

“Loess-palaeosol sections along the
Rhône Rift Valley (SE France) as Late
Quaternary palaeoenvironmental
archives”

Dissertation

for the award of the degree

"Doctor rerum naturalium" (Dr.rer.nat.)

of the Georg-August-Universität Göttingen

within the doctoral program Geography

of the Georg-August University School of Science (GAUSS)

submitted by

NORA PFAFFNER

from Dresden

Göttingen, 2022

Thesis Committee

Prof. Dr. Daniela Sauer

(Physical Geography Department / Georg-August University Goettingen)

Prof. Dr. Heinrich Thiemeyer

(Physical Geography Department / Goethe University Frankfurt)

Dr. Michael Klinge

(Physical Geography Department / Georg-August University Goettingen)

Members of the Examination Board

Reviewer 1:

Prof. Dr. Daniela Sauer

(Physical Geography Department / Georg-August University Goettingen)

Reviewer 2:

Prof. Dr. Heinrich Thiemeyer

(Physical Geography Department / Goethe Universität Frankfurt)

Further Members of the Examination Board

Dr. Michael Klinge

(Physical Geography Department / Georg-August University Goettingen)

Prof. Dr. Elisabeth Dietze

(Physical Geography Department / Georg-August University Goettingen)

Prof. Dr. Herrmann Behling

(Department of Palynology and Climate Dynamics / Georg-August University Goettingen)

Dr. Volker Karius

(Sedimentology - Environmental Geology Department / Georg-August University Goettingen)

Date of the oral examination: **10th March, 2023**

Acknowledgments

First, I would like to thank Prof. Dr. Daniela Sauer for introducing me into the fascinating world of “past” soils. I am deeply grateful to her for giving me the opportunity to start this Rhône journey by trusting me to teach our geography students that for understanding the evolution of a landscape properly you need to stay right in the middle of it, observing each soil, sediment and vineyard. Thank you for making it possible to continue the journey by giving me the opportunity, funding, support, advices and critics to realise this dissertation. I also sincerely appreciate your support of my scientific career by the numerous possibilities to continuously developing my soil “senses” in the various (field-) workshops and conferences. My sincere thanks to Prof. Dr. Heinrich Thiemeyer for co-supervising the thesis, your guidance and moreover, the interesting discussions during our meetings and field trips. My deepest appreciation to Dr. Annette Kadereit for her scientific and emotional support. Without your input and drive this Rhône journey would have not been proceeded so far.

I sincerely thank my former colleagues from the Physical Geography Department of the University Goettingen Stephen, Michael, Daniel, Barbara, Florian, Britta, Simon, Kwabena, Wiebke, and Steffen for their contributions, comments and mental support. I am grateful to Barbara for helping me with the field and laboratory work and Harold, Alexandra and Marie-France for solving some of the language difficulties. In particularly, I deeply thank my “work husband” and friend Stephen for always being there for me, no matter what, each step of the journey. My dearest Michael, Daniel and Britta, thank you for keeping me motivated, your (liquid) support, advises and the willingness to discuss endlessly any fact, anytime.

I thank Dr. Grotheer, Anja and Petra for their engagement in the laboratory and their continuous help with each small and large lab problem. I thank Lisa, Franziska and Marius for their support in the field with the preparation and measurements of the enormous number of samples. I am thankful to Dr. Volker Karius for introducing and helping me with the laser particle analysis. I thank Sophie Cornu, Pascal Bertran and Mathieu Bosq for welcoming us so in France. I thank Sebastian Kreutzer, Tobias Sprafke, Simon Meyer-Heintze and the members of the German working group palaeopedology for the fruitful scientific and non-scientific discussions. I also thank my current colleagues Marvin, Cornelius and the members of MoMok for being so understanding and supportive.

Special thanks to my long-lasting friends, which I have the privilege to call them my second family and without their mental support this journey would have been very short. Thank you to my “home” friends Hübi, Linda, Jana und Yvi for always pointing out what really matters in life. Friedi, Mülle, Susi, Charlie, Lisa, Tesi, Böhm, Myri thank you all for being there for me since we were little “academical rookies”. Especially, thank you Friedi, Mülle, Susi and Anja for

always being a home away from home. I also want to thank the Erbedinger family from the winery Bastianshauser Hof, your products helped more than once through slow thoughts and long working days/nights.

Finally, and most importantly my deepest appreciations to my entire family. Thank you to my mom for the love, trust and support during the entire period of the thesis. Thanks to my brothers and their lovely families, it is always happy time being with you guys. Thank you to my father, my uncles, cousins and special to my auntie Geli for being the best motivator, I know.

This thesis is dedicated to my grandparents, without you nothing like this would have happened.

Table of contents

Acknowledgments	iv
Table of contents.....	vi
List of Figures.....	xii
List of Tables.....	xvi
Summary.....	1
Chapter 1: Introduction	5
1.1 Context	5
1.2 Aim, objectives and hypotheses.....	8
1.3 Approach of research.....	8
1.4 Research area – Rhône Rift Valley	10
1.4.1 Geology and Geomorphology	10
1.4.2 Climate of the Rhône Rift Valley	13
1.4.3 The Pleistocene period in the Rhône Rift Valley	13
Chapter 2: Chronostratigraphy of two Late Pleistocene loess-palaeosol sequences in the Rhône Valley (southeast France) (study 1).....	19
Abstract	19
2.1 Introduction.....	20
2.2 Materials and methods.....	22
2.2.1 Study sites, description and sampling.....	22
2.2.2 Bulk magnetic susceptibility.....	24
2.2.3 Grain-size distribution and end-member modelling	24
2.2.4 Spectrocolourimetry.....	25
2.2.5 Geochemical analysis.....	26
2.2.6 Chronological data.....	29
2.3 Results.....	31
2.3.1 Lithofacies and soil horizons.....	31
2.3.2 Stratigraphy	33

2.3.3 Analytical data: magnetic susceptibility, colourimetry, grainsize and geochemistry	35
2.3.4 Variation in grain-size distribution and end-member modelling	37
2.3.5 Chronological data	38
2.4 Discussion	42
2.4.1 Eemian interglacial and Early Glacial pedocomplex (S1)	42
2.4.2 Lower Pleniglacial colluvium and bedded calcareous sandy loess (L1L2)	43
2.4.3 Middle Pleniglacial brown Bwk horizon (L1S1)	43
2.4.4 Upper Pleniglacial loess (L1L1)	46
2.4.5 Regional chronology	47
2.5 Conclusions	50
Declaration of competing interest	50
Acknowledgement	50
Appendix–Supplementary data	51
Appendix A	51
Appendix B	55
Chapter 3: Palaeosols in loess at Collias (SE-France) and their palaeoenvironmental significance (study 2)	75
Abstract	75
3.1 Introduction	76
3.2 Materials and methods	78
3.2.1 Geographical settings	78
3.2.2 Field sampling	79
3.2.3 Laboratory methods	81
3.3 Results – Characteristics of the horizons of Collias sections	82
3.3.1 Interglacial/Interstadial pedo-complex	82
3.3.2 Lower loess horizons	86
3.3.3 Interstadial soil-complex	87
3.3.4 Upper loess horizons	88
3.3.5 Holocene soil	89
3.3.6 Biopores and secondary carbonates	89

3.4 Discussion – soil formation and palaeoenvironmental context	93
3.4.1 Last Interglacial (Eemian) and Early Glacial soils	94
3.4.2 Early Glacial soils (MIS 5d to 5a, 115/110–71 ka)	97
3.4.3 Lower Pleniglacial horizons (MIS 4, 71–57 ka)	99
3.4.4 Middle Pleniglacial horizons (MIS 3, 57–29 ka ^{Lisietzki et al (2005)} /33 ka ^{Railsbeck et al. (2015), Railsback (2021)})	100
3.4.5 Upper Pleniglacial (MIS 2, 33–15 ka)	103
3.4.6 Recent soil formation (MIS 1, 14–0 ka)	105
3.5 Conclusions	106
Acknowledgement	107
Declaration of competing interest.....	107
Appendix	108
Chapter 4: Reconstructing the Eemian to Middle Pleniglacial pedosedimentary evolution of the Baix loess-palaeosol sequence (Rhône Rift Valley, southern France) – basic chronostratigraphic framework and palaeosol characterisation (study 3).....	115
Abstract	115
4.1 Introduction.....	116
4.2 Study site, sampling and methods	118
4.2.1 Study site	118
4.2.2 Field description and sampling	119
4.2.3 Methods	121
4.3 Results.....	126
4.3.1 General overview of the LPS Baix	126
4.3.1.1 Granulometry and carbonate contents.....	126
4.3.1.2 Micromorphology	126
4.3.2 Detailed characterisation of the lower 7 m of the LPS Baix.....	129
4.3.3 Luminescence screening results.....	132
OSL sensitivity	136
4.4 Discussion – Eemian to Middle Pleniglacial evolution of the Baix LPS and corresponding palaeoenvironmental conditions.....	136
4.4.1 The Eemian and Early Glacial period	136

4.4.2 Early Glacial to Lower Pleniglacial transition.....	138
4.4.3 The Lower Pleniglacial	139
4.4.4 The Middle Pleniglacial.....	140
4.5 Conclusion.....	141
Data availability	142
Competing interests.....	142
Disclaimer.....	142
Acknowledgement	142
Financial support	142
Review statement	143
Supplement	143
Chapter 5: The Late Pleistocene loess palaeosol-sequence Baix in SE France – stratigraphic insights and correlations (study 4)	165
Abstract	165
5.1 Introduction.....	166
5.2 Regional settings	168
5.3 Material and methods	170
5.3.1 Sampling and description	170
5.3.2 Analytical methods	172
<i>Texture and grain size proxies</i>	172
<i>Soil analysis, weathering proxies and colour</i>	173
5.3.3 Age determination	174
<i>Luminescence dating</i>	174
<i>AMS radiocarbon dating</i>	175
5.4 Results.....	175
5.4.1 Texture	175
5.4.2 Soil-chemical characteristics, colours, and micromorphology	176
<i>Micromorphology</i>	177
5.4.3 Chronological data.....	180
OSL screening results and block ages	180
AMS radiocarbon ages.....	182

5.5 Discussion	182
5.5.1 Soil and sediment formations and their palaeoenvironmental interpretation	182
Texture of Baix	182
Loess horizons of Baix LPS.....	183
(Palaeo)-soil of Baix LPS.....	184
5.5.2 Chronostratigraphy of Baix LPS and comparison with other European LPS	187
Last Interglacial (Eemian) and Early Glacial	187
Early Glacial to Lower Pleniglacial.....	188
Lower Pleniglacial to Middle Pleniglacial	190
Middle Pleniglacial to Upper Pleniglacial	191
5.6 Conclusions	192
Acknowledgement	194
Funding	194
Conflicts of Interest	194
Appendix	195
Supplement	196
Chapter 6: General discussion	261
6.1 Research objectives and hypotheses.....	261
6.2 Synthesis	262
6.3 Final conclusions and outlook	267
References.....	269

List of Figures

Chapter 1

Figure 1.1: Upper part: mean annual temperature of France of the year 2000	7
Figure 1.2: European Cenozoic Rift System (ECRIS) with research area “Rhône Rift Valley”	11
Figure 1.3: Map of aeolian (loess and sand), alluvial and fluvial deposits	17

Chapter 2

Figure 2.4: A) Map of aeolian deposits in Western Europe from Bertran et al. (2016)	21
Figure 2.5: Detailed stratigraphy of the Collias section	27
Figure 2.6: Detailed stratigraphy of the Lautagne section (Lautagne A) with the locations	28
Figure 2.7: A, B) Photographs of the main lithofacies of Collias	34
Figure 2.8: Photographs of selected thin sections (6.5 cm x 3.0 cm) of the Collias	36
Figure 2.9: Microfacies details of selected samples from Collias.....	39
Figure 2.10: Grain-size distribution of the samples from Collias	42
Figure 2.11: Contribution of the three end-members	44
Figure 2.12: Chronological data. A) Distribution of the OSL	45
Figure 2.13: A) Total AIS volume through the Last Glacial cycle (100–10 ka) from a	48
Figure A2.14: A) WNW-ESE topographic cross-section of the left bank of the Rhône River Valley	51
Figure A2.15: (A) Correlation coefficient (R^2) and (B) angular deviation goodness-of-fit.....	52
Figure A2.16: Energy-Dispersive X-Ray Fluorescence (ED-XRF) data were obtained	53
Figure A2.17: Energy-Dispersive X-Ray Fluorescence (ED-XRF) data were obtained	54
Figure A2.18: Age model of Lautagne A section used for Bayesian modelling	55
Figure B2.19: Boxplot of preheat dose-recovery test (left) and dose-recovery test.....	59
Figure B2.20: Preheat plateau tests (left) and dose-recovery tests (right)	60
Figure B2.21: Ternary diagram showing granulometric classes of the samples.....	61
Figure B2.22: Typical luminescence curves obtained during the SAR measurements	62
Figure B2.23: Dose distribution plots (here Abanico plots, Dietze et al. 2016).....	64
Figure B2.24: Dose distribution plots (here Abanico plots, Dietze et al. 2016).....	65
Figure B2.25: D_e distribution plots for the feldspar samples BDX21322.....	66
Figure B2.26: Example trace and density plots for sample BDX21327	67
Figure B2.27: Normalised ^{238}U plots to check for potential radioactive disequilibria	68
Figure B2.28: Nuclide concentration plots for one sample from Collias (A).....	69
Figure B2.29: The graph shows quartz and feldspar luminescence ages	71
Figure B2.30: Age-depth plots of the fine grain quartz ages of the site Lautagne	72

Chapter 3

Figure 3.31: A) Area map Collias. Yellowish areas denote loess and sandy loess	79
--	----

Figure 3.32: Main Collias-Wood LPS (A), Rhône Rift Valley, SE France	80
Figure 3.33: Stratigraphy of the Collias-Wood LPS, Rhône Rift Valley.....	83
Figure 3.34: Stratigraphy of the main loess-palaeosol section Collias-Wood.....	84
Figure 3.35: Photographs of special features of profiles of Collias LPS	86
Figure 3.36: Photos of biopore features of Collias-Wood LPS, Rhône Rift Valley.....	90
Figure 3.37: Variety of selected carbonate nodules from all Collias LPS	92
Figure 3.38: Potential soil formation phases at the loess-palaeosol sections (LPS) Collias	96
Figure 3.39: Selected generalised and simplified loess-palaeosol sections	102
Figure A3.40: Stratigraphy of Collias-North, Rhône Rift Valley, SE France	112
Figure A3.41: Stratigraphy of Collias-North_D112, Rhône Rift Valley, SE France.....	113
Figure A3.42: Stratigraphy of Collias-South_D112, Rhône Rift Valley, SE France	114
Chapter 4	
Figure 4.43: Location of the Baix loess–palaeosol sequence (LPS).....	117
Figure 4.44: Hillshade map of the area around the Baix LPS	118
Figure 4.45: Baix LPS, Rhône Rift Valley, SE France. (a) Overview photo.....	120
Figure 4.46: pIR-BLSL SAR protocol applied to minimally prepared	124
Figure 4.47: pIR ₆₀ IR ₂₂₅ SAR protocol applied to minimally prepared.....	124
Figure 4.48: Photos of whole thin sections (3 cm × 4 cm) of the Baix LPS	130
Figure 4.49: Photomicrographs of thin sections of the Baix LPS	131
Figure 4.50: Effective dose rates determined for the six selected samples.....	133
Figure 4.51: Results of the pIR-BLSL and pIR ₆₀ IR ₂₂₅ screening of the Baix LPS	134
Figure 4.52: Results of the luminescence sensitivity measurements.....	135
Figure 4.53: Synopsis of data for the lower 7 m of the Baix LPS, Rhône Rift Valley.....	139
Figure S4.54: Dose recovery test on eight aliquots of box sample HDS-1802	147
Figure S4.55: pIR-BLSL dose recovery test on eight aliquots	147
Figure S4.56: Dose recovery test on twelve aliquots of box sample HDS-1817.....	148
Figure S4.57: pIR-BLSL dose recovery test on twelve aliquots of box sample	148
Figure S4.58: Dose recovery test on the eight aliquots already used.....	150
Figure S4.59: Results of the dose recovery test on eight fresh aliquots.....	151
Figure S4.60: pIR ₆₀ IR ₂₂₅ dose recovery test on eight aliquots of box sample	152
Figure S4.61: Results of the water content determination from the box subsamples.....	156
Figure S4.62: Results of the g-value determination: BLSL ₁₂₅ signal.....	158
Figure S4.63: Results of the g-value determination: BLSL ₁₂₅ signal, box sample	159
Figure S4.64: Results of the g-value determination: IR ₂₂₅ signal, box sample	160
Figure S4.65: Results of the g-value determination: IR ₂₂₅ signal, box sample	161
Figure S4.66: Results of the pIR-BLSL and pIR ₆₀ IR ₂₂₅ -screening summarised.....	162

Figure S4.67: Representation of the age-depth relationship of the results of the pIR-BLSL	163
---	-----

Chapter 5

Figure 5.68: Map of aeolian deposits in western Europe	168
Figure 5.69: Map of aeolian and fluvial deposits in the Rhône Rift Valley area	169
Figure 5.70: Logarithmic distribution curves of 116 classes (<0.2 μm – 2000 μm).....	176
Figure 5.71: Loess-palaeosol section (LPS) Baix, Rhône Rift Valley, SE France	178
Figure 5.72: Photomicrographs of whole thin sequences (3 cm x 4 cm) and photomicrographs	179
Figure 5.73: Chronological data of the loess-palaeosol section (LPS) Baix	181
Figure 5.74: Compiling figure of marine and ice-core chronostratigraphy	188
Figure A5.75: Loess-palaeosol sequence Baix, Rhône Rift Valley, SE France.....	195
Figure A5.76: Loess-palaeosol sequence (LPS) Baix_west, Rhône Rift Valley	195
Figure S5.77: Equipment of the luminescence reader model Risø TL/OSL DA20	198
Figure S5.78: Normalisation dose test on bleached aliquots of sample HDS-1776	202
Figure S5.79: Normalisation dose test on bleached aliquots of sample HDS-1776	202
Figure S5.80: Dose recovery tests with LAB 2700 s and NRM (a) 7.5 %.....	204
Figure S5.81: Dose recovery tests with NRM 30 %	204
Figure S5.82: Dose recovery tests with NRM 30 %	205
Figure S5.83: Schematic representation of the pIR ₆₀ IR ₂₂₅ SAR protocol.....	205
Figure S5.84: Parameters of the D _e determination.	206
Figure S5.85: D _e determination on sample HDS-1776. Exponential plus linear fit.....	208
Figure S5.86: D _e determination on sample HDS-1777. Exponential plus linear fit.	208
Figure S5.87: D _e determination on sample HDS-1778. Exponential plus linear fit	209
Figure S5.88: D _e determination on sample HDS-1799.....	210
Figure S5.89: D _e determination on sample HDS-1800.....	210
Figure S5.90: D _e determination on sample HDS-1801.....	211
Figure S5.91: Equipment of the luminescence reader model Risø	212
Figure S5.92: Schematic representation of the pIR ₆₀ IR ₂₂₅ SAR protocol.....	213
Figure S5.93: Test measurement on 3 aliquots with the natural luminescence.....	214
Figure S5.94: Test measurement on 3 aliquots with the natural luminescence.....	214
Figure S5.95: Normalisation dose test on bleached aliquots of sample HDS-1776	217
Figure S5.96: Normalisation dose test on bleached aliquots of sample HDS-1776	218
Figure S5.97: Dose recovery test on bleached aliquots of sample HDS-1776	219
Figure S5.98: Schematic representation of the pIR ₆₀ IR ₂₂₅ SAR protocol.....	220
Figure S5.99: Parameters of the D _e determination	220
Figure S5.100: D _e determination on sample HDS-1776.....	222
Figure S5.101: D _e determination on sample HDS-1777.....	223

Figure S5.102: D_e determination on sample HDS-1778.....	224
Figure S5.103: D_e determination on sample HDS-1799.....	225
Figure S5.104: D_e determination on sample HDS-1800.....	226
Figure S5.105: D_e determination on sample HDS-1801.....	227
Figure S5.106: T_x/T_n sensitivity curves over the 8 measured SAR cycles	230
Figure S5.107: Mean T_x/T_n values per aliquot (y-axis) versus D_e value (x-axis).....	231
Figure S5.108: Equipment of the luminescence reader model Risø TL/OSL DA20	232
Figure S5.109: Typical examples of shine down curve, dose response curve	233
Figure S5.110: Combined preheat and dose recovery test.....	235
Figure S5.111: Combined preheat and dose recovery test.....	236
Figure S5.112: Combined preheat and dose recovery test.....	237
Figure S5.113: Dose recovery tests on sample HDS-1776	237
Figure S5.114: Dose recovery tests on sample HDS-1776	239
Figure S5.115: Dose recovery tests on sample HDS-1776	240
Figure S5.116: Schematic representation of the BLSL ₁₂₅ SAR.....	240
Figure S5.117: Parameters of the D_e determination.	241
Figure S5.118: D_e determination on sample HDS-1776.....	242
Figure S5.119: D_e determination on sample HDS-1777.....	243
Figure S5.120: D_e determination on sample HDS-1778.....	244
Figure S5.121: D_e determination on sample HDS-1799.....	245
Figure S5.122: D_e determination on sample HDS-1800.....	246
Figure S5.123: D_e determination on sample HDS-1801	247
Figure S5.124: Exemplary results of the scanning electron microscope (SEM)	248
Figure S5.125: Samples HDS-1777 to HDS-1781	251
Figure S5.126: LM OSL measurements of the samples HDS-1777	252
Figure S5.127: Four-component analyses of the natural LM-OSL.....	253
Figure S5.128: Samples HDS-1777 to HDS-1781	254
Figure S5.129: Samples HDS-1777 to HDS-1781, one aliquot each.....	255
Figure S5.130: Samples HDS-1777 to HDS-1781, one aliquot each.....	256
Figure S5.131: Timeline of Loess- palaeosol sequences (LPS) Baix and Collias	257
Figure S5.132: Uranium, thorium and potassium contents as determined with the.....	259
Chapter 6	
Figure 6.133: Chronostratigraphies of Baix and Collias loess-palaeosol sections	263
Figure 6.134: Derived climate conditions from Baix and Collias loess-palaeosol sections (LPS)	266

List of Tables

Chapter 2

Table 2.1: Authors contributions to study 1.....	19
Table 2.2: Final dose rates, equivalent doses (D_e) and luminescence age	30
Table 2.3: AMS radiocarbon ages of samples from the sections	32
Table 2.4: AMS radiocarbon ages of loess samples	46
Table 2.5: OSL ages of loess samples from other locations.	48
Table B2.6: SAR protocol settings applied for measuring the quartz fraction.....	58
Table B2.7: DRAC settings applied for the luminescence age calculation	59
Table B2.8: High-resolution γ -ray spectrometry results and applied water content.	69
Table B2.9: Final dose rates, equivalent (D_e) and age values	73

Chapter 3

Table 3.10: Authors contribution to study 2.....	75
Table A3.11: Main characteristics and observations of horizons of Collias profiles	108
Table A3.12: Results of infilled biopores and respectively surrounding sediments	111

Chapter 4

Table 4.13: Authors contribution to study 3.....	115
Table 4.14: Horizon designations and characteristics of the horizons of the Baix LPS	127
Table S4.15: Parameters of data analysis for D_e determination – pIR-BLSL SAR protocol.	145
Table S4.16: Parameters of data analysis for D_e determination – pIR60IR225 SAR protocol.....	149
Table S4.17: Results of the normalisation dose test for late light subtraction	150
Table S4.18: Dose recovery test on the eight aliquots already used	151
Table S4.19: Results of the dose recovery test on eight fresh aliquots	152
Table S4.20: Six subsamples (>3 g dry wt) of the box samples	154
Table S4.21: Analytical dose rate data and effective dose rates for the pIR ₁₂₅ BLSL ₁₂₅ -protocol.	157
Table S4.22: Analytical dose rate data and effective dose rates for the pIR60IR225-protocol.	157

Chapter 5

Table 5.23: Authors contribution to study 4.....	165
Table S5.24: Scheme of OSL sampling and sample preparation	196
Table S5.25: Results of the D_e range test with a not yet finally adapted pIR ₆₀ IR ₂₂₅ protocol.....	199
Table S5.26: Results of the normalisation dose test on sample HDS-1776	202
Table S5.27: Comparison of the signal strength of the IR ₆₀ and IR ₂₂₅ signals.....	207
Table S5.28: Results of the normalisation dose test for different D_e integrals	217
Table S5.29: Comparison of the signal strength of the IR ₆₀ and IR ₂₂₅ signals	221
Table S5.30: Combined preheat and dose recovery test.....	235

Table A5.31: Dose rate data for the pIR₁₂₅BLSL₁₂₅-protocol for Feldspar coarse grains..... 258

Summary

Loess-palaeosol sections (LPSs) represent ideal archives for gaining knowledge of past climatic conditions and changes, as their intermediate loess deposits and buried palaeosols reflect climate conditions of their specific locations. Detailed knowledge of past climatic changes is also beneficial for accurate modelling and forecasting since such past changes must have already shown similar trends. Although climate reconstructions from LPS from the last decades have improved our understanding concerning the cross-regional Pleistocene climate changes, there are wide knowledge gaps regarding reconstructions linking the central temperate and Mediterranean Europe. According to climate projections, the region between the Mediterranean and the temperate climate zone of central Europe is most vulnerable in Europe, as a northern expansion of Mediterranean conditions (e.g. higher temperatures, more arid months) is expected. Within this context, the climate reconstruction of the expansion of the Last Interglacial (Eemian) conditions is especially relevant, as this area is assumed to be several degrees warmer than current climate, a condition that is also expected for the future climate within the European vulnerable climatic transition zone.

The LPSs of the Rhône Rift Valley in southeast (SE) France were chosen for this investigate as the recent climate transition zone is located in the centre of this valley (Valence, ~45° N). Thus, the LPS present important tie-points between the central European and the Mediterranean LPS region. Previous investigations on the LPS in the Rhône Rift Valley were mainly based on observations, and provided only limited insights into the lithological properties of the loess deposits, the intercalated palaeosols and the resulting pedostratigraphy. This limitation also applied to the understanding of the changing degree of weathering and interpretations of the palaeosols with respect to their relative palaeoenvironments. In particular, numerical ages of the loess deposition and soil formation phases were scarce. We aimed in this thesis to fill these gaps by reconstructing the Last Interglacial-Glacial landscape evolution changes along the climate-sensitive transition zone from LPS of the Rhône Rift Valley. The results were linked with known European LPS in order to (i) verify our findings with LPS of similar conditions (e.g. climate conditions, valley position) and (ii) to identify where possible climatic boundaries were located during the Late Pleistocene, and how these boundaries may have fluctuated over time. We focused thereby on identifying possible stratigraphic marker horizons/complexes in the LPS, and establishing a reliable chronostratigraphy.

In several field campaigns, two main LPS, i.e. Baix LPS (in the climate transition zone) and Collias LPS (in the Mediterranean zone) and several aside profiles, have been investigated with multiple state-of-the-art-methods to establish reliable chronostratigraphies. The two LPS displayed several loess and weakly to strongly developed palaeosol horizons. Based on the

field observations and the laboratory analyses, both main LPS were subdivided in up to four pedo-stratigraphic units, interlaced by two main loess units, respectively and formation and deposition times of soils and sediments were correlated with various OSL ages.

Both LPSs begin from bottom to top with an Last Interglacial/Early Glacial soil-complex (MIS 5) represent by a mainly truncated Luvisol formation (Baix LPS: Stagnic Luvisol; Collias LPS: Chromic Luvisol + several Bw horizons), also well-know from other European LPSs (e.g. Rocourt complex). However, in contrast to European LPSs no humic-rich layer for late MIS 5 were observed in Rhône Rift Valley LPS. The following loess unit of the Lower Pleniglacial (MIS 4) comprises of least weathered silty and sandy loess (partly olive-ish at Collias LPS) and loess-like sediment horizons. At Baix LPS also a brown MIS 4 /MIS 3 Bw horizon was identified (lower interstadial soil), which may correlate with known palaeosol relicts of the Cambisol or Regosol-Cambisol types (e.g. Gräselberger Soil, Jackerath Soil, Reisberg Soil) from central Europe LPSs. The overlain pedo-unit, at both sites, is represented by a truncated Cambisol-complex (upper interstadial soil) with prominent in situ carbonate nodules and a striking former biopores system (mainly at Collias LPS). The soil remain is assumed to represents a pedo-complex spanning from (GI 15.1 or) GI 14 to GI 9 and correlates well with brown soil horizons (e.g. Remagen Soils, Gräselberg Soils) of European LPSs. Thus, the striking Cambisol soil-complex may be regarded as a stratigraphic marker horizon within the Rhône Rift Valley and serve as a Middle Pleniglacial-unit for supra-regional correlation of central European and Mediterranean LPS. In contrast to central European LPSs with further Cambisol formation (e.g. Lohne Soil complex, Sinzig Soils) for the milder climate periods GI 8 to GI 4 (ca 38–29 ka) during upper MIS 3, at Baix and Collias LPSs no significant soil formation could be detected or may not exist. Thus, times favourable of soil formation (and soil conservation) appear to alternate between the Mediterranean (early MIS 3 prior to Heinrich 4 event) and the central European loess landscapes (later MIS 3, after the Heinrich 4 event). The deposits of the following Upper Pleniglacial (MIS 2) are represented at both LPSs mainly by silt and sand sized loess with varying intensity of weathering. Also no further (weak) soil formation, e.g. tundra gley soils, especially redoximorphic features related to freeze-thaw dynamics, was observed, thus agree with assumed less severe climate conditions during loess accumulations at both LPS sites compared to central Europe. The Holocene soil formation displays similar to European LPSs a Cambisol formation, although the conditions for a Luvisol formation along the entire climatic transect is given, but the difference in terms of disturbance and duration of time period have to be respected.

Based on our findings we could show that the main (pedo) -stratigraphies of Collias and Baix LPSs generally agree with the central and western European LPSs (e.g. MIS 5, MIS 3 pedo-stratigraphic marker horizons). However, the syn-sedimentary, intensively reworked and

bioturbated character of the Rhône Rift Valley loess deposits as well as their partly polygenetic soils and soil-complexes reflect clearly a gradient of decreasing magnitude of Late Pleistocene climate changes from central Europe to southern Europe.

Furthermore, no clear northern expansion of Mediterranean conditions based solely on soil characteristics during the Last Interglacial could be unambiguously verified. However, other archives do support a northern expansion of Mediterranean conditions in the northern Rhône Rift Valley and we can conclude that the climate conditions in the central and southern Rhône Rift Valley seemed to be significantly more humid than today. The comparison of the Last Interglacial and the recent soil formation to determine similarities and differences of the climate conditions within the Rhône Rift Valley is challenging due to various factors (e.g. different insolation, geomorphological position, intense anthropogenic use). As our results are inconclusive concerning the Last Interglacial climate conditions within the recent climatic transition zone, statements how these boundaries within the Rhône Rift Valley respond to future climate changes have to be carefully made and thus, more research to conclusively verify the intensity of rubefication under similar conditions, regionally and within the climate transect is needed.

Chapter 1: Introduction

1.1 Context

In Europe, loess-palaeosol sections (LPSs) have been widely used for reconstructing Pleistocene (Quaternary) environments (Antoine et al. 1999, 2001, 2009a, 2016, 2021; Frechen et al. 2001, 2007; Haesaerts et al. 2016; Lehmkuhl et al. 2016; Schirmer, 2016; Rousseau et al. 2018, Fischer et al. 2019, 2021). Loess deposits are generally attributed to cold conditions of stadial phases, involving processes like the formation and aeolian transportation of silt-sized particles, their deposition and syn- and post-sedimentary weathering (Pécsi and Richter, 1996; Kehl, 2010). The formation of palaeosols is attributed to warm and (temporarily) moist conditions of the interglacials and interstadial phases. Thus, LPS are the result of alternating dry/cold and warm/moist conditions, reflecting their palaeoenvironments and therefore provide valuable insights into the dynamics of the Pleistocene climate changes. Furthermore, the loess source and sink areas, as well as the local topography of the loess deposition regions are influencing factors, which established broad variations of LPS throughout Europe (Lehmkuhl et al. 2021).

In the last decades, supra-regional palaeoenvironmental reconstructions from western to eastern Europe (Zöller, 2010; Terhorst et al. 2015; Lehmkuhl et al. 2016; Rousseau et al. 2018), as well as in the Mediterranean region (Wacha et al. 2011a, 2011b, 2018; Boixadera et al. 2015; Costantini et al. 2018, Wolf et al. 2018, 2019) have gained attention to fill the knowledge gaps, especially regarding the climates of the Late Pleistocene period. However, overarching climate reconstructions linking central and southern Europe are lacking, although the knowledge of this cross-regional Pleistocene climate evolution is crucial for the understanding of climate drivers and feedback mechanisms. Especially as this transition zone between the temperate mid-latitude and the northern Mediterranean zone is expected to respond most sensitively to climate changes in the future (Giorgi, 2006). Climate models predict northward shifts of the atmospheric circulation zones for the end of the 21st century, accompanied by higher temperatures especially during the summer, and lower humidity for the northern Mediterranean summer, thus an increased frequency and length of dry periods (Giorgi and Lionello, 2008; Alessandri et al. 2014; Lionello and Scarascia, 2018; Sgubin et al. 2018; Lee et al. 2021) (Fig. 1.1). The possible effects on the hydrology, ecosystems, agriculture, and other human livelihoods needs a detailed picture of the future changes in this climate zone. This suggest that by reconstructing the environmental changes along the climatic transect from the mid-latitude temperate to the northern Mediterranean, we can provide deeper insights into the processes and mechanisms that can be used to predict such similar conditions in the coming future for the region. Especially, reconstructing the Last Interglacial (Eemian)

palaeoenvironmental conditions along these climatic transect has a particular relevance as it is assumed that the Eemian was several degrees warmer compared to today (e.g. Kukla et al. 2002; North-GRIP Members, 2004; Brewer et al. 2008), which is relevant in view of current global warming effects (Fig. 1.1). Thus, the corresponding palaeoenvironmental boundaries may serve as estimates for the environments and boundaries that might be established by the end of the century in response to the currently ongoing climate change. Although, a climatic synopsis between the Eemian and the Anthropocene should be regarded within reservation (e.g. different insolation pattern in the northern latitudes (e.g. Brewer et al. 2008; Pedersen et al. 2017)).

The Rhône Rift Valley in SE France with its north-south course (46° N to 43° N) is located exactly in the transition area between temperate and Mediterranean climatic zone, and thus represents the optimal area to study the shift of climatic boundaries. The recent climate boundary is approximately located around Valence ~44.56° N (Lelièvre et al. 2010) (Fig. 1.1). Another advantage for choosing the Rhône Rift Valley as research area is, that the valley represents the southern part of the European Cenozoic Rift System (ECRIS), whereas the Bresse Graben and the Lower and Upper Rhine Graben outline parts of the northern extension of the ECRIS shown in Fig. 1.2. The northern parts of the ECRIS are drained by the Rhine River, flowing to the North Sea, whereas the southern ECRIS is drained by the Rhône River into the Mediterranean Sea. Originating in the Alps, the Rhine and Rhône Rivers formed braided river systems during glacial periods, fed by summer meltwaters. Their wide and periodically dry riverbeds served as sources of dust, which was blown out and accumulated in thick loess deposits at various sites along the margins of the rift system (Haase et al. 2007). As a result, they provide several exceptionally detailed and well-investigated LPSs in the northern, e.g. Garzweiler, Rheindahlen, Schwalbenberg I-II (Schirmer, 2000, 2002, 2012, 2016) and central parts of the rift system, e.g. Riegel, Heitersheim, Bahlingen, Nussloch/Schatthausen (Guenther, 1961, 1987; Bronger, 1966; Khodary-Eissa, 1968; Bronger and Hädrich, 1969; Hädrich, 1985; Zöller et al. 1988; Hädrich and Stahr, 1992, Antoine et al. 2001, 2009a; Bibus et al. 2007; Frechen et al. 2007; Zech et al. 2012; Kadereit et al. 2013; Moine et al. 2017, Schulze et al. 2022) for comparison along the ECRIS.

In contrast to the northern ECRIS, only a limited number of studies have been carried out on LPSs in the southern ECRIS (e.g. Aubagne, Quincieux, Lautagne, Collias (Magnin, 1993, 2014; Franc et al. 2017; Bosq et al. 2018, 2020a, 2020b)), so far. One possible reason for the lack of studies is, that most of these LPSs are highly disturbed due to geomorphic activities and/or bioturbation, which hampers the possibility to connect reconstructed palaeoenvironmental conditions to specific periods.

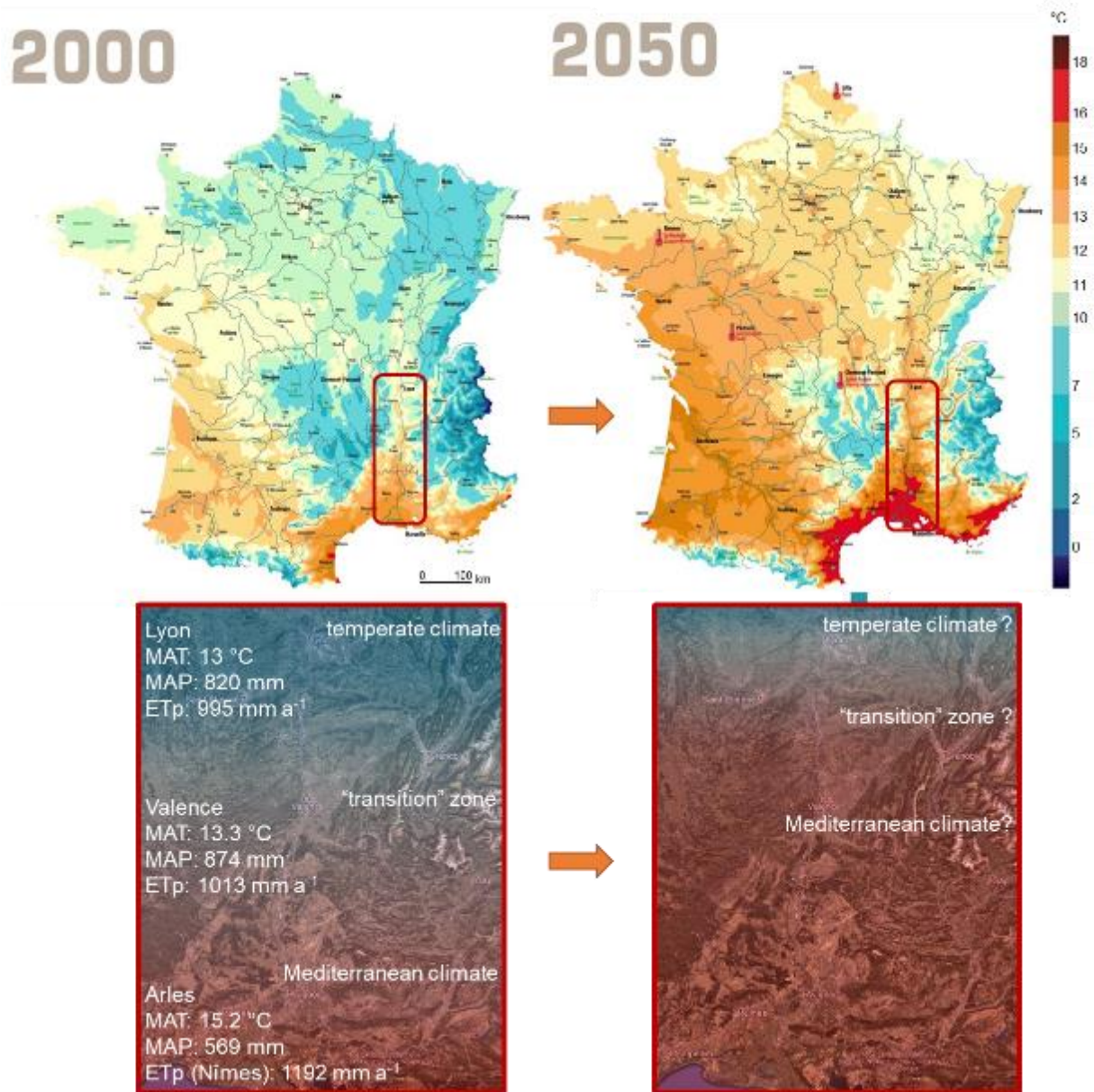


Figure 1.1: Upper part: mean annual temperature of France of the year 2000 and for the year 2050 (red square outlines the Rhône Rift Valley) (source: Datar, 2022). Lower part, left: recent temperate and Mediterranean climate zone and their climatic transition zone of the above outlined Rhône Rift Valley with mean annual temperature (MAT), mean annual precipitation (MAP) and mean annual potential Evapotranspiration (ETp) of the cities Lyon, Valence and Arles. Right: Possible shifted climate zones during the Last Interglacial (Eemian) period and potential future boundaries of climate zones (sources: Meteo-France, 2022a, 2022b, 2022c, 2022d).

Furthermore, as a result of high geomorphic activities, most of the LPSs of the southern ECRIS mentioned above do not comprise sediments and palaeosols from the whole Last Interglacial-Glacial cycle, which aggravates especially a synopsis of the Last Interglacial conditions in this area. Thus, a comparison of the Rhône Rift Valley–LPSs with other LPSs providing comparable conditions, e.g. valley position, climatic conditions and periods, will be helpful. Using well-known LPSs from eastern Spain (Brosche and Walther, 1977; Günster, 1999; Günster et al. 2001 Boixadera et al. 2015) to northern Italy (Cremaschi, 1990a, Ferraro, 2009,

2014; Zerboni et al. 2015, Costantini et al. 2018) and western Croatia (Cremaschi, 1990b; Durn, 2003, Durn et al. 2018a, 2018b; Mikulčić Pavlaković et al. 2011; Wacha et al. 2011a, 2011b, 2018; Zhang et al. 2018) as tie-points, would help to identify similarities and differences within the interglacial, interstadial and stadial periods. After the comparison with LPSs with similar conditions, the connection with LPSs of the north-directed ECRIS presents ideal conditions to evaluate past shifts of the climatic transitions zone between the Mediterranean and the mid-temperate central Europe.

1.2 Aim, objectives and hypotheses

The thesis was aimed to reconstruct Late Pleistocene palaeoenvironmental changes along the climate-sensitive transition zone (Rhône Rift Valley) between central and southern Europe to link those obtained characteristics to known European LPS for establishing a synopsis of palaeoenvironments along central and southern Europe.

This aim was achieved by accomplishing two main objectives as followed:

- I. identify possible stratigraphic marker horizons/complexes in the LPS along the Rhône Rift Valley, which allows cross-regional correlations with other European LPS;
- II. establish a reliable chronostratigraphy by dating soil formation processes and loess depositions.

Based on the state-of-the-art knowledge of reconstructed palaeoenvironments from European LPS (section 1.1) and other archives (e.g. marine cores, ice cores, pollenstratigraphies, speleothem records) the following hypotheses were developed from the objectives:

- i) The Mediterranean zone extended further north during the Last Interglacial (Eemian, marine isotope stages (MIS) 5e).
- ii) During the Middle Pleniglacial (MIS 3) more pronounced temperate conditions (i.e. higher precipitation) prevailed in the Rhône Rift Valley compared to central Europe.
- iii) During the Upper Pleniglacial (MIS 2) the transition zone was marked by less pronounced cold and arid conditions compared to central Europe.

1.3 Approach of research

To achieve the objectives and test the hypotheses, a multi method-approach combining data from the macro- to micro scale level, was used. A series of field campaigns to the Rhône Rift Valley took place between 2016 and 2021, visiting various LPS described in the literature. The goal of these visits was to identify suitable LPS that are likely to represent Late Pleistocene climate changes by covering the climatic conditions of all glacial, interglacial and interstadial periods. The preliminary investigations confirmed that almost all LPS in the Rhône Rift Valley are disturbed by erosive/colluvial processes, and the (palaeo-) soils mainly remained as soil-

sediment mixtures. Finally, the “Baix” LPS within the recent climate transition zone and the “Collias” LPS in the Mediterranean region were chosen as they appeared to be the least disturbed and seemed to include remains from the Last Interglacial-Glacial cycle (Figs. 1.2, 1.3). Additional, to the two main sections, smaller side sections (Collias-North, Collias-South_D112, Collias-North_D112 and Baix_west) were chosen to study the palaeosol formation in greater detail and to understand their spatial variability at the local scale.

The field characteristics of the sections were described in detail and cleaned sections were sampled for pedological-sedimentological analyses. For micromorphological analyses, orientated samples from the loess sediment and the palaeosols were carved out with the help of steel-framed Kubiëna boxes. The results of the granulometric and soil-chemical analyses were used to generate palaeo-proxies (e.g. weathering indices, grain size index) in order to identify weathering intensities of the loess sediment and (palaeo-) soils. The results from the micromorphological analyses were also used to determine weathering intensities (e.g. presence of clay coatings) and to identify possible in situ formations or disturbances through relocation and/or bioturbation, respectively. The interpretation of the combined field observations and analytic results allowed to i) identify similar pedogenic and sediment cycles, with in the LPS ii) determine (palaeo-) soil types according to IUSS Working Group WRB (2022), and iii) derive former climatic conditions.

A central aspect of the study was to discern a reliable chronological framework into which the reconstructed palaeoenvironmental conditions can be placed. For obtaining the chronometric frame, ages were determined using i) luminescence screening on minimally prepared material, ii) optically stimulated luminescence (OSL) dating on different grains of various sizes and iii) accelerator mass spectrometry (AMS) radiocarbon dating from gastropod shells and earthworm calcite granules. The obtained ages were put in context with the warm interglacial and cold glacial periods derived from oxygen isotope data of marine sediment cores (marine isotope stages (MIS)) and stage boundaries used according to Lisiecki and Raymo (2005) and Railsback et al. (2015). Furthermore, the results were correlated with the INTIMATE event stratigraphy, which includes additionally to terrestrial and marine records, ice core records from the last glacial period climate fluctuations known as Dansgaard-Oeschger events, which were numbered systematically as Greenland interstadials (GI) and Greenland stadials (GS) (Rasmussen et al. 2014). Subsequently, the set-up chronostratigraphies of the LPSs were correlated with other local, regional and supra-regional known European LPS. With respect to their geographic locations and the fact that these archives have their own multitude of proxies, other terrestrial and marine archives were used to confirm or deny reconstructed climate conditions within the Rhône Rift Valley.

The findings were outlined in four studies, representing the cumulative compilation of this thesis. Study 1 (chapter 2) and study 2 (chapter 3) focused thereby on dated key palaeosols of the Collias LPS and obtained palaeoenvironmental conditions of southern (Mediterranean) region of the research area and their connection with Mediterranean LPSs of similar characteristic. In study 3 (chapter 4) and 4 (chapter 5) the focus was set on the recent climatic transition area near Valence with the Baix LPS. Within study 3, a detailed chronological frame together with correlations to local archives allowed to reconstruct the palaeoenvironmental conditions of the climate transition zone. With the gained knowledge of the studies 1, 2 and 3, it was possible in study 4 to use the north-south transect-approach, to characterise the main palaeosol horizons in their (sub-) regional context, and to characterise their changes from central Europe, along the transition area to southern Europe. In chapter 6, the central findings of two LPSs were discussed and synthesised in order to accomplish the research aim.

1.4 Research area – Rhône Rift Valley

1.4.1 Geology and Geomorphology

The Rhône Rift Valley and its northern extensions, the Bresse Graben and the Rhine Graben are part of the European Cenozoic Rift System (ECRIS), a large N-S orientated graben structure, extending over 1100 km, from the North Sea to the Mediterranean Sea (Fig. 1.2) (Dèzes et al. 2004; Ziegler and Dèzes, 2007). The formation of the ECRIS and thereby of the Rhône Rift Valley started in the Eocene, as a consequence of the Alpidic orogenesis. In the following stages the Rhône Rift Valley was filled with Oligocene to Miocene deposits (Ziegler and Dèzes, 2007). Due to uplifting, dissecting and eroding of the diverse geology, the Rhône Rift Valley is characterised by an alternation of wide basins and epigenetic constrictions. The north is marked out by the northern Lyon basin, framed by the north-eastern Dombes plateau, composed of Miocene, Pliocene and Pleistocene material. At the Bresse Graben the ECRIS continues, consisting of molasse and Pleistocene sediments. The north-western part of the valley is limited by the Palaeozoic metamorphic and plutonic rocks of the Massif Central. Remnants of Jurassic and Cretaceous sediments are only found as discontinuous formations in the marginal areas e.g. Monts du Mâconnais, Mont d'Or lyonnaise, Crussol massif (Bourdier, 1958). Further south-west, the Massif Central withdraws and the limestone plateau of the Languedoc-Rhodanian (Ardèche, Gard) with its Eocene and Oligocene deposits appear, presenting a karst landscape with sunken molasse basins (Pletsch and Uterwedde, 2003). The eastern boundary of the valley is presented by the French Alps composed of Mesozoic and Palaeozoic material (Debelmas, 1974). The southern Rhône Rift Valley is surrounded by the northern Alpilles, the western Nîmes fault, the eastern Salon Cavaillon fault and seawards by the continental shelf (Boyer et al. 2005; Jamagne et al. 2011). The delta consists mainly of Pliocene and Pleistocene sediments.

The Rhône Rift Valley is affected by tectonic and micro-tectonic movements. Mainly, south-eastern tectonic features at the Gulf of Lion (Costière du Gard/ Nîmes plateau) indicate tectonic activity during Pleistocene (Vella and Provansal, 2000; Debelmas et al. 2004). Subsidence from recent tectonic activity are confirmed by archaeological data (Vella and Provansal, 2000; Boyer et al. 2005). Pyroclastites prove several volcanic eruption events during the Middle and Upper Pleistocene (Puaud et al. 2015).

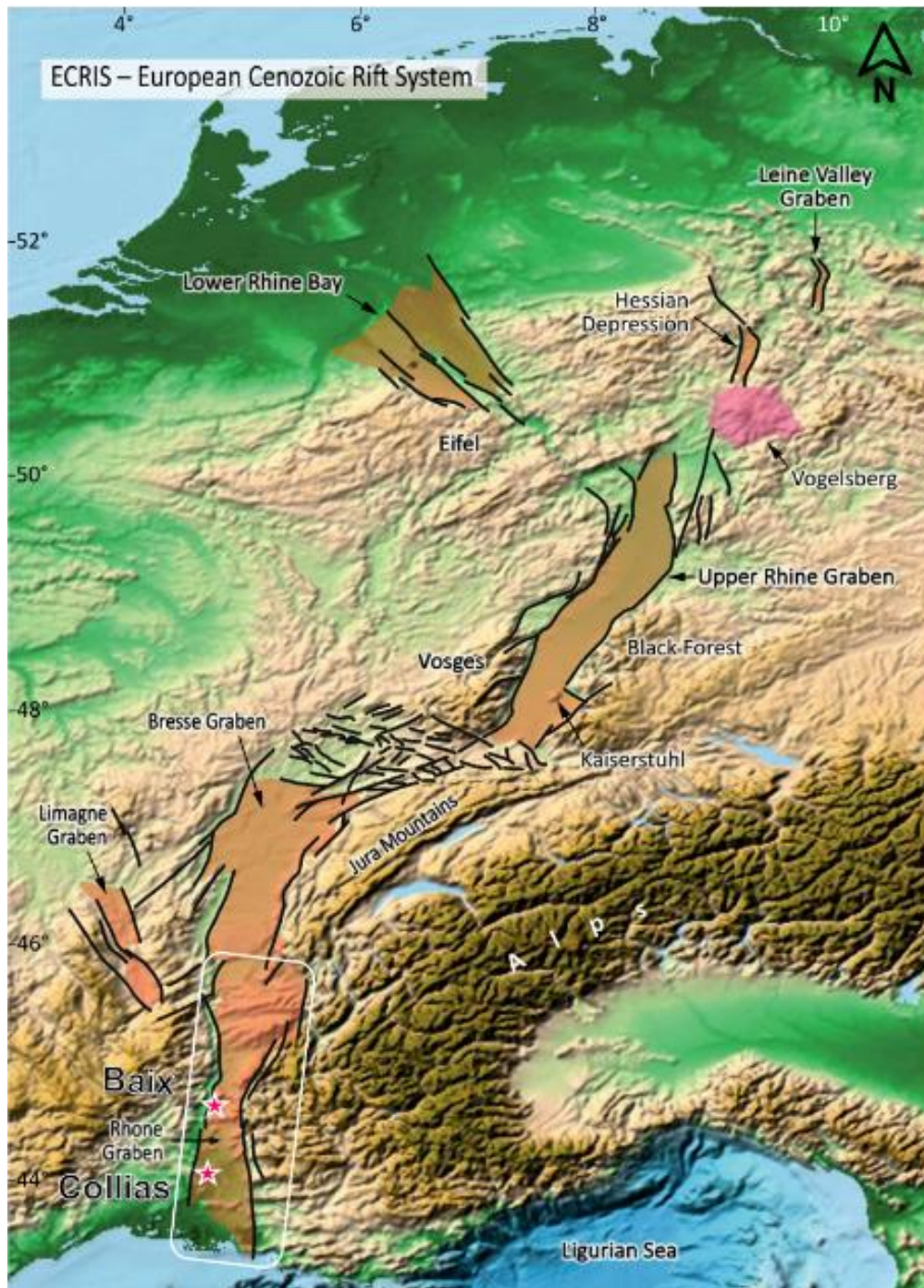


Figure 1.2: European Cenozoic Rift System (ECRIS) with research area “Rhône Rift Valley” (white rectangle) and locations of the investigated Baix and Collias loess-palaeosol sections (pink stars) (source: Meschede and Warr, 2019 (mod.)).

Hydrology of the Rhône Rift Valley

The Bresse Graben is drained by the Saône, which originates in the Vosges mountains and flows into the Rhône at Lyon. The Rhône River (810 km long) originates from the Rhône/Rotten glacier located at the Swiss Alps (canton Wallis, 2341 m a.s.l.). The river passes in east-west direction Lake Léman (Geneva), crosses between the Alps and the Jura Mountains and drains north into the alluvial fan of Bas-Dauphiné. West of the Jura Mountains the Ain River flows into the Rhône. At Lyon, the Rhône changes the direction and drains southwards into the Mediterranean Sea (Olivier et al. 2009). Before draining into the Mediterranean Sea, the Rhône subdivides into the Grand Rhône and the Petit Rhône. The Grand Rhône, drains east of the delta (sub-straight channel) and supplies an active pro-delta in the Mediterranean (Arnaud-Fassetta and Provansal, 2014). The Petit Rhône marks the western edge of the Camargue and, whereas it flows into the Mediterranean. The delta is part of the Gulf of Lion, a wide embayment of the French Mediterranean coastline (Arnaud-Fassetta, 2003). The eastern tributaries of the Rhône, e.g. Isère, Drôme, Durance originating in the Alps, have a higher sediment load, compared to steep shorter rivers (e.g. Ardèche, Gardon, Cèze) from the Massif Central (Olivier et al. 2009).

Vegetation of the Rhône Rift Valley

The potential temperate vegetation zone in the plains (<700 m) is characterised by deciduous oak mixed forest. The hills and mountains of the Alps and the Massif Central are characterised by a mixture of *Fagus* and *Abies* (Beaudouin et al. 2007; Ollivier et al. 2014). The Mediterranean coastline vegetation (<500 m) shows sclerophyllous forests with evergreen *Quercus* and *Laurus nobilis* (Beaudouin et al. 2007). Higher altitudes of the Mediterranean vegetation show mainly *Quercus pubescens* associated with *Buxus sempervirens* (Beaudouin et al. 2007). Mountainous forest (1450–2500 m) are characterised by conifers, while at the Alpine belt plants like *Ericaceae* with *Poaceae* emerge (Beaudouin et al. 2007). The actual vegetation is presented by large cultivated plantations represented by fruit cultivations in the north and more frost-sensitive fruits, like wine or olives in the south. The vegetation of the Rhône delta is adapted to dune and swampy vegetation e.g. *Salicornia*, *Limonium* (Pletsch and Uterwedde, 2003). Based on the favourable climatic and geomorphological conditions, the Rhône-Saône Valley is described as an early settlement region (Delhon et al. 2009; Daujeard et al. 2012; Doyen et al. 2015; Moncel et al. 2015; Richard et al. 2015). Thus, anthropogenic influence on deforestation, the change of natural vegetation distribution (deciduous oak by *Quercus ilex* through human activity) (Beaulieu et al. 2005) and intense agriculture (Reille and Beaulieu, 1990; Preusser et al. 2011) started at an early stage.

1.4.2 Climate of the Rhône Rift Valley

The recent climate of the Rhône Rift Valley is characterised by a gradual change from temperate climate conditions in the north to Mediterranean conditions in the south (Fig. 1.1). The temperate climate of the northern valley is distinguished by warm summers (up to 3 arid month) and cold, humid winters (mean annual temperature (MAT): ~13 °C) with mean annual precipitation (MAP) between 800 mm and 900 mm (Meteo-France, 2022a). The mountainous and eastern regions of the valley reached higher MAP of 1200–1400 mm and summer storms are common (Diodato et al. 2016). The Mediterranean climate is characterised by hot, dry summers with 5 arid months, MAT: ≥ 14 °C and humid winters with MAP: ≥ 500 mm (Meteo-France, 2022d, 2022e). The wind system of the valley is influenced by different origins of advect air masses (Mediterranean, maritime, polar maritime and subtropical), which led to synoptic circulations and resulting in a high yearly and seasonal variability of precipitation and wind intensities (Diodato et al. 2016). The dominating wind systems are the cold blowing Mistral and Tramontane. The strong north-northwestern blowing Mistral travels as well as the western blowing Tramontane, through the channelled valleys before opening into the Mediterranean Sea (Obermann et al. 2018). Both wind regimes occur consequently often at the same time, most likely during winter months and are accompanied by cold air and rain (Jacq et al. 2005; Obermann et al. 2018). The Mistral can reach maximal wind speeds up to 140 km h^{-1} and last for several days (Jacq et al. 2005). For the south-west Rhône Rift Valley flash flood events are common. Here, the 2022 event stands out, with daily precipitation maxima between 600 and 700 mm (Diodato et al. 2016).

1.4.3 The Pleistocene period in the Rhône Rift Valley

During the penultimate (Rissian) and Last Glacial period (Würmian), parts of the north-eastern Rhône Rift Valley were covered by glaciers. The glaciers of Arve, Arc, Isère and Rhône formed within the internal part of the French northern Alps and the Jura mountains a complex ice net, from which the so-called Lyonnais ice lobe advanced into the Rhône Rift Valley (Mandier et al. 2003; Coutterand et al. 2009; Buoncristiani and Campy, 2011). The glaciers Isère, Arc and Romache extended into the Isère Valley, north of the Massif Vercors representing the southern-most extension of the glaciation concerning the Rhône Rift Valley. During the Rissian period, the northern Dombes plateau was entirely covered by ice, creating an ice-dammed lake with glacial-lacustrine deposits. During the last glacial maximum (LGM), the extension of both ice lobes (Lyonnais and Isère) were more limited. The age of the LGM within the Rhône Rift Valley is still a matter of debate. Ages of 27 ka or 22 ka (MIS 2) are proposed (Schoeneich, 1998; Coutterand, 2010; Buoncristiani and Campy, 2011), but even earlier phases for the maximum advances (MIS 5d or MIS 4) are considered (Ivy-Ochs et al. 2008).

In the Massif Central small ice-caps, valley and piedmont-glaciers occurred during the Würmian (Buoncristiani and Campy, 2004). Due to the topography of the Massif Central (larger ice masses in the west than the east) it is assumed that the glacial impact in terms of debris and sediment input into the Rhône Rift Valley was minor, compared to the Alps (Buoncristiani and Campy, 2004).

The southern part (south of Valence) of the Rhône Rift Valley is assigned to the periglacial zone, in which Tzedakis et al. (2013) assumed the present of tree “refugias” during LGM. Andrieux et al. (2016) reconstructed the southern limit of continuous permafrost during the LGM at 47° N and of discontinuous permafrost at 45–44° N (region between Lyon and Valence). However, various frost features were observed in sediments along the entire southern ECRIS, especially at the Costière de Nîmes plateau in the Rhône delta (Arnal 1971; Bornand 1978; Ollivier et al. 2014), indicating at least strong seasonal frost during the LGM (Bertran et al. 2013; Andrieux et al. 2016).

Pleistocene moraine and terrace deposits of the Rhône Rift Valley

The research on the Pleistocene terraces of the Rhône Rift Valley started in the early 20th century by Penck and Brückner (1909), Kilián and Gignoux (1911), Chapotat (1935), Bourdier (1958), Mandier (1969, 1974, 1984, 1988), Bonnet and Bornand (1970) and Arnal (1974), Bornand (1978) until more recently Molliex et al. (2013) aimed to establish a chronological frame of the terrace formation periods.

In the northern Rhône Rift Valley only a very limited number of terraces remained, as Pleistocene deposits have been almost entirely eroded. With exceptions of scarce Riss-Würmian or Inter-Würmian lignite formations, only Würmian retreat moraines and post-Würmian sediments can be found. These moraines and fluvio-glacial deposits were divided by Mandier (1984) into five stages (A–E). Stage A presents the maximal extension of the glacier (LGM) located east of Lyon, whereas stages B and C present different end moraine stages. Stage D presents an early retreat of the ice and stage E finally marks the complete ablation (Mandier et al. 2003). Proposed radiocarbon dates for the retreat of the ice lobe for stage E are between 22.000 and 18.200 cal BP. (Mandier et al. 2003). The fluvio-glacial terraces of the northern valley are defined as “terrace rhodanienne” (Bornand, 1978; Jamagne et al. 2011). They appear mainly on the eastern river bench with ranging thicknesses between 10 and 50 m (Bornand 1978; Jamagne et al. 2011). The terraces are composed of sandy debris, which originated from the molasse or calcic substrate of the Rhône Rift Valley (Jamagne et al. 2011).

At Bièvre-Valloire, in the middle Rhône Rift Valley, the fluvial and fluvio-glacial terraces are remarkably preserved and comprises of deposits from the entire Pleistocene (Bourdier, 1958). The good preservation status is mainly related to alpine tectonics, with the oldest strata being

more uplifted than the youngest. The Valence basin presents the transition area from fluvio-glacial terraces to fluvial terraces. Rissian and Würmian fluvial terraces of the Rhône and the Isère (“terraces Prealps”) prevail in the basin located at the eastern river bench (Bourdier, 1958; Bambier et al. 1979). The approx. 10 m thick terraces are located on sandy molasse material from the Prealps, which is dominated by calcium (>95 %) and flint (Bornand, 1978; Jamagne et al. 2011). The depression between Saint-Péray and Saint-Georges-les-Bains on the western river bench represents an early (probably Günz-Mindel) paleo-channel of the pre-Rhône (Mandier, 1974).

The terraces on the western river bench in the mid- and lower Rhône Rift Valley are defined as “terraces Massif central” and further south as “terrace Ardèche”. Their thickness ranges between 5 m and 10 m and they comprise of the gravelly debris material (mixture out of crystalline, siliceous or basaltic material) from the Massif Central and the Ardèche, respectively (Bornand, 1978; Jamagne et al. 2011).

Within the lower Rhône Rift Valley, the old non-disturbed terraces (Villafranchian or Günz to Würm) submerge beneath the Holocene deposits in southward direction. In the west, the Rhône delta comprises of Pleistocene alluvial layers of the “Costière de Nîmes”/du Gard plateau (60–140 m over the delta) and of the Pliocene alluvial material from the Durance of the Costière de la Crau in the east (Jamagne et al. 2011). Due to tectonic movements, the chronostratigraphic classification of the plateaus is more challenging (Bourdier, 1958). The eastern and southern parts of the delta display a mixture of eroded Pleistocene fluvial and marine terraces, lacustrine and postglacial fluvial deposits. A correlation to other terraces of the delta via altitudinal is difficult, as these sediments have been reshaped by tectonic movements and erosion (Monjuvent et al. 1991).

During the Pleistocene, the palaeo-Rhône drained into the palaeo-coastal fringe, 120 m under present day sea level (Arnaud-Fassetta and Provansal, 2014). At present day, the Rhône channel is located at the top of a large alluvial ridge and characterised by fluvial, brackish (salty lagoons) and coastal (sandbars) deposits. At the western delta plain, sand ridges are well preserved, while at the eastern part they are eroded and/or buried (Boyer et al. 2005).

Loess deposits of the Rhône Rift Valley

In relation with other Pleistocene deposits, loess deposits were already described in the 19th century by Benoit (1858), Falsan and Chantre (1879) or in the early 20th century by Penck and Brückner (1909). First detailed descriptions of the aeolian deposits, especially loess, were done by Marcelin (1926), whereas Suen (1934) was among the first who extensively mapped the occurrence of loess along the Rhône. In the following loess research in the Rhône Rift Valley was further expanded by Perrin (1948), Viret (1948), Marcelin (1950), Tricart (1952),

Mazenot (1956, 1957, 1959, 1965), Bourdier (1958), Alimen (1965), Bonifay (1952, 1962, 1965) and more recently by Franc et al. (2017) and Bosq et al. (2018, 2020a, 2020b).

Source of the Rhône Rift Valley loess are alluvial deposits from the valley originated from glacial and fluvio-glacial deposits from the Alps and Massif Central (Suen, 1934; Bosq et al. 2018, 2020a). They cover the Dombes plateau and the large basins and terraces of the northern valley (Figs. 1.3, 2.4, 4.43, 5.69). They appear on both sides of the Rhône River, whereas on the western river bench, loess deposits are located at depressions and rives. On the eastern bench, the loess covers largely the Bas-Dauphiné depression. Further south, the deposits mainly occur along the tributaries cover partially bedrock, partially, the fluvial terraces, north and south of the confluences with the Rhône and smaller side valleys of the Rhône (Figs. 1.3, 2.4, 4.43, 5.69). The southern-most loess deposits are located on the Nîmes plateau.

According to Suen (1934), Bourdier (1958), Bonifay (1965), Mazenot (1965) and Bosq et al. (2018, 2020b), the following characteristics of the loess deposits in the Rhône Rift Valley were summarised. The loess deposits:

- vary in thickness between several centimetres and up to 10 m, locally.
- are dominated by large silt particles with a unimodal to polymodal grain-size distribution.
- show a discontinuous distribution of silty sands and colluviated loess within the southern parts of the valley.
- are generally intensively reworked and redeposited
- change in colour from yellow in the north to brown or red in the south of the valley.
- show a varying carbonate content between 15 and 35 % CaCO₃.
- contain striking carbonate nodules (French: “poupées”), which occur in various shapes and sizes up to few meters thick cemented carbonate layers.
- contain various faunal fossils all along the valley.

The chronology of the loess deposits was generally based on faunal remains, Palaeolithic artefacts or the stratigraphical positions of their palaeosols and their comparison with the chronology of the Alpine glaciations (Suen, 1934; Tricart, 1952; Bourdier, 1958; Bonifay, 1965, Mazenot, 1965). Suen (1934), suggested that the main loess formation period corresponds to the Late Pleistocene. According to Tricart (1952) and Bonifay (1965), in the southern Rhône Rift Valley two series of loess are visible, dating to the last two glaciations (Rissian and Würmian), separated by the Last Interglacial soil. Bonifay (1965) also describes silty cave infilling of aeolian origin, which he accounts to the Mindelian period. Although without any numerical dating, the author provides a detailed stratigraphical description of the “older” Rissian loess and the “recent” Würmian loess. He subdivided the Würmian loess into four units, separated by palaeosol formations, beginning from the bottom with I to IV (Bonifay, 1965). The

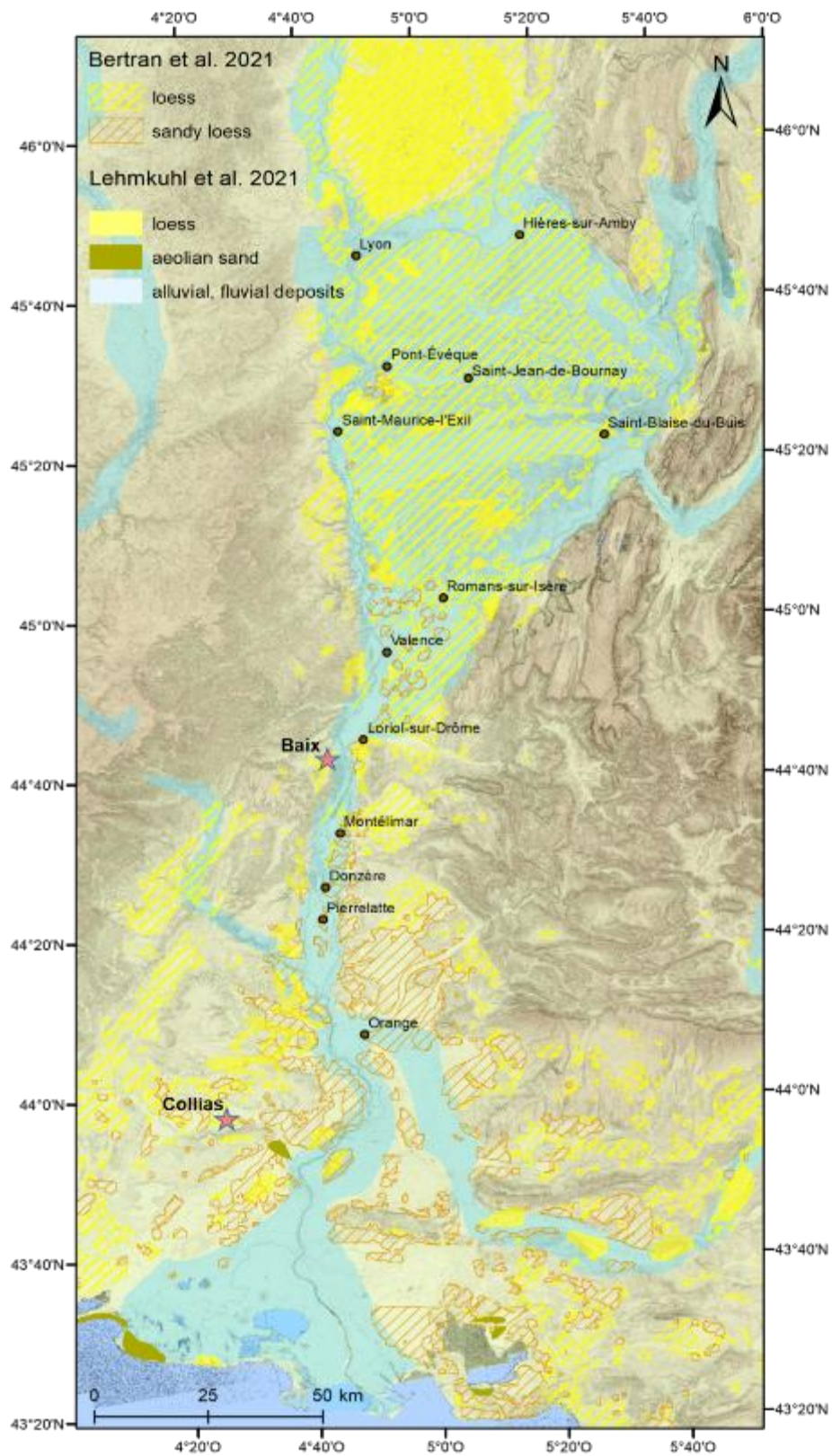


Figure 1.3: Map of aeolian (loess and sand), alluvial and fluvial deposits in the Rhône Rift Valley area derived from Bertran et al. (2021) and Lehmkuhl et al. (2021) with locations of loess-palaeosol section (LPS) Baix and Collias (pink stars) (map data: Digital Elevation Model (DEM) with a 12 m x 12 m resolution derived from the TanDEM-X data Mission (2011–2015) from the German Aerospace Centre (DLR)).

loess unit I overlays the 1.50 m thick red Last Interglacial soil and is dominated by an orange, or reddish, or even red colour. The loess unit I is generally subdivided into two levels, a red lower level bearing the trace of a small soil alteration in its upper part, and an orange or yellowish upper level. The loess unit II displays a typical loess facies and is overlain by a grey or reddish-brown soil (Bonifay, 1965). Loess unit III begins with a layer of cryoclastic debris, followed by a typical beige or greyish, sometimes sandy loess. The loess can be subdivided by a thin grey and a gravelly soil. At the top of the recent loess III is a grey or reddish-brown soil. The loess facies of unit IV is slightly sandy and the deposits are surmounted by colluvial material and the post-glacial soil (Bonifay, 1965). Bourdier (1958) describes a similar stratigraphy for the last glacial loess-palaeosol sequences and even suggest older deposition ages (Middle Pleistocene) for the lowermost loess.

More recent research by Magnin (2014) and Magnin and Bonnet (2014) in the southern part of the valley, presents ^{14}C ages from molluscs, suggesting favourable climate conditions for soil formation. Datings correspond to a MIS 3 interstadial (Hengelo-Charbon (38–37.000 BP) or Moershoofd-Pile interstadial complex (50–43.000 BP). A possibly corresponding brown palaeosol was dated in the LPS Lyon-Apollinaire, north of the valley, although the ages are more variable between 27 and 40 ka and remained to be discussed according to Franc et al. (2017). Furthermore, OSL and ^{14}C ages obtained from a brownish horizon of LPS Quincieux, close to LPS Lyon-Apollinaire, are coherent around 20 ka, suggesting another younger soil formation phase.

Chapter 2: Chronostratigraphy of two Late Pleistocene loess-palaeosol sequences in the Rhône Valley (southeast France) (study 1)

Mathieu Bosq¹, Sebastian Kreutzer^{2,3}, Pascal Bertran^{1,4}, Jean-Philippe Degeai⁵, Pauline Dugas^{1,6}, Annette Kadereit⁷, Philippe Lanos^{2,8}, Olivier Moine⁹, Nora Pfaffner¹⁰, Alain Queffelec¹, Daniela Sauer¹⁰

¹) PACEA, UMR 5199 CNRS, Université Bordeaux, Bâtiment B2, Allée Geoffroy Saint Hilaire, 33615, Pessac, France

²) IRAMAT-CRP2A, UMR 5060 CNRS, Université Bordeaux Montaigne, Maison de l'Archéologie, 33607, Pessac, France

³) Geography & Earth Sciences, Aberystwyth University, Aberystwyth, SY23 3DB, Wales, United Kingdom

⁴) Inrap, 140 Avenue Du Maréchal Leclerc, 33130, Bègles, France

⁵) ASM, UMR 5140 CNRS, Université de Montpellier III, Route de Mende, 34199, Montpellier, France

⁶) Adera, PACEA-Transfert Sédimentologie & Matériaux, 162 Avenue Du Docteur Schweitzer, 33600, Pessac, France

⁷) Heidelberg Luminescence Laboratory, Institute of Geography, University of Heidelberg, Germany

⁸) Géosciences Rennes, Université de Rennes I, 35042, Rennes, France

⁹) LGP, UMR 8591 CNRS, Université Paris I Panthéon-Sorbonne/Université Paris-Est-Créteil-Val-de-Marne (UPEC), Place Aristide Briand, 92195, Meudon, France

¹⁰) Institute of Geography, University of Göttingen, Germany

Manuscript published in Quaternary Science Review. DOI: <https://doi.org/10.1016/j.quascirev.2020.106473>.

Table 2.1: Authors contributions to study 1.

Authors	Contribution to study
Mathieu Bosq	Conceptualisation, Methodology, Writing -original draft, Formal analysis, Investigation, Visualisation.
Sebastian Kreutzer	Methodology, Writing - original draft, Writing - review & editing, Formal analysis, Investigation, Visualisation
Pascal Bertran	Conceptualisation, Writing - review & editing, Supervision, Project administration, Funding acquisition
Jean-Philippe Degeai	Investigation, Writing - review & editing
Pauline Dugas	Investigation, Formal analysis
Annette Kadereit	Validation, Writing - review & editing.
Philippe Lanos	Formal analysis, Software
Olivier Moine	Investigation, Writing - review & editing
Nora Pfaffner	Investigation, Writing - review & editing
Alain Queffelec	Methodology, Software, Formal analysis, Resources
Daniela Sauer	Investigation, Writing - review & editing

Abstract

A sedimentological and chronostratigraphical investigation was carried out on two loess sections located in the Mediterranean area in southeast France along the Rhône River (Lautagne) and the lower reach of a tributary of the Rhône River (Collias). High-resolution sampling (5–20 cm) for magnetic susceptibility, grain size distribution (including non-

parametric end-member modelling), colour reflectance and geochemistry was performed. The chronology was based on luminescence dating of quartz grains and radiocarbon dating of small gastropod shells, coupled with hierarchical Bayesian modelling. The Collias section (~8 m thick) records the whole last climatic cycle. It comprises a thick red basal pedocomplex S1 developed during the Last Interglacial and the Early Glacial, similar to that observed elsewhere in southern and southeastern Europe. Loess deposition occurred during the Lower (L1L2) and the Upper Pleniglacial (L1L1). It was interrupted by soil formation during the Middle Pleniglacial, of which a brown Bwk horizon has been preserved (L1S1). By contrast, the ~5 m thick Lautagne section provides a detailed record of the Upper Pleniglacial. Weakly developed hydromorphic soils are correlated with the Greenland Interstadials GI-4 to GI-2, while the main period of coarse loess sedimentation corresponds to the Greenland Stadials GS-5 to GS-2. At a regional scale, the time of loess deposition ranges between 38.5 ka and 12 ka, with a peak at ~28–24 ka, overlapping with the maximal advance of the Alpine Ice Sheet (AIS). This strongly suggests that regional glacier dynamics was the main driver of loess sedimentation.

Keywords: Loess, Southeast France, Chronology, Geochemistry, Grain-size distribution, Last Glacial

2.1 Introduction

Loess deposits are widespread across the European continent and constitute key terrestrial archives for reconstructing the palaeoenvironments of the last climatic cycle. During the Last Glacial, drastic reduction of the vegetation cover, increase in wind intensity and decrease in precipitation favoured the global emission of dust (Lunt and Valdes, 2002; Mahowald et al. 2006; Hopcroft et al. 2015; Schaffernicht et al. 2020). Loess accumulated at the periphery of the Eurasian Ice-Sheet (EIS) and on the banks of major rivers draining mountain ice caps. Past advances of luminescence-dating methods, such as optically simulated luminescence (OSL, Huntley et al. 1985) on quartz, and infrared stimulated luminescence (IRSL, Hütt et al. 1988) or post-IR IRSL (pIRIR, Thomsen et al. 2008) on feldspar and polymineral grains, have enabled the establishment of a robust chronological framework of the phases of loess accumulation and soil formation (e.g. Frechen and Schirmer, 2011; Thiel et al. 2011a; Kreuzer et al. 2012a, 2012b; Fuchs et al. 2013; Zöller et al. 2013; Lomax et al. 2014; Moska et al. 2015, 2019; Sauer et al. 2016; Guérin et al. 2017a; Zens et al. 2018). Simultaneous improvements of radiocarbon dating by Accelerator Mass Spectrometry (AMS) made it possible to analyse small charcoal pieces and carbonate biomineralisations (e.g. small terrestrial gastropod shells, earthworm calcite granules) and also greatly contributed to support and refine previous loess chronology in some regions (e.g. Újvári et al. 2016b; Moine et al. 2017;). Overall, the progress in dating accuracy over the past decades highlighted the impact of millennial climate variations such as Dansgaard-Oeschger (D-O) cycles upon loess sedimentation in Europe.

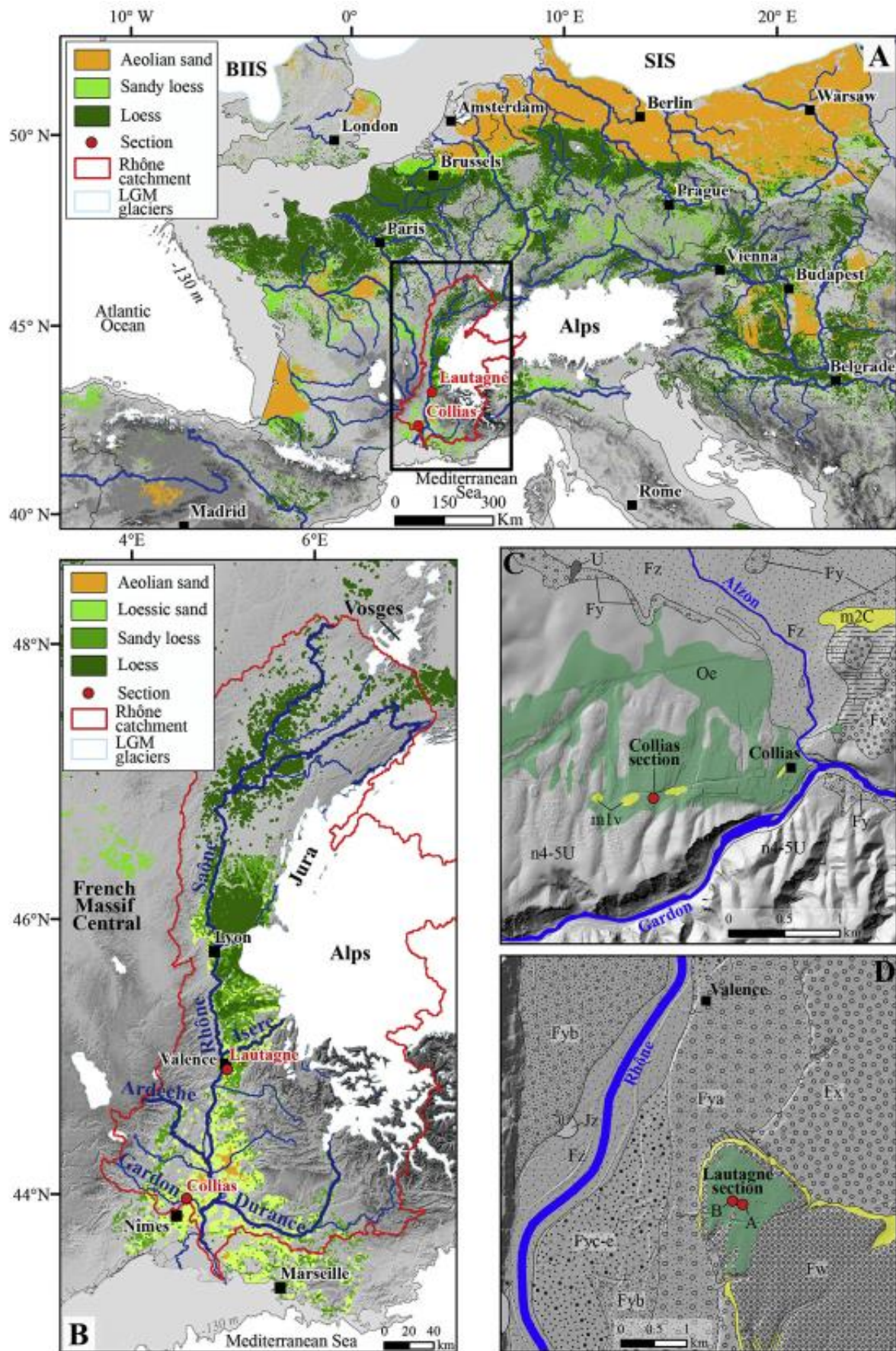


Figure 2.4: A) Map of aeolian deposits in Western Europe from Bertran et al. (2016) with additional data from Bosq et al. (2018) and Lindner et al. (2017), showing the location of the sections studied in the

Rhône Valley and within the Rhône catchment (red line). The British-Irish Ice Sheet (BIIS) and Scandinavian Ice Sheet (SIS) are from Hughes et al. (2016). The Alpine Ice Sheet (AIS) and other LGM glaciers are from Ehlers and Gibbard (2004). Sea-level drop to 130 m below sea level during the LGM is assumed (Lambeck et al. 2014). Palaeocoastlines are from Zickel et al. (2016). The map is based on a Digital Elevation Model (DEM) (ETOPO1; Amante and Eakins, 2009), ETRS89-LAEA projected geographic coordinate system. B) Spatial distribution of aeolian deposits in the study area (Bosq et al. 2018). C, D) Close-up maps of the Collias (C) and Lautagne (D) areas, based on a DEM with 5 m resolution from RGE ALTI® (<http://professionnels.ign.fr>). The geological formations were redrawn from the 1:50,000 geological map (<http://infoterre.brgm.fr>). Abbreviations: Fz = Holocene floodplain, Fy, Fyc-e, Fyb, Fya, Fw, Fv = Pleistocene terraces, Jz = alluvial fans, m1v/m2C = Miocene molasses (yellow), n4-5U = Cretaceous limestone, Oe = loess (green), U = travertine. (For interpretation of the references to colour in this figure legend, the reader is referred to the Web version of this article.) Yet, because of its patchy distribution and variable thickness, peri-Mediterranean loess remains poorly documented except for some publications (Calvo et al. 2016; Profe et al. 2016; Costantini et al. 2018; Wacha et al. 2018). Recent studies in the Po plain in Italy (Cremaschi, 1990a; Cremaschi et al. 2015; Zerboni et al. 2015) and Croatia (Wacha et al. 2018), as well as in the Ebro (Boixadera et al. 2015) and Tagus basins (Wolf et al. 2018, 2019) in Spain suggested, however, that Pleistocene loess covers considerable areas in peri-Mediterranean regions. Last Glacial loess is also widespread in the Rhône Valley, southeast France (Bosq et al. 2018, 2020a and references therein). These deposits have specific characteristics when compared to loess from the North-European Loess Belt (NELB), including a coarser texture (main grain-size mode around 60 µm), polymodal grain-size distribution, locally great thickness but discontinuous spatial distribution, high carbonate content and abundant syn-sedimentary bioturbation. Such pattern is assumed to reflect the capture of particles in saltation and short-term suspension by shrub vegetation close to the fluvial sources, in a milder climate than that of the North European plains. Geochemical analyses show that loess deposits derived from the rivers (Rhône, Rhine, Danube and Po) draining the Alpine Ice Sheet (AIS) have a similar, Ca-rich composition (cf. Bosq et al. 2020a). They are referred here as to “perialpine loess”.

This paper has the following objectives: (1) high-resolution multi-proxy analysis of two sections (Collias and Lautagne) representative of the loess-palaeosol sequences of the Rhône Valley, southeast France, (2) development of an accurate chronological framework using a hierarchical Bayesian model based on OSL and AMS ¹⁴C ages of the section of Lautagne, and (3) comparison of the chronology of loess deposition with AIS fluctuations and the North Greenland Ice Core Project (NGRIP) ice record.

2.2 Materials and methods

2.2.1 Study sites, description and sampling

The sequence Collias (43.953° N; 4.466° E; 100 m a.s.l.) is located on the left bank of the Gardon River, upstream of its confluence with the Rhône (Fig. 2.4A and B). In this area, loess deposits reaching locally 10 m thickness were recognised in the 1950s and 1960s (Tricart, 1952; Mazonot, 1956; Bonifay, 1962). Loess overlies Lower Miocene molasse (noted m1v on

the 1:50.000 geological map, <http://infoterre.brgm.fr/>) and extends from the foot of a Lower Cretaceous (n4–5U) limestone massif to the alluvial plain of the Alzon River (Fig. 2.4C). A previous study has demonstrated that the geochemical composition of alluvium from the Gardon River (as well as all the rivers from the French Massif Central) differs from that of loess of the Rhône Valley, including the Collias samples (Bosq et al. 2020a). The geochemical data also revealed that the dust was mainly supplied by the bed of the Rhône River (at that time a braided river, carrying the sediment loaded meltwater of the Alpine (and Jura) glaciers). Bonifay (1962) distinguished two loess generations and assigned them to the Last Glacial ("Series I") and the Penultimate Glacial ("Series II"). According to the same author, the two generations are separated by an erosional discontinuity attributed to the Last Interglacial. The studied section is a subvertical outcrop created during the construction of a forest road. A Mediterranean climate with low rainfall (Mean Annual Precipitation, MAP = 763 mm), hot summers ($T_{\max} \geq 22$ °C) and relatively high annual temperatures (Mean Annual Temperature, MAT = 15.2 °C) characterises the area (meteorological data for the period 1981-2010; <https://donneespubliques.meteofrance.fr>).

The sequence Lautagne (44.904 °N; 4.897 °E; 177 m a.s.l.) is located south of Valence on the left bank of the Rhône (Fig. 2.4D), on a river terrace (Fw) attributed to the Middle Pleistocene (Mandier, 1988), showing a well-developed rubefied palaeosol. Two test pits were dug during archaeological excavations led by the *Institut national de recherches archéologiques préventives* (Inrap) (see Fig. A2.14 in Appendix A). The fluvial gravel is buried by loess, reaching a thickness of up to 5 m (profile A) and gradually decreasing towards the edges of the plateau (profile B). Lautagne is located at the transition between a semi-continental climate to the north and a Mediterranean climate to the south, with a MAP = 923 mm and a MAT = 13.3 °C.

Excavation and manual cleaning of the sections created successive vertical panels (1 m to 2 m high and >1 m wide) separated by steps, making description and sampling easier. The lithofacies codes were taken from Miall (1996), and the soil horizons were classified according to the FAO Guidelines for Soil Description (FAO, 2006) and the World Reference Base for Soil Resources (IUSS Working Group WRB, 2015). Samples were collected for magnetic susceptibility, grain-size distribution and colourimetry at 5 cm depth-resolution, and for geochemistry at 20 cm depth-resolution. In total, 164 (Collias) and 98 (Lautagne) samples were collected and analysed (Figs. 2.5 and 2.6). In addition, eight blocks of sediment (15 cm x 10 cm x 7 cm) were extracted from each section for thin section preparation according to the method described by Guilloré (1980). The micromorphological description of the samples was carried out according to the recommendations of Stoops (2003).

2.2.2 Bulk magnetic susceptibility

Measurements of the specific-mass magnetic susceptibility (χ) of each sample were performed in the laboratory using a Bartington MS2B at room temperature. The results are expressed in $10^{-6} \text{ m}^3/\text{kg}$. The dry, bulk sedimentary material was homogenised and compressed in a 10 ml plastic cylinder. χ values reflect the concentration of minerals with ferrimagnetic properties (mainly magnetite and maghemite). Nevertheless, this proxy can be biased by the grain-size distribution of magnetic grains. Indeed, ferrimagnetic grains of the superparamagnetic grain-size (SP, $<0.03 \text{ mm}$) have a significantly higher χ than single-domain (SD, $>0.03 \text{ mm}$) or multi-domain (MD, $>10 \text{ mm}$) particles (Thompson and Oldfield, 1986). The use of the frequency dependent magnetic susceptibility (χ_{FD}) partially resolves these limitations (Obrecht et al. 2019). This parameter is the relative difference between the mass magnetic susceptibility values measured at low frequency (0.46 kHz) and high frequency (4.65 kHz) (χ_{LF} and χ_{HF} respectively). χ_{FD} (expressed in %) was calculated as follows:

$$\chi_{\text{FD}} = \frac{(\chi_{\text{LF}} - \chi_{\text{HF}})}{\chi_{\text{LF}}} \times 100$$

χ_{FD} is a measure of the relative contribution of SP ferrimagnetic particles approaching the SP-SD threshold that are formed exclusively in situ (e.g. Maher and Taylor, 1988; Dearing et al. 1996). Therefore, χ_{FD} is considered to be a very efficient proxy for determining the weathering intensity (Dearing et al. 1996; Buggle et al. 2014).

2.2.3 Grain-size distribution and end-member modelling

The samples for grain-size distribution analysis were processed using a Horiba LA-950 laser particle size analyser. After passing the samples through a 2 mm sieve to remove the coarser fraction (secondary carbonate concretions, shells, gravels and roots), the sample pre-treatment included suspension in sodium hexametaphosphate (5 g l^{-1}) and hydrogen peroxide (35 %) at room temperature for 12 h. As recommended by Schulte et al. (2016), the carbonates were not removed. Then, the suspension was subjected to 60 s ultrasonification to achieve optimal dispersion. The Mie solution to Maxwell's equation provided the basis for calculating the particle size distribution (ISO, 2009; Jones, 2003), using a refractive index of 1.333 for water and $1.55i-0.01i$ for the particles (see Appendix of Sitzia et al. (2017) for details on the procedure). The upper limit of clay measured by laser granulometry was set at $8 \text{ }\mu\text{m}$ after calibration by the sieve-pipette method as described in Bosq et al. (2018). Finally, the Grain Size Index (GSI) defined by Antoine et al. (2009a) was calculated. The GSI is the ratio between coarse silt ($52-26 \text{ }\mu\text{m}$) and fine silt plus clay ($<26 \text{ }\mu\text{m}$).

Grain-size distribution can provide key information on the provenance, mechanisms and/or distance of transport, and the depositional environment of sediments (e.g. Bagnold and

Barndorff-Nielsen, 1980; Vandenberghe, 2013; Újvári et al. 2016a). Two approaches have been developed to decompose grain-size distributions and to quantify dominant subpopulations in aeolian sediments: (i) parametric curve fitting using a mixture of log-normal (Qin et al. 2005; Bosq et al. 2018) or Weibull distribution functions (Sun et al. 2002) and (ii) non-parametric endmember modelling analysis (EMMA) (Weltje, 1997; Vriend and Prins, 2005; Weltje and Prins, 2007; Dietze et al. 2012; Dietze and Dietze, 2019). In this study, the EMMA approach was applied using the MATLAB® GUI software of AnalySize developed by Paterson and Heslop (2015). The main advantage of this method is that it describes an entire grain-size dataset as a mixture of distinct unimodal or polymodal subpopulations (Weltje, 1997; Weltje and Prins, 2007; Dietze et al. 2012). The analysis was arbitrarily restricted to the grain-size class [$>1 \mu\text{m}$ to $<678 \mu\text{m}$] to eliminate a large number of zeros that cause numerical instabilities in the treatment. The determination coefficient R^2 was calculated to identify the minimum number of end-members (EMs) (q) necessary for correct statistical interpretation. Following this principle of parsimony, an EM model with $q = 3$ was chosen as it allowed a significant improvement of R^2 from 2 to 3 EMs while the improvement was reduced from 3 to 4 EMs (see Fig. A2.15). This model explains 97.8 % of the total variance of the dataset. Then, the distribution of each EM was split into different populations by the parametric curve fitting method using the R (R Core Team, 2019) package 'mixdist' (Macdonald and Du, 2015) to identify the different modes. A log-normal distribution was used.

2.2.4 Spectrocolourimetry

The colour of moist sediments was determined in the field using the Munsell soil colour chart (Munsell, 2000). The colour of the dry, crushed and homogenised samples was then measured in the laboratory using an Avantes AvaSepc-2048 fibre-optic spectrometer. The instrument was equipped with an optic fibre probe (1 mm diameter) that was placed at a short distance (2 mm) from the smooth surface of the sample. An AvaLight-Hal was used as the light source, and the equipment was calibrated with a white reference sample (Halon D65). Three measurements per sample were performed, and the average was then calculated. The spectral information obtained was converted into the CIELAB (L^* , a^* , b^*) system (CIE, 1976) using Avasoft 7.5 software. The variable L^* indicates the lightness on a scale from 0 (black) to 100 (white) while the variables a^* and b^* express the colour in chromatic coordinates on the red-green (positive a^* - negative a^*) and blue-yellow (positive b^* - negative b^*) scales.

Colour differences between yellowish loess and reddish-brown palaeosols are mainly a consequence of goethite and hematite concentrations (Ji et al. 2001). The chromaticity values a^* is closely related to the relative abundance of pedogenic hematite (e.g. Lukić et al. 2014).

2.2.5 Geochemical analysis

The sediment was passed through a 100 mm sieve to remove coarse sand grains, ferruginous nodules, carbonate concretions and other debris such as calcified roots, mollusc shells and earthworm calcite granules, which may disturb the results of the geochemical analysis. The fine fraction <100 mm was ground and pressed into pellets for X-ray fluorescence (ED-XRF) using a portable Bruker Tracer 5i. Two measurements were taken under vacuum on all samples, one at 15 kV and 100 μ A for 300 s without a filter to quantify light elements (Na, Mg, Al, Si, P, K, Ti, V, Cr, Mn, Fe) and the other at 50 kV and 35 mA for 120 s with the Cu75, Ti25, Al200 filter for heavy elements (Ni, Zn, Ga, As, Rb, Sr, Y, Zr, Nb, Ba, La, Ce, Nd, Hf, Pb, Th) and Ca. The instrument was calibrated by use of the CloudCal v3.0 application (Drake, 2018; <https://github.com/leedrake5/CloudCal>), using the algorithm proposed by Lucas-Tooth and Price (1961). The calibration was performed using the geochemical composition of 43 loess and alluvial samples determined by Inductively Coupled Plasma-Atomic Emission Spectroscopy (ICP-AES) and ICP-Mass Spectrometry (ICP-MS) at the Service d'Analyse des Roches et des Minéraux (CRPG-SARM, Nancy, France) according to a previously published methodology (Bosq et al. 2020a). Only the elements for which the determination coefficient R^2 between the analytical results of the ED-XRF and the ICP-AES/ ICP-MS was greater than 0.7 were considered (cf. Figs. A2.16 and A2.17).

A wide variety of geochemical indices based on major and trace elements has been developed to study dust provenance, grain-size sorting and weathering intensity in European loess (cf. Bosq et al. 2020a). For the purposes of this study, we focused on the following element ratios and indices: Ti/Al, Si/Al, CPA, Rb/K, Fe/Al, and Ca/Al. Al is considered here as the invariant element. Ti, mainly in the form of oxides (anatase, brookite, rutile), forms inclusions in mafic minerals, especially biotite, which is concentrated in the fine fraction (Young and Nesbitt, 1998). The Ti/Al ratio is used here as an indicator of the homogeneity of the sedimentary source (Sheldon and Tabor, 2009). The Si/Al ratio is sensitive to grain-size sorting since Si-rich tectosilicates (quartz, feldspars) are over-represented in the coarser fractions, whereas Al-rich phyllosilicates constitute a large part of the finer fractions (Bouchez et al. 2012; Liang et al. 2013; Guo et al. 2018). Weathering indices are based on the selective removal of soluble and mobile elements (particularly alkali and alkaline earth elements) during pedogenesis (Nesbitt and Young, 1982; Buggle et al. 2011). The weathering intensity of silicates was quantified using the Chemical Proxy of Alteration (CPA) (in molar proportion):

$$CPA = 100 \times \frac{Al_2O_3}{(Al_2O_3 + Na_2O)}$$

CPA (originally called Chemical Index of Weathering (CIW') by Cullers, 2000) was considered a proxy for plagioclase weathering intensity by Buggle et al. (2011). The CPA is particularly

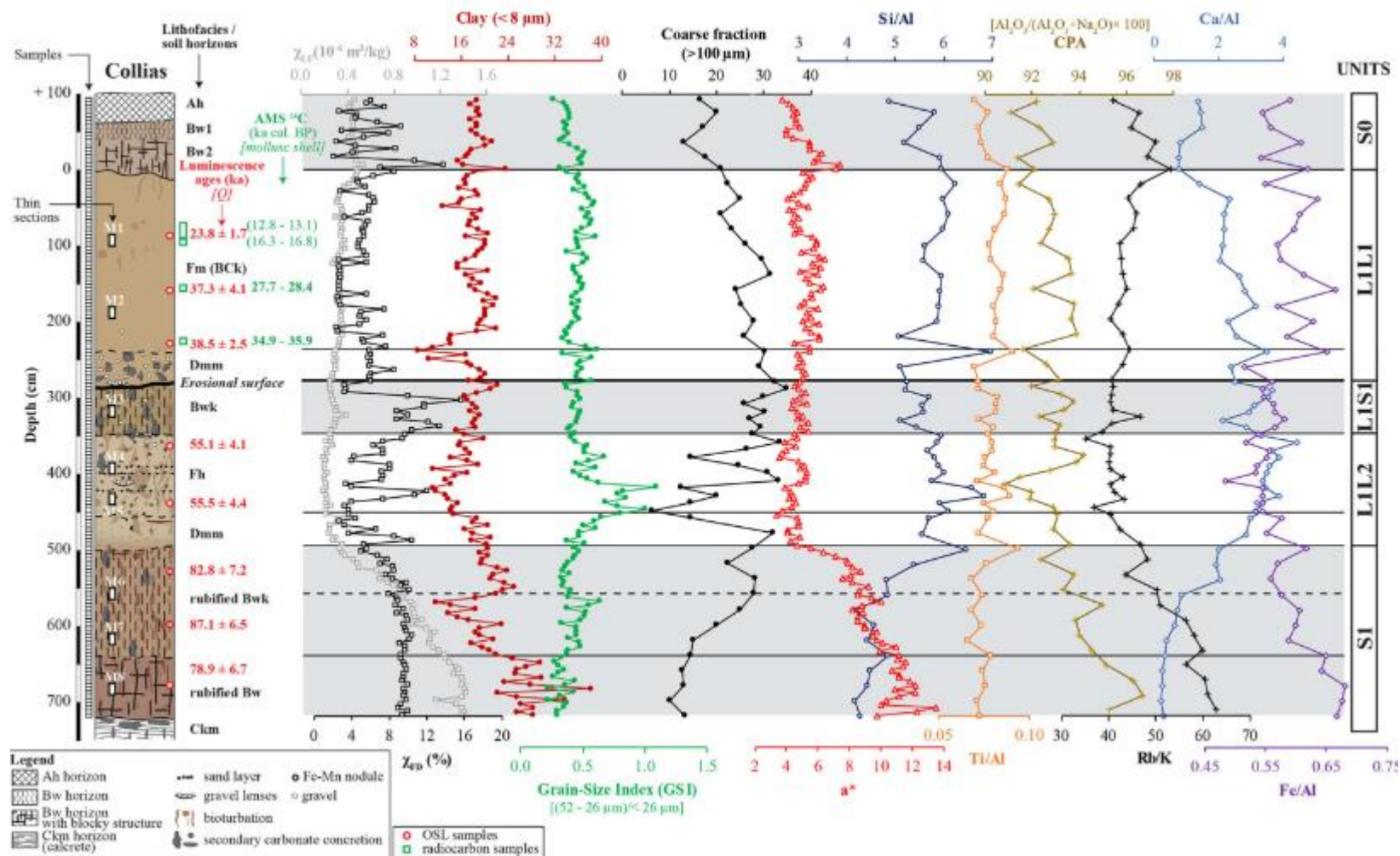


Figure 2.5: Detailed stratigraphy of the Collias section with the locations of the samples for sedimentological and micromorphological analyses. Curves: low-frequency mass-specific magnetic susceptibility (χ_{LF}) expressed in $10^{-6} \text{ m}^3/\text{kg}$, frequency dependent magnetic susceptibility (χ_{FD}) expressed in %, grain-size parameters (clay, GSI, coarse fraction), colour reflectance (a^*), geochemical ratios (Si/Al, Ti/Al, CPA, Rb/K, Ca/Al, Fe/Al). Details on luminescence dating results (red) are provided in Table 2.2 and on radiocarbon dating results (green) in Table 2.3. The grey bars indicate soil formation. (For interpretation of the references to colour in this figure legend, the reader is referred to the Web version of this article.)

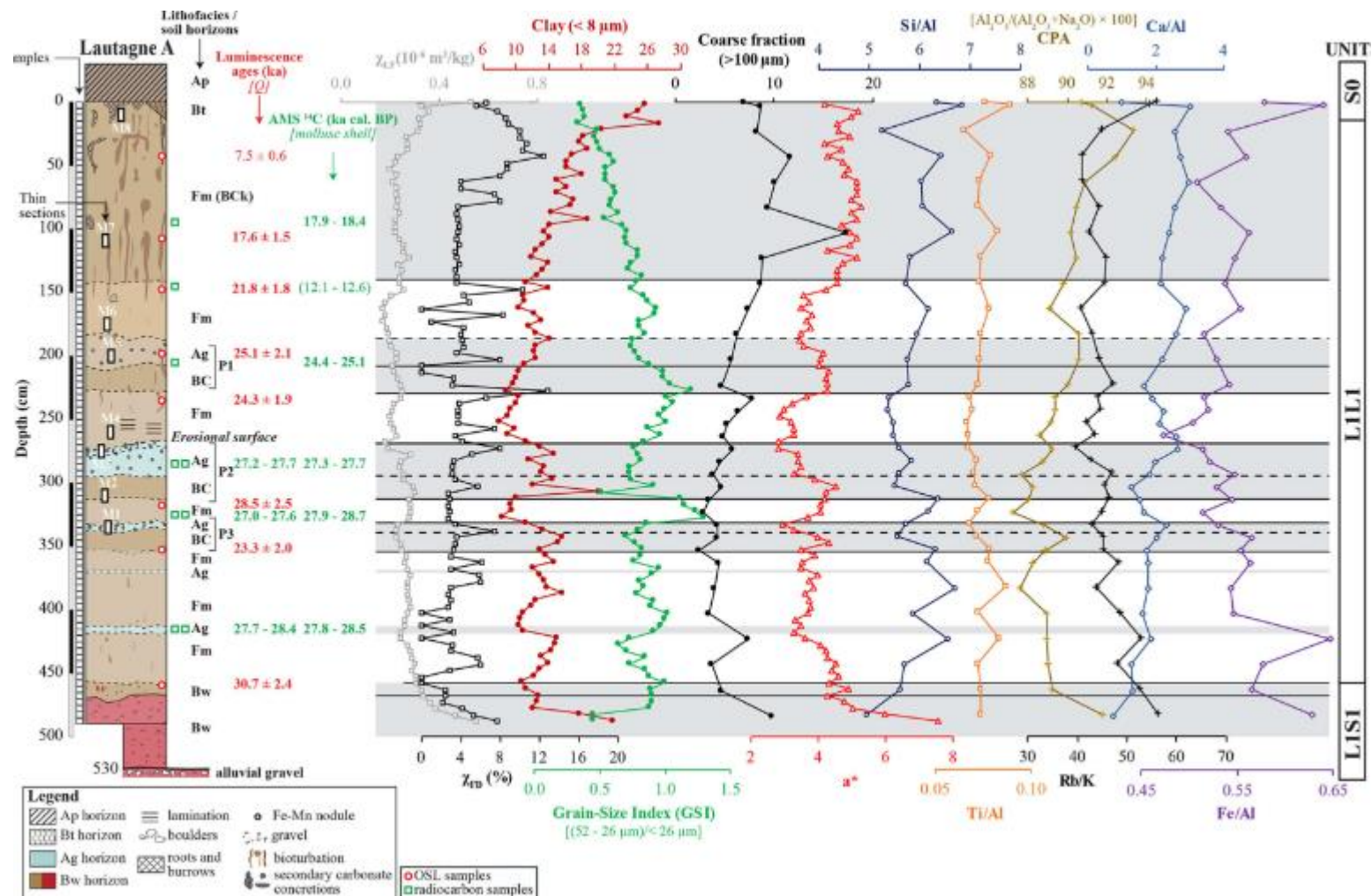


Figure 2.6: Detailed stratigraphy of the Lautagne section (Lautagne A) with the locations of the samples for sedimentological and micromorphological analyses. Curves: low-frequency mass-specific magnetic susceptibility (χ_{LF}) expressed in $10^{-6} \text{ m}^3/\text{kg}$, frequency dependent magnetic susceptibility (χ_{FD}) expressed in %, grain-size parameters (clay, GSI, coarse fraction), colour reflectance (a^*), geochemical ratios (Si/Al, Ti/Al, CPA, Rb/K, Ca/Al, Fe/Al). Details on luminescence dating results (red) are provided in Table 2.2 and on radiocarbon dating results (green) in Table 2.3. The grey bars indicate soil formation. (For interpretation of the references to colour in this figure legend, the reader is referred to the Web version of this article.)

adapted to poorly weathered sediments since weathering first impacts plagioclases rather than K-feldspars (Nesbitt and Young, 1989). Besides the CPA, the K/Rb ratio was used to estimate the weathering intensity of K-bearing minerals (Nesbitt et al. 1980; Wronkiewicz and Condie, 1990), since K is more mobile than Rb due to its smaller ionic radius. Rb is hosted by K-feldspars, micas and clay minerals (Heier and Billings, 1970; Nesbitt et al. 1980). As Ca is essentially hosted by calcite, the Ca/Al ratio allows to evaluate the depth distribution of calcite along the sequence, in particular the secondary precipitation of calcite of pedogenic origin at certain profile depths, provided that the contents of plagioclases and primary calcium carbonate are roughly constant across the profile. The Fe/Al ratio is used to distinguish the B horizons of soils that are relatively enriched in Fe, due to the formation of immobile iron oxides such as magnetite (Fe_3O_4), hematite (Fe_2O_3) and goethite ($\text{FeO}(\text{OH})$) (Reimann et al. 2014).

2.2.6 Chronological data

2.2.6.1 Luminescence dating

The two sites Lautagne and Collias were subjects to luminescence dating at the IRAMAT-CRP2A (Université de Bordeaux-Montaigne) between 2016 and 2019. In both cases, the samples were extracted under daylight using steel cylinders. In total, we prepared 18 samples (10 from Lautagne, including 8 from section A and 2 from section B, and 8 samples from Collias) to extract the fine-grain (4–11 μm) (Lautagne) and coarse-grain (90–200 μm) (Collias) quartz fractions (see Table 2.2).

Additionally, we extracted coarse-grain quartz separates for Lautagne and the K-feldspar fraction of 2 samples from Collias for cross-checks. The sample preparation was supported by the luminescence laboratories of the Justus-Liebig University Giessen (Germany) and the University of Bayreuth (Germany), following routine luminescence dating preparation methods (e.g. Preusser et al. 2008). The quartz samples were subjects to OSL measurements, applying the single aliquot regenerative (SAR) dose protocol (Murray and Wintle, 2000). Equivalent doses (D_e) were measured on Freiberg Instruments *lexsyg research* luminescence readers (Richter et al. 2013), and the data analysis was performed with the R (R Core Team, 2019) package ‘Luminescence’ (Kreutzer et al. 2012b, 2020). We applied the average dose model (Guérin et al. 2017b) to samples from Lautagne and the ‘baSAR’ approach (Combès et al. 2015; Mercier et al. 2016) to samples from Collias to calculate the average dose and the central dose respectively, and their corresponding standard errors. Dose-rate measurements relied on in situ gamma-dose rate measurements at Lautagne (cf. Løvborg and Kirkegaard, 1974; Mercier and Falguères, 2007) and high-resolution gamma-ray spectrometry (procedure at the IRAMATCRP2A, cf. Guibert and Schvoerer, 1991). In addition, we measured U, Th, K concentrations for all samples from both sites. The online calculator DRAC (Durcan et al. 2015)

in version 1.2 provided the final luminescence ages. We detail the luminescence dating, including further references, in Appendix B.

2.2.6.2 AMS radiocarbon dating

Last Glacial loess-palaeosol sequences (LPS) in southeast France lack organic remains that can be easily dated by the radiocarbon method. To overcome this problem, recent studies have been undertaken, which have shown that calcitic biomineralisations such as terrestrial gastropod shells or earthworm granules can be used to obtain a precise chronology (e.g. Újvári et al. 2016b; Moine et al. 2017). The advantage of this approach is that these carbonates are relatively abundant in loess. In the past, mollusc shells have often been avoided for dating because large taxa incorporate carbon from the substrate, which causes apparent radiocarbon-age increases up to several thousand years (Evin et al. 1980; Goodfriend and Stipp, 1983). However, several studies have shown that this effect is much more limited and generally negligible for small (<10 mm) gastropods (Brennan and Quade, 1997; Pigati et al. 2010).

Table 2.2: Final dose rates, equivalent doses (D_e) and luminescence age values of the Collias and Lautagne A sections. Uncertainties are quoted as 1s, rounded to one digit. Final ages used for this study are quoted in bold numbers. For more details, see Appendix B.

Sample name	Laboratory code	Mineral	Depth (m)	External dose rate (water corr.)			Internal dose rate		D_{cosm}	D_{ext}	D_{int}	D_{env}	D_e	Age (ka)	Posterior calib. date ka b2k (HPD, 95%)
				D_x	D_β	D_γ	D_x	D_β							
Collias BAY	BDX21322	Q	0.90	0.0 ± 0.0	1.1 ± 0.1	0.8 ± 0.0	0.0 ± 0.0	0.0 ± 0.0	0.3 ± 0.0	2.2 ± 0.1	0.0 ± 0.0	2.2 ± 0.1	51.4 ± 2.6	23.8 ± 1.7	–
Collias BAY	BDX21323	Q	1.60	0.0 ± 0.0	1.0 ± 0.1	0.8 ± 0.0	0.0 ± 0.0	0.0 ± 0.0	0.2 ± 0.0	1.9 ± 0.1	0.0 ± 0.0	1.9 ± 0.1	71.6 ± 7.0	37.3 ± 4.1	–
Collias BAY	BDX21324	Q	2.30	0.0 ± 0.0	1.0 ± 0.1	0.8 ± 0.0	0.0 ± 0.0	0.0 ± 0.0	0.2 ± 0.0	1.9 ± 0.1	0.0 ± 0.0	1.9 ± 0.1	72.0 ± 3.1	38.5 ± 2.5	–
Collias BAY	BDX21325	Q	3.65	0.0 ± 0.0	0.9 ± 0.0	0.7 ± 0.0	0.0 ± 0.0	0.0 ± 0.0	0.1 ± 0.0	1.7 ± 0.1	0.0 ± 0.0	1.7 ± 0.1	94.7 ± 5.3	55.1 ± 4.1	–
Collias BAY	BDX21326	Q	4.40	0.0 ± 0.0	1.0 ± 0.1	0.8 ± 0.0	0.0 ± 0.0	0.0 ± 0.0	0.1 ± 0.0	1.9 ± 0.1	0.0 ± 0.0	1.9 ± 0.1	106.8 ± 6.7	55.5 ± 4.4	–
Collias BAY	BDX21327	Q	5.30	0.0 ± 0.0	1.1 ± 0.1	0.9 ± 0.0	0.0 ± 0.0	0.0 ± 0.0	0.1 ± 0.0	2.0 ± 0.1	0.0 ± 0.0	2.0 ± 0.1	169.1 ± 12.1	82.8 ± 7.2	–
Collias BAY	BDX21328	Q	6.00	0.0 ± 0.0	1.3 ± 0.1	1.0 ± 0.0	0.0 ± 0.0	0.0 ± 0.0	0.1 ± 0.0	2.4 ± 0.1	0.0 ± 0.0	2.4 ± 0.1	212.4 ± 12.0	87.1 ± 6.5	–
Collias BAY	BDX21329	Q	6.80	0.0 ± 0.0	1.4 ± 0.1	1.1 ± 0.1	0.0 ± 0.0	0.0 ± 0.0	0.1 ± 0.0	2.6 ± 0.1	0.0 ± 0.0	2.6 ± 0.1	202.5 ± 14.1	78.9 ± 6.7	–
Lautagne A FGQ	BDX18944	FGQ	0.73	0.3 ± 0.1	1.1 ± 0.1	0.7 ± 0.0	0.0 ± 0.0	0.0 ± 0.0	0.2 ± 0.0	2.3 ± 0.1	0.0 ± 0.0	2.3 ± 0.1	17.3 ± 0.4	7.5 ± 0.6	–
Lautagne A FGQ	BDX18945	FGQ	1.07	0.3 ± 0.1	1.2 ± 0.1	0.7 ± 0.0	0.0 ± 0.0	0.0 ± 0.0	0.2 ± 0.0	2.4 ± 0.1	0.0 ± 0.0	2.4 ± 0.1	42.5 ± 2.0	17.6 ± 1.5	16.0–20.8
Lautagne A FGQ	BDX18946	FGQ	1.47	0.3 ± 0.1	1.2 ± 0.1	0.8 ± 0.0	0.0 ± 0.0	0.0 ± 0.0	0.2 ± 0.0	2.5 ± 0.1	0.0 ± 0.0	2.5 ± 0.1	53.8 ± 2.0	21.8 ± 1.8	18.8–24.4
Lautagne A FGQ	BDX18947	FGQ	1.98	0.3 ± 0.1	1.2 ± 0.1	0.8 ± 0.0	0.0 ± 0.0	0.0 ± 0.0	0.2 ± 0.0	2.5 ± 0.1	0.0 ± 0.0	2.5 ± 0.1	63.0 ± 2.5	25.1 ± 2.1	20.9–27.2
Lautagne A FGQ	BDX18948	FGQ	2.35	0.4 ± 0.1	1.3 ± 0.1	0.8 ± 0.0	0.0 ± 0.0	0.0 ± 0.0	0.2 ± 0.0	2.7 ± 0.1	0.0 ± 0.0	2.7 ± 0.1	64.8 ± 1.8	24.3 ± 1.9	22.3–27.9
Lautagne A FGQ	BDX18949	FGQ	3.18	0.4 ± 0.1	1.4 ± 0.1	0.9 ± 0.0	0.0 ± 0.0	0.0 ± 0.0	0.1 ± 0.0	2.8 ± 0.1	0.0 ± 0.0	2.8 ± 0.1	80.8 ± 4.0	28.5 ± 2.5	24.7–31.4
Lautagne A FGQ	BDX18950	FGQ	3.53	0.3 ± 0.1	1.3 ± 0.1	0.9 ± 0.0	0.0 ± 0.0	0.0 ± 0.0	0.1 ± 0.0	2.7 ± 0.1	0.0 ± 0.0	2.7 ± 0.1	63.5 ± 2.6	23.3 ± 2.0	21.3–28.7
Lautagne A FGQ	BDX18953	FGQ	4.60	0.4 ± 0.1	1.5 ± 0.1	1.1 ± 0.1	0.0 ± 0.0	0.0 ± 0.0	0.1 ± 0.0	3.0 ± 0.1	0.0 ± 0.0	3.0 ± 0.1	93.4 ± 2.4	30.7 ± 2.4	27.9–34.3

Q: coarse grain quartz; D_e values quotes as mean ± standard error of the mean.

BAY: coarse grain quartz (90–200 μm); D_e representing the 'baSAR' central dose and the standard error of the central dose.

FGQ: fine grain quartz (4–11 μm); D_e values quoted as mean ± standard error determined with the average dose model.

The final age calculations include the following systematic errors: D_x : 1%, D_β : 1%, D_γ : 5% (*in situ* measurements), D_γ : 3% (γ -ray spectrometry), β -source calibration: 3%.

Ten litres of bulk sediment have been wet sieved on a 425-μm mesh. Then, gastropod shells and earthworm calcite granules were cleaned by ultrasonic treatment and were analysed in

the following laboratories: (i) the AMS facilities of the Hertelendi Laboratory of Environmental Studies, Institute for Nuclear Research at Debrecen (Hungary) (Molnár et al. 2013); (ii) the Radiocarbon dating centre at Lyon (France) within the framework of the ARTEMIS programme and (iii) the Centre for Isotope Research at Groningen (Netherlands) (Dee et al. 2020). Conventional radiocarbon ages were calibrated to calendar ages with the IntCal13 calibration curve (Reimer et al. 2013), using the software Calib in version 7.0.4 (Stuiver and Reimer, 1993). Calibrated ages are reported as age ranges at the 2 sigma (σ) confidence level (95.4 %)

2.2.6.3 Bayesian age modelling

In order to obtain a robust chronology of the best-dated sequence (Lautagne A), a Bayesian age model was built using the software ChronoModel (version 2.0.18) (Lanos and Philippe, 2015, 2017; Lanos and Dufresne, 2019). This software allows the calculation of a posteriori ages by considering the stratigraphic constraints between the samples. After removal of outliers, an age model was built for the period 35–15 ka cal. b2k (before the year 2000). We used the default configuration of Monte-Carlo Markov Chain (MCMC) parameters proposed by the software (3 chains, 1000 burn iterations, and 500 batch iterations with a maximum of 20 batches, and 100,000 acquisition iterations with a thinning interval of 10). This approach may result in slightly underestimated age uncertainties because ChronoModel does not yet allow to specify shared systematic uncertainties. However, given the large uncertainties of the OSL ages, this potential problem does not affect the overall interpretation of our results. In total, 15 ^{14}C and OSL dates were used for establishing the chronology of the section Lautagne A (see Fig. 2.6). The highest posterior density (HPD, 95 %) of the ^{14}C and OSL ages was calculated according to the method detailed by Banks et al. (2019). The posterior age probability distributions for each sample are compiled in Tables 2.2. and 2.3.

2.3 Results

2.3.1 Lithofacies and soil horizons

2.3.1.1 Homogeneous loess (Fm)

This lithofacies consists of massive, homogeneous calcareous yellowish brown (10 YR 5/4 to 2.5Y 6/4) coarse silt and fine sand (Fig. 2.7A). Bioturbation features (root channels, burrows) and secondary carbonate concretions (rhizoconcretions, pseudomycelium) are abundant (Figs. 2.7, 2.8E and 2.8F, 2.9E and 2.9F). At Lautagne, a platy microstructure due to former segregation ice lenses (e.g. van Vliet-Lanoë, 1985) is visible between 1.9 m and 3.2 m depth (Fig. 2.9G). This lithofacies is dominant in both sections and interpreted as being of aeolian origin. Due to abundant secondary calcium carbonate, these loess units are designated as Ck or BCK horizons according to FAO (2006).

Table 2.3: AMS radiocarbon ages of samples from the sections Collias and Lautagne A (calibration by use of IntCal13 according to Reimer et al. 2013). Final ages used for this study are quoted in bold numbers.

Sample name	Laboratory code	Depth (m)	Material (species)	¹⁴ C (a BP) (1σ)	Unmodeled ¹⁴ C (a cal. BP)	Posterior calib. date (a b2k)
					(2σ) Min - Max	HPD (95%) From - To
Collias - 70/90	DeA-21816	0.800	shell (<i>P. muscorum</i>)	11078 ± 49	12805–13067	-
Collias - 90/100	DeA-21817	0.950	shell (<i>P. muscorum</i>)	13683 ± 61	16268–16785	-
Collias - 150/160	DeA-21818	1.550	shell (<i>P. muscorum</i>)	23996 ± 123	27754–28369	-
Collias - 220/230	DeA-21819	2.250	shell (<i>P. muscorum</i>)	31515 ± 214	34894–35917	-
Lautagne A - 50/60	Ly-51291	0.550	earthw. calcite granules	8560 ± 35	9489–9554	-
Lautagne A - 90/100	DeA-18280	0.950	shell (<i>P. muscorum</i>)	14893 ± 64	17876–18355	17955–18347
Lautagne A - 95/100	GrA-68030	0.975	earthw. calcite granules	19250 ± 90	22918–23486	-
Lautagne A - 140/150	Ly-51292	1.450	earthw. calcite granules	9490 ± 40	10591–11069	-
Lautagne A - 140/150	DeA-18281	1.450	shell (<i>P. muscorum</i>)	10486 ± 48	12138–12575	-
Lautagne A - 190/200	Ly-51293	1.950	earthw. calcite granules	12530 ± 50	14420–15111	-
Lautagne A - 200/210	DeA-18282	2.050	shell (<i>P. muscorum</i>)	20527 ± 108	24358–25112	24410–25159
Lautagne A - 240/250	DeA-19359	2.450	earthw. calcite granules	18134 ± 73	21765–22253	-
Lautagne A - 240/250	DeA-19423	2.450	earthw. calcite granules	19929 ± 81	23722–24234	-
Lautagne A - 250/260	Ly-51294	2.550	earthw. calcite granules	17200 ± 70	20534–20969	-
Lautagne A - 270/275	GrA-68028	2.725	earthw. calcite granules	14790 ± 70	17791–18216	-
Lautagne A - 280/290	Ly-51295	2.850	earthw. calcite granules	14970 ± 60	17982–18372	-
Lautagne A - 280/290	GifA18096.1	2.850	shell (<i>P. muscorum</i>)	23260 ± 120	27302–27724	27334–27712
Lautagne A - 280/290	GifA18096.2	2.850	shell (<i>P. muscorum</i>)	23140 ± 130	27184–27667	27269–27678
Lautagne A - 320/330	GifA18097.1	3.250	shell (<i>P. muscorum</i>)	23040 ± 150	27068–27624	27228–27746
Lautagne A - 320/330	GifA18097.2	3.250	shell (<i>P. muscorum</i>)	24280 ± 150	27941–28670	27857–28563
Lautagne A - 335/340	GrA-68027	3.375	earthw. calcite granules	22040 ± 110	25989–26551	-
Lautagne A - 380/390	DeA-19360	3.850	earthw. calcite granules	19656 ± 80	23420–23949	-
Lautagne A - 410/420	GifA18098.1	4.150	shell (<i>P. muscorum</i>)	24110 ± 160	27800–28535	27905–28559
Lautagne A - 410/420	GifA18098.2	4.150	shell (<i>P. muscorum</i>)	23940 ± 160	27695–28381	27824–28484
Lautagne A - 415/420	GrA-68026	4.175	earthw. calcite granules	22400 ± 110	26329–27095	-
Lautagne A - 440/450	DeA-19361	4.450	earthw. calcite granules	21077 ± 90	25181–25659	-
Lautagne A - 440/450	DeA-19424	4.450	earthw. calcite granules	19561 ± 75	23287–23853	-

2.3.1.2 Bedded calcareous sandy loess (Fh)

This facies consists of regularly alternating sandy and light yellowish-brown silty (2.5Y 6/4) beds with lenses of small subangular limestone fragments (Fig. 2.8B). The lenses are ca 1 cm thick and generally up to 1 m wide (Fig. 2.7B). This lithofacies is interpreted as loess mixed with local coarser material, redistributed by overland flow.

2.3.1.3 Massive loess colluvium (Dmm)

Massive brown coarse silty deposits, containing scattered gravels, and characterised by poor sorting, greater porosity and few charcoal fragments, are interpreted as colluviated loess (Figs. 2.5, 2.7B and 2.8A).

2.3.1.4 Ploughed topsoil horizon (Ap)

The topsoil horizon at Lautagne contains bricks, pottery and charcoal fragments and results from the reworking of loess caused by agricultural practices during the Holocene.

2.3.1.5 Buried topsoil horizons with redox features (Ag)

Five units in the section Lautagne A consist of thin (10–20 cm), slightly bleached (2.5Y 6/4 to 2.5Y 5/6), calcareous silt with scattered small Fe-Mn nodules. Their boundaries are sharp and show deformations due to stretching downslope (Fig. 2.7E). These horizons are characterised by (i) bleaching resulting from hydromorphic processes (iron reduction and removal from the horizon); (ii) a slightly finer texture compared to the underlying loess; (iii) weak staining by organic matter and (iv) abundant carbonate concretions.

These units, which often overlie BC horizons, are interpreted as topsoil Ag horizons, indicating seasonal waterlogging (FAO, 2006) that have been deformed by slope dynamics after burial, probably in a periglacial context, possibly by solifluction.

2.3.1.6 Brown Bwk and BC horizons

These horizons are characterised by moderate weathering as indicated by (i) a higher proportion of clay; (ii) a brown colour (10 YR 5/6 to 10 YR 6/6) related to the formation of iron oxides; (iii) partial dissolution of carbonates associated with carbonate precipitation in the underlying horizon. The Bwk horizon underwent strong secondary accumulation of calcite forming large rhyzoliths, which justifies the addition of the suffix -k. Poorly developed (incipient) horizons showing a range of features otherwise typical of Bw horizons are here referred to as BC horizons.

2.3.1.7 Rubefied Bw and Bwk horizons

Yellowish red (5 YR 4/6) to reddish brown (7.5 YR 4/6), compact calcareous clayey silt units, exhibiting a massive or prismatic to blocky structure, are interpreted as rubefied Bw horizons. Bioturbation (burrows and roots) is abundant, and black Fe-Mn hypocoatings cover many ped faces (Fig. 2.9D). There is no microscopic evidence of clay illuviation (e.g. clay coatings, clay papules) (Fig. 2.8C). Decalcification of the groundmass is complete, while some channels are filled by slightly calcareous loessic sediment. Secondary carbonate impregnations are also visible.

2.3.1.8 Calcrete (Ckm horizon)

At Collias, the redistribution of CaCO_3 led to the formation of an indurated laminar crust and vertical rhizoconcretions more than 10 cm long at the bottom of the profile, designated as Ckm horizon (Fig. 2.7A and C).

2.3.2 Stratigraphy

The section Collias comprises five main stratigraphic units, from bottom to top (Figs. 2.5 and 2.7):

- Calcrete (Ckm horizon) overlain by rubefied Bw and Bwk horizons, forming a pedocomplex referred to as S1;
- Bedded calcareous sandy loess (L1L2), 2.5 m thick, with bioturbation and diffuse lower boundary;
- Brown Bwk horizon (L1S1), 0.5-0.6 m thick, whose upper boundary is an erosional surface;
- Colluvium (0.2 m) overlain by 2.8 m thick primary loess (L1L1);

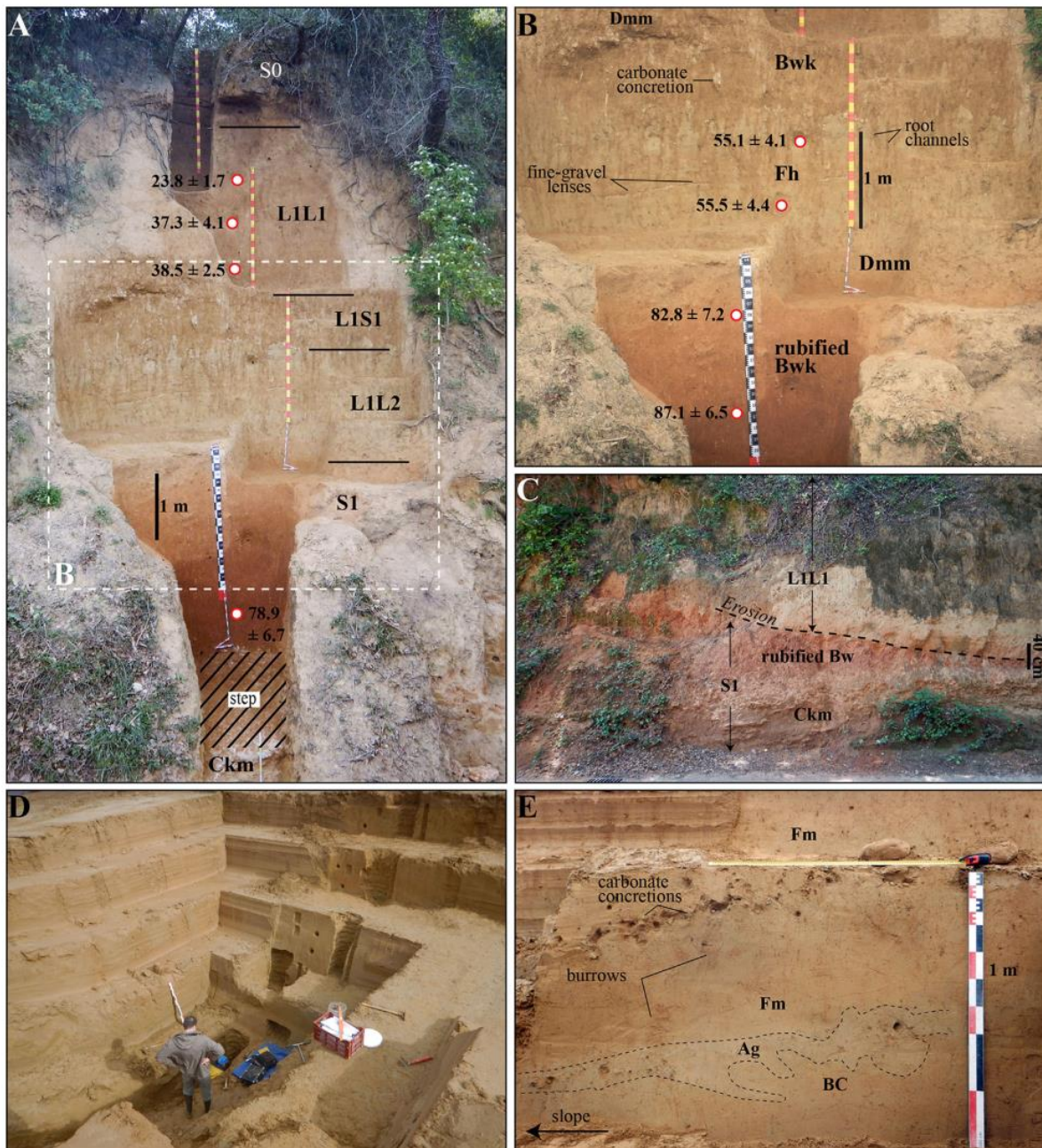


Figure 2.7: A, B) Photographs of the main lithofacies of Collias with luminescence ages. C) Close-up view of the erosional surface above the rubified pedocomplex (S1) exposed in a roadcut approximately 100 m from the Collias section; D) Overview of the Lautagne section (Lautagne A) during archaeological excavations; E) Detail of the deformed incipient palaeosol (P2) of Lautagne (Lautagne B). Photograph A were taken by D. Sauer, Photographs B–E were taken by M. Bosq.

- Holocene brown Cambisol (S0), about 1 m thick, predominantly composed of material that has been reworked and translocated in the course of agricultural land use and terracing of the above land (presently used as olive plantation).

The loess sequence at Lautagne (Fig. 2.6) covers Pleistocene gravels that were reached at a depth of 5.3 m during the archaeological excavation. Three main units (I-III) were distinguished:

- Reddish colluviated loess, up to 0.5 m thick (L1S1);

- Sandy, calcareous loess, 4.7 m thick (L1L1), including three incipient palaeosols (P3, P2 and P1), each consisting of an Ag-BC profile;
- Holocene Luvisol (S0), locally preserved from erosion due to agriculture within Gallo-Roman pits, and with a ploughed topsoil (Ap horizon).

2.3.3 Analytical data: magnetic susceptibility, colourimetry, grainsize and geochemistry

An overview of the main physical and chemical properties of the two sequences is provided in Figures 2.5 and 2.6. Both sections are characterised by large GSI fluctuations with maximum values in the bedded loess at Collias (between 4.15 m and 4.50 m depth) and in the homogeneous (primary) loess at Lautagne A (at 3.15–3.30 m depth). The proportion of the coarse fraction (>100 μm) ranges from 6.3 % to 34.8 % at Collias and reflects slope material inputs mixed with aeolian dust and/or pedogenic carbonate concretions. The variations in low-frequency magnetic susceptibility (χ_{LF}) coincide with lithofacies changes in both sequences. The highest values ($\chi_{\text{LF}} \geq 0.4 \cdot 10^{-6} \text{ m}^3/\text{kg}$) are found in palaeosol horizons while the lowest values are typical of primary loess (L1L1) and bedded loess (L1L2), except for the Bwk horizon L1S1 at Collias that has relatively low χ_{LF} values (between 0.25 and 0.39 $\times 10^{-6} \text{ m}^3/\text{kg}$). L1S1 has also χ_{FD} values above 10 %, indicating in situ neoformation of superparamagnetic (<0.03 μm) pedogenic particles. The lack of correlation between χ_{LF} and χ_{FD} values suggests that larger ferrimagnetic minerals (MD and SD) have little or no contribution to increased magnetic susceptibility.

A correlation exists between magnetic susceptibility and other proxies such as clay content and chromaticity a^* . The highest values of chromaticity a^* range between 5.6 and 13.5 and are associated with clay contents higher than 25 %, especially in the pedocomplex S1 at Collias. At Lautagne A, the BC horizons are characterised by relatively high a^* values (≥ 4), and an increase in clay content. In contrast, a^* values and clay contents decrease in homogeneous loess (on average 8–14 % clay at Lautagne A and 9–19 % clay at Collias).

In both sequences, the element ratio Ti/Al is almost constant, with values between 0.07 and 0.09, indicating stable and homogeneous sediment sources. The Si/Al ratio covariates with CSI and increases significantly in loess while it decreases in palaeosol horizons, which reflects enrichment in aluminosilicates (clay minerals) in the latter. Plagioclase and K-feldspar weathering, represented by CPA and Rb/K, respectively, is more intense in B and BC horizons than in underlying loess. The weathering indices record maximum values in S1 with a CPA of about 96 and a Rb/K ratio of 63. Ag horizons exhibit higher concentrations of K-bearing minerals than BC horizons, which is related to the presence of illite in the fine fraction.

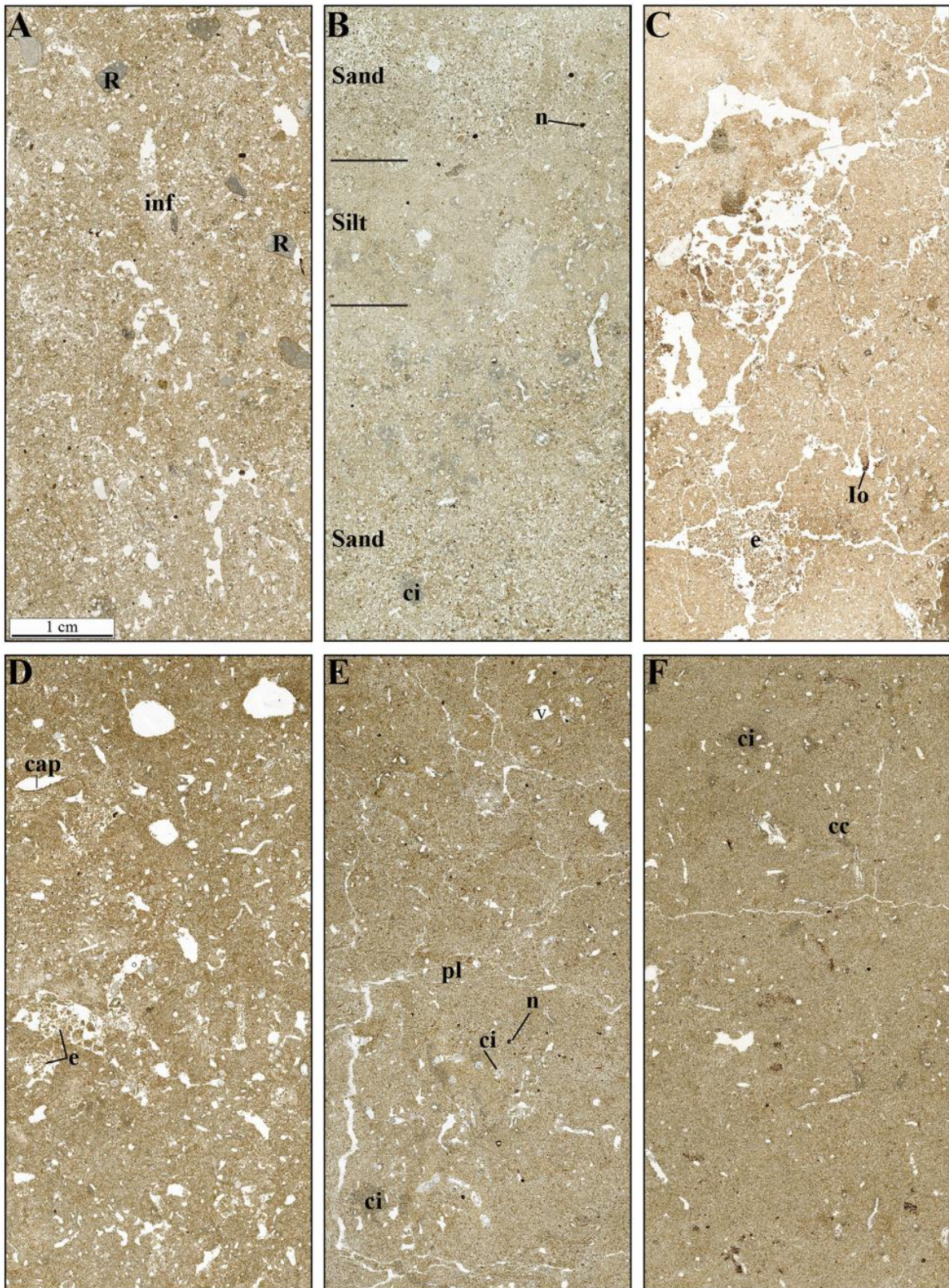


Figure 2.8: Photographs of selected thin sections (6.5 cm x 3.0 cm) of the Collias (A, B and C) and Lautagne (D, E and F) sections. A) Brown Bwk horizon around 320 cm depth – channel microstructure with scattered rock fragments showing thin, clayey silt coatings (M3). B) Calcareous sandy loess (L1L2) around 400 cm depth - 3 cm to 5 cm thick beds of sand and silt, massive to channel microstructure with abundant secondary calcite impregnations; few scattered Fe/Mn nodules (M4). C) Rubefied Bw horizon around 680 cm depth – subangular blocky macroaggregates (one to several centimetres in diameter) with completely decalcified reddish groundmass, diffuse Fe/Mn nodules and coatings. At the base of the thin section, loose discontinuous infillings with disintegrated excrements of enchytraeids or collembolas

(M8). D) L1L1 loess near the top of the sequence - channel to vughy microstructure with complex packing voids and large abundant loose infillings of voids by disintegrated excrements (M8). E) Homogenous loess (L1L1) around 260 cm depth -poorly developed subangular blocky structure with carbonate impregnations. In places platy microstructure, partly destroyed by bioturbation (M4). F) Ag horizon around 280 cm depth - massive microstructure with weakly impregnated orthic Fe-hydroxyde nodules (M3). Abbreviations: cap = clayey silt capping, cc = carbonate coating, ci = carbonate impregnation, e = organo-mineral excrements, inf = infilling, lo = amorphous Fe-Mn hydroxides, n = Fe-Mn nodule, pl = platy microstructure, R = rock fragment. (For interpretation of the references to colour in this figure legend, the reader is referred to the Web version of this article.)

2.3.4 Variation in grain-size distribution and end-member modelling

The grain-size distribution of all samples is polymodal, with the main mode around 60–70 μm (Fig. 2.10A and B). The EM modelling algorithm is able to distinguish three components (EM-1, EM-2 and EM-3) that explain well the observed variability in grain-size distribution ($R^2 > 0.9$ for 95 % of the samples analysed, i.e. 248 out of a total of 261).

EM-1 is characterised by a unimodal distribution with the main mode at 68 μm (Fig. 2.10C). This subpopulation explains 49.2 % of the variance at Lautagne and 19.3 % at Collias respectively. EM1 is interpreted as coarse particles that were transported by wind, through saltation and short-term suspension at very low altitude during storm events (Tsoar and Pye, 1987; Vandenberghe, 2013).

EM-2 has a roughly bimodal distribution with one mode in the medium silt fraction (45 μm) and another in fine silt (16 μm). It represents 40.3 % of the variance at Collias and 33.0 % at Lautagne A. The coarse mode (45 μm), common in loess deposits, involves short-term transport over greater distances than EM-1 (Pye, 1995; Muhs and Bettis III, 2003; Li et al. 2018). Recent observations in China showed that dust of the same grain-size mode (~40 μm) is collected 10 m above the ground during spring and early summer (Sun et al. 2003). The finest mode (16 μm) corresponds to dust transported through long-term suspension in the atmosphere at high altitude (tens to hundreds of metres above the ground (Sun et al. 2003). Observations in the Célé oasis (China) showed that these two components (45 μm and 16 μm) could derive from a single local source (Lin et al. 2016).

EM-3 is poorly sorted and has a polymodal distribution with the main mode of 183 μm and three minor modes (82 μm , 15 μm and 3 μm) (Fig. 2.10C). EM-3 explains 40.4 % of the variance at Collias and 17.8 % at Lautagne A. The presence of medium to coarse sand and poor sorting indicate mixing of materials from different sources (in surface horizons especially by agricultural practices) and the addition of autochthonous materials into the aeolian sediments by slope processes. EM-3 has probably a polygenic origin (aeolian and colluvial). Fine grains (~3.0 μm mode) are represented by a tail in the grainsize distribution curves of all three subpopulations (Fig. 2.10C). This tail is sometimes considered as an artefact (Nottebaum et al. 2015), and is reported in most European and Asian loess deposits (Vandenberghe, 2013). The fine particles could indicate long-term suspension transport in the atmosphere

(“continuous background dust”) (Sun et al. 2002). Alternative hypotheses include: (i) fine particles transported by wind as aggregates (Újvári et al., 2016a); (ii) clay adhesion on coarser grains (Qiang et al. 2010) or (iii) pedogenic processes (Bronger and Heinkelé, 1990; Sun et al. 2000). Both sequences show the same overall pattern of EM distribution (Fig. 2.11), i.e. glacial loess deposits are dominated by the coarse component (mainly EM-1), whereas interglacial and interstadial palaeosol horizons are dominated by the fine component (EM-2). Topsoils and bedded loess that have undergone reworking are characterised by a higher EM-3 score.

2.3.5 Chronological data

2.3.5.1 Luminescence ages

Table 2.2 lists the luminescence ages for the two sections. Additional information is provided in Appendix B.

2.3.5.2 Luminescence characteristics and equivalent doses

All investigated quartz samples showed overall acceptable brightness and reproducibility (Appendix B). However, compared to the samples from Collias, the quartz fine grain (ca 10^6 grains per aliquot) samples from Lautagne appeared rather dim, and additional tests on the coarse grain fraction (ca 10^2 grains per aliquot) were not continued due to the low signal intensity.

Collias and Lautagne, showed broad D_e distributions but without any obvious pattern. In the case of the samples from Collias this scatter may reflect poor bleaching, dose rate heterogeneities and/or sediment mixing. The presumed short transport distance from the Rhône Valley may not have yielded a full luminescence signal depletion. More likely, however, post-depositional mixing in conjunction with multiple short-distance erosion and deposition events occurred. Slope-wash and/or creep processes are evidenced by sand-sized and even fine-to medium-gravel sized particles, particularly in the L1L2 unit and the colluvial layer at the bottom of L1L1 at Collias (Fig. 2.5). Syn- and post-sedimentary bioturbation is also likely to have been involved.

For the samples from Lautagne (Fig. B2.24), the scatter is rather large for fine grain quartz samples with ca 10^6 grains per aliquot and the expected averaging effects. However, the inter-aliquot scatter is dominated by the individual errors. Thus, these aliquots represent a common central dose.

2.3.5.3 Dose rate results

Th and K concentrations are comparable for the sites Collias and Lautagne (Appendix B). In both sites, the Th and K concentrations show a trend towards higher values in the lower Bw

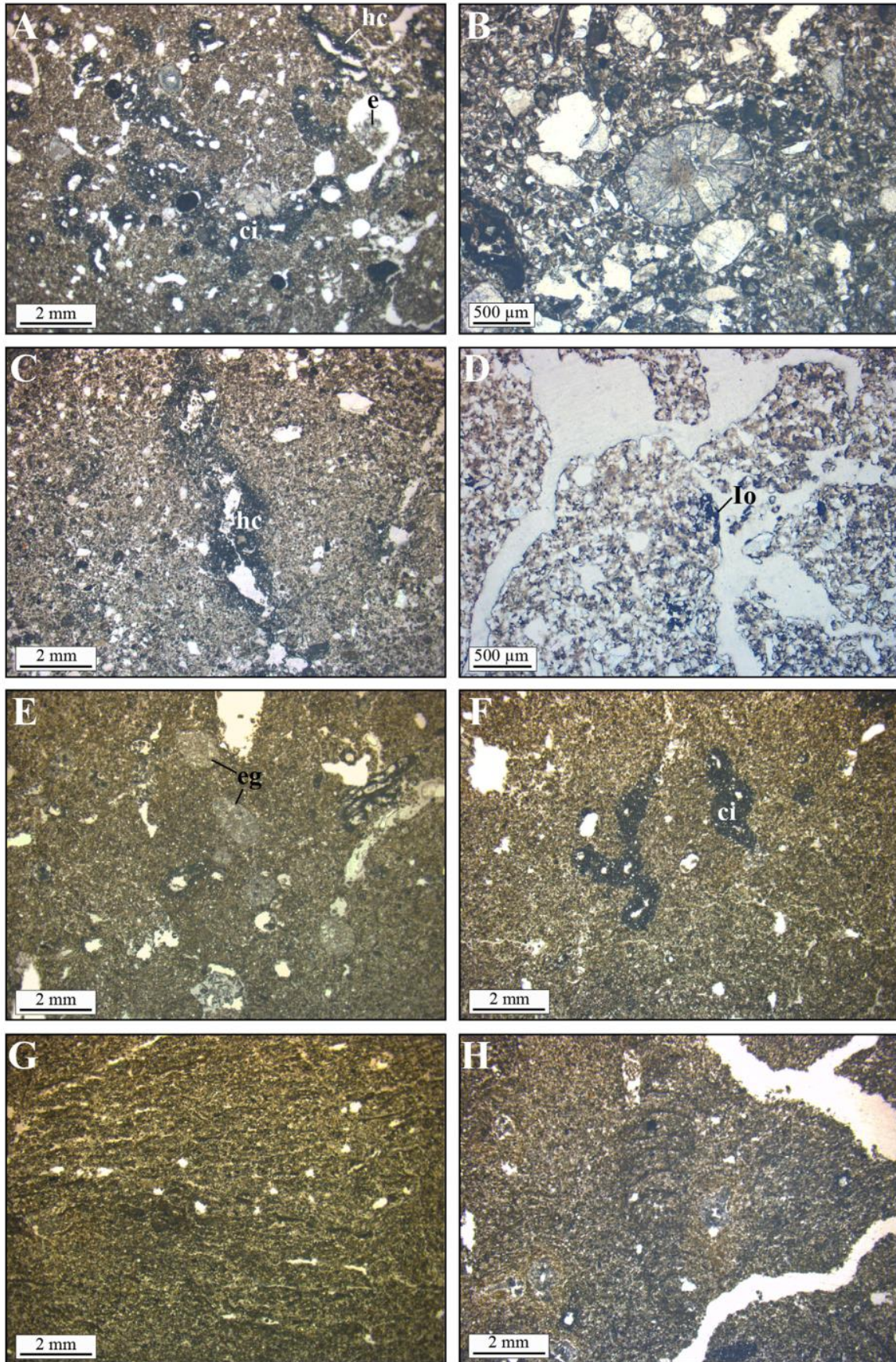


Figure 2.9: Microfacies details of selected samples from Collias (A, B, C and D) and Lautagne A (E, F, G and H) sections (see Figs. 2.4 and 2.5) (plane-polarized (PPL)). A) L1L1 loess around 90 cm depth -

dense incomplete micritic infillings and hypocoatings, and loose infilling of channels by porous organo-mineral microaggregates (M1). B) Brown Bwk horizon around 320 cm depth - earthworm granule showing radially arranged sparite crystals (M3). C) Calcareous sandy loess (L1L2) around 400 cm depth - calcite hypocoating around channel (M4). D) Rubefied Bw horizon around 680 cm depth – Fe-Mn hypocoatings and quasicoatings (M8). E) L1L1 loess around 110 cm depth - earthworm granules (M7). F) Homogenous loess (L1L1) around 170 cm depth - calcitic impregnation (M6). G) Homogenous loess (L1L1) around 260 cm depth - platy microstructure (M4). H) Ag horizon around 280 cm depth - crescent fabric in silty groundmass, resulting from bioturbation by soil mesofauna (M3). Abbreviations: ci = carbonate impregnation, e = organo-mineral excrements, eg = earthworm granule, Hc = calcite hypocoating, lo = amorphous Fe-Mn hydroxides. (For interpretation of the references to colour in this figure legend, the reader is referred to the Web version of this article.)

horizons (potential Th adsorption on clay particles). We found radioactive disequilibria in the U-decay chain at both sites. However, the onset of these disequilibria could not be determined, leading us to calculate an average value of the U concentration (see Appendix B).

2.3.5.4 Luminescence ages results

The OSL ages obtained for the loess deposits at Collias range from ~100 ka to ~25 ka. Age inversions overlap within uncertainties and are not considered significant. While the general pattern is similar for ages calculated as mean \pm standard error of the mean (Fig. B2.29, displayed in blue) and those using the 'baSAR' modelling approach (Fig. B2.29, displayed in red), the Bayesian approach leads to significantly older ages in the lower part of the section. Nevertheless, given the luminescence ages and D_e values close to commonly accepted saturation values for quartz luminescence measured in the UV wavelength region, an age underestimation cannot be excluded, and the values must be interpreted cautiously.

The OSL ages obtained for the loess of the Lautagne A sequence range from 31.1 ± 2.4 ka to 7.5 ± 0.6 ka, and the ages are stratigraphically consistent within uncertainties (Fig. B2.30). Figure 2.6 shows that the OSL estimates are consistent with the radiocarbon ages obtained from gastropod shells. Only samples BDX18944 (7.5 ± 0.6 ka) and DeA-18281 (12.1–12.6 ka cal. BP) appear significantly underestimated and were not considered in the Bayesian age model. We assume that these young ages reflect an admixture of recent soil material through bioturbation.

2.3.5.5 Radiocarbon ages

A total of 27 radiocarbon dates were determined from unit L1L1, including 23 at Lautagne A and 4 at Collias (Table 2.3).

At Lautagne A, the ages from *Pupilla muscorum* shells appear to be consistent with the stratigraphy and the OSL ages (Fig. 2.12B), while those from earthworm calcite granules show major stratigraphic inversions and younger ages (Table 2.3). The inconsistency of the latter can be explained by the following factors:

(i) lack of precise identification of the earthworm species that secreted these granules. Canti and Pearce (2003) show that some species (e.g. *Apporrectodea icteria*) deposit their granules at some depth, unlike other species (*Lumbricus terrestris* or *L. rubellus*) which preferentially release them on the soil surface. According to these authors, granules larger than 0.4 mm (i.e. the sieve mesh used in this study) can be produced only by a few earthworm species (mostly the genus *Lumbricus*). However, this statement needs to be confirmed as this study was based on current populations in the UK that are known to have smaller body sizes than those in more southerly latitudes, which acted as refuge areas during glacial period (Mathieu and Davies, 2014);

(ii) post-depositional movements resulting in granule redistribution along the soil profile. Earthworms commonly transport surface material (coarse sand, leaves, twigs) to the basal chamber of their burrows that can be located at up to 2 m depth (Canti, 2007). Syn-sedimentary bioturbation by roots may have been also involved.

Consequently, the ages from earthworm granules were excluded from the analysis to build the age-depth model of the sequence. However, only two dates (Ly-21291 and Ly-51292) among the 14 dates obtained from earthworm granules from the primary loess units yielded post-glacial ages. Thus, although the granules were not in a correct stratigraphic location, they provide reliable information on the age of loess deposition as a whole. Therefore, the ages obtained from Lautagne A (Table 2.3) and other loess sections (Table 2.4) were kept to calculate the age distribution of the Rhône Valley loess (see section 2.4.5).

2.3.5.6 Collias

The sediment from the upper part of the S1 pedocomplex yielded ages (1σ) between ca 87.1 ± 6.5 ka and 82.8 ± 7.2 ka (Fig. 2.12A), suggesting that it was deposited during the Early Glacial. The lower loess (L1L2) was deposited between 82.8 ± 7.2 ka and 55.1 ± 4.4 ka, i.e. during the Lower Pleniglacial (~MIS 4–very beginning of MIS 3), and the upper loess (L1L1) between 38.5 ka and <23.8 ka, during the Upper Pleniglacial (late MIS 3–MIS 2). The Bwk horizon (L1S1) corresponds to the Middle Pleniglacial (~MIS 3). Discrepancies between ^{14}C and OSL ages at the top of L1L1 prevent an accurate estimation of the end of loess sedimentation.

2.3.5.7 Lautagne A

According to a posteriori ages, the L1L1 loess of Lautagne A (4.60 m–0.95 m depth) accumulated between ~31 ka and 18 ka (Fig. 2.12B), during the Greenland Stadials GS-5.2 to GS-2.1 (Rasmussen et al. 2014). This period was interspersed with the Greenland Interstadials GI-5.1 to GI-2.1, favourable for the genesis of palaeosols. As suggested by the age-depth model provided by ChronoModel, the incipient Ag-BC palaeosols within the L1L1 loess likely

correlate with the interstadials. The 95.4 % confidence interval of the a posteriori ages (27.6–27.2 ka and 27.7–27.3 ka obtained for the most developed palaeosol P2 overlaps with the interstadial GI-3. With less certainty, P1 may be correlated to GI-2 and P3 to GI-4.

2.4 Discussion

2.4.1 Eemian interglacial and Early Glacial pedocomplex (S1)

The basal pedocomplex S1 at Collias is characterised by intense reddening, high clay content, chemical weathering, decalcification and precipitation of secondary carbonates in the underlying horizon, forming an indurated Ckm horizon (Fig. 2.5). Fe-Mn hypocoatings on the ped faces suggest occasional waterlogging (Figs. 2.8C and 2.9D). These characteristics are typical of red Mediterranean soils and testify a forest environment with strong seasonal moisture contrast leading to reddening (Yaalon, 1997; Fedoroff and Courty, 2013; Durn et al. 2018a).

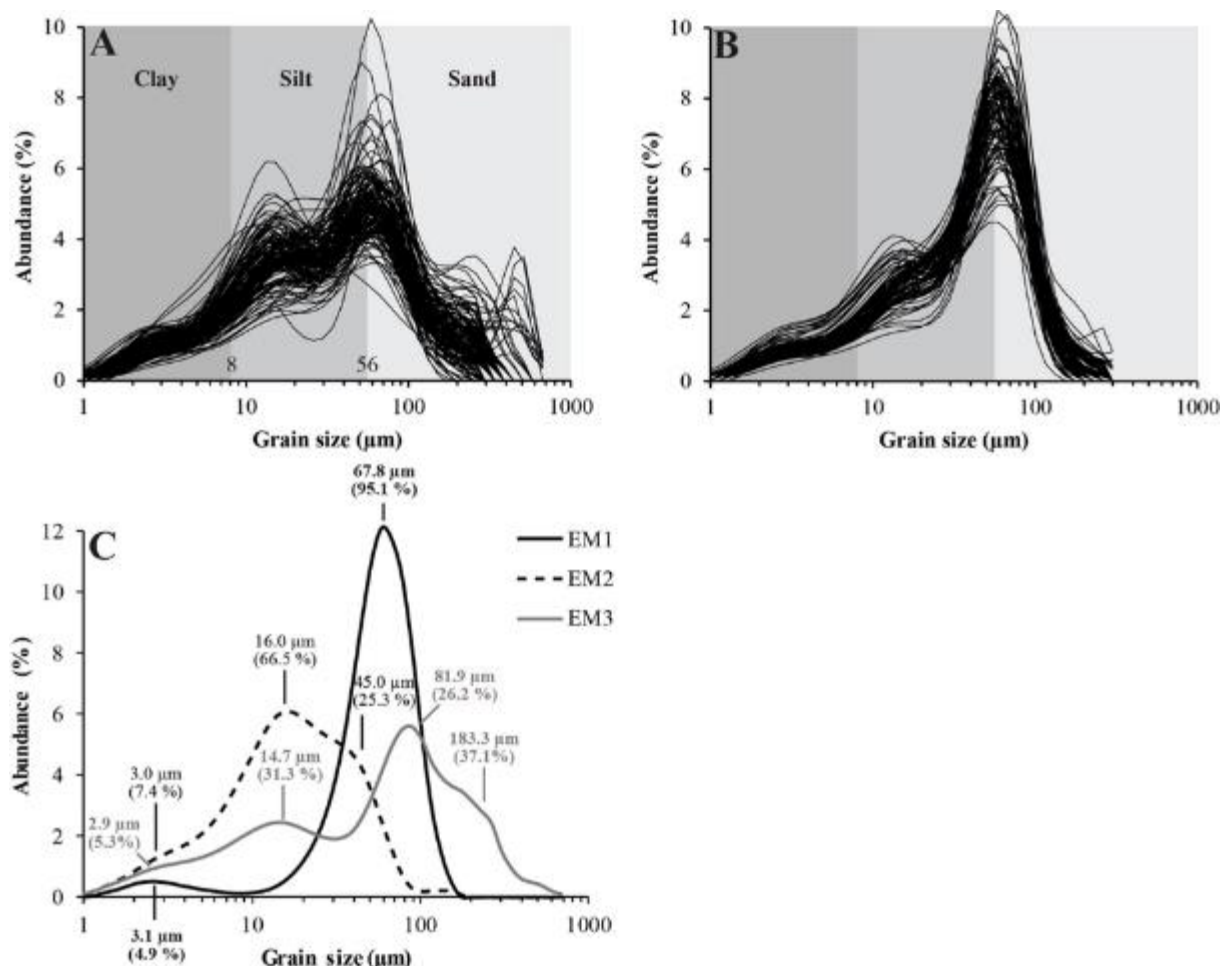


Figure 2.10: Grain-size distribution of the samples from Collias (A) and Lautagne A (B). The upper limits of the grain-size classes used here are: 8 µm for clay and 56 µm for silt. C) Endmember modelling results of the grain-size dataset of both sections. The main modes of the three end-members were determined by parametric curve-fitting using the R package 'mixdist' (Macdonald and Du, 2015).

Considering the uncertainties associated with the OSL ages (82.8 ± 7.2 ka and 87.1 ± 6.5 ka), the material, in which the upper Bwk horizon of the pedocomplex formed, is attributed to the Early Glacial (MIS 5a-d). The underlying Bw and Ckm horizons can thus be correlated with the Last Interglacial (Eemian, MIS 5e) (Figs. 2.5 and 2.12A).

2.4.2 Lower Pleniglacial colluvium and bedded calcareous sandy loess (L1L2)

The Lower Pleniglacial started with the emplacement of loessic colluvium, comprising scattered gravel and reddish lenses containing charcoal fragments (Fig. 2.6). The colluvium reflects reworking of the red Interglacial/Early Glacial Bw horizons exposed along the slope.

Then, increased aridity and wind intensity led to the deposition of coarse-grained calcareous loess that has been redistributed and sorted by slopewash during rainstorm and/or snowmelt (Figs. 2.6 and 2.11A). The coarse texture indicates abundant sand transport from the sources, probably from the bed of the Rhône River (Bosq et al. 2020a) since the particle size of the aeolian deposits becomes coarser towards this river (Fig. 2.4B). The presence of lenses of calcareous rock debris (Figs. 2.7A and 2.7B) indicates active frost weathering of limestone outcrops. Slopewash during rainstorms or snowmelt during summer are thought to be the main factor involved in the deposition of these lenses.

The OSL ages around 55 ka (BDX21325: 55.5 ± 4.4 ka and BDX21326: 55.1 ± 4.1 ka) suggest that loess deposition took place during late MIS 4 and/or the very beginning of MIS 3 (Fig. 2.12A). These periods are characterised by an increase in dust concentration in the Northern Hemisphere records, including the Greenland ice record (NGRIP; Ruth et al. 2003) and the Eifel Laminated Sediment Archive (ELSA) lake record in Germany (Seelos et al. 2009; Sirocko et al. 2016).

2.4.3 Middle Pleniglacial brown Bwk horizon (L1S1)

The brown Bwk horizon shows slight dissolution of carbonates, increased clay content and an increase in the concentration of pedogenic ultrafine magnetic grains. The lack of significant variation of weathering indices (CPA, Rb/K) indicates moderate silicate weathering (Fig. 2.5). Large rhizoliths formed below due to carbonate leaching and reprecipitation. The carbonate rhizoliths within the brown horizon must result from an interplay between pedogenesis and moderate loess accumulation rates. Thereby, the loess input led to an upward movement of the soil surface and addition of primary carbonates, whereas pedogenesis involved leaching of these fresh inputs and accumulation of secondary carbonates within the lower part of the brown horizon (Fig. 2.7B). Thus, this brown Bwk horizon implies a decrease (possibly multiphased) in loess sedimentation and a moister climate favourable to the development of vegetation. The soil has been truncated by erosion and covered by colluvial material.

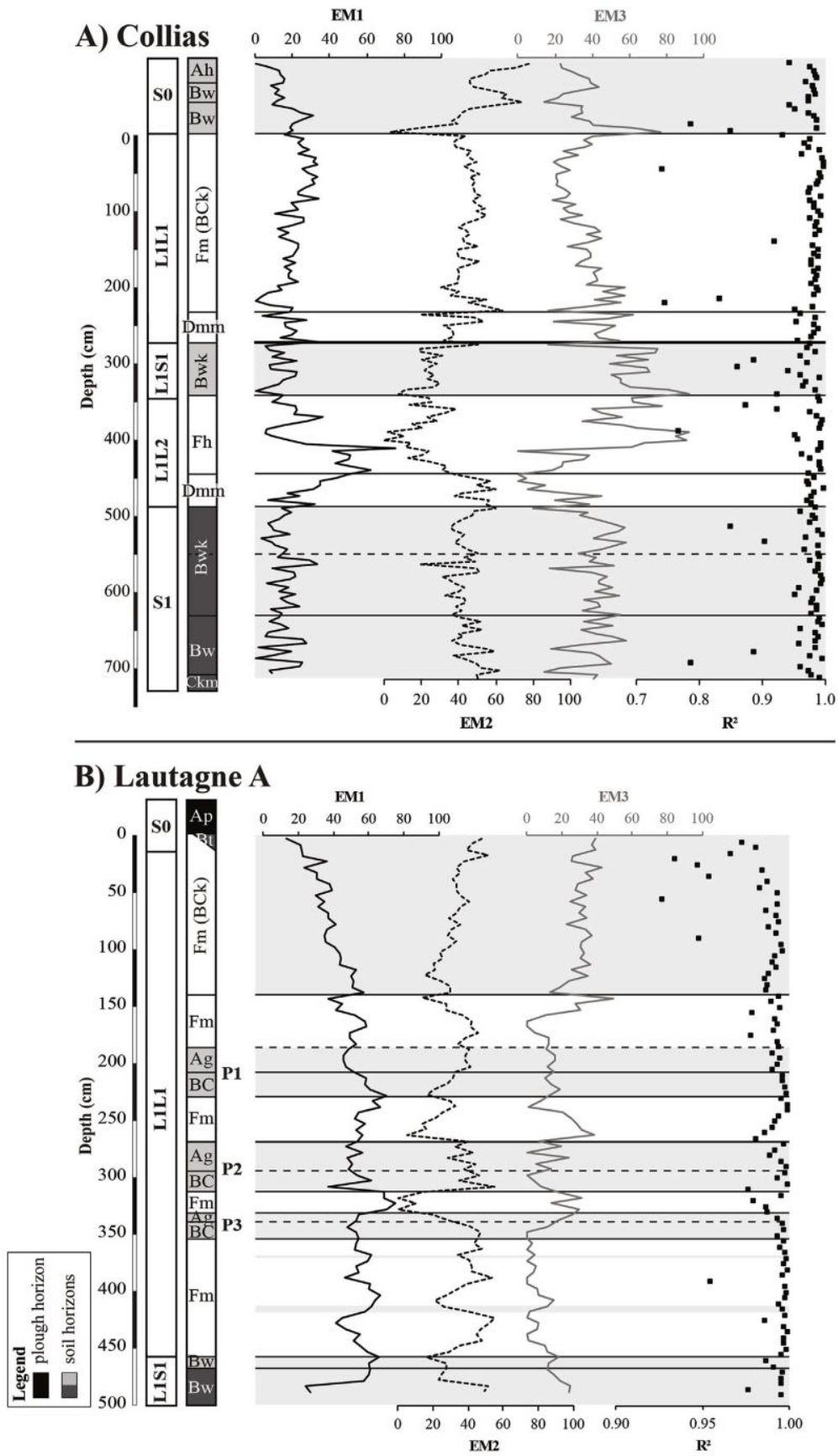
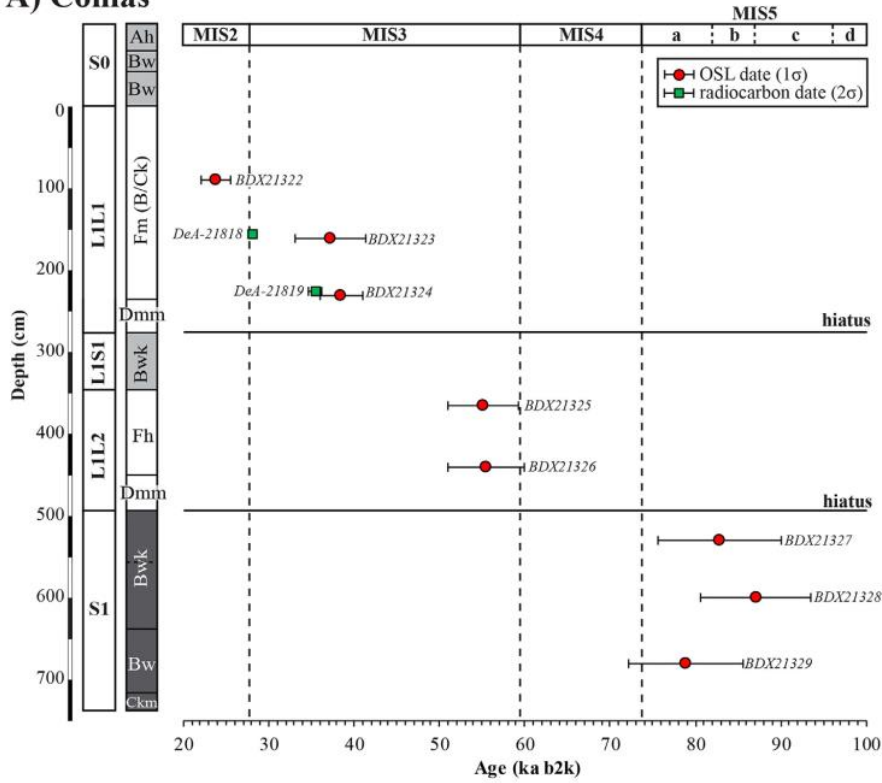


Figure 2.11: Contribution of the three end-members and coefficient of determination (R^2) for each sample from the sections Collias (A) and Lautagne A (B).

A) Collias



B) Lautagne A

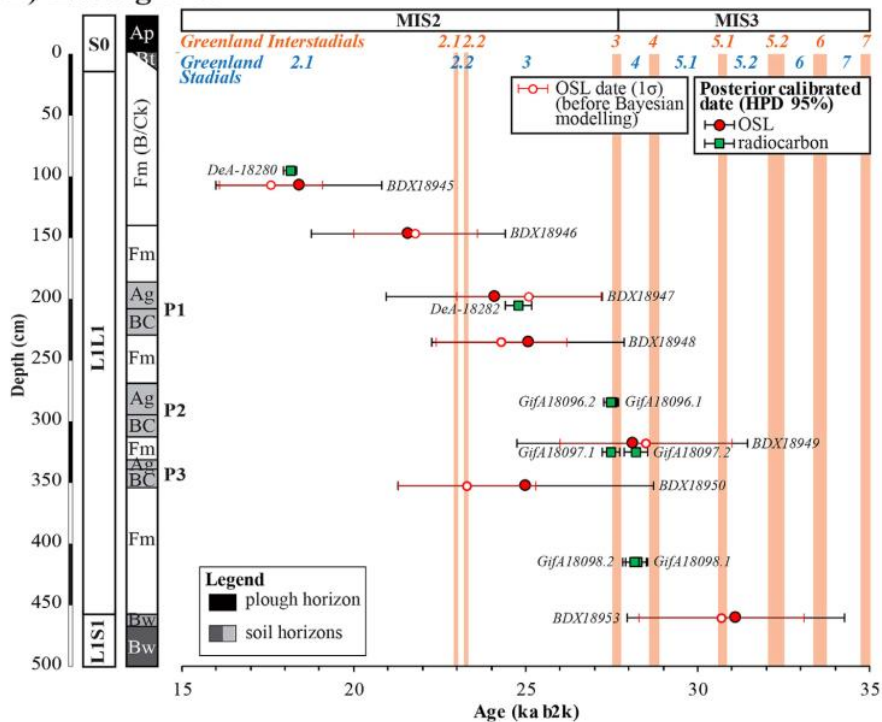


Figure 2.12: Chronological data. A) Distribution of the OSL and radiocarbon ages of the section Collias obtained in this study. B) Posterior distribution (95 %) of the ages for each sample derived from the Bayesian age model of the Lautagne section using ChronoModel. The OSL ages are generally consistent with the ^{14}C ages, although they have large error. Greenland interstadials from the NGRIP record on the GICC05 age model (Rasmussen et al. 2014) are indicated in orange. (For interpretation of the references to colour in this figure legend, the reader is referred to the Web version of this article.)

According to our chronological data, the soil to which the truncated Bwk horizon belonged formed between 55.1 ± 4.1 ka and 38.5 ± 2.5 ka (Fig. 2.12A), i.e. within a long interval during MIS 3.

Table 2.4: AMS radiocarbon ages of loess samples from other locations in the Rhône Valley (calibration by use of IntCal13 according to Reimer et al. 2013).

Sample name	Laboratory code	Material	^{14}C (a BP) (1σ)	Unmodeled ^{14}C a	Reference
				cal. BP (2σ) Min - Max	
Lautagne B - 105/100	GrA-68025	earthw.calcite granules	13250 ± 60	15722–16134	this study
Lautagne B - 165/160	GrA-68024	earthw.calcite granules	17000 ± 90	20221–20763	this study
Lautagne B - 260/255	GrA-68023	earthw.calcite granules	15340 ± 70	18440–18775	this study
Mauves Sud 1	Ly-14666	earthw.calcite granules	26870 ± 250	30651–31284	this study
Mauves Sud 2	Ly-14667	earthw.calcite granules	29370 ± 350	32698–34171	this study
Saint-Paul-les-Durance 3	Ly-14670	earthw.calcite granules	22880 ± 160	26776–27536	this study
Saint-Paul-les-Durance 4	Ly-14671	earthw.calcite granules	13030 ± 60	15324–15827	this study
Collias 5	Ly-14668	earthw.calcite granules	27540 ± 720	30976–31918	this study
Saint-Désirat 2	Ly-14669	earthw.calcite granules	21500 ± 140	25542–26043	this study
Saint-Péray 3	Ly-15407	earthw.calcite granules	19490 ± 100	23112–23784	this study
Sathonay 1	Ly-15408	shell (<i>S. oblonga</i>)	20020 ± 100	23809–24360	this study
Sathonay 2	Ly-15409	shell (<i>S. oblonga</i>)	22630 ± 140	26543–27316	this study
Soyons 1	Ly-15410	shell (<i>S. oblonga</i>)	18660 ± 90	22344–22769	this study
Soyons 2	Ly-15411	shell (<i>S. oblonga</i>)	27220 ± 230	30876–31456	this study
Bouzil	Ly-390/AA-23353	charcoal	23570 ± 200	27390–28031	Bazile (2007)
Mirabeau 11	Poz-17284	charcoal	11420 ± 140	13040–13547	Ollivier (2006)
Géménos-Aubagne	AA-16474	charcoal	32230 ± 490	35023–37596	Magnin (2014)

2.4.4 Upper Pleniglacial loess (L1L1)

2.4.4.1 Loess deposits

The L1L1 loess reaches more than 2 m thickness at Collias and 4 m at Lautagne A (Fig. 2.7). Similar homogeneous yellowish, up to 5 m thick loess deposits were observed in many outcrops along the Rhône Valley (Bosq et al. 2018).

They share common characteristics with the loess of the southern part of the Carpathian basin (e.g. Antoine et al. 2009b; Bokhorst et al. 2009; Marković et al. 2009; Novothny et al. 2011), including (i) coarse texture, (ii) lack of well-developed palaeosols; (iii) absence of structures of periglacial origin (ice-wedge pseudomorphs, soil wedges) except for platy microstructure; (iv) absence of laminated deposits of niveo-aeolian origin such as those commonly observed in NW Europe (Antoine et al. 2016; Lehmkuhl et al. 2016; Zens et al. 2018) and (v) abundant syn-sedimentary bioturbation.

The EM-1 subpopulation, which is predominant in the samples from Lautagne A (Fig. 2.11B), indicates a relatively limited transport distance, in the order of a few kilometres to tens of

kilometres. This fraction originates from the Rhône riverbed, where the particles derived from the AIS were subjected to deflation. Riparian vegetation was probably involved in the trapping of wind-transported particles (e.g. Bosq et al. 2018).

The GSI peaks are interpreted as reflecting periods of increasing wind carrying capacity (Vandenberghe et al. 1985; Antoine et al. 2009a; Schirmer, 2016). According to the chronological data of Lautagne (Fig. 2.12B), the highest GSI values occurred during GS-3 and GS-4, whereas they slowly decreased during GS-2.1 (Fig. 2.6).

2.4.4.2 Incipient palaeosols

Weakly developed palaeosols (P1 to P3) are visible within the L1L1 loess at Lautagne A (Fig. 2.6). The Ag horizons are finer-grained than primary loess. They exhibit hydromorphic features and low organic matter content. The abundant carbonate concretions are interpreted as resulting from secondary carbonate precipitation during the accumulation of overlying loess, favoured by the finegrained texture. The BC horizons have higher clay content, slight carbonate depletion and a slightly darker and reddish colour.

Their genesis indicates short periods of decrease or cessation of loess sedimentation due to milder climate. The hydromorphic features in the topsoils can be explained by two hypotheses, which are not mutually exclusive:

(1) The soils developed during a period of climatic improvement associated with increased precipitation and snow accumulation. Waterlogging in the topsoil resulted from snow cover and subsequent snowmelt above still frozen ground that did not allow for meltwater infiltration. Permafrost was absent in the southern part of France during the coldest periods of the Pleistocene (Andrieux et al. 2016) and waterlogging occurred only during limited periods each year.

(2) Reducing conditions in the topsoil horizon occurred upon burial, as a consequence of soil organic matter degradation by soil microorganisms. Unlike the humic horizons described in the loess sections of continental Eastern Europe (e.g. Veres et al. 2018), soil-forming conditions in less continental regions led to the formation of poorly condensed organic matter with low “black carbon” content (Schmidt and Noack, 2000; Eckmeier et al. 2007;), which was less resistant to degradation.

2.4.5 Regional chronology

In addition to the ages obtained in this study, we compiled the ages available for the loess deposits in southeast France from the literature to assess the chronology of the main regional sedimentation phases. Overall, 21 OSL dates on quartz and 43 ¹⁴C dates on gastropod shells, earthworm granules and charcoal were selected (Tables 2.2–2.5). The age distribution was

calculated using the Kernel Density Estimation (KDE) (Vermeesch, 2012), which helps to identify how ages cluster. The clusters provide a chronological estimate of the main periods of dust accumulation, assuming that sampling was equally distributed throughout the loess sequences. Although the analysis must be considered preliminary because of the limited number of available dates ($N = 64$), the comparison of the KDE graph with the modelled AIS volume (expressed in metres of sea level equivalent) (Seguinot et al. 2018) together with the Rhine (Preusser et al. 2011) and the Tagliamento (Monegato et al. 2007) glacial systems for which robust chronological constraints are available on the one hand, and the dust concentration recorded in the NGRIP ice core (Ca^{2+} in ppb) on the other hand, lead to the following conclusions (Fig. 2.13):

Table 2.5: OSL ages of loess samples from other locations.

Sample name	Laboratory code	Material	Age ka (1σ)	Reference
Les Croisieres - UPS30	GdTL-1878	Quartz (125–200 μm)	12.0 \pm 0.5	Varenes et al. (2015)
Les Croisieres - UPS9	GdTL-1877	Quartz (125–200 μm)	12.2 \pm 0.8	Varenes et al. (2015)
Garons ZAC Mitra V - PR116	GdTL-2839	Quartz (45–63 μm)	27.0 \pm 1.5	Laroche et al. (2020)
Favary - PR1109	GdTL-2190	Quartz (45–63 μm)	12.7 \pm 0.7	Thirault et al. (2020)
Lautagne B - OSL8 180 cm	BDX18951	Quartz (4–11 μm)	26.3 \pm 2.2	This study
Lautagne B - OSL9 240 cm	BDX18952	Quartz (4–11 μm)	23.4 \pm 1.8	This study

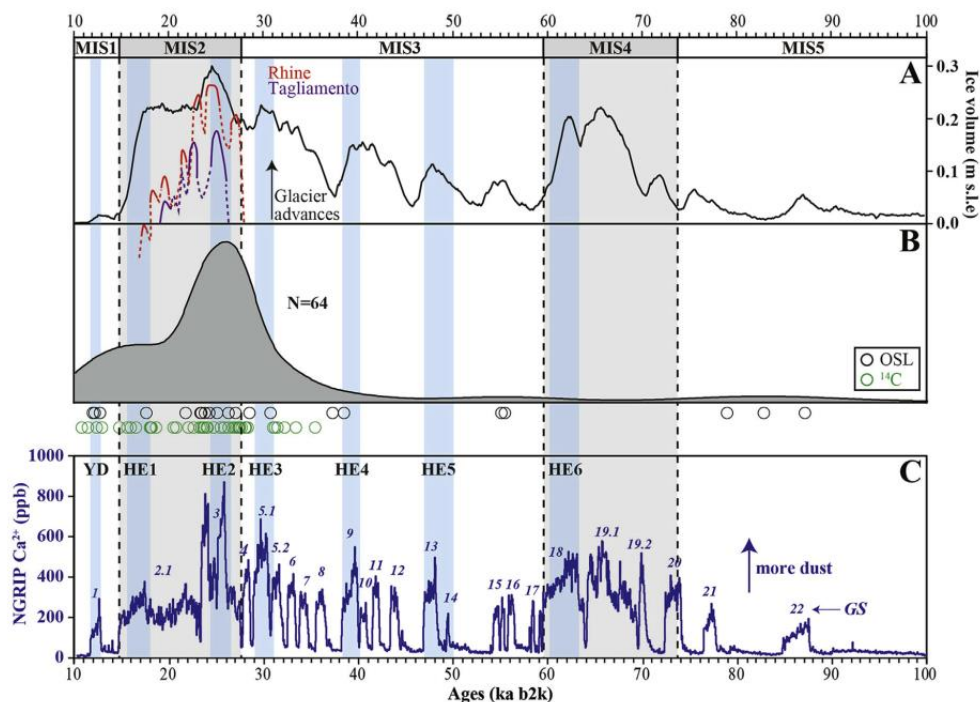


Figure 2.13: A) Total AIS volume through the Last Glacial cycle (100–10 ka) from a recent simulation using the Parallel Ice Sheet Model (PISM) with climate forcing derived from WorldClim and the ERA-Interim reanalysis (Seguinot et al. 2018). Modelled ice volume is expressed in meters sea level

equivalent (m s.l.e.). Fluctuations of the Rhine (red) (Preusser et al. 2011) and Tagliamento (purple) (Monegato et al. 2007) glaciers. B) Kernel Density Estimation (KDE) of ages for the OSL- and radiocarbon-dated loess from the Rhône Valley (this study, Ollivier, 2006; Bazile, 2007; Magnin, 2014; Varennes et al. 2015; Laroche et al. 2020; Thirault et al. 2020). The KDE bandwidth used is 2.5 ka. C) NGRIP Ca²⁺ curve over the last 100 ka according to the revised Greenland Ice Core Chronology (GICC05) proposed by Rasmussen et al. (2014). The chronological intervals for the Younger Dryas (YD) period and Heinrich Events (HEs) are depicted in blue. They are taken from Sanchez Goñi and Harrison (2010). The chronological limit of each MIS is also taken from Sanchez Goñi and Harrison (2010). (For interpretation of the references to colour in this figure legend, the reader is referred to the Web version of this article.)

(1) For the period before ca 40 ka, only a few dates (N = 5) are available, which suggests weak dust accumulation. Surprisingly, no age falls with certainty into MIS 4, a cold period that was marked by substantial AIS development. The reason behind remains unclear (weak deposition, subsequent erosion, loess recycling?).

(2) For the Upper Pleniglacial, the age distribution shows an approximate synchronicity between loess deposition and AIS fluctuations. The peak of loess ages at 28–24 ka, i.e. GS-3, coincides with the maximum AIS volume (26–23 ka, Preusser et al. 2011; Luetscher et al. 2015; Monegato et al. 2017; Ivy-Ochs et al. 2018; Seguinot et al. 2018) and the highest CSI values. This period includes Heinrich Event 2 (HE-2, Sanchez Goñi and Harrison, 2010), which was responsible for cold and arid conditions on the European continent (Fletcher et al. 2010; Duprat-Oualid et al. 2017).

(3) During the late Last Glacial Maximum (late LGM) (ca 23–19 ka, Clark et al. 2009), the AIS entered a recessional phase and lost 80 % of its volume at 17.5 ka (Ivy-Ochs et al. 2008; Monegato et al. 2017). Following the deglaciation during GS-2, a significant glacial re-advance (not visible in the simulation) occurred during the Gschnitz stadial at 17–16 ka, in response to the HE-1 cooling (Ivy-Ochs et al. 2006, 2008; Ivy-Ochs, 2015). Accordingly, the age density decreases sharply during GS-2, while aeolian accumulation may have resumed somewhat during HE-1. Overall, GSI values gradually declined over this period.

(4) The aeolian activity persisted until the Younger Dryas cooling (GS-1) at 12.9–11.7 ka.

These preliminary results suggest that the peak of dust accumulation in the Rhône Valley was concomitant with the maximum AIS extension. The link between these two phenomena could reside in the modulation of the amount of glacially abraded fine particles by the advances and retreats of the ice sheet. These particles, which were transported by the Rhône River and its tributaries, and then remobilised by deflation, formed the main source of dust as shown by Bosq et al. (2020a).

Therefore, glacier dynamics was probably the primary factor influencing loess deposition, whereas millennial climate fluctuations (HEs), including periods of enhanced dryness and associated changes in vegetation acted as a modulator of the primary signal.

2.5 Conclusions

The high-resolution multi-proxy sedimentological and chronostratigraphical analysis of two loess sections in the Rhône Valley allow to draw the following conclusions:

(1) A ~8 m thick loess record of the Last Climate Cycle is preserved at Collias. Loess deposition occurred during the Lower and Upper Pleniglacial (L1L2 and L1L1). The loess overlies a thick red pedocomplex (S1) developed during the Last Interglacial and the Early Glacial, similar to those observed elsewhere in southern and southeastern Europe (e.g. Fedoroff and Courty, 2013; Durn et al. 2018a). A brown Bwk horizon (L1S1) developed during the Middle Pleniglacial. In the Lautagne section, the ~5 m thick loess deposits provide a detailed record of the Upper Pleniglacial.

(2) The chronological data (AMS ^{14}C and OSL) show that the main phase of loess deposition (L1L1) corresponds to the stadials GS-5 to GS-2. The loess is coarse, calcareous and is interspersed with three incipient palaeosols at Lautagne A. These palaeosols are correlated with the Greenland Interstadials GI-4 to GI-2.

(3) At a regional scale, the numerical ages obtained on the upper loess (L1L1) range between ca 38.5 ka and 12 ka with a main peak at 28–24 ka, which coincides with the maximum AIS advance.

At a European scale, the aeolian systems composed of coversands and loess formed disconnected geographical units, each characterised by specific regional environmental conditions (i.e. regionally varying temperature, precipitation, and vegetation). It thus seems plausible that the phases of aeolian accumulation were not strictly synchronous across Europe, because the controlling factors (i.e. sediment availability, soil moisture, permafrost) varied considerably, both in time and space. This hypothesis remains, however, to be studied in more detail.

Declaration of competing interest

The authors declare that they have no known competing financial interests or personal relationships that could have appeared to influence the work reported in this paper.

Acknowledgement

This research was conducted in the PACEA laboratory with the financial support of the LaScArBx (research program of the Agence Nationale de la Recherche ANR-10-LABX-52), involving the University of Bordeaux and the University of Bordeaux-Montaigne. The preparation of the samples from Lautagne was greatly supported by the luminescence team from the Justus-Liebig University of Giessen (head: Prof Dr Markus Fuchs), namely Veit van Dienenhoven and Urs Tilmann Wolpert, who helped out in times of need. The preparation of

the samples from Collias was made possible by the luminescence team from the University of Bayreuth (head: Dr Christoph Schmidt) who gave us access to their sieving equipment. The remaining sample preparation in Bordeaux was supported by Julie Faure and Pierre Bidaud. Additional support was also provided by the Institut national de recherches archéologiques Préventives (Inrap). C. Ronco and E. Morin who provided us an access to the archaeological excavations of Lautagne are warmly acknowledged. We also acknowledge the archaeologists who conducted the excavations and survey of Garons Mitra V, Soyons and Saint-Péray, particularly M. Laroche, J.-M. Lurol, B. Gely, J.-M. Le Pape, F. Derym. We would like to thank M. Rué, C. Recq, A. Ajas and J.-L. Brochier for providing us with their OSL dating results. We warmly thank Lee Drake for his invaluable help in calibration of the ED-XRF portable Bruker Tracer 5i. Finally, the two reviewers, F. Lehmkuhl and D.-D Rousseau are acknowledged for their valuable comments.

Appendix–Supplementary data

Supplementary data to this article can be also found online at <https://doi.org/10.1016/j.quascirev.2020.106473>.

Appendix A

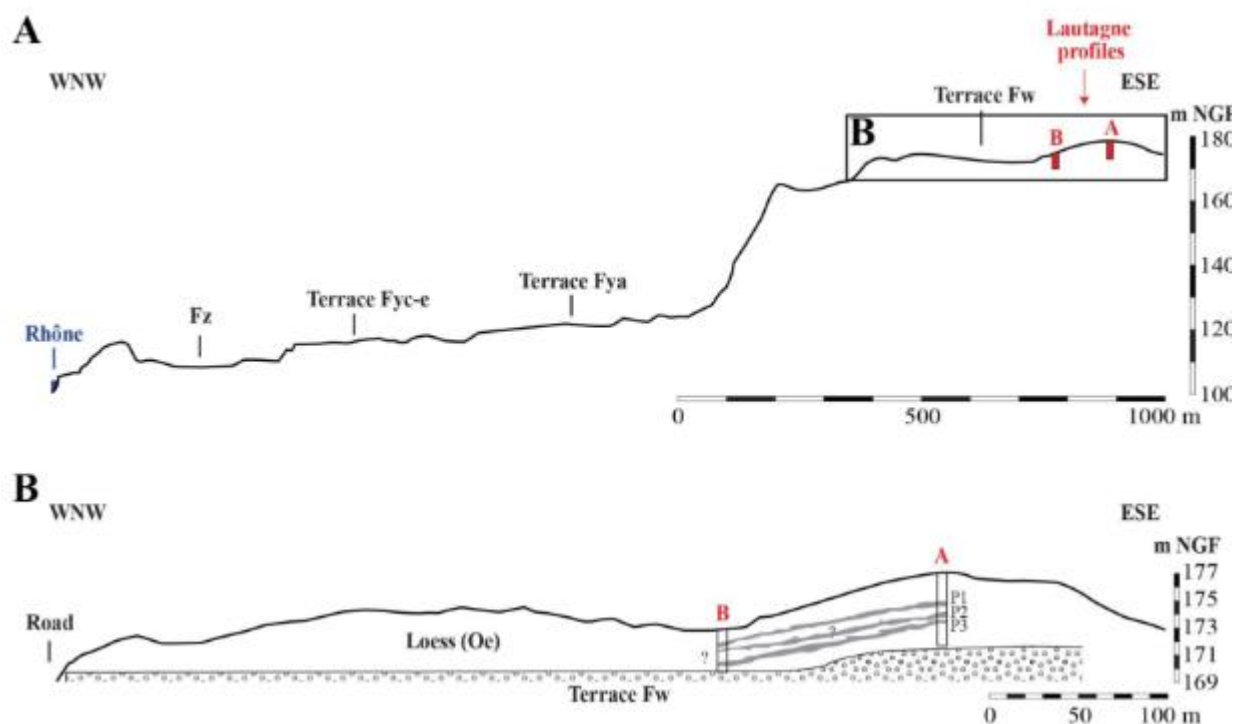


Figure A2.14: A) WNW-ESE topographic cross-section of the left bank of the Rhône River Valley highlighting the fluvial terraces according to the 1:50.000 geological map (<http://infoterre.brgm.fr/>) and the location of Lautagne profiles (A and B) (topography according to Google Earth Pro 2018). B) Stratigraphic correlations between the two profiles Lautagne A and B (palaeosols P1, P2 and P3 are shown in grey colour).

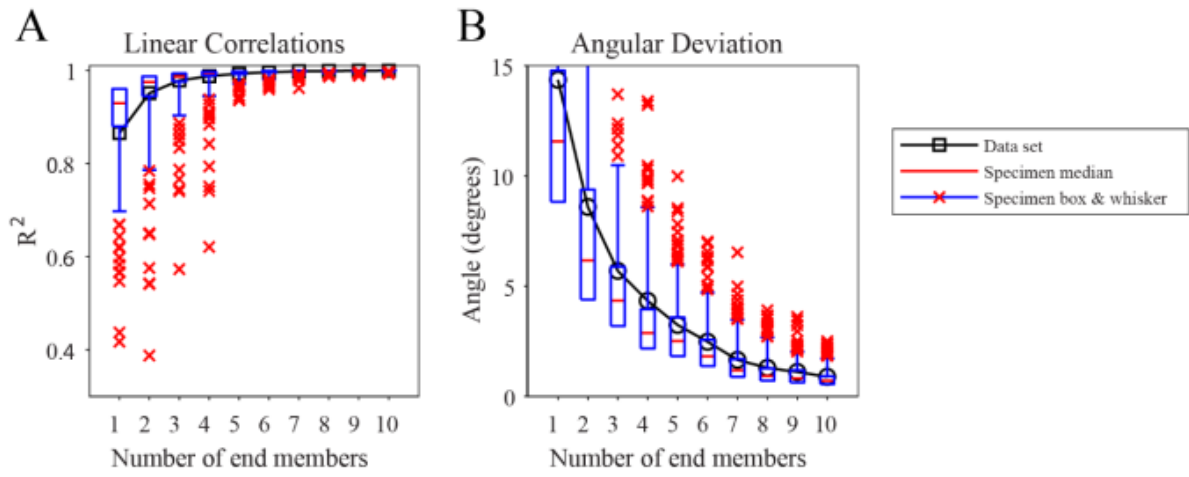


Figure A2.15: (A) Correlation coefficient (R^2) and (B) angular deviation goodness-of-fit statistics for various numbers of end members provided by grain size modelling. The red crosses represent outlying specimens (i.e. specimens that lie outside of the 95 % coverage interval).

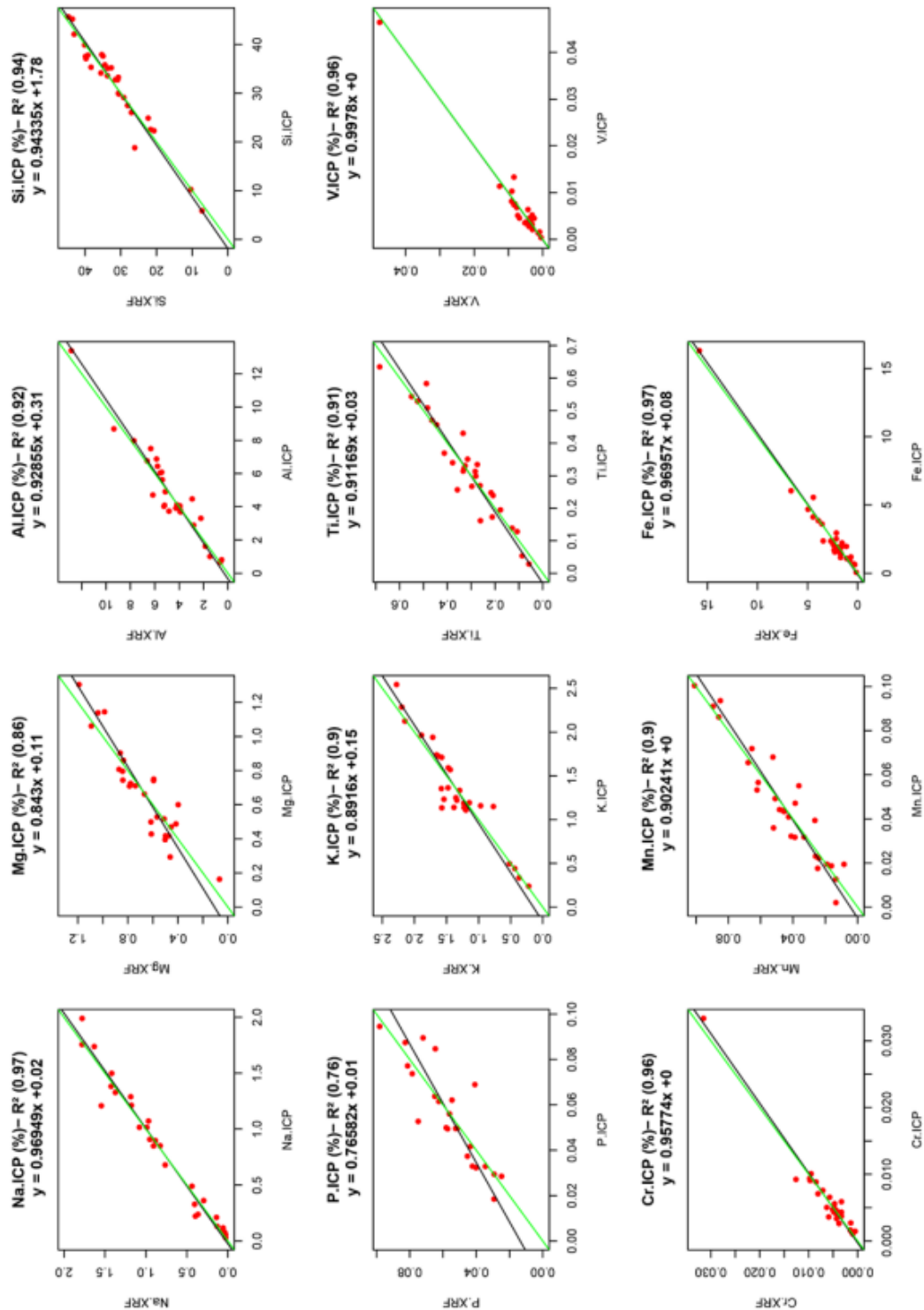


Figure A2.16: Energy-Dispersive X-Ray Fluorescence (ED-XRF) data were obtained on pressed pellets made of 97 % of ground sediment and 3 % of specific XRF wax, with acquisition parameters set to 15 kV, 100 μ A and 300 s of counting time. Quantitative results are provided for 11 light elements (Na, Mg, Al, Si, P, K, Ti, V, Cr, Mn, Fe) following an empirical calibration based on the Lucas-Tooth and Price (1961) method, using the ICP-AES/ICP-MS composition of 30 samples of loess and surficial sediments measured at the SARM-CRPG (Carignan et al. 2001). Only elements with a coefficient of determination (R^2) equal or greater than 0.7 between ED-XRF and ICP-AES/ICP-MS values were considered. Calibration was performed using the CloudCal v3.0 application (Drake, 2018 ; <https://github.com/leedrake5/CloudCal>).

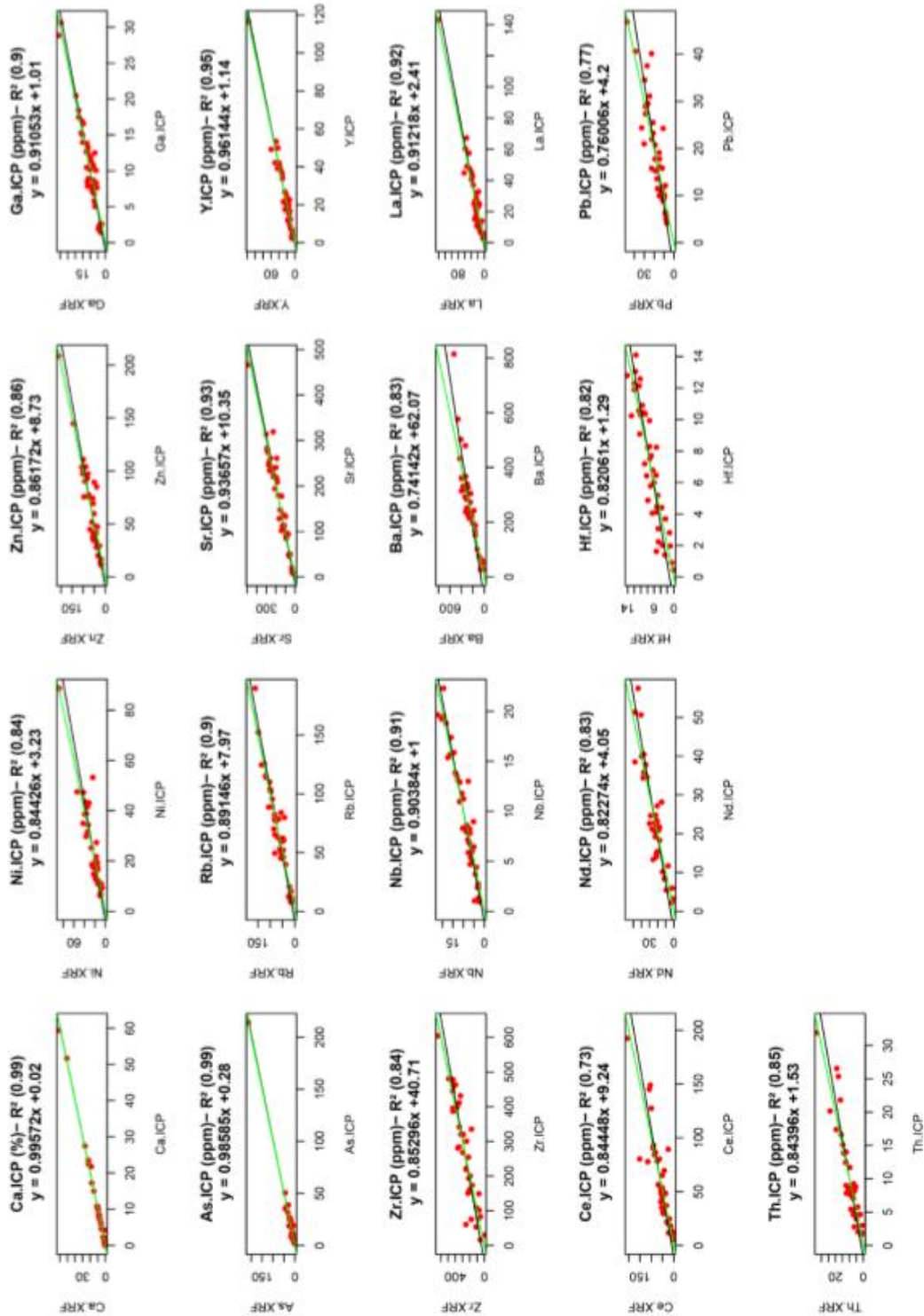


Figure A2.17: Energy-Dispersive X-Ray Fluorescence (ED-XRF) data were obtained on pressed pellets made of 97 % of ground sediment and 3 % of specific XRF wax, with acquisition parameters set to 50 kV, 35 μ A and 120 s of counting time with a filter composed of 75 μ m Cu, 25 μ m Ti and 200 μ m Al. Quantitative results are provided for 16 heavy elements (Ni, Zn, Ga, As, Rb, Sr, Y, Zr, Nb, Ba, La, Ce, Nd, Hf, Pb, Th) and Ca following an empirical calibration based on the Lucas-Tooth and Price (1961) method, using the ICP-AES/ICP-MS composition of 43 samples of loess and surficial sediments measured at the SARM-CRPG (Carignan et al., 2001). Only elements with a coefficient of determination (R^2) equal or greater than 0.7 between ED-XRF and ICP-AES/ICP-MS values were considered. Calibration was performed using the CloudCal v3.0 application (Drake, 2018 ; <https://github.com/leedrake5/CloudCal>).

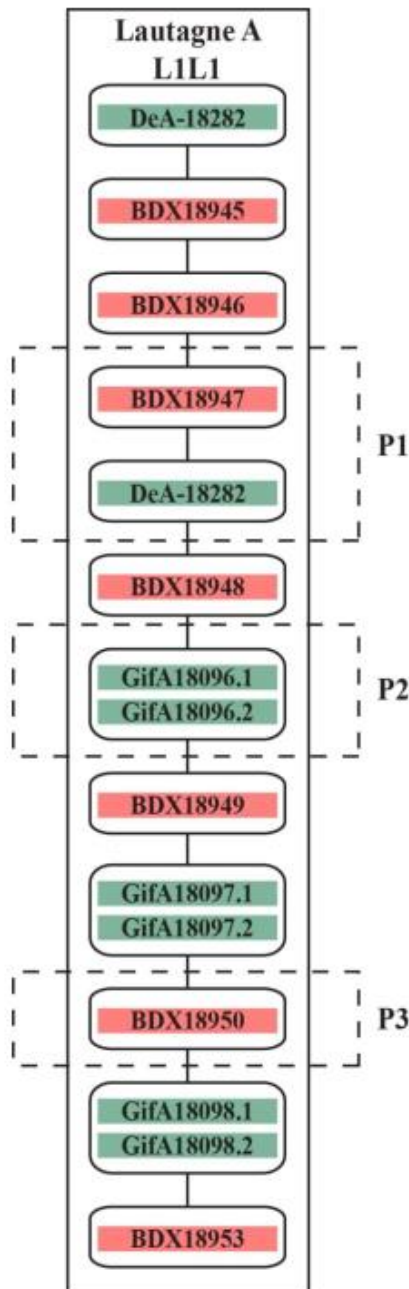


Figure A2.18: Age model of Lautagne A section used for Bayesian modelling in the software ChronoModel. Seven OSL dates (red boxes) and eight ¹⁴C (green boxes) dates were used. Stratigraphic relationships between events are indicated with black lines.

Appendix B

Note: We prepared the following text intending to be comprehensible without switching back and forth between this document and the main text. The text in the main text represents an extract of what is detailed here, and partly phrases are identical in both documents. This situation happens for phrases first drafted in the Appendix and then being recycled for the main text without deleting the original text here. However, this was intentional; otherwise the text here would have become a stump, left behind intelligible.

B 1 Details luminescence dating

B 1.1 Material and methods

B 1.1.1 Sampling and preparation

Samples were collected during daylight using steel-cylinders (diameter ca 4 cm, length ca 20 cm). Sample preparation was carried out in three different luminescence dating laboratories: (1) Justus-Liebig University Giessen, Germany (samples from Lautagne), (2) the University of Bayreuth, Germany (samples from Collias), and (3) IRAMAT-CRP2A, Université Bordeaux Montaigne, France (etching, other post-treatment). The sample preparation followed standard luminescence sample preparation procedures to extract (1) fine grain (4–11 μm) quartz, (2) coarse grain (90–200 μm) quartz, and (3) coarse grain K-feldspar bearing separates (e.g. Preusser et al. 2008). The grain-size fraction was extracted by wet-sieving and gravimetric separation using Atterberg cylinders (fine grain fraction). Further treatments involved HCl (10 %) and H_2O_2 (30 %) to remove organic sand carbonates, respectively. The fine grain quartz fraction was extracted using H_2SiF_6 (30 %). The coarse grain fraction was further treated with lithium heteropolytungstate (LST) and sodium heteropolytungstate (NST) heavy liquids with densities of 2.72 g cm^{-3} for separating heavy minerals, and 2.58 g cm^{-3} for separating quartz and feldspar. To further purify the quartz enriched fraction and to remove the zone affected by α -particles the samples were further treated with HF (40 %, 1 h) and afterwards rinsed in HCl (10 %; overnight) and distilled water. The coarse grain feldspar fraction was not further etched.

To account for potentially poor bleaching characteristics, additionally we prepared the coarse-grain quartz fraction for two samples from the site Lautagne. However, due to the very dim luminescence characteristic of the quartz grains from Lautagne, only ca 10 % of the aliquots produced a sufficient amount of light above the machine background. Therefore we continued only with the quartz fine grain fraction.

For luminescence measurements, the aliquots were mounted on stainless steel cups using silicon oil as adhesive. Cups were prepared as multiple grain aliquots with ca 106 grains for the fine grain fraction (1 mg/cup) and ca 800 grains for the coarse grain fraction.

B 1.1.2 Measurement equipment

The samples from Lautagne and Collias were measured over two years on two Freiberg Instruments lexsyg research readers (Richter et al. 2013) equipped with a $^{90}\text{Sr}/^{90}\text{Y}$ β -source delivering ca 6.6 Gy min^{-1} (calibrated for quartz on stainless steel cups using Risø calibration quartz Batch 90; Hansen et al. (2015); fine-grain calibration see below).

For optically stimulated luminescence (OSL) measurements, the systems were equipped either with LEDs (blue, IR) or laser diodes (blue, IR) (sample related settings see Table B2.6.

We consistently used the laser diodes for the fine grain samples from Lautagne and the LEDs for the coarse grain samples from Collias and Lautagne. IR stimulation was applied to test for potential feldspar contamination. The OSL signal was detected through a Hoya U340 (2.5 mm) glass filter in conjunction with a Delta BP 365/50 EX interference filter in front of a Hamamatsu H7360-02 photomultiplier tube (PMT). The system used for the infrared-radiofluorescence (IR-RF) test measurements, is similar to the system used by Frouin et al. (2017). Key components: Freiberg Instrumentslexsyg research reader with a $^{90}\text{Sr}/^{90}\text{Y}$ β -source (ring-source design, Richter et al. 2013), Hamamatsu H7421-50 photomultiplier tube, Chroma D850/40 interference filter, and inbuilt solar simulator.

B 1.1.3 Source calibration fine-grain quartz (Lautagne)

The inbuilt β -source used for the irradiation fine grain quartz samples from Lautagne was calibrated using a coastal dune quartz sample (BDX16651) from the Médoc area (south-west France) (Kreutzer et al. 2018a). The sample was first gently crushed, and the grain-size fraction of 4–11 μm was extracted by applying the Stokes' law. Before irradiation, the material was heated to 700 °C in air and additionally tested for feldspar contamination using IRSL. Two batches of the sample were shipped for irradiation to the Gif-sur-Yvette laboratory and irradiated with a γ -dose of 2.5 Gy (rel. SE: 3 %) and 5 Gy (rel. SE: 3 %). The irradiation was carried out using a homemade irradiator equipped with a ^{137}Cs γ -source (Valladas, 1978). The source is a ring consisting of six single circularly arranged ^{137}Cs sources with the sample placed in the centre.

All two batches were measured, and the source-dose rate was deduced from the slope of the regression line of the measured vs the given dose. The so obtained source-doserate ($0.107 \pm 0.005 \text{ Gy s}^{-1}$ at calibration date) of the quartz fine-grain fraction is ca $5.5 \pm 5.2 \%$ lower than the corresponding source dose rate of the coarse (100–200 μm) grain quartz fraction on the same reader. This grain size-related deviation in the source-dose rate is lower than results reported by Armitage and Bailey (2005) (ca 12 % deviation between the two grain-size fractions). However, our results are consistent within uncertainties.

B 1.1.4 Quartz measurements protocol

For measuring the quartz samples, we applied the single aliquot regenerative (SAR) dose protocol by Murray and Wintle (2000). The measurement parameters (preheat and cutheat temperatures) were deduced from preheat-plateau test (natural samples) and preheat dose-recovery tests (artificially irradiated samples) carried out on (1) three coarse grain quartz samples from Collias (BDX21322, BDX21326, BDX21329) and (2) two fine-grain quartz samples from Lautagne (BDX18948, BDX18953). The results of these tests are shown in Figs. B2.19, B2.20. For the samples from Collias we applied a preheat cutheat combination of 260

°C and 200 °C, and for 200 °C and 160 °C for the samples from Lautagne. The used protocol settings are summarised in Table B2.6. We measured up to 40 aliquots per sample for Collias and up to 20 aliquots for Lautagne.

For all measurements, we applied a channel resolution of 10 channels/s. Integration limits were set to channels 1–2 (signal) and channels 300–399 (background). Before every subsequent measurement step, the temperature was cooled down to 60 °C (preheat, cutheat, OSL). For potential feldspar contamination of the quartz, the fraction was tested using IRSL stimulation at the end of each SAR cycle. The dose given before the IRSL stimulation was similar to the one used for the repeated OSL regeneration dose point, and both signals were compared. Aliquots were rejected if the IRSL/OSL signal ratio was >5 %. Further rejection criteria: Recycling ratio: max. \pm 10 % (Lautagne: 20 %), max. recuperation rate: 10 %. For the fitting of the dose-response curve, we used an exponential + linear function.

Table B2.6: SAR protocol settings applied for measuring the quartz fraction of the samples from Collias and Lautagne.

#	Sequence step		Detection
	Collias	Lautagne	
1	Irradiation (regeneration dose)		-
2	Preheat to 220 °C for 10 s	Preheat to 260 °C for 10 s	-
3	blue-OSL@125 °C for 40 s	at 50 mW cm ⁻² temp. stabilisation 5 s	$L_{n,x}$
4	Irradiation (test dose)		-
5	Cutheat to 200 °C	Cutheat to 160 °C s	-
6	blue-OSL@125 °C for 40 s	at 50 mW cm ⁻² temp. stabilisation 5 s	$T_{n,x}$
7	Hotbleach@280 °C	-	-

Heating rates were set to 5 K/s (preheat and OSL)

The stimulation wavelengths were set to 458 Δ 5 nm (Collias) and 445 Δ 3 nm (Lautagne).

B 1.1.5 Feldspar measurements

For two samples from the profile Collias (BDX21322 and BDX21329) we measured the coarse grain K-feldspar fraction using infrared radiofluorescence (Trautmann et al. 1998, 1999) in conjunction with the RF70 protocol suggested by Frouin et al. (2017).

B 1.1.6 Data analysis

Luminescence data analysis was carried out using the R (R Core Team, 2019) package 'Luminescence' (Kreutzer et al. 2012b, 2020). Other used R package are cited at their appropriate location below. For dose rate and age calculation, the software DRAC (Durcan et al. 2015) in version 1.2 was used; for applied settings cf. Table B2.7. For calculating the central dose (D) for the samples from Collias we used the approach by Combès et al. (2015) implemented in the R package 'Luminescence' by Mercier et al. (2016) (analyse baSAR()).

The average dose (samples Lautagne) followed the approach by Guérin et al. (2017b) (function `calc AverageDose()` in the R package 'Luminescence').

Table B2.7: DRAC settings applied for the luminescence age calculation. For details on the meaning of the parameters, we refer to the online reference manual of DRAC. For all settings and data see the DRAC input table provided as supplement.

Parameter	DRAC input	APPLIED?	Reference
Dose rate conversion factors	Guerinetal2011	to all	Guérin et al. (2011)
Calc. extern. Rb from K conc.?	Y	Collias & Lautagne	Mejdahl (1987)
Calc. internal. Rb from K conc.?	Y	Collias (feldspar)	Mejdahl (1987)
Internal U (ppm) (quartz)	0.08 0.02	Collias & Lautagne	Vandenberghé et al. (2008)
Internal Th (ppm) (quartz)	0.18 0.03	Collias & Lautagne	Vandenberghé et al. (2008)
Internal K (%) (feldspar)	12.5 0.5	Collias (feldspar)	Huntley and Baril (1997)
β -etch depth attenuation factor	Bell1979	Collias (quartz)	Bell (1979)
β -grain size attenuation	Guerinetal2012-Q	Collias & Lautagne	Guérin et al. (2012)
β -grain size attenuation	Guerinetal2012-F	Collias (feldspar)	Guérin et al. (2012)
α -grain size attenuation	Brennanetal1991	to all	Brennan et al. (1991)
α -efficiency quartz fine grain	0.035 0.01	Lautagne	Lai et al. (2008)
α -efficiency feldspar IR-RF	0.07 0.02	Collias (feldspar)	Kreutzer et al. (2018b)
Cosmic-dose rate	43.95 4.78 100	Collias	Prescott and Hutton (1994)
Cosmic-dose rate	44.9 4.9 178	Lautagne	Prescott and Hutton (1994)

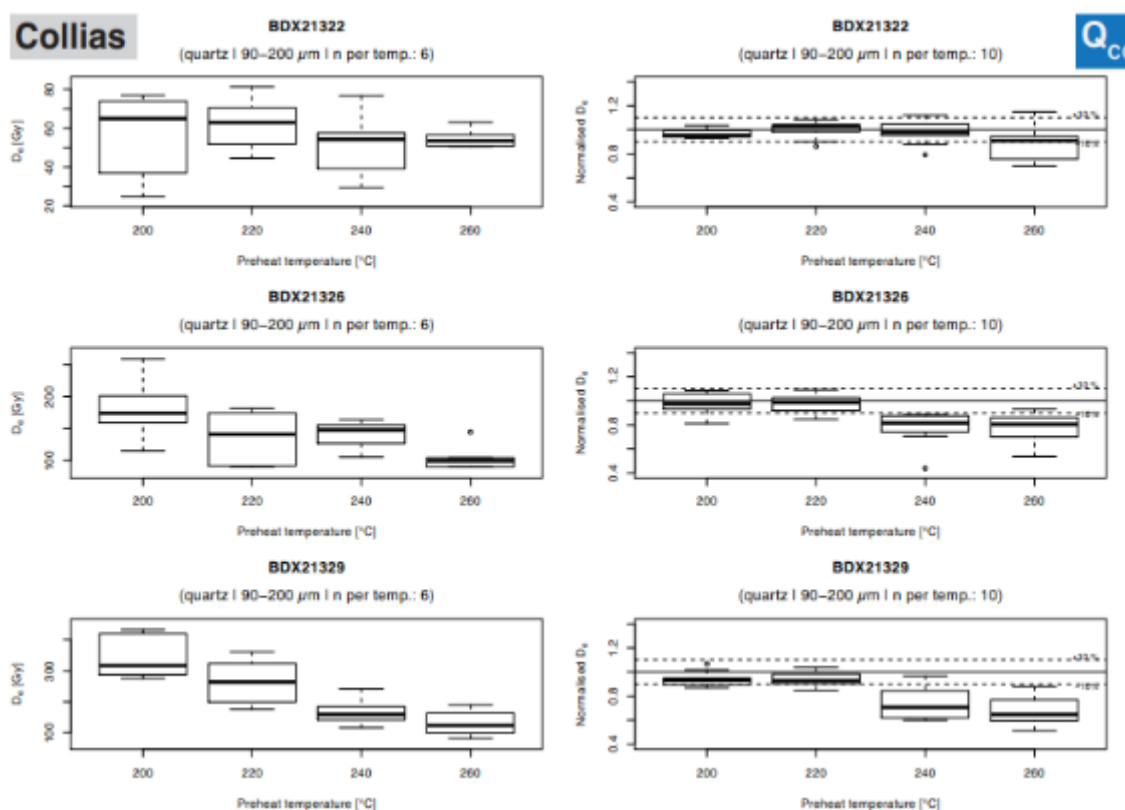
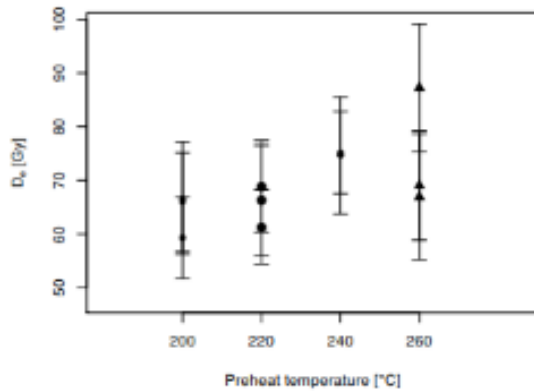
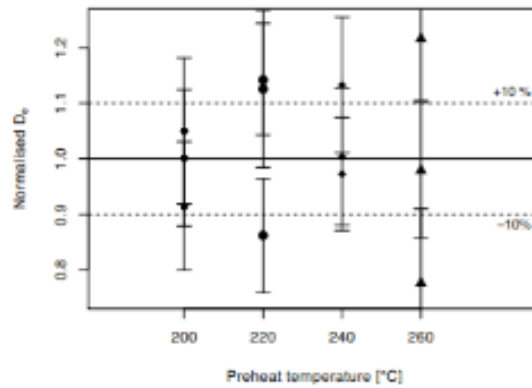


Figure B2.19: Boxplot of preheat dose-recovery test (left) and dose-recovery test (right) results for three coarse grain quartz samples from Collias. For each sample measured we measured six (left figure, preheat-plateau test) or ten (right figure, dose-recovery test) aliquots. For all experiments the cutheat temperature was kept at 200 °C. The given dose (dose-recovery experiments were set to the expected D_e for each sample. For the final D_e measurements we selected a preheat temperature of 220 °C.

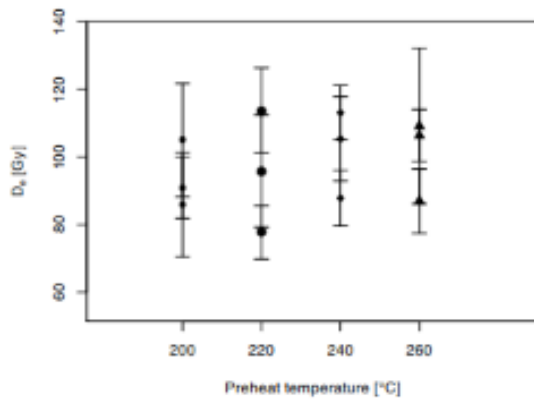
Preheat Plateau Test – BDX18948



Dose Recovery Test – BDX18948



Preheat Plateau Test – BDX18953



Dose Recovery Test – BDX18953

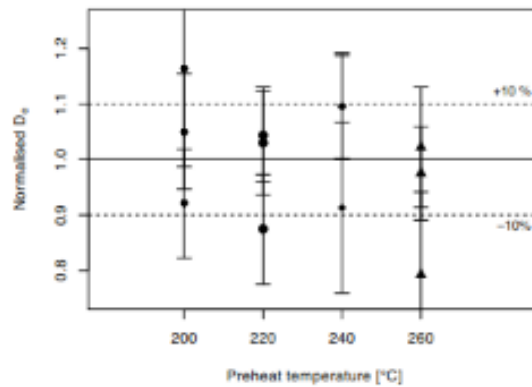


Figure B2.20: Preheat plateau tests (left) and dose-recovery tests (right) for two fine grain quartz samples from the upper (BDX18984) and the lower (BDX18948) part the profile Lautagne. Three aliquots were measured for each preheat temperature. The cutheat temperature was kept at 160 °C. Within uncertainties the different preheat temperatures are similarly suitable. For the final D_e measurements we selected a preheat temperature of 200 °C.

B 1.1.7 Dose-rate determination

Nuclide concentration

To estimate the U, Th and K nuclide concentrations high-resolution γ -ray spectrometry measurements were carried out at the IRAMAT-CRP2A (Guibert and Schvoerer, 1991) on ca 80 g to 90 g of the dried fraction sampled along with each luminescence sample. Data analysis was performed using a self-written MS Excel™ sheet.

In situ γ -ray spectrometry

For the site Lautagne we, additionally to the high-resolution γ -ray spectrometry in the laboratory in situ, employed in situ γ -dose rate measurements using a portable γ -ray spectrometer (Canberra Inspector 1000, 1.500 x 1.500 , LaBr probe). Final γ -dose rates were

derived applying the threshold approach (principle described in Løvborg and Kirkegaard 1974; Mercier and Falguères 2007; Guérin and Mercier, 2011).

Water content

To estimate the water content range needed to calculate the luminescence ages, we adopted an approach reported in Sauer et al. (2016) (their supplementary 2, sect. 2.1 and attached XLS-files). Based on the granulometric composition Sauer et al. (2016) calculated a meaningful water content range based on the pore volume distribution given in Blume et al. (2010) for sands, silts and clays. The data given by Blume et al. (2010) distinguishes between coarse, medium and fine pores. Sauer et al. (2016) considered fine pores as constantly water saturated, while the coarse pores are, only occasionally filled by rainwater, assumed empty. Hence, the uncertainty in the water content is determined by the medium pores alone, considering the pore volume for the silt fraction (Fig. B2.21; cf. Table B2.8). For sample BDX212329 we used a slightly higher water content of 20 % to account for the slightly higher clay concentration.

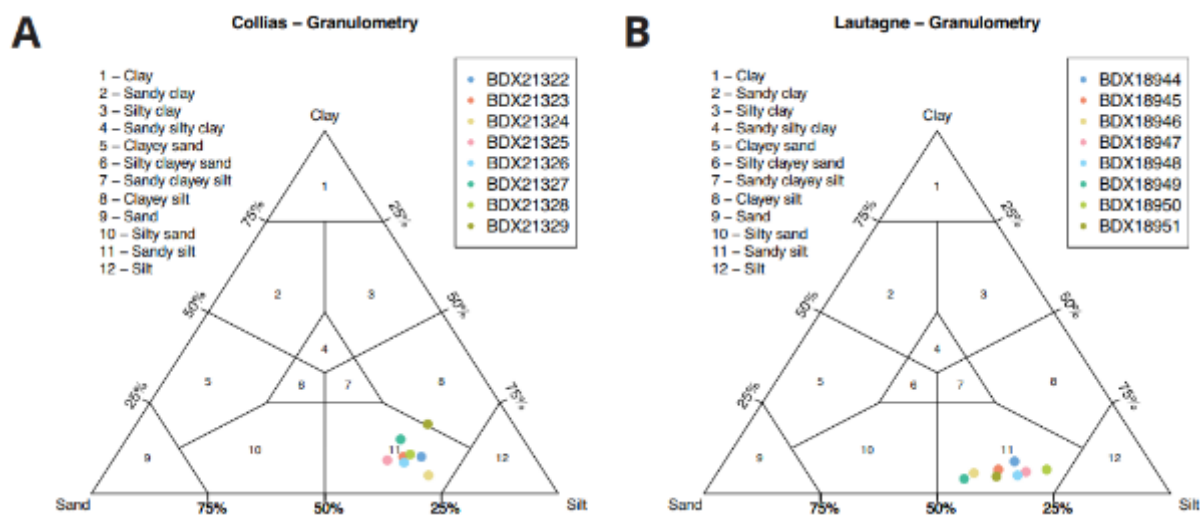


Figure B2.21: Ternary diagram showing granulometric classes of the samples according to Shepard (1954) for samples from Collias (A) and Lautagne (B). For Lautagne grain size data are only available for the first eight samples. The figure was produced using the R package 'rysgran' (Gilbert et al. 2014). The grain size data were used to estimate realistic water content values for the samples using pore volume data. The grain size data were measured at the PACEA (Université de Bordeaux) using a Horiba LA-950 laser particle size analyser. For Lautagne no grain-size data are available for the samples BDX18952 and BDX18953. For these samples, we assumed similar granulometry as for the other samples. For further and more detailed information on the grain size, please see the main text.

B 1.2 Results

B 1.2.1 Luminescence measurements and D_e determination

All investigated quartz samples show suitable luminescence characteristics in terms of brightness and reproducibility (see Fig. B2.22 for typical OSL curves from Collias and Lautagne). Nevertheless, samples from Lautagne appeared to be rather dim. Luminescence

measurements on the coarse-grain fraction even failed (data not shown) due the very low luminescence intensity of the samples. Furthermore, samples from both sites show a rather larger inter-aliquot scatter (Figs. B2.23, B2.24) already observed previously by (Bosq et al. 2018, their supplement) for two quartz samples taken from a quarry close to Avignon. A pattern that might render itself typical for the samples from the Rhône Valley.

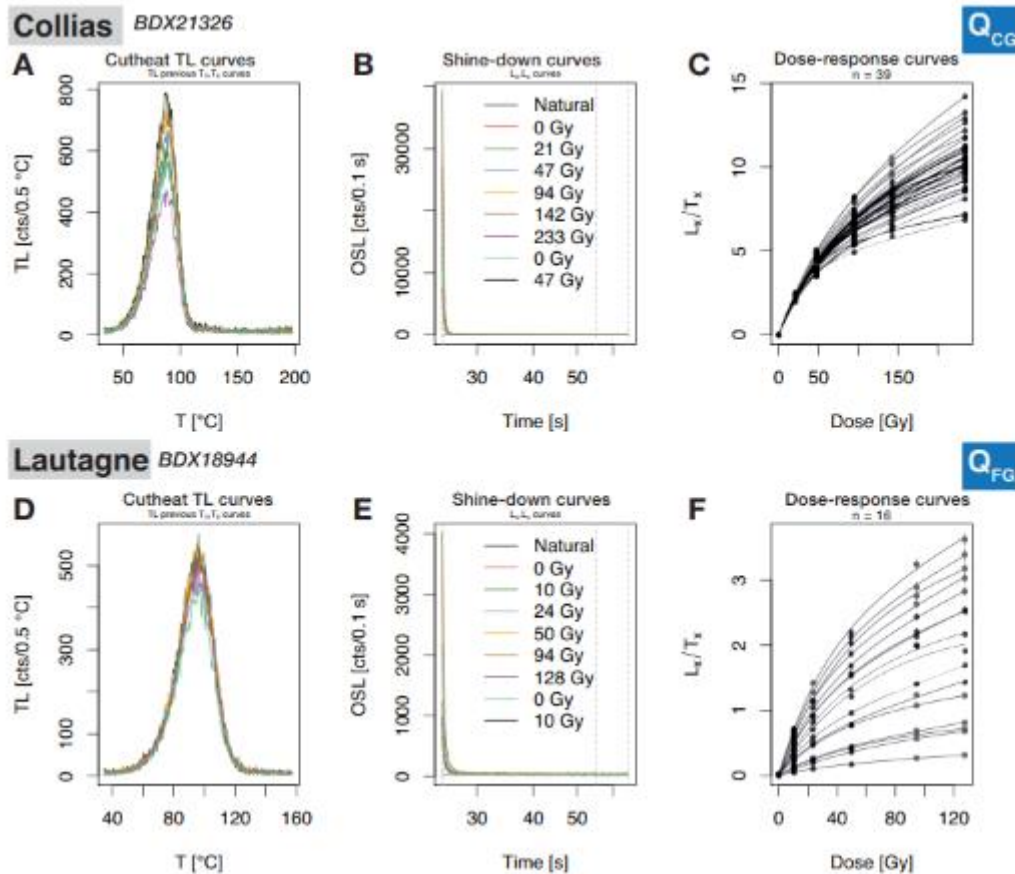


Figure B2.22: Typical luminescence curves obtained during the SAR measurements for samples BDX21326 (quartz coarse grain, Collias, A–C) and BDX18944 (quartz fine grain, Lautagne, D–E). Shown are cutheat TL curves (A, D), blue OSL shine-down curves (B, E), and dose-response curves (C, F). Vertical dashed lines (middle plot) show the chosen integration limits for signal and background, respectively.

Collias. The distribution plots for Collias and Lautagne (Figs. B2.23, B2.24) show no obvious pattern but a large dispersion. In the case of the samples from Collias this scatter may reflect poor bleaching, dose rate heterogeneities and/or real sediment mixing. At Collias, the additionally measured feldspar aliquots (BDX21322 and BDX21329) exhibit D_e values significantly higher than obtained for the quartz fraction (Fig. B2.25). Required bleaching times are longer for feldspar measured with IR-RF (ca 3 h for a full reset; Frouin et al. 2017) than for quartz OSL (e.g. ca 100 s even on a cloudy day Lindvall et al. 2017). Thus the presumed short transport distance in the Rhône Valley may not have yield a full signal depletion for the feldspar fraction and also the quartz fraction may be affected. More likely, however, appears a post-depositional mixing in conjunction with multiple short-distance erosion and deposition cycles.

Such slope-wash and/or sediment-creep processes are evidenced by sand-sized and even fine- to medium-gravel sized particles in the sediment-soil sequence at Collias (e.g. between 250 cm and 500 cm; Fig. 2.5). Furthermore, originating from the palaeo-soil-horizons former root channels reach deeply into the underlying units. This affects especially the units from 300 cm downwards. In the upper part of the lowermost Bt horizon (650–720 cm) up to 40 % by area are made up of dominantly light-coloured silty root infillings within the clayey-loamy solum. Without separation of these two components, numeric dating will inevitably lead to age underestimation. Next to these post-depositional pedogenic and bioturbation processes, the above addressed pre-depositional sedimentary processes most likely led to age overestimation.

The true origin of the scatter at Collias cannot be deciphered, but it appears to be of different origin than for the samples from Lautagne (see below). The Abanico plots (Fig. B2.23) indicate a substantial overdispersion in each sample. Moreover, the D_e values range from ca 50 Gy (BDX21322) to ca 172 Gy (BDX21328), and the samples BDX21327–BDX21329 reach a dose region where signal saturation of the fast-component dominated OSL signal in UV wavelength region (detection) have been reported (e.g. Roberts, 2008), and doubts have been raised on the overall reliability of the SAR protocol for those samples (e.g. Duller, 2007). Heydari and Guérin (2018) investigated different statistical models regarding the variability and reproducibility in a laboratory controlled experiment for a given dose close to saturation and concluded that the approach proposed by Combès et al. (2015) allows a correct recovery of a known central dose even for largely dispersed samples. While the distribution displayed in Fig. B2.23 refer to a data analysis using the conventional approach, all samples were re-analysed using the function analyse baSAR() (cf. Mercier et al. 2016) to calculate the central dose D (example curves: Fig. B2.26). Further parameter settings: `distribution = "normal", fit.method = "EXP+LIN", n.MCMC = 10000.`

Lautagne. For the samples from Lautagne (Fig. B2.24), the scatter is rather large for fine-grain quartz samples with ca 10^6 grains per aliquot and the expected averaging effects. However, the inter-aliquot scatter is dominated by the individual errors (nearly all points lay within the grey 2σ polygon, Fig. B2.24). In other words, these aliquots represent a common central dose. For the samples from Lautagne, we decided to apply the average-dose model (Guérin et al. 2017b) to determine the best central dose and its standard error. The intrinsic overdispersion value σ_m (parameter `sigma_m` in the function `calc_AverageDose()`) deduced from the dose-recovery experiments was set to 0.1. Results are listed in Table B2.9.

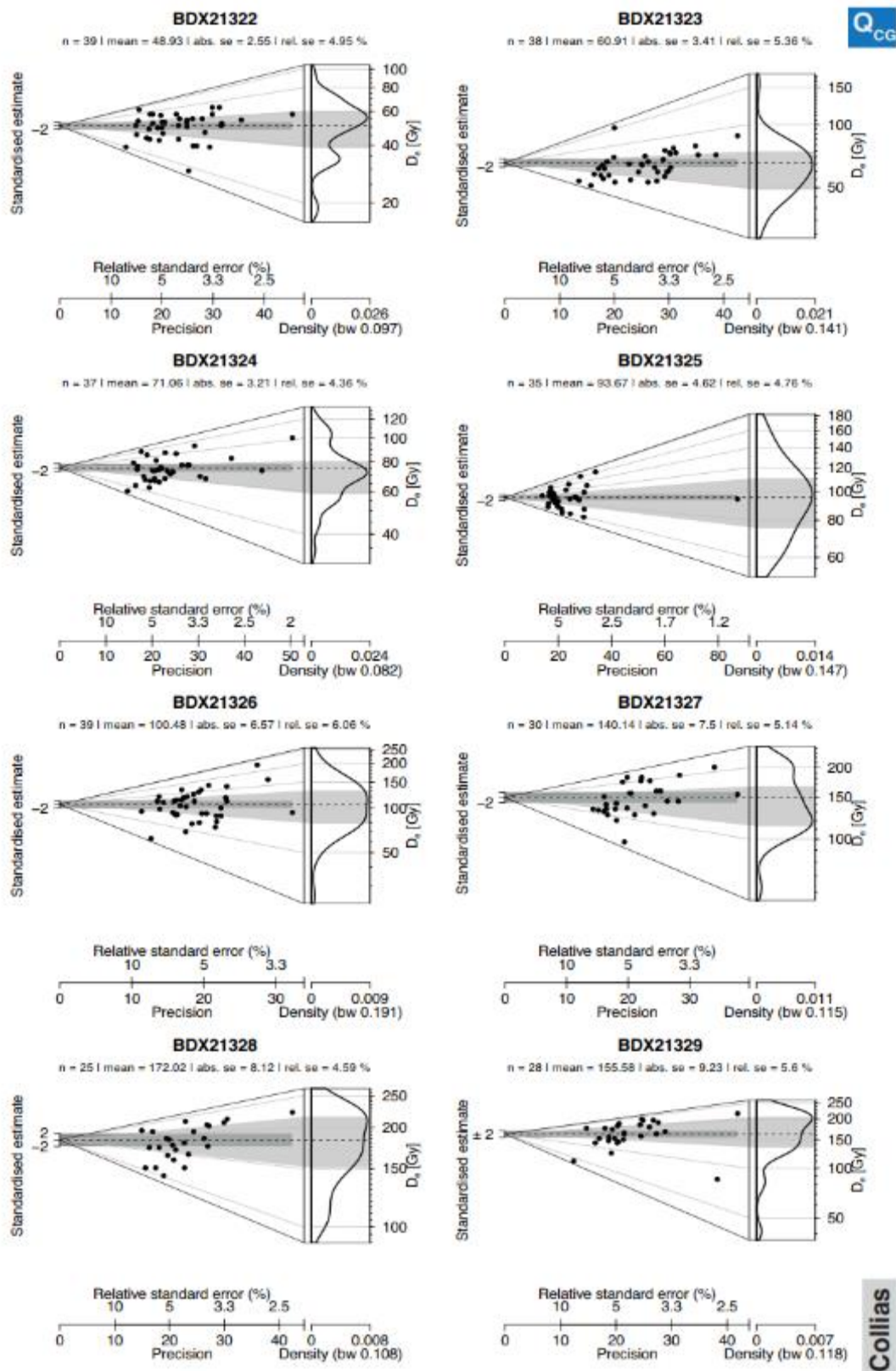


Figure B2.23: Dose distribution plots (here Abanico plots, Dietze et al. 2016) for all coarse grain quartz samples from Collias. All samples show a rather large dispersion.

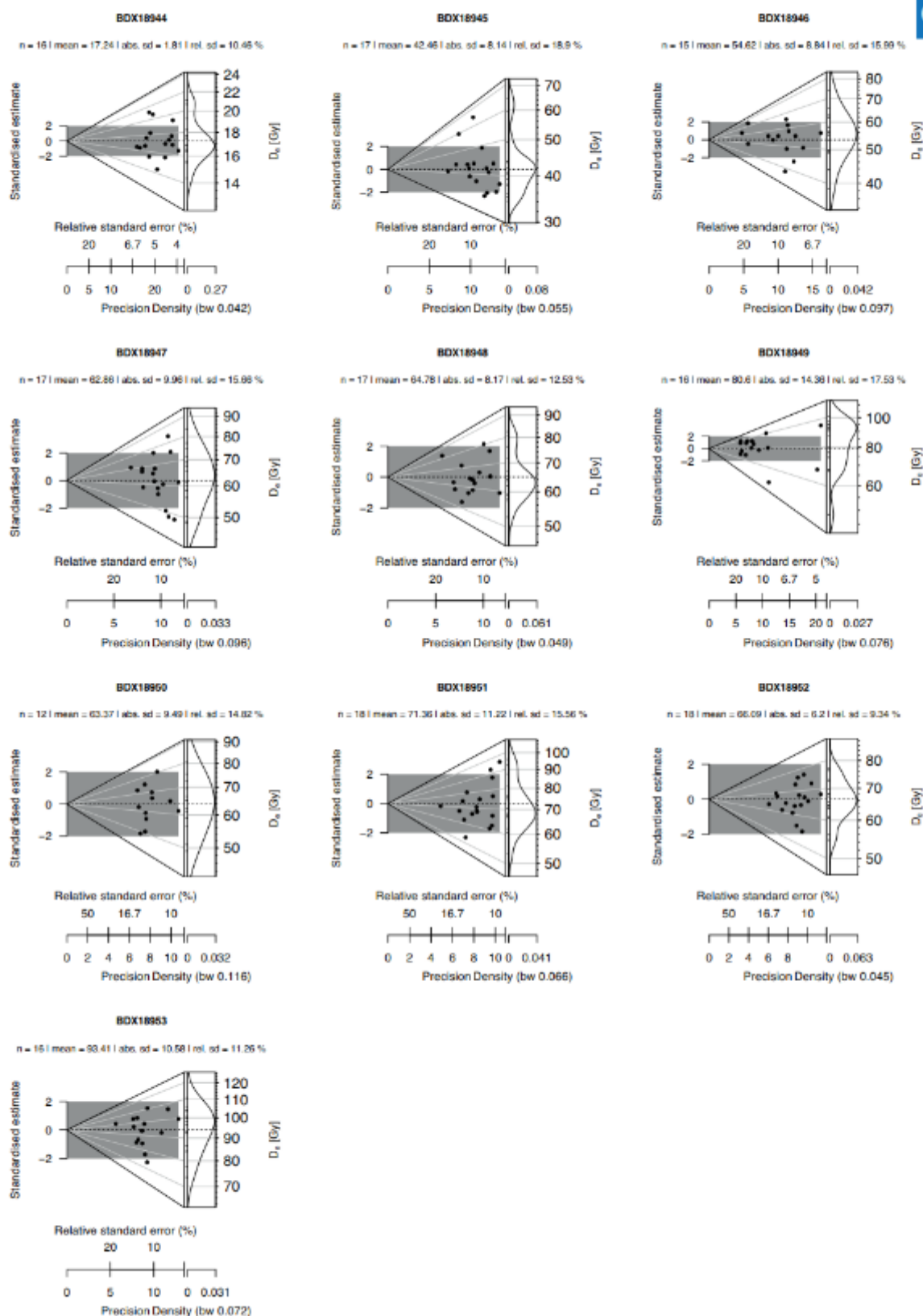


Figure B2.24: Dose distribution plots (here Abanico plots, Dietze et al. 2016) for all fine grain quartz samples from Lautagne. All samples show a large dispersion. However, due to the significant individual standard errors, almost all aliquots fall within the 2σ range of the central dose of each sample.

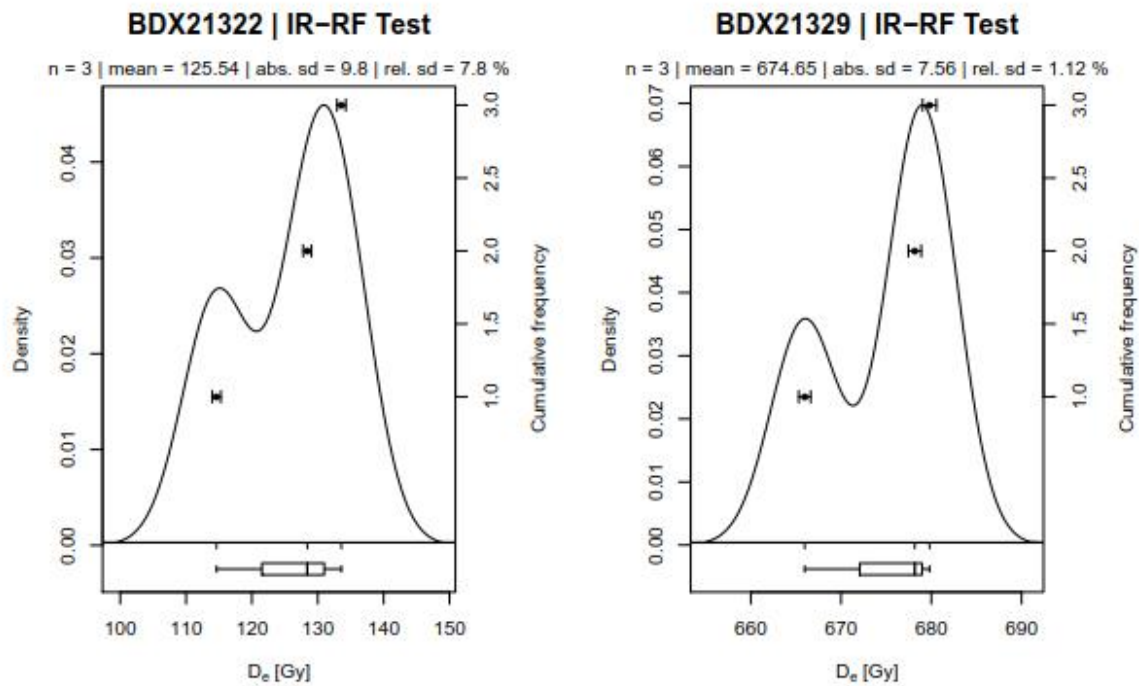


Figure B2.25: D_e distribution plots for the feldspar samples BDX21322(left) and BDX21329 (right) measured using the IR-RF. Both samples show consistent D_e values reflected by the narrow distributions (the individual statistical standard errors are even lower, and likely too small). However, in both cases the resulting ages overestimate the corresponding quartz ages, probably due to an insufficient signal resetting during the presumed short distance sediment transport.

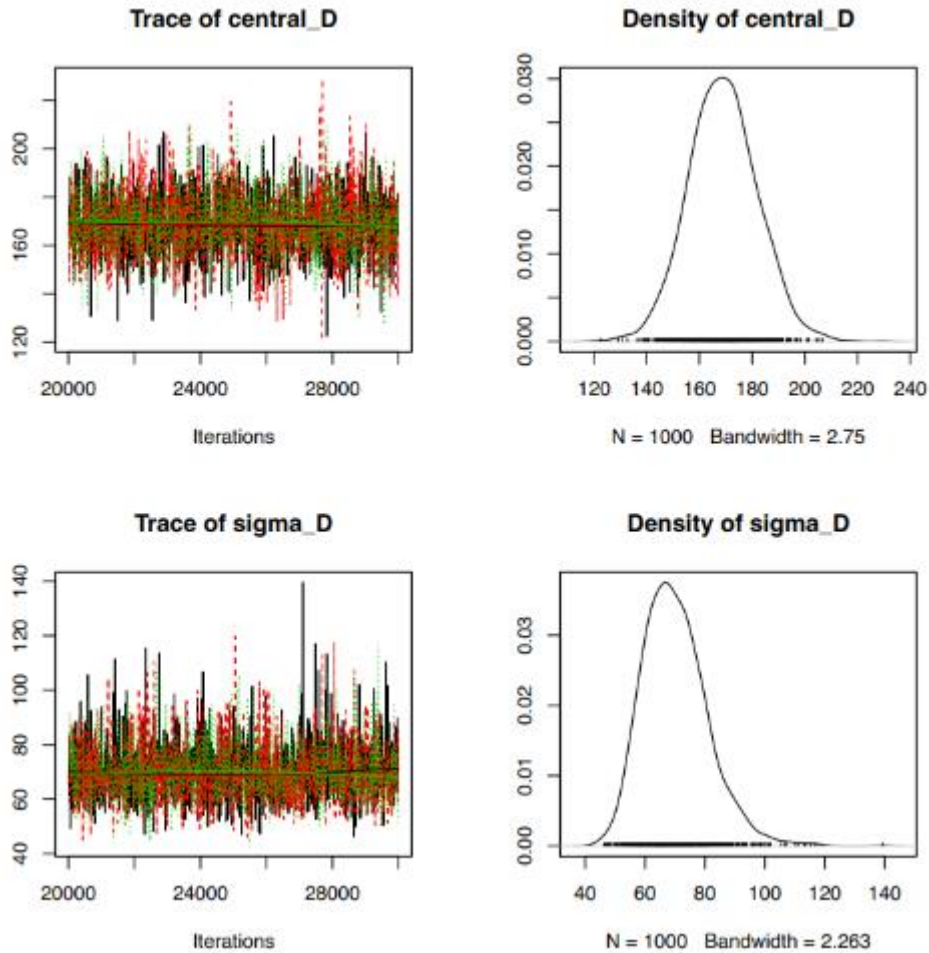


Figure B2.26: Example trace and density plots for sample BDX21327 generated from the output of the function `analyse baSAR()` while calculating the central equivalent dose. The lower plots ('`sigma_D`') show the dispersion of the individual doses around the central dose. Colours code Monte-Carlo Markov Chains (MCMC).

B 1.2.2 Dose rate results

High-resolution γ -ray spectrometry results (Table B2.8) reveal Th and K concentrations comparable for the sites Collias and Lautagne. The concentration values ranges from Th: ca 7.7–14.2 ppm (Collias) and 7.8–11.0 ppm (Lautagne) and K: ca 0.9–1.4 % (Collias) and 1.0–1.3 % (Lautagne). In both sites, the Th and K concentrations show a trend towards higher values in the lower part of the profile where the Bt/Bw horizons are more extensively developed (potential Th aggregation on clay particles). For both sites, we observed radioactive disequilibria in the U-decay chain. Figure B2.27 compares normalised equivalent ^{238}U concentration values deduced from pre- and post-Ra nuclides. In Collias the lowermost three samples are in secular equilibrium, while all other samples show higher U-concentrations when determined from post-Ra nuclides. The γ -ray spectrometry measurements from Lautagne render a similar picture, except that at Lautagne all samples show a radioactive disequilibrium.

It appears that those disequilibria are higher at the top of the profile than at the bottom of the profile indicating a (near) surface water circulation dominated process. Figures B2.28A and B

display theoretical equivalent U-values derived from each measured nuclide. The figure exhibit two peculiarities for a scenario of Ra excess. In the figure from Collias (Fig. B2.28A) the Ra excess occurred rather recent (<10 ka) and a secular equilibrium with daughter nuclides did not (yet) take place (the alternative interpretation would be ^{210}Pb leaching due to rainfall). Figure B2.28B (Lautagne) shows a similar picture but for a secular equilibrium with the daughter nuclides of ^{226}Ra . Results of the variance test (data are not shown) as suggested by Guibert et al. (2009) further support the hypothesis of a Ra excess in both profiles. For Collias and Lautagne, the geochemical alteration induced variance is in both cases significantly higher for post-Ra equivalent U-concentrations. Nevertheless, the onset and duration of the disequilibria cannot be determined beyond doubt. Thus, for calculating the dose-rate values used for the age calculation (Table B2.9) we calculated a mean U concentration derived from, both, from nuclides from the upper part of the U decay chain and the lower part (cf Table B2.8). For the samples from Lautagne, the γ -dose rate was obtained via in situ measurements and not from the mean U concentration. In summary, the environmental dose rate ($D_{\text{env.}}$) varies for both profiles between ca 1.7 Gy ka $^{-1}$ to 3 Gy ka $^{-1}$.

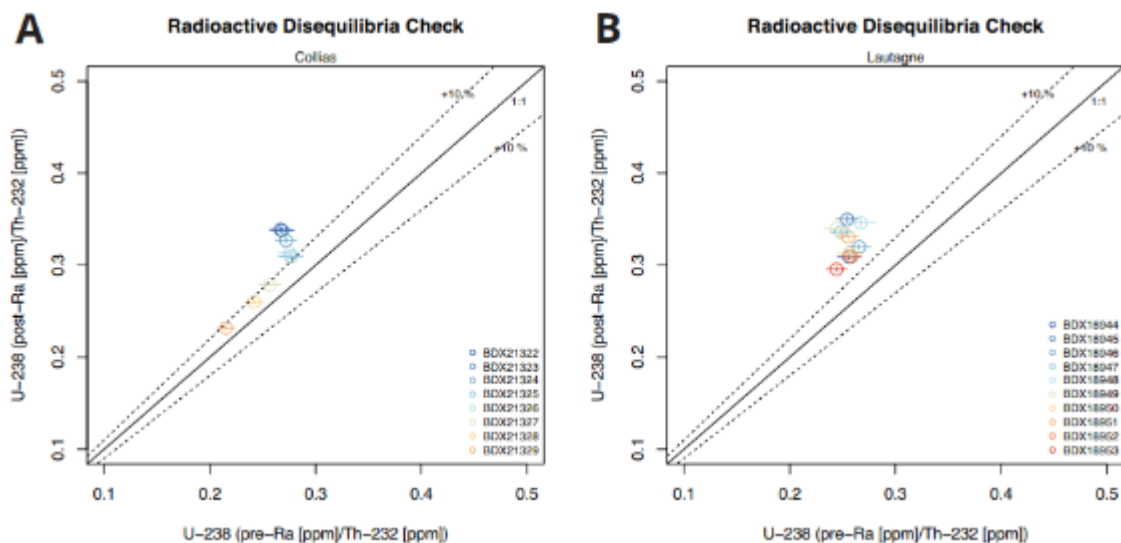


Figure B2.27: Normalised ^{238}U plots to check for potential radioactive disequilibria after Guibert et al. (2009) in the samples from Collias (A) and Lautagne (B). Except for the three lowermost samples, all samples of the site Collias show a radioactive disequilibrium in terms of higher post-Ra derived ^{238}U concentrations. The samples from the site Lautagne render a very similar picture with all samples showing a radioactive disequilibrium.

Table B2.8: High-resolution γ -ray spectrometry results and applied water content.

ID	High-resolution γ -ray spectrometry						$W_{\text{mea.}}$ [%]	$W_{\text{app.}}$ [%]
	Th [ppm]	K [ppm]	U (pre- ^{226}Ra) [ppm]	U (post- ^{226}Ra) [ppm]	U (^{210}Pb) [ppm]	$U_{\text{app.}}$ [ppm]		
<i>Collias</i>								
BDX21322	9.129 ± 0.079	1.008 ± 0.014	2.437 ± 0.100	3.093 ± 0.028	2.685 ± 0.162	2.765 ± 0.051	4.09	17 ± 5
BDX21323	8.457 ± 0.075	0.936 ± 0.013	2.271 ± 0.094	2.857 ± 0.026	2.433 ± 0.151	2.564 ± 0.049	3.72	17 ± 5
BDX21324	8.150 ± 0.066	0.942 ± 0.012	2.217 ± 0.081	2.664 ± 0.022	2.392 ± 0.133	2.441 ± 0.042	3.65	17 ± 5
BDX21325	7.647 ± 0.069	0.870 ± 0.013	2.116 ± 0.088	2.367 ± 0.023	2.069 ± 0.138	2.242 ± 0.046	2.41	17 ± 5
BDX21326	8.643 ± 0.075	0.990 ± 0.013	2.381 ± 0.094	2.708 ± 0.025	2.375 ± 0.149	2.545 ± 0.049	5.38	17 ± 5
BDX21327	9.643 ± 0.083	1.072 ± 0.015	2.474 ± 0.099	2.690 ± 0.026	2.172 ± 0.151	2.582 ± 0.051	10.98	17 ± 5
BDX21328	12.250 ± 0.094	1.349 ± 0.016	2.963 ± 0.106	3.186 ± 0.027	2.895 ± 0.162	3.075 ± 0.055	9.40	17 ± 5
BDX21329	14.209 ± 0.109	1.360 ± 0.017	3.056 ± 0.117	3.294 ± 0.029	2.720 ± 0.170	3.175 ± 0.060	10.86	20 ± 5
<i>Lautagne</i>								
BDX18944	7.820 ± 0.071	0.978 ± 0.014	2.002 ± 0.084	2.418 ± 0.024	2.437 ± 0.160	2.210 ± 0.044	11.45	17 ± 5
BDX18945	8.230 ± 0.071	1.051 ± 0.014	2.093 ± 0.085	2.880 ± 0.026	2.545 ± 0.160	2.487 ± 0.044	8.76	17 ± 5
BDX18946	8.516 ± 0.077	1.086 ± 0.015	2.263 ± 0.093	2.724 ± 0.027	2.762 ± 0.178	2.494 ± 0.048	8.30	17 ± 5
BDX18947	8.577 ± 0.073	1.083 ± 0.014	2.130 ± 0.085	2.886 ± 0.026	2.918 ± 0.195	2.508 ± 0.044	12.12	17 ± 5
BDX18948	9.309 ± 0.099	1.164 ± 0.020	2.488 ± 0.126	3.222 ± 0.036	3.136 ± 0.238	2.855 ± 0.066	11.42	17 ± 5
BDX18949	9.854 ± 0.095	1.316 ± 0.020	2.408 ± 0.115	3.350 ± 0.034	3.380 ± 0.266	2.879 ± 0.060	10.18	17 ± 5
BDX18950	9.459 ± 0.093	1.187 ± 0.019	2.427 ± 0.113	2.960 ± 0.032	2.971 ± 0.213	2.694 ± 0.059	13.32	17 ± 5
BDX18951	9.631 ± 0.080	1.155 ± 0.015	2.460 ± 0.093	3.185 ± 0.028	3.35 ± 0.192	2.823 ± 0.049	15.41	17 ± 5
BDX18952	10.58 ± 0.089	1.220 ± 0.016	2.732 ± 0.104	3.271 ± 0.030	3.539 ± 0.234	3.002 ± 0.054	18.64	17 ± 5
BDX18953	10.941 ± 0.093	1.332 ± 0.018	2.672 ± 0.106	3.234 ± 0.030	3.553 ± 0.231	2.953 ± 0.055	17.59	17 ± 5

$W_{\text{mea.}}$: Measured *in situ* water content | $W_{\text{app.}}$: water content value used for dose rate calculation

For both samples the water content was measured on arrival in the laboratory, however, for Collias this was a couple of months after the sampling in the field.

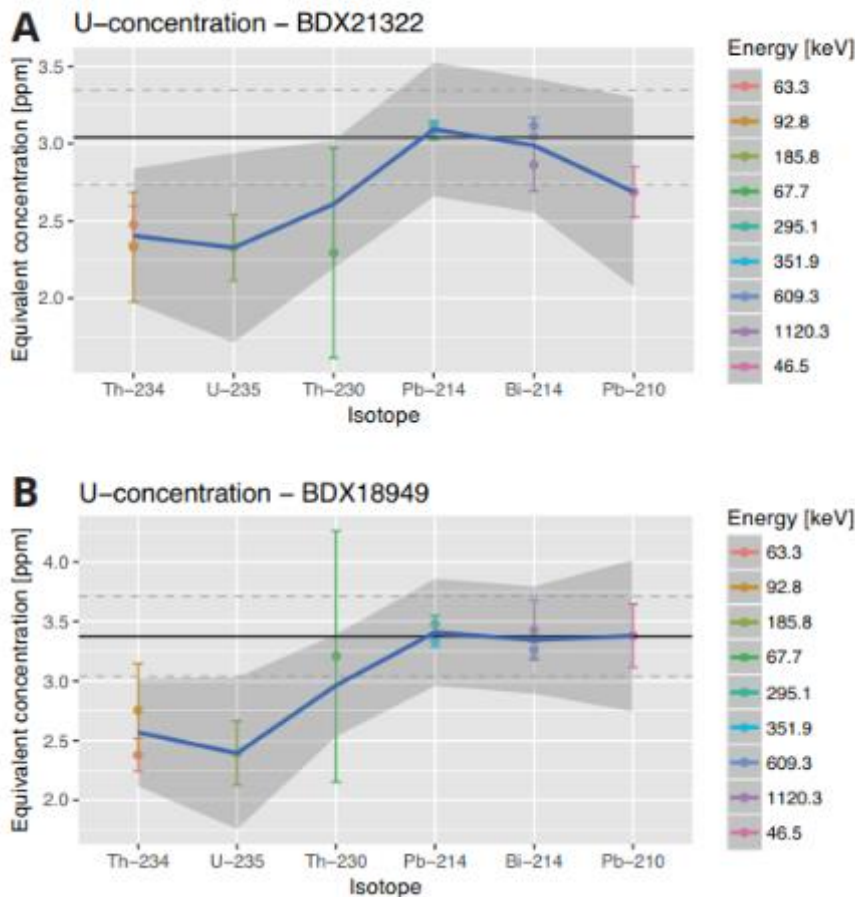


Figure B2.28: Nuclide concentration plots for one sample from Collias (A) and Lautagne (B) exemplifying the encountered radioactive disequilibria. In both cases, the equivalent U concentration obtained from pre-Ra nuclides results in lower values than equivalent U concentrations obtained from post-Ra nuclides. The presumed leaching of ^{210}Pb is not relevant in the considered time frame.

B1.2.3 Luminescence ages and interpretation

The final luminescence ages are displayed in Figs. B2.29 and B2.30 for Collias and Lautagne, and numerical results are listed in Table B2.9. Full details for all scenarios are provided as additional supplement (*DRAC* CSV-file). In both figures, age based on extreme dose-rate scenarios considering equivalent U values derived from pre-Ra and post-Ra nuclides are visualised using a diamond.

In Collias, all samples were taken from a single profile wall. All ages increase with depth (Fig. B2.29 displays samples order by their stratigraphy), but appear to reach a plateau in the lower part of the profile (BDX21327–BDX21329). The outer age margins are ca 25 ka (top) and 100 ka (bottom). Age inversions overlap within uncertainties and are not considered significant. While this pattern is similar for ages calculated as mean \pm standard error of the mean (displayed in blue) and using the ‘baSAR’ modelling approach (displayed in red), the Bayesian approach leads to considerable older ages in the lower part of the profile. Nevertheless, given the luminescence age and D_e values close to commonly accepted saturation values for quartz luminescence measured in the UV wavelength region, an age underestimation cannot be excluded and ages must be interpreted cautiously. Unfortunately, the IR-RF age results (samples BDX21322 and BDX21329; K-feldspar fraction) appear to suffer from insufficient signal bleaching. BDX21322 exhibits an age roughly two times as old as the age from the quartz fraction. In Fig. B2.29 the age result of sample BDX21329 is even off-scale and not shown in the plot.

Additionally, the cause of the aforementioned broad D_e distributions either due to poor bleaching during the periods of geomorphic activity in the first place, and/or secondary sediment mixing during the periods of geomorphic stability and pedogenesis, remain unresolved. Thus the OSL ages (see below) for Collias provide an important first estimate for the site, but should not be over-interpreted

At Lautagne, samples were taken from two different profiles in close vicinity and ages are displayed in two different age-depth plots (Figs. B2.30A–B). Ages range from ca 7.5 ka (top) to 31 ka (bottom) and increase slightly with depth. It appears that samples BDX18949 and BDX18950 show an age inversion, which is repeated in a similar stratigraphic (not similar depth) in the second profile (Fig. B2.30). Therefore, it is likely that both age inversions refer to a similar transportation process at the site of Lautagne.

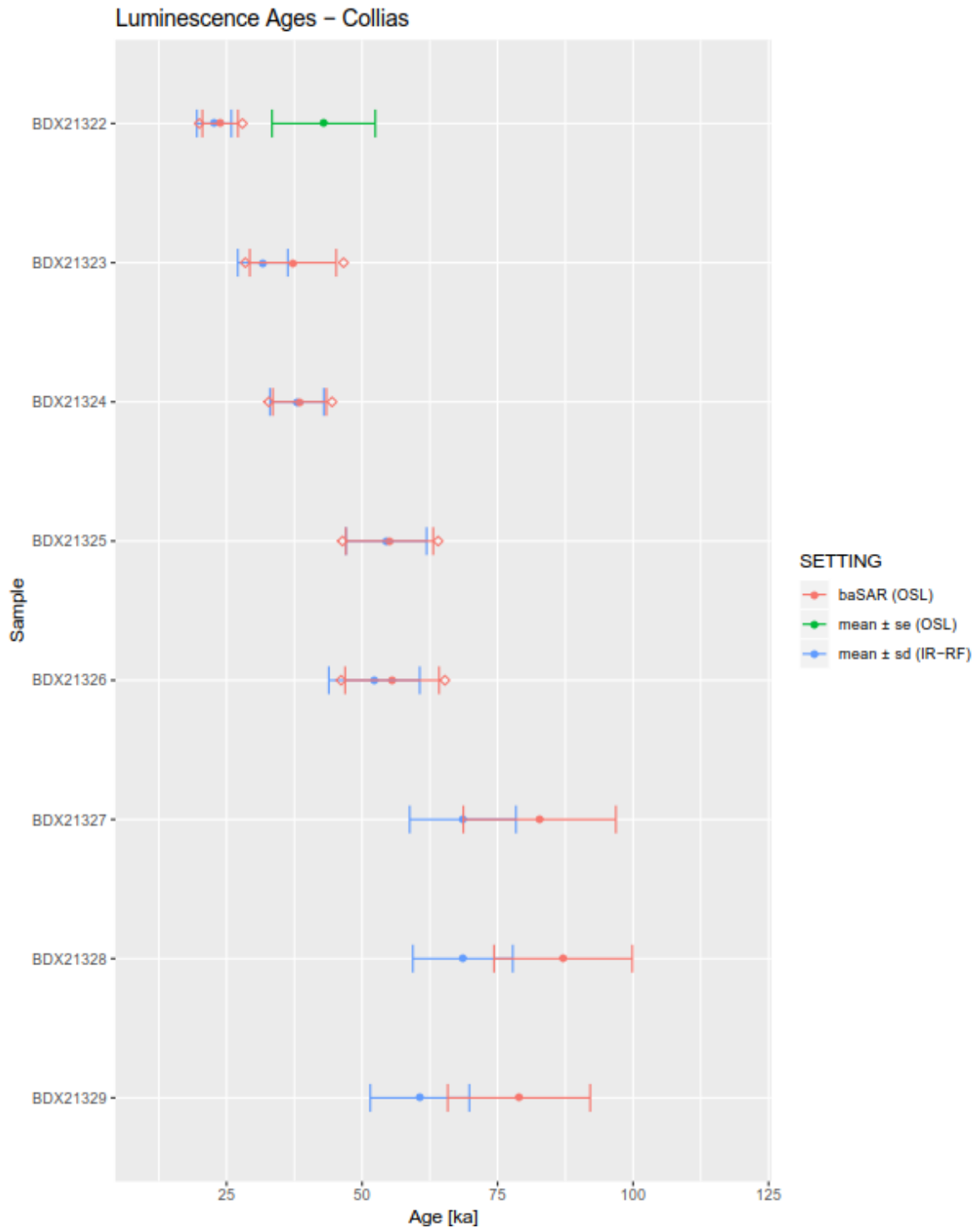


Figure B2.29: The graph shows quartz and feldspar luminescence ages stratigraphically ordered for the profile Collias. Red symbols show luminescence ages for which the central dose was obtained using model 'baSAR'. Other ages plotted as quoted in the legend. The IR-RF age of sample BDX21329 is off the scale (>125 ka; cf. Table B2.9). The red diamonds indicate minima and maxima ages for the two dose-rate scenarios taking into account the equivalent U concentration obtained from pre-Ra and post-Ra. Samples BDX21327–BDX21329 did not show a radioactive disequilibrium. Error bars show a 2σ interval.

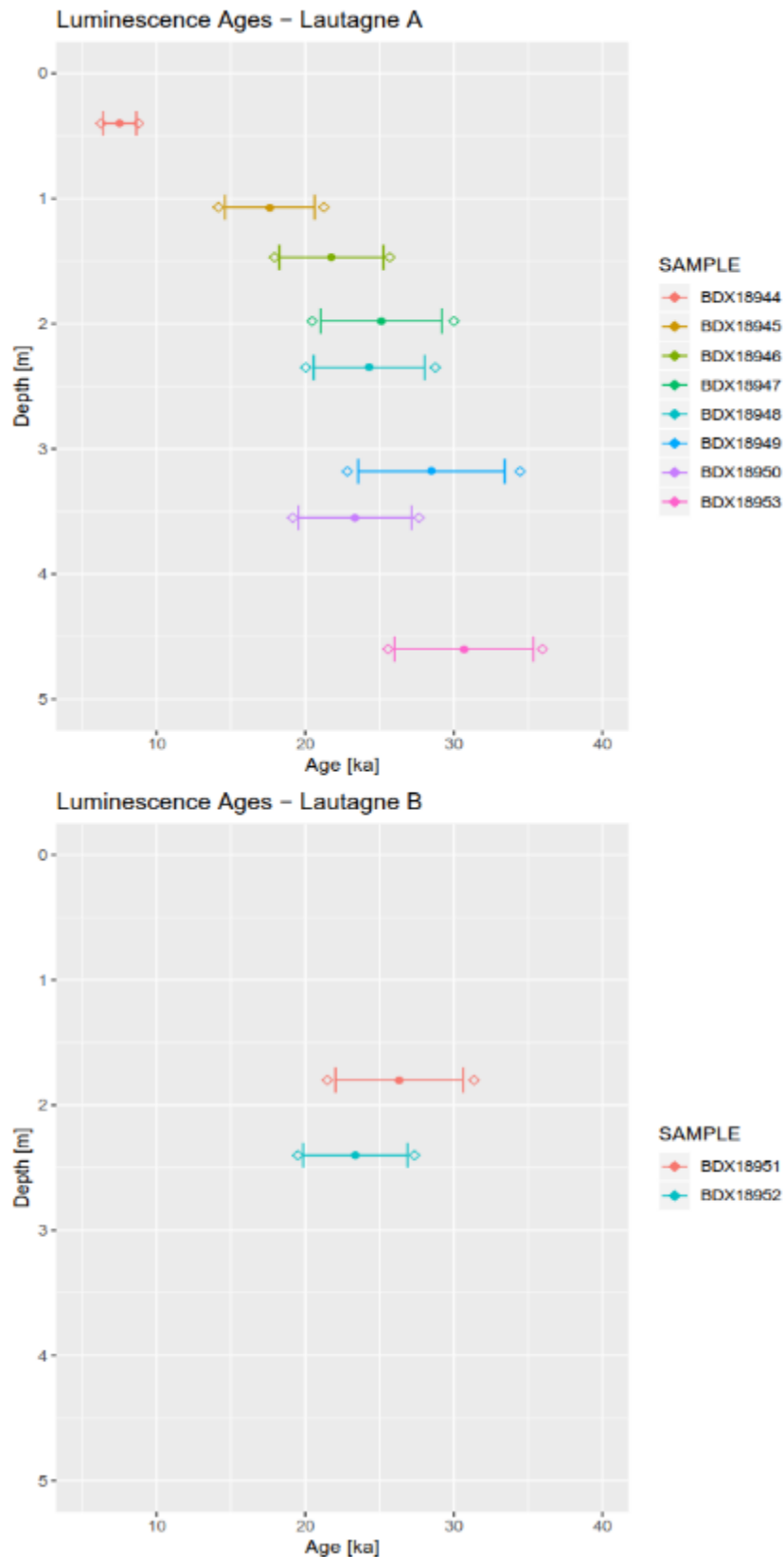


Figure B2.30: Age-depth plots of the fine grain quartz ages of the site Lautagne. Shown are mean ages and standard errors of the mean using the average dose model (2σ). The samples originate from two separate at the site Lautagne and are thus presented in two separate plots (A, top) and (B, bottom). The diamonds indicate the limits for the extreme dose-rate scenarios (equivalent U determined from pre-Ra and post-Ra).

Table B2.9: Final dose rates, equivalent (D_e) and age values. Standard errors are quoted as 1σ , rounded to one digit. Final ages taken for this study are quoted in bold numbers. For full details see the supplementary DRAC CSV-file.

Setting	Sample	M.	External dose rate (water corr.)			Internal dose rate			$D_{cosm.}$	$D_{ext.}$	$D_{int.}$	$D_{env.}$	D_e	Age
			D_{α}	D_{β}	D_{γ}	D_{α}	D_{β}	D_{γ}	[Gy ka ⁻¹]	[Gy ka ⁻¹]	[Gy ka ⁻¹]	[Gy]	[ka]	
Collias.Q	BDX21322	Q	0.0±0.0	1.1±0.1	0.8±0.0	0.0±0.0	0.0±0.0	0.0±0.0	0.3±0.0	2.2±0.1	0.0±0.0	48.9±2.5	22.7±1.6	
Collias.BAY	BDX21322	Q	0.0±0.0	1.1±0.1	0.8±0.0	0.0±0.0	0.0±0.0	0.0±0.0	0.3±0.0	2.2±0.1	0.0±0.0	51.4±2.6	23.8±1.7	
Collias.IRRF	BDX21322	F	0.1±0.0	1.1±0.1	0.8±0.0	0.0±0.0	0.6±0.2	0.6±0.2	0.3±0.0	2.3±0.1	0.6±0.2	125.5±9.8	42.9±4.9	
Collias.Q	BDX21323	Q	0.0±0.0	1.0±0.1	0.8±0.0	0.0±0.0	0.0±0.0	0.0±0.0	0.2±0.0	1.9±0.1	0.0±0.0	60.9±3.4	31.7±2.4	
Collias.BAY	BDX21323	Q	0.0±0.0	1.0±0.1	0.8±0.0	0.0±0.0	0.0±0.0	0.0±0.0	0.2±0.0	1.9±0.1	0.0±0.0	71.6±7.0	37.3±4.1	
Collias.Q	BDX21324	Q	0.0±0.0	1.0±0.1	0.8±0.0	0.0±0.0	0.0±0.0	0.0±0.0	0.2±0.0	1.9±0.1	0.0±0.0	71.1±3.2	38.0±2.5	
Collias.BAY	BDX21324	Q	0.0±0.0	1.0±0.1	0.8±0.0	0.0±0.0	0.0±0.0	0.0±0.0	0.2±0.0	1.9±0.1	0.0±0.0	72.0±3.1	38.5±2.5	
Collias.Q	BDX21325	Q	0.0±0.0	0.9±0.0	0.7±0.0	0.0±0.0	0.0±0.0	0.0±0.0	0.1±0.0	1.7±0.1	0.0±0.0	93.7±4.6	54.5±3.8	
Collias.BAY	BDX21325	Q	0.0±0.0	0.9±0.0	0.7±0.0	0.0±0.0	0.0±0.0	0.0±0.0	0.1±0.0	1.7±0.1	0.0±0.0	94.7±5.3	55.1±4.1	
Collias.Q	BDX21326	Q	0.0±0.0	1.0±0.1	0.8±0.0	0.0±0.0	0.0±0.0	0.0±0.0	0.1±0.0	1.9±0.1	0.0±0.0	100.5±6.6	52.3±4.3	
Collias.BAY	BDX21326	Q	0.0±0.0	1.0±0.1	0.8±0.0	0.0±0.0	0.0±0.0	0.0±0.0	0.1±0.0	1.9±0.1	0.0±0.0	106.8±6.7	55.5±4.4	
Collias.Q	BDX21327	Q	0.0±0.0	1.1±0.1	0.9±0.0	0.0±0.0	0.0±0.0	0.0±0.0	0.1±0.0	2.0±0.1	0.0±0.0	140.1±7.5	68.6±5.0	
Collias.BAY	BDX21327	Q	0.0±0.0	1.1±0.1	0.9±0.0	0.0±0.0	0.0±0.0	0.0±0.0	0.1±0.0	2.0±0.1	0.0±0.0	169.1±12.1	82.8±7.2	
Collias.Q	BDX21328	Q	0.0±0.0	1.3±0.1	1.1±0.1	0.0±0.0	0.0±0.0	0.0±0.0	0.1±0.0	2.5±0.1	0.0±0.0	172.0±8.1	68.6±4.7	
Collias.BAY	BDX21328	Q	0.0±0.0	1.3±0.1	1.0±0.0	0.0±0.0	0.0±0.0	0.0±0.0	0.1±0.0	2.4±0.1	0.0±0.0	212.4±12.0	87.1±6.5	
Collias.Q	BDX21329	Q	0.0±0.0	1.4±0.1	1.1±0.1	0.0±0.0	0.0±0.0	0.0±0.0	0.1±0.0	2.6±0.1	0.0±0.0	155.6±9.2	60.7±4.7	
Collias.BAY	BDX21329	Q	0.0±0.0	1.4±0.1	1.1±0.1	0.0±0.0	0.0±0.0	0.0±0.0	0.1±0.0	2.6±0.1	0.0±0.0	202.5±14.1	78.9±6.7	
Collias.IRRF	BDX21329	F	0.1±0.0	1.4±0.1	1.1±0.1	0.0±0.0	0.6±0.2	0.6±0.2	0.1±0.0	2.8±0.1	0.6±0.2	674.6±7.6	199.4±15.3	
Lautagne.FGQ	BDX18944	Q	0.3±0.1	1.1±0.1	0.7±0.0	0.0±0.0	0.0±0.0	0.0±0.0	0.2±0.0	2.3±0.1	0.0±0.0	17.3±0.4	7.5±0.6	
Lautagne.FGQ	BDX18945	Q	0.3±0.1	1.1±0.1	0.7±0.0	0.0±0.0	0.0±0.0	0.0±0.0	0.2±0.0	2.4±0.1	0.0±0.0	42.5±2.0	17.6±1.5	
Lautagne.FGQ	BDX18946	Q	0.3±0.1	1.2±0.1	0.8±0.0	0.0±0.0	0.0±0.0	0.0±0.0	0.2±0.0	2.5±0.1	0.0±0.0	53.8±2.0	21.8±1.8	
Lautagne.FGQ	BDX18947	Q	0.3±0.1	1.2±0.1	0.8±0.0	0.0±0.0	0.0±0.0	0.0±0.0	0.2±0.0	2.5±0.1	0.0±0.0	63.0±2.5	25.1±2.1	
Lautagne.FGQ	BDX18948	Q	0.4±0.1	1.3±0.1	0.9±0.0	0.0±0.0	0.0±0.0	0.0±0.0	0.2±0.0	2.7±0.1	0.0±0.0	64.8±1.8	24.3±1.9	
Lautagne.FGQ	BDX18949	Q	0.4±0.1	1.4±0.1	0.9±0.0	0.0±0.0	0.0±0.0	0.0±0.0	0.1±0.0	2.8±0.1	0.0±0.0	80.8±4.0	28.5±2.5	
Lautagne.FGQ	BDX18950	Q	0.3±0.1	1.3±0.1	0.9±0.0	0.0±0.0	0.0±0.0	0.0±0.0	0.1±0.0	2.7±0.1	0.0±0.0	63.5±2.6	23.3±2.0	
Lautagne.FGQ	BDX18951	Q	0.4±0.1	1.3±0.1	0.9±0.0	0.0±0.0	0.0±0.0	0.0±0.0	0.2±0.0	2.7±0.1	0.0±0.0	71.7±2.8	26.3±2.2	
Lautagne.FGQ	BDX18952	Q	0.4±0.1	1.4±0.1	0.9±0.0	0.0±0.0	0.0±0.0	0.0±0.0	0.2±0.0	2.8±0.1	0.0±0.0	66.6±1.4	23.4±1.8	
Lautagne.FGQ	BDX18953	Q	0.4±0.1	1.5±0.1	1.1±0.1	0.0±0.0	0.0±0.0	0.0±0.0	0.1±0.0	3.0±0.1	0.0±0.0	93.4±2.4	30.7±2.4	

Q: coarse grain quartz; D_e values quoted as mean ± standard error of the mean. BAY: coarse grain quartz; D_e represent the 'best-fit' central dose and the standard error of the central dose.

IRRF: coarse grain feldspar measured with infrared radiofluorescence; D_e values quoted as mean ± standard deviation.

FGQ: fine grain quartz; D_e values quoted as mean ± standard error determined with the average dose model.

The final age calculations include the following systematic errors: D_{α} : 1%, D_{β} : 1%, D_{γ} : 5% (as situ measurements), D_{β} : 3% (γ-ray spectroscopy), β-sources calibration: 3%.

Acknowledgements

The sample preparation of the samples from Lautagne was greatly supported by the luminescence team from the Justus-Liebig University of Giessen (head: Prof Dr Markus Fuchs), namely Veit van Diedenhoven and Urs Tilmann Wolpert, who helped out in times of need. The sample preparation of the samples from Collias was made possible by the luminescence team from the University of Bayreuth (head: Dr Christoph Schmidt) who gave us access to their sieving equipment. The remaining sample preparation in Bordeaux was supported by Julie Faure and Pierre Bidaud.

Chapter 3: Palaeosols in loess at Collias (SE-France) and their palaeoenvironmental significance (study 2)

Nora Pfaffner¹, Annette Kadereit², Sebastian Kreutzer^{2,3,4}, Sophie Cornu⁵, Mathieu Bosq⁶, Pascal Bertran^{6,7}, Daniela Sauer¹

¹) Department of Physical Geography, University of Göttingen, 37077 Göttingen, Germany

²) Heidelberg Luminescence Laboratory, Institute of Geography, University of Heidelberg, 69120 Heidelberg, Germany

³) Geography & Earth Sciences, Aberystwyth University, SY23 3DB Aberystwyth, Wales, United Kingdom

⁴) Archéosciences Bordeaux, UMR 6034, CNRS - Université Bordeaux Montaigne, Pessac, France

⁵) Cerege, 13545 Aix-en-Provence, France

⁶) PACEA, UMR 5199 CNRS–Université de Bordeaux-CNRS, 33615 Pessac, France

⁷) Inrap, 33130 Bègles, France

Manuscript in preparation.

Table 3.10: Authors contribution to study 2.

Authors	Contribution to study
Nora Pfaffner ^{1,2}	Investigation, Methodology, Data validation and interpretation, Writing -original draft, Visualisation
Annette Kadereit ³	Project-conceptualisation, Investigation, Methodology, Data validation and interpretation, Writing – review & editing, Visualisation
Sebastian Kreutzer ^{2,3,4}	Methodology, Writing - review & editing
Sophie Cornu ⁵	Investigation, Writing - review & editing
Mathieu Bosq ⁶	Investigation, Writing - review & editing
Pascal Bertran ^{6,7}	Writing - review & editing
Daniela Sauer ¹	Project-conceptualisation, Investigation, Data validation and interpretation, Writing – review & editing,

Abstract

Palaeosol horizons in loess-palaeosol sections (LPSs) serve as valuable palaeoenvironmental archives. Here, we present new insights of the LPS Collias (-Wood) and three nearby complementary sections, i.e., Collias-North, Collias-North_D112 and Collias-South_D112 situated in the southern, Mediterranean Rhône Rift Valley, SE France. The identified soil and sediment horizons were analysed for colour, particle-size distribution, carbonate content, and major element concentrations to apply geochemical indices. The MIS 5 soil-complex comprises of a truncated Chromic Luvisol, including a thick petrocalcic layer for the Eemian and several overlaying cambic horizons formed during the Early Glacial. For the MIS 3, a truncated brown Cambisol with large, elongated, vertically oriented calcium carbonate nodules and long, brown tongues defined as root-related biopores, was identified. The MIS 4 and 2 sediments display varying weathering intensities from yellow-olive C and BC horizons during MIS 4 to (yellow)-brown BC horizons during MIS 2. Considering possibly erosion, the Holocene Cambisol is assumed to originate from less recent precipitation as the assumed more humid

conditions for the MIS 5e and the interstadial phases of the MIS 3. The comparison with the Mediterranean LPS of NE Spain (Ebro Valley), Italy and NW Croatia (Po Valley) suggested similar major soil formation conditions during the Last Interglacial and Glacial period. However, less pronounced climatic shifts in terms of numbers of soil horizons especially during the MIS 3 at Collias, may indicate more stable and possible humid climate conditions in the southern Rhône Rift Valley.

Keywords: Loess, Palaeosols, Palaeoenvironment, Rhône Rift Valley; Mediterranean

3.1 Introduction

Palaeosol horizons in loess sections are important sources for better understanding palaeoenvironmental dynamics of the glacial-interglacial cycles. The modification of loess by pedogenic processes and their resulting properties can be interpreted as indicators (proxies) of former climatic conditions and their changes (Kemp, 2001). Thus, intensely developed soil horizons may indicate phases of comparably warm and/or moist conditions with a relatively stable land surface while less or no soil formation may signify cold and/or arid/dry climatic conditions with a geomorphologically more unstable landscape surface. Moreover, it is possible to connect pedo-features (e.g. size and position of secondary carbonate nodules, Fe-Mn nodules), the moisture regimes (e.g. active layers, ice wedges, sand wedges, redoximorphic features) and biogenic remains (e.g. former root channels, earthworm faeces) together with primary sedimentary facies characteristics (e.g. gravel contents) of the palaeosol horizons to the respective prevailing palaeoconditions. However, differentiating between the factors climate and time, when trying to reconstruct the extent of soil formation, is a well-known problem in palaeopedology (Catt, 1991; Kemp, 2001). However, in connection with a reliable chronostratigraphy, the identified soil characteristics can be correlated with known regional palaeoclimate conditions to understand their effects on the local soil formation, moisture regimes and erodibility, and to identify their patterns of change.

Understanding past-climatic changes is crucial for regions, which are highly vulnerable to expected future climate changes, like the Mediterranean region. The Mediterranean is regarded as a hot-spot of responsiveness by projections of future climate change (Giorgi and Lionello, 2008). So far, expected future changes comprise a possible increase in precipitation intensity and a raise of extreme temperatures, and resulting geomorphic processes like, e.g., slope wash (Goubanva and Li, 2007). However, the Mediterranean is a highly diverse region (e.g. geology, topography, vegetation) and thus shows great spatial climatic and palaeoenvironmental variability on a sub-regional level. Presently, the Mediterranean region is located in a transition zone between a subtropical desert climate to the south (northern Africa) and a humid-temperate climate to the north (central Europe) (Lionello et al. 2007). Slight northward shifts of the atmospheric circulation zones, accompanied by increased anticyclonic

circulation (Azores), as predicted for the end of the 21st century, may result in higher temperatures especially during the summer, and less humidity for the northern Mediterranean especially in summer (and for the southern Mediterranean especially in winter) (Giorgi and Lionello, 2008; Lionello and Scarascia, 2018). Mean annual precipitation (MAP) will be higher in the north-eastern Mediterranean, compared to the north-western regions (Lionello et al. 2007). For soil forming processes not only the annual amount but also the seasonal distribution of precipitation as well as the precipitation concentration and number of arid months are leading factors, which determine the variety of existing soil types (e.g. Calcisol, Cambisol, Luvisol) in the sub-humid Mediterranean area (Yaalon, 1997).

(Palaeo-)soil horizons with varying thicknesses in loess and loess-like sediments of the northern Mediterranean region are distributed along the foothills of major mountain ranges (Alps, Pyrenees, Pre-Alps, Apennines) along coast lines, on islands and in large (river) basins (Rhodenburg und Sabelberg, 1973; Brunnacker, 1974; Brosche und Walther, 1977; Cremaschi, 1990a, 1990b; Günster, 1999; Rose et al. 1999; Bogner et al. 2003; Ferraro, 2009; Wacha et al. 2011a, 2011b, 2018; Wagner et al. 2014; Boixadera et al. 2015; Cremaschi et al. 2015; Zerboni et al. 2015; Boretto et al. 2017; Constantini et al. 2018; Wolf et al. 2018, 2019; Zhang et al. 2018). Documentations of loess-palaeosol sections (LPSs) and corresponding palaeosol studies in SE France were carried out already in the beginning and middle of the last century by Marcelin (1926), Suen (1934), Tricart (1952), Mazenot (1956, 1957), Bourdier (1958), Alimen (1965), Bonifay (1965) and, more recently, by Franc et al. (2017) and Bosq et al. (2018, 2020a, 2020b). Early observations of LPS at Collias, southern Rhône Rift Valley (SE-France), identified two major loess deposits, intercalated by one reworked soil and underlain by a soil complex, but disagreement exists to which interglacial phase the complex belongs (Tricart, 1952; Mazenot, 1956; Bourdier, 1958; Bonifay, 1965). However, in order to decipher such pedo-complexes in greater detail, the character and intensity of pedogenic processes needs to be determined by measured soil-chemical proxies and the respective soil horizons have to be supported by a reliable chronostratigraphy. The study of Bosq et al. (2020b) provides an excellent sedimentological and chronostratigraphical investigation of one LPS at Collias (Collias-Wood).

In this study, we present four profiles from Collias LPS, focusing on the soil forming processes and conditions during the Last Interglacial-Glacial cycle by determining their soil-chemical properties and features. The aims are to i) classify the palaeosol types, thus contributing new information for a better understanding of the past climate conditions at the site and hence complementing the palaeoenvironmental picture for SE France and ii) compare the palaeosols to the recent soil formation. Especially, the reconstruction of the Last Interglacial (Eemian) palaeoenvironmental conditions has a high relevance, as the Eemian is supposed to having

been several degrees warmer than the present (e.g. Kukla et al. 2002; Brewer et al. 2008; North-GRIP Members, 2004; Wilcox et al. 2020), which – with reservations (e.g. different insolation pattern in the northern latitudes (e.g. Pedersen et al. 2017) – may be relevant in view of global climate warming. Although, the precise classification of the (palaeo)-soil types of Mediterranean LPSs, including the recent soil, is highly challenging due to complex post-formational processes like intense erosion/truncation and redeposition of the reworked soil material, enhanced by the long history of anthropogenic use (Yaalon, 1997; García-Ruiz et al. 2013). We compare our findings with LPSs in the northern Mediterranean region, i.e., eastern Spain, northern Italy and north-western Croatia. These sections were selected with respect to comparable geographical positions (big river valleys) in the sub-humid Mediterranean, considering the west-eastern climatic trend and variations in altitude.

3.2 Materials and methods

3.2.1 Geographical settings

The studied sections are situated at Collias, SE France (Fig. 3.31). They are located in the Uzès basin, a peripheral part of the Rhodanian (Rhône) basin in Miocene times (Reynaud et al. 2006), and at 80 km distance to the recent Mediterranean coast line. The Uzès basin is a 15 km wide synclinal depression formed during the Pyrenean orogeny in the latest Cretaceous in Mesozoic deposits, which cover the Palaeozoic basement of the Massif Central (Reynaud et al. 2012; Satterfield et al. 2019). It is framed by Cretaceous outcrops and filled up with Miocene (i.e. glauconitic sandstone, grey marls and bioclastic carbonates with a lime-mud matrix), Pliocene and Quaternary deposits (Berger-Levrault, 1968; Reynaud et al. 2012). The basin is drained by two rivers, the Alzon which east of Collias joins the Gard, which drains into the Rhône River (Fig. 3.31). While both rivers incise into the Urgonien limestone (Lower Cretaceous), following the hydrographic system, the Gard River eroded a gorge with exposing rock cliffs (Berger-Levrault, 1968; Sheffer et al. 2008). The loess deposits are located in foot-slope positions at the edges of the basin, with especially thick deposits (>9 m) in the south, trapped between a major outcrop and the basin border (Tricart, 1952; Bonifay, 1965; Berger-Levrault, 1968; Bosq et al. 2018, 2020b). The present-day climate is Mediterranean with warm dry summers (5 arid months) and mild humid winters (Mean Annual Temperature, MAT: 14.5 °C; Mean Annual Precipitation, MAP: 809 mm) (Meteo-France, 2022e). The precipitation occurs mainly in spring and autumn and becomes most intense in September/October reaching up to >100 mm month⁻¹ (Sheffer et al. 2008; Diodato et al. 2016). The wind regime is characterised by westerly winds and dominated by the Mistral, a northerly, low-level, in the north-south running Rhône Rift Valley orographically enhanced cold wind (Guenard et al. 2005). The recent vegetation is presented by sclerophyllous forests, respectively mixed shrub-tree forests. These forests correspond to matorral woodlands (Garrigue) with a dominance of

Quercus ilex and *Ericaceae* (Beaudouin et al. 2007). Human activity had and still has a major impact on the studied area, especially through soil erosion caused by intensive agricultural use since the early times (Berger-Levrault, 1968; Durand and Leveau, 2004).

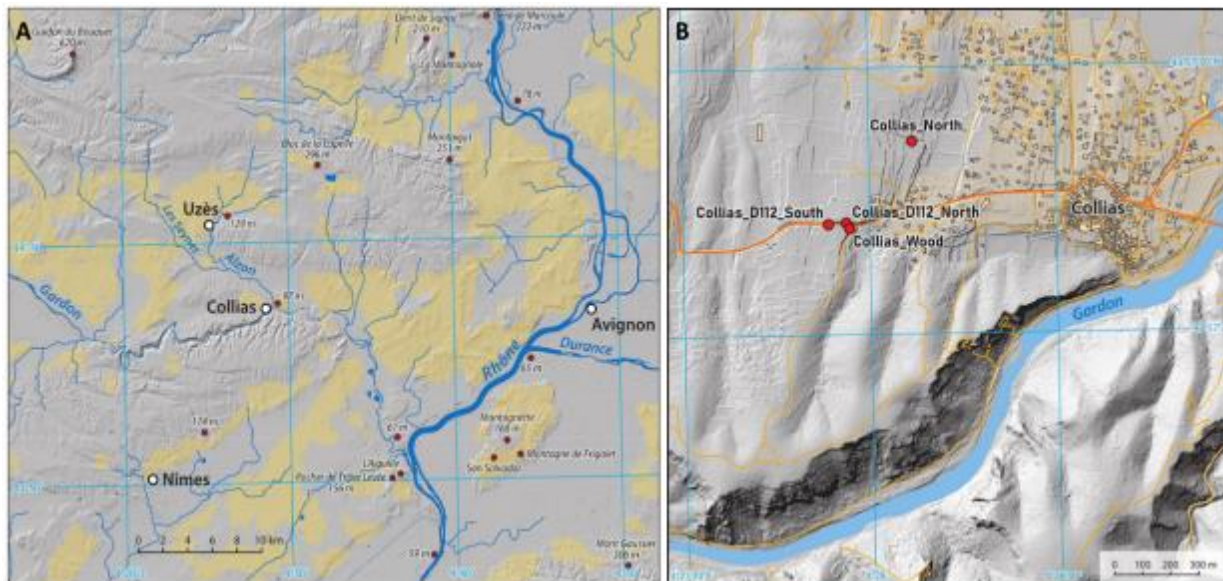


Figure 3.31: A) Area map Collias. Yellowish areas denote loess and sandy loess (cf. Bertran et al. 2021). Digital elevation model (DEM) based on TanDEM-X data (12 m resolution) provided by the German Aerospace Centre (DLR). B) Close-up map of the Collias research area, including the main section Collias-Wood and the additional sections Collias-North, Collias-North_D112 and Collias-South_D112. Orange-tinted colours representing settlement areas and roads. Shaded relief based on a DEM (1 m resolution) provided by the IGN-FRb géoservices (2021), Cartography: V. Schniepp).

3.2.2 Field sampling

During three field campaigns, the main Collias-Wood LPS (43°57'11.7 'N, 4°27'56.6 'E; 106 m a.s.l.) with a total thickness of 9 m, and three complementary profiles, i.e. Collias-North (4.5 m) (43°57'18.7 'N, 4°27'57.5 'E; 90 m a.s.l.), Collias-North_D112 (1.8 m) (43°57'12.7 'N, 4°27'54.5 'E; 113 m a.s.l.) and Collias-South_D112 (3.5 m) (43°57'12.6 'N, 4°27'56.1 'E; 115 m a.s.l.) were studied in detail (Fig. 3.32A-E). The profiles are located at the southern edge of the basin of Uzès, west of Collias (Fig. 3.31). Collias-Wood is situated in a middle slope position, exposed to the west and situated between erosional channels following the primary inclination from south to north. Collias-North_D112 and Collias-South_D112 are road cuts along the northern and southern side of road D112 constructed in a former erosional channel, following secondary inclination from west to east, and which are exposed to the south (Collias-North_D112) and the north (Collias-South_D112), respectively (Fig. 3.32). The terrain surface at all three sections is used for olive and wine cultivation and the surfaces have been levelled for creating terraced fields. Collias-North is situated ca 380 m NE of the other profiles in a footslope position and exposed to the north. The recent surface is covered by a semi-deciduous shrub-tree vegetation, but former agricultural use is evidenced in the profile by a relict Ap horizon. The additional profiles allowed to study the observed palaeosol horizons in

greater detail and to assess also the spatial variability of particular palaeosol horizons at a local scale.

The observed horizons and their characteristics are described and classified according to guidelines of the Food and Agriculture Organization of the United Nations (FAO, 2006) and corresponding soil types were classified afterwards according to World Reference Base for Soil Resources (IUSS Working Group WRB, 2022). Sediments and soils were sampled for soil-chemical analyses by taking mixed samples per horizon defined according to altering texture and colour. Horizons thicker than 30 cm were subdivided for sampling and special features (e.g. infilled biopores) were additionally sampled. The size and orientation of secondary carbonates were determined and their forms classified according to FAO (2006). After cleaning, a more detailed characterisation of their morphology was performed on a macroscale level. This was done to reconstruct their formation, considering the potential complexity of the formation mechanisms, in order to utilise them as palaeoenvironmental proxies (Becze-Deák et al. 1997; Barta, 2011a, 2016; Gocke et al. 2014; Zamanian et al. 2016).



Figure 3.32: Main Collias-Wood LPS (A), Rhône Rift Valley, SE France and additional profiles Collias-North_D112 (B), Collias-South_D112 (C) and Collias-North (E). View from W to E: Road D112 leading out of Collias in a west-east orientated erosion channel, where sections Collias-North_D112 (right) and Collias-South_D112 (left) are located (D) (photos taken by D. Sauer and N. Pfaffner (2016–2019)).

3.2.3 Laboratory methods

After drying, the samples were sieved (2 mm mesh size) and rock fragment content was determined by weighting and presented in wt %. The soil texture was obtained by determining the particle size distribution of the fine soil fraction (<2 mm). The organic matter was removed by 30 % H₂O₂ and samples were dispersed with a 0.1 % NaOH solution. Sediment particles larger than 63 µm were determined by the sieve method and particles smaller than 63 µm were measured using a SediGraph III Plus (Micromeritics). Particle sizes were determined in wt % and classified according to FAO (2006). The total clay content (≤2 µm) and the clay/silt ratio were used to obtain the degree of weathering. Soil organic carbon (SOC) contents were obtained by measuring total C contents with a CHN elemental analyser (TruSpec Micro, LECO) and subsequently the carbon contents of carbonates (CaCO₃) were subtracted from the total C contents. CaCO₃ contents were determined in wt % by the gas-volumetric method using a Scheibler apparatus (Blume et al. 2011).

Total contents of Fe, Al, Ca, Mg, Si, Mn were determined by fusing samples with a Li-meta-tetraborate mixture (ratio 1:4), diluted with 5 % HNO₃ and analysed by inductively coupled plasma optical emission spectrometry (ICP-OES, iCAP 7000, Thermo Scientific) (Potts, 1987). The total content of Na and K were determined by a flame spectrometer (Elex 6361, Eppendorf). Element concentrations were used to estimate weathering intensities by determining the following indices based on the molar element ratios: the WI_{MER} (weathering index based on the molar element ratio) calculated as $WI_{MER} = (Ca (Ca, \text{ after subtraction of Ca in } CaCO_3) + Mg + K + Na) / Al$ (Sauer, 2016). The CPA index (Chemical Proxy of Alteration), calculated as $CPA = Al_2O_3 / (Al_2O_3 + Na_2O) \times 100$ and the Si/Al ratio (Sheldon and Tabor, 2009; Buggle et al., 2011). Each index reflects most directly the loss of bases by silicate weathering due to pedogenesis. Further geochemical indices of Collias-Wood are presented in Bosq et al. (2020b).

Pedogenic Fe, Al and Mn contents were determined by Na₂S₂O₄ extraction and analysed by ICP-OES (iCAP 7000, Thermo Scientific) (Sparks and Bartels, 1996). The ratio of pedogenic iron oxide contents (Fe_d) to total iron oxide contents (Fe_t), as a function of depth, reflects the degree of weathering of Fe-containing primary silicates and helps to identify weathered zones compared to less and non-weathered zones. The colours were obtained by using Munsell Soil Colour Charts and a handheld spectrophotometer CM-700d (Konica Minolta). The samples were measured three times with the spectrophotometer and the mean value of the results was converted into the CIE colour index, reflected by the L* a*b* (CIE, 1976). Higher a* values may indicate the presence of Hematite (red colour), formed at lower water contents and higher temperatures than Goethite (brown colour).

Optically stimulated luminescence (OSL) ages from Bosq et al. (2020b) of the Collias-Wood section were used to correlate findings with oxygen isotope curves from marine sediment cores and associated marine isotope stages (MIS), as well as with the INTIMATE event stratigraphy (Güter et al. 2003; Rasmussen et al. 2014).

3.3 Results – Characteristics of the horizons of Collias sections

At the main Collias-Wood LPS in total 19 horizons were identified and their boundaries verified by their soil and sediment-chemical characteristics (Fig. 3.33, Table A3.11). In terms of soil formation the section begins from bottom to top with a red(dish)-orange Interglacial/interstadial pedo-complex, followed by a brown, cambic interstadial soil-complex with prominent carbonate nodules and ends with the Holocene soil formation. The soil units are subdivided by a lower yellow/olivish loess unit, interlaced by fine bands and lenses of gravel and fine sand and upper loess horizons, which can be more characterised as a highly bioturbated weathered loess (Fig. 3.33).

Generally, the horizons of the additional profiles concur with those of Collias-Wood. Although, one or more horizons are missing, either because they were not accessible (the base of Collias-North; the top of Collias-South_D112) or because the parent material had not been deposited at the site or the parent material or solum was subsequently re-eroded (gaps of interstadial soil horizons and lower loess horizons at Collias-North_D112) (Fig. 3.34). In the following description of the characterisations of each horizon of all profiles are compiled.

3.3.1 Interglacial/Interstadial pedo-complex

The pedo-complex comprises of varying intense weathered horizons, which are assumed to reflect several erosion and-soil formation phases. The subdivision of the complex is based on changes of colour, structure, weathering intensity and observed in situ carbonate nodules. The complex is underlain by a ≥ 50 cm thick carbonate encrusted indurated horizon, classified as petrocalcic Bkm horizon, respectively (Fig. 3.35C) (FAO, 2006; Candy and Black, 2009). The petrocalcic horizon developed in sandy deposits, most likely molasse sediments of the early Miocene (Burdigalian) (Reynaud et al. 2012).

Bw and Bt horizons

The colour of the lowermost horizons of Collias-Wood (850–790 cm) (5 YR 3/6) and Collias-North_D112 (180–155 cm) (2.5 YR 3/6) is an intense red with the highest a^* values (15–17). The colour is due to rubefication and displays a Munsell hue redder than 7.5 YR (moist), which allows to use the qualifier “chromic” for the horizon (Schwertmann, 1993; IUSS Working Group WRB, 2022).

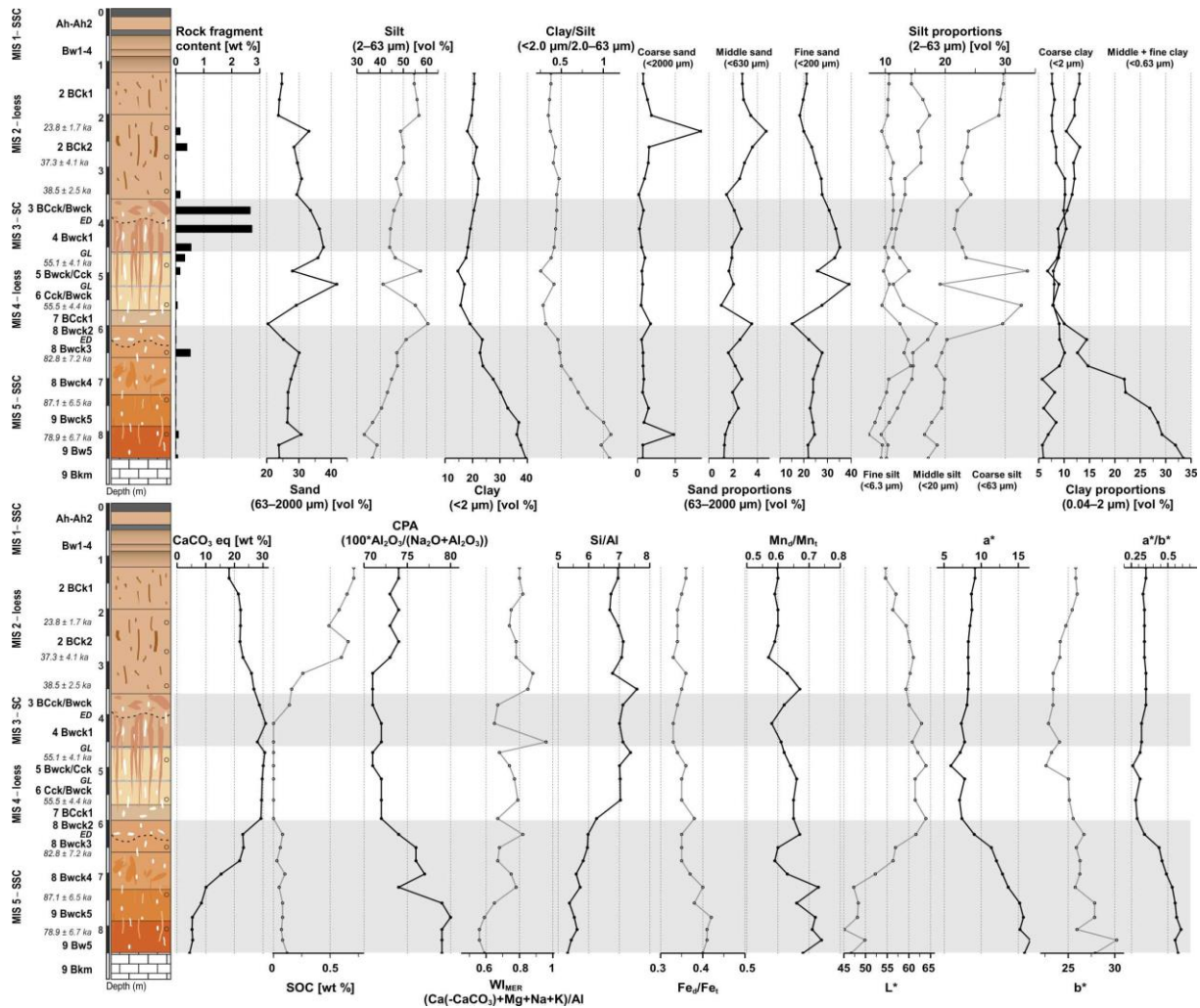


Figure 3.33: Stratigraphy of the Collias-Wood LPS, Rhône Rift Valley, SE France with palaeosol formation units marked as grey bars. Depth related upper curves of: rock fragment content [wt %], grain-size fractions of sand (63–2000 μm), silt (2–63 μm) and clay (<2 μm), in vol %; grain-size ratio of clay/silt (<2 $\mu\text{m}/2.0\text{--}63 \mu\text{m}$) and grain-size fractions of sand (fine sand: 63–200 μm , medium sand: 200–630 μm , coarse sand: 630–2000 μm), silt (fine silt: 2–6.3 μm , medium silt: 6.3–20 μm , coarse silt: 20–63 μm) and clay (fine clay + medium clay: <0.63 μm , coarse clay: 0.63–2 μm). Depth related lower curves of calcic carbonate equivalents in wt %, contents of soil organic carbon (SOC) in wt % and chemical proxy of alteration (CPA) ($100 \cdot \text{Al}_2\text{O}_3 / (\text{Na}_2\text{O} + \text{Al}_2\text{O}_3)$), weathering index of molar element ratio (Wl_{MER}) (Ca (after subtraction of Ca in CaCO_3) + $\text{Mg} + \text{K} + \text{Na}$) / Al), Si/Al and, ratios of pedogenic to total contents of iron and manganese (Fe_o/Fe_t , Mn_o/Mn_t) and colours of the CIE colour index, reflected by the parameters L^* , a^* , b^* and ratio of a^* and b^* . Black circles mark position of OSL samples, ages after Bosq et al. (2020b). SC: soil complex; SSC: soil -sediment-complex; GL: gravel lense; ED: erosional discontinuity.

The 3 Bt horizon of Collias-North_D112 displays the most intense weathering with maxima of clay (54 vol %), clay/silt (2.8), Fe_o/Fe_t (0.52) and CPA (84) as well as minima of Si/Al (4.5) and Wl_{MER} (0.41) (Fig. A3.41). The horizon has a clay texture with an angular to prismatic structure and abundant distinct clay and Mn coatings (Fig. 3.35D). Uniform contents of total sand as well as fine sand (63–125 μm) in the vertical direction implicate that soil formation took place in a

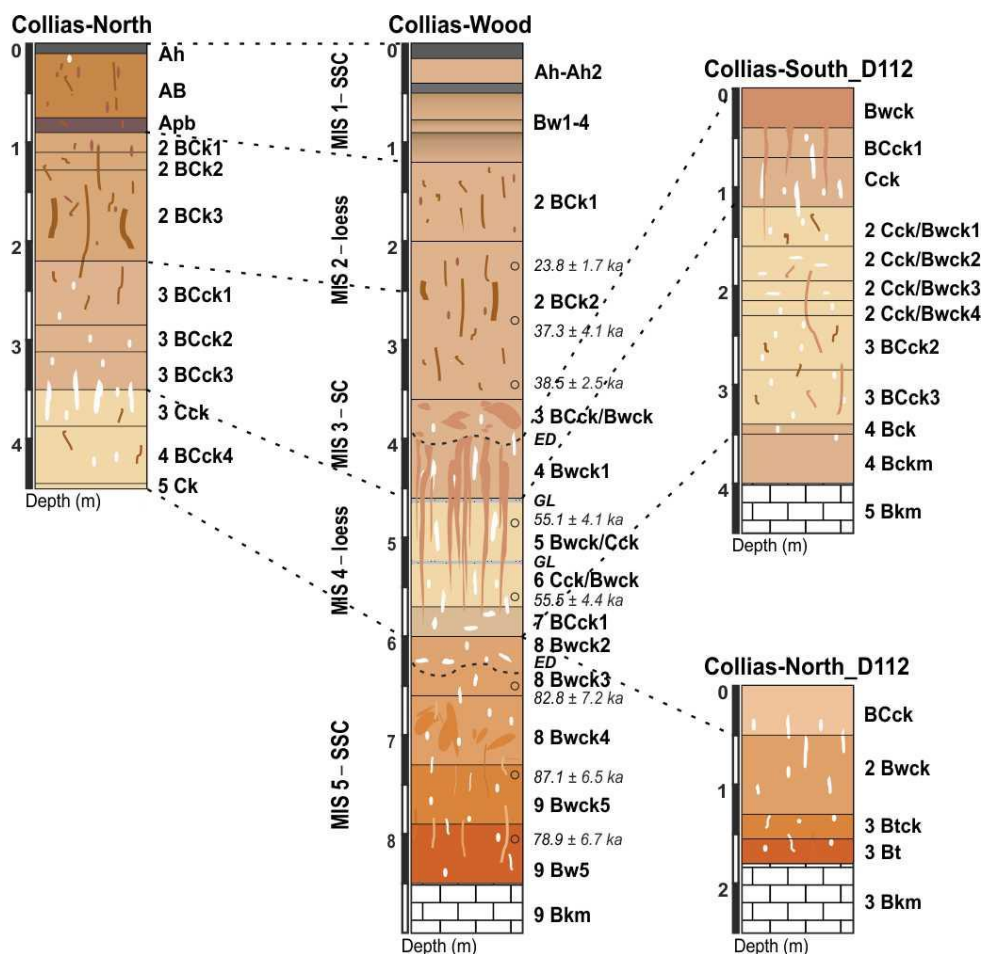


Figure 3.34: Stratigraphy of the main loess-palaeosol section Collias-Wood and correlation to horizons of the additional profiles Collias-North, Collias-South_D112 and Collias-North_D112, Rhône Rift Valley, SE France. SSC: soil sediment complex, SC: soil complex, ED: erosional discontinuity, GL: gravel lense. Black circles mark position of OSL samples (Bosq et al. 2020b).

lithologically uniform material, i.e. at Collias the loess sediment. The correlating 9 Bw5 horizon of Collias-Wood indicates less intense weathering with clay contents of 39 vol %; clay/silt: 1.1; Fe_d/Fe_t : 0.41; Si/Al: 4.9; WI_{MER} 0.52 and CPA: 82 (Fig. 3.33). The horizon is characterised by a clay loam texture, a subangular and angular structure and displays few to very few clay and Mn coatings (Fig. 3.35B). Both horizons contain up to 5 wt % $CaCO_3$, display few small in situ carbonate concretions and contain a marginal amount of rock fragments (0.02 wt %– 0.1 wt %).

In agreement with the field observations at both sites (Table A3.11) these horizons reflect the most intense weathering compared to all other horizons of the Collias sections. However, in contrast to the field observations, micromorphological evidence at Collias-Wood showed no clay coatings for the lowermost Bw horizon (Bosq et al. 2020b). We assume that in the middle-slope position of Collias-Wood a reworked soil-sediment was deposited, whereas in today's erosional channel of Collias-North_D112 parts of the in situ solum was preserved. The lack of clay coatings at Collias-Wood may be due to the reworking of the same soil material as observed at Collias-North_D112 and its redeposition as soil sediment. Thus, the red horizon

of Collias-North_D112 fits the criteria for an argic horizon and classified as Bt horizon (3 Bt, Fig. 3.35, A3.41), whereas the horizon of Collias-Wood shows cambic criteria, and is classified as Bw horizon (9 Bw5 horizon, Fig. 3.33) (FAO, 2006; IUSS Working Group WRB, 2022). We presume these horizons represent remains of a former Luvisol formation.

Bwck and Btck horizons

The four overlying Bwck horizons of Collias-Wood (790–600 cm; 9 Bwck5 to 8 Bwck2) are characterised by a gradual change of colour with decreasing depth from orange-red (5 YR 3/6) to orange (5 YR 4/4) to patchy brown-orange (7.5 YR 4/4) and brown (10 YR 4/4) (a^* value: 16 to 9). The uppermost brown 8 Bwck2 horizon represents the upper boundary with a change of colour between the lower brown-orange colour and the overlain loess unit with a yellow/olivish colour (Fig. 3.33). A similar trend of colour shifts (5 YR 3/6 to 5 YR 4/8 to 7.5 YR 4/6; a^* value: 17 to 14) was observed at Collias-North_D112 (155-50 cm). At this site the upper brown horizon is missing and the pedo-complex is directly overlain by a horizon designated to the upper loess unit (Fig. A3.41, Table A3.11).

The horizons of both sections show a vertical decrease of weathering intensity, indicated by a decrease of clay (48 vol % to vol 24 %); clay/silt (1.9 to 0.5); CPA (83 to 76) and Fe_d/Fe_t (0.43 to 0.35) and an increase of Si/Al (4.8 to 5.7), WI_{MER} (0.42 to 0.59) and $CaCO_3$ contents (8 wt % to 23 wt %). The texture at Collias-Wood changes from clay loam to silt loam and from an angular to a subangular structure; at Collias-North_D112 from clay to a clay loam and from an angular to a massive structure. The 2 Bwck and 3 Btck horizons at Collias-North_D112 contain many faint clay coatings and common to few Mn coatings, whereas at Collias-Wood only in the lower horizon very few clay and Mn coatings were observed, but in the upper brown horizon fine rounded soft Mn concretions (Figs. 3.33, A3.41, Table A3.11).

All horizons display enrichments of secondary carbonates, accumulated as in situ calcic nodules. Their size increases with decreasing depth, apart from the uppermost 8 Bwck2 horizon at Collias-Wood. Here, the carbonate concretions are relocated and the horizon contains up to 0.5 wt % of small rock fragments. The stronger accumulation of secondary carbonates in these horizons allowed to use the diagnostic criteria “cambic” for the Bwck at Collias-Wood and, due to the more intensely developed clay coatings, “argic” for the Btck at Collias-North_D112 (IUSS Working Group WRB, 2022).

Bck and Bckm horizon

At Collias-South_D112 (400+ – 340 cm) the lower horizons of the pedo-complex are missing and the calcrete is directly overlain by a yellow-brown horizon and a light brown horizon, which

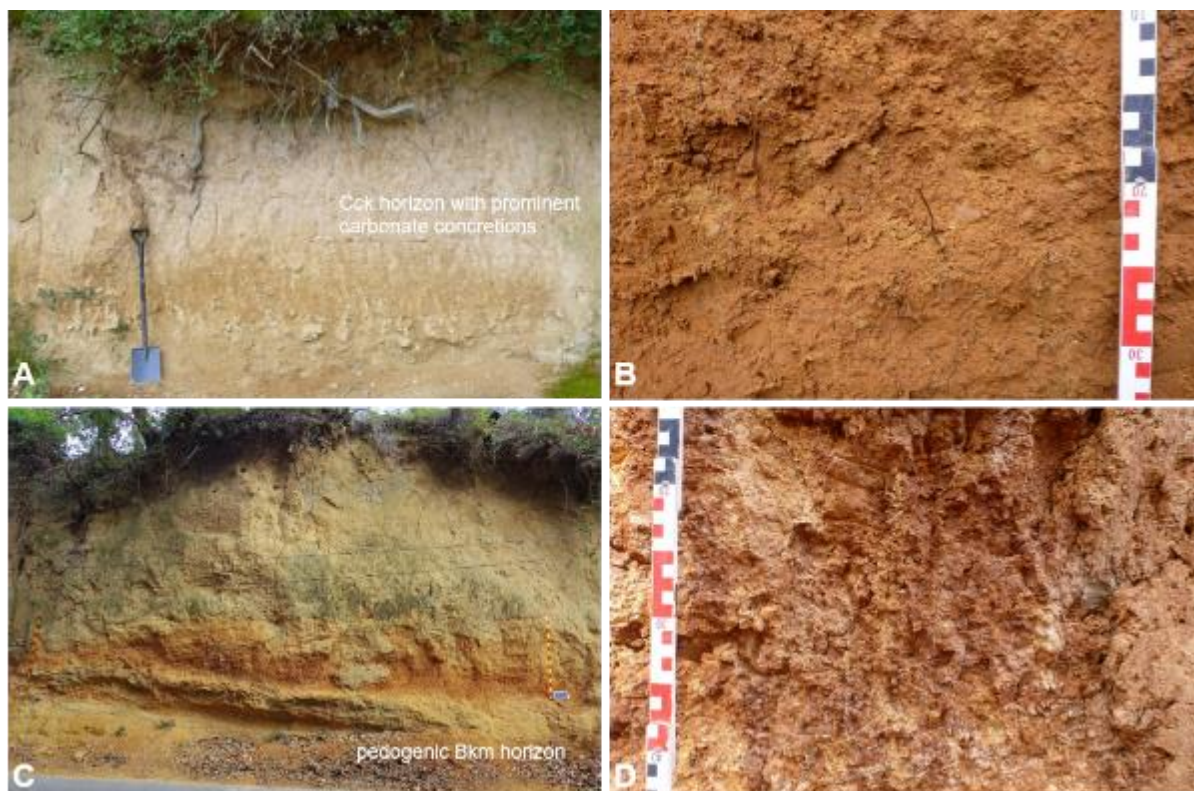


Figure 3.35: Photographs of special features of profiles of Collias LPS, Rhône Rift Valley, SE France. A) Prominent carbonate nodules in 3 Cck horizon of Collias-North before profile preparation. (B) Clay-loamy 9 Bw5 horizon of Collias-Wood with few to very few clay and Mn coatings. C) Petrocalcic Bkm horizon above Miocene sediments, showing, like road D112, a west-to-east inclination. Profile Collias-North_D112 at the right edge of the picture. D) Clayey 3 Bt horizon of Collias-North_D112 with a prismatic structure and abundant distinct clay and Mn coatings (photos taken by D. Sauer and N. Pfaffner (2016-2020)).

range from 10 YR 5/4 to 10 YR 6/4 (a^* value: ~ 7) (Fig. 3.32C, A3.42). The upper yellow-brown horizon contains small in situ carbonate nodules and is classified as 4 Bck horizon. The brighter brown colour (10 YR 6/4) of the lower horizon originates from the intense secondary carbonate enrichment, classifying it as a 4 Bckm horizon. The horizon has a massive structure and their characteristics (clay contents: ~ 26 vol %; clay/silt: 0.41–0.54; CPA: 71–72; Si/Al: 5.7–5.9; W_{MER} : 0.71 to 0.76; Fe_d/Fe_t : 0.39; $CaCO_3$: 27 wt %–34 wt %) indicate slightly less weathering than the uppermost corresponding horizons of the pedo-complex (8 Bwck2 at Collias-Wood, 2 Bwck at Collias-North_D112) and to not classify as cambic. Nevertheless, in consideration of the stratigraphic position of these horizons at Collias-South_D112 and the fact, they all have a silt loam texture, we assume they belong to the same pedo-complex.

3.3.2 Lower loess horizons

C(c)k, Cck/Bwck and BCck horizons

The colours of the horizons range from brown-olive (2.5 Y 3/3) to olive (2.5 Y 5/4) and yellow-olive (2.5 Y 5/4) (a^* value: 6–7) within decreasing depth. The horizons are characterised by abundant bioturbation evidenced by brown (10 YR 5/6) infilled biopores (section 3.4.1). They

are characterised by low contents of clay (15 vol % to 19 vol %) and clay/silt (0.30–0.38), medium Fe_d/Fe_t (0.37–0.38), medium CPA (69–75), medium WI_{MER} (0.59–0.85), medium $CaCO_3$ contents between 26 wt %–29 wt % and high Si/Al (5.9–8.0). They have a massive structure and a silt loam texture. Colour and texture indicate a re-deposited sediment-mixture of underlain brown Bwck (7 BCck1 at Collias-Wood, 3 BCck2-3 at Collias-South_D112) material of the underlain pedo-complex and superimposed olive C-horizon material. The horizons display various carbonate nodules, partly relocated (sect. 3.4.2, Table A3.11), and dominant Mn coatings at Collias-South_D112 (285–230 cm) and very fine, faint, rounded soft Mn concretions at Collias-Wood (600–570 cm). Due to their sediment-mixed character, the horizons were classified as BCck.

The characteristics of the upper olive and yellow-olive horizons (clay contents: 7 vol %–17 vol %; clay/silt: 0.26–0.86; CPA: 67–75; Si/Al: 6.9–4; WI_{MER} : 0.60–1.24; Fe_d/Fe_t : 0.34–0.36; $CaCO_3$: 27 wt %–30 wt %) rather indicate low weathering, but with a wide range of the measured values (Fig. A3.42). In contrast to the underlying brow-olive horizons, they have a massive to single grain structure with a texture alternating between sandy loam and silt loam. The varying colours and textures originate from two different (alternating) parent sediments, a coarser sediment, possibly the local reworked glauconitic sandstone and a finer loess sediment. The coarser texture challenges the comparison of the degree of weathering, but explains the scattering values. The horizons contain small angular rock fragments (up to 0.5 wt %). Collias-Wood displays two calcic carbonate encrusted gravel lenses (465–460 cm and 527–523 cm) (Fig. 3.36B), which delimit the two olive horizons (6 Cck/Bwck, 5 Bwck/Cck; 570 cm to 460 cm). At Collias-South_D112, no gravel lenses were observed, but they could be traced in the same sediment unit along the loess outcrop in the westward direction. Based on the low weathering of the horizons the olive sediment is designated as Cck or Ck depending on the appearance of the carbonate nodules, whereas the brown biopores are classified as Bwck due to their dominance occurrences.

3.3.3 Interstadial soil-complex

Cck, BCck and Bwck horizons

The horizons of this soil complex are characterised by an increase of weathering intensity with decreasing depth, reflected by a change of colour from yellow-brown (10 YR 5/6, 10 YR 6/4) to light brown (10 Y/R 5/4) to brown (10 Y/R 4/6) (a^* value: ~8). They display a gradual change of palaeoproxies from least to moderate weathered (47 wt % to 25 wt % $CaCO_3$; clay: 15 vol % to 25 vol %; clay/silt: 0.38 to 0.82; CPA: 66 to 75; Si/Al: 8.2 to 7.6; WI_{MER} : 1.61 to 0.58; Fe_d/Fe_t : 0.31 to 0.36), with decreasing amount of rock fragments (6.1 wt % to 0.4 wt %) and were classified as Cck to BCck to Bwck horizons (Figs. 3.33, A3.42, Table A3.11).

At Collias-South_D112 (120–0 cm), the brown Bwck horizon with its loam texture is underlain by a weakly weathered BCck and a no weathered Cck horizon. Both underlain horizons contain large, in situ carbonate nodules (Fig. 3.35A) and in-filled biopores (Fig. 3.36A-C). In consideration of the high amount of rock fragments of the Bwck horizon, we assume the horizons reflect at least one in situ Cambisol formation, whereas the upper part was truncated. In contrast, at Collias-Wood (460–400/410 cm), only one patchy yellow-brown 4 Bwck1 horizon with a silt loam texture and also pronounced brown infilled biopores with prominent carbonate nodules, remained. Although, the soil is mainly eroded and merely remains of it were mixed in the loess sediment, the horizon is classified as a cambic Bwck to signify the former soil formation.

An equivalent of the Bwck horizon is missing at Collias-North (350–220 cm), but parent material with pronounced carbonate nodules horizon (Cck) and overlying BCck horizons can be correlated to this horizon (Figs. 3.34, 3.35).

3.3.4 Upper loess horizons

BCck horizons

The upper loess horizons begin at Collias-Wood with the colluvial 3 BCck/Bwck horizon (400/410–360 cm), in which the loess sediment is classified as BCck and the in-worked soil remains from the underlain horizon (4 Bwck1 horizon) as Bwck. The horizon displays a silt loam texture, a weakly developed subangular blocky structure, a patchy brown (10 YR 4/6) and yellow-brown (10 Y/R 5/6) colour and high amount of rock fragments (2.7 wt %). A corresponding colluvial horizon, including reworked Bwck soil sediment, is missing at Collias-North. However, highest amounts of rock fragments (6.1 wt %) of the uppermost 3 BCck1 horizon suggests respective correlations.

The uppermost loess horizons displayed at Collias-Wood (360–120 cm), Collias-North (220 cm to 90 cm) and Collias-North_D112 (50–0+ cm) are weakly weathered horizons. At Collias-Wood the colour of the 2 BCk2 and 2 BCk1 horizons change from light brown (10 YR 5/4) and brown (10 YR 4/6) to grey-brown (10 YR 5/3) (a^* value: 8–9). In contrast, the corresponding horizons at Collias-North show a change from light brown (10 YR 5/4) and grey-brown (10 YR 5/3) to brown (10 YR 4/4) (a -value: 9), whereas the uppermost horizon of Collias-North_D112 has a light yellow-brown colour (10 YR 6/4) (a^* value: 10). The horizons display abundant features from biological activity, including former and recent roots as well as earthworm channels and infilled burrows. Together with an increase of soil structure and decrease of pseudomycelia they indicate initial soil formation with decreasing intensity. However, clay (20 vol % to 30 vol %) and weathering indices (CPA: 74–76; Si/Al: 5.9–7.1; WI_{MER} : 0.55–0.69), as well as Fe_d/Fe_t (0.34–0.35) display no noticeable changes (Figs. 3.33, A3.40).

We assume, that the brown colour similar to the Bwck horizons from the brown soil complex does not originate from similarly intense in situ weathering, but rather from relocated pre-weathered material with subsequently less intense in situ soil formation. The colluvial character is supported by contents of rock fragments (Figs. 3.33, A.3.40). Thus, the horizons are rather classified as BCK horizons.

3.3.5 Holocene soil

The recent soil formation at Collias is influenced by a long-time and intense agricultural use. At Collias-Wood (120–0 cm), the Ah horizon is underlain by four colluvial horizons, which each display a medium developed structure. With decreasing depth, the orange-brown matrix changes from an orange dominated to a brown dominated colour. Former Ah horizons may have delimited the colluvial horizons, but they were incorporated in the underlying material, most likely during different phases of terrace levelling. The colluvial horizons are classified as Bw (1–4) horizons according to the field observations. At Collias-North (90–0 cm), the recent Ah horizon is underlain by a brown colluvial horizon, followed by a former ploughed surface (A_{pb} horizon). The colluvial AB horizon above has a moderate subangular blocky structure, displays abundant dominant clay coatings and the horizons contain primary carbonate. The mixed characteristics are interpreted as former erosional processes of pre-weathered material with subsequent soil formation.

3.3.6 Biopores and secondary carbonates

Biopores

Biopores are defined as voids in the soil and sediment as the result of biological activity (e.g. plant roots growth, burrowing animals) strongly related to the formation of the soil structure (Kautz, 2015). The stratigraphical position, size, colour as well as the texture of the biopores and their infilling sediments can provide, combined with analysed palaeosol horizons and sediments, valuable information for reconstructing palaeoenvironmental conditions (Gocke et al. 2014).

The Collias sections are characterised by abundant recent and former (in-)filled biopores, as observed in all horizons. The size of the vertical oriented biopores varied from small (0.15 cm to 5 cm wide, up to 25 cm long) up to large tongues (5–10 cm wide, up to 2 m long), but large tongues are restricted to the Cambisol remain and the underlain loess horizons (Fig. 3.36A–B). The biopores are partly filled with sediment, partly encrusted by soft secondary carbonates and in situ carbonate nodules. The biopore infillings of the lower pedo-complex show a yellow to yellow-brown colour compared to the red-orange colour of the surrounding material (Fig.

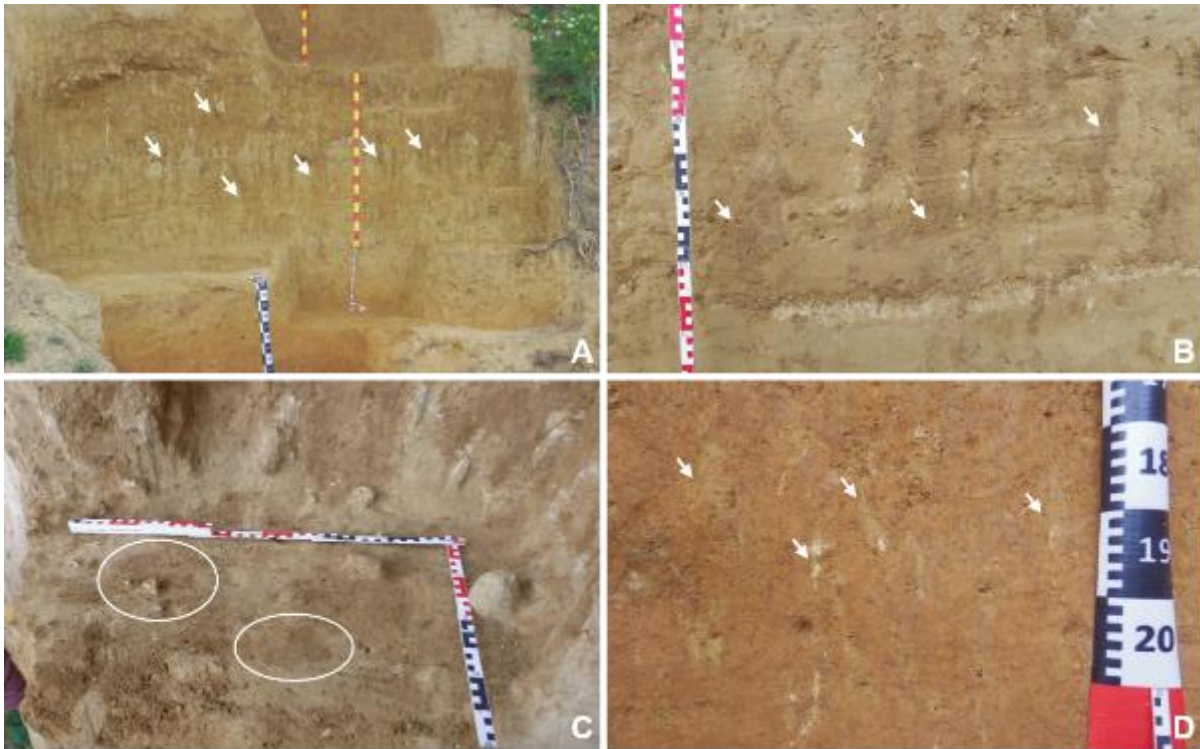


Figure 3.36: Photos of biopore features of Collias-Wood LPS, Rhône Rift Valley, SE France. A) large brown infilled biopores (5–10 cm wide, up to 2 m long) of the interstadial soil horizon reaching into the lower loess unit (360–570 cm), B) close up of smaller brown biopores surrounded by olivish sediment of 5 Cck horizon (0.15 cm to 5 cm wide, up to 25 cm long) of lower loess horizons at ~510 cm depth with gravel lens (523–527 cm). C) Horizontal 40 cm x 60 cm cross section (480 cm depth) (cutting) through large brown infilled biopores. D) Yellow to yellow-brown biopores, partly encrusted by soft secondary carbonates of interglacial/interstadial pedo-complex surrounded by red-orange soil sediment of 8 Bwck4 horizon (670–710 cm) (photos taken by D. Sauer (2019–2020)).

3.36D). In contrast, the infillings of the upper brown Cambisol show a darker browner colour compared to the surrounding yellow-brown coloured material (Fig. 3.36A–B). Based on the field observations, we hypothesise that the former biopore system presented zones of preferential flow within a surrounding denser matrix, by which overlying materials were leached into underlying horizons.

We investigated the phenomenon in more detail. Firstly, at 480 cm depth at Collias-Wood a horizontal cross section (40 cm x 60 cm) cutting through the large tongues in the 5 Bwck/Cck horizon was prepared to analyse their three-dimensional forms and distribution (Fig. 3.36C). Secondly, samples from infillings with surrounding sediment from 670–710 cm as well as 527–570 cm and 465–523 cm were taken to determine soil-chemical characteristics in order test the leaching hypothesis. The horizontal cross section revealed round cone-like shapes of the brown tongues with diameters of 3 cm to 8 cm and showed revealed that the forms were isolated, i.e. unconnected among each other, displaying an irregular and scattered distribution (Fig. 3.36C). Thus, periglacial features (ice or sand wedges, thermal cracks) as their origin can be excluded, because they would have induced a regular polygonal pattern (Bertran et al.

2014). Furthermore, a faunal origin, like animal burrows, can be excluded due to their vertical cone-shapes which confirm their root-related origin.

The lower yellow-brown infillings of the interglacial/interstadial pedo-complex display higher contents of CaCO_3 and ratios for W_{MER} , CPA, and lower contents of clay and a lower clay/silt ratio compared to the surrounding soil sediment (Table A3.12). Thus, less soil formation for the infillings is assumed, which supports the hypothesis of (vertical) leaching from above through biopores. The lower CaCO_3 contents, higher clay contents and clay/silt ratio of the brown infilling sediments beneath the brown Cambisol remain indicates more intense weathering compared to the surrounding sediment (Table A3.12). Therefore, brown soil material from the 4 Bwck1 horizon may leached down into the less weathered loess sediment (5 Bwck/Cck and 6 Cck/Bwck horizon). However, as differences in the texture of the 4 Bwck1 parent material and the surrounding sediment of the brown infilled-biopores was observed (Table A3.12; Bosq et al. 2020b). Thus, the comparison of weathering ratios is challenging. To clarify, if leaching of overlain 4 Bwck1 material or in situ weathering along the biopores took place, the consistence of the parent material was determined by the middle sand/coarse silt ratio (mS/cSi ratio). Both particle size classes are mainly composed of quartz, orthoclase or muscovite micas, and are therefore less vulnerable to weathering compared to the other particle size classes (Blume et al. 2011). We observed equal mS/cSi ratios for the brown infillings and the surrounding sediment compare to the 4 Bwck1 material, suggesting in situ weathering of the brown infillings (Table A3.12). We assume, the large brown tongues originate from preferential flow along previously developed biopores (Gocke et al. 2014; Zhang et al. 2016). After root decaying, leaching in the remaining voids favoured weathering of in situ material compared to the surrounding sediment.

Secondary carbonates

Secondary carbonates occur in LPS in various types, which imply different environmental conditions (Becze-Deák et al. 1997; Kovda et al. 2009; Barta, 2011b, 2011a; Zamanian et al. 2016; Li et al. 2018). So far, based on the classified forms of the FAO (2006), a differentiation of their differing origins, i.e. from biogenic (calcified earthworm granules; calcified root cells; rhizoliths; pseudomycels; needle-fibre calcite) or abiogenic (soft concretions; coatings; hypocoatings; nodules; calcretes) on a macroscale level is challenging (Becze-Deák et al. 1997; Gocke et al. 2014; Barta, 2016; Zamanian et al. 2016). Thus, in this study, the term “pseudomycelia” refers to all in the field visible carbonate concretions within the pore system and “carbonate concretions” to observed and sampled hard (hollow) concretions (Fig. 3.37A-F, Table A3.11).

At Collias sections, pseudomycelia are displayed in all moderately weathered lower horizons of and in the weakly developed horizons of the upper loess unit. Compared to the homogenous



Figure 3.37: Variety of selected carbonate nodules from all Collias LPS, Rhône Rift Valley, SE France. A) Reddish nodule (concretion) with prominent septarian structure from 3 Btck horizon of Collias-North_D112 (130–155 cm). B) yellow-brown nodule (upper left in photo) with septarian structure and hollow nodule (rhizoliths) (down and left in photo) from BCck and 2 Bwck horizons of Collias-North_D112 (0–110 cm). C) Brownish nodule (rhizolith) from 7 BCck1 horizon of Collias-Wood (595 cm). D) yellow-olive hollow carbonate nodule (rhizolith) from 2 Cck/Bwck2 horizon at Collias-South_D112 (160–175 cm). E) Vertically cut yellow-brown nodule with porous homogenous inner fabric from Collias-South_D112 (0–40 cm). F) yellow-brown carbonate concretion (>20 cm long, >10 cm wide) impregnated with small rock fragments from CCK horizon of Collias-South_D112 (0–40 cm) (Photos taken by N. Pfaffner (2019)).

distribution in the lower horizons, the amount of pseudomycelia increases with increasing depth in the upper loess unit. Based on their stratigraphical position, we assume for these horizons, that increasing amounts of pseudomycelia are due to leaching of bicarbonate solution from carbonate rich material deeper into the soil profile. For the lower horizons, the identification of pseudomycelia is uncertain and further research is required.

Beneath the last Interglacial/interstadial pedo-complex a carbonate cemented layer of ≤50 cm thickness was observed. The layer has a rough surface and is assumed to form by carbonate (re)precipitation (Fig. 3.35C). Hard carbonate nodules of different shapes and sizes were observed in the lower pedo- and loess units in all sections (Fig. 3.37A–F). In particular, abundant large elongated and cylindrical carbonate nodules (>20 cm long, >10 cm wide) occur in and underneath the Bwck, BCck and Cck horizons of the interstadial soil-complex, rendering it a conspicuous (carbonate nodules) zone in all profiles (except Collias-North_D112, where the respective unit was not accessible) (Figs. 3.36C, 3.37F). The prominent carbonate nodules occur in the loess matrix as well as in the large brown biopores. The nodules have a homogenous yellow-brown colour and show a pitted, porous surface impregnated with small rock fragments (Fig. 3.37F). The nodules were further investigated to determine their origin.

So called “rhizoliths” originate from water flow with soluble Ca^{2+} at the roots and precipitation of CaCO_3 along them or the release of HCO_3 by roots to compensate for the uptake of anions (Zamanian et al. 2016). Generally, rhizoliths have a typical hollow or toroidal inner fabric. Thus, exemplarily two of the large carbonate nodules of Collias-South_D112 were cut vertically to review their inside structure. They displayed in contrast to rhizoliths, a porous, uniform inner fabric with small rock fragments and cavities up to 1.5 mm in diameter (Fig. 3.37E). Therefore, they rather correlate with the descriptions of nodules/concretions from Zamanian et al. (2016) and Li et al. (2018). They assume that the nodules/concretions form in situ by cementation of the soil matrix, where precipitation of CaCO_3 minerals merging with the other compounds (e.g. rock fragment, mineral particle, organic particle). Barta (2011b) even distinguishes nodules (various form, do not fill pre-existing cracks, do not incorporate clastic material) and concretions (spheroidal or ellipsoidal shapes, incorporates clastic material). However, as the nodules from Collias-South_D112 display contradicting characteristics regarding Barta’s (2011b) descriptions, we chose the term “carbonate nodules”. We assume, they formed by reprecipitation of the bicarbonate solution, encrusting the sediment matrix favoured by the former biopore system. Additionally, the amount of rock fragments in these horizons acted as condensation cores, which may also explain the inner homogeneous structure of Collias concretions. Another possible explanation for the porous inner structure may state, that high amounts of small channels favoured hypocoatings in an early formation phase, which gradually cemented together (Barta, 2011a). Probably, a mixture of small rock fragments and hypocoatings acted as precipitation nuclides in the biopore system.

Smaller horizontal concretions, observed at Collias-Wood (7 BCck1, 570–635/640 cm), were nodules reworked by the downslope erosion by water. In contrast at Collias-South_D112 (2 Cck /Bwck1-4, 160–215 cm) the nodules show very fine bulges, which one would expect to get abraded if relocated. Therefore, we assume either the protuberances started to grow after the nodules had been redeposited at the site, or concretions possibly formed in situ due to horizontal/lateral water flow. In the 7 BCck1 horizon of Collias-Wood (595 cm), the 2 Cck/Bwck2 horizon at Collias-South_D112 (160–175 cm) and the BCck and 2 Bwck horizons of Collias-North_D112, hollow hard nodules, which fit the characteristics of rhizoliths, were observed (Fig. 3.37B–D) (Barta, 2011b; Zamanian et al. 2016). Within the 3 Btck horizon of Collias-North_D112 (130–155 cm) round, reddish concretions with a septarian crack structure, were observed fitting the criteria for nodules (Fig. 3.37A) (Barta, 2011b; Li et al. 2018).

3.4 Discussion – soil formation and palaeoenvironmental context

On the basis of the observed and measured soil characteristics and available OSL ages from Bosq et al. (2020b) a chronostratigraphy was established for the Collias-Wood LPS. The sequence of sediments and soils is reflected against the warm interglacial and cold glacial

periods as derived from oxygen isotope data of marine sediment cores (marine isotope stages, MIS) (Fig. 3.38). We use stage boundaries according to Lisiecki and Raymo (2005) and Railsback et al. (2015). Furthermore, phases were correlated with interstadial and stadial phases known from terrestrial archives (pollenstratigraphies), whereas local nomenclature for southern Europe was chosen (Guiot et al. 1993; Guiter et al. 2003; Wohlfarth, 2013) (Fig. 3.38). If possible, interstadial phases as reconstructed from soil development and OSL dating at the LPS were correlated with the INTIMATE event stratigraphy (Rasmussen et al. 2014). This stratigraphy includes, next to terrestrial and marine records, ice core records from the northern hemisphere displaying for the last glacial period climate fluctuation known as Dansgaard-Oeschger events, which were numbered systematically as Greenland interstadials (GI) and Greenland stadials (GS) (Rasmussen et al. 2014) (Fig. 3.38). OSL ages for the interglacial/interstadial pedo-complex range between 78.9 ± 6.7 ka and 87.1 ± 6.5 ka, which can be correlated with the Early Glacial (MIS 5 a-c/MIS 5.1–5.3). The ages of 55 ± 4.4 ka and 55 ± 4.1 ka correspond to the Lower to Middle Pleniglacial transition (MIS 4 to MIS 3) and early Middle Pleniglacial (MIS 3), whereas ages of the upper loess unit range from 38.5 ± 2.5 ka, i.e. the late Middle Pleniglacial (MIS 3), to 23.8 ± 2.5 ka, i.e. the Upper Pleniglacial (MIS 2). Thus, the sections also cover the Last Glacial Maximum (LGM), as determined for the Alpine Region with an expansion of glaciers since 32.5–30.5 ka, and with two distinct glacier advances around 26–25 ka and 23–22 ka (Ivy-Ochs et al. 2022).

The chronostratigraphy of the additional Collias profiles is based on stratigraphic correlations of the horizons with those of Collias-Wood (Fig.3.34). In combination with the results they provide the basis for reconstructing the soil forming conditions through time, and thus the changes of the palaeoenvironmental conditions at Collias from MIS 5 to MIS 1. We correlate our findings with those from Mediterranean LPS of eastern Spain, northern Italy and western Croatia taking into consideration chronological uncertainties due to the lack of numeric ages for most of the published sections (Fig. 3.39).

3.4.1 Last Interglacial (Eemian) and Early Glacial soils

Eemian soil MIS (5e, ca 130–115 ka/110 ka)

Whereas the Eemian is generally considered to having lasted from 130–115 ka ago (NEEM community members, 2013), thus conforming largely to MIS 5e (e.g. Chen et al. 1991; Shackleton et al. 2003), in contrast to northern Europe the Eemian is considered to having lasted until the beginning of the Melisey I stadial (GS 25, end of GI 25) in southern Europe, i.e. until ca 110 ka ago in MIS 5d (Guiot et al. 1993; Shackleton et al. 2003; Sánchez-Goñi et al. 2005; Brewer et al. 2008; Wohlfarth, 2013; Rasmussen et al. 2014). The Eemian soil at Collias is represented by a chromic, decalcified, clayey Bt horizon with an angular to prismatic

structure with clay and Mn coatings (cf. section Collias-North_D112). The intense red colour is attributed to the presence of hematite as a result of rubefication (Fig. 3.35B, 3.35D).

This process requires warm temperatures in combination with a xeric moisture regime (Boero and Schwertmann, 1989; Fedoroff and Courty, 2013). The Luvisol remain is underlain by a petrocalcic horizon formed by leaching and reprecipitation of a solution rich in hydrogen carbonate, requiring a xeric moisture regime, too (Yaalon, 1997; Candy and Black, 2009). These characteristics point clearly to a formation under Mediterranean climate conditions (hot, dry summer and rainy mild winter), for which effective rainfall intensity exceeds evapotranspiration. Our findings are in accordance with descriptions of the assumed Eemian soil from other Mediterranean sections (red-brown to red, rubefied, argic Bt(k) horizon, often hydromorphic features) (Fig. 3.39) (Bonifay, 1965; Brosche and Walther, 1977; Cremaschi, 1990a; Rose et al. 1999; Günster et al. 2001; Ferraro et al. 2004; Ferraro, 2009; Boixadera et al. 2015; Zerboni et al. 2015, Plata et al. 2021).

However, a yellowish-red to red Bw horizon with scarce rounded clay coatings classified by Durn et al. (2018a) as a hypereutric Chromic Cambisol was described for north-western Croatian LPS (Wacha et al. 2011a; Zhang et al. 2018). As the red palaeosol is mainly correlated to the Eemian period (Mikulčić Pavlaković et al. 2011; Wacha et al. 2011a; Zhang et al. 2018), the less intensely developed horizon may reflect less pronounced climate conditions, and therefore Durn et al. (2018a) assume that soil formation took place during the Penultimate Interglacial (MIS 7). Red soils, including limestone derived terra rossa soils, are well known from the Mediterranean region, but the determination of their origin and especially their precise formation age are still under debate (Yaalon, 1997; Durn, 2003; Fedoroff and Courty, 2013; Durn et al. 2018a). Numerical data of the assumed Eemian soil(s) in Mediterranean LPS are scarce and often they are solely identified by their stratigraphic position (Bonifay, 1965; Ferraro, 2009; Brosche and Walther, 1977; Günster et al. 2001). The hitherto existing ages are mainly inconclusive because of the polygenetic and/or mostly colluvial character of this soil (Fedoroff and Courty, 2013; Boixadera et al. 2015; Zerboni et al. 2015; Durn et al. 2018a; Zhang et al. 2018). These uncertainties illustrate how challenging a correlation of these horizon characteristics solely to the Eemian period is and that climate conditions may be misinterpreted.

The distinct thickness of the petrocalcic horizon of the Collias profiles raises the question, if climate conditions of the Eemian could have induced this indurated horizon or if a polycyclic formation took place. SE-Spanish LPS with similarly high amounts of carbonate as at Collias display also petrocalcic horizons (up to 1.2 m thickness) under the assumed Eemian soil (Günster, 1999). Petrocalcic horizons of LPS of Croatia are displayed in dune sands and/or similarly coarsely granulated substrates. In Italian LPS no calcrete horizon was observed due

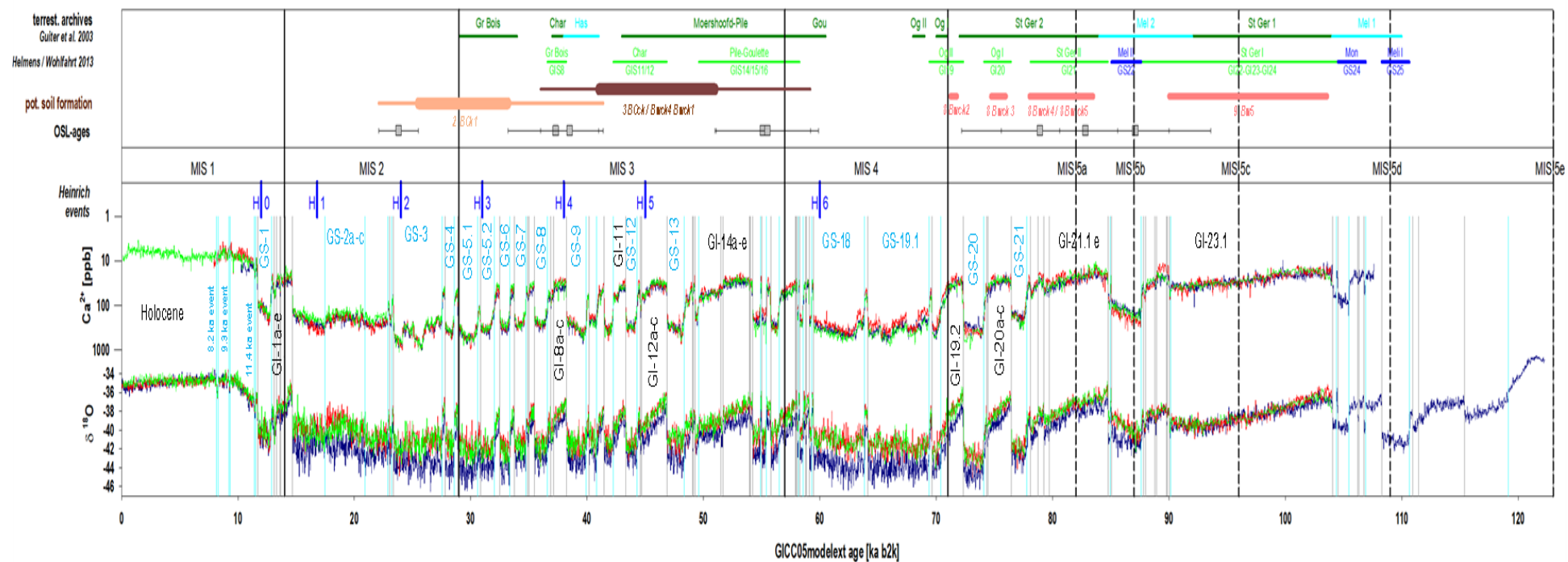


Figure 3.38: Potential soil formation phases at the loess-palaeosol sections (LPS) Collias reflected against (1) the OSL ages from the study site pointing to periods of sediment-soil reworking and deposition (Bosq et al. 2020b) and (2) marine, ice core (Rasmussen et al. 2014) and selected terrestrial archives (Guiter et al. 2003; Wohlfarth, 2013; Helmens, 2014). (MIS = Marine Isotope Stage; GI = Greenland).

to different underlying material (i.e., fluvio-glacial deposits, till, limestone) (Ferraro, 2009; Wacha et al. 2011a; Boixadera et al. 2015; Zerboni et al. 2015; Durn et al. 2018a). Described LPS of SE France equally petrocalcic horizons with similar thicknesses (up to 60 cm) or carbonate nodules enriched horizons beneath the assumed Eemian soil (Bonifay, 1965). These horizons are, like Collias, also underlain by coarser material (e.g. gravels, sands), which favours carbonate precipitation (Zamanian et al. 2016). Recently, palaeoclimatic studies suggest for the western Mediterranean region enhanced winter precipitation during the Eemian period and that, in favourable topographic positions with additional carbonate enrichment through subsurface interflow, possibly enhanced by underlying coarse sandy material, may supports the hypothesis of a single formation phase (Sauer et al. 2015; Zamanian et al. 2016; Pasquier et al. 2019; Dixit et al. 2020).

Furthermore, we exclude a polygenetic formation of the chromic Bt material of Collias, as assumed for Italian or Croatian LPS (Durn, 2003; Zerboni et al. 2015). The highly exposed topographical position makes it unlikely that soil material of preceding interglacial was preserved. In contrast to Tricart (1952), soil formation in the underlying local Miocene parent material during preceding interglacial periods can be excluded, as the texture is determined as coarse loess material, indicating penultimate (Rissian) loess deposits as parent material (Bonifay, 1965; Bosq et al. 2020b). We attribute the characteristics of the soil formation exclusively to the Eemian period and assume due to the displayed clay coatings (section Collias-North_D112), the in situ Eemian soil type was a Luvisol. The lack of clay coatings of the lowermost soil horizon of Collias-Wood (9 Bw5 horizon) (Bosq et al., 2020b) can be explained by its topographic position on a mid-slope. In agreement with the published OSL age (78.9 ± 6.7 ka) of this horizon, we suggest that the horizon reflects reworked Eemian soil material, in contrast to the in situ remains of the 3 Bt horizon of Collias-North_D112.

Thus, we presume for the Eemian period in SE France climate conditions with a pronounced seasonality marked by hot, arid summer months and mild winter months with a significant amount of precipitation. This assumption coincides not only with described palaeosol formations of terrestrial records, but also with pollen records of France and elsewhere in the Mediterranean, which display an abundance of summer-drought resistant, sclerophyllous taxa (e.g. *Ilex*, *Olea*, *Pistacia*, evergreen *Quercus*) (Beaulieu et al. 2005; Tzedakis, 2007) , and with precipitation patterns extracted from marine records (Pasquier et al. 2019; Dixit et al. 2020).

3.4.2 Early Glacial soils (MIS 5d to 5a, 115/110–71 ka)

With the onset of the Early Glacial, a slow decrease in temperature and an increase of humidity as well as an opening of the forest vegetation (cover) is described for the Mediterranean region (Beaulieu and Reille, 1984b; Guiter et al. 2003). Thus, the landscape surface became instable and geomorphic activity resulted in the truncation of the Eemian soils which became

redeposited in different topographic positions (cf., 9 Bw5 horizon of Collias-Wood vs. 3 Bt horizon of Collias-North_D112). The truncation of Eemian soils in European LPS has often been described (Brosche and Walther, 1977; Antoine et al. 1999, 2001, 2009a; Günster et al. 2001; Frechen et al. 2007; Fedoroff and Courty, 2013; Rousseau et al. 2018).

Structure, colour and texture class the lower four Bwck horizons of Collias-Wood as cambic horizon (IUSS Working Group WRB, 2022). We attribute the vertical decrease of weathering to several erosion-sedimentation cycles each followed by a less intense soil formation than during the Eemian period. We correlated these erosion-sedimentation cycles with the succession of colder stadials of MIS 5d (Mélisey I (110–104 ka) (Guiter et al. 2003); GS 25 (Wohlfarth, 2013); NAC25 (Helmens, 2014); GS 25, 110.6–108.3 ka (Rasmussen et al. 2014)) and MIS 5b (Mélisey II (92–84 ka) (Guiter et al. 2003); GS 22 (Wohlfarth, 2013); NAC 22–21 (Helmens, 2014); GS 22-20, 87.6–85.1 ka (Rasmussen et al. 2014)) (Fig. 3.38). Subsequent soil formation phases are correlated with the interstadial of MIS 5c (St Germain I (104–92 ka) (Guiter et al. 2003); GI 24-22 (Wohlfarth, 2013); NAW 24–22 (Helmens, 2014); GI 24.1c–22a, 106.8–87.6 ka (Rasmussen et al. 2014)) and MIS 5a (St Germain II (84–72 ka) (Guiter et al. 2003); GI 21 (Wohlfarth, 2013); NAW 21 (Helmens, 2014); GI 21.1e–19.2, 84.8–72.3 ka (Rasmussen et al. 2014)) of the Early Glacial (Fig. 3.38). However, the OSL ages of the lower samples do not show the expected age increase with depth and the lowermost sample may underestimate the true age of sediment deposition.

The soil characteristics indicate brunification processes and Bw horizons represent most likely (several phases of) Cambisol formation. The decreasing weathering intensity along with increasing silt contents suggest a change from more humid to drier and cooler climate conditions for the interstadial phases of the Early Glacial period. The infilled biopores in these Bwck horizons reflect these climate oscillations, too. The vegetation is described to having alternated between coniferous forest (*Pinus*, *Picea*), open boreal forest and open steppe-tundra vegetation during the stadial phases and temperate deciduous forest (*Carpinus*, *Corylus* and *Quercus*) during interstadial phases (Beaulieu and Reille, 1984a; Reille and Beaulieu, 1989; Allen et al. 1999; Guiter et al. 2003). We presume, that biopores were introduced during the interstadial phases and when the vegetation cover changed to an open forest loess material was leached into former biopores. Such leaching may well explain, why the OSL ages do not show the expected increase with depth.

Our assumptions agree with the observations from LPS from SE France (Durance valley) (Bonifay, 1965). Bonifay (1965) describes a lower reddish and an upper orange mixture of soil sediment and loess (local units Würmian I A and I B), separated by a thin, and weakly decalcified red soil. He assumes a temperate climate with seasonal changes of intense precipitation and strong aridity (Bonifay, 1965). Croatian LPS from Susak Island display a thick

orange-brown palaeosol, correlated to the late MIS 5/MIS 4, too (Mikulčić Pavlaković et al. 2011; Wacha et al. 2011a). The orange-brown palaeosol has similar characteristics (i.e. small carbonate concretions and vertical biopores up to few cm in length filled with secondary carbonate, (Wacha et al. 2011b) as the Bwck horizons at Collias. In Italian sections, the Early Glacial is represented by colluvial deposits, which show characteristics of the underlying Eemian soil and the overlying loess; at the section Bagaggera they were classified as a yellowish brown Bt horizon (Cremaschi et al. 1990; Ferraro et al. 2004). Rose et al. (1999) described also two brown soil formations for Early Glacial phases at LPS of Mallorca. In contrast, Günster (1999) describes for the Granada basin grey and greyish brown soils (Vertisol like), separated by humic sediments and were formed under a steppe vegetation (Günster et al. 2001). We assume, that with the beginning climate deterioration soil forming conditions in the NE region of the Mediterranean, especially at lower altitudes and in valleys and basins were still humid enough for brunification or clay illuviation processes (to proceed), compared to already drier conditions at higher altitudes of the Granada basin.

3.4.3 Lower Pleniglacial horizons (MIS 4, 71–57 ka)

The colluvial horizons at the base of the lower loess horizons at Collias-Wood (7 BCck1) and Collias-South_D112 (3 BCck2–3) represent transition horizons from the MIS 5 to MIS 4 or a period of reworking during the early MIS 4. We tentatively suggest the Ognon 1 and/or 2 interstadial, or rather an associated transition from an interstadial to a stadial period, as these times of pronounced environmental change are especially prone to landscape destabilisation and sediment reworking. Yet, the temporal position at least of the Ognon I interstadial is contentious. While traditionally it has been associated with MIS 4, a temporal placement at the end of MIS 5 appears more likely (for details cf. Wohlfarth, 2013; Helmens, 2014). Anyway, with respect to the INTIMATE-stratigraphy we would consider GI 19.2-19.1 (Ognon 2: GI 19, (Wohlfarth, 2013); NAW 19, (Helmens, 2014)), as likely interstadials, not excluding GI 20 (NAW 20, Helmens 2013; GI 20 Wohlfarth, 2013) with respect to a possible placement of the interstadial Ognon 1 in MIS 5a (GI 20c–20a, 76.4–74.1 ka; GI 19.2–19.1, 72.3–69.4 ka; GI 18, 64.1–63.8 ka (Rasmussen et al. 2014)). The horizon contains loess with pre-weathered material from the underlying pedo-complex, which underwent intense reworking, most likely through slope wash processes.

The centre values of ca 55 ka of the OSL ages for the sediment deposition of the overlying horizons (6 Cck/Bwck and 5 Bwck/Cck at Collias-Wood; Cck and 2 Cck/Bwck1–4 at Collias-South_D112) point to the early Middle Pleniglacial (early MIS 3). However, within error margins the ages (55.5 ± 4.4 ka; 55.1 ± 4.1 ka) cover a range between 59.9 ka and 51.0 ka, which also cover the latest MIS 4. Therefore, the respective horizons are vaguely attributed to the MIS 4/beginning of the MIS 3 in accordance with Bosq et al. (2020b). The sediment has a coarse

sandy loam to loamy sand texture, which generally suggests increased aridity and wind intensity, as it is also reported from sections of Italy and Croatia (Tricart, 1952; Cremaschi, 1990a, 1990b, 2015; Wacha et al. 2011a; Zhang et al. 2018; Bosq et al. 2020b). However, the olivish colour rather suggests a proximal source (Miocene greenish sandstone) of sediment supply, which could also imply non-aeolian processes, such as slope wash. Furthermore, it is assumed, that observed interlaced gravel (angularly shape) lenses are due to frost weathering and subsequent slope wash processes during seasonal climate amelioration (Tricart, 1952; Bourdier, 1958; Bosq et al. 2020b). Similar observations are described from Croatian and Italian LPS (Cremaschi, 1990a, 1990b; Ferraro et al. 2004). So far, these lenses present the only feature, which can be directly related to frost activity. The lenses appear at Collias-South_D112 as continuous layers and their thickness as well as size of contained rock fragments increases, following the (palaeo-)relief in the downslope direction (Tricart, 1952). Changing moisture conditions are marked by abundant Mn coatings and soft carbonate nodules in the horizons (Table A3.11). We conclude, that the climate for the MIS 4 was cold and dry, leading to seasonal frost activity and sediment accumulation (loess and fine sands; aeolian input and subsequent local reworking). The indicated run off processes suggest slight climate ameliorations, which may possibly correlate with the interstadial events of GI 17–15 (GI 17.2–15.1, 59.4–54.9 ka, Rasmussen et al. 2014). Within error margins of the OSL data also GI 14 would be possible, but the character of the interstadial succession changes from short-term to longer-term ameliorations starting with GI 14. We would consider repeated environmental changes from interstadial to stadial conditions favouring geomorphic activity, and longer-term interstadials favourable for more intense soil formation (cf. section 3.5.3).

3.4.4 Middle Pleniglacial horizons (MIS 3, 57–29 ka^{Lisietzki et al (2005)}/33 ka^{Railsbeck et al. (2015), Railsbeck (2021)})

The MIS 3 is marked by millennial-scaled climate changes (Voelker, 2002; Kjellström et al. 2010). The interstadials in terrestrial archives are termed as (i) Pile-(Moershoofd) complex, starting at the ending Lower Pleniglacial/beginning Middle Pleniglacial (GIS 16-14 (Helmens, 2013); GI 16.2–14a, 58.3–49.6 ka (Rasmussen et al. 2014)), (ii) Charbon (Hengelo) (GIS 11/12 (Helmens, 2013); GI 12c–11, 46.9–42.2 ka (Rasmussen et al. 2014)) and (iii) Grand Bois (Denekamp) complex (GIS 8 (Helmens, 2013); GI 8c–8a, 38.2–36.6 ka (Rasmussen et al. 2014)). The Cambisol remain (4 Bwck1 at Collias-Wood; Bwck at Collias-South_D112) imply at least one soil formation phase. The OSL ages of 55.1 ± 4.1 ka and 38.5 ± 2.5 ka below and above the remain span the maximum timeframe for the soil formation between ca 59 ka and ca 36 ka (GI 17.2–8a: 59.4–36.6 ka; start of GI 7c at 35.5 ka) already outside the time window; (Rasmussen et al. 2014) (Fig. 3.33). The time window matches the Pile complex and/or the Charbon interstadial. This period is characterised by a succession of long-lasting interstadial periods favouring soil formation, interrupted by short-lasting stadials (<1 ka; exceptions GS 13,

GS 9; corresponding to Heinrich (H) 5 and H 4 events, respectively, e.g. (Guillevic et al. 2014; Goldstein and Hemming, 2014), which may well explain the significant (possibly repeated) truncation of the palaeosol remain, often down to the large carbonate nodules, which largely increase the threshold of erosivity.

Tricart (1952) suggests that the cambic soil formation at Collias must have taken place under similar climate conditions as today as the soils show similar characteristics. Other archives of SE France also suggest comparable climate conditions to the recent ones (Magnin and Bonnet, 2014; Ollivier et al. 2014). However, observed large carbonate nodules of the MIS 3 soil are missing in the Holocene soil which may suggests more humid conditions for the early MIS 3. Thus, we presume for Collias less pronounced climatic shifts between stadial and interstadial phases with increased humidity during the early (and middle) MIS 3, resulting in one thick polygenetic (and subsequently truncated) Cambisol. In other words, we assume moderate accumulation of loess under humid conditions during stadial phases, which allowed pre-weathering in form of efficient carbonate leaching also during the stadial phases, and brunification during the interstadial phases. Along with the soil formation the biopore system was firstly introduced by intense rooting of (the described) mixed temperate forests (*Quercus*, *Carpinus*, *Abies*, *Picea*) during the interstadials as described by Beaudouin et al. (2007) and Ollivier et al. (2014). The subsequent climate deterioration seems to introduce more severe (cold and drier) conditions for the following middle to late MIS 3 time (likely from GS 9 or GS 8, if soil formation lasted until GI 8, to GS 6 (in the system of Railsback et al. (2015)) or GS 5.1; in the system of Lisiecki and Raymo (2005), respectively). This led to the truncation of the palaeosol and induced the observed patchy sediment in-mixture. Tricart (1952) attributes the patchy character of the horizon to cryogen processes. He defines it as a “Brodelsboden”, a result of refreezing of the active layer in a periglacial environment resulting in a pocket-like appearance of the material that freeze (last) between the upper and lower progressing frost fronts. However, our field observations did not give any evidence for cryoturbation processes. We assume, his description of the lower cryoturbation pockets fits to the observed large infilled biopores (sect. 3.3.6).

The interstadial phases of MIS 3 are represented mainly in northern Mediterranean LPS by several independent and/or polygenetic brown to brown-reddish soil horizons, separated by loess deposits accumulated during stadial phases (Bonifay, 1965; Brosche and Walther, 1977; Günster et al. 2001; Wacha et al. 2011a; Zhang et al. 2018; Bosq et al. 2020b) (Fig. 3.39). In the northern Rhône Rift Valley, Franc et al. (2017) observed a polygenetic, yellow-brown Bw horizon deposited ca between 51 ka and 35 ka. Günster (1999) describes up to three brown soil formations, which he correlated with the three described (above) interstadials from terrestrial archives. In NW Croatian LPS, two thick brown horizons, possibly correlated with

the Charbon or Grand Bois interstadials are followed by several thin brown horizons, correlated to late MIS 3 (Wacha et al. 2011a, 2011b). At the Bagaggera section in the Po Valley (Italy), the formation of an Alfisol of pre-weathered loess sediment (WRB: Luvisol, (FAO, 2006)), was correlated with the Charbon interstadial, reflecting wetter temperate conditions compared to other sections (Cremaschi et al. 1990). In contrast, the LPS of Val Sorda (Italy) and the upper part of the LPS of Susak island (Croatia), display organic-rich palaeosols (according to Bogнар et al. (2003) and Ferraro (2009) Chernozem-type soils), which rather suggest a colder and drier climate (Cremaschi, 1990a; Ferraro et al. 2004; Ferraro, 2009). However, it is also hypothesised that high organic carbon contents were caused by wildfires rather than decelerated decomposition of litter due to drier climatic conditions (Fedoroff and Courty, 2013; Cremaschi et al. 2015).

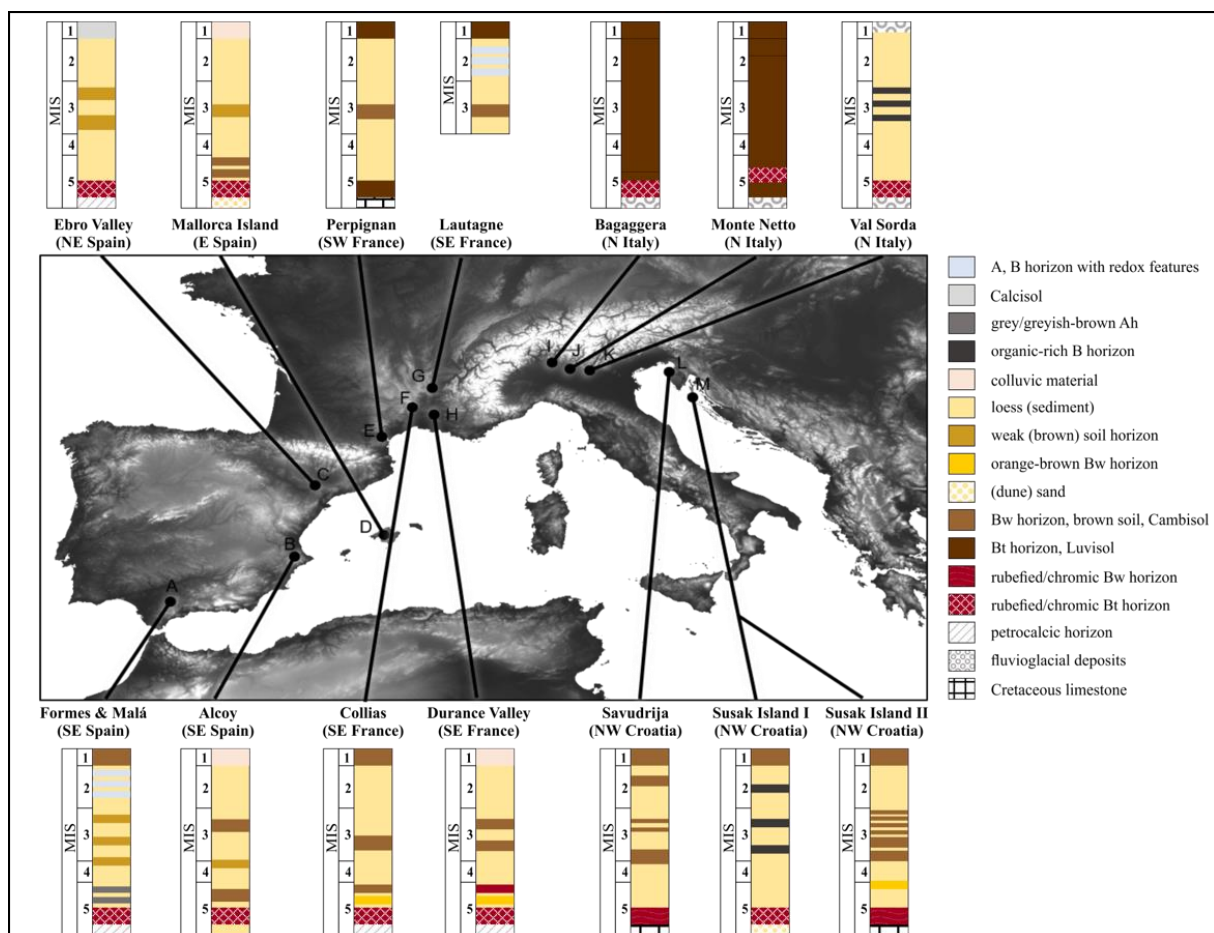


Figure 3.39: Selected generalised and simplified loess-palaeosol sections emphasising on palaeosol formation within the NW Mediterranean region. A) LPS of Formes and Malá from Granada basin (855–900 m a.s.l.), mean annual temperature (MAT): 15 °C, mean annual precipitation (MAP): >500 mm, 4 arid months (Günster, 1999; Günster et al., 2001). B) LPS of Alcoy (660 m a.s.l.), MAT: 14 °C, MAP: 506 mm, 4 arid months (Brosche and Walther, 1977). C) LPS of Ebro Valley (18–390 m a.s.l.), MAT: 15 °C; MAP: 300–400 mm, 2 arid months (Boixadera et al. 2015). D) LPS of Mallorca Island (5 m a.s.l.), MAT: 17 °C, MAP: 500 mm, 5 arid months (Rose et al. 1999). E) LPS of Perpignan (65 m a.s.l.) MAT: 15 °C, MAP: 586 mm, 4 arid months (Brosche and Walther, 1977). F) LPS of Collias (106 m a.s.l.), MAT: 15 °C, MAP: 763 mm, 3 arid months (Tricart, 1952; Bonifay, 1965; Bosq et al. 2020b). G) LPS of Lautagne (177 m a.s.l.), MAT: 13 °C, MAP: 923 mm, 2 arid months (Bosq et al., 2020b). H) LPS of Durance Valley (213 m a.s.l.), MAT: 13 °C, MAP: 640 mm, 3 arid months (Bourdier, 1958; Bonifay,

1965). I) LPS of Bagaggera (260 m a.s.l.), MAT: 13 °C, MAP: 1314 mm, no arid months, (Cremaschi et al. 1990). J) LPS of Monte Netto (200 m a.s.l.), MAT: 13 °C, MAP: 1310 mm, no arid months (Zerboni et al. 2015). K) LPS of Val Sorda (220 m a.s.l.), MAT: 12 °C, MAP: 830 mm, 1 arid month (Ferraro et al., 2004; Ferraro, 2009). L) LPS of Savudrija (1 m a.s.l.), MAT: 14 °C, MAP: 1049 mm, 1 arid month (Zhang et al. 2018). M) LPS of Susak Island (0 m a.s.l.), MAT: 14 °C, MAP: 992 mm, 3 arid months, Susak Island I (Cremaschi, 1990b), Susak Island II (Wacha et al. 2011a, 2011b; Durn, 2003; Durn et al. 2018a; Bognar et al. 2003; Mikulčić Pavlaković et al. 2011) (Data: map of northern Mediterranean region based on SRTM-data, <https://www2.jpl.nasa.gov/srtm/>, accessed: 18 March 2021).

Thus, the observed brown soil formation(s) of the early to middle MIS 3 supports the above assumed less pronounced climatic shifts and more stable humid conditions for the beginning of the Middle Pleniglacial. Additionally, similarly large carbonate nodules in NE Spanish LPS, although without confirmed formation ages and small, but abundant carbonate nodules in Savudrija LPS, NW Croatia coincide with nodules of Collias and assumed higher humidity (Brosche and Walther, 1977; Boixadera et al. 2015; Zhang et al. 2018). The diversity of soil formation intensity during MIS 3 can be explained by the geographic (altitude, topography), climatic and vegetational heterogeneity. More specific, soils of LPS located at higher altitudes (SE Spain) or at more continental positions (NE Italy, NW Croatia) may have formed under colder and/or drier conditions compared to soils of SE France or NE Spain (Bognar et al. 2003; Surić and Juračić, 2010).

The late MIS 3, like the following MIS 2, is marked by the main phase of loess accumulation at the Collias LPS (ca 4 m of altogether 8.5 m of the LPS; cf. also Bosq et al. 2020b). In contrast to above Mediterranean LPS, which exhibit two or more palaeosols, no other MIS 3 palaeosols were observed at Collias. As we assume, the Cambisol remains (4 Bwck and 3 BCck/Bw horizons at Collias-Wood) are part of a polygenetic soil complex including all interstadial soil formation phases before ca 38 ka. So far, no indications (e.g. relocated soil material in overlain 2 BCk2 horizon in Collias-Wood) for a Cambisol formation after 38 ka was found. Although, the overlain BCk horizons (2 BCk2 horizon of Collias-Wood, 2 BCk 3 horizon of Collias-North) indicate climate conditions intense enough to introduced slight weathering, within the general shift to colder and drier conditions.

3.4.5 Upper Pleniglacial (MIS 2, 33–15 ka)

The 2 BCk2 horizon of Collias-Wood was dated between 37.3 ± 4.1 ka and 23.8 ± 1.7 ka, placing it between the late MIS 3 and the early MIS 2, likely before the LGM. The horizons of Collias-Wood and Collias-North display abundant bioturbation and weak not depth-related weathering (weak structure, constant carbonate content, similar weathering indices as underlying horizons), which is explained by syn-sedimentary processes of coarse loess accumulation, contemporaneous carbonate leaching and an on-growing open wooded vegetation cover (Pye, 1995). Thicker loess deposits in the Po Valley for the late MIS 3, and main loess accumulation phases (late MIS 3 to MIS 2) of SE France, E Spain and NW Croatia

also indicate more pronounced shifts to colder and drier conditions (Wacha et al. 2011b; Boixadera et al. 2015; Costantini et al. 2018; Bosq et al. 2020b) (Fig. 3.39).

With the ongoing MIS 2, we assume, cold and mainly dry conditions, which are required for loess accumulation, but with respect to seasonality, allowing run-off processes, which redeposited pre-weathered material especially at the foot slopes. Furthermore, we suggest sufficient temperature and humidity for the existence of an open wooded vegetation and possibly even for a tree refugia of a temperate forest vegetation. Local tree refugia with temperate to Mediterranean forest taxa (*Acer*, *Taxus*, *Arbutus*, *Buxus*, *Ulmus*, *Phyllirea*, *Pistacia*, *Olea*) were observed in all northern Mediterranean pollen sequences (Beaulieu et al. 2005; González-Sampériz et al. 2005; Surić and Juračić, 2010; Guido et al. 2020). Pollen sequences of Les Échets (northern Rhône Rift Valley) also indicate arboreal pollen deposits of *Pinus*, *Alnus*, *Quercus*, *Abies* and *Picea*, suggesting tree refugia, which coincide with a pollen record from the Gulf of Lion indicating the presence of *Abies*, *Picea* and deciduous *Quercus* (Beaulieu and Reille, 1984a; Beaudouin et al. 2007; Ollivier et al. 2014). The hypothesis of a refugia position is supported by the fact, that no frost related features (i.e. platy structure, micro cracks) were observed in the upper horizons of the Collias sections. However, close to Collias, various frost features were observed (Arnal, 1971; Bornand, 1978; Ollivier et al. 2014), indicating at least strong seasonal frost and/or spatially sporadic permafrost during the LGM (Bertran et al. 2014; Andrieux et al. 2016). This would also agree with Andrieux et al. (2016), who reconstructed the southern limit of continuous permafrost during the LGM at 47° N and of discontinuous permafrost at 45–44° N. Furthermore, the LPS of Lautagne displays weakly developed Ag-horizons with redox features dated to MIS 2 (30.7 ± 2.4 to 21.8 ± 1.8 ka; GS 5.2–2.1). On the one hand, it is possible that soil features were destroyed and/or camouflaged by the Holocene soil formation (Berger-Levrault, 1968; Bertran et al. 2014). On the other hand, a possible refugia situation of the Collias profiles may be attributed to their geographical position, as the western Alpine ice cap extent was limited to the north-eastern flank of the Rhône Rift Valley, restricting the spatial occurrence of frost dynamics (Coutterand et al. 2009; Bosq et al. 2018).

This interpretation coincides with observed frost wedges and laminated zones in LPS of Quincieux at the northern Rhône Rift Valley (Franc et al. 2017). For the MIS 2 at NE Spain weak Bw(k) horizons and very few Ab horizons were recorded and also Croatian LPS display moderately weathered loess with a brown soil development, but no frost related features were observed (Cremaschi, 1990a; Wacha et al. 2011a; Boixadera et al. 2015; Zerboni et al. 2015; Zhang et al. 2018). MIS 2 soil features in Italian LPS were not reported, but loess of the Bagaggera section displays similar characteristics as the B_{Ck} horizons of Collias according to Cremaschi (1990a) induced by solifluction processes and mild pedogenetic activity (biological),

quasi-contemporary with the loess deposition. Frost related features were observed in Italian LPS, but restricted to the beginning of the Upper Pleniglacial and related to seasonal deep ice lensing or freezing rather than permafrost (Cremaschi and van Vliet-Lanoë, 1990; Kühn et al. 2006; Cremaschi et al. 2015). In contrast, Günster et al. (2001) describe a soil complex with up to three weakly developed slightly pseudogleyic palaeosols, indicating periodic frost action under relatively low temperatures, which can be explained by the altitude of the LPS, favouring more severe conditions compared to the other sections.

3.4.6 Recent soil formation (MIS 1, 14–0 ka)

The recent soil formation at Collias-Wood and Collias-North is characterised by up to four colluvial Bw horizons, including a former Ap horizon at Collias-North. The horizons display weathering characteristics, containing primary carbonate and thus are classified as Cambisol, which agrees with the Calcisol type (WRB: calcic Cambisol) of the regional soil map (Languedoc-Roussillon; (GisSol, 1999; Legros, 2006). For understanding and interpreting palaeoclimatic conditions, the recent soil type may provide valuable information. However, the classification is challenging due to the lack of recent in situ soil profiles and the long intense anthropogenic use. Especially, the planation of the agriculturally used terrain and the creation of terraces, including known fire clearance destroyed the natural soil horizons and features (Berger-Levrault, 1968).

Described Holocene soil types originating from loess parent material range in the Mediterranean region from Calcisols (NE Spain) to Cambisols (SE Spain, SE France, NW Croatia) and (chromic) Luvisols (SE France, N Italy, NW Croatia) (Brosche and Walther, 1977; Cremaschi et al. 1990; Jamagne et al. 2011; Bašić, 2013; Boixadera et al. 2015; Cremaschi et al. 2015). The possible increase of soil intensity from the NW to the NE in the northern Mediterranean region, would agree with the recent climate conditions, showing an increase in MAP. However, the anthropogenic influence in these LPS needs to be taken into account, as, e.g., the agriculturally used soils of Susak island are commonly classified as Regosols (Durn et al. 2018b). The influence of pre-weathered and colluvial loess as parent material as well as the different primary carbonate varying content must be considered, too.

Actually, the present conditions in the Mediterranean region (e.g. MAP, time, porosity of the parent material) are favourable for Luvisol development on loess (Quénard et al. 2011). Possible explanations for the missing argic horizon are that it (i) was destroyed through soil erosion and colluvial processes, (ii) was thwarted by anthropogenic influence, (iii) did not develop, because rainfall does not exceed evapotranspiration. Although, none of the explanations can be rejected, we assume the latter statement suits the Collias sections. The negative amount of annual effective rainfall (-383 mm, (Meteo-France, 2022d, 2022e)) does

not fulfil the required conditions for a Luvisol development and coincides with the determined in situ Cambisol (type).

We conclude, that the Cambisol type, along with the absence of secondary carbonates as well as missing rubefication originates from less recent precipitation as compared to the assumed more humid conditions for the Eemian (MIS 5e) and the interstadial phases of the early MIS 3. Although the Eemian is described to have lasted somewhat longer (approx. 17.000–18.000 years), than the ongoing Holocene, it is unlikely that the Cambisol will develop into a Luvisol with the present conditions prevailing (Bronger, 1976; Kukla et al. 2002; Guiter et al. 2003). It is rather likely, that assumed future increase of precipitation intensity and temperature effects less the soil moisture regime, but results in intense soil erosion. Thus, these soils are highly vulnerable to degradation and consequently at risk for their future agriculture potential (García-Ruiz et al. 2013).

3.5 Conclusions

In this study, the palaeosols of the Collias profiles were used to reconstruct the (local) palaeoenvironmental conditions supplementing the regional palaeoenvironmental picture of the Last Interglacial-Glacial period of SE France. The sections support the complex character of palaeosols and soil sediments of Mediterranean LPS and following conclusions can be drawn:

- 1) The Last Interglacial (Eemian, MIS 5e) climate conditions were warm and humid (with occurrence of arid months) enough to allow a Chromic Luvisol development with a thick underlying calcrete and under sclerophyllous vegetation. The Early Glacial (MIS 5d–5a) was marked by shifts between cold and drier (intense erosion and loess accumulation) and humid temperate conditions, forming Cambisols out of former colluvial soil sediments during terrestrial interstadial phases of St Germain I (GI 24.1c–22a) and St Germain II (GI 21.1e–19.2) under a deciduous forest vegetation.

- 2) The Lower Pleniglacial (MIS 4) was marked by the most severe (dry and cold) climate conditions without any soil formation, but with seasonal shifts (tentatively GI 17–15) in the moisture regime, allowing an open wooded vegetation.

- 3) The Middle Pleniglacial (MIS 3) was marked by less pronounced climate shifts with more humid conditions, allowing syn-sedimentary processes forming a Cambisol-complex, which correlates with the terrestrial Pile (Moershoofd) interstadial complex (GI 16.2–14a) and/or Charbon (Hengelo) (GI 12c–11) interstadial. Furthermore, humidity was sufficient for the development of a deciduous forest cover and prominent large carbonate concretions, acting as a marker horizon in the Collias sections. The late MIS 3 was characterised by more pronounced climate shifts with drier conditions reflected by increased loess accumulation.

4) The Upper Pleniglacial (MIS 2) is marked by cold and arid conditions, but no periglacial features were observed so that the site may have served as a tree refugia. Syn-sedimentary slight carbonate leaching occurred most likely under an open wooded vegetation cover.

5) The recent (MIS 1) Mediterranean climate is also warm, but humidity only suffices for a Cambisol formation.

The soil formation phases during the major climatic ameliorations likely coincide with those of the LPS of SE Spain, N Italy and NW Croatia. However, the climatic W-E trend (more continental positions) as well as the varying altitudes of the LPS, lead to differences in the soil forming intensity and characteristics. The Last Interglacial is present in all LPS generally by a Chromic Luvisol, indicating more humid Mediterranean conditions. In contrast, considering the anthropogenic influence, the recent Mediterranean conditions seem to be more differentiated as higher evapotranspiration in SE France does not support Chromic Luvisol formation in loessic parent material. Furthermore, enhanced run-off process induced by predicted increase of precipitation intensity and temperature may be expected for this region. The Early Glacial soils differ both from a Cambisol formation (SE France, N Italy, Mallorca Island, NW Croatia) and from steppic, organic-rich soils (SE Spain, N Italy). Most of these LPS display no soil developments for the Lower Pleniglacial. The Middle Pleniglacial soils are mostly presented by two up to six Cambisols of different weathering intensity and thickness. Chernozem soil-types were observed in LPS of N Italy and NW Croatia. Luvisol formation described for the Bagaggera section (N Italy) can be explained by the pre-weathered polygenetic character of the sediment. The Upper Pleniglacial sediments are partly characterised by frost related features (SE Spain, SE France, N Italy), but permafrost in form of gleyic soils was only observed in the high basin of Granada.

Acknowledgement

We warmly thank Dr Barbara von der Lühe, Dr Sophie Cornu, Dr Jean-Philippe Degeai and Dr Olivier Moine for the intense support and precious discussions in the field. We are grateful to the mayor of Collias for the possibility to work safely and the local support of the Association les Amis du Patrimoine de Collias. We thank Dr Grotheer, Anja Södje, Petra Voigt and Marius Friedrich, who contributed to this study by laboratory analyses. We acknowledge the German Aerospace Centre (DLR), which provided the TanDEM-X data for the study area (DEM_GEOL1263).

Declaration of competing interest

The authors declare no conflict of interest.

Appendix

A3.3 Results of Collias LPS

Table A3.11: Main characteristics and observations of horizons of Collias profiles, Rhône Rift Valley, SE France according to FAO (2006) (size of carbonate nodules: large: >20 cm long, >10 cm wide; small: <5 cm long, <4 cm wide), n.d. = not detected. WE = earthworm channels; WC = earthworm casts; PM = pseudomycelia; Mn = manganese. OSL ages described in Bosq et al. (2020b).

Depth [cm]	Horizon	Main characteristics	Carbonates
Collias-Wood			
0–120	Ah; Bw1; Ah2; Bw2; Bw3; Bw4	4 several colluvial layers interlace by former Ah horizons; brown-orange colour matrix with increasing orange part, former Ah3 in reworked sediment of Bw4	n.d.
120–200	2 BCk1	clear, smooth boundary; brown (10 YR 4/4) to grey-brown (10 YR 5/3) colour; SiL texture; moderate, fine and coarse subangular blocky structure; earthworm faeces; abundant WC; strongly rooted	PM
200–360	2 BCk2 (OSL ages 23.8 ± 1.7 ka 37.3 ± 4.1 ka 38.5 ± 4.4 ka)	gradual, smooth boundary; brown (10 YR 4/6) to light brown (10 YR 5/4) colour; SiL texture; size of moderate, fine, subangular blocky structure decreases to coherent structure within depth; dark brown root channels	increase of PM within depth
360–400/410	3 BCk/Bwck	clear, wavy boundary; yellow-brown (BCkc) (10 YR 5/6) and brown (Bwkc) (10 YR 4/6) colour; SiL texture; weak and moderate, fine and coarse, subangular blocky structure	in situ carbonate nodules in former root channels; PM only BCk
400/410–460	4 Bwck1	clear, wavy boundary; yellow-brown (10 YR 5/6) colour with brown tongues (10 YR 4/6); SiL texture; moderate, fine to coarse, subangular blocky structure	large in situ carbonate nodules; precipitated in brown tongues and horizon; few PM
460–527	5 Bwck/Cck (OSL age 55.1 ± 4.1 ka)	abrupt, smooth boundary; yellow-olive sediment (Ckc) (2.5 Y 4/6) with brown tongues (Bwck) (10 YR 5/6); SiL texture; Cck: massive structure, Bwck: moderate, fine and medium subangular blocky structure; gravel lenses from 460–465 & 523–527 cm, red fine-sand lenses	large in situ carbonate nodules penetrating from upper horizon; PM only in Bwck
527–570	6 Cck/Bwck (OSL age 55.5 ± 4.4 ka)	gradual, wavy boundary; yellow-olivish sediment (Ckc) (2.5 Y 4/6) with brown tongues (Bwck) (10 YR 5/6); SiL texture; massive structure; red fine-sand lenses	in situ carbonate nodules; few PM only in brown tongues; very fine, rounded Mn soft concretions
570–600	7 BCk1	clear, smooth boundary; brown-olive-ish (2.5 Y 3/3) colour; SiL texture; moderate, fine to coarse, angular and subangular blocky structure	dislocated carbonate nodules and penetrated by upper in situ carbonate concretions; partly carbonate encrusted former root channels; PM; very fine, rounded Mn soft concretions
600–635/640	8 Bwck2	clear, wavy boundary; brown colour (10 YR 4/4); SiL texture; moderate, fine to coarse, subangular blocky structure; reddish, fragmented soil aggregates; gravel lens 640 cm depth	dislocated carbonate nodules, carbonate encrusted former root channels; PM; very fine, rounded Mn soft concretions
635/640–660	8 Bwck3 OSL age 82.8 ± 7.2 ka	clear, wavy boundary; brown-orange colour (7.5 YR 4/6); SiL texture; moderate, fine to coarse, angular and subangular blocky structure; very few faint clay and few prominent Mn coatings	few large in situ carbonate nodules; PM
660–30	8 Bwck4	gradual, irregular boundary; orange colour (5 YR 4/4); CL texture; weak to moderate, fine to coarse, subangular blocky structure; very few prominent Mn coatings	small in situ carbonate nodules, carbonate encrusted former root channels; PM

730–790	9 Bwck5 (OSL age 87.1 ± 6.5 ka)	gradual, smooth boundary; patchy orange-red colour (5 YR 4/6); CL texture; moderate, coarse subangular blocky structure; very few faint clay and few prominent Mn coatings; recent roots	small in situ carbonate nodules, carbonate encrusted former root channels
790–850	9 Bw5 (OSL age 78.9 ± 6.7 ka)	abrupt, wavy boundary; red colour (5 YR 3/6); CL to SiCL texture; strong, coarse, angular and subangular blocky structure; very few distinct clay and few prominent Mn coatings; recent and former roots (10 YR 6/4)	small in situ carbonate nodules, carbonate encrusted former root channels (15 mm width)
850–900+	9 Bkm	white-grey petrocalcic horizon	
Collias-North_D112			
+50	BCck	clear, smooth boundary; light yellow-brown colour (10 YR 6/4); CL texture; massive structure	in situ calcic nodules concretions
50–130	2 Bwck	gradual, smooth boundary; brown-orange colour (7.5 YR 4/6); CL texture; massive structure	in situ calcic carbonate nodules; PM; disperse powdery lime
130–155	3 Btck	gradual, smooth boundary; orange-red (5 YR 3/6) C texture; moderate to strong, fine and medium, angular blocky structure; many faint clay and few faint Mn coatings	small in situ calcic carbonate nodules; PM; calcic soft concretions
155–180	3 Bt	abrupt, smooth boundary; red colour (2.5 YR 3/6); C texture; strong, fine, angular blocky to prismatic structure; abundant distinct clay and Mn coatings	calcic soft concretions
180+	4 Bkm	white-grey petrocalcic horizon	
Collias-South_D122			
+40	Bwck	gradual, smooth boundary; brown colour (10 YR 4/6); L texture; massive texture	in situ calcic carbonate nodules; PM
40–70	BCck1	gradual, smooth boundary; light brown colour (10 YR 5/4); L texture; massive structure	in situ calcic carbonate nodules; PM
70–120	Cck	clear, smooth boundary; light yellow-brown colour (10 YR 6/4); L texture; massive structure;	large in situ calcic carbonate nodules
120–160	2 Cck/Bwck1	gradual, smooth boundary; olive-ish colour (2.5 Y 5/4) with small brown root channels (Bwck); SL texture; massive to single grain structure;	in situ calcic carbonate nodules
160–195	2 Cck/Bwck2	clear, smooth boundary; olive-ish colour (2.5 YR 5/3) with small brown root channels (Bwck); LS texture; massive to single grain structure;	(in situ) horizontal orientated calcic carbonate nodules, small calcic root tubules
195–215	2 Cck/Bwck3	gradual, smooth boundary; olive-ish colour (2.5 Y 5/4) with small brown root channels (Bwck); SL texture at the bottom coarser material; massive to single grain structure;	(in situ) horizontal orientated calcic carbonate nodules; small calcic root tubules
215–230	2 Cck/Bwck4	gradual, smooth boundary; olive-ish colour (2.5 Y 5/4) with small brown root channels (Bwck); SiL texture; massive structure; few distinct Mn coatings;	in situ calcic carbonate nodules of various sizes; calcic soft concretions
230–285	3 BCck2	clear, smooth boundary; olive-ish colour (2.5 Y 5/4) changing to brown-yellow with increasing depth (10 YR 5/3) and small brown root channels; L to SL texture; massive structure; few distinct Mn coatings	in situ calcic carbonate nodules of various sizes; calcic soft concretions
285–340	3 BCck3	clear, smooth boundary; olive-ish colour (2.5 Y 5/4); SiL texture few distinct Mn coatings	in situ calcic carbonate nodules of various sizes
340–350	4 Bck	abrupt, wavy boundary; light brown colour (10 YR 5/4); SiL texture; massive structure; few distinct Mn coatings	small in situ calcic carbonate nodules; calcic soft concretions
350–400	4 Bckm	yellow-brown colour (10 YR 6/4); SiCL to SiL texture; massive structure	carbonate cemented
400+	5 Bkm	white-grey petrocalcic horizon	-
Collias-North			
0–10	Ah	clear, wavy boundary; dark brown colour (10 YR 2/3); CL texture; strong, very fine and fine,	none

		subangular blocky structure; abundant root channels	
10–75	Bw (not sampled)	gradual, smooth boundary; brown colour (n.d.); texture (n.d.); moderate, medium and coarse, subangular blocky structure; abundant distinct clay coatings; abundant dark brown root channels; WE	none
75–90	2 Apb	clear, smooth boundary; dark brown colour (10 YR 3/4); CL texture; moderate, fine and medium, angular and subangular blocky structure; abundant distinct clay coatings; abundant brown root channels; WE; WC	none
90–110	2 BCk1	gradual, smooth boundary; brown colour (YR 10 4/4); CL texture; moderate, medium and coarse, angular and subangular blocky structure; abundant distinct clay coatings; abundant brown root channels	PM
110–128	2 BCk2	gradual, smooth boundary; light brown colour (10 YR 5/4); CL texture; moderate, fine and medium, angular and subangular blocky structure; many faint clay coatings; abundant brown root channels	PM
128–220	2 BCk3	clear, wavy boundary; grey-brown colour (10 YR 5/3); CL texture; moderate, fine and medium, angular and subangular blocky structure; many faint clay coatings; abundant brown root channels	PM
220–285	3 BCk1	clear, smooth boundary; yellow-brown colour (10 YR 5/6); L texture; massive structure; abundant brown root channels; 230–240 cm gravel lens	carbonate nodules; disperse powdery lime
285–312	3 BCk2	clear, smooth boundary; light brown colour (10 YR 5/4); L texture; massive structure; brown root channels	carbonate nodules; disperse powdery lime
312–350	3 BCk3	clear, smooth boundary; yellow-brown colour (10 YR 5/6); L texture; massive structure; common faint clay coatings; brown root channels	large in situ carbonate nodules; PM; disperse powdery lime
350–387	3 Cck	clear, wavy boundary; olive-ish colour (2.5 Y 5/4); texture n.d.; massive structure	large in situ carbonate nodules; PM; disperse powdery lime
387–445	4 BCk4	clear, wavy boundary; yellow-olive-ish colour (2.5 Y 5/6); SiL texture; moderate, medium, angular blocky structure	carbonate nodules; soft concretions PM; disperse powdery lime
445–450+	5 Ck	yellow-olive-ish colour (2.5 Y 5/6); SL texture; massive structure	disperse powdery lime

Table A3.12: Results of infilled biopores and respectively surrounding sediments of Collias-Wood LPS, Rhône Rift Valley, SE France. Particle size classes are according to FAO (2006), SOC = soil organic content; CPA = chemical proxy of alteration; WI_{MER} = weathering index based on the molar element ratio).

	brown infilled biopores (465–523 cm depth)	surrounding sediment of 5 Bwck/Cck horizon	brown infilled biopores (527–570 cm depth)	surrounding sediment of 6 Cck/Bwck horizon	yellow infilled biopores (670–710 cm depth)	surrounding soil- sediment of 8 Bwck4 horizon
Absolute particle size distribution in wt % [μm]						
<2	17.14	14.61	17.0	13.69	23.55	31.55
2–20	8.87	8.83	8.33	7.01	10.12	10.08
20–63	14.24	14.29	13.91	11.7	14.28	14.81
63–125	24.82	29.16	27.56	35.16	20.29	21.18
125–200	22.46	23.63	21.98	18.48	17.64	15.08
200–630	10.74	7.26	9.84	9.35	7.51	4.86
630–1250	1.15	1.61	0.91	1.18	4.20	2.08
1250–2000	0.58	0.61	0.48	0.43	2.42	0.56
Proxies						
middle sand/coarse silt ratio	0.05	0.06	0.03	0.03	0.21	0.10
clay/silt ratio	0.28	0.36	0.34	0.25	0.53	0.68
CaCO ₃ eq [wt %]	19.63	25.52	20.32	22.97	15.84	7.77
SOC [wt %]	0.84	0.62	0.87	0.76	1.04	1.14
CPA ($100 \cdot \text{Al}_2\text{O}_3 / (\text{Na}_2\text{O} + \text{Al}_2\text{O}_3)$)	74	74	73	73	79	78
WI_{MER} (Ca(- CaCO ₃)+Mg+Na+K)/Al	0.98	1.06	1.00	1.03	0.80	0.66
Si/Al	6.86	6.85	6.96	6.70	5.52	5.02

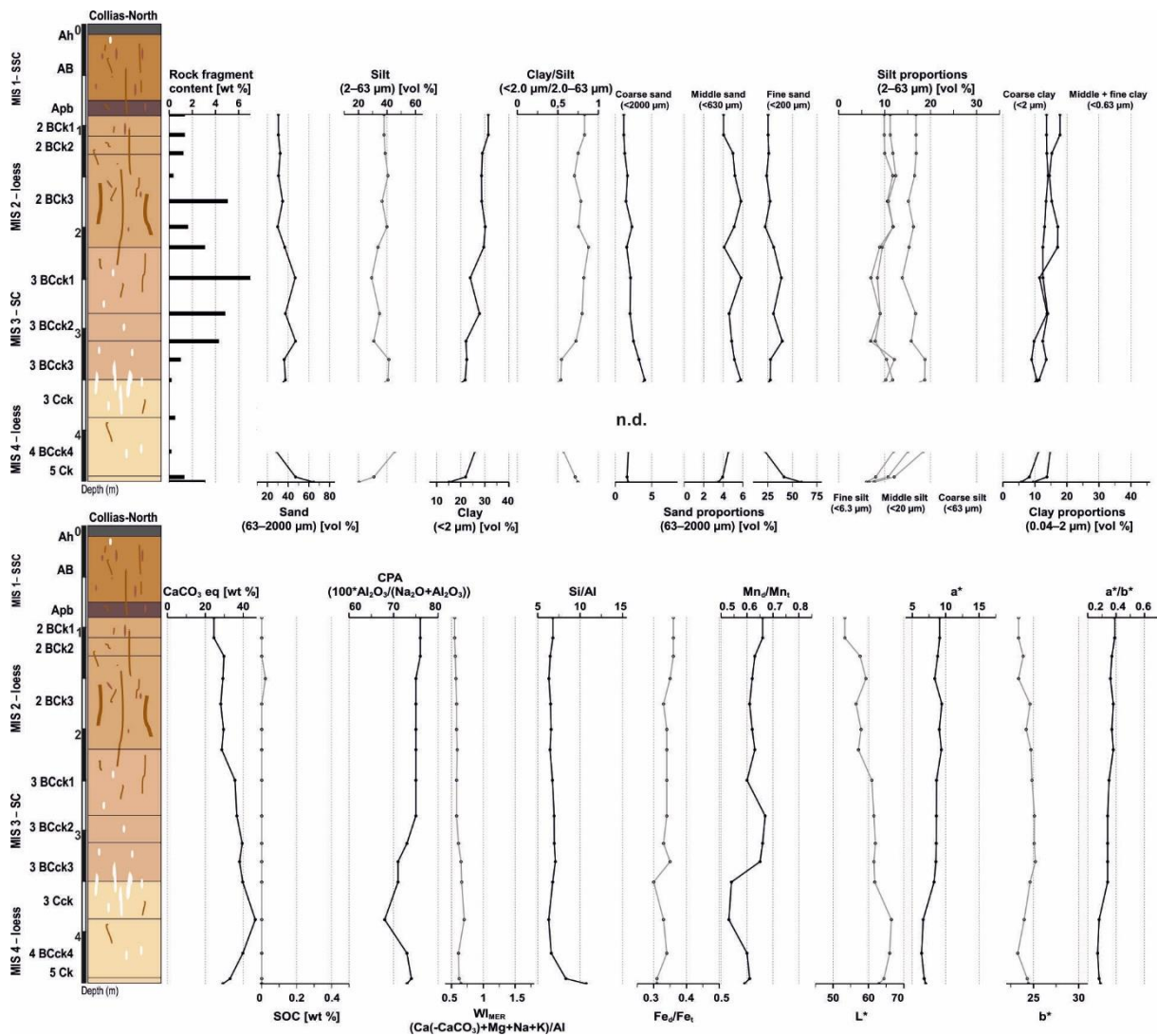


Figure A3.40: Stratigraphy of Collias-North, Rhône Rift Valley, SE France. Depth related upper curves of: rock fragment content [wt %], grain-size fractions of sand (63–2000 µm), silt (2–63 µm) and clay (<2 µm), in vol %; grain-size ratio of clay/silt (<2 µm/26–63 µm) and grain-size fractions of sand (fine sand: 63–200 µm, medium sand: 200–630 µm, coarse sand: 630–2000 µm), silt (fine silt: 2–6.3 µm, medium silt: 6.3–20 µm, coarse silt: 20–63 µm) and clay (fine clay + medium clay: <0.63 µm, coarse clay: 0.63–2 µm). Depth related lower curves of calcic carbonate equivalents in wt %, contents of soil organic carbon (SOC) in wt % and chemical proxy of alteration (CPA) ($100 \cdot \text{Al}_2\text{O}_3 / (\text{Na}_2\text{O} + \text{Al}_2\text{O}_3)$), weathering index of molar element ratio (W_{IMER}) (Ca (after subtraction of Ca in CaCO_3) + $\text{Mg} + \text{K} + \text{Na}$) / Al), Si/Al and, ratios of pedogenic to total contents of iron and manganese (Fe_d/Fe_t , Mn_d/Mn_t) and colours of the CIE colour index, reflected by the parameters L^* , a^* , b^* and ratio of a^* and b^* . SC: soil complex; SSC: soil -sediment-complex.

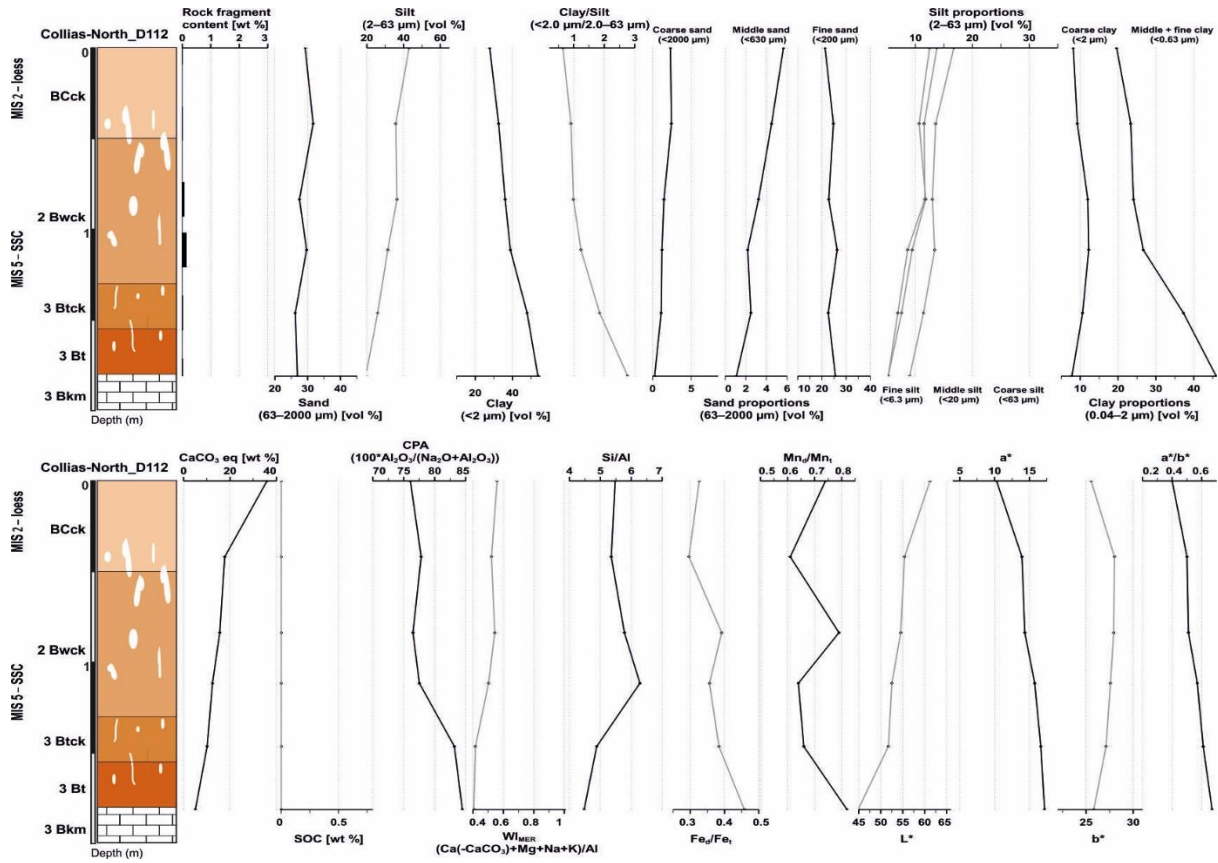


Figure A3.41: Stratigraphy of Collias-North_D112, Rhône Rift Valley, SE France. Depth related upper curves of: rock fragment content [wt %], grain-size fractions of sand (63–2000 µm), silt (2–63 µm) and clay (<2 µm), in vol %; grain-size ratio of clay/silt (<2 µm/26–63 µm) and grain-size fractions of sand (fine sand: 63–200 µm, medium sand: 200–630 µm, coarse sand: 630–2000 µm), silt (fine silt: 2–6.3 µm, medium silt: 6.3–20 µm, coarse silt: 20–63 µm) and clay (fine clay + medium clay: <0.63 µm, coarse clay: 0.63–2 µm). Depth related lower curves of calcic carbonate equivalents in wt %, contents of soil organic carbon (SOC) in wt % and chemical proxy of alteration (CPA) ($100 \cdot \text{Al}_2\text{O}_3 / (\text{Na}_2\text{O} + \text{Al}_2\text{O}_3)$), weathering index of molar element ratio (Wl_{MER}) (Ca (after subtraction of Ca in CaCO_3) + $\text{Mg} + \text{K} + \text{Na}$) / Al), Si/Al and ratios of pedogenic to total contents of iron and manganese (Fe_d/Fe_t , Mn_d/Mn_t) and colours of the CIE colour index, reflected by the parameters L^* , a^* , b^* and ratio of a^* and b^* . SC: soil complex; SSC: soil-sediment-complex.

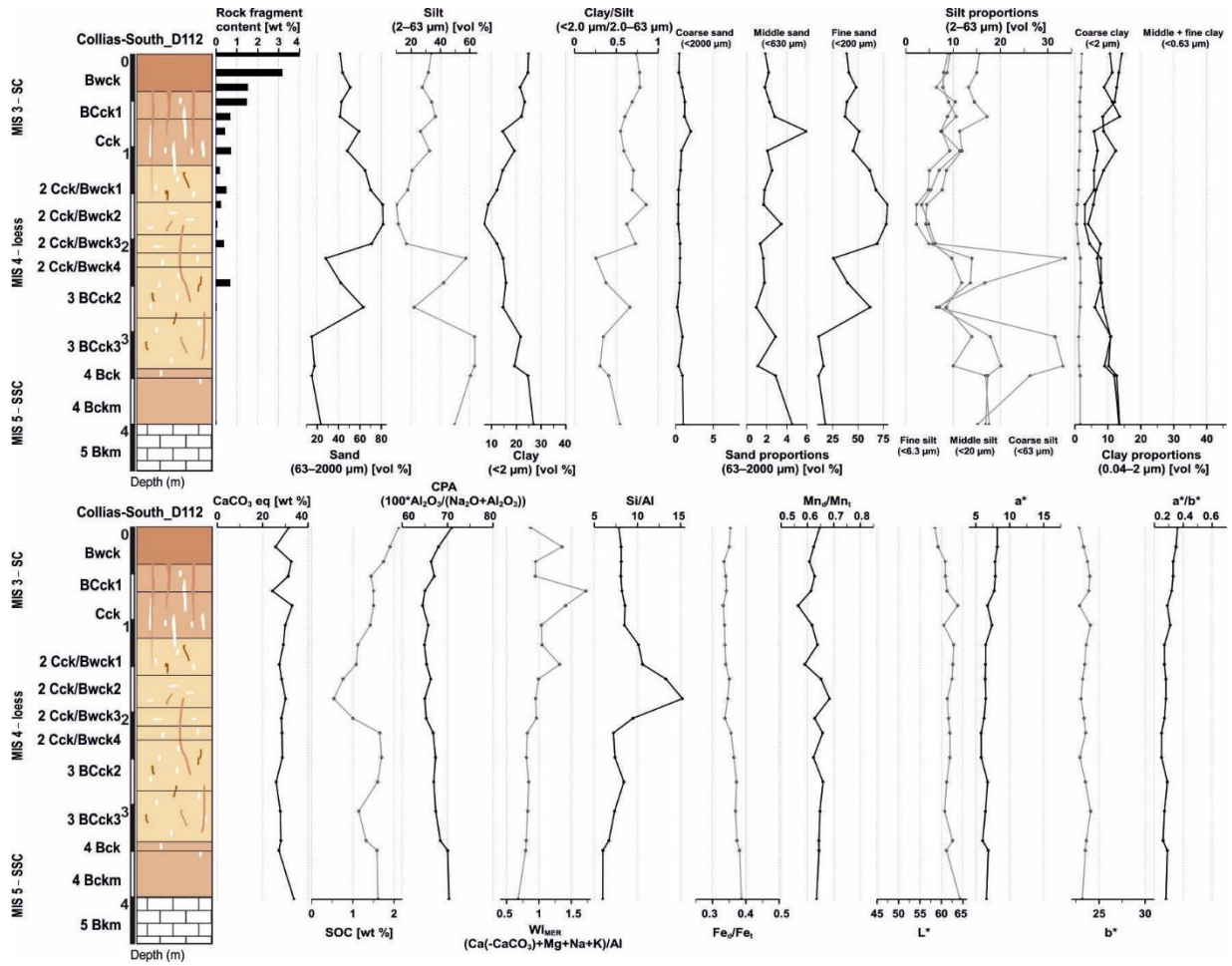


Figure A3.42: Stratigraphy of Collias-South_D112, Rhône Rift Valley, SE France. Depth related upper curves of: rock fragment content [wt %], grain-size fractions of sand (63–2000 μm), silt (2–63 μm) and clay (<2 μm), in vol %; grain-size ratio of clay/silt (<2 μm /26–63 μm) and grain-size fractions of sand (fine sand: 63–200 μm , medium sand: 200–630 μm , coarse sand: 630–2000 μm), silt (fine silt: 2–6.3 μm , medium silt: 6.3–20 μm , coarse silt: 20–63 μm) and clay (fine clay + medium clay: <0.63 μm , coarse clay: 0.63–2 μm). Depth related lower curves of calcic carbonate equivalents in wt %, contents of soil organic carbon (SOC) in wt % and chemical proxy of alteration (CPA) ($100 \cdot \text{Al}_2\text{O}_3 / (\text{Na}_2\text{O} + \text{Al}_2\text{O}_3)$), weathering index of molar element ratio (WI_{MER}) (Ca (after subtraction of Ca in CaCO_3) + $\text{Mg} + \text{K} + \text{Na}$) / Al), Si/Al and, ratios of pedogenic to total contents of iron and manganese (Fe_d/Fe_t , Mn_d/Mn_t) and colours of the CIE colour index, reflected by the parameters L^* , a^* , b^* and ratio of a^* and b^* . SC: soil complex; SSC: soil-sediment-complex.

Chapter 4: Reconstructing the Eemian to Middle Pleniglacial pedosedimentary evolution of the Baix loess-palaeosol sequence (Rhône Rift Valley, southern France) – basic chronostratigraphic framework and palaeosol characterisation (study 3)

Nora Pfaffner^{1,2}, Annette Kadereit³, Volker Karius⁴, Thomas Kolb⁵, Sebastian Kreutzer^{3,6,7}, Daniela Sauer¹

¹)Department of Physical Geography, University of Göttingen, 37077 Göttingen, Germany

²)Institute of Forest Ecosystems, Thünen Institute, 16225 Eberswalde, Germany

³)Heidelberg Luminescence Laboratory, Institute of Geography, University of Heidelberg, 69120 Heidelberg, Germany

⁴)Department of Sedimentology and Environmental Geology, University of Göttingen, 37077 Göttingen, Germany

⁵)Department of Geography, University of Gießen, 35390 Gießen, Germany

⁶)Geography & Earth Sciences, Aberystwyth University, Aberystwyth, SY23 3DB Wales, United Kingdom

⁷)Archéosciences Bordeaux, UMR 6034, CNRS - Université Bordeaux Montaigne, 33607 Pessac, France

Manuscript published in E&G Quaternary Sciences Journal. DOI:

<https://doi.org/10.5194/egqsj-74-1-2024>, 2024.

Table 4.13: Authors contribution to study 3.

Authors	Contribution to study
Nora Pfaffner^{1,2}	Investigation, Methodology, Data validation and interpretation, Writing -original draft, Visualisation
Annette Kadereit³	Project-conceptualisation, Investigation, Methodology, Data validation and interpretation, Writing - original draft, Writing – review & editing, Visualisation
Volker Karius⁴	Methodology, Review & editing
Thomas Kolb⁵	Methodology, Review & editing
Sebastian Kreutzer^{6,7}	Methodology, Review & editing
Daniela Sauer¹	Project-conceptualisation, Investigation, Data validation and interpretation, Writing - review & editing

Abstract

Loess–palaeosol sequences (LPSs) are important archives of landscape evolution, recording alternating periods of geomorphic activity (dust deposition and slope processes) and landscape stability (soil formation). LPSs of the Rhône Rift Valley are located along a spatial climatic gradient from the mid-latitudes to the Mediterranean region. This position renders them extremely valuable archives for correlating LPSs in the European loess belt and the Mediterranean region. Despite this important function, Rhône Rift Valley LPSs have been little investigated. In this study, we aimed to narrow this knowledge gap, in a first step towards linking LPS-based mid-latitude and Mediterranean palaeoenvironmental reconstructions. We studied the ~ 14 m thick Baix LPS located at the western edge of the Rhône Rift Valley near Valence. Here, we focus on the lower ~ 7 m of the LPS, which comprises 12 of 19 soil horizons

overall, and record regional palaeoenvironmental variations from the Eemian to the Middle Pleniglacial (~ marine isotope stage (MIS) 5 to MIS 3). Our reconstruction is based on detailed field description, complemented by granulometry (10 cm vertical resolution), and micro-morphological analyses. Luminescence screening of cut-out soil-sediment columns subsampled with ~5 cm vertical resolution (126 subsamples over 7 m) provides a preliminary chronometry. The loess deposits of the Baix LPS are strongly calcareous and predominantly silty but also contain sandy and fine gravelly laminae typical of loess deposits subjected to slope-wash processes. From bottom to top, the investigated part shows three intensely pedogenised levels: (1) a basal sequence of reddish-brown Btg and Bt horizons of a thick Eemian Stagnic Luvisol (MIS 5e); (2) an Early Glacial yellowish-brown Bw horizon (MIS 5d-a); and (3) a yellowish-brown Bw horizon with large cone-shaped carbonate nodules in the associated underlying Bk horizon, interpreted as a truncated Middle Pleniglacial (MIS 3) Calcic Cambisol. The Baix LPS is in parts very similar to the Collias LPS ~100 km further south but also exhibits differences, reflecting its position at the spatial climatic transition between the presently temperate and the Mediterranean zone.

4.1 Introduction

Loess–palaeosol sequences (LPSs) are valuable palaeoenvironmental archives, as they preserve information on, for example, past phases of (i) deposition of dust eroded from bare hillslopes and dried-out riverbeds and (ii) soil development and vegetation cover (e.g. Moine et al. 2005; Marković et al. 2009; Zech et al. 2012). In Europe, LPSs of large river basins have been intensively investigated in the mid-latitude region, e.g. in the Seine, Somme and Rhine basins (Bibus and Semmel, 1977; Guenther, 1987; Antoine et al. 2001, 2009, 2016, 2021; Schirmer, 2002, 2016; Fischer et al. 2021) as well as in the Mediterranean region, e.g. in the Ebro, Tagus and Po basins (Ferraro, 2009; Wacha et al., 2011b; Boixadera et al. 2015; Zerboni et al. 2015; Costantini et al. 2018; Wolf et al. 2019). Yet, LPSs in the transition between the European mid-latitudes and the Mediterranean zone have remained rarely investigated. A few exceptions are early studies from the first half of the 20th century (Suen, 1934; Mazonot, 1956; Bonifay, 1965), when modern techniques of LPS analysis were not yet available.

The Rhône Rift Valley in SE France is a natural N–S-orientated corridor leading from the mid-latitudes to the Mediterranean zone. The area around 45° N (near Valence, Fig. 4.43) denotes the present-day transition between temperate and Mediterranean climate (Joly et al. 2010). Loess along the Rhône Rift Valley was intensively studied in the middle of the last century (Suen, 1934; Mazonot, 1956; Bourdier, 1958; Bonifay, 1965), when major construction works facilitated access to thick profiles. Source areas of the loess were the dried-out riverbeds of the Rhône River and its tributaries from the Alps and the Massif Central, which during glacial

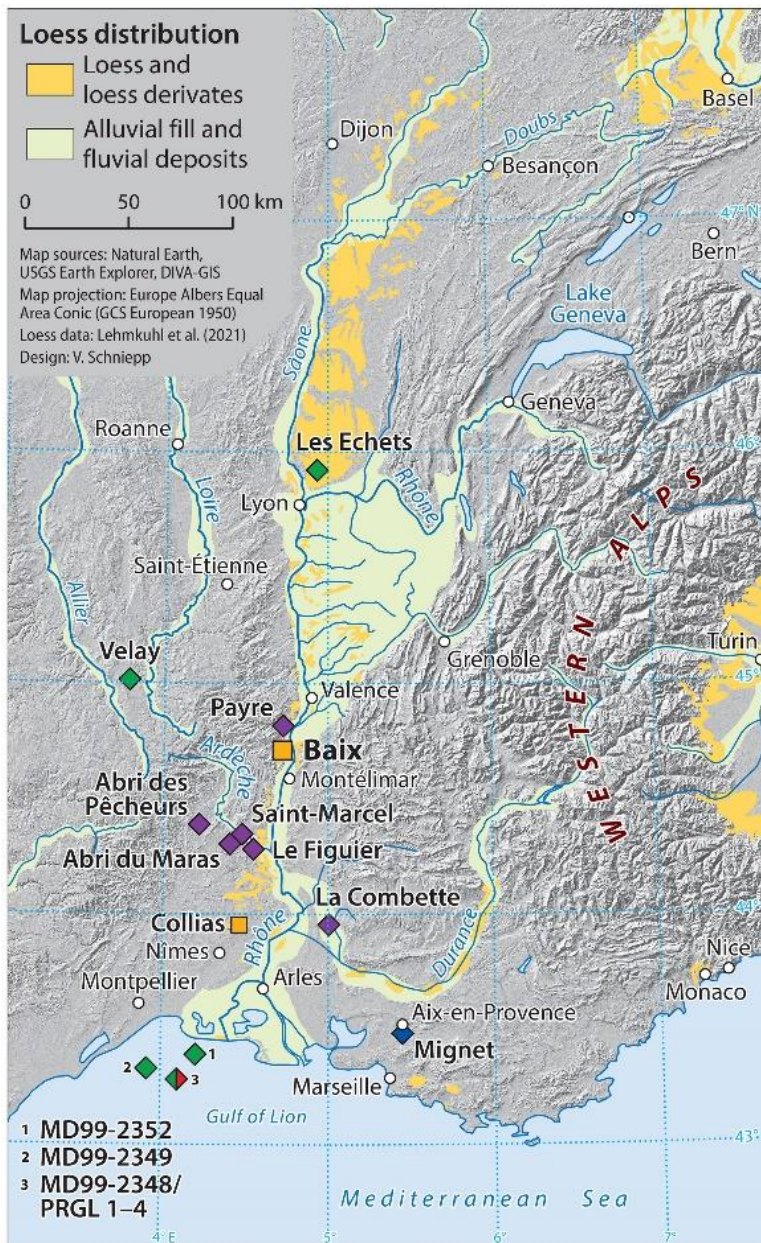


Figure 4.43: Location of the Baix loess–palaeosol sequence (LPS) at the western edge of the Rhône Rift Valley and published archives used for comparison and complementation of the palaeoenvironmental reconstruction. The Baix and Collias LPSs are marked by orange squares. Pollen records (green diamonds) from lacustrine sediments of Les Échets (Beaulieu and Reille, 1984a, b); maar lakes in the Velay region, Lac du Bouchet, Ribains and Praclaux (Reille and Beaulieu, 1990; Reille et al. 2000); and marine sediments from the Gulf of Lion (cores: MD 99-2349, MD99-2352, MD99-2348/PRGL1-4; Beaudouin et al. 2005). Archaeological sites (purple diamonds) of Payre (Valladas et al. 2008; Rivals et al. 2009), La Combette (Kreutzer et al. 2021; Mologni et al. 2021), and the Ardèche area (Abri des Pêcheurs, Saint-Marcel, Le Figuier, Abri du Maras) (Moncel et al. 2015). Molluscan record (blue diamond) of Aix-en-Provence (Magnin and Bonnet, 2014). Marine sediment record (half-red diamond) from the Gulf of Lion (core/borehole PRGL1-MD99-2348; Sierra et al. 2009).

periods were fed with fine-grained material abraded by the glaciers in the western Alps and the Massif Central (Bosq et al. 2020a). Only recently has loess research in the area been resumed, applying state-of-the-art investigation methods, including numerical dating (Franc et al. 2017; Bosq et al. 2018, 2020a, 2020b; Kreutzer et al. 2021; Mologni et al. 2021). One of the recently reinvestigated LPSs is the Collias LPS, located in the Mediterranean zone of SE

France (Fig. 4.43). There, a prominent Middle Pleniglacial (marine isotope stage (MIS) 3) yellowish-brown palaeosol horizon was observed. Optically stimulated luminescence (OSL) dating (e.g. Aitken, 1998) suggested a time window for the formation of this palaeosol of between $\sim 55 \pm 4$ ka (deposition of the sediment the palaeosol had developed in) and $\sim 39 \pm 3$ ka (sediment accumulation on top of the palaeosol) (Bosq et al. 2020b). The underlying soil horizon exhibited large cone-shaped carbonate nodules, resulting from substantial carbonate leaching from the Middle Pleniglacial palaeosol horizon and associated carbonate reprecipitation below. We observed these characteristic carbonate nodules in several LPSs along the Rhône Rift Valley.

4.2 Study site, sampling and methods

4.2.1 Study site

The Baix LPS ($44^{\circ}42'36.30''\text{N}$, $4^{\circ}43'20.80''\text{E}$) is located at the western edge of the Rhône Rift Valley, SW of Valence and ca 4 km west of the Rhône River at an elevation of 155 m a.s.l. (Figs. 4.43, 4.44). It is situated on the foot slope of a convex ridge that forms the northern edge of a small basin, consisting of Lower Cretaceous limestone and marl, covered by Cretaceous debris and Pleistocene sediments (Chenevoy et al. 1977; Saint Martin, 2009).

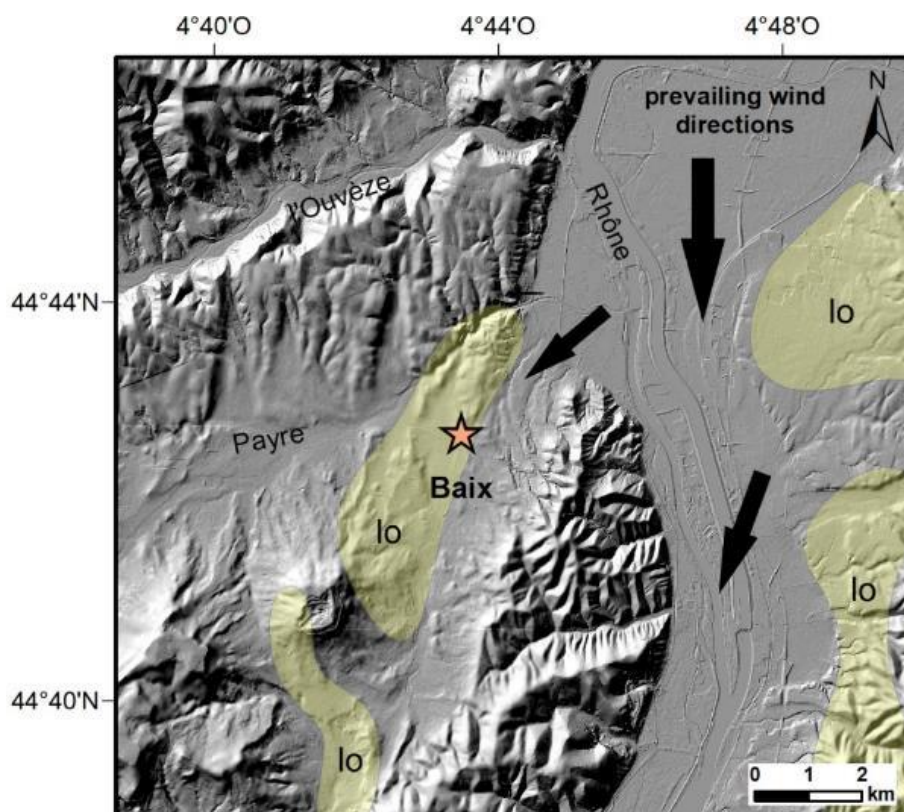


Figure 4.44: Hillshade map of the area around the Baix LPS, Rhône Rift Valley, SE France, with prevailing wind directions and distribution of loess and loess derivatives (lo) derived from Lehmkuhl et al. (2021) (map data: DEM with a $5 \text{ m} \times 5 \text{ m}$ resolution derived from IGN-FRA, 2020).

To the south, the basin is bordered by the basaltic plateau of the Coiron volcanic province with the Montagne d'Andance (530 m a.s.l.), a volcano that was active until the Late Miocene to Pliocene times (Chenevoy et al. 1977; Pastre et al. 2004). Several episodic creeks drain the basin via the rivers Ouvèze and Payre in an eastern direction towards the Rhône River (Fig. 4.44). The present climate is characterised by a mean annual temperature of 13.3 °C and mean annual precipitation of 874 mm, with a precipitation maximum in October or November (Meteo-France, 2022b). The predominant wind regime is the mistral, a strong northerly wind that is channelled within the Rhône Rift Valley and accelerated southward (Guenard et al. 2005). At the opening of the western shoulder of the Rhône Rift Valley near Baix, a part of the wind flow gets diverted westward into the small basin on whose northern edge the Baix LPS is located (Fig. 4.44). The Baix LPS is situated in the wind shadow with respect to the wind that blows from the Rhône Rift Valley into the basin immediately south of the low crest on whose foot slope the Baix LPS is located. This situation explains the occurrence of the thick loess patch at this south-facing foot slope. The Baix LPS was first mentioned by Suen (1934) and named "Baix" by Mazenot (1956). Solely based on field observations, Mazenot (1956) subdivided the Baix LPS into four parts, comprising (1) a palaeosol at the base, containing debris of basalt and Cretaceous limestone, overlain by (2) decarbonated red loamy loess, superimposed by (3) typical yellow loess, and (4) typical loess on top. Mazenot (1956) interpreted the entire Baix LPS as having developed in one single loess deposit, arguing that the intensive alteration of the basal part occurred due to a high groundwater table in former periods.

4.2.2 Field description and sampling

4.2.2.1 Field description, palaeosol classification, sampling for granulometry and analyses of carbonate content and micromorphology

We cleaned a main vertical profile of 13.7 m on the eastern wall of a small loam pit during three field campaigns in the years 2018–2020 (Fig. 4.45a–e) and described it according to the Guidelines for soil description (FAO, 2006). Palaeosols were later classified according to the World Reference Base for Soil Resources (IUSS Working Group WRB, 2022). Sampling for granulometric analysis was done by taking mixed samples integrating over 10 cm, thus continuously sampling the whole section at 10 cm vertical resolution. Where a horizon boundary (characterised by distinct changes in texture, structure and/or colour) occurred in less than 10 cm distance, the sampling interval was adjusted to the horizon boundary. The samples were air-dried, sieved (<2 mm mesh size) and homogenised. The coarse material (≥2 mm) was treated with 10 % HCl to dissolve possibly included carbonate nodules. It was then weighed to determine the rock-fragment content of the sediment as an important indicator of loess re-working through slope-wash processes. Three undisturbed, orientated blocks were

collected from the main palaeosol horizons (5 Bw2, 7 Bt1) and unweathered loess (5 Ck2) for micromorphological analysis. These samples were taken in Kubiëna boxes (6 cm × 8 cm × 4 cm) that were gently inserted into the profile wall, steadily supported by a knife.

4.2.2.2. Sampling for luminescence screening

Material for luminescence screening was sampled semi-continuously from the lower ~ 7 m of the previously cleaned profile wall. For this purpose, we carved into the profile wall to separate the sediment columns to be sampled (12 cm width; Fig. 4.45e). Then, we placed a plastic flower box vertically onto the uppermost section of the uppermost sediment column, with its opening towards the wall. We obtained a sediment block of ca 43 cm × 12 cm × 10 cm by carving around the side walls of the flower box with long knives and saws. We repeated this procedure from the top to bottom of the sediment columns, obtaining one flower pot filled with a sediment block after the other. An unsampled space of 3 cm remained between two consecutive sediment blocks due to the protruding rims of the flower boxes. Irregularities in the profile wall that might affect the luminescence signal were avoided by sampling in four columns that were



Figure 4.45: Baix LPS, Rhône Rift Valley, SE France. (a) Overview photo with white rectangles marking the positions of the close-up photos in panels (b), (c), (d) and (e). (b) In situ carbonate nodules of horizon 5 BCk4 (~ 850 cm depth). (c) Hydromorphic features of 7 Btg horizon (1199–1275 cm depth) of the basal Stagnic Luvisol. (d) Bleached root channel with lepidocrocite fringe (5–7 mm wide) in 7 Btg horizon (1227–1275 cm depth). (e) Vertically carved-in slots mark the positions of the sediment columns collected in boxes from 680 to 1360 cm depth for optically stimulated luminescence (OSL) screening (photos: Daniela Sauer, 2020).

slightly horizontally offset from one another (Fig. 4.45e). When the sampling shifted horizontally from one column to another, we used this chance to place the upper rim of the next flower box 10 cm above the depth of the lower rim of the previous flower box so that the block samples overlapped in these parts (partial columns 2, 3 and 4). Four partial sediment columns (subsections: 663–982 cm, 983–1072 cm, 1062–1150 cm, 1140–1368 cm) in 17 flower boxes represent one semi-continuous block sample, i.e. a vertical sediment column covering the lower ~7 m of the profile wall. Empty spaces in the flower boxes were filled with paper wadding to prevent the sediment blocks from breaking during transport. The flower boxes with the samples were finally tightly wrapped with clingfilm to stabilise them and preserve the water content in the sediment samples. Laboratory codes of the box samples range from HDS-1802 (top) to HDS-1817 (bottom).

4.2.3 Methods

4.2.3.1 Granulometry, analysis of carbonate content and micromorphological analysis

Particle size distribution was measured by use of a laser diffraction particle size analyser (Beckman Coulter LS 13 320). First, soil organic matter of 10 g homogenised fine earth material (<2 mm) was removed by adding 25 mL of 30 % H₂O₂ + 20 ml of deionised H₂O to the samples at 60 °C and allowing the samples to react for 12 h. This treatment was repeated until no visible reaction was observed (ISO 11277, 2020). Then, the samples were dispersed in 25 ml Na₄P₂O₇ × 10 H₂O (0.1 mol l⁻¹) + 200 ml deionised H₂O, shaken for 18 h in an overhead shaker and subsequently evaporated (ISO 11277, 2020). Carbonates were not removed because calcium carbonate grains constituted a substantial portion of the primary mineralogical and granulometric composition of the loess, which we did not want to lose. Samples containing high iron oxide contents (samples of Bt and Btg horizons) were additionally pre-treated with a solution of 4 % Na₂S₂O₄ + 0.3 mol l⁻¹ C₂H₃NaO₂ to dissolve the iron oxides following ISO 11277 (2020). Samples were shaken for 12 h in an overhead shaker. They were then washed by adding deionised H₂O, centrifuging (5 min, 3500 rpm) and removing the supernatant by pipette. The treatment was repeated until the samples had completely lost their brownish colour. An aliquot of the pre-treated and dried sample was ultrasonicated for 30 s in deionised H₂O and inserted in the mixing chamber of the laser particle sizer. The arithmetic mean of three measurements of each sample was used to calculate the particle size distribution based on an optical model according to Mie theory with a complex refraction index (RI) of 1.56-i0.1 suitable for quartz (ISO 13320, 2020). The laser measurements yielded 116 particle size classes (0.04 to 2000 µm) which were grouped into particle size classes of clay, silt and sand (vol %). The limits of the classes were set according to Bosq et al. (2018, 2020b), i.e. at <8 µm (clay), 8–56 µm (silt) and >56 µm (sand). We chose the high limit for clay (i) because it is commonly used to compensate for the known underestimation of clay content by laser diffraction (Konert and

Vandenbergh, 1997; Beuselinck et al. 1998; Újvári et al. 2016a) and (ii) because it allows for comparing the granulometric data of the Baix LPS with those of the Collias LPS. We used the U ratio ($16\text{--}44\ \mu\text{m} / 5.5\text{--}16\ \mu\text{m}$) to identify changes in sedimentary conditions during loess accumulation phases and the clay / silt ratio ($<8\ \mu\text{m} / 8\text{--}56\ \mu\text{m}$) to identify phases of pedogenesis (Antoine et al. 2009a; Újvári et al. 2016a; Schulte and Lehmkuhl, 2018; Schulte et al. 2018). Carbonate content was determined by the gas-volumetric method using a Scheibler apparatus and calculated as calcium carbonate (CaCO_3) equivalents in weight percent (wt %; Blume et al. 2011). The soil blocks for micromorphological analysis were subjected to acetone exchange of the remaining pore water. Then, the blocks were impregnated with resin (Palatal), cut, glued on 28 mm \times 48 mm glass slides and polished to a thickness of $\sim 25\ \mu\text{m}$. Micromorphological analysis was carried out in plane-polarised light (PPL) and cross-polarised light (XPL), using a Keyence VHX-7100 and/or VHX-E100 digital microscope, following the guidelines of Stoops (2021).

4.2.3.2 Luminescence screening

In recent years, various attempts have been made to profile sediment archives with luminescence techniques, also termed luminescence screening, i.e. in the case of optically stimulated luminescence, “OSL screening” (e.g. Sanderson et al. 2003; Burbidge et al. 2007; Sanderson and Murphy, 2010; Muñoz-Salinas et al. 2011; Kinnaird et al. 2012; Bateman et al. 2015; Portenga and Bishop, 2016; May et al. 2018; Fitzsimmons et al. 2022).

In contrast to conventional luminescence dating, luminescence screening involves minimal sample preparation, measurement of a few aliquots (usually one to three) and/or considerably shortened measurement procedures. The profiling maps the brightness (sensitivity) of one or more luminescence signals, for example, blue-light-stimulated luminescence (BLSL), infrared-stimulated luminescence (IRSL) or thermally stimulated luminescence (TL), e.g. along a sediment core (changes with depth) or in two dimensions across a profile wall. The use of a portable luminescence reader during fieldwork (cf. Scottish Universities Environmental Research Centre (SUERC) portable OSL reader; Sanderson and Murphy, 2010) may help to optimise the positions of OSL samples and to understand the stratigraphy of a sediment archive if the luminescence sensitivities correlate with different sediment units (Sanderson et al. 2003; Muñoz-Salinas et al. 2011). Among others, the sensitivity may reflect the characteristics of the minerals (usually quartz and feldspar), the amount of the palaeodose accumulated over time since the last exposure to daylight and varying local dose rates within the sediment deposit. However, in order to relate the luminescence counts gained by a portable OSL reader to the natural dose accumulated by a sample since the last sediment reworking, the sample material needs to be artificially irradiated, e.g. by an external gamma source, to allow for comparison of the natural signal of a sample to that received after the irradiation with

a calibrated source (Sanderson and Murphy, 2010). Further, some sort of dose rate estimation is required to transform the palaeodose estimates into a rough age estimate. Luminescence profiling has been successfully applied in different sedimentary environments, such as colluvium and alluvium (Muñoz-Salinas et al. 2014; Portenga and Bishop, 2016), coastal sand dunes (Bateman et al. 2015), swamp deposits (May et al. 2018), and loess (Fitzsimmons et al. 2022), including deposits at archaeological and prehistoric sites influenced by humans (Sanderson et al. 2003; Burbidge et al. 2007).

Luminescence profiling can be improved by applying the single-aliquot regeneration (SAR) protocol (Murray and Wintle, 2000) to closely spaced samples that are minimally prepared in the dark luminescence laboratory for measurements on a conventional automated luminescence reader, equipped also with a calibrated radiation source. Burbidge et al. (2007) and Kinnaird et al. (2012) applied a simplified SAR protocol to different mineral and grain size fractions of their samples, while May et al. (2018) measured one cycle of a complete SAR protocol (the natural luminescence signal, L_n , and the OSL signal received after an applied test dose, T_n) without grain size separation. L_n/T_n values were further normalised by the dose rates, which varied considerably along the profile. Fitzsimmons et al. (2022) used IRSL from unprepared bulk material of Rhine Valley loess read out at 50 °C (IR_{50}). Again, the luminescence signal was normalised by a test dose signal (L_n/T_n). The variation in the test-dose-normalised signal sensitivity was regarded as a proxy for varying source areas of the loess deposits. Thus, approaches to luminescence screening do not follow a strict protocol and are adjusted according to the aims of a study.

Luminescence screening “age estimates”

In this study, we performed luminescence screening to support the stratigraphy based on detailed field observation, hypothesising that the lower ~7 m of the Baix LPS reflect the Eemian to Middle Pleniglacial palaeoenvironmental changes. Therefore, we collected data on the luminescence sensitivity, the (approximate) palaeodoses and the dose rates. In addition, we applied a sensitivity approach following Fitzsimmons et al. (2022) but using the coarse fraction and performing an additional step for inter-aliquot normalisation to obtain a proxy indicating the likely provenance of the material. Here, we give a brief outline of the procedure, while a detailed description is given in the supplement (“S4.2 Methods – Luminescence screening”).

A semi-continuous sequence of material was collected from the lower ~7 m of the Baix LPS in 16 vertically aligned boxes (laboratory codes of the OSL box samples are HDS-1802 (top) to HDS-1817 (bottom) (cf. sect. 4.2.2). In the dark luminescence laboratory, up to eight ca 1 cm³ small subsamples (A–H) were extracted at intervals of 5 cm from each box sample (altogether 126 subsamples). Additional material was taken for water content and radionuclide determination, both needed for calculating an effective dose rate. Minimal sample preparation

included wet sieving (125 µm mesh size) and preparation of small aliquots (a few hundred grains) from the retained polymineral coarse-grain fraction (>125 µm).

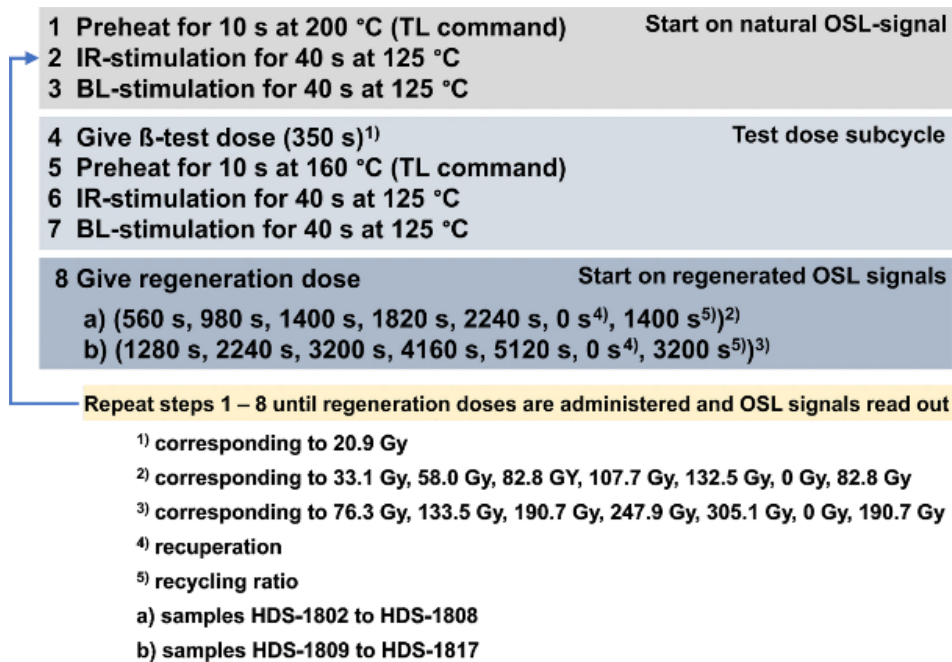


Figure 4.46: pIR-BLSL SAR protocol applied to minimally prepared polymineral coarse grains from 126 miniature (1 cm³) subsamples.

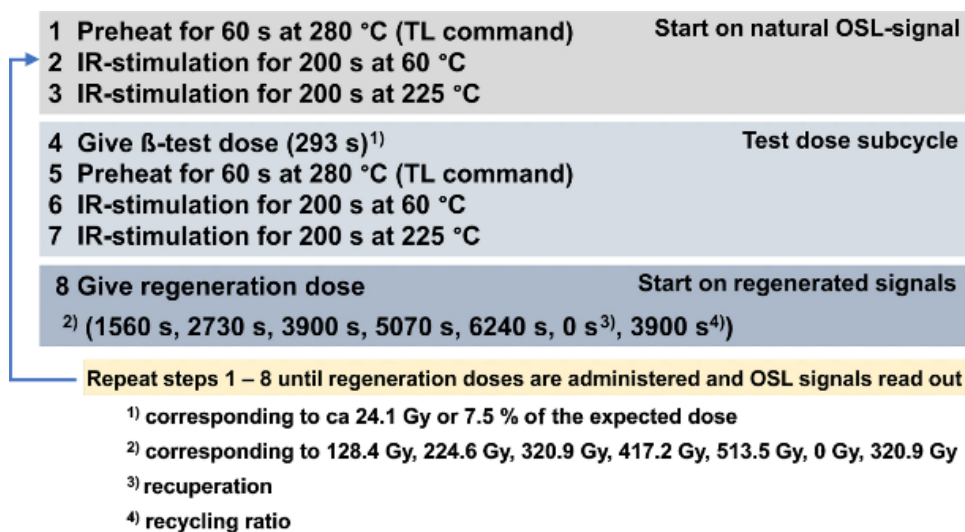


Figure 4.47: pIR₆₀ IR₂₂₅ SAR protocol applied to minimally prepared polymineral coarse grains from 126 miniature (1 cm³) subsamples.

To provide a time frame, we applied the SAR protocol establishing dose–response curves with several test dose-normalised regeneration-dose points (L_x/T_x), including dose points for testing the recuperation and recycling ratio, once with a BLSL protocol (Murray and Wintle, 2000) after IR stimulation (pIR-BLSL) and signal detection in the UV (Hoya U340) and once with a post-infrared (at 60 °C) infrared (at 225 °C) protocol (pIR₆₀IR₂₂₅) (Thomsen et al. 2008) with detection of the blue emission around 410 nm (through interference filter CH-30D410-44.3). All measurements were performed on two automated luminescence Risø reader models,

TL/OSL DA15 and TL/OSL DA20 (an update of TL/OSL DA15), respectively (Lapp et al. 2012, 2015). The protocols are illustrated in Figs. 4.46 and 4.47

We aimed to extract a quartz-dominated signal with the pIR-BLSL protocol and a potassium-feldspar-dominated signal with the pIR₆₀IR₂₂₅ protocol. For adapting the pIR-BLSL and the pIR₆₀IR₂₂₅ protocols to the Baix samples, we performed a series of tests, including D_e -range tests, dose recovery tests, normalisation dose tests (pIR₆₀IR₂₂₅ protocol only) and tests of anomalous fading. Thus, our OSL-screening approach contained all relevant preparatory measurement steps needed for elaborated SAR OSL dating. In contrast to proper OSL dating, however, the D_e measurements were performed on only three aliquots per subsample for the pIR-BLSL approach and one aliquot per subsample for the pIR₆₀IR₂₂₅ protocol in order to save measurement time. For dose rate assessment, radionuclide determination was performed with the novel μ Dose system (Tudyka et al. 2018, 2020; Kolb et al. 2022) on six samples regarded as representative of the Baix sediments and palaeosols. Assuming radioactive equilibrium, the radionuclide concentrations were transformed to dose rates (Guérin et al. 2011), while the cosmic dose rate was calculated with the R package “Luminescence” (Kreutzer et al. 2012b). Following standard procedures, we assumed an internal potassium content of 12.5 ± 1.25 wt % for the pIR₆₀IR₂₂₅ protocol, a values of 0.1 ± 0.02 for the pIR₆₀IR₂₂₅ approach (Kreutzer et al. 2014) and 0.035 ± 0.02 (Lai et al. 2008) for the pIR-BLSL approach and water content as suggested by Sauer et al. (2016) and applied to the Collias LPS by Bosq et al. (2020b). While our OSL “age estimate” calculation relies on 126 D_e measurements for the pIR₆₀IR₂₂₅ protocol and the triple number of D_e measurements for the pIR-BLSL protocol, a mean effective dose rate was used for each of the two SAR protocols. Due to the reduced number of aliquots used for D_e determination and the use of a representative mean effective dose rate for each of the two SAR approaches, we called them “age estimates” and put them into quotation marks. We consider our luminescence screening approach for deriving OSL “age estimates” adequate for testing the field hypothesis of whether the lower ~ 7 m of the Baix LPS contains an Eemian to Middle Pleniglacial record. We will additionally perform OSL dating on selected samples in future studies.

Luminescence sensitivity

Varying luminescence sensitivities in a loess profile may serve as a proxy for different source areas or materials (Fitzsimmons et al. 2022). We compared the IR signal of the aliquots measured with the pIR-BLSL protocol to the subsequently readout BLSL signal, using all measured test dose signals (T_x) for this procedure. For determining the luminescence sensitivities, first, the T_x signals of a complete SAR measurement (eight measurement points) were averaged for each aliquot (T_{x_mean} of an aliquot) before a mean with the standard error of the three aliquots of each subsample was calculated (T_{x_mean} of a subsample). Finally, the ratio

of the signals of the two stimulations was derived (T_{x_IR}/T_{x_BLSL}). While samples with a dominant IR signal may point to the predominance of feldspar (emitting in the UV), the dominance of a BLSL signal could indicate the predominance of quartz in the polymineral coarse grains. Thus, larger values (ratios) would point to more feldspar emitting around 340 nm and smaller ratios to a quartz dominance emitting in that range.

4.3 Results

4.3.1 General overview of the LPS Baix

The overall 13.7 m thick Baix LPS was subdivided into 19 horizons, developed in (mostly reworked) loess and soil sediments that overlie slope deposits with a large share of rock fragments from local bedrock (Table 4.14). Four levels of soil formation were identified, in the following termed “Holocene soil”, “upper interstadial palaeosol”, “lower interstadial palaeosol” and “interglacial palaeosol complex”. Several erosional discontinuities were observed, e.g. above the 7 Btg and 5 Bw2 horizons. Various forms and sizes of secondary carbonate accumulation, i.e. pseudomycelia, hard nodules and soft carbonate concentrations, were observed (Table 4.14, Fig. 4.45b). All horizons showed abundant bioturbation features such as root channels and earthworm burrows, which make it a challenge for luminescence dating.

4.3.1.1 Granulometry and carbonate contents

The mean particle size distribution in the lower 7 m of the Baix LPS included 26 vol % clay, 55 vol % silt and 19 vol % sand. The palaeosol horizons exhibited the highest clay contents with up to 30 vol % clay, whereas the only slightly weathered loess horizons showed the highest silt (60 vol %) and sand (26 vol %) contents. The main mode was in the coarse silt fraction (34 μm), and the mean particle size was in the range 29–41 μm , with an arithmetic mean of 33 μm . Rock-fragment contents ranged from 0 wt % up to 80 wt %. U ratios were in the range 1.55–2.59, exhibiting maxima in the only slightly weathered loess deposition phases and decreasing in the palaeosol horizons (Fig. 4.53). Clay/silt ratios showed an opposite trend, overall ranging between 0.35 and 0.58. The least weathered loess (5 Ck2 horizon) contained 23 wt % CaCO_3 , which was the maximal measured CaCO_3 content. The lowest CaCO_3 content (0.3 wt %) was found in the 7 Bt1 horizon, belonging to the interglacial palaeosol complex.

4.3.1.2 Micromorphology

The groundmass of the three thin sections of the Baix LPS displayed quartz and carbonate grains with lower quantities of feldspars and biotite. All horizons showed calcitic and/or textural pedofeatures. They had massive (Fig. 4.48b) to weakly subangular blocky (Fig. 4.48c) microstructures and calcitic crystallitic (Fig. 4.49d) to stipple-speckled and porostriated (Fig.

Table 4.14: Horizon designations and characteristics of the horizons of the Baix LPS according to the Guidelines for soil description (FAO, 2006) and interpretation with respect to sedimentary and pedogenic processes. Soil colour is given according to Munsell Soil Colour Charts (moist). Abbreviations and definitions: PM, pseudomycelia; HC, hard carbonate nodules; HHC, hard hollow carbonate nodules; SC, soft carbonate nodules; very small carbonate nodules, ca 1 to 5 mm in diameter (\emptyset); small carbonate nodules, ca 0.5 to 1.5 cm \emptyset ; medium-sized carbonate nodules, 1.5 to 5 cm \emptyset ; large carbonate nodules, ≥ 5 cm \emptyset ; WE, earthworm channels; WC, earthworm casts; Mn, manganese.

No.	Horizon	Depth [cm]	Subdivision [cm]	Main characteristics	Interpretation
1	Ah	0–20		disturbed surface; clear smooth lower boundary; dark brown colour (10 YR 3/2); fine and medium granular structure; many WC	colluvial deposit, Holocene Cambisol
2	Bw1	20–65	20–30	clear smooth lower boundary; dark brown colour (10 YR 4/4); moderate fine and medium subangular blocky structure; many WE, burrows, infilled small burrows	Holocene soil
			30–45	gradual smooth lower boundary; intense brown colour (10 YR 4/6); moderate fine and medium subangular blocky structure; PM; many WE, burrows, infilled small burrows	
			45–65	gradual smooth lower boundary; brown colour (10 YR 5/6); moderate medium subangular blocky structure; PM; many WE, infilled small burrows	
3	Bk1	65–95		gradual smooth lower boundary; brown colour (10 YR 5/4); weak medium subangular blocky structure; PM; small few HC, HHC; common WE	
4	Bck1	95–240	95–200	gradual smooth lower boundary; light brown colour (10 YR 6/4); massive structure; PM, small few HC, HHC	slope-washed loess with varying degrees of pre-weathering
			200–240	gradual smooth lower boundary; brown colour (10 YR 5/4); massive structure; small HC, SC	
5	Ck1	240–374	240–280	gradual smooth lower boundary; light brown colour (10 YR 6/4); massive structure; few PM, small HC; mollusc-shell fragments	
			280–374	gradual smooth lower boundary; yellowish brown colour (10 YR 6/3); massive structure; few PM, few very small HC; very few very fine soft Mn concentrations	
6	CBk	374–500		gradual smooth lower boundary; greyish brown colour (10 YR 5/3); massive structure; long PM, very small HC; very few very fine spheroidal soft Mn concentrations; charcoal pieces	Loess
7	2 Bck2	500–570/590		gradual smooth lower boundary; light brown colour (10 YR 5/4); strong massive structure; PM, few small HC; very few very fine spheroidal soft MN concentrations	
8	3 Bck3	570/590–700		gradual smooth lower boundary; light brown colour (10 YR 5/4); strong massive structure; PM, few small in situ HC; very few very fine round soft Mn concentrations	
9	4 Bck/Bw	700–735		clear to gradual smooth lower boundary; light brown colour (10 YR 5/6); strong massive structure; PM, very	mixture of reworked soil

				few small HC; very few very fine spheroidal soft Mn concentrations	sediment and loess	
10	5 Bw2	735–775		gradual smooth lower boundary; brown colour (10 YR 4/6); massive to weak coarse subangular blocky structure; few PM, very few very small HC; loess-coloured infillings in WE; contains small rock fragments	truncated Bw horizon of Cambisol	Upper interstadial palaeosol
11	5 Bk2	775–820		gradual smooth lower boundary; brown colour (10 YR 4/6); massive to weak coarse subangular blocky structure; PM, few small in situ HC	slightly weathered, lower in situ horizon of Cambisol	
12	5 Bck4	820–853		gradual smooth lower boundary; brown colour (10 YR 5/4); strong massive to subangular blocky structure; PM, many large in situ HC (up to 8–15 cm long, 4–6 cm width); contains small rock fragments	In situ carbonate accumulation horizon of Cambisol	
13	5 Ck2	853–995	853–915	gradual smooth lower boundary; light brown colour (10 YR 6/4); strong massive structure; few PM, HC; few incompletely infilled former root channels; many recent root channels; rock fragments	slope-washed loess with varying degrees of pre-weathering	Loess
			915–995	gradual smooth lower boundary; yellowish brown colour (10 YR 6/3); strong massive structure; few PM, HC; darker brown sediment-filled former root channels; few recent root channels; small rock fragments		
14	5 Bck5	995–1080		clear smooth lower boundary; brown colour (10 YR 5/4); massive structure; very few very small in situ HC; very few very fine spheroidal soft Mn concentrations; small rock fragments		
15	6 Bw3	1080–1155	1080–1120	gradual smooth lower boundary; brown colour (10 YR 4/6); massive structure; very few very fine round soft Mn concentrations; small rock fragments	Bw horizon developed in a mixture of reworked soil sediment and loess	Lower interstadial palaeosol
			1120–1155	gradual smooth lower boundary; brown colour (10 YR 4/6); massive structure; very few faint clay coatings; few very small in situ HC; very few very fine spheroidal soft Mn concentrations; loess-infilled former root channels; small rock fragments		
16	6 Bck/Btg	1155–1199	1155–1178	clear smooth lower boundary; brown colour (10 YR 5/8); massive structure; few small HC; few very fine spheroidal soft Mn concentrations; rock fragments	mixture of reworked soil sediment and loess	Loess
			1178–1199	clear smooth lower boundary; yellowish brown (10 YR 5/8) and reddish-brown colour (7.5 YR 5/6); weak massive to subangular blocky structure; very few faint to distinct clay coatings; SC, few small HC; common fine to medium irregular flat soft Mn concentrations; lower part with iron-oxide mottles and depletion zones		
17	7 Btg	1199–1315	1199–1227	clear to gradual smooth lower boundary; reddish orange-brown colour (7.5 YR 4/6); weak coarse and very coarse subangular blocky structure; few distinct clay coatings; few in situ HC; many fine to medium irregular flat soft Mn concentrations; iron-oxide mottles and depletion zones	Bt and Btg horizons of Stagnic Luvisol (subdivision based on the intensity of hydromorphic features) developed in reworked soil sediment	Interglacial palaeosol complex
			1227–1275	clear to gradual smooth lower boundary; reddish orange-brown colour (7.5 YR 5/8); weak coarse and very coarse subangular blocky structure; common distinct clay coatings; few in situ HC; many fine and medium spheroidal soft Mn concentrations; iron oxide		

			mottles and depletion zones; bleached root channels seamed by Lepidocrocite hems (5–7 mm thick); depth where hydromorphic features are most prominent	
		1275–1315	gradual smooth lower boundary; reddish orange-brown colour (7.5 YR 5/8); weak coarse and very coarse subangular blocky structure; common distinct clay coatings; many very fine and fine spheroidal soft Mn concentrations; iron oxide mottles and depletion zones; bleached root channels seamed by Lepidocrocite hems (2–3 mm thick); root channels incompletely filled with sediment	
18	7 Bt1	1315–1360	abrupt smooth lower boundary; reddish brown colour (7.5 YR 5/6); weak coarse and very coarse, subangular blocky structure; few distinct clay coatings; many very fine spheroidal soft Mn concentrations; few WE filled with WC; rock fragments	
19	8 Bt2	1360–1370	clear wavy lower boundary; reddish brown colour (7.5 YR 6/6); strong massive structure; weathered (soft) and unweathered rock fragments	mixture of reworked soil sediment, loess and local rock debris
20	Cw	1370+	debris of Lower-Cretaceous limestone and marl, and basalt	slope deposit of local rock debris

4.49f) b-fabrics. Voids mainly included channels, chambers and vughs (Fig. 4.48a–c). The number and size of orthic and disorthic Fe nodules increased with depth (Fig. 4.48a–c). Calcite earthworm granules and/or calcified root cells were observed in all three thin sections (Fig. 4.49c–d).

4.3.2 Detailed characterisation of the lower 7 m of the LPS Baix

4.3.2.1 Basal interglacial palaeosol complex

The basal interglacial palaeosol complex of the Baix LPS was classified as a Stagnic Luvisol (IUSS Working Group WRB, 2022), of which a Btg horizon and two underlying Bt horizons were preserved (Table 4.14), all characterised by an intense reddish-brown to orange-brown colour and massive to subangular blocky structure. This palaeosol complex exhibited the highest clay contents (25 vol %–37 vol %) and lowest silt contents (45 vol %) of the investigated part of the Baix LPS. Thereby, the slightly carbonated (8 wt %) 8 Bt2 horizon had the highest rock-fragment content (80 wt %) and the highest clay content (37 vol %), although no clay coatings were observed. The overlying 7 Bt1 and 7 Btg horizons had clay contents of up to 30 vol % and displayed clay coatings that were observed both in the field and in the thin sections. Both disturbed and/or relocated clay coatings (Fig. 4.48c) and undisturbed clay and clay–silt coatings along voids, indicating in situ clay migration (Fig. 4.49e–f), were identified under the microscope. The 7 Bt horizon contained up to 12 wt % rock fragments (in its basal part), whereas the overlying 7 Btg horizon had no rock fragments. It showed in situ stagnic

properties, i.e. bleached root channels and prominent undisturbed Mn and Fe concentrations and coatings (Fig. 4.45c–d).

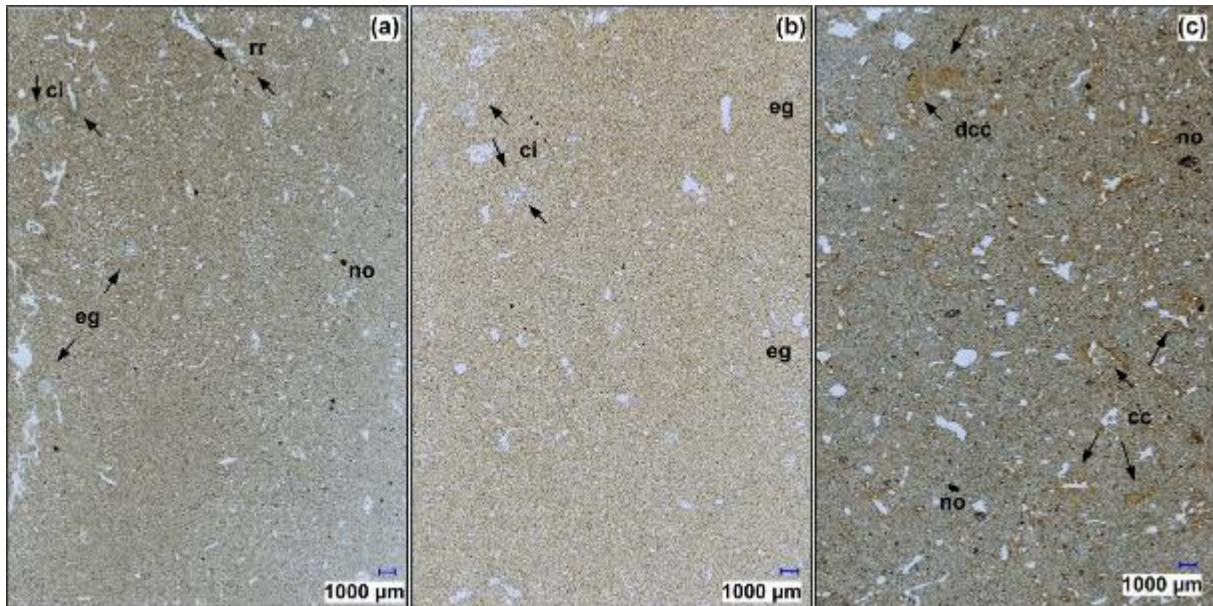


Figure 4.48: Photos of whole thin sections (3 cm × 4 cm) of the Baix LPS, Rhône Rift Valley, SE France. (a) Decarbonated 5 Bw2 horizon (755–763 cm): weakly subangular blocky microstructure (in places crumbly, channel microstructure). Voids: channels and vughs. Voids impregnated with calcite hypo- and quasi-coatings, channel infillings, and porous and dense rounded microaggregates. Typic, rounded and digitated elongated disorthic Fe / Mn nodules and digitated Fe/Mn impregnations. Calcite earthworm granules with clay–silt capping and root residues. (b) 5 Ck2 horizon (935–943 cm depth): massive, vuggy microstructure. Voids: vughs and channels, some infilled with dense rounded microaggregates, partially with calcite hypocoatings. Few small Fe/Mn nodules. Calcite earthworm granules. (c) Decarbonated 7 Bt1 horizon (1335–1343 cm depth): weak subangular blocky, crumbly microstructure. Voids: channels, vughs and chambers. Some channels infilled with porous to dense microaggregates. Voids with limpid orange (relocated) clay coatings. Abundant round, digitated, elongated disorthic Fe/Mn nodules; large (\varnothing 380 μ m) Fe impregnations. Abbreviations: cc, clay coating; ci, calcite impregnation; dcc, disturbed clay coating; eg, calcite earthworm granule; no, Fe nodules; rr, root residues.

4.3.2.2 Lower and upper interstadial palaeosols

The lower interstadial palaeosol was represented by the decarbonated bipartite brown 6 Bw3 horizon with massive structure. The horizon was marked by increased clay (27 vol %–29 vol %) and decreased silt (52 vol %–57 vol %) and sand (15 vol %–19 vol %) contents. It contained up to 1 wt % of rock fragments. The lower part of the bipartite horizon displayed faint clay coatings and loess-infilled former root channels (Table 4.14). The upper interstadial soil was represented by the brown decarbonated 5 Bw2 horizon and the underlying 5 Bk2 and 5 BCK4 horizons. The 5 Bw2 horizon had massive to weak subangular blocky structure. Its clay (27 vol %–30 vol %), silt (52 vol %–54 vol %) and sand (16 vol %–21 vol %) contents were similar to those of the 6 Bw3 horizon of the lower interstadial palaeosol. The 5 Bw2 horizon of the upper interstadial soil contained up to 7 wt % of rock fragments. Under the microscope, rounded microaggregates, dusty silt-clay coatings along pores, in situ Fe nodules, partially decomposed root remains, and calcite earthworm granules were observed (Figs. 4.48b, 4.49a–b). The 5

Bk2 and 5 Bck4 horizons underlying the 5 Bw horizon were characterised by reprecipitation of the carbonates leached from the 5 Bw horizon, forming large in situ carbonate nodules. The largest carbonate nodules (8 to 15 cm long, 4 to 6 cm wide) were found at 810–860 cm depth (Fig. 4.45b). The carbonate nodules were yellowish brown; contained silicate grains including rock fragments; and displayed a porous, homogenous structure.

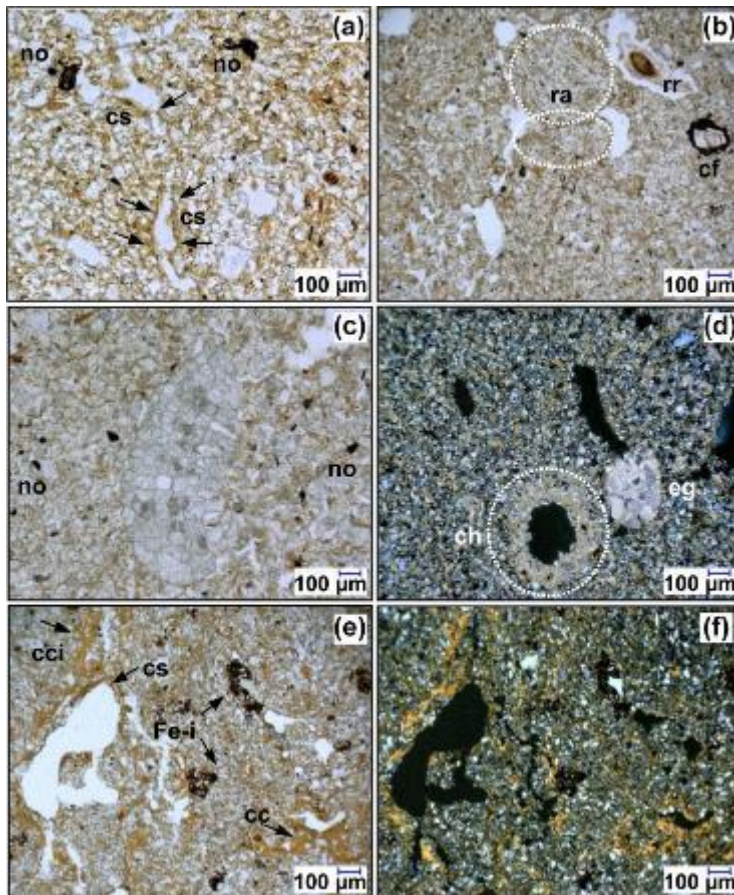


Figure 4.49: Photomicrographs of thin sections of the Baix LPS, Rhône Rift Valley, SE France. (a) Brown clay–silt coatings along voids in the 5 Bw2 horizon (755–763 cm) and elongated and digitated Fe / Mn nodules (plane-polarised light; PPL). (b) Rounded (bioturbated) aggregates in the 5 Bw2 horizon (755–763 cm) with root residues and in situ weathered calcite fragment. (c) Calcified root cells in 5 Ck2 horizon (935–943 cm depth) with elongated anorthic Fe / Mn nodules and digitated Fe impregnations (PPL). (d) Subrounded (relocated) calcite earthworm granule and calcite hypocoatings along voids in the carbonated groundmass of the 5 Ck2 horizon (935–943 cm depth) (cross-polarised light; XPL). (e) Limpid orange clay and dusty-brown silt coatings and infillings with disorthic Fe impregnations in the 7 Bt1 horizon (1335–1343 cm depth) (PPL). (f) Same area as panel (e) under XPL, Stipple-speckled, partly porostriated b-fabric of the 7 Bt1 horizon (1335–1343 cm depth). Abbreviations: cc, clay coating; cci, clay coating infilling; cf, calcite fragment; ch, calcite hypocoatings; cs, clay–silt coating; eg, calcite earthworm granule; Fe-i, Fe impregnation; no, nodule; ra, rounded aggregate; rr, root residues.

4.3.2.2 Erosional discontinuities and characteristics of the slightly to moderately weathered loess

Major erosional discontinuities were observed above the interglacial palaeosol complex and above the upper interstadial palaeosol. Both of these discontinuities were followed by a layer of mixed sediment, containing clearly recognisable portions of reworked palaeosol material

and only slightly weathered loess (6 BCK/Btg and 4 BCK/Bw). These mixed layers displayed high rock-fragment contents (up to 20 wt %). The parts of the Baix LPS where the sediment was only slightly to moderately weathered (5 BCK5, 5 Ck2, 5 BCK 4, 5 Bk2, 3 BCK3) had yellow-brown (Ck), light-brown (BCK) and brown (Bk) colours; had massive to weak subangular blocky structure; and contained 5 wt %–22 wt % CaCO₃, reflecting their different weathering degrees (Table 4.14). The least weathered 5 Ck2 horizon displayed the highest silt content (60 vol %), high sand content (24 vol %) and the lowest clay content (20 vol %) of the investigated part of the Baix LPS. Otherwise, the slightly to moderately weathered loess was composed of 49 vol %–59 vol % silt, 16 vol %–26 vol % sand and 21 vol %–28 vol % clay. Rock-fragment contents were in the range of 0 vol %–6 wt %. Abundant bioturbation features were observed in the thin sections, including calcite earthworm granules, calcified root cells and former root channels coated by micritic carbonate precipitates (Figs. 4.48b,4.49c–d).

4.3.3 Luminescence screening results

Examples of pIR-BLSL and pIR₆₀IR₂₂₅ shine-down, dose–response curves and graphical results of the fading tests are given in the second part of the supplement (“S4.2 Results – Luminescence screening”) (all *g* values normalised to 2 d). While four aliquots measured with the pIR-BLSL protocol showed *g* values, which within error margins agreed with zero, eight aliquots exhibited *g* values pointing to fading. For the pIR₆₀IR₂₂₅ protocol, four aliquots exhibited *g* values which conform with zero, while the other four aliquots showed *g* values above zero (mean of all eight aliquots 6.45 ± 1.16). As this is not expected for pIR-IR measurements (Thomsen et al. 2008), we eliminated the prompt readouts for *g*-value determination. This produced a mean *g* value over all eight aliquots of 1.24 ± 2.48 , conforming with zero (no fading). Therefore, we assumed that the larger *g* values for the pIR₆₀IR₂₂₅ protocol were measurement artefacts (cf. Thiel et al. 2011b). Such measurement artefacts may be produced if prompt readouts are included in fading measurements and no minimum time after irradiation and preheating is considered (see final public response to discussion of Kadereit et al. 2020). As no correlation between the size of a *D_e* of an aliquot and its *g* value was observed, we expect the pIR₆₀IR₂₂₅ protocol to deliver reliable data.

The results of the effective dose rate determination for the six selected samples are presented in Fig. 4.50. They show a relatively narrow spread, justifying the use of a mean effective dose rate for the OSL screening. For pIR-BLSL measurements, supposed to sample quartz, the effective dose rates ranged between 2.43 ± 0.18 and 2.93 ± 0.23 Gy ka⁻¹ (dark-blue symbols), giving a mean value of 2.80 Gy ka⁻¹ (blue line). For pIR₆₀IR₂₂₅ measurements, likely sampling potassium feldspar, the effective dose rates range between 3.52 ± 0.19 Gy ka⁻¹ and 4.15 ± 0.24 Gy ka⁻¹ (red symbols), providing a mean value of 3.98 Gy ka⁻¹ (red line). These values were used for OSL “age estimate” calculation. For the lowermost silt loam sample, a higher

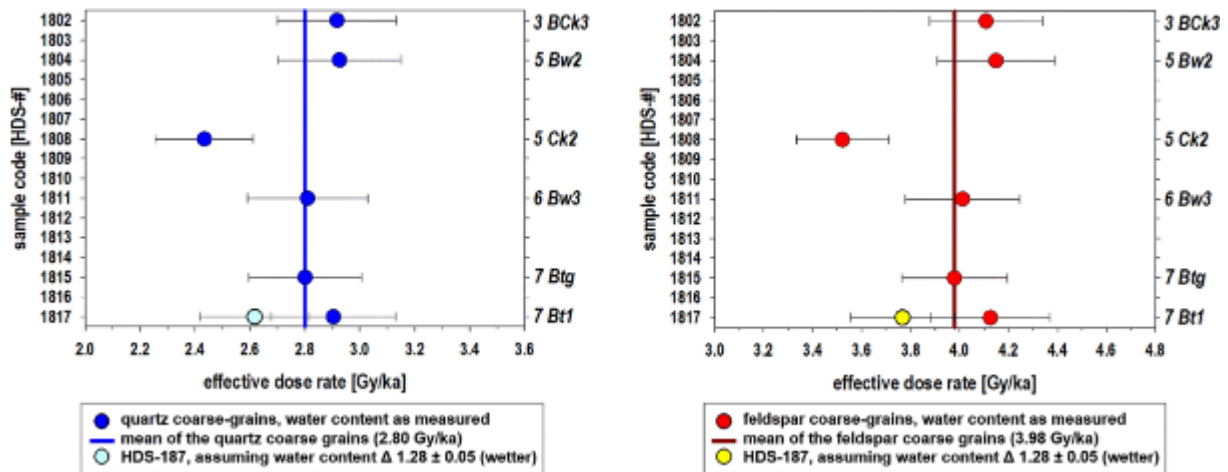


Figure 4.50: Effective dose rates determined for the six selected samples subjected to measurements with the μ Dose device to determine the radionuclide concentrations. The error bars take the water contents of the subsamples into account, expressed as moist weight/dry weight = 1.17 ± 0.05 . Because of stagnic properties in the basal part of the Baix LPS, we additionally calculated effective dose rates for wetter conditions (1.28 ± 0.05) for sample HDS-1817. The water content estimates are based on Sauer et al. (2016).

water content was also assumed (light-blue and yellow symbols) for dose rate assessment, accounting for its hydromorphic features. While for “age estimate” calculation, D_e errors and beta source calibration errors were taken into account, only the mean values of the dose rate without assuming an error were considered. Thus, the OSL screening gives an idea of the course of the burial doses along the lower 7 m of the Baix LPS, divided by an effective dose rate regarded as representative, to produce a profile of approximate “age estimates” (Fig. 4.51). A graph summarising OSL “age estimates” block-wise for each of the 16 boxes HDS-1802 to HDS-1817 following the central age model approach of Galbraith et al. (1999) is provided in Fig. S4.66. Throughout the investigated part of the profile, pIR-BLSL “age estimates” are smaller than pIR₆₀IR₂₂₅ “age estimates”.

While the course of “age estimates” gained with both the pIR-BLSL and the pIR₆₀IR₂₂₅ protocol shows a trend of increasing data values from top to ca 12.3 m depth, surprisingly, the values do not increase further below that depth for the pIR-BLSL protocol. Further, several aliquots measured with the pIR-BLSL SAR protocol show “age estimates” younger than the Last Glacial Maximum (LGM) limit (cf. yellow line in Fig. 4.51), which is not logical for loess deposits, especially not at depths several metres below the ground level. Although the incorporation of quartz grains from the surface and younger deposits by bioturbation cannot be excluded, with quartz being bleachable faster than feldspar (Godfrey-Smith et al. 1988), this assumption does not seem appropriate as an explanation for the comparably young(er) “age estimates” produced by the pIR-BLSL SAR protocol.

In general, we suppose that the pIR-BLSL “age estimates” are less reliable than the pIR₆₀IR₂₂₅ “age estimates” produced by our OSL-screening approach. We assume that the IR depletion

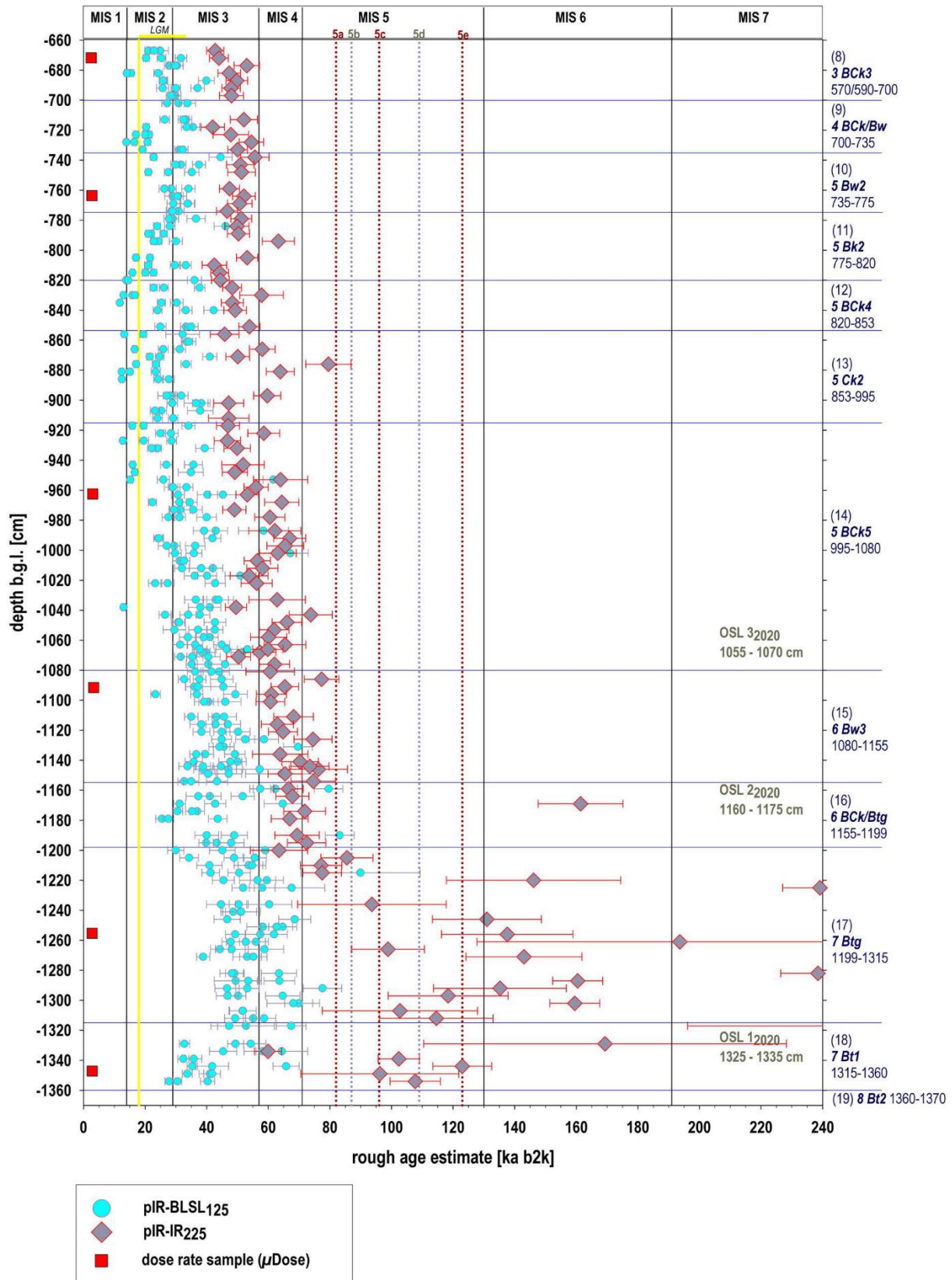


Figure 4.51: Results of the pIR-BLSL and pIR₆₀IR₂₂₅ screening of the Baix LPS, Rhône Rift Valley, SE France. Solid vertical lines denote the boundaries of marine isotope stages (MISs), while dotted lines denote the peaks of the MIS 5 sub-stages. Boundaries after Lisiecki and Raymo (2005) and Railsback et al. (2015) (LGM denotes the Last Glacial Maximum).

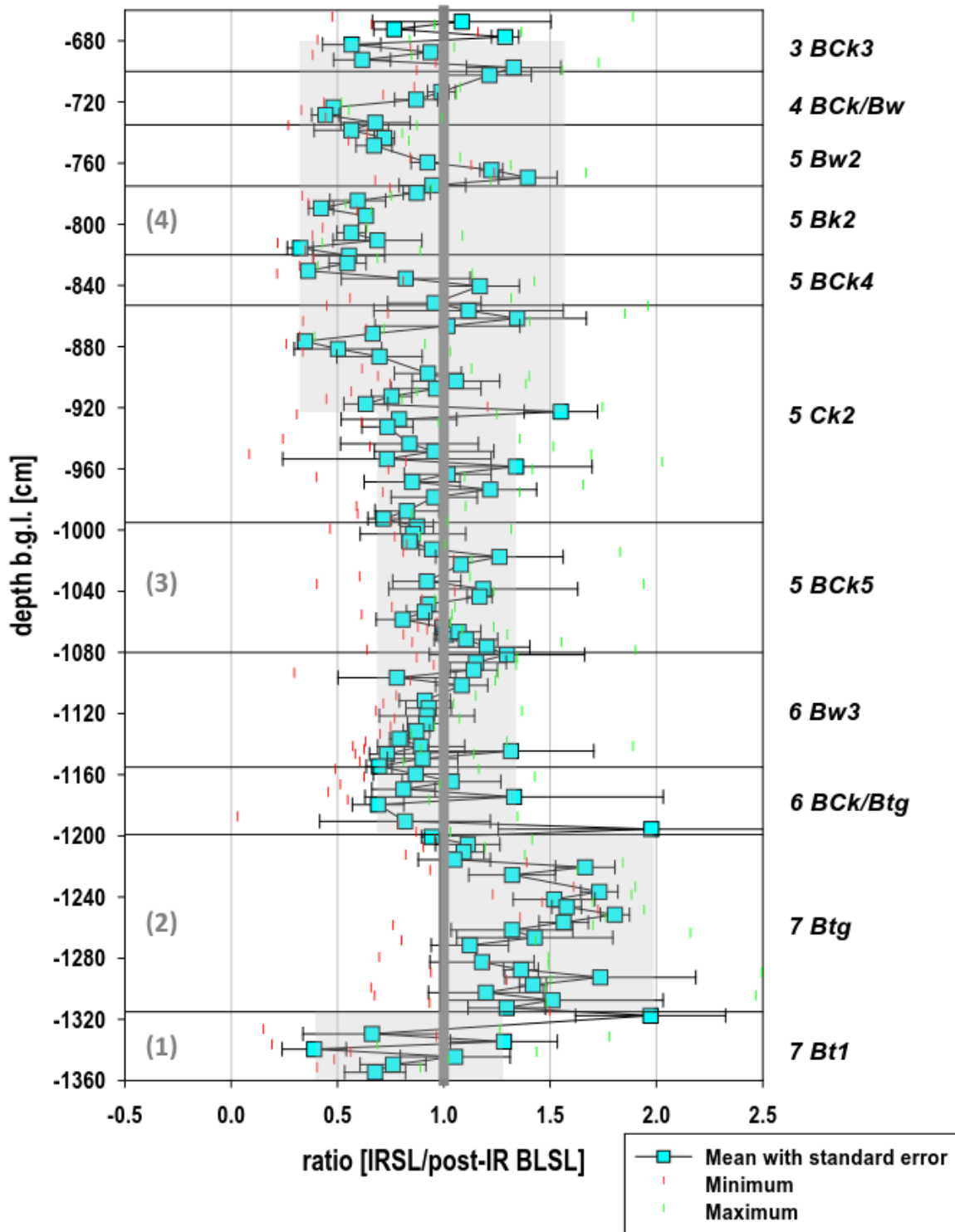


Figure 4.52: Results of the luminescence sensitivity measurements (IRSL/post-IR BLSL signal strength; IRSL denotes infrared-stimulated luminescence, and BLSL denotes blue-light-stimulated luminescence) of the Baix LPS, Rhône Rift Valley, SE France. Mean values with standard error of three aliquots measured per subsample with the BLSL protocol after IR simulation (pIR-BLSL protocol; blue squares and error bars in black) and respective minimum (red) and maximum (green) values (further details sect. 4.3.3, “Luminescence screening”). Grey boxes mark subdivision into four units. The two upper data values are not included, as they may or may not point to a narrower scattering of data values around the balance line, similar to unit (3).

of the polymineral coarse grains was too incomplete to get a more or less “pure” BLSL signal from quartz. It is likely that the polyminerals emitted an unstable UV emission from feldspar, especially as preheating and pIR-BLSL readout occurred at significantly lower temperatures and for considerably shorter times than for the pIR₆₀IR₂₂₅ protocol. This assumption agrees with the partly considerable *g* values observed by the fading tests. For these reasons, we disregard the age assessments associated with the pIR-BLSL measurements and only consider the pIR₆₀IR₂₂₅ “age estimates” for the discussion. The derived “age estimates” of the OSL screening are tentatively reflected against the MIS as defined by Lisiecki and Raymo (2005) (Fig. 4.51). As the MIS stratigraphy rather reflects global climate changes, we correlated our OSL “age estimate” results with stadial and interstadial phases derived from European terrestrial (LPSs, pollen and lacustrine sequences) archives (Woillard, 1978; Beaulieu and Reille, 1992; Guiter et al. 2003; Haesaerts et al. 2016).

OSL sensitivity

The OSL sensitivity values (IRSL/pIR-BLSL ratios) originate from coarse-grain separates and therefore do not represent the far-transported aeolian main component of the LPSs but rather accessories. They ranged between ca -0.5, likely pointing to subdued contribution from feldspar, and ca +1.5 (Fig. 4.52), likely pointing to an increased contribution from feldspar (or feldspar having a stronger signal in the UV range if the depletion of the OSL signal was insufficient by the IR stimulation).

Low values of around -0.5 occurred in the lowermost horizon, 7 Bt1. The largest concentration of values around 1.5 occurred in the overlying 7 Btg horizon. “Balanced” values scattering closely around 1 occurred in the overlying horizons, i.e. 6 Bck/Btg to 5 Ck2. Values alternating between these two extremes are observed in the 5 Ck2 to 3 Bck3 horizons. Thus, the OSL screening seemed to serve as a proxy for variations in the sediment sources, as suggested by Fitzsimmons et al. (2022), and supported a subdivision into four parts marked in Fig. 4.52.

4.4 Discussion – Eemian to Middle Pleniglacial evolution of the Baix LPS and corresponding palaeoenvironmental conditions

4.4.1 The Eemian and Early Glacial period

The basal interglacial palaeosol complex was composed of three horizons, whereby the lowermost horizon (8 Bt2) had developed not in loess but in a slope deposit with high content of local rock debris. Its difference in parent material is also reflected in its different OSL sensitivity ratio (Fig. 4.52). Most likely, its high clay content was partially inherited from the pre-weathered slope deposit. The reddish-brown colour and the presence of in situ clay coatings in the overlying 7 Bt1 horizon suggested warm and at least seasonally humid conditions. Relocated aggregates and broken clay coatings in the matrix indicated intense bioturbation. The uppermost reddish- to orange-brown 7 Btg horizon of the basal interglacial palaeosol

complex showed similar characteristics to the 7 Bt1 horizon but in addition exhibited strong stagnic properties (Table 4.14). The sediment in which these two upper horizons of the interglacial palaeosol complex had developed yielded penultimate-glacial to Eemian “age estimates” and exhibited an above-average OSL sensitivity ratio over the entire thickness of the two horizons. Thus, the sediment was clearly different from the last-glacial slope-wash loess that made up the overlying part of the Baix LPS. We thus interpreted the basal interglacial palaeosol complex as an Eemian palaeosol complex, developed in slope deposits with predominant penultimate-glacial loess component, corresponding to the basal red palaeosol in the Collias LPS ~100 km further south (Bosq et al. 2020b). The declining OSL “age estimates” at the base appear to indicate an age reversal. However, in the simplified approach applied in the present study, a common dose rate was assumed for all samples, neglecting the stagnic conditions that clearly prevailed for some time at the base of the Baix LPS, and thus reducing the effective dose rate and increasing the “age estimates” accordingly. Assuming an increased water content (Fig. 4.50), the “age estimate” at the base would be in agreement with the expected stratigraphy. This issue needs to be addressed in more detail in future studies with more sophisticated OSL approaches. The apparent Eemian “age estimates” for the lower and central part of the 7 Btg horizon may be owed to reworking by short-distance slope-wash processes. The uppermost part of the 7 Btg horizon may have even developed in a younger deposit, possibly reworked and deposited during the late Early Glacial period (e.g. *Mélisey I*, with subsequent pedogenesis during *St Germain I*), as incorporation of soil peds eroded from the underlying horizon and re-sedimentation of insufficiently bleached material could lead to age overestimation. Possible reworking phases correlate most likely with the stadials *Mélisey I* and *Mélisey II* (MIS 5d, 5b; Hering, Rederstall (Guiter et al. 2003); *St Nicolas*, *Saint Haon* (Reille et al. 2000)) of the Early Glacial period (Beaulieu and Reille, 1984b; Guiot et al. 1993). The subsequent periods of landscape stability, reflected in the Baix LPS, again by soil formation, possibly correlate with the interstadials *St Germain I* and *St Germain II* (MIS 5c, 5a; Amersfoort–Brørup, *Odderade* (Guiter et al. 2003); *St Geneys 1*, *St Geneys 2* (Reille et al. 2000)) (Beaulieu and Reille, 1984b).

Thus, we assume that the basal Eemian palaeosol complex in the Baix LPS started to develop under conditions of dry, warm summers and wet, mild winters, leading to the 7 Bt1 and 8 Bt2 horizons. After a period of reworking (during *Mélisey I* and/or *Mélisey II*), soil formation continued into the middle and late Early Glacial period in the reworked material of the Eemian soil. Eemian Luvisol formation and subsequent truncation and/or reworking are well known from European LPSs (Antoine et al. 2001, 2009a, 2016; Günster et al. 2001; Haesaerts et al. 2016). However, Early Glacial palaeosol horizons in mid-latitude European LPSs generally reflect drier conditions compared to the Eemian conditions (*Mosbacher Humus zones*) (Antoine et al. 2001, 2016; Schirmer, 2016), whereas in Mediterranean LPSs, more humid

conditions seem to be reflected by polygenetic Eemian to Early Glacial palaeosol complexes (Günster et al. 2001; Ferraro, 2009; Wacha et al. 2011b). Within the Rhône Rift Valley, the Eemian palaeosol complex in the Baix LPS is in accordance with LPSs from the south (Bourdier, 1958; Bonifay, 1965; Bosq et al. 2020b). Especially the reworking of the Eemian soil material as observed in the Baix LPS, followed by another phase of in situ pedogenesis, forming the 7 Btg horizon, agrees well with the deposits at the top of the S1 unit identified at the Collias LPS, ca 100 km further south (Bwk developed in a reworked soil sediment with an OSL age of ca 83 ka) and with similar horizons reported from LPSs in the Durance Valley (Fig. 4.43) (Bonifay, 1965; Bosq et al. 2020b).

Other local archives near the Baix LPS and in the Rhône Rift Valley also reflect our derived Eemian and Early Glacial climate conditions (Fig. 4.43). Eemian pollen records display summer-drought-resistant sclerophyllous taxa, with *Ilex*, *Olea*, *Pistacia* and evergreen *Quercus* (Beaulieu and Reille, 1984a; Tzedakis, 2007) and, at higher altitudes, mixed oak forest with the presence of *Buxus* and *Taxus* (Reille et al. 2000). The following change in vegetation towards tundra or steppe (Reille and Beaulieu, 1990; Mologni et al. 2021) was associated with a change to colder, drier, more continental climatic conditions, whereas the temperate deciduous vegetation recorded in between suggests a milder climate with higher precipitation and possibly higher temperatures. The gradual climate deterioration of the late Eemian is also reflected by the erosion of intensely weathered (partly red) sediments and a change within the pollen and human occupation remains derived from archaeological sites along the Ardèche and Payre Rivers (Valladas et al. 2008; Rivals et al. 2009; Moncel et al. 2015) (Fig. 4.43).

4.4.2 Early Glacial to Lower Pleniglacial transition

The erosional discontinuity above the 7 Btg horizon reflects an unstable phase with slope-wash processes, during which material of the 7 Btg horizon was mixed with slope-wash loess, followed by a phase of loess accumulation. In a subsequent more stable phase, the lower interstadial palaeosol (represented by the 6 Bw3 horizon) developed. Loess accumulation again set in, while pedogenesis continued, as indicated by the gradual upper boundary of the lower interstadial palaeosol, which reflects the transition from predominating pedogenesis to predominating loess accumulation.

The OSL screening yielded “age estimates” of around 65–75 ka for the 6 BCK/Btg and 6 Bw3 horizons, suggesting the deposition took place during the transition from the late Early Glacial period (MIS 5a) to the Lower Pleniglacial (MIS 4). Thus, the erosion phase may correlate with Mélisey II (Guiter et al. 2003), whereas the subsequent more stable phase probably correlates with St Germain II (St Geneys 2 (Reille et al. 2000)) and/or Ognon I (Beaulieu and Reille, 1984b, 1989). The transition from the Early Glacial period to the Lower Pleniglacial in the Baix

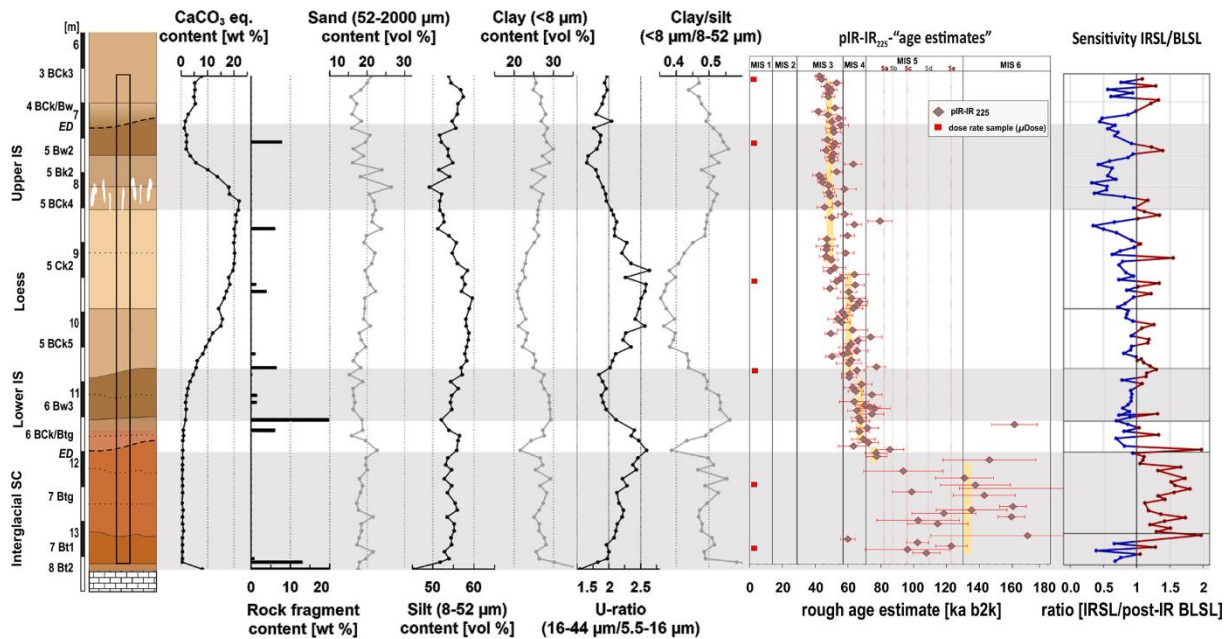


Figure 4.53: Synopsis of data for the lower 7 m of the Baix LPS, Rhône Rift Valley, SE France. From left to right: profile sketch (grey bars mark phases of soil formation); carbonate content (as CaCO_3 equivalent); rock-fragment content; contents of sand, silt and clay in the fine earth; U ratio; clay/silt ratio; "age estimates" based on the $\text{pIR}_{60}\text{IR}_{225}$ screening (solid lines denote the boundaries of marine isotope stages (MISs), dotted lines denote the peaks of the MIS 5 substages) and luminescence sensitivity (IRSL/pIR-BLSL) based on the $\text{pIR}_{125}\text{BLSL}_{125}$ protocol (SC, palaeosol complex; IS, interstadial palaeosol; ED, erosional discontinuity).

LPS is thus characterised by a marked climate deterioration. This agrees with central European LPSs, where unstable conditions are reflected by the Niedereschbach zone or Harmignies colluvial deposit (Antoine et al. 2016; Lehmkuhl et al. 2016). At the Collias LPS in the Rhône Rift Valley, this lower interstadial soil was not observed. However, intense slope-wash processes (Dmm horizon) during this period indicated unstable conditions at Collias as well (Bosq et al. 2020b). The pollen records of Les Échets and Velay (Beaulieu and Reille, 1984a, 1984b) also indicate a shift to cooler and drier conditions, including a warmer phase within the general trend of climatic deterioration.

4.4.3 The Lower Pleniglacial

The following enhanced loess accumulation (highest silt content and U ratio) and decreasing weathering intensities (lowest clay content and clay/silt ratio) reflect drier and colder conditions (Fig. 4.53). The coarse silt fraction is interpreted as having been transported in short-term, near-surface to low suspension clouds within a relatively limited distance (Tsoar and Pye, 1987; Vandenberghe, 2013; Újvári et al. 2016a). As it has been proven for other LPS sites along the Rhône Rift Valley (Bosq et al. 2018, 2020b), we also assume that the major part of the source of the loess deposits at the Baix LPS was the seasonally dried-out riverbed of the Rhône River during glacial times.

The only weakly weathered loess (5 Bck5 and 5 Ck2 horizons) reflects the predominance of loess accretion rates over soil formation rates during the Lower Pleniglacial at Baix, indicating generally dry and cold conditions. Also, the observed diverse forms and sizes of secondary carbonate accumulation (i.e. pseudomycelia, hard and soft carbonate nodules) and the upwardly increasing CaCO₃ contents suggest a weakening of carbonate leaching under increasingly drier conditions (Fig. 4.53). This phase of enhanced loess deposition coincides with increased loess accumulation in most of the European, including Mediterranean, LPSs (Antoine et al. 2001; Ferraro, 2009; Zerboni et al. 2015) and with high sedimentation rates at other sites in the Rhône Rift Valley (Tricart, 1952; Sierro et al. 2009; Bosq et al. 2020b). The associated cold and dry climate is also reflected in the decline of trees to semi-open boreal landscape with partly steppe vegetation in the valley (Beaulieu and Reille, 1989; Reille et al. 2000; Moncel et al. 2015).

4.4.4 The Middle Pleniglacial

The upper interstadial palaeosol in the Baix LPS is interpreted to represent a strongly truncated and partially reworked Calcic Cambisol, including the reworked 5 Bw2 horizon, underlain by the in situ 5 Bk2 and 5 Bck4 horizons. Its basal large carbonate nodules require a corresponding carbonate source, i.e. a thick decarbonated soil horizon above. Therefore, we assume that the most intensively weathered upper part of the Calcic Cambisol was eroded. A phase of increased loess accumulation followed. The deposits in which the horizons 5 Ck2, 5 Bck4, 5 Bk2, 5 Bw2, 4 Bck/Bw and 3 Bck3 developed accumulated during the end of MIS 4 and into MIS 3 (Figs. 4.51, 4.53). The uppermost subsamples analysed from the 3 Bck3 horizon may point to slightly younger “age estimates” (~40 ka), as would be expected for sediment deposits above an in situ palaeosol. Fine-tuned alterations of screening “age estimates” may be camouflaged by possible subsample-to-subsample variations in radionuclide concentrations and water contents, which both have an impact on effective dose rates and OSL “age estimates” but were not considered for the simplified approach of the OSL screening. Nevertheless, the OSL screening supports the hypothesis that the strongly truncated upper interstadial Calcic Cambisol represents Middle Pleniglacial palaeosol remains. The soil formation phase might correspond to the interstadial periods of Pile–Goulotte (Moershoofd) dated to 50–43 ka and/or Charbon (Hengelo) (38–37 ka) (Guiot et al. 1993; Guiter et al. 2003). The assumed soil formation intensity of the Calcic Cambisol remains, including the prominent carbonate nodules, suggests temperate conditions with at least one phase of intense carbonate dissolution and reprecipitation. Comparably intensely developed brown truncated soil horizons are found in most of the European and Mediterranean LPSs, e.g. Remagen soils, Gräselberg soils (Antoine et al. 2001; Schirmer, 2016; Fischer et al. 2021; Wacha et al. 2011b). In the Collias LPS in SE France, a very similar brown Bwk horizon with similar prominent carbonate nodules was identified. The likely period of this soil formation was

after ~55 ka and had ended by ~39 ka, as suggested by OSL dating (Bosq et al. 2020b). During our field surveys, we observed the prominent carbonate nodules not only at Baix and Collias but also in several other LPSs in the Rhône Rift Valley. Therefore, these large cone-shaped carbonate nodules that underlie truncated remains of a brown Calcic Cambisol may serve as a useful stratigraphic marker in LPSs along the Rhône Rift Valley. Another possibly comparable brown soil horizon, although without any age provided, was described for the LPS of the Durance Valley (Bonifay, 1965).

The local assumed temperate conditions are supported by the pollen of the MIS 3 interstadials, pointing to deciduous *Quercus* (at least from 39.405 ± 2250 BP), associated with *Abies* and *Carpinus* (Beaudouin et al. 2005). Thus, around ~40.000 BP, the vegetation in the wider region was mainly composed of broad-leaved temperate taxa, whereas at higher altitudes, the last regional presence of *Picea* was recorded (Reille and Beaulieu, 1990; Beaudouin et al. 2005). With respect to the local hydrology, malacological analyses of a palustrine level at the site of Mignet College in Aix-en-Provence, correlating also with the Pile–Goulotte (Moershoofd) interstadial, pointed to a marsh habitat, which may support assumed enhanced humidity in the region for this period (Magnin and Bonnet, 2014).

4.5 Conclusion

Our investigations of the lower ca 7 m of the Baix LPS in the Rhône Rift Valley confirm the importance of this archive for reconstructing regional Eemian to Middle Pleniglacial palaeoenvironmental changes. The obtained palaeoenvironmental reconstruction can be well correlated with other regional archives and can point out the different conditions compared to the central European LPSs. From bottom to top of the investigated part, we identified Eemian (MIS 5e) to Early Glacial (MIS 5d-a) soil formation, resulting in a polygenetic reddish Stagnic Luvisol; an Early Glacial (MIS 5a/4) to Lower Pleniglacial (MIS 4) brown horizon of a weakly developed Cambisol; a Lower to Middle Pleniglacial (MIS 4 to MIS 3) loess package showing subordinate syn-sedimentary pedogenesis; and, most prominently, a strongly truncated Middle Pleniglacial (MIS 3) Calcic Cambisol, underlain by characteristic large cone-shaped carbonate nodules. Thus, we can conclude that the generally characteristics of Baix in terms of the main soil formation and loess depositions phases coincide with central European LPSs, although their characteristics induced by climatic differences seem to reflect the transitional position of the LPSs.

However, we observed multiple reworkings and bioturbation, which are typical of the loess–palaeosol landscape of the Rhône Rift Valley and challenge numerical dating (Tricart, 1952; Bonifay 1965; Franc et al. 2017; Bosq et al. 2018, 2020b). We performed an optically stimulated luminescence (OSL) screening by applying a pIR₆₀-BLSL₁₂₅ and a pIR₆₀-IR₂₂₅ single-aliquot regeneration (SAR) protocol to minimally prepared polymineral coarse grains on 126

ca 1 cm³ subsamples collected at vertical intervals of ca 5 cm. Whereas the pIR-BLSL approach gave erroneously young “age estimates”, the pIR-IR technique seems to provide a realistic time corridor ranging from bottom to top from MIS 5 into MIS 3, thus corroborating the field hypotheses of the likely temporal positions of the different loess and palaeosol horizons. We also monitored OSL sensitivity changes in the minimally prepared coarse grains along the investigated part of the profile wall and found patterns which appear plausible when related to the likely evolution of the terrestrial archive, i.e. with respect to weathering and pedogenesis as well as material input by aeolian and/or slopewash processes. Finally, among the known LPSs along the Rhône Rift Valley, the Baix LPS provides the most detailed, dated palaeoenvironmental record of the Eemian to Middle Pleniglacial landscape evolution. These promising results encourage continuation of the palaeoenvironmental analysis of the Baix LPS.

Data availability

All data are provided in the figures and table, and they are available upon request.

Competing interests

At least one of the (co-)authors is a member of the editorial board of E&G Quaternary Science Journal. The peer-review process was guided by an independent editor, and the authors also have no other competing interests to declare.

Disclaimer

Publisher’s note: Copernicus Publications remains neutral with regard to jurisdictional claims made in the text, published maps, institutional affiliations, or any other geographical representation in this paper. While Copernicus Publications makes every effort to include appropriate place names, the final responsibility lies with the authors.

Acknowledgement

We are very grateful to Louis Garnier for allowing us to prepare and investigate the Baix LPS in his loam pit. We thank Barbara von der Lühe and Tianhao Wang for their help in the field and Marius Friedrich and Jutta Asmuth for the laboratory analyses. We also thank the European Union’s Horizon 2020 research and innovation programme under the Marie Skłodowska-Curie grant agreement no. 844457 (CREdit), who supported Sebastian Kreutzer during the writing phase of this paper. We thank the two anonymous reviewers for their very constructive comments and suggestions, supporting the improvement and finalisation of the manuscript.

Financial support

This open-access publication was funded by the University of Göttingen.

Review statement

This paper was edited by Jan-Hendrik May and reviewed by two anonymous referees.

Supplement

The supplement related to this article is also available online at: <https://doi.org/10.5194/egqsj-74-1-2024-supplement>.

S4.2 Methods – Luminescence screening

The luminescence screening aimed at a vertical sequence of roughly assessed OSL age estimates for the lower ca 7 m of the loess palaeosol sequence at the Baix section. The profiling encompassed two analytical steps: (1) rough assessment of the palaeodose of minimally prepared samples by applying the single aliquot regeneration (SAR) protocol (Murray and Wintle, 2000), and (2) determination of radionuclide concentrations for dose-rate assessment on a limited number of representative samples. While preparatory steps and palaeodose assessment were performed in the Heidelberg luminescence laboratory under strongly subdued indirect red light, radionuclide determination was performed in the Giessen luminescence laboratory. As the here applied luminescence screening provides only rough OSL age estimates, “age estimates” will be placed in quotation marks.

S4.2.1 A sequence of 1-cm³ subsamples

First, the sediment-soil blocks sampled in the flower boxes (hereinafter box samples) in the field were sub-sampled to obtain material not affected by daylight. We extracted small subsamples (1 cm x 1 cm x 1 cm) with a square frame for cutting out cubes (similar to those used for collecting 1 cm³-subsamples for pollen analyses from lake-sediment cores). We sampled along a vertical centre line of the sediment block at intervals of 5 cm (midpoint to midpoint; base area 1 cm x 1 cm; 4 cm distance from sample rim to sample rim), leaving 3.5 cm (midpoint 4 cm) distance from the possibly light-influenced rims at the top and bottom. We retrieved 8 subsamples (A–H) from each block (6 subsamples A–F from the lowermost box block, 1325–1357/1362 cm depth); in total 126 subsamples. The subsamples were weighed, dried at 50 °C and weighed again to determine the water content. We reserved material of some representative subsamples for radionuclide determination (cf. sect. S4.2.7).

Beneath each dose-rate sample, a second 1 cm³-cube sample was collected for luminescence analyses. Between the sampling of the first (upper, dose-rate sample) and the second 1 cm³-cube (lower, luminescence sample), the surface of the sediment-soil block was cleaned using a vacuum cleaner to prevent contamination with possibly light-influenced material from near the block-surface

S4.2.2 Preparation of polymineral coarse grains and aliquot preparation

The 1 cm³-luminescence samples were minimally prepared, omitting, e.g. the destruction of organic matter and carbonates. The preparation included: wet sieving (125 µm) with dest. H₂O retaining the coarse-grain fraction ≥125 µm. This fraction was dried and used for preparing small aliquots (a few 10² grains) of polymineral coarse grains, strewn on aluminium cups (ø ca 10 mm, 1 mm thick) through a hole mask (ø 4 mm) and fixed with silicon oil. The theoretical maximum grain size fitting in the pit of the “spoon” used for aliquot preparation is ca 1 mm. However, such large grain sizes were not part of the coarse-grain aliquots as (1) we did not prepare single-grain aliquots; (2) the smaller grains accumulating in the bottom pit of the sample tube were deliberately spooned out, and (3) larger grains were shaken off the sample carrier. Therefore, grains are ≤500 µm in diameter. Microscopic inspection of aliquots after the OSL measurements confirmed this assumption but revealed that the aliquots might have included particles <125 µm. We assume that due to the omission of sample treatment with acetic acid and hydrogen peroxide and due to using soft-screen fabric instead of metal sieves for the rapid preparation soil aggregates were not disaggregated completely prior to/during the sieving but only later when spooned out of the sample container for aliquot preparation. Yet it is reasonable to assume that the dominant OSL signal originates from the coarse-grain fraction.

S4.2.3 Measurement equipment for equivalent dose (D_e) determination

SAR measurements for equivalent dose (D_e) determination were performed on two luminescence readers, i.e. a Risø reader model TL/OSL DA20 (serial number 240, nicknamed “Athenaeum”) and a Risø reader model TL/OSL DA15, updated DA20 (serial number 83) (cf. Lapp et al. 2012, 2015). Both readers were equipped with a turntable with 48 sample positions, three clusters of infrared emitting diodes (7 LEDs each; 870 Δ 40 nm; plus longpass filter RG830 (Schott) for No. 83) for infrared stimulated luminescence (IRSL), four clusters of blue light-emitting diodes (7 LEDs each; 470 Δ 30 nm) for blue light stimulated luminescence (BLSL), a bialkali PMT EMI 9235QB15 for signal detection, a ⁹⁰Sr/⁹⁰Y β-source (No. 240: ca 5.0 Gy min⁻¹ at the time of measurements 2020–2021; No. 83: ca 3.6 Gy min⁻¹) for laboratory irradiation. The system was run with Risø MiniSys software version 4.08 (12.01.2016). Measurements were run with the Risø sequence editor v4.36 (2015-09-10). OSL measurements were performed in an N₂ atmosphere after an atmosphere stabilisation period of ca 4 min at the beginning of a SAR measurement.

S4.2.4 Adapting the single-aliquot regeneration (SAR) protocols

For the luminescence screening, palaeodose determination on the polymineral coarse grains was performed in a twofold manner, once with a blue-light stimulated luminescence (BLSL)

SAR protocol (Murray and Wintle, 2000), including IR-bleaching prior to the BLSL readout (pIR-BLSL), and once with a post-infrared (at 60 °C) infrared (at 225 °C) stimulation (pIR₆₀IR₂₂₅) protocol (Thomsen et al. 2008). For the BLSL measurements, 3 aliquots were analysed from each of the 126 subsamples (HDS-1802 A to HDS-1817 F). For the pIR₆₀IR₂₂₅ protocol, we limited the measurements to one aliquot per subsample, as the latter measurements lasted significantly longer.

The uppermost (HDS-1802) and the lowermost sample (HDS-1817) were used to adapt the measurement parameters of the SAR protocols. For data analysis and for D_e determination, we used the software “Analyst” (Duller, 2015 Version 4.31.9, Build 23rd May 2020; for details of the data analysis, cf. Table S4.15 and Table S4.16). Examples of pIR-BLSL and pIR₆₀IR₂₂₅ shine-down, as well as dose-response curves, are provided in sections S4.2.4.1.2 (Fig. S4.54), S4.2.4.1.3 (Fig. S4.56) and S4.2.4.2.3 (Figs. S4.58, S4.59).

S4.2.4.1 pIR-BLSL SAR protocol

For the pIR-BLSL SAR protocol, signal detection occurred in the ultra-violet spectrum around 340 nm through a set of glass filters U340 (Schott; 3 x 2.5 mm each) on luminescence reader No. 83. The IR- and BL-stimulation power was set to 90 %.

IR-stimulation at 125 °C which was performed to deplete a potential signal of feldspar, thus “enriching” the signal of quartz from the polymineral coarse-grains (cf. also Banerjee et al. 2001), and BL-stimulation at 125 °C were each performed for 40 s (250 data channels; 0.16 s per data channel) (cf. Table S4.15). Dose-response curves were fitted with a single exponential function. The D_e integral was set to (0–0.16 s) and the background integral to 32.16–40.0 s. The SAR protocol as adapted in a series of pre-tests (sect. S4.2.4.1.1 to S4.2.4.1.3) is shown in Fig. 4.47 of the main text.

Table S4.15: Parameters of data analysis for D_e determination – pIR-BLSL SAR protocol.

Software:	Luminescence Analyst, version 4.31.9 (Duller 2015)
Curve fitting:	Exponential fit
Integral [channel]:	1 - 1 (0 - 0.16 s)
Background [channel]:	201 - 250 (32.16 - 40.0 s)
Use recycled points for fitting:	Yes
Measurement error [%]	1.5
Incorporate error on curve fitting:	Yes
Use errors when applying criteria:	Yes
Recycling ratio limit [%]:	10
Maximum test dose error [%]:	10
Maximum recuperation [% of N]:	10
Tn signal > 3 sigma above background:	Yes

S4.2.4.1.1 D_{es} -range test

The potential range of D_{es} was investigated on unprocessed sediment material crumbled on aluminium cups (\varnothing ca 10 mm) and fixed with silicon oil. This was done with a pIR-BLSL SAR protocol using preheat 1 of 200 °C and preheat 2 of 160 °C and seven regeneration dose points (560 s, 980 s, 1400 s, 1820 s, 2240 s, 0 s, 1400 s) spanning the range ca 33.5–109 Gy and a normalisation dose (test dose) of 830 s (49.7 Gy). The dose-response curve conforms to an expected dose of ca 84 Gy representing 100 %, with regeneration dose points at 40 %, 70 %, 100 %, 130 %, 160 %, 0 % (testing signal recuperation) and 100 % (recycling dose point) of the expected dose. The range test was applied on 42 aliquots from the uppermost box sample (HDS-1802, subsamples A–H) and the lowermost box sample (HDS-1817, subsamples A–F), 3 aliquots per subsample. D_e determination occurred on the first data channel (0–0.16 s), with the last 50 data channels (32.16–40 s) used for late light subtraction. Criteria of acceptance were a 10 % recycling ratio, a maximum test dose error of 10 % and a maximum recuperation of 10 %. For this initial test, also D_{es} that had to be extrapolated beyond the largest regeneration dose point were accepted. The obtained D_{es} varied between 72–193 Gy (results not shown).

As fine grain material may coat coarser grains and aggregate as soil peds, for further measurements, the fraction <125 μm was eliminated by wet sieving, and the strategy changed from no sample preparation to minimal sample preparation (cf. sect. S4.2.2).

Further tests (not shown here) investigated whether the normalisation dose could be reduced to 350 s (ca 21 Gy), corresponding to 60 % to 25 % of the expected dose. As these tests proved positive, the lower normalisation dose was applied in further tests.

S4.2.4.1.2 Dose recovery uppermost sample (HDS-1802 A–H)

A dose-recovery test was performed on eight aliquots of the uppermost box sample HDS-1802, subsamples A–H, one aliquot each, bleached under the solar simulator for 3 h prior to irradiation. The administered laboratory dose was 1400 s (ca 84 Gy), and – like in the previous tests – the positions of the seven regeneration dose points were at 40 %, 70 %, 100 %, 130 %, 160 %, and 0 % of the laboratory dose (cf. Fig. S4.54) and the normalisation dose was 350 s (25 %) (henceforth the 1400 s growth curve). As a result, most aliquots met the expected D_e within error margins, and all aliquots were within a tolerance of 10 %. The expected dose was met within error margins by the mean (1345.3 ± 75.6 s), but the centre values (mean, central dose) underestimated the given dose slightly by 4–5 % (Fig. S4.55).

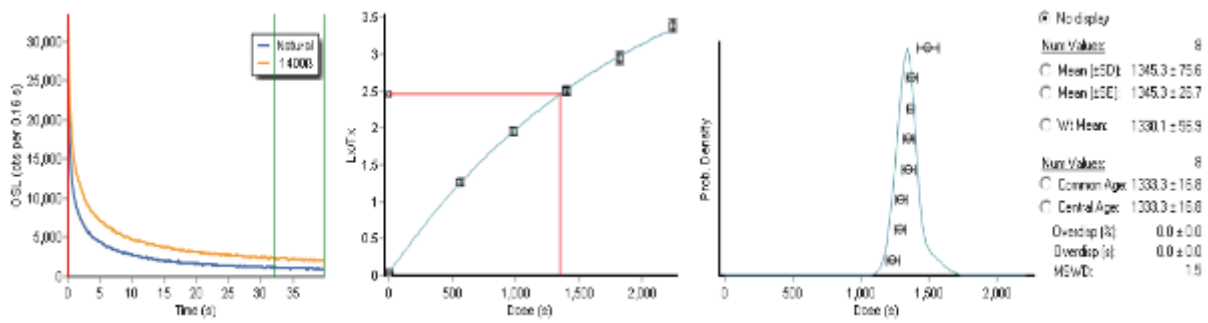


Figure S4.54: Dose recovery test on eight aliquots of box sample HDS-1802, subsamples A–H, one aliquot each. Example of shine down curves (left), SAR dose response curve (center) and probability density plot of recovered doses. The laboratory dose of ca 84 Gy (1400 s) was recovered within a tolerance of 10 %. Graphical output from “Analyst” (Duller, 2015).

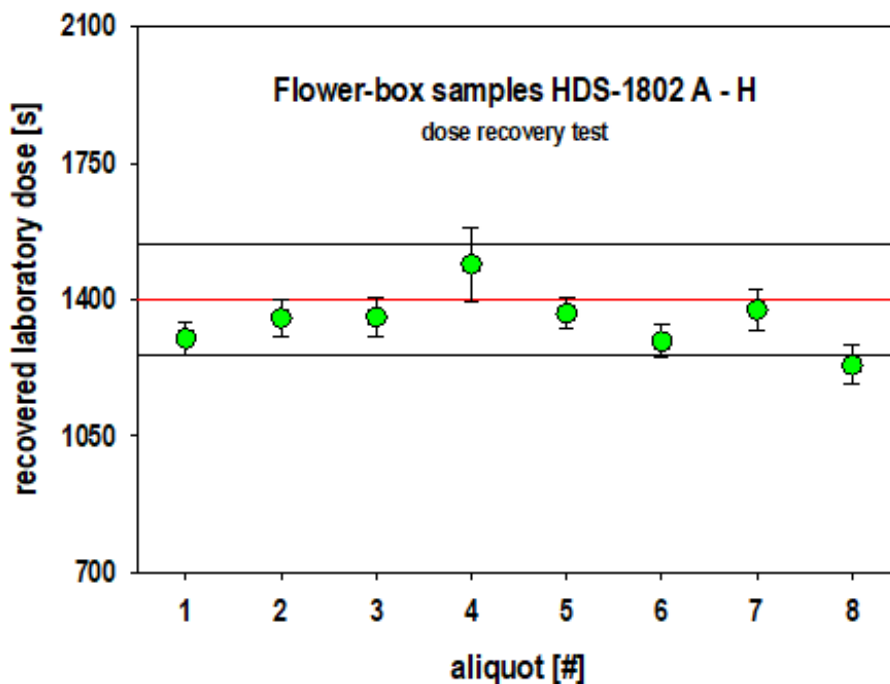


Figure S4.55: pIR-BLSL dose recovery test on eight aliquots of box sample HDS-1802, subsamples A–H, one aliquot each. The laboratory dose of ca 84 Gy (1400 s) was recovered within a tolerance of 10 %.

S4.2.4.1.3 Dose recovery tests lowermost sample (HDS-1817 A–F)

Another dose recovery test was performed on twelve aliquots of the lowermost box sample HDS-1817, subsamples A–F, two aliquots each. The laboratory dose was set to ca 191 Gy, and the seven regeneration dose points at 40 %, 60 %, 100 %, 130 %, 160 %, 0 % and 100 % of the expected dose were adjusted accordingly (1280 s, 2240 s, 3200 s, 4160 s, 5120 s, 0 s and 3200 s) (henceforth the 3200 s growth curve) (cf. Fig. S4.56). As for the dose recovery test with the 1400 s growth curve on sample HDS-1802, the normalisation dose was 350 s (for deposited doses in Gy cf. Fig. 4.46 of the main text). As a result, the centre value of the mean and central dose underestimated the expected dose slightly by ca 5 %. All recovered D_{es} were recovered within 10 % of the expected dose (Fig. S4.57).

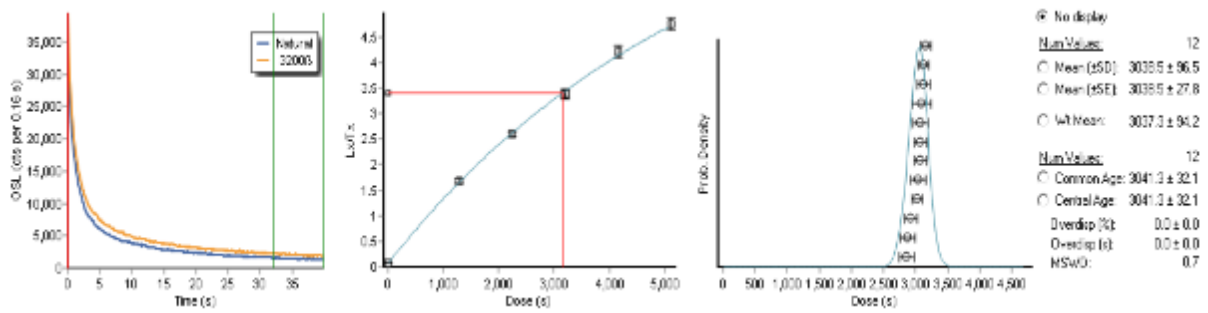


Figure S4.56: Dose recovery test on twelve aliquots of box sample HDS-1817 subsamples A–F, two aliquots each. Example of shine down curves (left), SAR dose-response curve (centre) and probability density plot of recovered doses. The laboratory dose of ca 191 Gy (3200 s) was recovered within a tolerance of 10 %. Graphical output from “Analyst” (Duller, 2015).

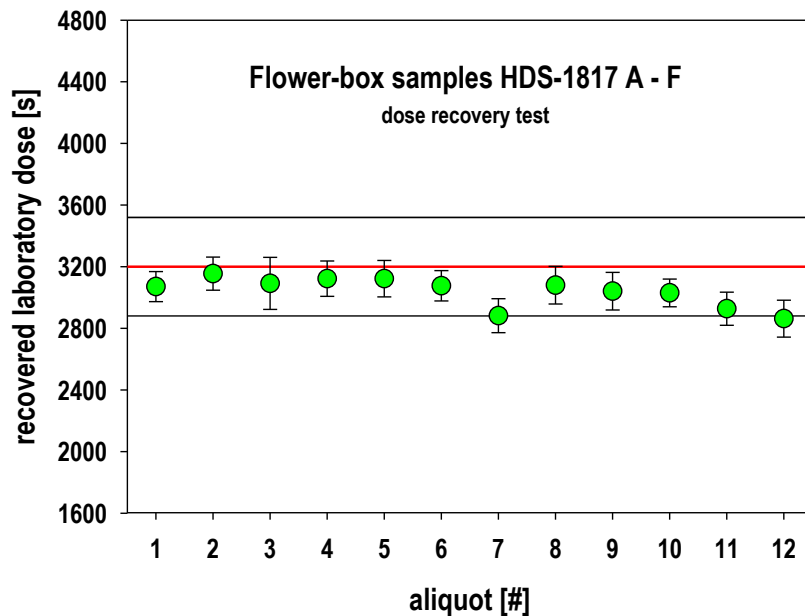


Figure S4.57: pIR-BLSL dose recovery test on twelve aliquots of box sample HDS-1817, subsamples A–F, two aliquots each. The laboratory dose of ca 191 Gy (3200 s) was recovered within a tolerance of 10 %.

We considered the results of both dose-recovery tests acceptable for the intended OSL screening. Therefore, the pIR-BLSL protocol was used for the “dating” measurements applying the 1400 s dose-response curve for samples HDS-1802 to HDS-1808 and the 3200 s dose-response curve for samples HDS-1809 to HDS-1817 (cf. Fig. 4.46 of the main text).

S4.2.4.2 pIR₆₀IR₂₂₅ measurements

The pIR₆₀IR₂₂₅ signal was detected in the blue-violet spectrum around 410 nm through an interference filter CH-30D410-44.3 (Chroma) on the luminescence reader “Athenaeum”. Only every second turntable position was used for SAR measurements to minimise unwanted optical cross-talk during IR stimulation (Kreutzer et al. 2013). The stimulation power was set to 90 %. IR-stimulation at 60 °C and subsequently at 225 °C was performed for 200 s (1 s per data channel) (cf. Table S4.16). For the data analysis, the first four seconds were used as D_e .

integral, while the integral 51–60 s was used for background subtraction (testing also other D_e -integral and background combinations, which all provided same results within error margins; cf. Tables S4.17–S4.19). The pIR-IR SAR protocol, as adapted in a series of pre-tests (sect. S4.2.4.2.1 to S4.2.4.2.3) is shown in Fig. 4.47 of the main text.

Table S4.16: Parameters of data analysis for D_e determination – pIR60IR225 SAR protocol.

Software:	Luminescence Analyst, version 4.31.9 (Duller 2015)
Curve fitting:	Exponential fit
Integral [channel]:	1 - 4 (0 - 4 s)
Background [channel]:	51 - 60 (51 - 60 s)
Use recycled points for fitting:	Yes
Measurement error [%]:	1.5
Incorporate error on curve fitting:	Yes
Use errors when applying criteria:	Yes
Recycling ratio limit [%]:	10
Maximum test dose error [%]:	10
Maximum recuperation [% of N]:	10
Tn signal > 3 sigma above background:	Yes

S4.2.4.2.1 D_e -range test

A pIR₆₀IR₂₂₅-SAR-protocol was applied to 14 aliquots of the uppermost sample HDS-1802 (8 subsamples, A–H, one aliquot each) and the lowermost sample HDS-1817 (6 subsamples, A–F, one aliquot each) to get an idea of the possible D_e range of the box samples. The preliminary dose-response curve was constructed with regeneration dose points at ca 33.1 Gy, 57.8 Gy, 82.6 Gy, 107.4 Gy, 132.2 Gy, 0 Gy and 82.6 Gy. The normalisation dose (test dose) was set to 600 s (ca 49.6 Gy, or 60 % of the 100 % regeneration dose point). The measurement started after 4 min (120 s + 120 s) N-purge. IR-stimulation at 60 °C and subsequently at 225 °C was performed for 200 s (1 s per data channel). The first four seconds were used as D_e integral for the data analysis. The integral 51–60 s was used for background subtraction. For IR₂₂₅, three aliquots were not analysable, as the potential D_e value was too large to be met by the (extrapolated) SAR dose-response curve, the D_{es} of the remaining 11 aliquots had to be extrapolated beyond the largest regeneration dose point. D_{es} scattered between ca 2000 s to 8200 s (ca 165–678 Gy) (results not shown).

S4.2.4.2.2 Normalisation dose test

IR SAR and pIR-IR SAR measurements respond sensitively to the size of the normalisation dose (unpublished data in the Heidelberg luminescence laboratory; Colarossi et al. 2018). Therefore, eight aliquots of HDS-1802 A–H (one aliquot each) were subjected to a combined dose-recovery and normalisation dose test. Based on the D_e range test (cf. sect. S4.2.4.2.1) and keeping the spreading of the regeneration dose points at 40 %, 70 %, 100 %, 130 %, 160 %, 0 % and 100 % of the expected dose, the regeneration dose points were set at 1560 s,

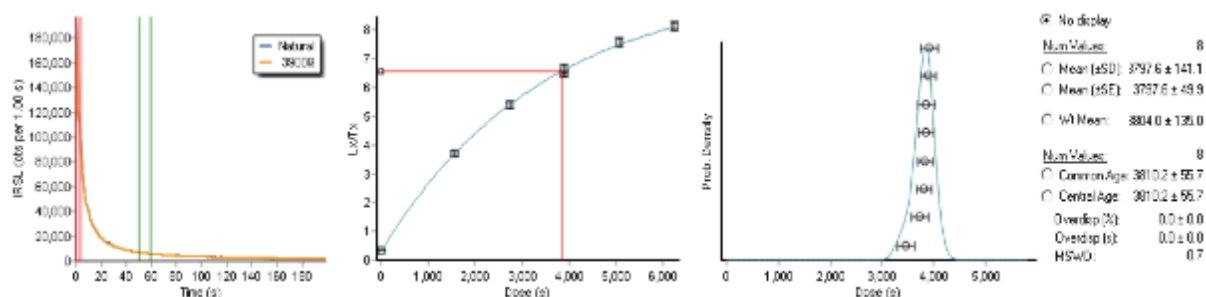
2730 s, 3900 s, 5070 s, 6240 s, 0 s and 3900 s with 3900 s corresponding to 321.3 Gy and 6240 s corresponding to 514.2 Gy (3900 s dose-response curve). We tested which size of the normalisation dose would be appropriate for the given dose-response curve, testing 98 s, 195 s, 293 s, 390 s, 780 s, 1170 s, 1560 s, 1950 s, corresponding to 2.5 %, 5 %, 7.5 %, 10 %, 20 %, 30 %, 40 % and 50 % of the expected dose. Using again the integral 51–60 s for late light subtraction, the D_e determination shows within error margins the same results for different lengths of the D_e integral varying from one to four seconds (Table S4.17). Whereas the smallest two normalisation doses of 2.5 % and 5 % of the expected dose appear to overestimate the given dose (more strongly curved dose-response curve), the largest five normalisation doses seem to underestimate the laboratory dose slightly. Therefore, we chose 293 s (ca 24.1 Gy; 7.5 % of the expected dose) as normalisation for further tests and measurements.

Table S4.17: Results of the normalisation dose test for late light subtraction 51–60 s and four different D_e integrals.

normalisation dose	0 - 1 s		0 - 2 s		0 - 3 s		0 - 4 s	
[% of expected dose]	DE [s]		DE [s]		DE [s]		DE [s]	
2.5	4321.87	± 311.31	4308.89	± 292.71	4338.25	± 288.70	4328.72	± 294.48
5	4431.09	± 270.47	N.A.		4408.31	± 249.13	4425.11	± 247.50
7.5	3975.52	± 164.97	3992.28	± 163.79	3991.09	± 162.31	3993.61	± 161.83
10	3684.01	± 194.39	3730.01	± 177.66	3705.55	± 170.96	3696.81	± 172.75
20	3775.38	± 137.88	3799.88	± 132.67	3782.96	± 127.59	3749.76	± 125.23
30	3864.34	± 139.05	3852.31	± 128.61	3855.32	± 127.51	3860.00	± 127.49
40	3296.93	± 135.32	3365.37	± 131.58	3315.31	± 127.13	3315.33	± 126.48
50	3841.49	± 136.91	3813.95	± 128.56	3815.51	± 129.27	3795.68	± 126.49

S4.2.4.2.3 Dose-recovery tests (HDS-1802 A–H)

A dose-recovery test with an administered dose of 3900 s and a normalisation dose of 293 s was performed on the eight previously measured aliquots of HDS-1802 A–H (one aliquot each). D_e analysis occurred with a late light subtraction of the integral 51–60 s. As a result, the expected dose is recovered well (cf. Fig. S4.58, Table S4.18). The mean recuperation is 4.9 % for the D_e integral 0–4 s and 4.8 % for the integral 0–1 s.



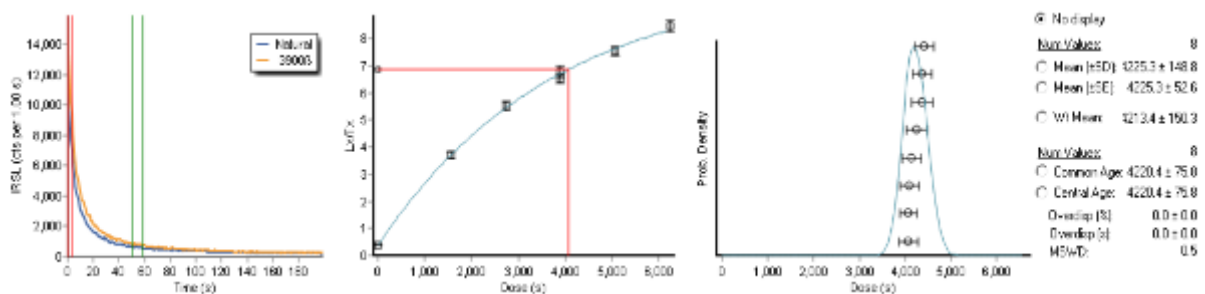
D_e integral 0–4 s

Figure S4.58: Dose recovery test on the eight aliquots already used in the previous normalisation dose test with a normalisation dose of 293 s (7.5 % of expected dose). Graphical output from “Analyst” (Duller, 2015).

Table S4.18: Dose recovery test on the eight aliquots already used in the previous normalisation dose test with a normalisation dose of 293 s (7.5 % of expected dose).

aliquot	0 - 1 s		0 - 2 s		0 - 3 s		0 - 4 s	
[turntable position]	DE [s]		DE [s]		DE [s]		DE [s]	
1	3900.96	± 172.35	3858.07	± 163.51	3862.69	± 163.67	3849.25	± 162.86
3	3816.54	± 156.18	3811.22	± 152.53	3846.35	± 154.64	3846.49	± 153.94
5	3881.11	± 146.21	3886.13	± 142.19	3901.84	± 142.58	3899.61	± 142.97
7	3790.21	± 217.63	3860.51	± 192.39	3761.31	± 177.68	3741.60	± 169.23
9	3825.75	± 167.62	3792.26	± 152.46	3816.67	± 151.13	3823.42	± 149.78
11	3988.69	± 170.88	3942.14	± 158.66	3840.26	± 150.13	3836.75	± 149.18
13	3785.95	± 211.60	3582.07	± 177.33	3489.28	± 166.45	3472.45	± 166.63
15	3992.57	± 205.95	3852.80	± 176.19	3880.96	± 171.56	3911.10	± 172.09

In a further dose-recovery test with a given dose of 3900 s and a normalisation dose of 239 s, eight aliquots of HDS-1802 A–H (one aliquot each) were analysed, which had been bleached for 3 h under the solar simulator (Fig. S4.59). The results show that the expected dose was overestimated by ca 8 % (here: D_e integral 0–1 s, late light 51–60 s; mean with standard deviation and standard error $4225.3 \pm 148.8 \pm 52.6$ s; central dose 4220.4 ± 75.8 s). Yet all recovered D_e values were reproduced within a range of 10 % of the expected value (Fig. S4.60). No dependency was observed on the D_e integral and/or the integral used for late light subtraction (Table S4.19). Like the dose recovery test on the previously measured aliquots, the mean recuperation was ca 5 % (here D_e integral 0–4 s, late light subtraction 51–60 s).



D_e integral 0–4 s, late light integral 51–60 s

Figure S4.59: Results of the dose recovery test on eight fresh aliquots bleached under the solar simulator with a normalisation dose of 293 s (7.5 % of expected dose). Graphical output from “Analyst” (Duller, 2015).

Table S4.19: Results of the dose recovery test on eight fresh aliquots bleached under the solar simulator with a normalisation dose of 293 s (7.5 % of expected dose).

late light	51 - 60 s		51 - 60 s		51 - 60 s		51 - 60 s		5 - 6 s	
aliquot	0 - 1 s		0 - 2 s		0 - 3 s		0 - 4 s		0 - 1 s	
[turntable position]	De [s]		De [s]		De [s]		De [s]		De [s]	
1	4555.36	± 264.61	4289.56	± 216.80	4335.93	± 212.05	4379.03	± 207.60	4684.07	± 383.98
3	4399.35	± 226.94	4429.46	± 222.55	4441.49	± 225.83	4415.74	± 223.90	4409.43	± 249.60
5	4085.18	± 268.00	3935.28	± 225.06	4025.33	± 215.23	4066.29	± 214.89	4198.90	± 450.01
7	4424.18	± 298.52	4395.39	± 254.14	4259.88	± 226.22	4372.11	± 231.07	5150.97	± 613.59
9	4205.14	± 259.28	4090.86	± 222.31	4043.40	± 212.95	4091.24	± 215.13	4214.32	± 346.01
11	4614.07	± 366.87	4461.79	± 304.13	4354.10	± 267.77	4256.15	± 245.28	4434.31	± 527.35
13	3963.13	± 202.50	3989.48	± 184.38	4077.71	± 185.10	4071.44	± 180.86	3930.60	± 261.32
15	4167.14	± 266.13	4192.96	± 229.95	4165.17	± 219.48	4150.44	± 211.97	4064.28	± 368.20

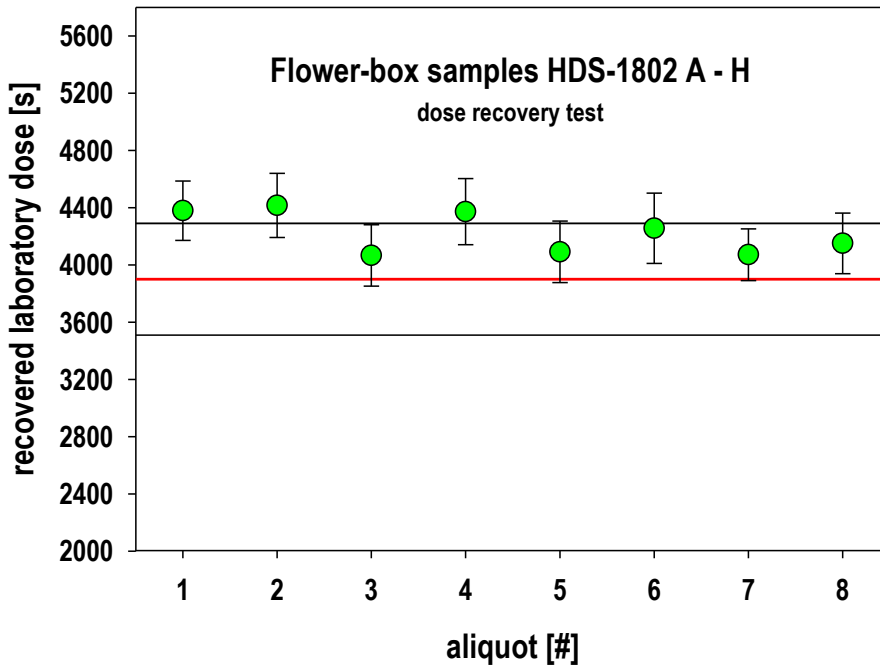


Figure S4.60: $pIR_{60}IR_{225}$ dose recovery test on eight aliquots of box sample HDS-1802, subsamples A–H, one aliquot each. The laboratory dose of ca 321.3 Gy (3900 s) was recovered within a tolerance of 10 %.

As the results appeared acceptable for the intended OSL screening (rather than proper OSL dating) and as sample material was scarce, no further tests potentially improving the $pIR_{60}IR_{225}$ SAR protocol were performed. We used one dose-response curve suitable for interpolating all, or at least most, of the expected palaeodoses. Due to the measurement time, only one aliquot per subsample was analysed. Figure 4.47 of the main text gives a schematic overview of the $pIR_{60}IR_{225}$ SAR protocol applied for the palaeodose assessments.

S4.2.5 Testing for anomalous signal fading

In luminescence dating, feldspar is known for a phenomenon termed athermal signal fading (Wintle, 1973), i.e. an unwanted signal loss. Therefore, fading tests are usually associated with luminescence dating measurements of feldspar (e.g. Auclair et al. 2003). Here we tested the 8 aliquots of the 8 subsamples of sample HDS-1803 and the 6 aliquots of the 6 subsamples of

sample HDS-1817 for the pIR₆₀IR₂₂₅ protocol. The signal readout was performed two times promptly, after ca 1 day, 2 days, 4 days, and promptly again.

As IR-bleaching in the pIR-BLSL protocol reduces the signal detected from feldspar but does not exclude signal from feldspar during the subsequent BLSL step completely, few aliquots measured with the pIR-BLSL aliquot were also subjected to a fading test: the 6 aliquots of subsamples F and G of sample HDS-1802 as well as 6 aliquots of sample HDS-1817, subsamples A and C (2 aliquots each), and B and D (1 aliquot each). A signal readout on HDS-1802 was two times prompt, after ca 4 h, 1 day, 2 days and prompt again; on HDS-1817, readout occurred two times prompt, after ca 1 day, 2 days, 4 days, and prompt.

Data analysis and *g*-value determination were performed with the function `analyse_FadingMeasurements` (Kreutzer and Burow, 2020) from the R package 'Luminescence' (Kreutzer et al. 2012b). Results of the fading measurements are provided in S4.3 "Results – Luminescence screening").

S4.2.6 Converting beta-irradiation time to deposited energy

Beta irradiation must be converted to deposited energy in the analysed mineral grains, which is accomplished using a calibrated beta source. The amount of deposited energy per unit time is known (e.g. Gy per min or s irradiation time). The luminescence readers used in this study had been calibrated using a grain-size fraction of 90–125 µm (corresponding to a grain-size fraction ca 130–165 µm before HF-etching). However, the ca 1 cm³ samples were too small for rigorous sieving for technical reasons. Therefore, only the lower boundary of the grain-size fraction was well defined (cf. sect. S4.2.2), while the upper boundary was estimated at 500 µm at maximum. However, the amount of energy deposited in mineral grains by beta irradiation in luminescence readers does not change significantly for grain size diameters varying in the range ca 100–500 µm (Armitage and Bailey, 2005; Mauz et al. 2021). Potential errors in the beta-source calibration of few percentages due to slightly differing grain sizes in the here analysed grain-size spectrum is a minor issue when compared to other challenges associated with gamma to beta transfer calibration (Kadereit and Kreutzer, 2013; Tribolo et al. 2019; Richter et al. 2020).

S4.2.7 Dose rate determination

From the 1 cm³-cubes used for water-content determination, six samples were selected for radionuclide determination (Table S4.20). The samples originate from: (1) the top of the sampled sediment-soil column (BCk3; 575/590–700 cm); (2) the upper interstadial soil (5 Bw2: 745–775 cm); (3) the loess deposit beneath (5 Ck2: 915– 995 cm); (4) the lower interstadial soil (6 Bw3: 1080–1155 cm); (5, 6) and the possibly reworked palaeosol remains of the interglacial soil-complex (7 Btg: 1227–1275 cm; 7 Bt1: 1315–1360 cm). The selected

subsamples were regarded as adequate for deriving a “representative” mean dose rate to be used for OSL “age estimate” assessments.

Table S4.20: Six subsamples (>3 g dry wt) of the box samples HDS-1802 to HDS-1817 were selected for dose-rate determination with the μ Dose system.

Flower-Box [Lab.-code]	Subsample [A - H]	Depth b.g.l. [cm]	Weight dry mass [g]	Soil horizon [after FAO 2014/2015]	Comment
HDS-1802	C	672.5		3.95 (11) 575/590 - 700 cm: 3 Bck3	representing "everything" above MIS 3 soil
HDS-1803					
HDS-1804	B	764.5		5.80 (13) 745 - 775 cm: 5 Bw2	MIS 3 soil (?)
HDS-1805					
HDS-1806					
HDS-1807					
HDS-1808	E	963.5		4.15 (18) 915 - 995 cm: 5 Ck2	with brown sediment infillings in former root channels
HDS-1809					
HDS-1810					
HDS-1811	F	1091.5		5.65 (20) 1080 - 1120 cm: 6 Bw3	with soft Mn concretions
HDS-1812					
HDS-1813					
HDS-1814					
HDS-1815	E	1256.5		4.85 (26) 1227 - 1275 cm: 7 Btg	hydromorphic features and bleached root channels
HDS-1816					
HDS-1817	E	1349.5		3.65 (28) 1315 - 1360 cm: 7 Bt1	reworked Eem Bt (?)

As the samples were relatively small, weighing ca 2.05–6.95 g each (dry wt), the recently developed μ Dose-system (Tudyka et al. 2018, 2020) was regarded as especially suitable for dose-rate determination within the here performed luminescence screening at the Baix site. The selection of representative samples from different B and C horizons occurred among those that had provided at least 3 g of dry matter. A comprehensive performance test of the novel device for dose-rate determination has recently been conducted by Kolb et al. (2022), which showed that the μ Dose-analytics delivers mostly equally correct results as established techniques such as, e.g. low-level gamma-ray spectrometry. μ Dose measurements were performed in the Giessen luminescence laboratory, where the samples were dried at 105 °C before 3 g of each sample were placed and sealed in the μ Dose sample holders.

S4.2.8 “Age estimate” calculations

OSL scanning “age estimates” were calculated not for mean burial doses of a set of aliquots but for individual aliquots. In contrast, a mean value was assumed for the dose rate based on the six representative dose rate samples. Assuming radioactive equilibrium, radionuclide concentrations were transformed to dose rate values by applying the dose-rate conversion factors of Guérin et al. (2011). The cosmic dose rate was calculated with the R package ‘Luminescence’ (Kreutzer et al. 2012b) but contributed only between 0.1044 ± 0.0104 Gy ka⁻¹ (uppermost sample at 6.72 m depth) and 0.0586 ± 0.0059 Gy ka⁻¹ (lowermost sample at 13.49 m depth). For the mineral grains responding to IR stimulation by emitting a luminescence signal around 410 nm (likely potassium feldspar), an internal potassium content of 12.5 ± 1.25 wt % was assumed. Considering the efficiency of the external alpha radiation (*a*-value) for the pIR-IR feldspar measurements at 225 °C an *a*-value of 0.1 ± 0.02 (cf. Kreutzer et al. 2014) and for

the mineral grains responding to BL-stimulation after IR-depletion (assumed to originate dominantly from quartz) an a -value of 0.035 ± 0.02 (cf. Lai et al. 2008) was taken into account, assuming that alpha particles penetrate 20 μm into the coarse grains and adapting the fine-grain a -values accordingly.

The water contents of the samples as measured (cf. Fig. S4.61) were not considered to be representative of the dating period. Therefore, we estimated a uniform water content (ratio of wet sample wt to dry wt) of $\Delta 1.17 \pm 0.05$, based on the considerations of Sauer et al. (2016), who calculated realistic water contents for pore volume distributions typical of loess. As also Bosq et al. (2020) had followed this recommendation for OSL dating at the Collias site ca 100 km further to the south, the procedure allows comparing the OSL dating results for the two sites. Only for the lowermost sample, a silt loam, in addition to a water content of $\Delta 1.28 \pm 0.05$ was assumed, thus simulating stagnant conditions.

S4.2.9 Luminescence sensitivity

Varying luminescence count rates (sensitivities) within a loess profile may proxy different source areas or source material (Fitzsimmons et al. 2022). We measured both the IR- and the post-IR BL-stimulated luminescence of the minimally prepared box subsamples (cf. sect. S2.4.1). We used the ratio of both signals as a down-the-profile-normalised proxy, as the luminescence yield may also depend on the amount of material on a sample carrier rather than the mere luminescence sensitivity of a material. It is assumed that the IRSL signal indicates the presence of feldspar, while the BLSL signal points to quartz (e.g. Banerjee et al. 2001). However, as the IR stimulation does not fully erase the OSL signal in feldspar, the post-IR BLSL signal is likely a composite of quartz and feldspar. The comparatively mild preheat procedure of 10 s duration at 200 °C, suitable for quartz measurements, might further cause the preservation of a feldspar signal. Nevertheless, possible variations in the signal ratio likely indicate different provenance or weathering conditions (cf. Fitzsimmons et al. 2022).

The signal ratios were determined using the function `Luminescence:calc_OSLLxTxRatio()` of the R package 'Luminescence', version 0.9.16 (Kreutzer et al. 2021), pretending that the IR-induced signal was the L_x/L_n -signal and the post-IR BLSL-induced signal was the T_x/T_n signal (therefore larger ratios would point to more feldspar emitting around 340 nm, in the simplified model here taken as a basis). IRSL and BLSL signals were gained from the test-dose-induced luminescence. First, the 8 test-dose signals of a

complete SAR measurement were averaged for each aliquot; then, the mean with standard error of the three aliquots measured of each subsample was calculated.

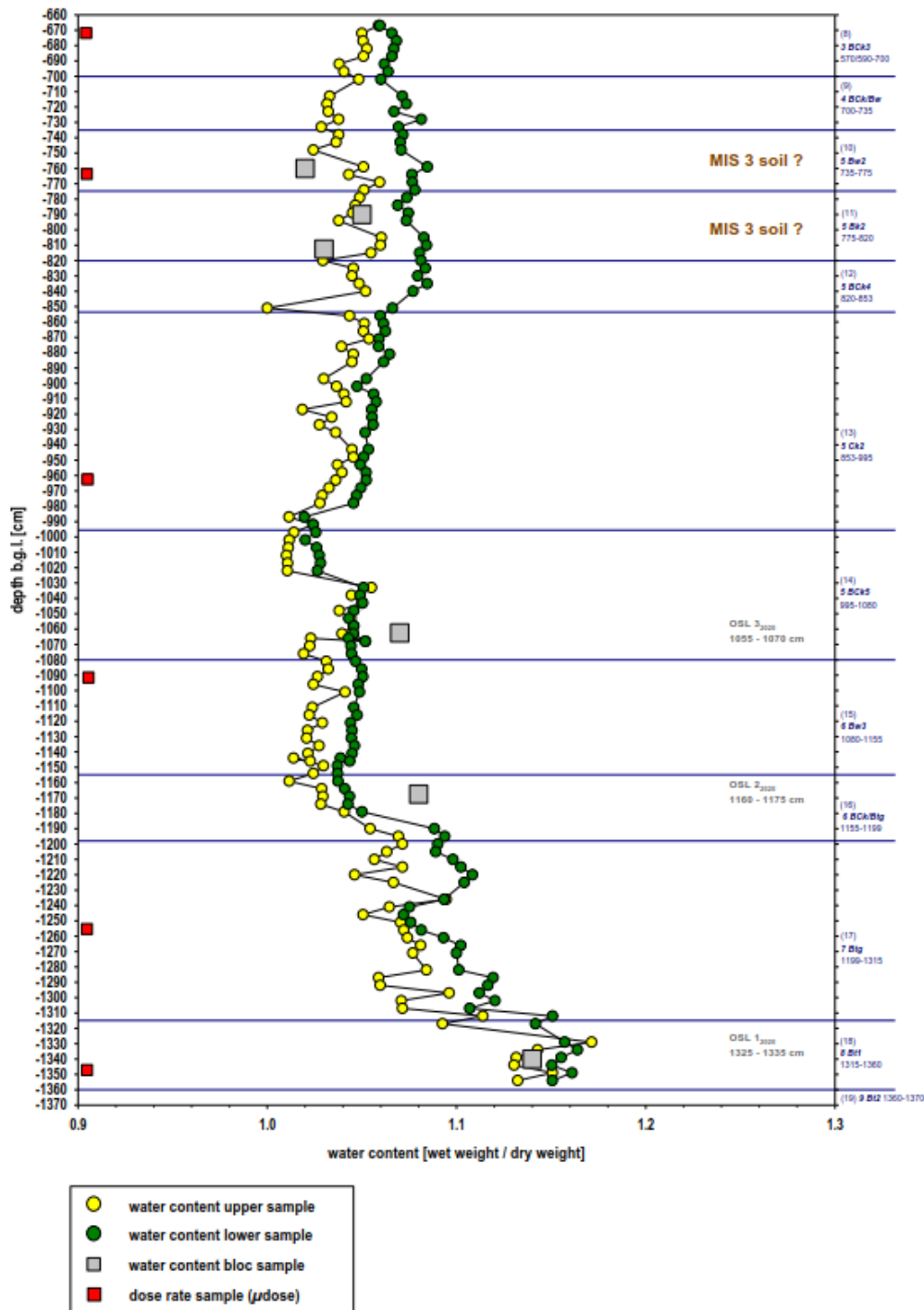


Figure S4.61: Results of the water content determination from the box subsamples. The lower samples (luminescence samples) are systematically slightly wetter than the upper samples (dose rate samples), likely due to water percolating in the downward direction into the horizontally stored sample blocks. Red squares denoting positions of dose rate samples used for μ Dose analyses. Grey squares illustrating water contents measured in additional block samples not further analysed in the present study. All data values within an error margin of ± 0.05 . Smallest values above 1178 cm b.g.l. (6 BCK/Btg to top; mean ca 1.04 upper samples; ca 1.06 lower samples). Largest values in lowermost 8 Bt1 (1315–1360 cm b.g.l.; ca 1.14 upper samples; ca 1.16 lower samples). Intermediate resp. increasing values from 7 Btg to 6 BCK/Btg (ca 1.07 upper samples; ca 1.10 lower samples)..

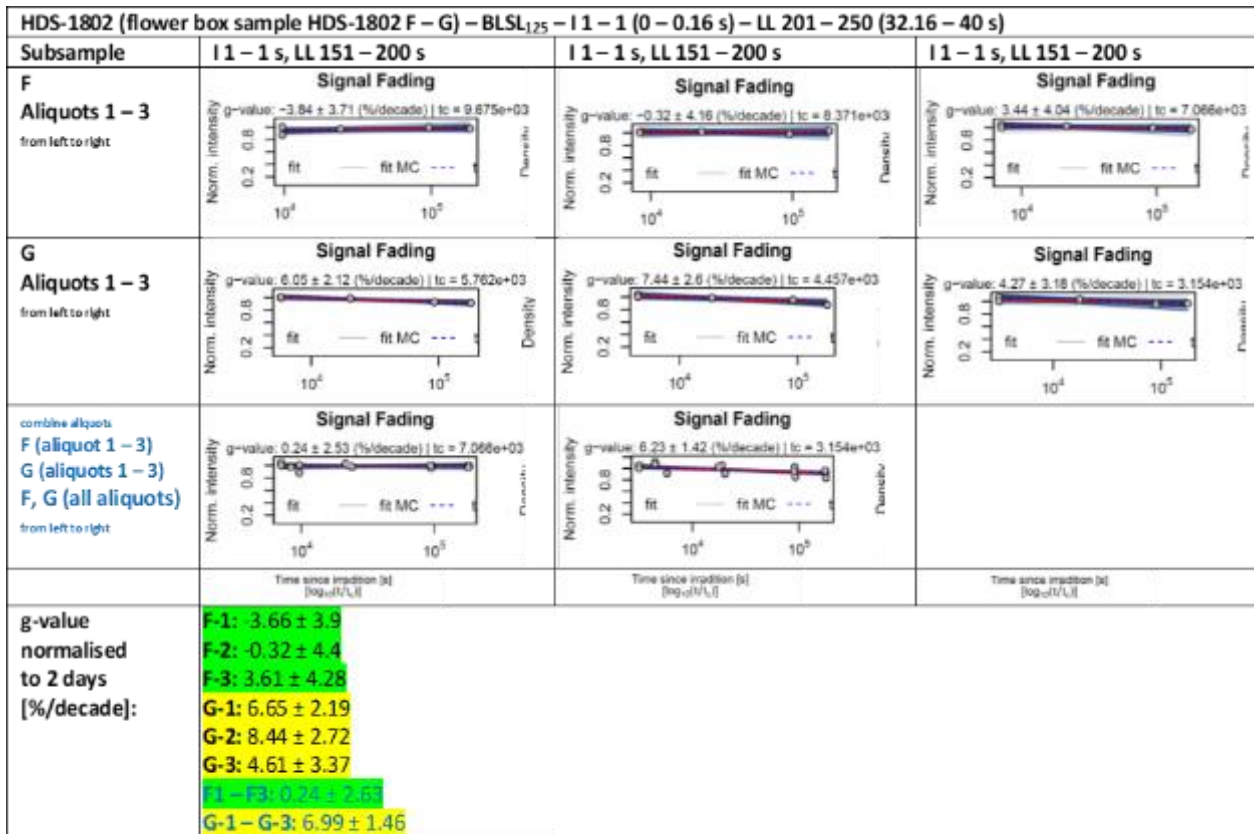
S4.3 Results – Luminescence screening

Table S4.21: Analytical dose rate data and effective dose rates for the pIR₁₂₅BLSL₁₂₅-protocol.

Lab.-No./subsample/depth/horizon	DL_kosm	Err_DL_kosm U	Err_U	Th	Err_Th	K	Err_K	Water_meas	Water_mod	Err_Water_mod	a_value.fine_grain	Err_a_value.fine_grain	K_grain_intern	Err_K_grain_intern	Grain_min	Grain_max	a_value	Err_a_value	DL_eff	Err_DL_eff	
HDS-1802_C_672.5 cm_3Bck3	0.1044	0.0104	2.600	0.320	11.831	1.043	1.534	0.049	1.065	1.17	0.05	0.035	0.02	0	0	125	212	0.0295	0.0168	2.9168	0.2167
HDS-1804_B_764.5 cm_5Bw2	0.0957	0.0096	2.384	0.310	13.746	1.126	1.452	0.048	1.075	1.17	0.05	0.035	0.02	0	0	125	212	0.0295	0.0168	2.9258	0.2252
HDS-1808_E_963.5 cm_5Ck2	0.0801	0.0080	1.596	0.240	11.585	0.820	1.310	0.045	1.050	1.17	0.05	0.035	0.02	0	0	125	212	0.0295	0.0168	2.4345	0.1776
HDS-1811_F_1091.5 cm_6Bw3	0.0719	0.0072	2.741	0.320	11.762	1.110	1.409	0.047	1.046	1.17	0.05	0.035	0.02	0	0	125	212	0.0295	0.0168	2.8093	0.2189
HDS-1815_E_1256.5 cm_7Btg	0.0629	0.0063	2.072	0.220	13.207	0.750	1.482	0.046	1.086	1.17	0.05	0.035	0.02	0	0	125	212	0.0295	0.0168	2.8006	0.2053
HDS-1817_E_1349.5 cm_7Bt1	0.0586	0.0059	2.858	0.330	12.018	1.213	1.480	0.049	1.157	1.17	0.05	0.035	0.02	0	0	125	212	0.0295	0.0168	2.9039	0.2269
HDS-1817_E_1349.5 cm_7Bt1 - wetter	0.0586	0.0059	2.858	0.330	12.018	1.213	1.480	0.049	1.157	1.28	0.05	0.035	0.02	0	0	125	212	0.0295	0.0168	2.6165	0.1984

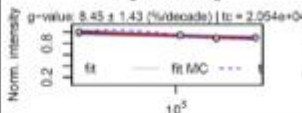
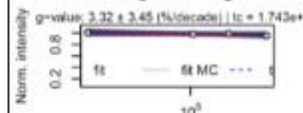
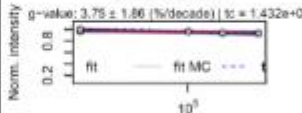
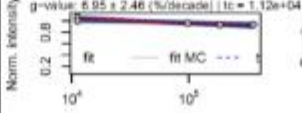
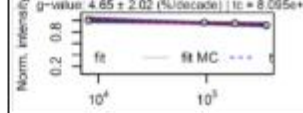
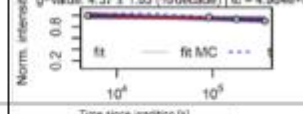
Table S4.22: Analytical dose rate data and effective dose rates for the pIR60IR225-protocol.

Lab.-No./subsample/depth/horizon	DL_kosm	Err_DL_kosm U	Err_U	Th	Err_Th	K	Err_K	Water_meas	Water_mod	Err_Water_mod	a_value.fine_grain	Err_a_value.fine_grain	K_grain_intern	Err_K_grain_intern	Grain_min	Grain_max	a_value	Err_a_value	DL_eff	Err_DL_eff	
HDS-1802_C_672.5 cm_3Bck3	0.1044	0.0104	2.600	0.320	11.831	1.043	1.534	0.049	1.065	1.17	0.05	0.1	0.02	12.5	1.25	125	212	0.0842	0.0168	4.1083	0.2307
HDS-1804_B_764.5 cm_5Bw2	0.0957	0.0096	2.384	0.310	13.746	1.126	1.452	0.048	1.075	1.17	0.05	0.1	0.02	12.5	1.25	125	212	0.0842	0.0168	4.1492	0.2396
HDS-1808_E_963.5 cm_5Ck2	0.0801	0.0080	1.596	0.240	11.585	0.820	1.310	0.045	1.050	1.17	0.05	0.1	0.02	12.5	1.25	125	212	0.0842	0.0168	3.5212	0.1882
HDS-1811_F_1091.5 cm_6Bw3	0.0719	0.0072	2.741	0.320	11.762	1.110	1.409	0.047	1.046	1.17	0.05	0.1	0.02	12.5	1.25	125	212	0.0842	0.0168	4.0126	0.2334
HDS-1815_E_1256.5 cm_7Btg	0.0629	0.0063	2.072	0.220	13.207	0.750	1.482	0.046	1.086	1.17	0.05	0.1	0.02	12.5	1.25	125	212	0.0842	0.0168	3.9786	0.2154
HDS-1817_E_1349.5 cm_7Bt1	0.0586	0.0059	2.858	0.330	12.018	1.213	1.480	0.049	1.157	1.17	0.05	0.1	0.02	12.5	1.25	125	212	0.0842	0.0168	4.1257	0.2424
HDS-1817_E_1349.5 cm_7Bt1 - wetter	0.0586	0.0059	2.858	0.330	12.018	1.213	1.480	0.049	1.157	1.28	0.05	0.1	0.02	12.5	1.25	125	212	0.0842	0.0168	3.7673	0.2111



HDS-1802 (flower box sample HDS-1802, subsample F (aliquot 1 – 3) and subsample G (aliquot 1 – 3) – BLSL₁₂₅ – including the three prompt readouts. Delays: „prompt“, ca. 4 hours, ca. 1 day, ca. 2 days, „prompt“.

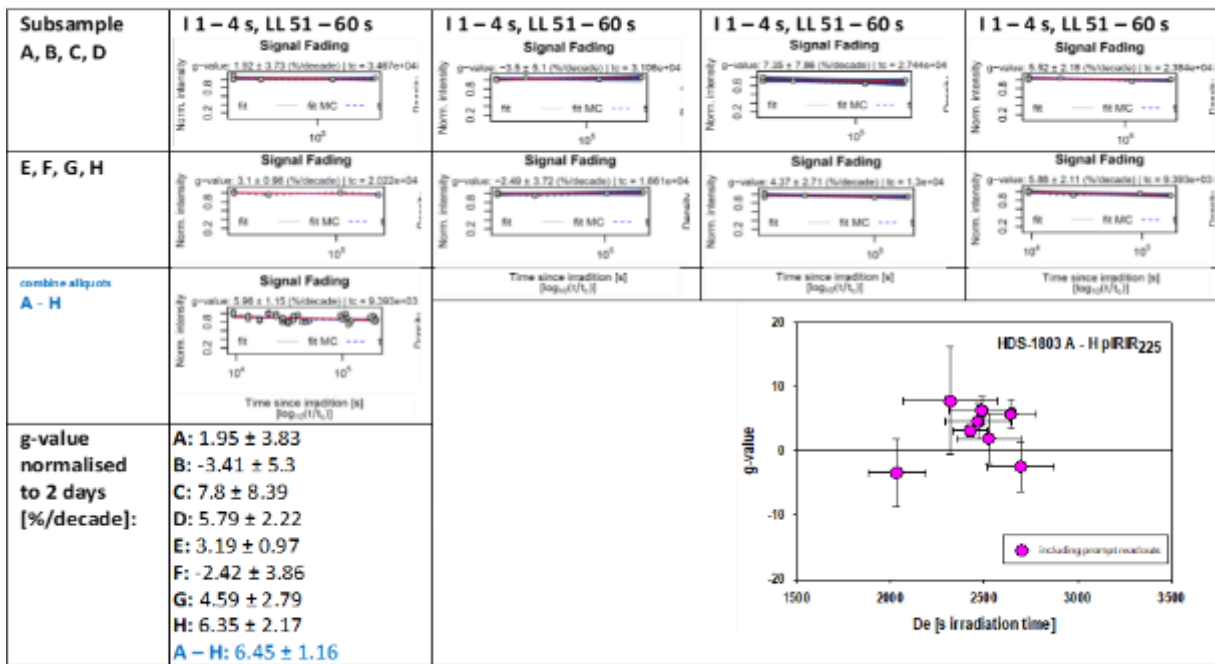
Figure S4.62: Results of the g-value determination: BLSL₁₂₅ signal, box sample HDS-1802, subsamples F–G. While the three aliquots of subsample HDS-1802 F show within error margins g-values around zero (no fading), the three aliquots of subsample HDS-1802 G show g-values around ca 7.

HDS-1817 (flower box sample HDS-1817 A, B, C, D) – BLSL ₁₂₅ – I 1 – 1 (0 – 0.16 s) – LL 201 – 250 (32.16 – 40 s)			
Subsample	I 1 – 1 s, LL 151 – 200 s	I 1 – 1 s, LL 151 – 200 s	I 1 – 1 s, LL 151 – 200 s
A Aliquots 1 [1], 3 [3] from left to right	Signal Fading g-value: 8.45 ± 1.43 (%/decade) $t_c = 2.054e+04$ 		Signal Fading g-value: 3.32 ± 3.45 (%/decade) $t_c = 1.743e+04$ 
B Aliquots 1 [4] from left to right	Signal Fading g-value: 3.75 ± 1.86 (%/decade) $t_c = 1.432e+04$ 		
C Aliquots 1 [7], 3 [9] from left to right	Signal Fading g-value: 6.95 ± 2.46 (%/decade) $t_c = 1.12e+04$ 		Signal Fading g-value: 4.65 ± 2.02 (%/decade) $t_c = 8.095e+03$ 
D Aliquots 3 [12] from left to right			Signal Fading g-value: 4.37 ± 1.83 (%/decade) $t_c = 4.984e+03$ 
g-value normalised to 2 days [%/decade]:	Time since irradiation [h] [log ₁₀ (t/t ₀)] A-1 [1]: 9.17 ± 1.44 A-3 [3]: 3.43 ± 3.57 B-1 [4]: 3.91 ± 1.9 C-1 [7]: 7.58 ± 2.53 C-3 [9]: 4.95 ± 2.07 D-3 [12]: 4.69 ± 1.88	Time since irradiation [h] [log ₁₀ (t/t ₀)]	Time since irradiation [h] [log ₁₀ (t/t ₀)]

HDS-1817 (flower box sample HDS-1817, subsample A (aliquot 1, 3), subsample B (aliquot 1, turntable position 4), subsample C (aliquot 1, 3, position 7, 9) and subsample D (aliquot 3, position 12) – BLSL₁₂₅ – including the three prompt readouts. Delays: „prompt“, ca. 1 day, ca. 2 days, ca. 4 days, „prompt“.

Figure S4.63: Results of the g-value determination: BLSL₁₂₅ signal, box sample HDS-1817, subsamples A, B, C, D. While one aliquot of subsample HDS-1817 A shows a g-value which within the comparably large error margin does not differ from zero, the other aliquots show g-values between ca 4 and 9.

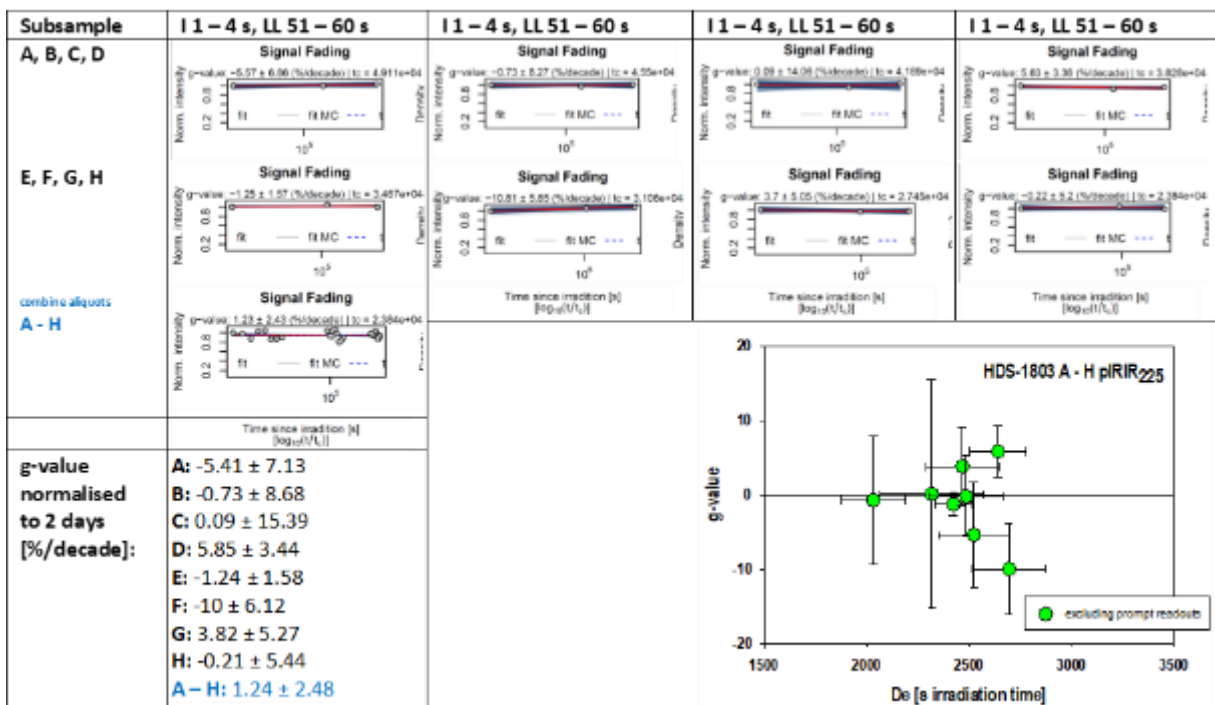
HDS-1803 (flower box sample HDS-1803 A - H) – IR₂₂₅ – including the three prompt readouts



HDS-1803 (flower box sample HDS-1803 A - H) – IR₂₂₅ – including the three prompt readouts

(a)

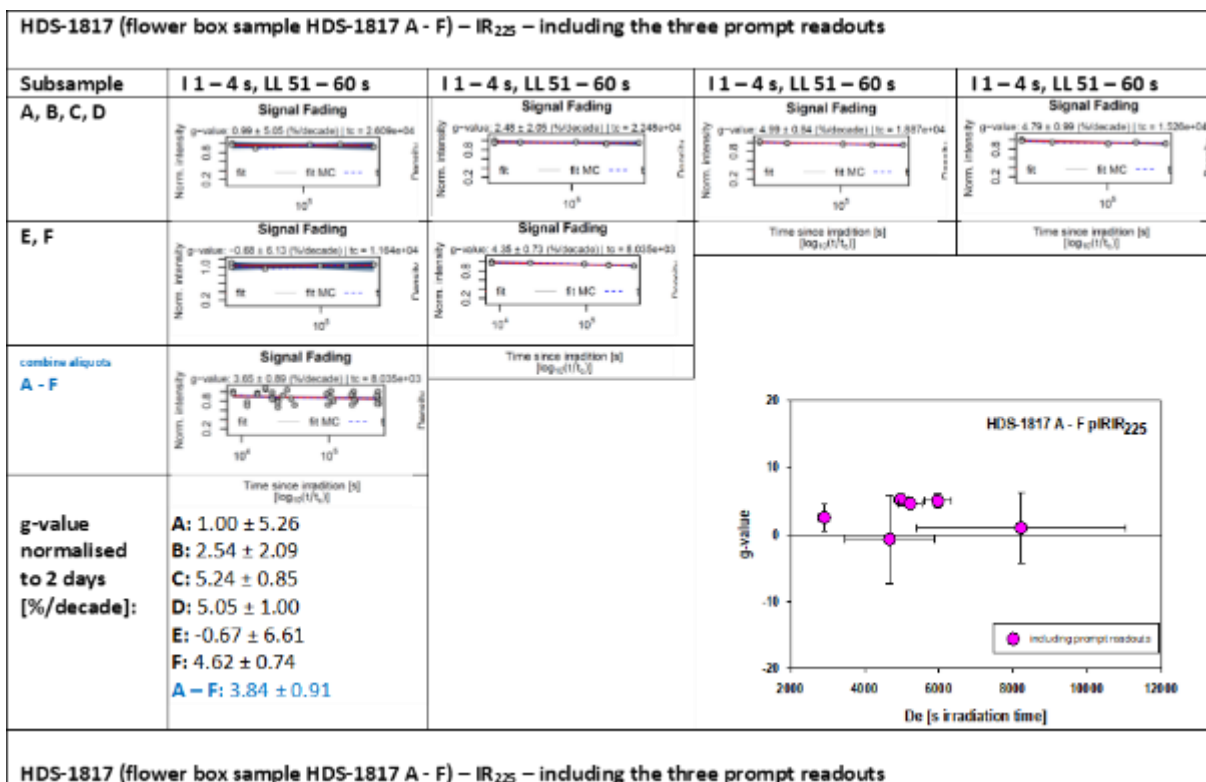
HDS-1803 (flower box sample HDS-1803 A - H) – IR₂₂₅ – excluding the three prompt readouts



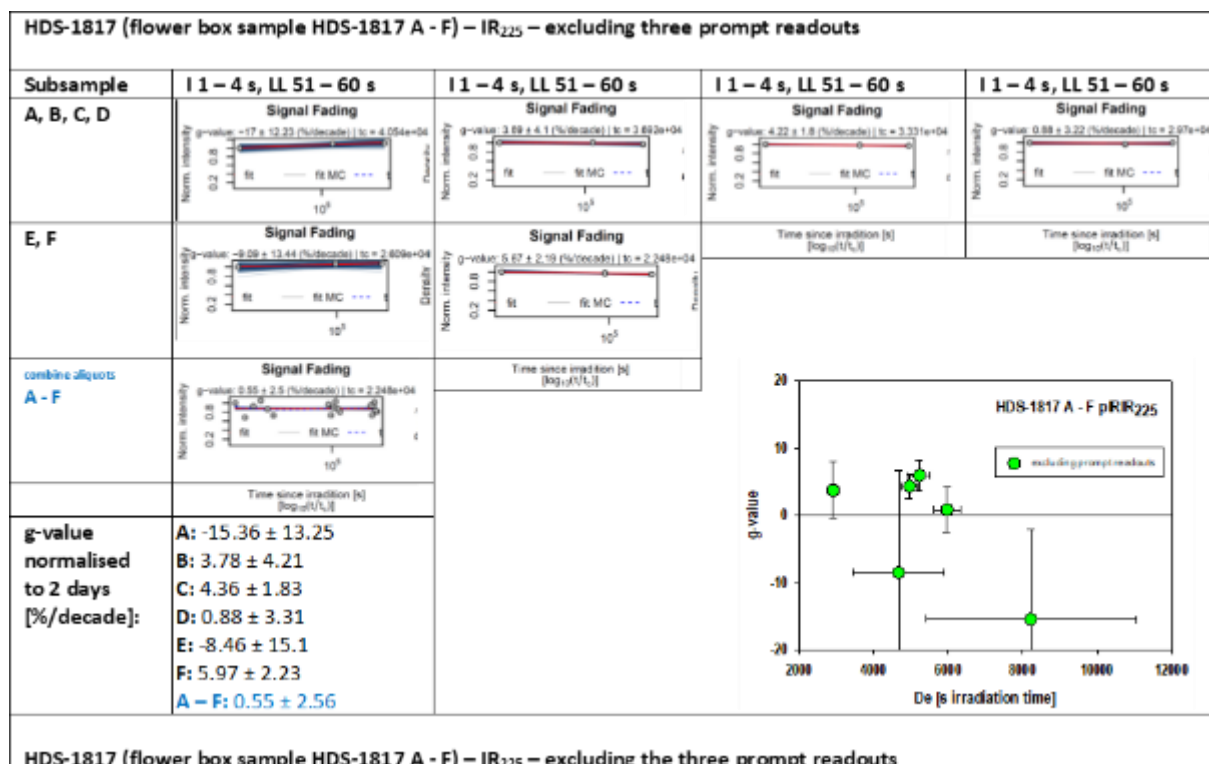
HDS-1803 (flower box sample HDS-1803 A - H) – IR₂₂₅ – excluding the three prompt readouts

(b)

Figure S4.64: Results of the g-value determination: IR₂₂₅ signal, box sample HDS-1803, subsamples A–H. (a) including the three prompt readouts, (b) excluding the three prompt readouts. Eliminating the prompt readouts leads to smaller g-values, mostly in agreement with zero-fading.



(a)



(b)

Figure S4.65: Results of the *g*-value determination: IR₂₂₅ signal, box sample HDS-1817, subsamples A–F. (a) including the three prompt readouts, (b) excluding the three prompt readouts. Eliminating the prompt readouts leads to smaller *g*-values, mostly in agreement with zero-fading.

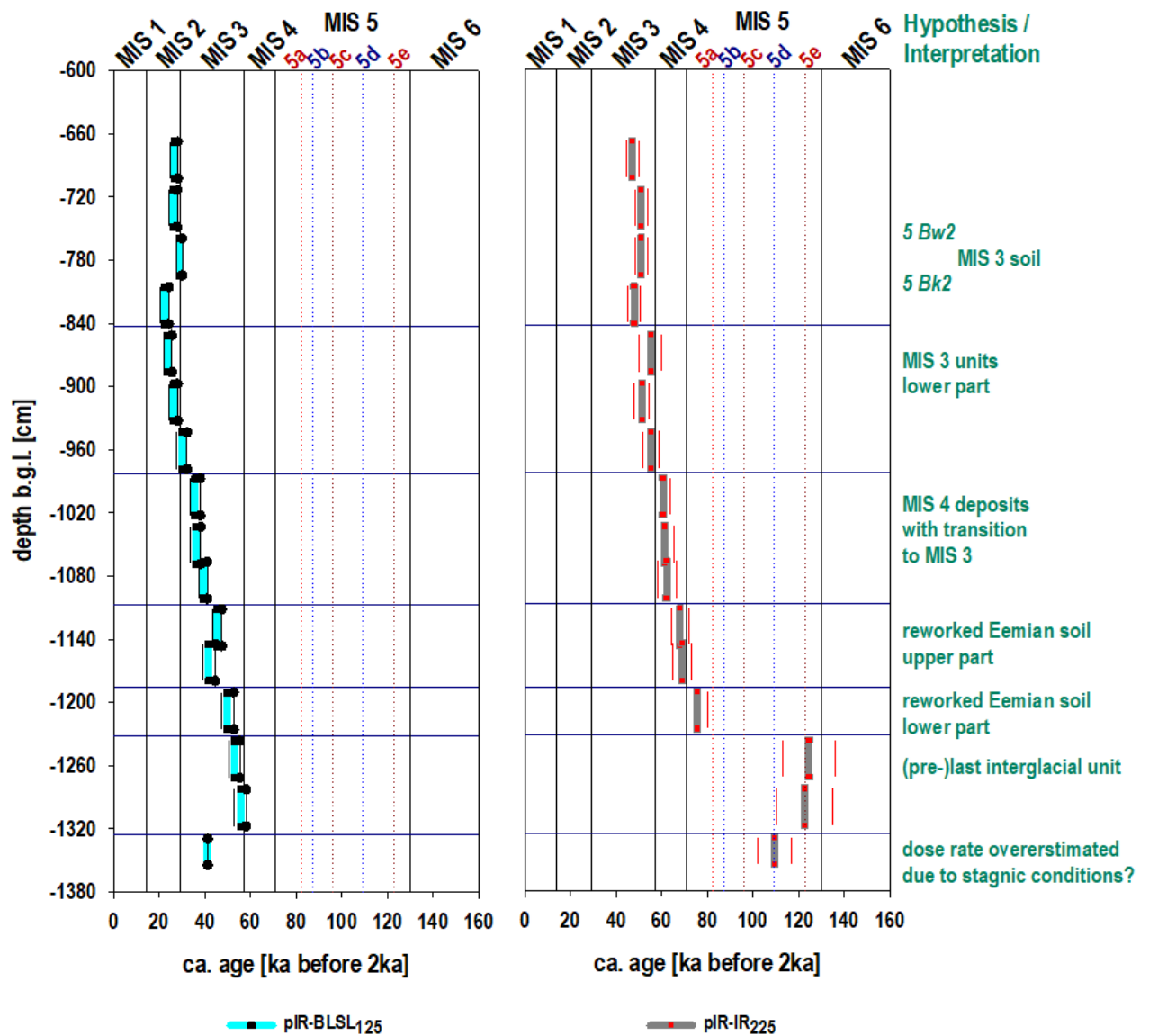


Figure S4.66: Results of the pIR-BLSL and pIR₆₀IR₂₂₅-screening summarised per box (HDS-1802 to HDS-1817, from top to bottom). Central “ages” (Galbraith et al. 1999) represented by broad light blue and grey bars, error ranges by thin black and red lines. Des determined with the software Luminescence Analyst, Duller, 2015). “Age” assessments by assuming a representative effective dose rate of 2.80 Gy/ka for the pIR-BLSL protocol and 3.98 Gy/ka for the pIR₆₀IR₂₂₅ protocol. For details on the dose rate assessment cf. S4.2 “Methods – Luminescence screening”.

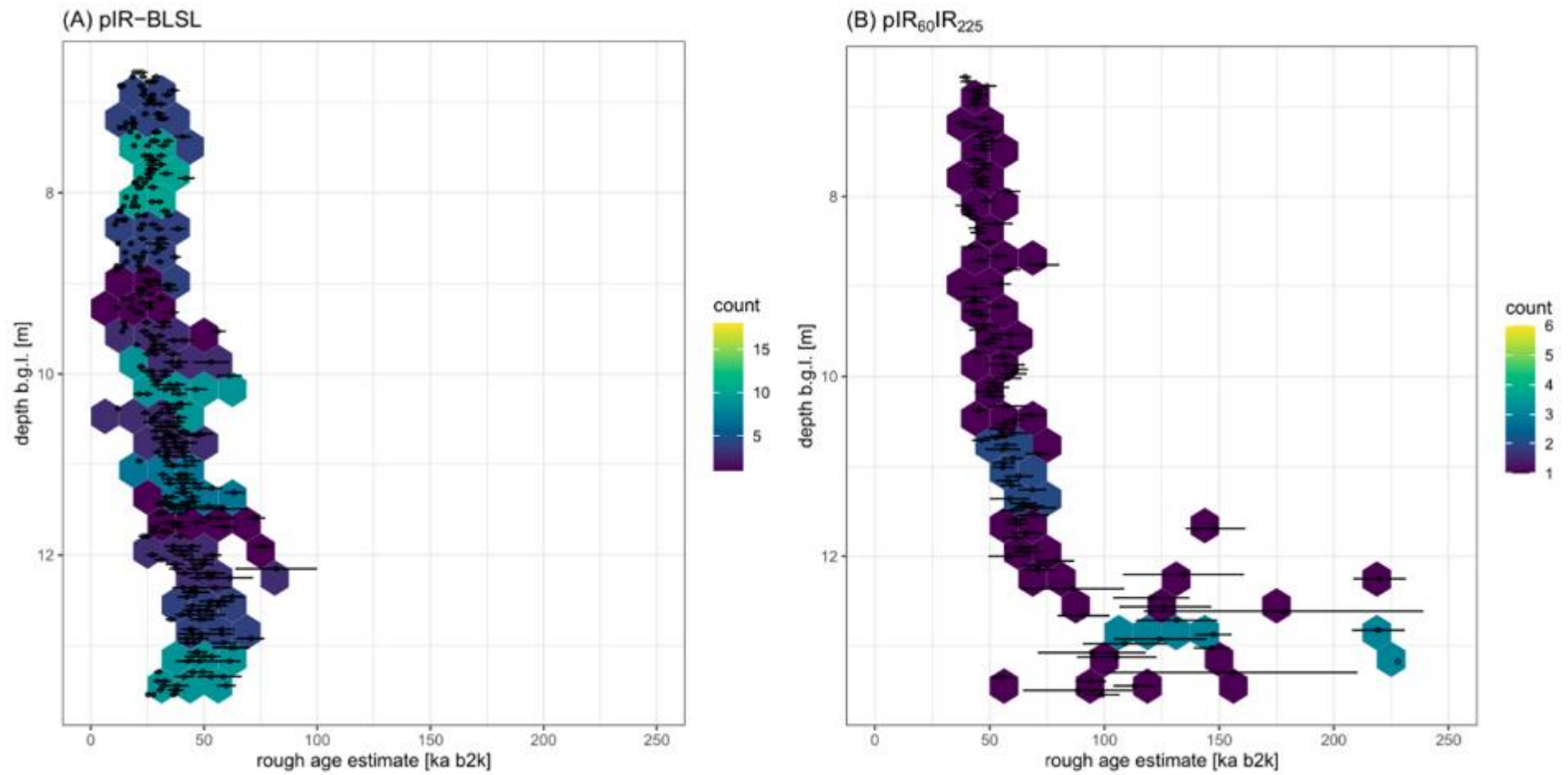


Figure S4.67: Representation of the age-depth relationship of the results of the pIR-BLSL and pIR₆₀IR₂₂₅-screening as hexbinplot (also hexplot), in which the scattering of the data is reduced by binning (here maximum of 20 per hexagon). Counts equal the number of “ages” in one hexagon area. The figure shows the general pattern of the “ages”, which generally increase with depth. The pIR₆₀IR₂₂₅ “ages” are systematically older than the pIR-BLSL-“age estimates”.

Chapter 5: The Late Pleistocene loess palaeosol-sequence Baix in SE France – stratigraphic insights and correlations (study 4)

Nora Pfaffner¹, Annette Kadereit², Sebastian Kreutzer^{2,3,4}, Thomas Kolb⁵, Tianhao Wang⁶, Pascal Bertran^{7,8}, Mathieu Bosq⁸, Christine Hatté⁹, Daniela Sauer¹

¹ Department of Physical Geography, University of Göttingen, 37077 Göttingen, Germany

² Heidelberg Luminescence Laboratory, Institute of Geography, University of Heidelberg, 69120 Heidelberg, Germany

³ Geography & Earth Sciences, Aberystwyth University, SY23 3DB Aberystwyth, Wales, United Kingdom

⁴ Archéosciences Bordeaux, UMR 6034, CNRS - Université Bordeaux Montaigne, 33607 Pessac, France

⁵ Department of Geography, University of Gießen, 35390 Gießen, Germany

⁶ Dalian University, College of Life and Health, 124221 Dalian, China

⁷ Inrap, 33130 Bègles, France

⁸ PACEA, UMR 5199 CNRS – Université de Bordeaux-CNRS, 33615 Pessac, France

⁹ Laboratoire des Sciences du Climat et de l'Environnement (LSCE), UMR CEA-CNRS-UVSQ 8212, 91191 Gif-sur-Yvette, France

Manuscript in preparation.

Table 5.23: Authors contribution to study 4.

Authors	Contribution to study
Nora Pfaffner¹	Investigation, Methodology, Data validation and interpretation, Writing -original draft, Visualisation Conceptualisation, Investigation, Data validation and interpretation, Writing – review & editing
Annette Kadereit²	Conceptualisation, Investigation, Methodology, Data validation and interpretation, Writing – review & editing, Visualisation
Sebastian Kreutzer^{2,3,4}	Methodology, Review & editing, Visualisation
Thomas Kolb⁵	Methodology, Writing - review & editing.
Tianhao Wang⁶	Investigation, Writing - review & editing
Pascal Bertran^{7,8}	Investigation, Data validation and interpretation Writing - review & editing, Visualisation
Mathieu Bosq⁸	Investigation, Data validation and interpretation, Writing - review & editing, Visualisation
Christine Hatté⁹	Methodology, Writing - review & editing.
Daniela Sauer¹	Project-conceptualisation, Investigation, Data validation and interpretation, Writing - review & editing

Abstract

Loess palaeosol-sequences (LPS) provide valuable terrestrial archives, preserving palaeoclimatic and palaeoenvironmental information over long periods. LPS in the central European loess belt, in the temperate zone to the north and the Mediterranean further to the south, were studied intensively in the past. Here we present new results for the LPS Baix, situated in the northernmost part of the Mediterranean zone, linking (palaeo-)climatic conditions from the Mediterranean to the temperate zone during the Late Pleistocene. The ca 14 m thick LPS Baix, located in the Rhône Rift Valley, SE France, was investigated using

sedimentological and palaeopedological methods combined with optically stimulated luminescence- and AMS radiocarbon dating from mollusc shells. The LPS Baix was formed over the Last Interglacial to the present-day by loess sedimentation, (palaeo-)soil formation, (bio-)turbation and local reworking of both loess and soil horizons. Thicker loess deposits between the preserved palaeosols are attributed to the MIS 4 and MIS 2, respectively. The unimodal grain-size distribution resonates with findings from central European LPS. For the Last Interglacial/Early Glacial (MIS 5), a polygenetic, Stagnic Luvisol with its Bt(g) horizons confirms more humid conditions during late MIS 5 compare to central European LPS. The thick MIS 4 loess deposits contain a biparted brown Bw soil, which formed during late MIS 4 to MIS 3, suggesting changing moisture conditions. A Calcic Cambisol complex with striking carbonate nodules was formed during the MIS 3. Cambisols are present in the Mediterranean and the temperate zone LPS. However, Mediterranean LPS are associated with an underlying horizon with prominent carbonate nodules, suggest at least on intense leaching phase (marker function). Unlike in the temperate zone, at Baix, no palaeosols and/or active-layer soils are present in the Upper Pleniglacial (MIS 2) deposits. Contrary, the recent Cambisol appears less weathered than the palaeosols due to intense anthropogenic activity. Thus, the syn-sedimentary, intensively reworked and bioturbated character of the loess deposits as well as their partly polygenetic soils and soil complexes of the Baix LPS reflect a gradient of decreasing magnitude of Late Pleistocene climate changes from central Europe to southern Europe

Keywords: Loess-Palaeosol-Sequence, Late Pleistocene, Palaeoenvironment, Pedology, Rhône Rift Valley

5.1 Introduction

Loess-palaeosol sequences (LPS) are valuable archives to reconstruct changes in palaeolandscapes in response to climatic shifts. Throughout the Pleistocene, larger riverbeds presented sources of dust deflation, while river terraces and valley slopes were prominent accumulation zones (Fig. 5.68). LPS display typical stratigraphic patterns due to a supra-regional climatic forcing, with prominent pedo-stratigraphy characteristics reflecting regional and local climate conditions (Pye, 1995). LPS of temperate regions are generally highly resolved records, with distinct responses to climatic shifts in the form of various palaeosol horizons and permafrost-related features (Semmel, 1968; Bibus and Semmel, 1977; Guenther, 1987; Antoine et al. 1999, 2016, 2021; Frechen et al. 2007, Schirmer 2012, 2016; Fischer et al. 2021, Lehmkuhl et al. 2021). In contrast, Mediterranean LPS are marked by a less diversified pedo-stratigraphy, and loess and palaeosol units are generally highly reworked and (bio)-turbated hampering pedo- and chronostratigraphic analyses and interpretation. Furthermore, Mediterranean LPS display scattered frost-related features (Bonifay, 1965; Brunnacker, 1974; Ferraro, 2009; Wacha et al. 2011a, 2011b; Boixadera et al. 2015; Zerboni

et al. 2015; Costantini et al. 2018; Wolf et al. 2019; Bertran et al. 2021; Lehmkuhl et al. 2021). These LPS are each typical “representatives” of the prevailing northern (N) temperate and southern (S) Mediterranean conditions. By contrast, LPS in the transition zone along the N-S gradient remain hardly studied. Amid the ongoing pivotal climate change debate, it is crucial to understand past climatic responses of susceptible sensitive transition zones, particularly those areas within the expected northward shift of the boundary between the Mediterranean and temperate environments (Ottlé et al. 2001; Gao and Giorgi, 2008; Giorgi and Lionello, 2008). Most northern Mediterranean LPS are cut off from temperate regions beyond high mountain ranges (e.g. the Pyrenees, the Alps, Apennines, Dinaric Alps, Pindus mountains) (Fig. 5.68). Thus, the LPS of the Rhône Rift Valley in SE France presents unique archives as the N–S orientated Rift Valley is marked by a change from temperate to Mediterranean climate conditions with around 45° N (Valence), denoting the present-day transition between the two zones (Meteo-France, 2020).

Loess in the Rhône Rift Valley was studied in the past by Suen (1934), Mazenot (1956), Bourdier (1958), Bonifay (1965), Dubar (1979) and more recently, including numeric dating, by Franc et al. (2017) and Bosq et al. (2018, 2020a, 2020b). According to loess maps of Haase et al. (2007) and Lehmkuhl et al. (2021), the distribution of aeolian sediments is patchy in the southern Rhône Rift Valley, whereas the map of Bertran et al. (2021), derived from grain sizes of topsoils, suggests a more widespread distribution of loess and sandy loess (Fig. 5.69). Furthermore, the map of Bertran et al. (2021) and observations by Bosq et al. (2018, 2020b) suggest a change of the loess facies from loess to sandy loess. This change indicates a possible alteration of LPS characteristics within the Rhône Rift Valley, whereas the region near Valence (~45° N) represents a transition area. The area around Valence coincides with the recent transition zone from temperate to Mediterranean conditions. The LPS study site Baix is located within that area, 25 km southwest of Valence (Figs. 5.68, 5.69).

We present results from soil-colour measurements, physical and chemical soil-sediment analyses to reconstruct the palaeoenvironmental evolution at the site. For chronostratigraphic correlations ages from the lower 7 m of the profile gained by i) a luminescence screening on minimally prepared material (Pfaffner et al. 2024) ii) optically stimulated luminescence (OSL) dating on feldspar coarse grains, polymineral fine grains and quartz fine grains from six OSL block samples and (iii) accelerator mass spectrometry (AMS) radiocarbon dating on gastropod shells from the upper part of the sequence was applied.

The results will be used to investigate on a pedo-stratigraphic level whether the present-day transition character of the area was archived in the Baix LPS and/or at which times in the Last Interglacial-Glacial cycle the Baix LPS shows typical characteristics of temperate or Mediterranean conditions. These settings enables us to discuss (i) the changes in the aeolian

deposits in the Valence area (Haase et al. 2007; Bosq et al. 2020b; Bertran et al. 2021; Lehmkuhl et al. 2021) and (ii) to test the hypothesis of Brunnacker (1974) that the extension of the Mediterranean climate conditions during the Last Glacial corresponds to the recent climate setting. Thus, Baix will be compared with well-known LPS from temperate central European regions and northern Mediterranean LPS of Italy and western Croatia to the south.

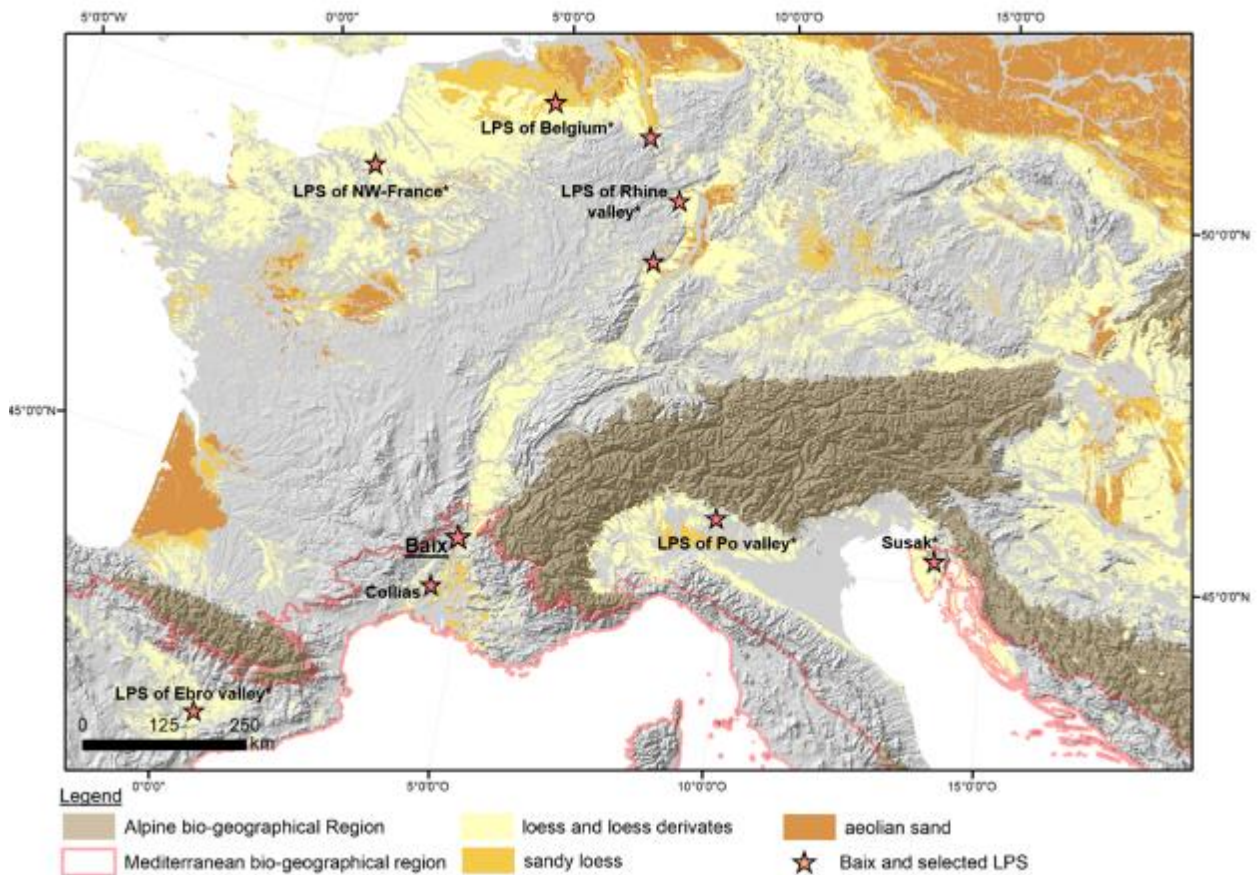


Figure 5.68: Map of aeolian deposits in western Europe based on Bertran et al. (2021) and Lehmkuhl et al. (2021), location of loess-palaeosol sequence (LPS) Baix, Collias and selected LPS of NW-France* (incl. Havrincourt, Renancourt, Saint-Acheul, Saint-Illiers, Saint-Pierre-lès-Elbeuf, Saint-Sauflieu, Villiers-Adam (Antoine et al., 1999, 2016, 2021)), LPS of Belgium* (incl. Harmignies, Kesselt, Rocourt, Remicourt, (Frechen et al. 2001; Antoine et al. 2016; Haesaerts et al. 2016)), LPS of the Rhine Valley* (incl. Achenheim, Garzweiler, Grafenberg, Nussloch, Schwalbenberg, Remagen, Schatthausen (Antoine et al. 2001, 2009a; Rousseau et al. 2002; Schirmer, 2002, 2012, 2016; Frechen et al. 2007; Gocke et al. 2014; Fischer et al. 2019, 2021) LPS of Collias (SE-France, Bosq et al. 2020b), LPS of the Ebro Valley* (incl. Guiamets, Tivissa, Mas de l'Alerany, Batea, Almenara (Boixadera et al. 2015)), LPS of the Po Valley* (incl. Bagaggera, Monte Netto, Val Sorda (Ferraro et al., 2004, Ferraro, 2009; Zerboni et al. 2015; Costantini et al. 2018)), LPS of Susak* (incl. Sand Pit, Bok, Savudrija (Wacha et al. 2011a, 2011b 2018; Zhang et al. 2018)). Extension limits of the Mediterranean bio-geographical conditions and Alpine bio-geographical regions. (Data: Elevation map of Europe (1 km x 1 km) and shapefiles of bio-geographical regions provided by European Environment Agency (EEA), 2021.)

5.2 Regional settings

The Baix LPS (44°42'36.30" N, 4°43'20.80" E, 155 m a.s.l) is located in a former quarry at Brune, 25 km SW of Valence, with in the middle of the Rhône Rift Valley (Figs 5.68, 5.69). The

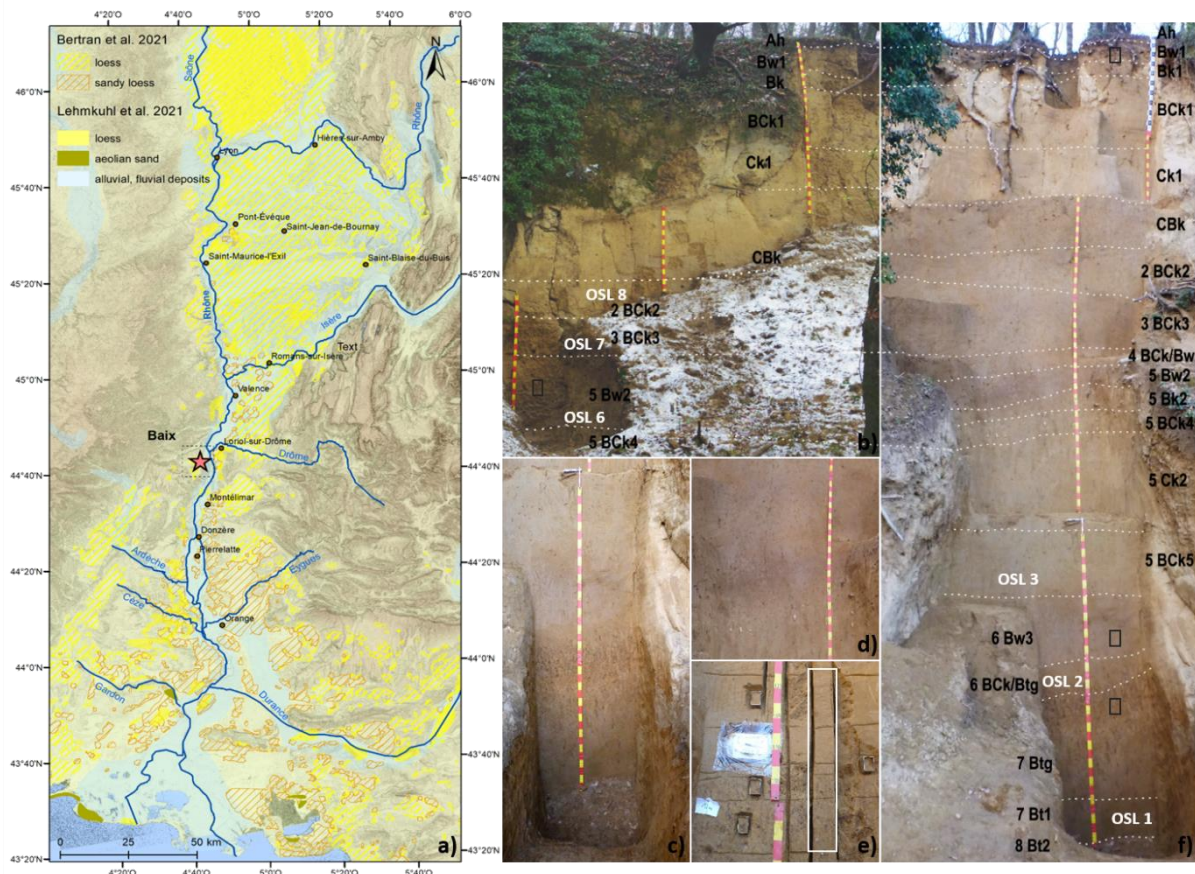


Figure 5.69: Map of aeolian and fluvial deposits in the Rhône Rift Valley area derived from Bertran et al. (2021) and Lehmkühl et al. (2021) and location of loess-palaeosol sequence (LPS) Baix. (Map data: Digital Elevation Model (DEM) with a 12 m x 12 m resolution derived from the TanDEM-X data Mission (2011-2015) from the German Aerospace Centre (DLR). b & f) Profile photos of “Baix_west” (b) and main profile “Baix” (f), Rhône Rift Valley, SE France with designated soil horizons. White optical luminescence labelling (OSL-6 to OSL-8 and OSL-1 to OSL-3) marks sample positions for OSL dating; black rectangles marks positions of thin section samples. c) Interglacial palaeosol complex of Baix LPS represented by a Stagnic Luvisol with prominent hydromorphic features. d) Upper interstadial palaeosol of Baix LPS represented by a truncated Calcic Cambisol underline by prominent in situ carbonate nodules. e) Sampling scheme of Baix LPS: vertically carved in slots highlighted with the white rectangle marks sediment columns collected in flower boxes for OSL screening (Pfaffner et al., 2024); plastic foil covered sediment blocks marks samples for OSL dating and used Kubiěna frames for micromorphological investigation (Photos: D. Sauer (2017-2020)).

Rhône Rift Valley is part of the European Cenozoic Rift System (ECRIS), a wide north-south orientated graben structure (Ziegler and Dèzes, 2007). Bounded by the Massif Central and the Alps composed of Palaeozoic rocks and Mesozoic and Cenozoic rocks, respectively, the graben is mainly filled with deposits reaching from the Oligocene and Miocene to the Pliocene and Pleistocene (BRGM 2021). Due to uplifting, dissecting and eroding of the diverse geology, the Rhône Rift Valley is characterised by an alternation of wide basins and epigenetic constrictions with various smaller side basins (Fig. 5.69). Loess deposits of the Rhône Rift Valley originated from glacial and fluvio-glacial deposits from the Alps and Massif Central (Suen, 1934; Bosq et al. 2018, 2020a). In the northern part of the valley, loess mainly covers the plateaus, large basins, and terraces, whereas in the south, the deposits primarily occur

along the tributaries covering partially bedrock, partially, the fluvial terraces and the smaller side valleys of the Rhône (Fig. 5.69) (Suen, 1934; Mazonot, 1956; Bosq et al. 2018). The valley is drained by the Rhône River and several side tributaries, whereas the eastern tributaries of the Rhône (e.g. Isère, Drôme, Durance) originating in the Alps, are described to provide a higher/more intense sediment load, compared to steep shorter rivers (e.g., Ardèche, Gardon, Cèze) from the Massif Central (Olivier et al. 2009) (Fig. 5.69). The present-day climate in the valley is characterised by a gradual change from temperate climate conditions in the north to Mediterranean conditions in the south. The temperate climate of the northern valley is distinguished by warm summers (up to 3 arid month) and cold, humid winters (mean annual temperature (MAT): ~ 13 °C) with mean annual precipitation (MAP) between 800 mm and 900 mm (Meteo-France, 2022a). The mountainous and eastern regions of the valley reached higher MAP of 1200–1400 mm and summer storms are common (Diodato et al. 2016). The Mediterranean climate is characterised by hot, dry summers with 5 arid months, MAT: ≥ 14 °C and humid winters with MAP: ≥ 500 mm (Meteo-France, 2022c, 2022d). The wind system of the valley is influenced by different origins of advect air masses (Mediterranean, maritime, polar maritime and subtropical), which led to synoptic circulations and resulting in a high yearly and seasonal variability of precipitation and wind intensities (Diodato et al. 2016). The dominating wind systems are the cold blowing Mistral and Tramontane. The strong north-northwestern blowing Mistral travels as well as the western blowing Tramontane, through the channelled valleys before opening into the Mediterranean Sea (Obermann et al. 2018). The lower foothills of the Cévennes form along the western side of Rhône Rift Valley a small side basin filled with debris of Cretaceous limestone and basalts. The Baix LPS is situated in the wind shadow at the south-eastern foot slope of the small side basin (Pfaffner et al. 2024). Thus, both the general wind situation and the topographic position of the Baix LPS explain the patchy occurrence of a loess patch just at the LPS site Baix. It is known that the source area(s) of the loess deposits at the site Baix was the dried-out river bed of the river Rhône, as it has been proven for other loess sites along the Rhône valley (Bosq et al. 2020a). This does not exclude the possible admixture of material from more proximal sources like river beds of smaller local tributaries (e.g. Payre, l'Ouvèze) or hill slope above the LPS site.

5.3 Material and methods

5.3.1 Sampling and description

We studied the main profile “Baix” with a total thickness of 13.7 m during three field campaigns between 2018 and 2020. An additional profile, “Baix_west” (thickness 8.50 m), was cleaned to assess the spatial variability of the sediments and palaeosol horizons (Fig. 5.69b, 5.69f). The observed characteristics and horizon designations were described according to the Food and Agriculture Organization guidelines of the United Nations (FAO, 2006), and corresponding soil

types were afterwards classified according to World Reference Base for Soil Resources (IUSS Working Group WRB, 2022). The horizons of profile Baix_west generally concur with those of the main profile (Fig. 5.69b, 5.69f). In both profiles, a prominent carbonate nodules horizon appears at a depth of ~850 cm. However, small differences in the position of the upper loess horizons suggest a gentle southwestern inclination, which coincides with the local convex ridge-relief. Both profiles show abundant bioturbation features, exhibiting recent and sediment-filled former root channels and filled earthworm channels (Pfaffner et al. 2024). While the main trends of the determined weathering proxies of Baix_west (cf. Fig. A5.76) coincide with those of the upper part of the main profile, we refer in the following results and discussion solely to the results of the main profile of Baix.

The main profile Baix comprises in total of 19 soil and loess horizons. More detailed from bottom to top:

Interglacial soil-complex:

consisting of two well-developed, reddish-brown Bt horizons (8 Bt2, 7 Bt1) and an reddish-orange-brown 7 Btg horizon, imprinted with in situ hydromorphic features and clay coatings, classified as a Stagnic Luvisol (Fig. 5.69c).

Lower interstadial soil:

is represented by a brown bisected Bw horizon (6 Bw3) underlain by an erosional 6 BCk/Btg horizon, representing a mixture of yellow-brown loess and reworked reddish-brown Btg material from the beneath interglacial palaeosol complex.

Upper interstadial soil:

represents a truncated Calcic Cambisol remain consisting of a reworked brown 5 Bw2, followed by an in situ brown 5 Bk2 horizon and a brownish 5 BCk4 horizon, both containing striking large carbonate nodules (~850 cm depth) (Fig. 5.69d).

Holocene soil:

the recent brown intensively bioturbated Cambisol comprising of the Ah, Bw1, Bk1 horizons.

Intercalated loess deposits:

several light brown, grey-brown to yellow-brown loess horizons (3 BCk3, 2 Bck2, CBk, Ck1, BCk1) with varying degree of pre-weathering.

A detailed description of the field characteristics of the main profile Baix is presented in Pfaffner et al. (2024).

We sampled a vertical column continuously every 10 cm for chemical and texture analyses, respecting distinct changes in texture and colour. The samples were air-dried, sieved (<2 mm mesh size) and homogenised. Four samples from the palaeosol horizons (Bk1, 5 Bw2, 6 Bw3 and 7 Btg) were carved out with the help of Kubiëna boxes for micromorphological analyses (Fig. 5.69b, 5.69e, 5.69f).

For OSL dating (Huntley et al. 1985) loess material for (i) screening was sampled continuously in plastic flower boxes (5 cm resolution) from the lower ca 7 m (Fig. 5.69e, Pfaffner et al. 2024) and (ii) 6 block samples, which also stratigraphically covers the lower ca 7 m of the main profile, were collected. Three samples OSL 1 to OSL 3 (HDS-1799 to HDS-1801) were collected from the main profile Baix from the Early Glacial to Lower Pleniglacial horizons (7 Bt1, 6 Bck/Btg and 5 Bck5) (Fig. 5.69e). The other three samples OSL 6 to OSL 8 (HDS-1776 to HDS-1799) were collected from the additional profile Baix_west from the assumed Middle Pleniglacial palaeosol remains from horizons 5 Bw2, 3 Bck3 and 2 Bck2. These horizons correspond to 5 Bk2, 3 Bck3 to 4 Bck/Bw and 2 Bck2 to 3 Bck3 in the main profile (Fig. 5.69b, 5.69f).

Ten samples of bulk sediment, each of approximately 10 l, were taken at regular intervals from the upper 7 m of the LPS to collect mollusc shells for 14C-AMS dating at the Laboratoire des Sciences du Climat et de l'Environnement (LSCE) de Gif-sur-Yvette (France). The samples were wetly sieved on a 425 µm mesh, and the mollusc shells were cleaned by ultrasonic treatment.

5.3.2 Analytical methods

Texture and grain size proxies

High-resolution grain size distribution (GSD) data provide valuable information about transport mechanisms of aeolian sediments under consideration of their complex environmental situations such as topography, microclimate, vegetation and influence of post-depositional processes (Pye, 1995; Rousseau et al. 2002; Vandenberghe, 2013; Lehmkuhl et al. 2016; Újvári et al. 2016a; Schulte et al. 2018; Vandenberghe et al. 2018; Varga et al. 2019). Granulometric data was measured with a Laser Diffraction Particle Size Analyzer (Beckman Coulter LS 13320), for analysis samples were prepared following ISO 11277 (2020) and 13320 (2020). For GSD determination, an optical model according to the Mie theory with RI 1.56i0.1 suitable for quartz was applied (ISO 13320, 2020) and besides using the statistical parameters (e.g., mean, mode of GS) of the 116 grain size classes from 0.04 µm to 2000 µm, primed particle-size classes for clay, silt and sand in vol % (FAO, 2006) was additionally used. However, clay contents (<2 µm) are known to be underestimated by the laser diffraction method, and slightly higher contents can be assumed (Konert and Vandenberghe, 1997; Beuselinck et al. 1998; Újvári et al. 2016a)

To identify modes and GS variations, thus reconstructing environmental and climate conditions, variable proxies were used, each influenced by different factors (e.g., wind speed, distal and local transport, post-depositional process) (Újvári et al. 2016a; Schulte et al. 2018; Schulte and Lehmkuhl, 2018). A logarithmic distribution characterises total and mean abundance of GS of loess and soil horizons. Additionally, the GSI ($26\text{--}52\ \mu\text{m}/<26\ \mu\text{m}$), the U-ratio ($16\text{--}44\ \mu\text{m}/5.5\text{--}16\ \mu\text{m}$) was chosen to reduce the influence of pedogenic clay, and the Si/Al ratio was considered an indicator for particle sorting (Vandenberghe et al. 1985; Antoine et al. 2009a; Liang et al. 2013). The clay/silt ratio and fine to coarse clay ($<0.04\ \mu\text{m}/0.63\text{--}2.0\ \mu\text{m}$) ratio were applied to determine palaeosol horizons and the amount of illuvial clay in assumed palaeosol horizons.

Soil analysis, weathering proxies and colour

Major element concentrations were used to apply geochemical indices based on their molar proportions to identify the loss of bases from silicate weathering due to pedogenesis. The following indices were used: the WI_{MER} calculated as $WI_{\text{MER}} = (\text{Ca (after subtraction of Ca in CaCO}_3\text{)} + \text{Mg} + \text{K} + \text{Na})/\text{Al}$ (Sauer, 2016) and the CPA index (Chemical Proxy of Alteration), calculated $\text{CPA} = \text{Al}_2\text{O}_3/(\text{Al}_2\text{O}_3 + \text{Na}_2\text{O}) * 100$ (Sheldon and Tabor, 2009; Buggle et al. 2011). The Si/Al ratio was also applied to detect the enrichment of aluminosilicates (Liang et al. 2013). Total contents of Fe, Al, Ca, Mg, Si, and Mn were obtained by fusing samples with a Lithium-meta-tetraborate mixture (ratio 1:4), diluted with 5 % HNO_3 and analysed by inductively coupled plasma optical emission spectrometry (ICP-OES, iCAP 7000, Thermo Scientific). The total content of Na and K was determined by a flame spectrometer (Elex 6361, Eppendorf). Pedogenic Fe, Al and Mn contents were determined by $\text{Na}_2\text{S}_2\text{O}_4$ extraction and analysed by ICP-OES (iCAP 7000, Thermo Scientific) (Sparky and Bartels, 2009). The ratios of Fe_d/Fe_t and Mn_d/Mn_t as depth functions reflect the degree of weathering and changing hydromorphic processes, which helps identify weathered zones compared to less and non-weathered zones. Calcic carbonate contents (CaCO_3) were measured by the gas-volumetric method using a Scheibler apparatus and stated in calcium equivalents in wt % (Blume et al. 2011). Soil organic carbon (SOC) contents were obtained by quantifying total carbon (C) contents with a CHN elemental analyser (TruSpec Micro, LECO) in wt %, and subsequently, CaCO_3 was subtracted from the total C contents.

LPS colour changes reflect changing palaeoenvironmental conditions (Pécsi and Richter, 1996; Sprafke, 2015; Wang et al. 2016). Thus, a light yellow(-ish) colour most likely results from calcareous loess deposits during cold-dry conditions, whereas darker brown and/or red colours indicate the presence of Goethite and Hematite built under temperate-warm climates with differing humid conditions (Pécsi and Richter, 1996; Sprafke et al. 2020). Quantified colour-based stratigraphy attained more attention recently, e.g., in LPS studies of Chen et al.

(2002), Gocke et al. (2014), Sprafke (2015), Wang et al. (2016), Zeeden et al. (2017), Sprafke et al. (2020), Krauss et al. (2021) and Laag et al. (2023). To detect and quantify colours more sensitively, we used a handheld spectrophotometer CM-700d (Konica Minolta). Fine earth samples were measured three times (10° standard observer, SCI) and the mean results were converted into the CIE colour index, reflected by the $L^*a^*b^*$ by SpectraMagic NX software (CIE, 1976). L^* (metric lightness function) represents the brightness or luminance (range 0–100), and a^* and b^* the chromaticity coordinates opponent red-green scales (a^*) and opponent blue-yellow scales (b^*) (Viscarra Rossel et al. 2006). Although it is not possible to separate between in situ and reworked soil material or secondary carbonate enrichments, the chromatic parameter a^* and derived ratios are valuable tools to detect the influence of weathering on sediments.

For thin section analyses the remaining pore water of the undisturbed, orientated blocks for was gradually exchanged with acetone. After, the blocks were impregnated with hardening resin (Palatal), cut into smaller blocks, glued on a glass slide (28 mm x 48 mm) and (hand-) polished to <30 μm thickness. According to Stoops (2021), semi-quantitative characterisations of the thin sections were carried out and photomicrographs taken with a Keyence VHX-7100/-E100 polarising, digital microscope in-plane polarised and crossed polarised light.

5.3.3 Age determination

Luminescence dating

In addition to the luminescence screening on 126 minimally prepared small subsamples (ca 1 cm x 1 cm x 1 cm) from sediment samples (“flower-box samples” HDS-1802 to HDS-1817) of the lower ca 7 m of the profile Baix (Pfaffner et al. 2024), for the present study, we collected 6 block samples for optically stimulated luminescence (OSL, Huntley et al. 1985) dating (HDS-1776 to HDS-1778; HDS-1799 to HDS-1801), which stratigraphically also cover the lower ca 7 m of the main profile. For luminescence dating, both fine grains (4–11 μm) and coarse grains (125–212 μm) were available, but quartz coarse grains turned out too scarce for luminescence dating. Details of the sample preparation are given in the supplement (Table S5.24). For OSL dating, the single aliquot regeneration (SAR) approach was applied (Murray and Wintle, 2000). While quartz fine grains were measured with a blue-light stimulated (BLSL) SAR protocol (Murray and Wintle, 2000) detecting the ultra-violet luminescence emission around 340 nm, feldspar coarse grains and polymineral fine grains were measured with a post-infrared (at 60 °C) infrared (at 225 °C) stimulation ($pIR_{60}IR_{225}$) protocol (Thomsen et al. 2008) detecting the blue-violet emission around 410 nm. Details on measurement configurations, pretests for adapting the protocols to the Baix samples, parameters of data analyses as well as results of the equivalent doses (D_e) of individual aliquots and the D_e distribution of a sample are given in the supplement (“S5.4 Results”). In addition, for the quartz fine grains, the results of a series

of additional tests are provided in the supplement, which were conducted to investigate possible reasons for the unexpectedly large quartz fine grain ages. Furthermore, the analyses of the feldspar coarse grain measurements are accomplished by tests investigating the suitability of the T_x/T_n sensitivity curves as a proxy of (1) material source or (2) poor bleaching (Chen et al. 2013). For dose rate estimation, the contents of radionuclides were determined with the μ Dose system in the luminescence laboratory at Gießen University (Kolb et al. 2022). For further information on the radionuclide contents and the age calculation see the supplement (Fig. S5.131, S5.132).

AMS radiocarbon dating

Two small mollusc taxa were selected for dating depending on their respective abundance in the samples, i.e. *Pupilla muscorum* and *Trochulus hispidus*. These species live on vegetation and are assumed to be suitable for chronological investigations (e.g., Pigati et al. 2010; Újvári et al. 2016b). Radiocarbon ages were calibrated to calendar ages with the IntCal20 calibration curve (Reimer et al. 2020), using the software Calib in version 8.2 (Stuiver et al. 2021). Calibrated ages are reported as age ranges at the 2 sigma (σ) confidence level (95.4 %).

5.4 Results

5.4.1 Texture

The mean percentages of the main grain-size classes read clay: 11 %, silt: 72 % (coarse silt, 20–63 μm : 44 %), and sand 17 % (finest sand, 63–125 μm : 15 %) for the main profile Baix (Fig. 4). Loess horizons contain the highest proportion of the silt fraction (76 %) and the lowest proportion of clay (9 %), soil units are marked by the highest clay contents of 13–18 % (Fig. 5.71).

The curve shape of the GSD of all samples shows a unimodal-like distribution with the main mode at the coarse silt fraction (~44–50 μm), indicating an aeolian origin of the sediment (Fig. 5.70). Two subpopulations in the fine/middle silt (~5–12 μm) and middle clay ranges (~0.2–0.3 μm) within the fine tail of the distribution curve can be associated with soil formation (Fig. 5.70). Throughout the profile, the mean GS ranges between 29 μm and 65 μm with an average of 36 μm , while the median grain size ranges from 23 μm to 41 μm , and the average is 30 μm . The curve is generally slightly positively skewed (Fig. A5.75). Thus, GS tends to coarsen. The class-wise and subpopulation changes and shifts of the mean, median and double standard deviation of GS along the depth axis is presented in Fig. A5.75 in the appendix. The upper 2 m (Holocene soil and upper loess horizons) and horizons of the upper interstadial soil are marked by shorter variations in GS, poor sorting and high kurtosis and skewness, which shifts at larger depth to a highly sorted, fine-skewed sediment with an unvaried kurtosis, respectively (Figs. 5.71, A5.75). Thus, these deposits suggest either grain transport over short distances

or, more likely, sediment reworking, whereas the lower sediments of the profile instead suggest in situ deposited loess. In the field, no layering/sorting of the sediment was observed. However, most of the horizons contain a scattered number of small gravels and charcoal pieces, and in accordance with the foot slope position of Baix, a gentle erosion and re-accumulation of loess are suggested. All horizons consist of homogenous silts, whereas for the intercalated loess horizons, an increase of the GIS towards the top, accompanied by a constant decrease of the silt fraction and an increase of the fine sand fraction, was observed respectively and reflected by an increase of mean and median GS (Fig. A5.75). The U-ratio (1.55–3.03), GSI (0.34–0.79) and Si/Al (4.55–6.64) show maxima within assumed loess depositions and decrease in palaeosol horizons, whereas clay/silt (0.13–0.27), fine clay/coarse clay (0.16–0.57) ratios acting oppositely (Fig. 5.71).

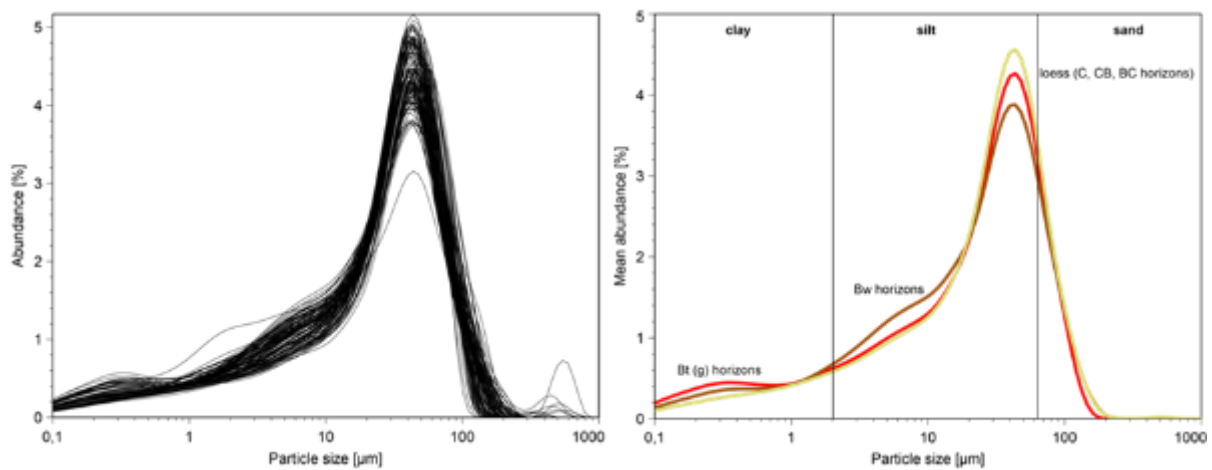


Figure 5.70: Logarithmic distribution curves of 116 classes ($<0.2 \mu\text{m} - 2000 \mu\text{m}$) of the grain size (GS) of the fine earth fraction of loess-palaeosol sequence Baix. Left: Absolute abundance in vol % $<2 \text{ mm}$ of the 130 soil samples. Right: Mean grain size of determined soil horizon types (red colour: Bt (g) horizons; brown colour: Bw horizons; yellow colour: different intensively weathered loess horizons (C, CB and BC)).

5.4.2 Soil-chemical characteristics, colours, and micromorphology

The interstadial palaeosol complex displays decalcified material with ca 0.3 to 2.5 wt % eq. CaCO_3 . In addition, two cycles of decalcification are visible. Both start with maxima of ca 23 wt % eq. CaCO_3 , firstly from beneath the Holocene soil secondly from beneath the upper interstadial soil (Fig. 5.71). From the Bk1 horizon until the 7 Btg horizon relocated and in-situ, hard carbonate nodules of various sizes are observable, which indicates a constant cycle of leaching and enrichment of secondary carbonates.

The soil organic carbon (SOC) contents fluctuated between 0 wt % and 0.5 wt % (maximal value for Ah horizon with 2.5 wt %), showing increasing trends in the upward direction (Fig. 5.71). The weathering indices record their maximum values within the palaeosol horizons and their minima in the loess sediment.

- well-developed Bt (g) horizons: highest Fe_d/Fe_t : 0.90; Mn_d/Mn_t : 1.35; CPA: 80 ratios and lowest WI_{MER} : 0.49 and Si/Al: 4.5 ratios,
- Bw, Bk horizons: medium Fe_d/Fe_t : 0.60; Mn_d/Mn_t : 1.1; CPA: 74; WI_{MER} : 0.70 and Si/Al: 5.0–5.9 ratios,
- loess horizons ranging from Bck to Ck: lowest Fe_d/Fe_t : 0.55–0.45; Mn_d/Mn_t : 1.17–0.86; CPA: 73–68 ratios and highest WI_{MER} : 0.70–0.95 and Si/Al: 5.1–6.6 ratios (Fig. 5.71).

The variations of the colour values show a clear pattern. The fluctuation of the lightness (L^* value) throughout the profile reflects the diversity of the colour of the deposits (Fig. 5.71). Generally, lower L^* values for the soil horizons and higher values for the loess sediments were observed. The chromatic values of a^* and b^* display a similar pattern, with maxima values for palaeosol horizons (a^* :11; b^* :32), attributed to the formation of Fe oxides and minima for the loess horizons (a^* : 5; b^* : 22). The minima values coincide with the least weathered loess horizons designated Ck horizons. Like the L^* values, the values a^* and b^* for the recent Ah horizon do not conform to the sediments and soil horizons below (Fig. 5.71). By combining chromatic parameters (a^* and b^*), sediment and soil horizons are differentiated (Fig. 5.71).

Micromorphology

The four thin sections taken from each investigated soil of Baix and Baix_west are generally composed of quartz, feldspars, biotite, calcites and very few garnet minerals (Fig. 5.72a-d). Their microstructures range from massive, channel, vughy (Fig. 5.72c) over subangular and rounded/vermicular (Fig. 5.72a) to a weakly subangular to angular blocky microstructure (Fig. 5d). Whereas the Holocene soil and the brown Bw horizons display a crystalline to stippled speckled b-fabric (Fig. 5.72h, 5.72j, 5.72l, 5.72n), shows the 7 Btg horizon a clear poro-striated b-fabric (Fig. 5.72r, 5.72t). The void system of all sections is dominated by biogenic pores, e.g., channels and chambers with some vughs (Fig. 5.72a–d). Although, the soils are decalcified, except for the Holocene soil, they show enrichments of secondary carbonates in terms of micrite hypocoatings (Fig. 5.72p). In all soil horizons redoximorphic nodules of various size, shape and origin are displayed, generally define as orthic and disorthic Fe/Mn nodules (Fig. 5.72m, 5.72k). Within the thin section of the 6 Bw3 horizon a Fe depletion zone was observed (Fig. 5c). Furthermore, in the 6 Bw3 and the 7 Btg horizons, two large reddish anorthic nodules containing Fe and limpid clay coatings were observed (Fig. 5.72c, 5.72d). Due to the clay coatings they are interpreted as relocated aggregates of various distances and intensities (Fig. 5.72o). Further pedofeatures, like clay and clay-silt coatings are observed in all thin sections along the voids and aggregate surfaces (Fig. 5.72g, 5.72i, 5.72k, 5.72s). In situ as well as fragmented, limpid layered clay coatings were only observed in the 7 Btg horizon (Figs. 5d, 5q, 5s). The layers along the void wall seem to begin with limpid orange clay coatings

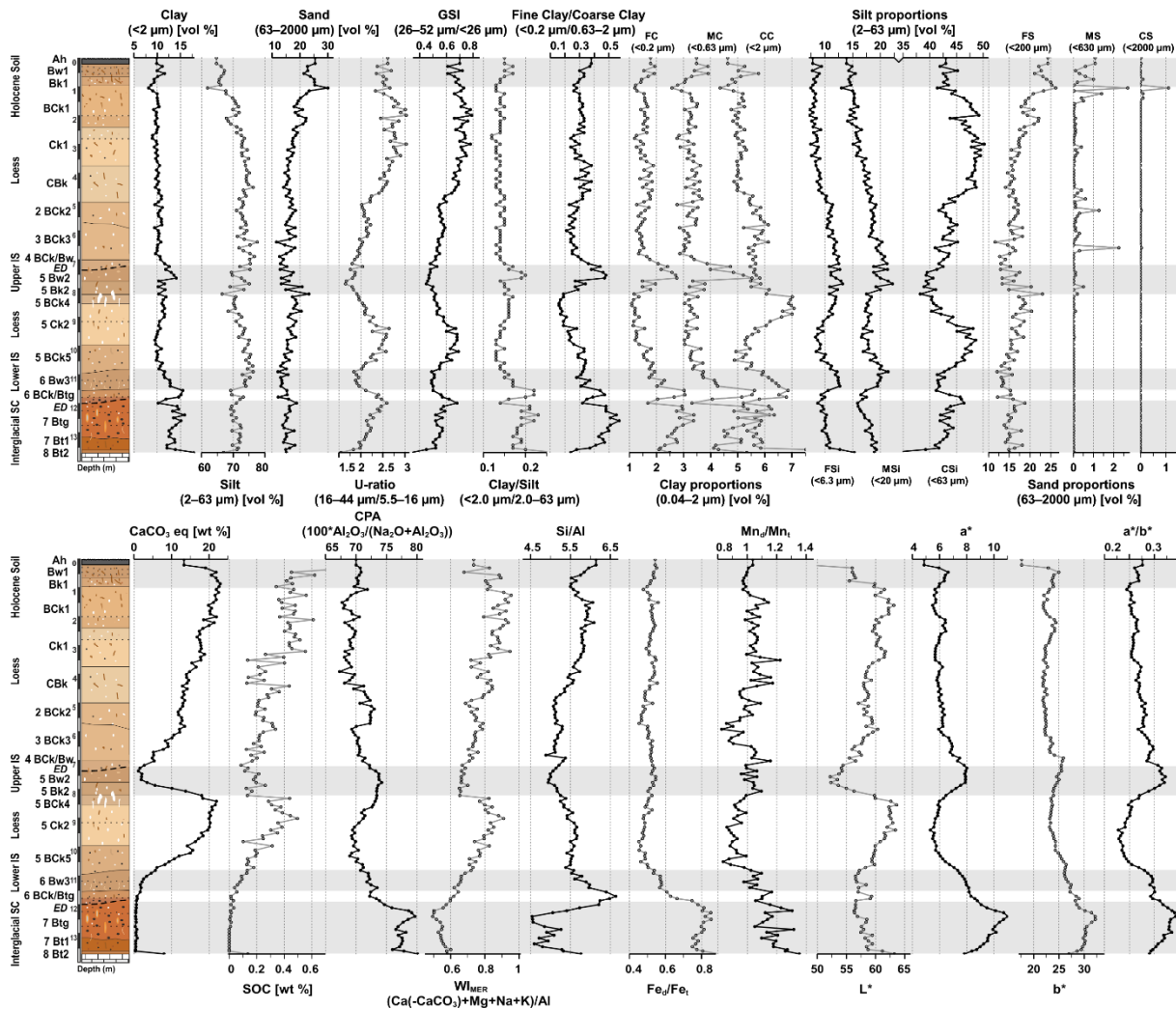


Figure 5.71: Loess-palaeosol section (LPS) Baix, Rhône Rift Valley, SE France with soil formation units marked as grey bars. Depth related upper curves of: grain-size fractions of clay (<2 μm), silt (2–63 μm) and sand (63–2000 μm) in vol %; grain-size ratios: U-ratio (16–44 $\mu\text{m}/5.5\text{--}16\ \mu\text{m}$), grain-size index (GSI) (26–52 $\mu\text{m}/<26\ \mu\text{m}$), clay/silt (<2.0 $\mu\text{m}/26\text{--}63\ \mu\text{m}$), fine clay/coarse clay (<0.2 $\mu\text{m}/0.63\text{--}2\ \mu\text{m}$) and grain-size fractions of clay (fine clay (FC): 0.04–0.2 μm , medium clay (MC): 0.2–0.63 μm , coarse clay (CC): 0.63–2 μm), silt (fine silt (FSi): 2–6.3 μm , medium silt (MSi): 6.3–20 μm , coarse silt (CSi): 20–63 μm) and sand (fine sand (FS): 63–200 μm , medium sand (MS): 200–630 μm , coarse sand (CS): 630–2000 μm). Depth related lower curves of calcic carbonate equivalents in wt %, contents of soil organic carbon (SOC) in wt % and chemical proxy of alteration (CPA) ($100 \cdot \text{Al}_2\text{O}_3 / (\text{Na}_2\text{O} + \text{Al}_2\text{O}_3)$), weathering index of molar element ratio (Wl_{MER}) (Ca (after subtraction of Ca in CaCO_3) + $\text{Mg} + \text{K} + \text{Na}$) / Al), Si/Al and, ratios of pedogenic to total contents of iron and manganese (Fe_d/Fe_t , Mn_d/Mn_t) and colours of the CIE colour index, reflected by the parameters L^* , a^* , b^* and ratio of a^* and b^* . SC: soil complex; SSC: soil-sediment-complex; GL: gravel lense; ED: erosional discontinuity.

followed by dusty, grey-brown clay-silt coatings and ending with Fe coatings, which suggests different conditions during their formation (Fig. 5.72s). Using a λ retardation plate, a parallel orientation (shown by a blue colour and clear extinctions) to the void walls could be determined, supporting the assumed in situ illuvial process. Thus, verifying an in situ 7 Btg horizon. However, considering the fragmented clay coatings within the ground matrix and the relocated aggregate, two explanation for these contradicting features are possible: i) different generations/phases of illuviation including relocation of the soil aggregates or ii) dis/relocation of coatings and aggregates induced by local intense bioturbation. Considering the position of

the profile, the first scenario seems highly likely, although the occurrence of various passage features rather indicate that both scenarios took place simultaneously. Passage/bioturbation features and calcite earthworm granules are observed through all horizons (e.g. 5.72a, 5.72e, 5.72f).

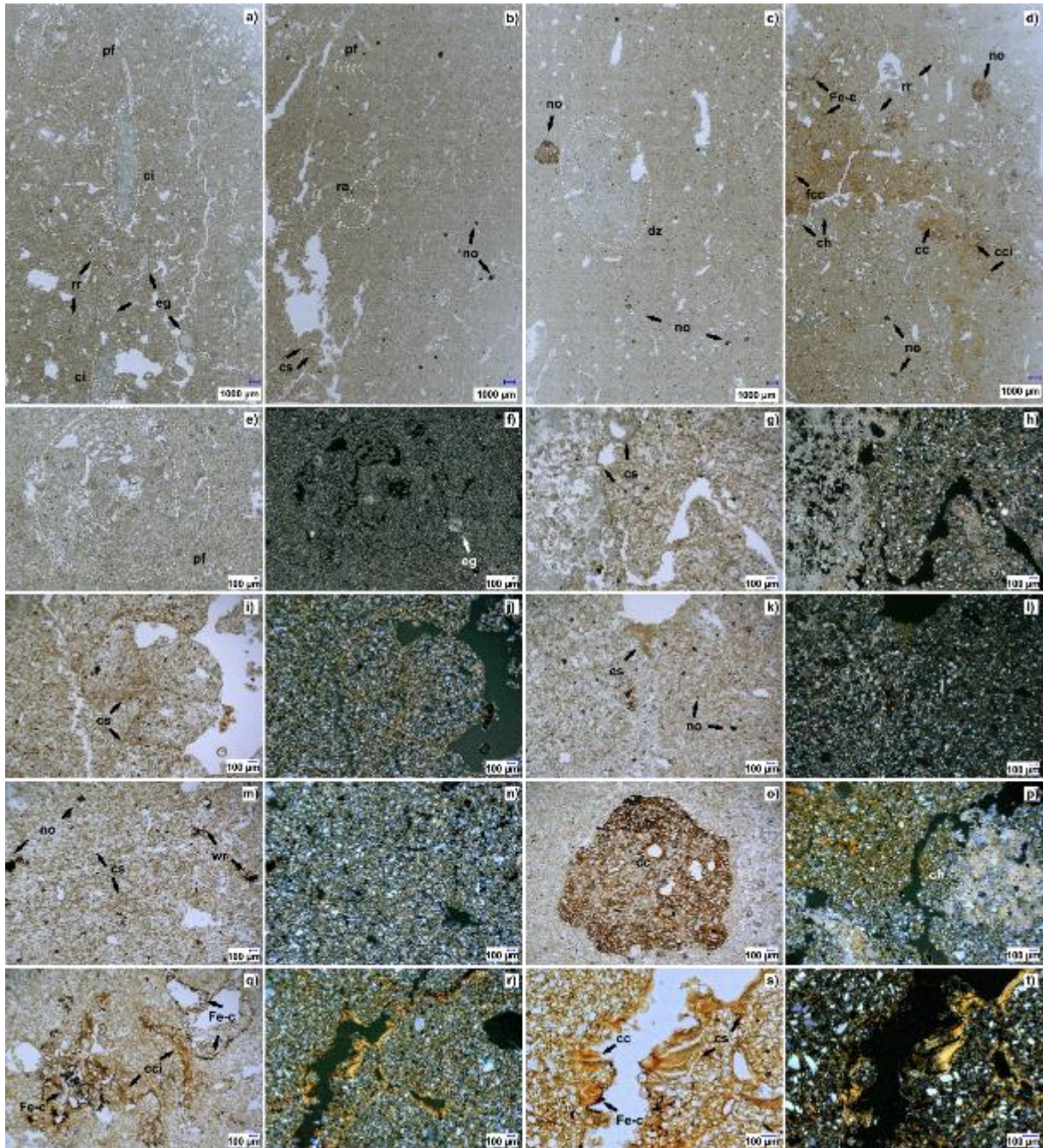


Figure 5.72: Photomicrographs of whole thin sequences (3 cm x 4 cm) and photomicrographs with various magnifications of the profiles Baix and Baix_west, Rhône Rift Valley, SE France. a) Baix, light brown, calcified Bw1 horizon (43–51 cm): with a subangular and rounded/vermicular microstructure due to intense bioturbation. Equable, rounded brown aggregates, micrite hypocoatings along voids dense calcite infillings. Remains of calcite earthworm granules (\varnothing 670 μ m) and root residues (plane-polarised light; PPL). b) Baix_west, brown 5 Bw2 horizon (734–742 cm): subangular-blocky microstructure with accommodated voids. Channels are partly infilled with rounded, bioturbated, aggregates. Frequent disorthic, rounded, elongated, digitated Fe/Mn nodules and typical, digitated orthic Fe nodules (\varnothing 580 μ m) with fine bulgs (PPL). c) Baix, brown, decalcified 6 Bw3 horizon (1133-1141 cm), massive to channel,

vughy microstructure. In situ channels partly filled with porous microaggregates. Orthic and disorthic, rounded and digitated Fe/Mn nodules (\varnothing 350 μ m). Bleached zone induced by depletion of clay and Fe oxides. (PPL).d) Baix, reddish-orange brown, decalcified 7 Btg horizon (1209-1217 cm), weakly subangular to angular blocky microstructure with channels and vughs. Large, red, rounded anorthic nodule with Fe and clay coatings and fragmented clay coatings. Common small round, digitated, elongated, disorthic Fe/Mn nodules; larger typical orthic Fe nodules. e) Large, rounded passage feature in a partly vermicular structure in upper left corner of panel (a) within the Bw1 horizon (43–51 cm). f) Passage feature under cross-polarised light (XPL), showing crystalline and stippled speckled b-fabric with calcite earthworm granule. g) Calcite infillings (needle-fibre calcites) and clay-silt coatings along in situ voids of Bw1 horizon. h) Same area as panel (g) with stippled speckled b-fabric (XPL) i) Rounded, brown aggregate of brown 5 Bw2 horizon of Baix_west with clay-silt coatings along the edges of the aggregate (PPL). j) Same area as panel (i) with striated and stippled speckled b-fabric (XPL). k) In situ dusty clay-silt coatings at the bottom of the void of 6 Bw3 horizon of Baix with abundant anorthic Fe nodules (PPL). l) Same area as panel (k) with stippled speckled b-fabric (XPL). m) Dusty clay-silt coatings along voids within the 6 Bw3 horizon of Baix. Typical to concentric orthic and anorthic Fe nodules (PPL). n) Same area as panel (m) with stippled speckled b-fabric (XPL, HDR).o) One large rounded, reddish anorthic nodule (\varnothing 2200 μ m) containing Fe and clay coatings (PPL) of 6 Bw3 horizon of Baix. p) Poro-striated b-fabric and calcite hypocoatings of 7 Btg horizon of Baix (XPL, HDR). q) Fe-coatings, and infillings clay coatings along voids of 7 Btg horizon of Baix (PPL). r) Poro-striated b-fabric and limpid clay coatings of 7 Btg horizon of Baix (XPL). s) In situ limpid orange clay and grey-brown clay-silt coatings along voids of 7 Btg horizon of Baix (PPL, HDR). t) Same area as panel (s) with poro-striated b-fabric (XPL, HDR). Abbr.: bz = depleted zone; cci= clay coating infilling; cc= clay coating; ch= calcite hypocoating; ci = calcite infilling; cs = clay-silt coating; dz = depleted zone; eg = calcite earthworm granule; fcc = fragmented clay coating; Fe-c = Fe coating; no = Fe/Mn nodule; pf = passage feature; ra rounded aggregate; rr = root residue; wr= weathered rock fragments.

5.4.3 Chronological data

OSL screening results and block ages

Both pIR₆₀IR₂₂₅ feldspar coarse-grain and pIR₆₀IR₂₂₅ polymineral fine-grain ages follow well the results of the OSL screening (Pfaffner et al. 2024) (Fig. 5.73). While the results of the pIR₆₀IR₂₂₅ dating provide methodically very reliable single-point data, the closer-spaced OSL screening data accomplish the picture with a more continuous chronometric “backbone”. The course of the OSL screening data and the pIR₆₀IR₂₂₅ ages meet the stratigraphic expectations derived from the fieldwork and pedo-sedimentary analyses (cf. Pfaffner et al. 2024). By contrast, the quartz fine grain ages overestimate the other data in each case. This finding is surprising, as the luminescence signal of quartz is assumed to reset faster than that of feldspar (Godfrey-Smith et al. 1988). Additional investigations of the quartz fine grains showed that the thermally stimulated (TL) glow curves of the natural samples, but not of the artificially regenerated samples, exhibit a high-temperature peak, similar to a Precambrian quartz sample with a geologic dose of ca 1.5 Ga published by Schmidt and Woda (2019). This finding corroborates the assumption that geologically old fine-grained quartz was incorporated into the Baix loess deposits, likely during hill wash processes. Two scenarios are likely: (1) Quartz fine grain was enriched in the last interglacial Bt horizon due to intensive weathering and pedogenic processes and was later incorporated into younger loess deposits during downslope sediment reworking. (2) Quartz fine grains were provided from the in situ geologic bedrock, likely Cretaceous marl stones. In both scenarios, fresh aeolian dust input was contaminated by older quartz fine grains, which could explain the unexpected age overestimation – with respect to

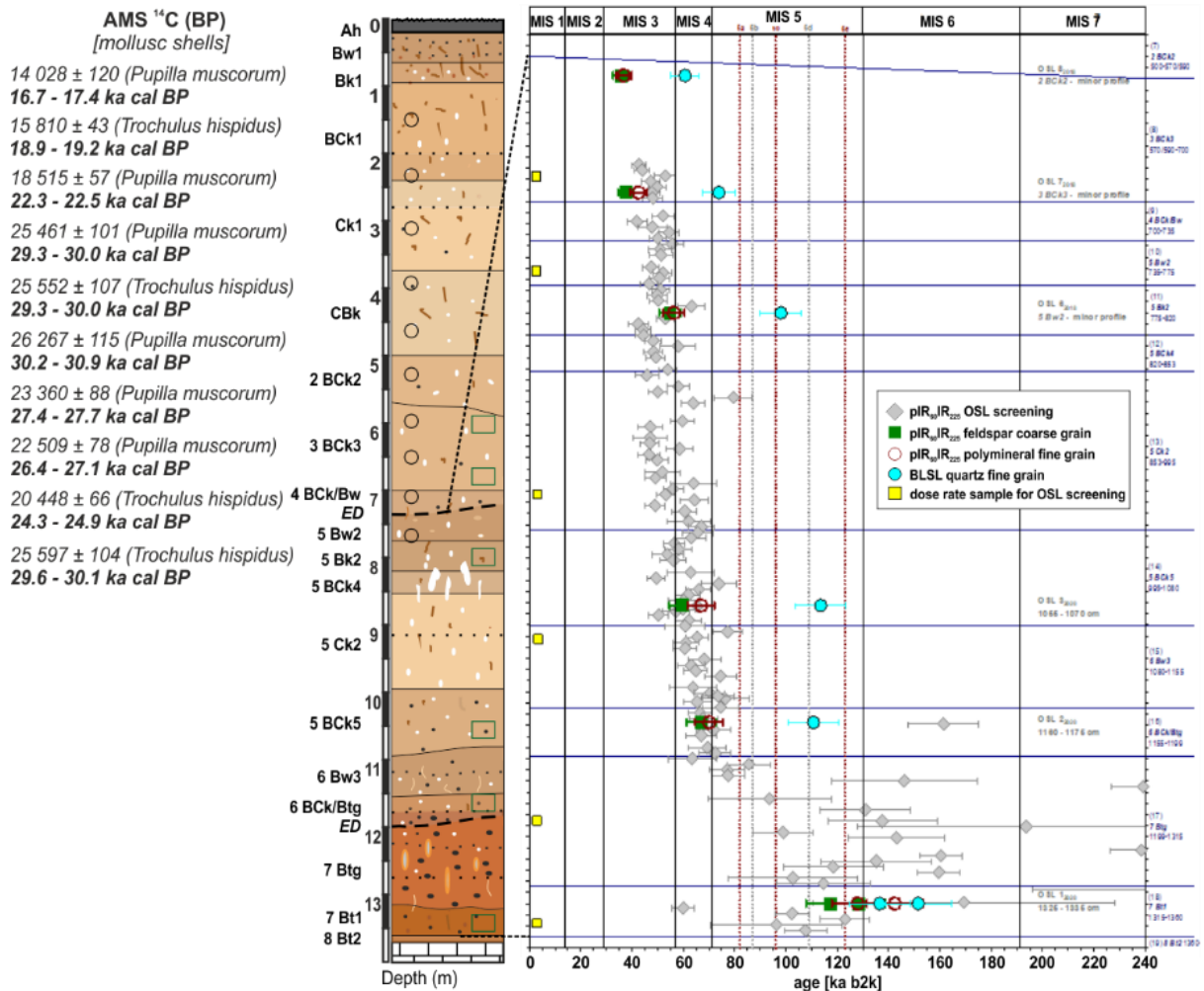


Figure 5.73: Chronological data of the loess-palaeosol section (LPS) Baix, Rhône Rift Valley, SE France. Left: AMS ^{14}C radiocarbon ages derived from mollusc taxa, marked as black circles in the profile scheme. Right: Results of the OSL screening ($p\text{IR}_{60}\text{IR}_{225}$, grey diamonds) on minimally prepared coarse grains from 126 box subsamples (HDS-1802 to HDS-1817, each A to H; Pfaffner et al. 2024) as well as OSL dating on feldspar coarse grains ($p\text{IR}_{60}\text{IR}_{225}$, green squares), polymineral fine grains ($p\text{IR}_{60}\text{IR}_{225}$, red circles) and quartz fine grains (BLSL, blue filled circles) from six OSL block samples (lower green squares in profile OSL 1 to OSL 3 (HDS 1799 to HDS-1801) of main profile Baix and upper green squares OSL 6 to OSL 8 (HDS 1776 to HDS-1778) from profile Baix_west) following standard sample preparation. The yellow squares mark the positions of the dose rate samples used to gain a representative dose rate for the OSL screening procedure (Pfaffner et al. 2024), whereas the dose rates for the OSL block samples were derived for each sample individually, like for the OSL screening also by the μDose system (Tudyka et al. 2018; 2020; Kolb et al. 2022). For the lowermost sample HDS-1799 from the 7 Bt1 horizon, the OSL ages were modelled for the generally assumed water content ($\Delta 1.17$) (Sauer et al. 2016; Bosq et al 2020), but also for stagnant conditions ($\Delta 1.28$), as suggested, e.g., by the observation of Mn-concretions in the lowermost soil horizons. The respective older ages are associated with the higher water content. Solid vertical lines denote the boundaries of the marine isotope stages (MISs) and dotted lines mark the peaks of the substages of MIS 5 (MIS boundaries after Lisiecki and Rayno, 2005 and Railsback et al. 2015).

the stratigraphic expectations and the results of the SAR $p\text{IR}_{60}\text{IR}_{225}$ dating. Therefore, in the following, we disregard the quartz fine grain ages and base our discussion on the results of the OSL screening (Pfaffner et al. 2024) and the $p\text{IR}_{60}\text{IR}_{225}$ dating of the feldspar coarse grains and the polymineral fine grains (Fig. 5.73, Table S5.25). As, by nature, the coarse grain ages

come with a smaller error than the polymineral fine-grain ages, in the discussion we will refer to the $pIR_{60}IR_{225}$ feldspar coarse grain ages.

The pedo-sedimentary horizons are correlated with the oxygen isotope stages of marine sediment cores, referred to as MIS stages with stage boundaries according to Lisiecki and Raymo (2005) and Railsback et al. (2015). Stages are grouped and named as known Eemian (MIS 5e), Early Glacial (MIS 5a-d), Lower (MIS 4), Middle (MIS 3) and Upper Pleniglacial (MIS 2) (Fig. 6). Possible Greenland stadials (GS) and interstadials (GI) from the INTIMATE event stratigraphy (Rasmussen et al. 2014) are cautiously proposed, especially for palaeosol horizons, as they are expected to respond to more supra-regional climate forces.

AMS radiocarbon ages

The calibrated ^{14}C ages range from ~17 ka to ~30 ka (Fig; 5.73). However, we observed substantial scatter and age inversions. Putting together all ^{14}C ages on shells from loess sequence studied in the Rhône Rift Valley does not allow us to detect systematic mollusc species' specific age offsets depending. Bioturbation and/or sediment reworking, for instance, due to slope wash and deflation likely contributed to the age scatter. Overall, the chronological data points to an end of MIS 3 to MIS 2 age for the deposition of the upper loess horizons, which is consistent with other regional data (Bosq et al. 2020b), as well as elsewhere in Europe (Antoine et al. 2016; Lehmkuhl et al. 2021).

5.5 Discussion

5.5.1 Soil and sediment formations and their palaeoenvironmental interpretation

Texture of Baix

Most samples from horizons of pedogenetically little to unaltered loess (C, CB, BC) show unimodal grain-size distributions with a peak in the coarse silt fraction (~44–50 μm), which is also dominant in pedogenetically overprinted loess (Bw, Bt(g)) (Fig. 5.70). The dominating coarse silt mode suggests one regional source and deposition during severe cold phases (Vandenberghe, 2013). In the literature (Tsoar and Pye, 1987; Vandenberghe, 2013; Újvári et al. 2016a), this coarse silt fraction is defined to be short transported within near-surface clouds, whereas as the closed by source area assumed to be bare alluvial or fluvio-glacial sediments that were eroded originally from glaciated mountains and subsequently redistributed by rivers. These findings agree with Bosq et al. (2020a, 2020b), who suggested that the floodplain of the Rhône River was the main particle source. The local relief with its NSW-oriented limestone ridge advanced the accumulation of loess at the lee-position of the slope, assuming prevailing northern winds (Pfaffner et al. 2024). According to the observed asymmetry of aeolian deposits with silt loess depositions over fluvio-glacial fans to the north of Valence and sandy loess to

the south, the LPS Baix coincides with the “northern Rhône Graben type” of Bosq et al. (2018, 2020b), Bertran et al. (2021) or the subdomain IIIa according to Lehmkuhl et al. (2021).

The tailing at the middle/fine silt and clay fractions may be attributed to a long-term suspension in the atmosphere, weaker wind activities or to transported silt-and/or sand-sized aggregates (Tsoar and Pye, 1987; Pye, 1995; Vandenberghe, 2013) or to post-depositional weathering processes (Bronger, 1976; Újvári et al. 2016a; Schulte et al. 2018; Bosq et al. 2020b; Sprafke et al. 2020). Pedogenesis in loess sediments is known to favour grain size variation due to a decrease of the coarse silt proportion to enhance medium/fine silt and clay proportions (Sun et al. 2000; Günster et al. 2001; Újvári et al. 2016a; Wacha et al. 2018). These findings concur with subpopulations observed in the palaeosols and the Holocene soil, which display the main mode at the coarse silt fraction, high amounts of fine-/middle silt in the Bw horizons and fine clay proportions in the Bt horizons (Figs. 5.70, 5.71).

Furthermore, within the loess horizons from bottom to top, an increase in GSI and U-ratio combined with a decrease in the silt proportion and an increase in the fine sand proportion was observed (Fig. 5.71). Similar trends of upward GS coarsening were observed in comparable units of the LPS Lautagne (Bosq et al. 2020b), possibly in grain-size zone 2 of the LPS Val Sorda (Ferraro, 2009), in Croatian LPSs of Susak (Wacha et al. 2018) and central European LPS (Antoine et al. 2001, 2009a; Schirmer, 2016; Fischer et al. 2019). General explanations of coarsening are increased local wind intensity and source material (Rousseau et al. 2002; Antoine et al. 2009a; Wacha et al. 2018). An increased wind speed seems likely as the median and mean grain-size and GS ratios increase gradually, as well as the Si/Al ratio in the upper loess horizons (Figs. 5.71, A5.75). However, another possible explanation could be a change in the vegetation cover (Tsoar and Pye, 1987; Bosq et al. 2018; Bertran et al. 2021). The Rhône Rift Valley, especially the riparian and basin areas, is considered as refugia for higher developed vegetation (tree, shrubs) during stadial periods, especially during the last glacial period (Beaudouin et al. 2007; Tzedakis et al. 2013). Thus, in accordance with an observed increase of SOC contents, coarsening of GS caused through trapping by shifts to taller developed vegetation seems to be a considering factor (Field et al. 2012). This observation was also implemented in the sediment depositional model suggested by Bosq et al. 2018, who assign a prominent role to the vegetation cover in the Rhône Rift Valley.

Loess horizons of Baix LPS

The loess horizons are generally characterised by increased accumulation (peaks of U-ratio, GSI, highest primary carbonate contents) induced by increased aridity. Although, the gradual leaching of calcic carbonate with depth, appearance of secondary carbonate nodules of various sizes, weak shifts in the weathering ratios and fluctuations of SOC contents as well as chromatic parameters a^* and a^*/b^* indicate different intensities of initial soil formation during

continuing loess deposition (Fig. 5.71). Thus, syn-sedimentary soil development is assumed, with changing weathering intensities reflecting variations in temperature and humidity during generally cold and dry conditions. Therefore, Ck horizons are interpreted to reflect most cold and arid conditions, indicated by peaks of U-ratio, GSI and chromatic b^* values and least weathering with zero SOC contents as well as least fluctuations of Mn_d/Mn_t ratios (Fig. 5.71). Shifts from coldest and driest to less severe, milder, and humid climate conditions are reflected by increasing SOC contents and CPA values and decreasing WI_{MER} values. The gradual changes of slightly weathered sediments are represented by CBk to BCK to Bw horizons. The mixed sediment horizons (6 BCK/Btg, 4 BCK/Bw) are characterised by abrupt changes of the GSD (increased U-ratio, GSI, Si/Al), lower a^* and a^*/b^* ratio and low weathering (lower CPA, Fe_d/Fe_t , higher WI_{MER}), which indicates a climatic deterioration triggering erosion and re-accumulation of soil material and the recurrence of aeolian processes (Figs. 5.71, 5.75).

The upper loess horizons with lacking palaeosol formation, are typical for the Rhône Rift Valley and agree with the findings of Bosq et al. (2018, 2020b). The gradual shifts of weathering ratios, $CaCO_3$, and SOC contents of the two superimposed horizons (3 BCK3, 2 BCK2) indicate varying humid conditions during syn-sedimentary processes of continuous loess accumulation and primary carbonate leaching. Slightly enhanced CPA, lower WI_{MER} and L^* values within the horizon boundary of 2 BCK2 to 3 BCK3 may implies the existence of a further Bw horizon (Fig. 5.71). However, this could also result from the underlying upper interstadial complex. Their proxies' overlaying loess horizons reflected decreasing humidity and increasing aridity (Fig. 5.71).

Within the loess horizons, but also throughout the entire profile, no lamellar, platy/prismatic structures, cracks, ice-wedge cast, or other features related to frost-thaw processes can be found. The missing features are attributed to less dry, cold climate conditions during loess accumulation phases, according to the suggested maximum extension of permafrost south of 47° N (Andrieux et al. 2016). Thus, solifluction processes in Baix are rather reduced, and reworking of the sediment seems to reflect runoff/sheet wash processes during climate deterioration and/or rainstorm/snowmelt events. Considering the relief position, GS distribution and gravel contents, these sediments originates from short-distance slope wash processes of changing intensities.

(Palaeo)-soil of Baix LPS

Interglacial soil complex

The horizons of the Interglacial soil complex are characterised by decalcification, intense chemical weathering (highest Fe_t , Fe_d/Fe_t ratio, Mn_d/Mn_t , CPA and lowest WI_{MER} , Si/Al) and slight rubefication with maximum values of chromatic value a^* and a^*/b^* ratio (Fig. 5.71). The

lowermost 8 Bt2 horizon displays the highest amounts of clay (18 %), and is interpreted as a reworked horizon, whereas highest clay proportions are most likely induced by local long-term weathering of the debris rather than intense pedogenesis (Pfaffner et al. 2024). In contrast, the overlying 7 Bt(g) horizons display the highest fC/cC ratio and showing in situ clay coatings suggesting in situ lessivage (clay migration) processes, inducing a Luvisol (Figs. 5.71, 5.72q, 5.72s). The intensity of pedogenesis of the loess sediment by silicate weathering (commonly micas and feldspars) and the formation of secondary clay minerals is favoured by warm and humid climate conditions.

The slight rubefication of the Interglacial soil complex coincide with European LPS (e.g., Nussloch: “brown red clay coatings”) (Antoine et al. 2001). In contrast, chromic characteristic or red/rubefied colours were described at the LPS of the Mediterranean (Ferraro, 2009; Wacha et al. 2011b; Boixadera et al. 2015, Durn et al. 2018a, Zhang, 2018, Bosq et al. 2020b). Two assumptions are possible for the slight rubefication of Baix LPS: i) the climate conditions were the same as in Europe ii) the position of the Baix LPS at the slope foot may favoured moisture availability and necessary dry periods for the rubefication process was not given. So far no other in situ last Interglacial soil within LPS in this climatic transition zone was described. However, from other nearby archives Mediterranean climate conditions has been described (Beaulieu and Reille, 1984; Tzedakis, 2007 Valladas et al. 2008; Rivals et al. 2009; Moncel et al. 2015), thus we tend to assumption two.

The observed weakly developed soil structure of the Bt(g) horizons, the fluctuations of weathering indices and fine and medium clay particle-sized proportions as well as the different layers of clay coatings indicate a polygenetic soil formation (Figs. 5.71, 5.72d). Thus, we assume that relocated pre-weathered soil sediment of a previous Luvisol formation was possibly subjected again to clay illuviation, filtrating down, and forming with the lower 7 Bt1 horizons a dense substrate, which slowed down soil water circulation and promoted the formation of hydromorphic features. Whether (seasonally) stagnic conditions are induced by underlying dense soil material or by a change of the moisture regime is difficult to determine. However, the Fe coatings as a last “layer” within the pore walls of the 7 Btg horizons support the idea of changing moisture conditions (Fig. 5.72q, 5.72s). Anyhow, the relocation of pre-weathered soil material indicates a climatic deterioration followed by a stable period with climate conditions intense enough to allow renewed clay illuviation to form a polygenetic Stagnic Luvisol. Polygenetic Luvisol formation is described for various European and Mediterranean LPS (Antoine et al. 1999, 2001; Günster et al. 2001; Ferraro, 2009; Haesaerts et al. 2016, Kehl et al. 2024).

Lower interstadial soil

The lower interstadial soil is represented by a decalcified two-parted brown 6 Bw3 horizon (Pfaffner et al. 2024). The weathering ratios and the peak of fine silt proportion (subpopulation of GSD ~5–12 μm) reflect pedogenesis intensities corresponding to characteristics of a Bw horizon (FAO, 2006) (Figs. 5.70, 5.71). The lower part of the 6 Bw3 horizon displays relocated reddish aggregates and depleted zones similar to the 7 Btg horizon of the Interstadial soil complex as well as in situ clay-silt coatings (Figs. 5.72c, 5.72k). We assume that the Bw formation began within the relocated, pre-weathered soil material and was followed by syn-sedimentary processes of sediment deposition and carbonate leaching, explaining the upwards decreasing pedogenesis. Thus, the climate conditions seemed to be favourable (humid) enough to allowed clay-silt coatings to develop.

Upper interstadial soil

This soil unit developed, a strongly through slope wash, reworked loess sediment, reflected by a poor GS sorting and peaks of mean GS and median GS (Figs. 5.71, A5.75). The decalcified 5 Bw2 horizon displays similar characteristics (equal values of W_{MER} , CPA, clay contents, peak at fine silt proportion, U-ratio, GIS, silt-clay coatings along with pores) as the lower 6 Bw3 horizon, implying similar climate conditions during soil formation (Figs. 5.71, 5.72b, 5.72j). Similar characteristics of this Bw horizon were observed in the LPS Collias further south of France (Bosq et al. 2020b). Bosq et al. (2020b) suggested an interplay between soil formation and moderate loess deposition rates. The fresh loess input induced an upward growing soil surface and addition of primary carbonates, while soil formation involved leaching these fresh inputs and accumulating secondary carbonates within lower horizons (Bosq et al. 2020b). However, the complete decalcification of the 5 Bw2 horizon and the occurrence of prominent carbonate nodules in one specific depth at Baix (~850 cm) indicates at least one soil formation phase of increased humid conditions without loess input. We assume, that the intensively weathered upper soil part was truncated.

Holocene soil

A Cambisol formation reflects the recent soil formation. Compared to the lower palaeosol Bw horizons (6 Bw3, 5 Bw2), the recent Bw1 horizon is not completely decalcified, and lower weathering ratios may reflect less intense weathering (Fig. 5.72a, 5.72g). This observation may suggest less moisture or enhanced evapotranspiration for the recent climate conditions. However, time needs to be considered, as the soil had less time to evolve. Furthermore, a repeatedly well-known surface disturbance due to, e.g., agricultural use is expected, which prevents the formation of more intense soil features (e.g., decalcification, forming aggregates) and complicates the comparisons with Holocene soil formations from other LPS.

5.5.2 Chronostratigraphy of Baix LPS and comparison with other European LPS

Last Interglacial (Eemian) and Early Glacial

The lowermost sample (OSL 1) collected from the likely last Interglacial (Eemian, MIS 5e) palaeosol gives a pIRIR-age of 117.5 ± 9.7 ka (Fig. 5.73). However, as detailed by Pfaffner et al. (2024), stagnic conditions are most likely for most of the time during the year for the lowermost part of the profile, if not since sediment deposition then since the formation of the clay rich subsoil (7 Bt1, 8 Bt2) and the underlying pedogenic carbonate crust, i.e., likely since Eemian times (ca 126–115 ka; in the Mediterranean likely until 110 ka (cf. Sánchez-Goñi et al. 1999). Therefore, Pfaffner et al. (2024) assumed a soil moisture content of $\Delta 1.28 \pm 0.05$ for the lowermost section of the main profile. Adopting this value for the present study would yield an age of 128.5 ± 10.5 ka, conforming the field assumption. Thus, the 7 Bt1 horizon correlates with the Eemian (MIS 5e; GI 25) and is in accordance with reconstructions from other European LPS (Bourdier, 1958; Bonifay, 1965; Rose et al. 1999; Antoine et al. 2001; Ferraro, 2009; Wacha et al. 2011a, 2011b; Boixadera et al. 2015; Schirmer, 2016; Bosq et al. 2020b).

Considering the determined characteristics of the superimposed 7 Btg horizon, the topographic position and its widely scattering OSL screening data, the sediment in which the horizon formed, is assumed to be relocated concerning OSL analyses likely insufficiently bleached, Eemian soil material (Fig. 5.73). Relocation and subsequent soil phases, which induced the polygenetic, Stagnic Luvisol, can be correlated most likely with the known stadial phases of MIS 5 d/b and interstadial phases MIS 5 c/a (Fig. S5.131). The hydromorphic features are suggested to be caused by humid conditions, which were also observed in LPS between Cadarache and Saint-Estève (Durance Valley, southern Rhône Rift Valley) (Bonifay, 1965; Mologni et al. 2021). In contrast, western and central European LPS suggest more continental (drier) conditions, represented by several interlaced humic horizons (Fig. 5.74) (Antoine et al. 2001, 2016; Haesaerts et al. 2016; Schirmer, 2016).

Concluding, the interpreted MIS 5 climate conditions at Baix were characterised at the beginning by a stable interglacial warm-temperate climate, which decreased gradually to glacial cold and arid conditions. On the one hand, the deterioration was marked by cold and dry climate conditions (first erosion with subsequent loess deposition), similar to central European LPS. On the other hand, stable phases with increased humidity and temperature are intense enough to introduce a polygenetic Stagnic Luvisol (MIS 5d-a). Similar pedostratigraphic units for the MIS 5 are described from LPS of south France (Bonifay, 1965; Bosq et al., 2020b), Spain (Lachar LPS) (Günster et al. 2001) and Croatian LPS of Susak (Wacha et al. 2011b; Profe et al. 2018). Thus, compared to central European LPS, where increasing continentality is represented by up to three humus-enriched horizons (e.g. Bettencourt soil overlaying St. Sauflieu complex, upper Rocourt pedocomplex overlaying humus complex of

Remicourt, the upper part of Garzweiler pedocomplex, Mosbacher humus zones) the LPS Baix reflects more humid conditions during soil formation phases, which decreased gradually within the climatic deterioration (Antoine et al. 1999, 2016; Schirmer, 2002, 2016; Frechen et al. 2007; Lehmkuhl et al. 2021).

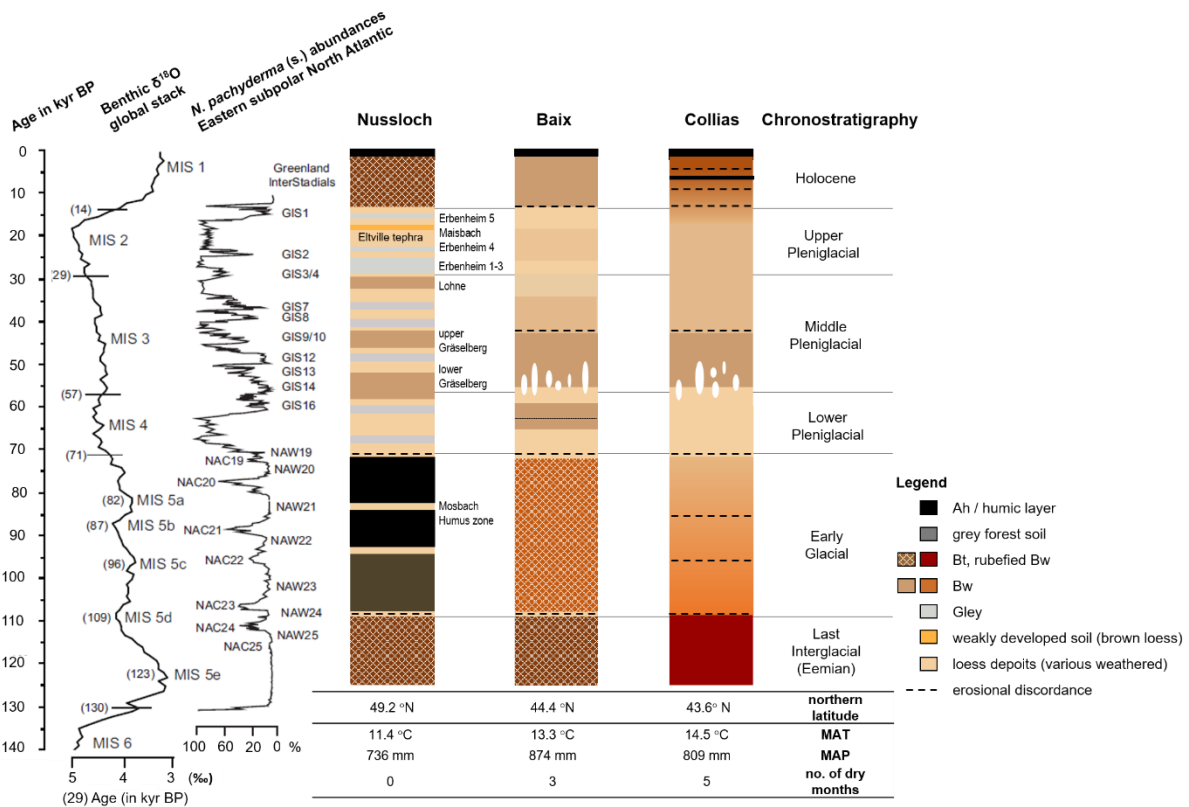


Figure 5.74: Compiling figure of marine and ice-core chronostratigraphy for the last 140 kyr, including Marine Isotope Stages (MIS) derived from global benthic stack (Lisiecki and Raymo, 2005), North Atlantic Cold (NAC) and North Atlantic Warm events (NAW) and Greenland interstadials (GIS) (Johnsen et al. 1992; Dansgaard et al. 1993; McManus et al. 1994) modified from Helmens (2013). The author combined data from North Atlantic cores to the curve of *N. pachyderma* abundances and Eastern subpolar North Atlantic and stretched the curve minimal for the time-intervals between 130–75 kyr BP and between 75–60 kyr BP to obtain a better match with the NorthGRIP time-scale (North-GRIP Members, 2004). Right: Generalised loess palaeosol-sequence (LPS) of Nussloch (Antoine et al. 2001, 2009a; Kadereit et al. 2013) and LPS Baix and LPS Collias (Bosq et al. 2020b) emphasising on soil formation phases during chronostratigraphical stages of the Late Pleistocene with their latitudinal position, recent mean annual temperature (MAT), mean annual precipitation (MAP) and number of arid months (dwd, 2021a, 2021b; meteo-france 2022a, 2022c).

Early Glacial to Lower Pleniglacial

The OSL sample (OSL 2) from the 6 BCK/Btg horizon gives an age of 67.0 ± 5.7 ka which corresponds to the transition from the Early Glacial (MIS 5d-a) to the Lower Pleniglacial (MIS 4), a period of widespread sediment reworking commonly found in the western and central parts of the European loess belt in the temperate zone (e.g., Keldach discordance and Niedereschbach zone; Hermies, Harmignies colluvial deposit) (Semmel, 1998; Antoine et al. 2016; Lehmkuhl et al. 2016). It possibly conform with the GS 19.1 (cf. Fig. S5.131). Indications

of sediment reworking was observed also for the respective part of the LPS Baix both during the field analysis of the profile (Pfaffner et al. 2024). Therefore, tentatively we propose a supraregional period of sediment reworking during MIS 4 (71–57 ka) spanning not only larger parts of central Europe as suggested by numerous previous studies but covering also the northern part of the Rhône Rift Valley as evidenced here for the first time by the LPS Baix.

The next-upper OSL-block sample (OSL 3) gives an age of 59.8 ± 5.3 ka, which fits late MIS 4 (71–57 ka) or the transition MIS 4/MIS 3 (Fig. 5.73). The time of sediment reworking could possibly conform with GS 15, 16, 17 and/or 18 and/or Heinrich (H) 6 event. The age of sediment deposition narrows down the time window for the development of the 6 Bw3 palaeosol remains beneath. The age suggests soil development during the later part of MIS 4 and/or the beginning of MIS 3. We assume, that after relocation of the interglacial soil and loess sediment-mixture, the (re-)formation of the 6 Bw3 horizon began in the climatically mild excursions of GI 18, or more likely GI 17.2–GI 16.1 a (or GI 15.1) and continued as syn-sedimentary process within a younger phases (Fig. S5.131). If soil formation started in GI 18, Heinrich 6 event corresponding to GS 18 could possibly also explain the bipartitioning of 6 Bw3. For central Europe MIS 4 to MIS 4/MIS 3 palaeosol relicts of the Cambisol or Regosol-Cambisol types have been evidenced at several LPS sites (e.g. Gräselberger Soil, Semmel 1968; Jackerath Soil, Reisberg Soil Schirmer 2002; Havrincourt, Antoine et al. 2016; Malplaquet Soil, Haesaerts et al. 2016; stratigraphic units 12, 20, 23 and above the MIS 4/MIS 3 boundary unit 26, all remains of the Calcaric Cambisol type (Bw), Fischer et al. 2021). Whereas the temporal positioning of some soils seems clear (e.g., Jackerath Soil in the Lower Pleniglacial (MIS 4)), at other sites the allocation appears less unequivocal, but suggests a temporal placement somewhere near the MIS 4/MIS 3 boundary (cf. Lower Gräselberg Soil, Antoine et al. 2009a; Lower Remagen Soils, Schirmer 2012), which may resemble more the situation at Baix.

So far, to our knowledge, palaeosol formation during MIS 4 in the Mediterranean loess-palaeosol landscapes have been only identified for the Bok section in terms of thin brown palaeosols (Wacha et al. 2011a). Also an orange-brown palaeosols of the Bok section 1 (Wacha et al. 2011b) is assumed to have developed after 98.3 ± 7.3 ka and prior to 54.3 ± 4.9 ka (not only during MIS 5c – 5a but also later during MIS 4) and therefore may correspond to the brown horizon identified at the LPS Baix. Thus, the LPS Baix serve as an further important stratigraphic link between the central European and the Mediterranean loess-palaeosol landscapes for last glacial Lower to Middle Pleniglacial times and the lowermost last glacial brownish soils of the Cambisol type (here 6 Bw3) may be used as a (set of) marker horizon(s) for a quick stratigraphic orientation in the field.

Lower Pleniglacial to Middle Pleniglacial

The pIRIR ages gained on the upper three OSL block samples have to be transferred from the minor profile to the main profile (Figs. 5.69, 5.73). The OSL 6 sample assigned to the 5 Bk2 horizon produced an age of 54.8 ± 5.2 ka. The OSL age overlaps within error margins with the age from 5 Bck5 right above the MIS 4 marker soil horizon (6 Bw3). Sedimentation rates between OSL 3 and OSL 6 increase by a factor of ca 3.6 as compared to those between OSL 2 and OSL 3. Therefore, it is likely that both sediment units (in which 5 Bck5 and 5 Bk2 developed), and those in between, represent a relatively short period of intensive sediment reworking. This is similar to the site Collias where OSL ages of 55.5 ± 4.4 ka and 55.1 ± 4.1 ka represent ca 2 m sediment deposits between ca 5–3 m b.g.l. (Bosq et al. 2020b). For Baix the OSL ages of OSL 3 and OSL 6, which cover a depth of ca 2.6 m between 10.6–8.0 m b.g.l., suggest a sedimentation rate of ca 0.5 m ka^{-1} . At both sites, Collias and Baix, coarse clasts point to sediment reworking by slope wash processes. The sediment sequence in between the OSL samples 3 and 6 does not exhibit any soil horizons showing browning or loaming which could point to intermediate periods of mild climate excursions.

Yet soil formation leading to the brownish MIS 3 soil with the prominent carbonate concretions in the corresponding Bk and Bck horizons could possibly have started in GI 15.1, or more likely in GI 14 (Fig. S5.131). Also similar to Collias, the OSL age of sample OSL 7 from Baix, collected from the slope-washed, pre-weathered 3 Bck3 loess horizon points to an end of the formation of the prominent MIS 3 palaeosol prior to 37.5 ± 3.1 ka, perhaps during GS 9 and/or Heinrich 4 (40.2–38.3 ka) (Figs. 5.73, S5.131). Therefore, it is likely that the prominent MIS 3 soil, as identified at Baix and Collias, represents a pedo-complex possibly spanning (GI 15.1 or) GI 14–GI 9. A similar, intensive red-brown soil horizon, including carbonate nodules, is described on Susak Island (Wacha et al. 2011b, 2018; Zhang et al. 2018). Furthermore, a comparably intense developed brown truncated soil horizon (Cambisol) is found in most of the European LPS (although without the description of the carbonate nodules), i.e. in northern and southern France (e.g. Saint-Acheul/Villiers-Adam soil complex) (Bonifay, 1965; Antoine et al., 2003, 2016), Belgium (Les Vaux) (Haesaerts et al. 2016) and in Germany, sometimes preserved in several brown soil horizons (e.g., Remagen Soils, Gräselberg Soils) (Antoine et al. 2001; Schirmer, 2002, 2016; Frechen et al. 2007; Gocke et al. 2014; Fischer et al. 2021) (Fig. 5.74). Thus, the striking Cambisol soil complex at Baix may be regarded as a stratigraphic marker horizon within the Rhône Rift valley and serve as a Middle Pleniglacial-unit for supra-regional correlation of central European and Mediterranean LPS.

As at both sites, Baix and Collias, significant soil formation could not be detected above the MIS 3 Bw palaeosol remain with the prominent carbonate nodules in the corresponding Bk horizon beneath, it seems that Baix does not conform with the central European loess

landscapes after ca 40 ka (Heinrich 4 event; GS 9), but conforms to the Mediterranean pattern, where the lack of sufficient humidity likely prevents intense soil formation leading to the development of diagnostic horizons.

In Mediterranean LPS, the upper MIS 3 soils are highly diverse depending on their geographical and geomorphological position (Brunnacker, 1974; Coudé-Gaussen, 1990). Thus, soils vary from up to three Chernozem palaeosols in Italy (Ferraro, 2009, Pasquetti et al. 2023) to up to four thin brown soil horizons in the Susak LPS (Wacha et al. 2011a). For the northern Rhône Rift Valley, Franc et al. (2017) also described a correlating brown soil, whereas complementary horizons seem to be challenging to determine (Bourdier, 1958; Bonifay, 1965) or also missing in LPS of the southern Rhône Rift Valley (Bosq et al. 2020b). At Baix, it is challenging to identify a separate upper MIS 3 soil formation as brown aggregates could belong to the older underlying Cambisol or possibly to a younger formation. Anyhow, as younger MIS 3 soil formation are difficult to identify or may not exist, the upper MIS 3 at the middle Rhône Rift Valley (transition zone) may seem to be influenced by more constant climate conditions, in contrast to Italy and Croatia with more pronounced shifts, and also central European LPS, which exhibit further (boreal) Cambisol formations (Antoine et al. 2001; Ferraro, 2009; Wacha et al. 2011b; Kadereit et al. 2013; Schirmer, 2016; Fischer et al. 2019).

For the central European loess landscapes formation of soils of the Cambisol type is typical for the milder climate periods GI 8 to GI 4 (ca 38–29 ka) during MIS 3, which at several sites has led to the formation of the Lohne Soil complex or its equivalents e.g. Sinzig Soils, upper part of the Saint-Acheul/Villiers-Adam soil complex (Antoine et al. 2001; Schirmer, 2002, Kadereit et al. 2013; Moine et al. 2017; Fischer et al. 2019). Thus, times favourable of soil formation (and soil conservation) appear to alternate between the Mediterranean (early MIS 3 prior to Heinrich 4 event) and the central European loess landscapes (later MIS 3, after the Heinrich 4 event).

Middle Pleniglacial to Upper Pleniglacial

Another time mark of $ca\ 35.8 \pm 3.2$ ka is given by sample OSL 8. The data point is situated already above the level of the OSL screening, which ended slightly above the sample point of OSL 7. For the two subsamples at the uppermost end of the sediment column sampled in flower boxes it could not be decided whether they indicate a trend towards smaller “ages” or whether they represent mere scattering (Pfaffner et al. 2024). However, AMS ^{14}C ages derived from the loess horizons are correlating with the middle to end of the MIS 3 and MIS 2 (Fig. 5.73). The pIRIR ages of ca 38 ka and 36 ka of the block samples OSL 7 and OSL 8 support the assumption of a trend towards smaller ages in the upper part of the 3 BCK 3 horizon.

Rates of sedimentation, derived from thicknesses of loess, are challenging to determine as generally intense erosional processes are expected in the region. Nevertheless, the sedimentation rates of ca 0.6 m ka⁻¹ appear comparatively high with a factor of ca 9.5 times larger than between OSL 6 and OSL 7 which frame the MIS 3 soil formation period. Although MIS 3 ends and MIS 2 starts at 29 ka, the terrestrial systems often respond to some kind of climate triggering already a few thousand years earlier (Lüthgens et al. 2011). Ca 39–37 ka, the sedimentation rates seem to be quite high also at Collias (ca 0.6 m ka⁻¹). The combined effects of climate deterioration of GS 9 and Heinrich 4 event may have triggered palaeoenvironmental conditions favourable for dust deposition. Greenland stadials and especially Heinrich events led to dramatic decline of forest vegetation and established semi-desert vegetation (Fletcher and Sánchez-Goñi, 2008). Recent publications suggest for the Mediterranean glacier retreat during Heinrich events due to aridity (Allard et al. 2021), but also an increase of areas affected by permafrost and frost weathering as well as high sediment load of Mediterranean rivers (e.g. Woodward et al. 2008; Lewis et al. 2009), which function as dust source areas when drying out. Glacier advance during the milder excursions may lead to dust input also during the periods more favourable for pedogenesis and explain, e.g., the fading out of the 6 Bw3 horizon at its top. With respect to the LPS Baix it is interesting to note that coarser clasts, pointing to sediment reworking by slope wash processes, which are typical for the lower part of the profile are no longer present in the upper 7 m.

Aeolian input of mainly silt and sand sized grains becomes dominant from ca 36 ka onwards. In this respect the LPS Baix correlates to the central European system in terms of recorded acceleration of loess input rates (Antoine et al. 2009a, 2016; Ferraro, 2009; Bosq et al. 2018, 2020b). As stated before, in the upper loess horizons at Baix LPS, no further (weak) soil formation, e.g. tundra gley soils, especially redoximorphic features related to freeze-thaw dynamics, was observed as they are, in contrast, described for the Lyon region and the southern Durance valley (Bonifay, 1965; Franc et al., 2017) or central European LPS (Antoine et al. 2001, 2016; Rousseau et al. 2002; Schirmer, 2016) (Fig. 5.74)). Thus, earlier suggested less severe climate conditions during loess accumulations in the northern Mediterranean LPS region (Brunnacker, 1974; Coudé-Gaussen, 1990; Ferraro, 2009; Wacha et al. 2011b) as compared to central Europe conditions, agrees with observations at Baix.

5.6 Conclusions

The generally more disturbed characters of Mediterranean LPS caused by reworking and (bio-) turbation creates a challenging setting for pedo- and chronostratigraphic analyses and interpretation. Despite the encountered difficulties, we have shown that the well resolved and profound examination of the LPS Baix made it possible to extract relevant information. Our findings agree with described LPS further south and north and showed that the LPS Baix is a

relevant terrestrial palaeoarchive of the Last Interglacial-Glacial cycle with the potential to link the loess-palaeosol landscapes of the Mediterranean zone to those of the temperate zone. In summary, the main loess accumulation phases occurred during MIS 4 and MIS 2 periods. The unimodal GSD correlates well with characteristics of central European LPS, and the loess accumulation was mainly controlled by the local wind regime, the topography and vegetation cover. The general pedo-stratigraphy of the LPS Baix agrees with the known supra-regional European pedo-stratigraphy of the Last Interglacial-Glacial cycle. However differences in their characteristic are due to the geomorphological and latitudinal position and following conclusions can be drawn:

- I. A well-preserved record of the Eemian and Early Last Glacial period (MIS 5) with a polygenetic, slightly rubefied Stagnic Luvisol verifies a warm-temperate climate with changing humidity followed by a gentle/slow climatic deterioration in terms of humidity and temperature. Within the N-S transect the intensity of rubefication seem to increase southwards into the Mediterranean. Although a northern expansion of Mediterranean conditions during the Eemian solely based on the soil characteristics (intensity of rubefication) of Baix could not be conclusively verified, other archives do support a northwards expansion. Within the following climate deterioration the entire Rhône Rift Valley was marked by more humid and temperate conditions compare to more arid and colder conditions of central European, mostly reflected by humic-rich layers.
- II. A brown two-parted Bw horizon referring to the late MIS 4 and/or beginning of MIS 3. Within the syn-sedimentary processes of loess accumulation and primary carbonate leaching, humid phases allowed the formation of a brown silt-clay ground matrix.
- III. A pedo-stratigraphic marker horizon of a Calcic Cambisol complex formed during the beginning and middle MIS 3. In contrast to the temperate zone, this marker horizon is in the Mediterranean and at Baix, associated with an underlying horizon with prominent carbonate nodules, suggesting at least one intense humid phase. As the observed carbonate nodules are missing or have not been described for MIS 3 soils in central European LPS, we attributed this feature to a more intense humidity during the early and mid MIS 3, in contrast to central Europe.
- IV. During the generally cold and arid conditions of the MIS 4 and MIS 2 aeolian inputs of mainly silt and sand sized grains becomes dominant and thus compares with central European systems. However, manifold tundra gleys which are typical of the central European LPS and which may serve as marker horizons for the correlation of the sections representing the Last Glacial Maximum (LGM) of the LPS are absent at Baix due to the lack of permafrost. The area's less severe conditions during the coldest glacial periods are also one of the main reasons for intensified bioturbation and

sediment reworking by slope-wash processes. In this respect the LPS Baix resembles the LPSs of the Mediterranean loess landscapes.

- V. The recent Cambisol formation appears less intensively weathered than all observed palaeosols, but variable anthropogenic disturbances have led to erosion and rejuvenation. Therefore, it is difficult to evaluate whether the clay-rich and -illuviated Last Interglacial soil represents the potential outcome of present-day soil-forming conditions or whether it instead shows an equivalent that might develop under ongoing climate change, as modelling of both Eemian climate and future climate change result in similar temperature increases as compared to the present.

Thus, Baix displays characteristics of both central European and Mediterranean LPS “representatives” and announced transition zone from Brunnacker (1974), Bosq et al. (2018, 2020b) and Lehmkuhl et al. (2021) (subdomain IIIa to VIa) at Valence area agrees with proposed findings. Finally, our study provides new and unique information for correlations of the loess palaeosol-stratigraphy of the Last Interglacial-Glacial cycle in south-eastern France.

Acknowledgement

We are very grateful to Monsieur L. Garnier for allowing us to prepare the profile in his quarry. We thank Dr. Barbara von der Lühe for the help in the field, and Dr. Volker Karius, Dr. Jürgen Grotheer, Anja Södje, Petra Voigt, Marius Friedrich and Jutta Asmuth for the laboratory analyses. We thank Dr Sophie Cornu to provide us with high resolution DEM data (5 m x 5 m) of France. We acknowledge the German Aerospace Centre (DLR), which provided the TanDEM-X data for the study area (DEM_GEOL1263). Sebastian Kreutzer was supported by the European Union’s Horizon 2020 research and innovation programme under the Marie Skłodowska-Curie grant agreement no. 844457 (CREDit).

Funding

This work was funded by the University of Goettingen.

Conflicts of Interest

The authors declare no conflict of interest.

Appendix

A5.4 Results

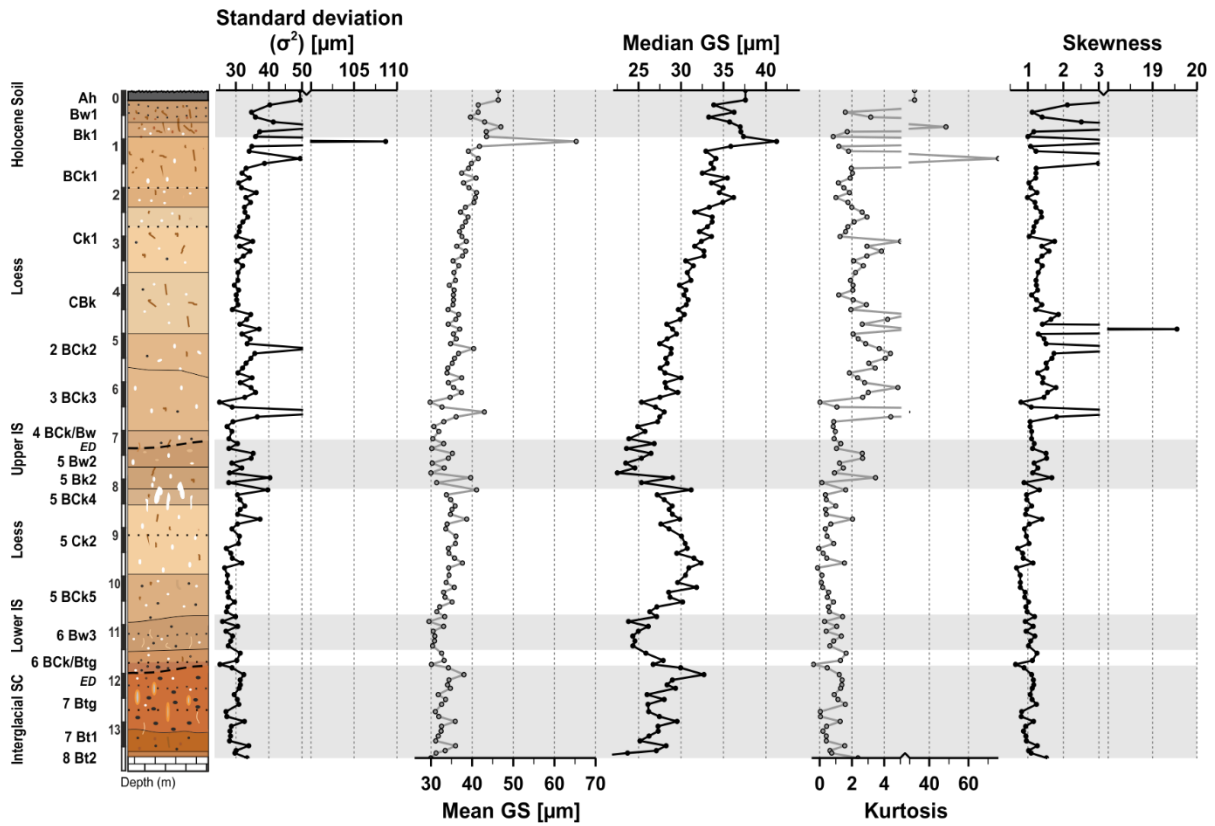


Figure A5.75: Loess-palaeosol sequence Baix, Rhône Rift Valley, SE France with soil formation units marked as grey bars and depth profiles of statistical parameters of standard deviation, mean and median grain-size in μm , kurtosis and skewness.

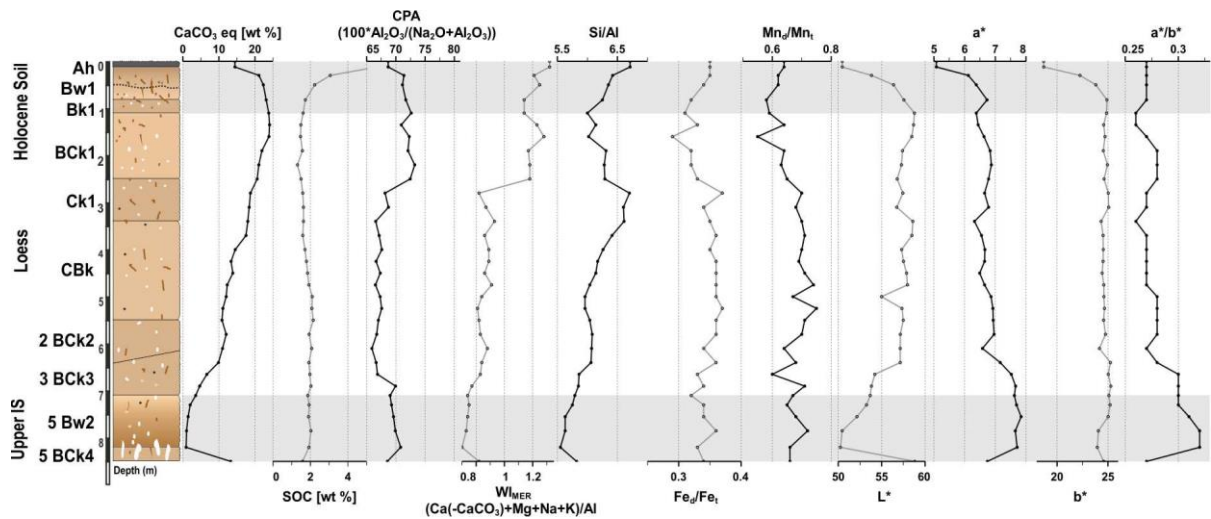


Figure A5.76: Loess-palaeosol sequence (LPS) Baix west, Rhône Rift Valley, SE France with soil formation units marked as grey bars. Depth related curves of calcic carbonate equivalents in wt %, contents of soil organic carbon (SOC) in wt % and chemical proxy of alteration (CPA) ($100 \cdot \text{Al}_2\text{O}_3 / (\text{Na}_2\text{O} + \text{Al}_2\text{O}_3)$), weathering index of molar element ratio (W_{MER}) (Ca (after subtraction of Ca in CaCO_3) + $\text{Mg} + \text{K} + \text{Na}$) / Al), Si/Al and, ratios of pedogenic to total contents of iron and manganese (Fe_d/Fe_t , Mn_d/Mn_t) and colours of the CIE colour index, reflected by the parameters L^* , a^* , b^* and ratio of a^* and b^* .

Supplement

S5.3 Material and methods

Table S5.24: Scheme of OSL sampling and sample preparation from loess-palaeosol sequence Baix, Rhône Rift Valley, SE France.

Sampling in the field	
	<ul style="list-style-type: none">• Collect samples in opaque metal cylinders, metal boxes, PE liner-tubes or similar• Carve out larger blocks (dried/hardened sediment only)
Sample preparation in the luminescence laboratory under strongly subdued red light	
[1]	<ul style="list-style-type: none">• Eliminate outer, potentially light affected sample rims<ul style="list-style-type: none">○ Retain not light-affected sample for luminescence dating (1)○ Retain outer sample rims for dose rate determination (2) (not further considered in this work flow)
[2]	<ul style="list-style-type: none">• Use (1) and determine sample's wet weight• Use (1) and dry at 50 °C; weigh repeatedly until no further loss of weight is observed (3)• Determine sample's water content (wet weight : dry weight; needed for dose rate determination)
[3]	<p>Only if there is a surplus of fine-grained material (silt, clay) and little coarse-grained material (fine sand)</p> <ul style="list-style-type: none">• Use dried inner sample part (3) and dilute in aqua_{demin}; separate muddy components (3a) from coarser components (3b); proceed with steps [4]–[7] on the two fractions (3a) and (3b) separately• Proceed with dried inner sample part (3); or with subfractions (3a) and (3b), respectively
[4]	<ul style="list-style-type: none">• Eliminate carbonate content with acetic acid (CH₃COOH; 20 %); rinse with aqua_{demin} (4)
[5]	<ul style="list-style-type: none">• Eliminate organic content with hydrogen peroxide H₂O₂ (10 % and 30 %); rinse with aqua_{demin} (5)
[6]	<ul style="list-style-type: none">• Disperse sample (5) with sodium oxalate (Na₂C₂O₄, 0.01 N); rinse with aqua_{demin} (6)
[7]	<ul style="list-style-type: none">• Sieve sample (6)<ul style="list-style-type: none">○ For coarse grains with mesh sizes of 212 µm and 125 µm; retain fraction < 125 µm (7); retain fraction 125–212 µm (8)○ For fine grains use fraction < 125 µm (7); sieve with mesh size 63 µm; retain fraction < 63 µm (9)
	<ul style="list-style-type: none">• Extract polymineral fine grains (4–11 µm)
[8]	<ul style="list-style-type: none">○ Use fraction < 63 µm (9); separate fraction < 11 µm in aqua_{demin} (beaker or Atterberg cylinder); retain fraction < 11 µm (10)
[9]	<ul style="list-style-type: none">○ Use fraction < 11 µm (10); remove fraction < 4 µm in aqua_{demin} (centrifuge); retain resulting mineral separate 4–11 µm as <i>polymineral fine grains (4–11 µm)</i> (11)
	<ul style="list-style-type: none">• Extract quartz fine grains (4–11 µm)
[10]	<ul style="list-style-type: none">○ Use polymineral fine grains (11); etch in fluorosilicic acid (H₂[SiF₆]; 35 %) for 5 days in PET beaker (sample : acid = 1 : 4); swirl beaker once every workday); rinse with aqua_{demin} (5 times)
[11]	<ul style="list-style-type: none">○ Remove fluorides with hydrochloric acid (HCl, 10 %) over night; stir 3 times (usually 2 times first day, 1 time second day); rinse with aqua_{demin} (until pH = 7); retain resulting mineral separate as <i>quartz fine grains (4–11 µm)</i> (12)

- **Extract quartz coarse grains (125–212 μm)**

- [12] ○ Use fraction 125–212 μm (8); remove heavy minerals (fraction > 2.74 g/cm³) in lithium polytungstate (LST, 2.74 g/cm³); retain fraction < 2.74 g/cm³ (13)
- [13] ○ use fraction < 2.74 g/cm³ (13) to separate lighter minerals < 2.64 g/cm³ from heavier minerals > 2.64 g/cm³ in LST (2.64 g/cm³); retain fraction 2.64–2.74 g/cm³ (14) and fraction < 2.64 g/cm³ (15) (the latter for feldspar preparation)
- [14] ○ Use fraction 2.64–2.74 g/cm³ (14); etch in hydrofluoric acid (48 %; magnetic stirrer on low level) for 45 min in teflon beaker; rinse with aqua_{demin} (5 times)
- [15] ○ Remove fluorides with hydrochloric acid (HCl, 10 %) over night; rinse with aqua_{demin} (until pH = 7); retain resulting mineral separate as *quartz coarse grains (125–212 μm) (16)*

- **Extract potassium feldspar and sodium feldspar coarse grains (125–212 μm)**

- [16] ○ Use fraction < 2.64 g/cm³ (15); separate generally lighter potassium feldspar and generally heavier sodium feldspar in LST (2.58 g/cm³)
- Retain resulting mineral separate < 2.58 g/cm³ as *potassium feldspar coarse grains (125–212 μm) (17)*
- Retain resulting mineral separate 2.58–2.64 g/cm³ as *sodium feldspar coarse grains (125–212 μm) (18)*

S5.4 Results

S5.4.1 Report polymineral fine grains – pIR₆₀IR₂₂₅ – DA240 “Athenaeum”

Instrumentation

Post infrared (at 60 °C) infrared (at 225 °C) (pIR₆₀IR₂₂₅) single aliquot regeneration (SAR) (Murray and Wintle, 2001) measurements of polymineral fine grains (4–11 μm) were carried out on a luminescence reader model Risø DA20 (serial no. 240; nicknamed “Athenaeum”; Kadereit and Kreutzer 2013), equipped as depicted in Fig. S5.77.

Luminescence reader: Risø model TL/OSL DA20 (No. 240, "Athenaeum")			
turntable: 48 measurement positions use every 2 nd position (or wider spacing) to avoid IR cross talk			
IR stimulation: IR at 60 °C and IR at 225 °C IR-LEDs; 3 clusters; 7 LEDs each; 870 Δ 40 nm measurements with 90 % diode-power, after 10 s warmup			
Blue light stimulation: not used for pIR ₆₀ IR ₂₂₅ SAR protocol blue light emitting diodes; four clusters; 7 LEDs each; 470 Δ 30 nm measurements with 90 % diode-power, after 10 s warmup			
Detection: bialkali PMT EMI 9235QB15			
Detection filter: CH-30D410-44.3 (Chroma)			
Detected emission: violet-blue, around 410 nm			
β-dose rate:	0.08527 ± 0.00300	Gy/s	10.11.2021 (start this study)
	5.1 ± 0.2	Gy/min	
	0.08418 ± 0.00296	Gy/s	24.05.2022 (end this study)
	5.05 ± 0.18	Gy/min	
Nitrogen use: ca. 4 minutes at start of measurement			

Figure S5.77: Equipment of the luminescence reader model Risø TL/OSL DA20 used for pIR₆₀IR₂₂₅ SAR measurements of the polymineral fine grains (4–11 μm).

D_e-range test

For a first test on the D_e range of the here investigated samples HDS-1776 to HDS-1778 and HDS-1799 to HDS-1801, the pIR₆₀IR₂₂₅ protocol as adapted for the minimally prepared coarse grains from the flower box samples (HDS-1802 to HDS-1817) of the same site Baix was applied (cf. luminescence screening in Pfaffner et al. (2024)). Two aliquots were measured per sample. The regeneration dose points for dose response construction were set at 1560 s (128.4 Gy), 2730 s (224.6 Gy), 3900 s (320.9 Gy), 5070 s (417.2 Gy), 6240 s (513.5 Gy), 0 s (0 Gy; to determine the recuperation) and 3900 s (320.9 Gy; recycling ratio), and the normalisation dose (test dose) was 293 s (24.1 Gy). IR₆₀ and subsequent IR₂₂₅ readout were performed for 200 s, each (200 data channels; 1 s per data channel). De determination occurred with the software Analyst (version 4.31.09; Duller, 2015) for the integrals 0–1 s and 0–4 s, respectively, and a late light subtraction 51–60 s (for both De integrals) applying an exponential plus linear fit for dose response curve modelling. The smallest D_{es} were gained for the uppermost sample HDS-1778 (ca. 1500 s; ca. 130 Gy), the largest D_{es} for the lowermost sample HDS-1799 (ca 5560 s; ca 480 Gy) (Table S5.25).

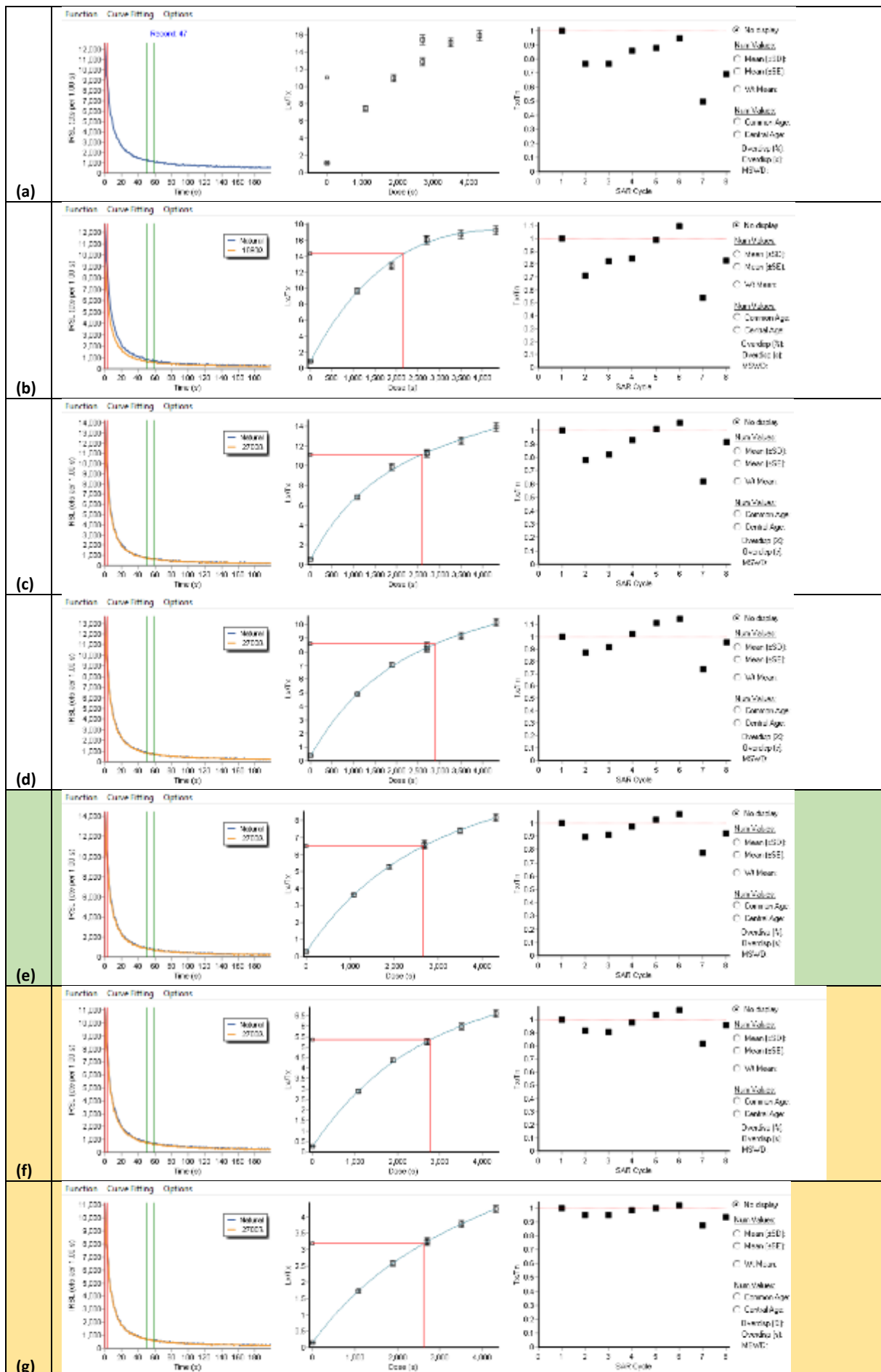
Table S5.25: Results of the D_e range test with a not yet finally adapted $pIR_{60}IR_{225}$ protocol.

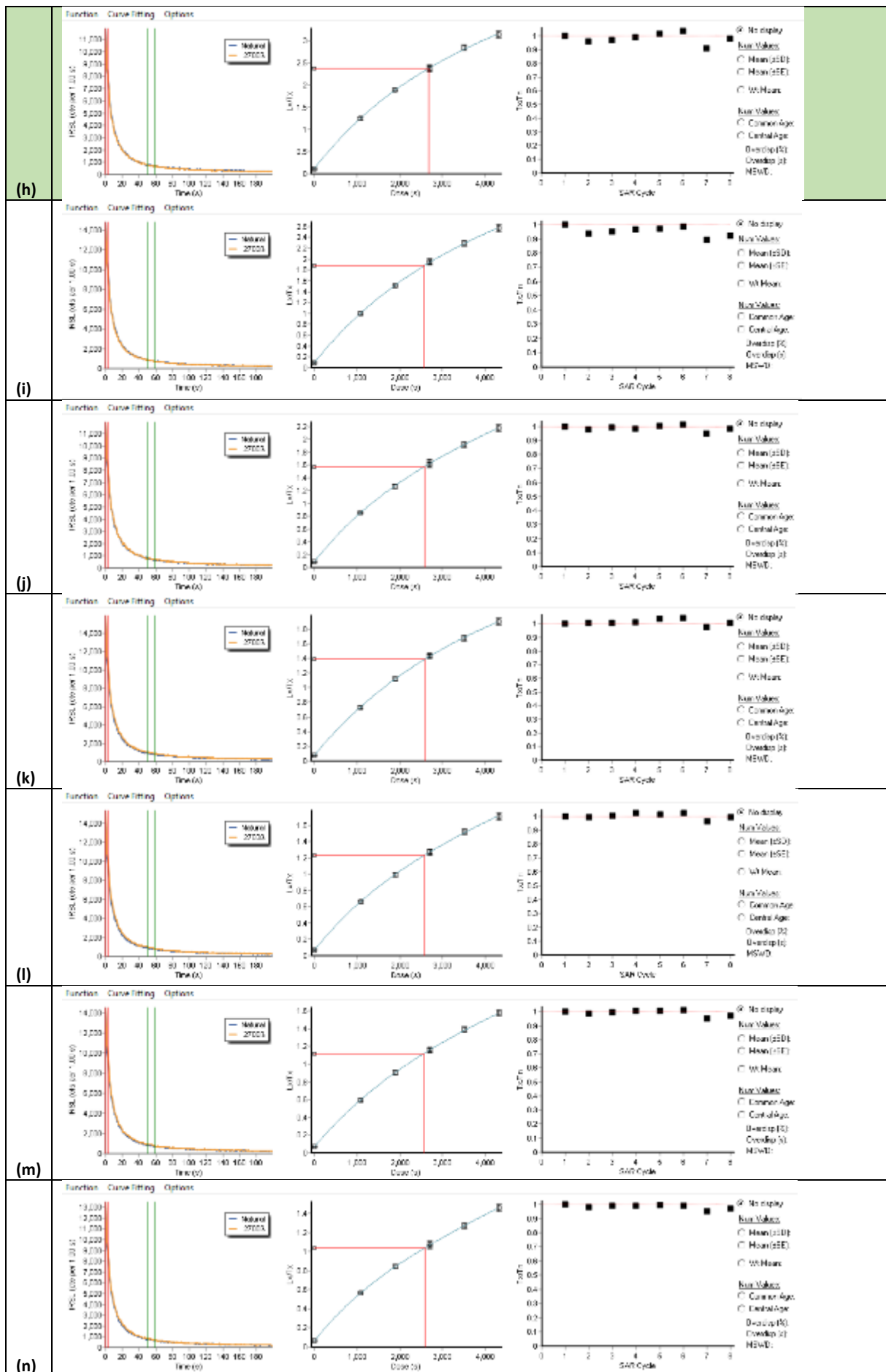
sample	turntable position	aliquot	recovered dose	recovered dose
[HDS-no.]	[#]	[#]	[s irradiation time]	[s irradiation time]
			[0 - 1 s]	[0 - 4 s]
HDS-1776	1	1	2346.99	129.07
HDS-1776	3	2	2433.00	163.11
HDS-1777	5	3	2148.17	116.14
HDS-1777	7	4	2307.92	163.98
HDS-1778	9	5	1320.52	150.31
HDS-1778	11	6	1471.47	127.62
HDS-1779	13	7	5287.26	374.48
HDS-1779	15	8	5364.57	301.37
HDS-1800	17	9	3014.88	160.58
HDS-1800	19	10	3249.08	166.31
HDS-1801	21	11	2827.86	178.83
HDS-1801	23	12	2649.51	127.78

Normalisation dose test

Initially not considering the largest D_{es} of sample HDS-1799 gained by the D_e test, for further tests a dose response curve was constructed for an expected dose of 2700 s (100 %; 226.0 Gy) with regeneration dose points at 40 % (1080 s; 90.4 Gy), 70 % (1890 s; 158.2 Gy), 100 % (2700 s; 226.0 Gy), 130 % (3510 s; 293.8 Gy), 160 % (4320 s; 361.6 Gy), 0 % (0 s; 0 Gy) (testing for recuperation) and 100 % (2700 s; 226.0 Gy) (determining the recycling ratio) (2700 s dose response curve).

For this expected dose a normalisation dose test (cf. Colarossi et al. 2018) was performed with normalisation doses (NRM) at 0.5 % (14 s), 1 % (27 s), 2.5 % (68 s), 5 % (135 s), 7.5 % (203 s), 10 % (270 s), 20 % (540 s), 30 % (810 s), 40 % (1080 s), 50 % (1350 s), 60 % (1620 s), 70 % (1890 s), 80 % (2160 s), 90 % (2430 s) and 100 % (2700 s) of the expected dose (one aliquot of sample HDS-1776 each). The samples which received a laboratory dose (LAB) of 2700 s (226.0 Gy), had been bleached for 3 h under a solar simulator (model Dr. Hönle, SOL 2) while covered by an UVILEX glass filter and placed on a watercooled copper plate (ca 22 °C), and – prior to the SAR measurement – stored for at least 24 h in the dark at room temperature. For D_e determination the D_e integrals 0–1 s, 0–4 s and 0–10 s were analysed, using in each case the integral 51–60 s for late light subtraction. For dose response curve modelling a single exponential and an exponential plus linear fit were applied. As a result the different variants of D_e determination gave the same results within error margins. With respect to the expected dose the best results were gained for normalisation doses of/from 7.5 % and/to 30 % of the expected dose (Fig.S5.78, Fig. S5.79, Table S5.26).





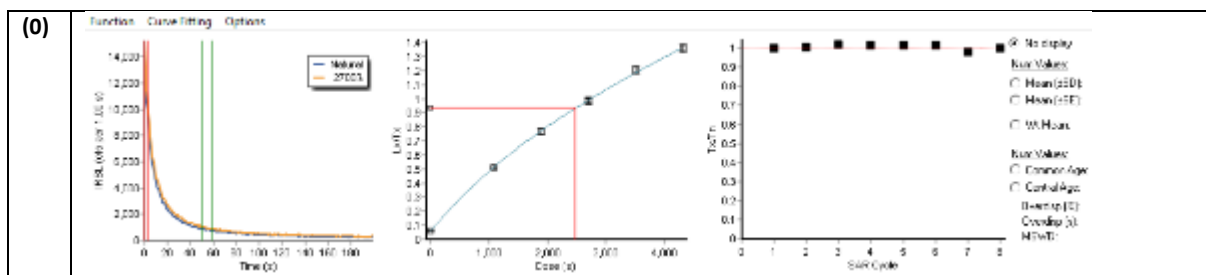
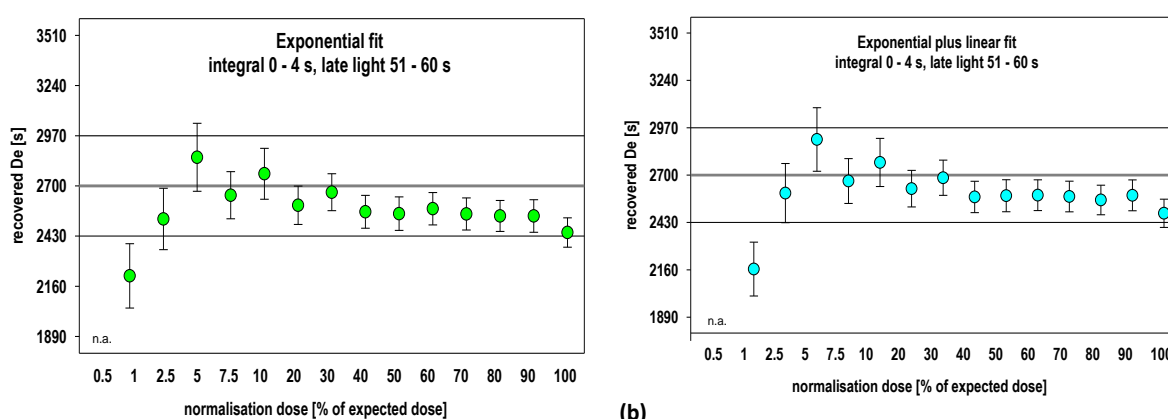


Figure S5.78: Normalisation dose test on bleached aliquots of sample HDS-1776 with a laboratory dose of 2700 s (ca 226 Gy). Exponential plus linear fit for dose response modelling. Late light subtraction 51–60 s; D_e integral 0–4 s. Normalisation doses of (or from) 7.5 % (203 s) and (or to) 30 % (810 s) of the laboratory dose (2700 s) delivered the best results. Normalisation doses above 30 % underestimate the expected value.



(a) Figure S5.79: Normalisation dose test on bleached aliquots of sample HDS-1776 with a laboratory dose of 2700 s (ca 226 Gy). (a) Single exponential and (b) exponential plus linear fit for dose response modelling. Late light subtraction 51–60 s; D_e integral 0–4 s. Normalisation doses of/from 7.5 % (203 s) and/to 30 % (810 s) of the laboratory dose (2700 s) delivered the best results. Normalisation doses above 30 % systematically underestimate the expected value, those below 7.5 % show an erratic pattern or no determinable D_e (0.5 %).

Table S5.26: Results of the normalisation does test on sample HDS-1776 with a laboratory dose of 2700 s (226 Gy).

aliquot position	normalisation dose [% of expected dose]	normalisation dose [s]	single exponential late light 51 - 60 s				((I1 - 4 s) - (I1 - 1 s))		((I1 - 10 s) - (I1 - 1 s))		
			I1 - 1 s De [s]	I1 - 4 s De [s]	I1 - 10 s De [s]	[%]	[%]	[%]	[%]		
1	1	0.5	14	1781.14	184.97	n.a.	n.a.	n.a.	n.a.		
2	3	1.0	27	2021.09	180.09	2216.18	173.15	2177.06	153.80	9.65	7.72
3	5	2.5	68	2401.27	224.47	2522.24	165.02	2558.74	165.72	5.04	6.56
4	7	5.0	135	2913.20	250.22	2853.88	182.96	2722.23	150.40	-2.04	-6.56
5	9	7.5	203	2688.07	168.01	2649.90	126.67	2658.66	123.08	-1.42	-1.09
6	11	10.0	270	2699.57	173.02	2765.34	136.82	2729.04	127.45	2.44	1.09
7	13	20.0	540	2571.32	123.00	2595.93	103.07	2620.57	102.37	0.96	1.92
8	15	30.0	810	2713.15	124.01	2666.08	99.38	2669.94	97.29	-1.73	-1.59
9	17	40.0	1080	2573.20	98.36	2561.00	88.44	2610.13	89.80	-0.47	1.44
10	19	46.2	1246	2524.12	99.30	2550.69	90.13	2556.79	90.68	1.05	1.29
11	21	60.0	1620	2568.12	99.45	2577.35	87.19	2566.29	85.45	0.36	-0.07
12	23	70.0	1890	2490.44	91.55	2549.01	86.27	2537.15	84.34	2.35	1.88
13	25	80.0	2160	2575.06	93.90	2538.56	83.29	2518.17	82.57	-1.42	-2.21
14	27	90.0	2430	2533.63	92.29	2538.33	87.56	2498.11	85.22	0.19	-1.40
15	29	100.0	2700	2418.92	83.54	2449.34	79.14	2428.95	78.63	1.26	0.41
MEAN:										1.16	0.67

aliquot position	normalisation dose		exponential plus linear									
	[% of expected dose] [s]		late light 51 - 60 s									
			I 1 - 1 s	I 1 - 4 s	I 1 - 10 s	(I 1 - 4 s) - (I 1 - 1 s)	(I 1 - 10 s) - (I 1 - 1 s)					
		De [s]	De [s]	De [s]	De [s]	De [s]	De [s]	De [s]	De [s]	De [s]	De [s]	De [s]
1	1	0.5	14	1745.97	156.21							
2	3	1.0	27	1989.66	161.46	2164.61	153.27	2138.88	140.45	8.79	7.50	
3	5	2.5	68	2451.99	232.87	2597.39	168.67	2616.75	169.62	5.93	6.72	
4	7	5.0	135	2989.46	235.55	2903.05	181.19	2794.65	148.67	-2.89	-6.52	
5	9	7.5	203	2746.41	169.23	2666.45	127.79	2680.01	124.18	-2.91	-2.42	
6	11	10.0	270	2798.08	168.47	2772.16	136.96	2768.46	128.09	-0.93	-1.06	
7	13	20.0	540	2606.42	124.54	2622.90	104.16	2683.24	102.09	0.63	2.95	
8	15	30.0	810	2737.49	124.92	2685.00	100.17	2708.44	97.58	-1.92	-1.06	
9	17	40.0	1080	2610.56	100.00	2575.50	89.30	2632.41	90.68	-1.34	0.84	
10	19	46.2	1246	2561.26	100.71	2582.55	91.17	2589.78	91.93	0.83	1.11	
11	21	60.0	1620	2584.94	100.14	2585.52	87.59	2592.69	86.27	0.02	0.30	
12	23	70.0	1890	2509.03	93.03	2578.29	87.41	2556.18	85.26	2.76	1.88	
13	25	80.0	2160	2631.37	93.68	2558.22	84.13	2532.78	83.33	-2.78	-3.75	
14	27	90.0	2430	2544.43	85.57	2584.54	87.86	2542.02	85.45	1.58	-0.09	
15	29	100.0	2700	2451.70	79.93	2482.46	80.62	2457.87	79.95	1.25	0.25	
MEAN:										0.65	0.48	

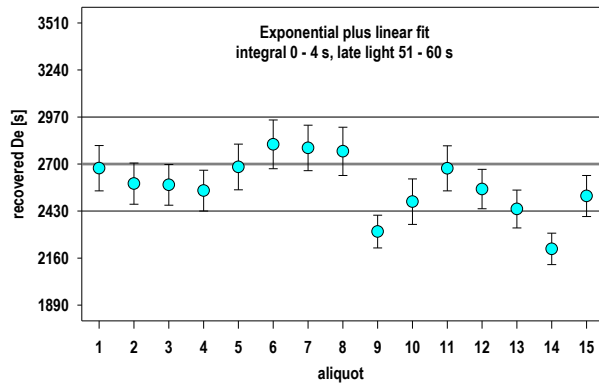
EXP+LIN - EXP

I 1 b 1 s	I 1 b 4 s	I 1 b 10 s	I 1 b 1 s	I 1 b 4 s	I 1 b 10 s
[s]	[s]	[s]	[%]	[%]	[%]
-35.17			-1.97		
-31.43	-51.57	-38.18	-1.56	-2.33	-1.75
50.72	75.15	58.01	2.11	2.98	2.27
76.26	49.17	72.42	2.62	1.72	2.66
58.34	16.55	21.35	2.17	0.62	0.80
98.51	6.82	39.42	3.65	0.25	1.44
35.10	26.97	62.67	1.37	1.04	2.39
24.34	18.92	38.50	0.90	0.71	1.44
37.36	14.50	22.28	1.45	0.57	0.85
37.14	31.86	32.99	1.47	1.25	1.29
16.82	8.17	26.40	0.65	0.32	1.03
18.59	29.28	19.03	0.75	1.15	0.75
56.31	19.66	14.61	2.19	0.77	0.58
10.80	46.21	43.91	0.43	1.82	1.76
32.78	33.12	28.92	1.36	1.35	1.19
MIN:			-1.97	-2.33	-1.75
MAX:			3.65	2.98	2.66
MEAN:			1.17	0.87	1.19

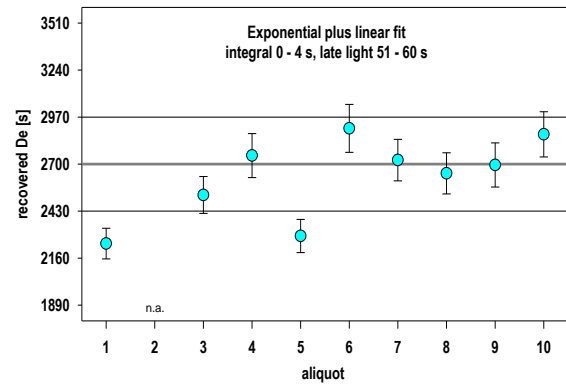
Dose recovery tests

Next, three dose recovery tests on sample HDS-1776, each with a laboratory dose of 2700 s (226 Gy) and a normalisation dose of 7.5 % of the expected dose (203 s) (15 aliquots), 10 % (270 s) (10 aliquots) and 30 % (810 s) (10 aliquots) were performed using the regeneration dose points of the 2700 s dose response curve. The results show that the expected dose of 2700 s is slightly underestimated for the two lower normalisation doses (recovered central doses 2563.7 ± 45.1 s with an overdispersion (OD) of 5.0 ± 0.4 % and 2611.7 ± 76.8 s with OD 7.6 ± 0.8 %, respectively; Fig. S5.80a, Fig. S5.80b), but met by the 30 % normalisation dose (2715.2 ± 32.0 s, OD 0.0 %) (results for the exponential plus linear fit, D_e integral 0–4 s, late light 51–60 s) (Fig. S5.80c). Therefore, in a next step two further dose recovery tests (10 aliquots each), one with a laboratory dose of 1500 s (ca. 125.6 Gy; cf. Table S5.25, sample HDS-1778) and the other with a laboratory dose of 3200 s (ca. 267.9 Gy; cf. Table S5.25, samples HDS-1800 and HDS-1801) were performed using the 2700 s dose response curve with the 30 % normalisation dose. For both, the lower and the larger laboratory dose, the

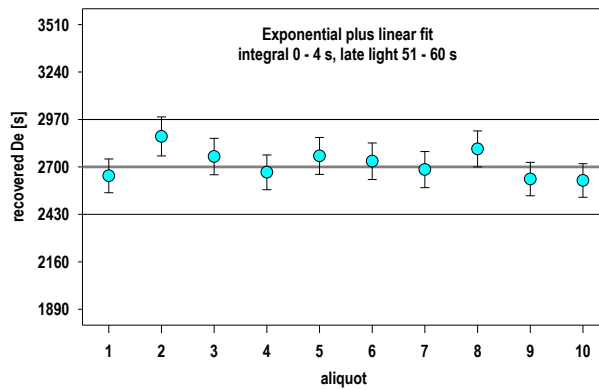
recovered central doses met the expected dose reasonably well (1571.3 ± 16.9 s; 3224.8 ± 39.3 s), and in both cases with zero OD (Fig. S5.81a-b).



(a)

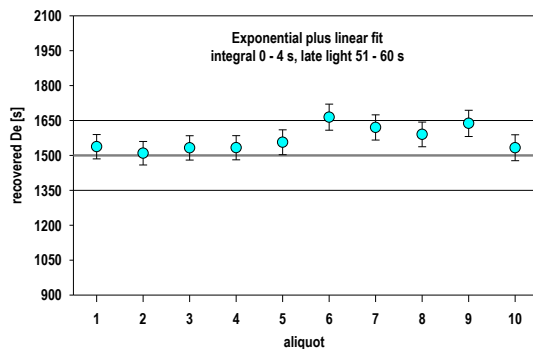


(b)

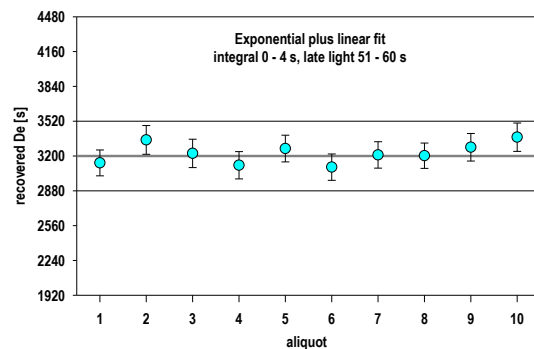


(c)

Figure S5.80: Dose recovery tests with LAB 2700 s and NRM (a) 7.5 %, (b) 10 % and (c) 30 % of LAB. Although most aliquots meet the expected dose within D_e errors within a range of 10 %, the best results are gained for NRM 30 %.



(a)



(b)

Figure S5.81: Dose recovery tests with NRM 30 % (of 2700 s; 2700 s dose response curve) for (a) LAB 1500 s (125.6 Gy) and (b) 3200 s (267.9 Gy). All aliquots of both tests meet the expected dose within a range of 10 % within D_e errors.

As for the lowermost sample (HDS-1779), the central dose was beyond the largest regeneration dose point (REG) (4320 s resp. 361.6 Gy), a further dose recovery test with the 30 % normalisation dose was performed, using an extended dose response curve with two more regeneration dose points (see Fig. S5.84). The test was performed on 10 bleached and

dosed aliquots of sample HDS-1776. As a result, the expected dose was reproduced well (Fig. S5.83; central dose 5456.9 ± 74.1 s) and again the OD was zero.

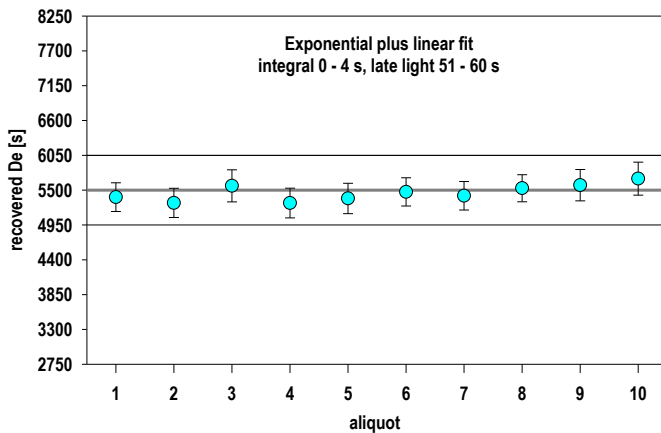


Figure S5.82: Dose recovery tests with NRM 30 % (of 2700 s; 2700 s dose response curve) for LAB 5500 s (460.4 Gy), applying an extended growth curve as depicted in Fig. S5.83. All aliquots meet the expected dose within error margins.

PIR₆₀IR₂₂₅ SAR protocol

Based on the pretests the SAR protocol for D_e determination of the polymineral fine grains (4–11 μm) from the 6 block samples was adapted as outlined in Fig. S5.83. The SAR measurements were processed after flooding the measurement chamber of the luminescence reader for 4 minutes with liquid nitrogen without applying the run-one-at-a-time mode. 16 aliquots were measured of each sample, placed on every second turntable position to avoid potential cross bleaching (Kreutzer et al. 2013).

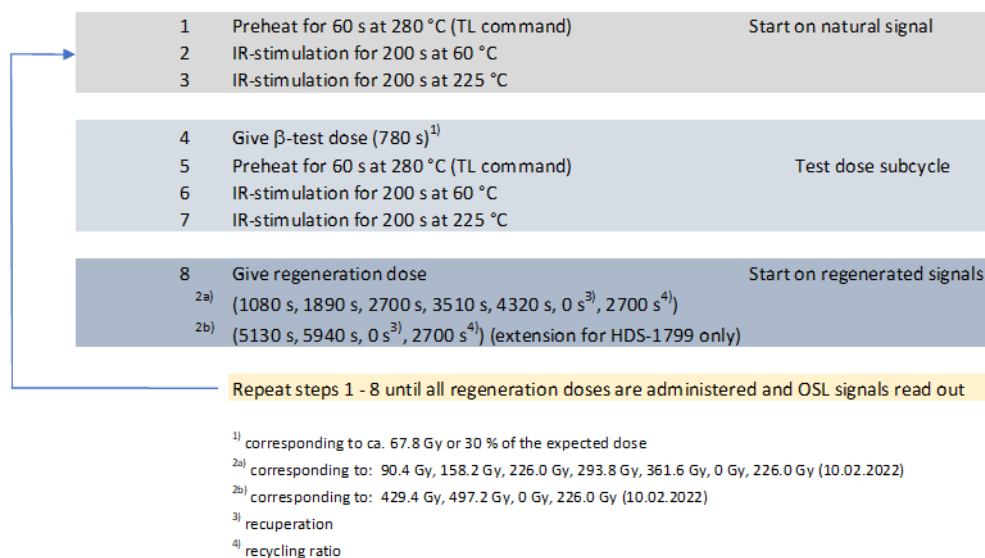


Figure S5.83: Schematic representation of the PIR₆₀IR₂₂₅ SAR protocol applied to polymineral fine grains (4–11 μm) of the 6 block samples HDS-1776 to HDS-1778 and HDS-1799 to HDS-1801.

As for the lowermost sample (HDS-1779), the central dose was beyond the largest regeneration dose point (REG) (4320 s resp. 361.6 Gy), for this sample two more recycling dose points were added at the upper end of the dose response curve (5130 s resp. 429.43 Gy; 5940 s resp. 497.23 Gy), followed by another zero dose point (recuperation) and another 2700 s dose point (recycling ratio). For results of the corresponding dose response test cf. Fig. S5.82.

D_e determination

The D_e determination occurred with the software Analyst (version 4.31.09; Duller, 2015) applying the parameters of data analysis as depicted in Fig. S5.84.

Software:	Luminescence Analyst, version 4.31.9 (Duller 2015)
Curve fitting:	Exponential plus linear
Integral [channel]:	1 - 4 (0 - 4 s)
Background [channel]:	51 - 60 (51 - 60 s)
Use recycled points for fitting:	Yes
Measurement error [%]:	1.5
Incorporate error on curve fitting:	Yes
Use errors when applying criteria:	Yes
Recycling ratio limit [%]:	10
Maximum test dose error [%]:	10
Maximum recuperation [% of N]:	10
Tn signal > 3 sigma above background:	Yes

Figure S5.84: Parameters of the D_e determination.

The analysis of the counts of the first data channel resp. first second of the shine down curve of sample HDS-1776 shows that the strength of the subsequently read out IR₂₂₅ signal of the polymineral fine grains, in contrast to the feldspar coarse grains, is only ca. 70 % of the strength of the previously read out IR₆₀ signal (Table S5.27).

Table S5.27: Comparison of the signal strength of the IR₆₀ and IR₂₂₅ signals. The comparison is based on the mean counts of the initial signal (0–1 s) of all normalisation doses (set number 9 (IR₆₀) and 10 (IR₂₂₅); 8 records each) of the 16 measured aliquots.

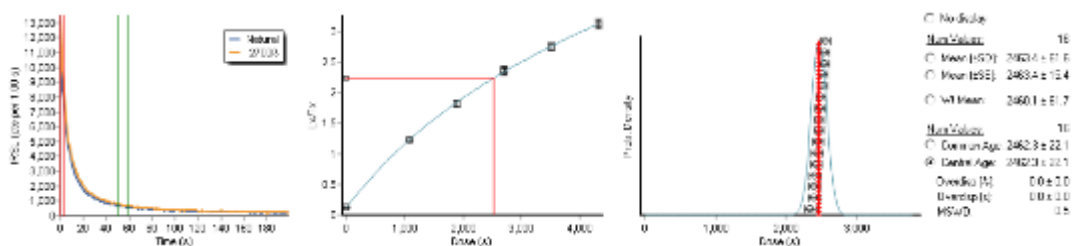
Position	NRM - IR ₆₀			NRM - IR ₂₂₅			NRM - IR ₂₂₅ / NRM - IR ₆₀
	Mean [cts]	SD [cts]	SD [%]	Mean [cts]	SD [cts]	SD [%]	
1	8321.00	290.13	3.49	5639.38	288.83	5.12	0.7
3	9746.13	589.60	6.05	5750.25	289.63	5.04	0.6
5	6808.13	427.40	6.28	4700.50	212.01	4.51	0.7
7	6121.88	144.81	2.37	4949.88	194.51	3.93	0.8
9	6905.63	367.35	5.32	5365.75	279.95	5.22	0.8
11	8353.88	358.65	4.29	5542.25	318.87	5.75	0.7
13	9610.88	570.48	5.94	5751.50	320.49	5.57	0.6
15	8044.13	426.38	5.30	5447.13	292.71	5.37	0.7
17	6575.50	299.32	4.55	4826.25	223.74	4.64	0.7
19	7376.13	392.20	5.32	5282.63	289.50	5.48	0.7
21	7552.63	378.62	5.01	5246.88	254.03	4.84	0.7
23	9466.75	517.58	5.47	5920.00	344.73	5.82	0.6
25	10544.00	684.31	6.49	6345.13	296.08	4.67	0.6
27	8868.50	407.53	4.60	5821.25	285.21	4.90	0.7
29	7406.38	426.35	5.76	5583.75	267.61	4.79	0.8
31	7761.13	466.72	6.01	5349.00	297.38	5.56	0.7

MEAN:	0.7
MIN:	0.6
MAX:	0.8

SAR measurements

Results of the De measurements are presented in Fig. S5.85 to Fig. S590. Comparison of the very early De integral 0–1 s vs. the integral 0–4 s shows no systematic differences for the two intervals, which could possibly point to insufficient (partial) bleaching during the last cycle of sediment reworking.

HDS-1776

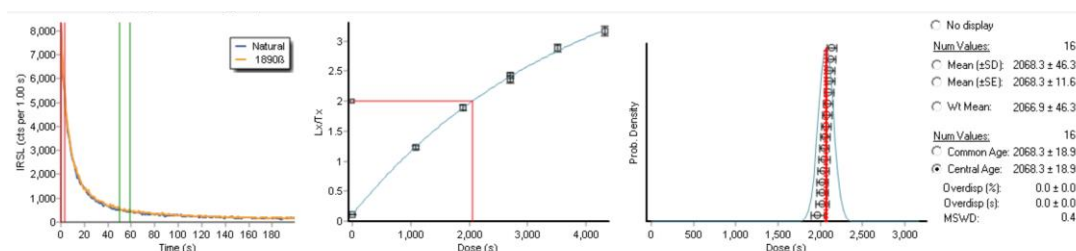


turntable position [#]	aliquot [#]	determined dose		determined dose		
		[s irradiation time] [0 - 1 s]	[s irradiation time] [0 - 4 s]	[s irradiation time] [0 - 4 s]	[s irradiation time] [0 - 4 s]	
	1	1	2420.90	106.37	2520.01	91.25
	2	2	2558.25	101.63	2486.25	86.09
	3	3	2407.73	105.05	2464.95	91.89
	4	4	2466.72	97.03	2541.71	89.24
	5	5	2464.73	106.55	2521.65	91.20
	6	6	2486.47	107.30	2397.66	84.93
	7	7	2488.22	108.49	2467.51	87.68
	8	8	2445.19	97.35	2471.83	87.20
	9	9	2521.99	105.94	2551.81	94.17
	10	10	2290.10	100.56	2405.25	87.89
	11	11	2446.08	108.17	2537.91	93.67
	12	12	2394.35	102.32	2452.90	88.65
	13	13	2363.48	95.30	2427.99	85.47
	14	14	2441.92	101.94	2432.18	87.14
	15	15	2390.12	104.26	2395.53	86.01
	16	16	2319.39	97.85	2338.89	84.16

central dose: 2432.20 25.70 2462.30 22.10

Figure S5.85: D_e determination on sample HDS-1776. Exponential plus linear fit. Example of shine down curve and dose response curve (D_e integral 0–4 s), and weighted histogram of all analysable aliquots ($N = 16$; $OD = 0.0\%$).

HDS-1777



turntable position [#]	aliquot [#]	determined dose		determined dose		
		[s irradiation time] [0 - 1 s]	[s irradiation time] [0 - 4 s]	[s irradiation time] [0 - 4 s]	[s irradiation time] [0 - 4 s]	
	1	1	2031.15	91.81	2047.72	71.26
	2	2	2006.23	86.16	2023.48	75.76
	3	3	2144.41	95.25	2123.07	77.17
	4	4	2112.66	90.54	2026.28	74.72
	5	5	2137.78	93.04	2107.70	76.44
	6	6	2046.38	82.05	2041.38	74.11
	7	7	2091.41	92.70	2135.48	77.64
	8	8	2065.57	93.98	2082.04	76.93
	9	9	2242.45	102.53	2116.22	78.20
	10	10	2046.58	88.25	2068.74	75.95
	11	11	2081.82	91.60	2117.29	76.93
	12	12	2024.32	93.83	1965.82	74.07
	13	13	2084.28	96.79	2054.96	75.53
	14	14	1957.55	85.25	2023.78	73.32
	15	15	2091.29	90.42	2093.97	74.29
	16	16	2094.39	99.50	2064.39	77.19

central dose: 2076.60 22.90 2068.30 18.90

Figure S5.86: D_e determination on sample HDS-1777. Exponential plus linear fit. Example of shine down curve and dose response curve (D_e integral 0–4 s), and weighted histogram of all analysable aliquots ($N = 16$; $OD = 0.0\%$).

HDS-1778

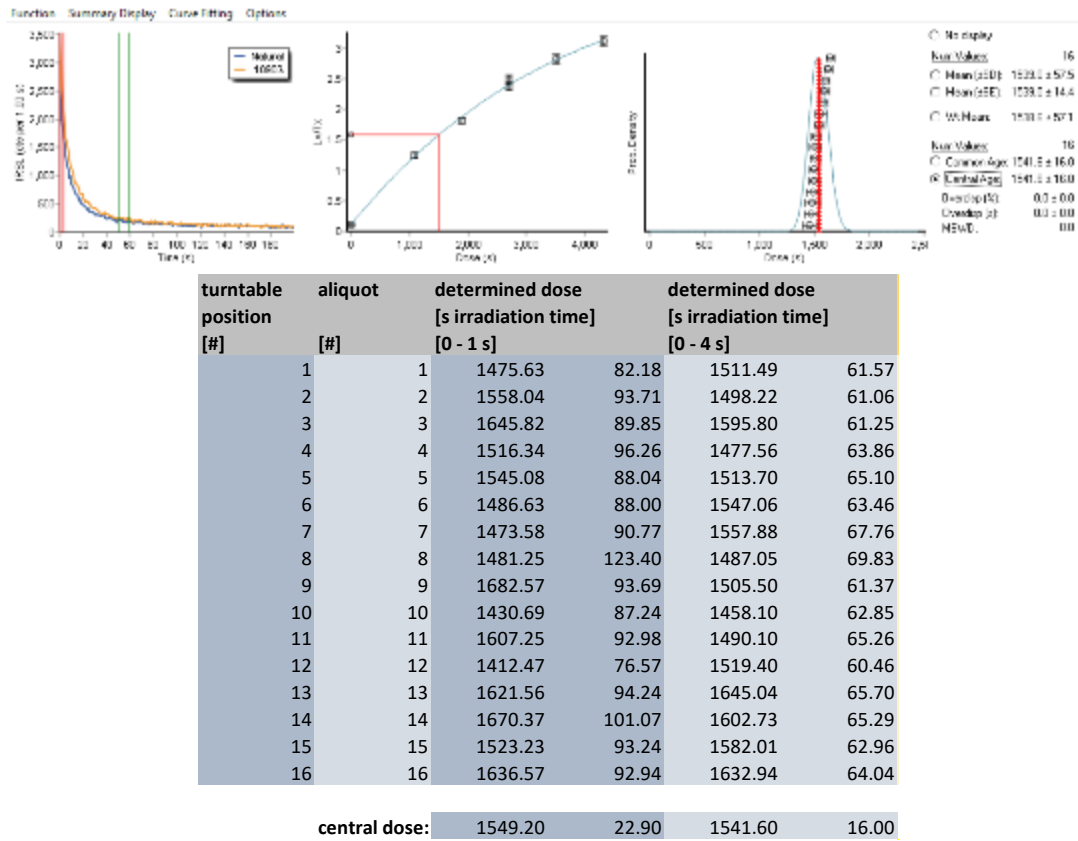
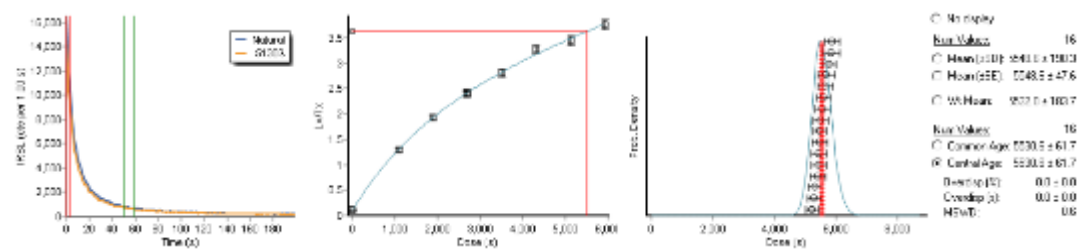


Figure S5.87: D_e determination on sample HDS-1778. Exponential plus linear fit. Example of shine down curve and dose response curve (D_e integral 0–4 s), and weighted histogram of all analysable aliquots ($N = 16$; $OD = 0.0\%$).

HDS-1799



turntable position [#]	aliquot [#]	determined dose [s irradiation time]		determined dose [s irradiation time]	
		[0 - 1 s]		[0 - 4 s]	
1	1	5504.75	306.04	5518.70	241.77
2	2	5888.44	317.93	5856.74	301.21
3	3	5549.88	300.46	5478.73	247.88
4	4	n.a.	n.a.	5668.36	251.33
5	5	5658.80	282.60	5795.72	243.17
6	6	5328.12	294.08	5482.13	224.61
7	7	5427.39	246.68	5612.08	238.61
8	8	5521.94	354.92	5701.83	300.35
9	9	5673.58	272.16	5576.85	252.15
10	10	5463.84	294.39	5427.71	252.57
11	11	5560.68	333.02	5461.03	245.20
12	12	5453.53	295.28	5239.42	227.07
13	13	5218.78	263.37	5334.22	222.17
14	14	5139.38	249.94	5309.54	221.16
15	15	5953.40	302.16	5869.07	295.76
16	16	5538.52	299.66	5445.89	236.27
central dose:		5517.90	75.00	5530.60	61.70

Figure S5.88: D_e determination on sample HDS-1799. Exponential plus linear fit. Example of shine down curve and dose response curve (D_e integral 0–4 s), and weighted histogram of all analysable aliquots ($N = 16$; $OD = 0.0\%$).

HDS-1800

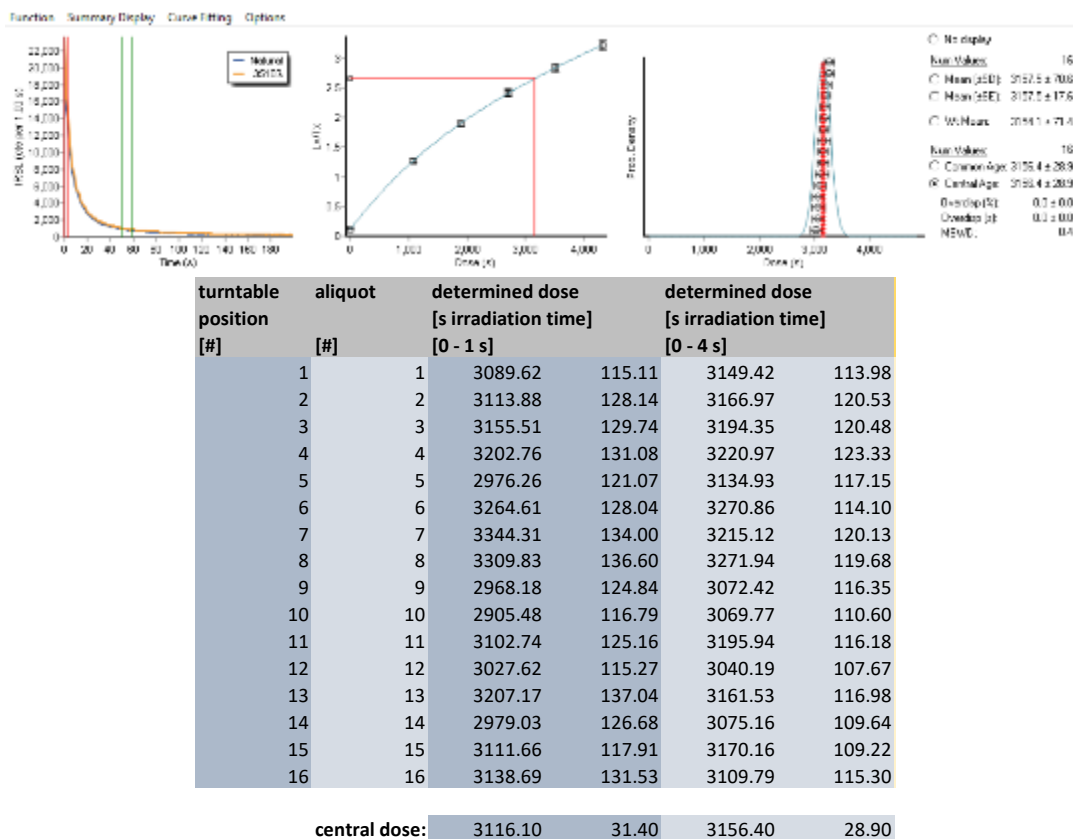


Figure S5.89: D_e determination on sample HDS-1800. Exponential plus linear fit. Example of shine down curve and dose response curve (D_e integral 0–4 s), and weighted histogram of all analysable aliquots ($N = 16$; $OD = 0.0\%$).

HDS-1801

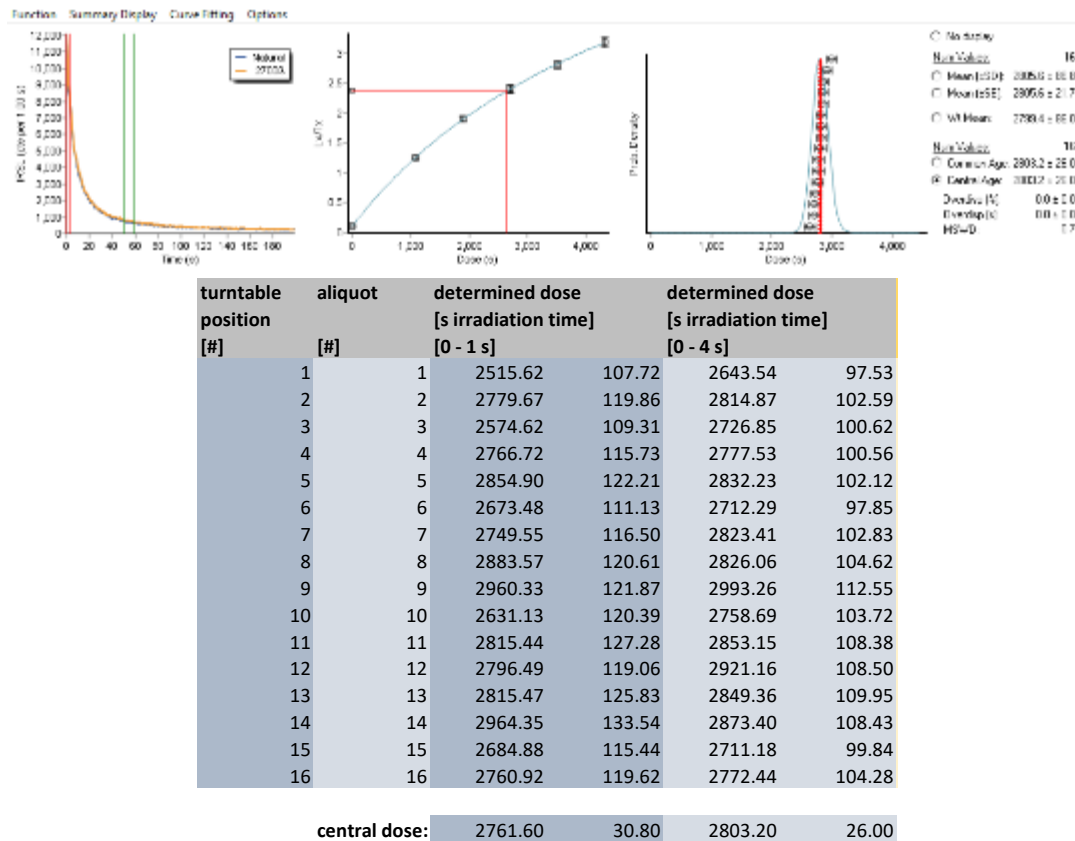


Figure S5.90: D_e determination on sample HDS-1801. Exponential plus linear fit. Example of shine down curve and dose response curve (D_e integral 0–4 s) and weighted histogram of all analysable aliquots ($N = 16$; OD = 0.0 % for D_e integral 0–4 s, but 1.2 ± 0.7 % for D_e integral 0–1 s).

S5.4.2 Report coarse grains – pIR₆₀IR₂₂₅ – DA240 “Athenaeum”

Instrumentation

Post infrared (at 60 °C) infrared (at 225 °C) (pIR₆₀IR₂₂₅) single aliquot regeneration (SAR) (Murray and Wintle, 2001; Thomsen et al. 2008) measurements of feldspar coarse grains (125–212 μm) were carried out on a luminescence reader model Risø DA20 (serial no. 240; nicknamed “Athenaeum”; Kadereit and Kreutzer 2013), equipped as depicted in Fig. S5.91.

Luminescence reader: Risø model TL/OSL DA20 (No. 240, "Athenaeum")			
turntable: 48 measurement positions use every 2 nd position (or wider spacing) to avoid IR cross talk			
IR stimulation: IR at 60 °C and IR at 225 °C IR-LEDs; 3 clusters; 7 LEDs each; 870 Δ 40 nm measurements with 90 % diode-power, after 10 s warmup			
Blue light stimulation: not used for pIR ₆₀ IR ₂₂₅ SAR protocol blue light emitting diodes; four clusters; 7 LEDs each; 470 Δ 30 nm measurements with 90 % diode-power, after 10 s warmup			
Detection: bialkali PMT EMI 9235QB15			
Detection filter: CH-30D410-44.3 (Chroma)			
Detected emission: violet-blue, around 410 nm			
β-dose rate:	0.08057 ± 0.00408	Gy/s	16.06.2021 (start this study)
	4.8 ± 0.2	Gy/min	
	0.07987 ± 0.00405	Gy/s	26.10.2021 (end this study)
	4.79 ± 0.24	Gy/min	
Nitrogen use: ca. 4 minutes at start of measurement			

Figure S5.91: Equipment of the luminescence reader model Risø TL/OSL DA20 used for pIR₆₀IR₂₂₅ SAR measurements of the feldspar coarse grains (112–225 μm).

D_e range

A separate test on the D_e range was not carried out on the potassium feldspar coarse grain separates, as pIR₆₀IR₂₂₅ SAR measurements had been performed in an earlier study, i.e. a luminescence screening on minimally prepared samples from the lower ca 7 m of the Baix section (Pfaffner et al. 2024) covering the range of the 6 block samples investigated in the present study. Therefore, a dose response curve aiming at an expected dose (100 %) of 3900 s (ca 313.4 Gy) was constructed with 7 regeneration dose points (REG) at 40 % (1560 s; ca 125.4 Gy), 70 % (2730 s; ca 219.4 Gy), 100 % (3900 s; ca 313.4 Gy), 130 % (5070 s; ca 407.5 Gy), 160 % (6240 s; ca. 501.5 Gy), 0 % (0 s; 0 Gy) and 100 % (3900 s; ca 313.4 Gy), using the latter two also to investigate the signal recuperation after zero dosing and the recycling ratio of a repeatedly measured dose point, respectively. Thus, the 3900 s dose response curve is identical to the one applied by (Pfaffner et al. 2024).

Test on the strength of the luminescence signal using different aliquot sizes

To evaluate how much the number of analysed mineral grains per aliquot could be reduced, in a first test 3 aliquots of sample HDS-1776 (lowermost sample, likely largest D_e) with the natural luminescence were measured, one small (10^2 grains), one tiny (10^1 grains) and one supertiny (10^0 grains) sized aliquot, using the pIR₂₂₅IR₂₉₀-protocol as adapted for the screening of the flower-box samples (cf. Pfaffner et al. 2024; Fig. S5.92). The integral 51–60 s was used for late light subtraction, while the initial integrals 0–1 s, 0–4 s and 0–10 s were tested for D_e determination. Data analysis of this test, as well as for all other test measurements and D_e determination, occurred with the software Analyst (version 4.31.09; Duller, 2015). The results show that the smallest aliquot size is suitable for D_e determination. Therefore all following pretests and the D_e measurements were performed on supertiny aliquots (100 grains). An

exponential plus linear fit for dose response curve modelling was regarded as more appropriate than a single exponential fit meeting better the uppermost regeneration dose point (Fig. S5.93, Fig. S5.94). The D_{es} varied between ca 2571 s (ca. 207 Gy) (tiny aliquot) and ca 3050 s (ca 245 Gy) (small aliquot).

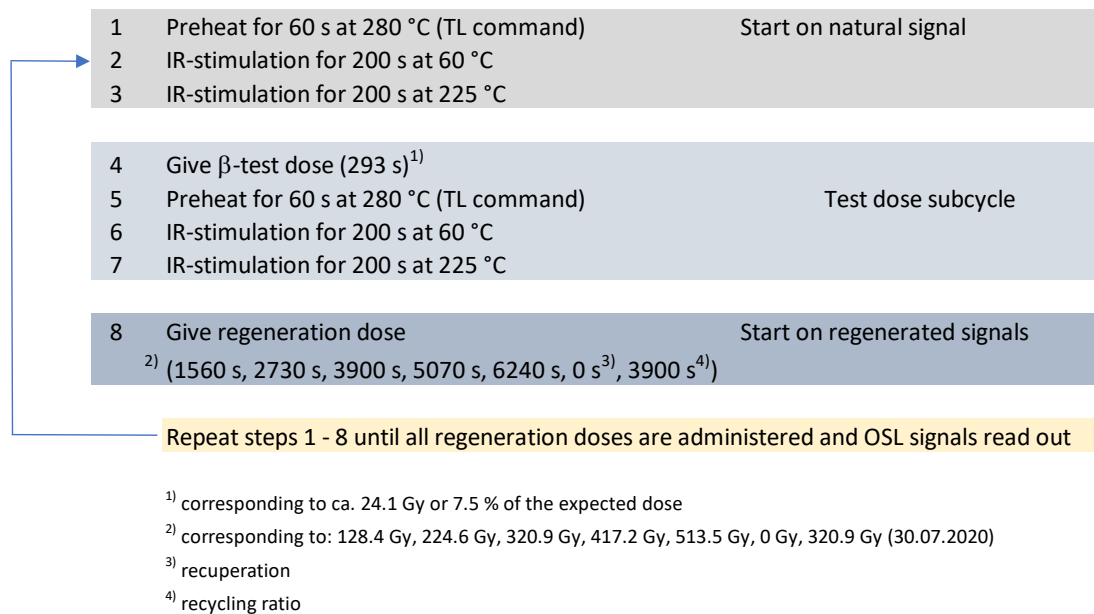


Figure S5.92: Schematic representation of the $pIR_{60}IR_{225}$ SAR protocol applied to minimally prepared polymineral coarse grains from 126 miniature (1 cm³) subsamples (A–H) of the flower box samples HDS-1802 to HDS-1817 (figure from Pfaffner et al. 2024). The protocol as adapted for the flower box samples was used for a first test measurement on potassium feldspar coarse grains with aliquots of varying size (sample HDS-1776).

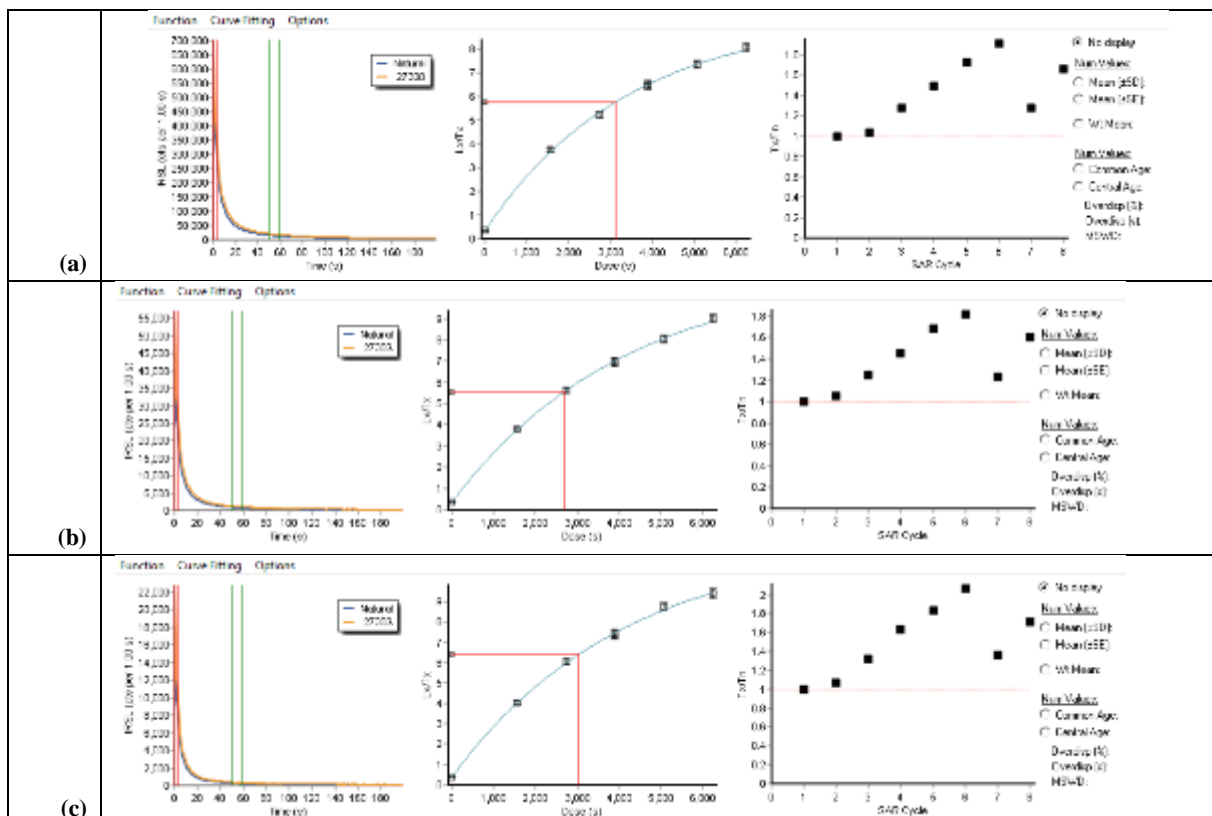


Figure S5.93: Test measurement on 3 aliquots with the natural luminescence (a) small (102 grains), (b) tiny (101 grains) and (c) supertiny (100 grains). Exponential fit. D_e integral 0–4 s, late light integral 51–60 s.

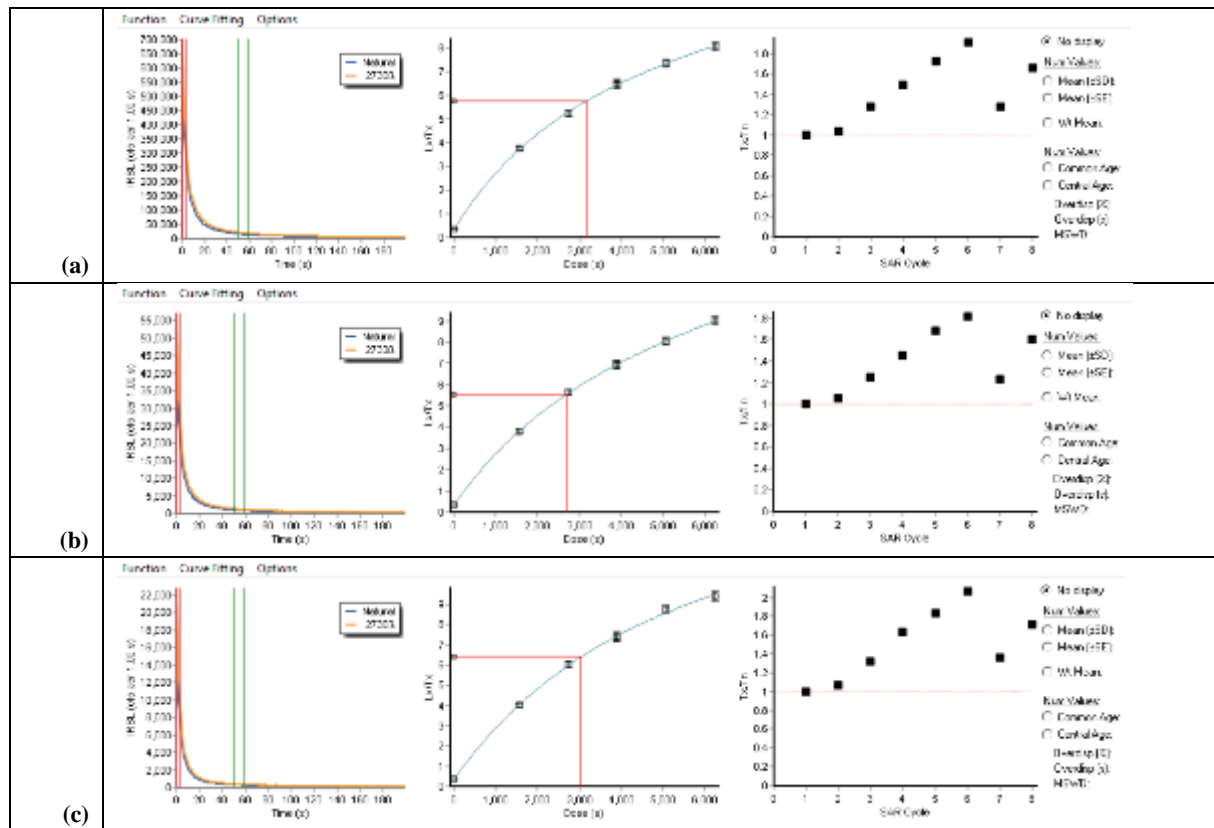


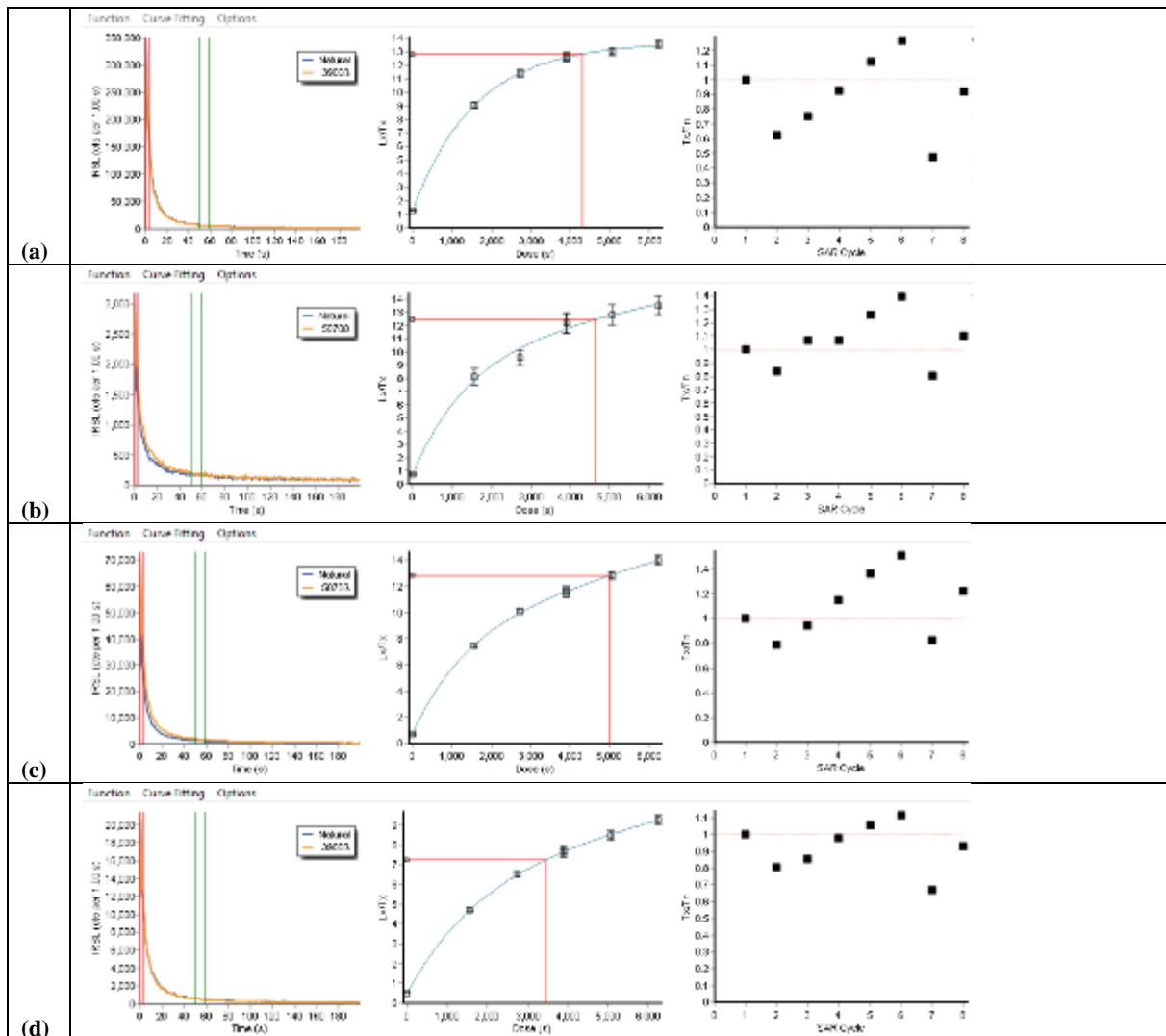
Figure S5.94: Test measurement on 3 aliquots with the natural luminescence (a) small (102 grains), (b) tiny (101 grains) and (c) supertiny (100 grains). Exponential plus linear fit. D_e integral 0–4 s, late light integral 51–60 s.

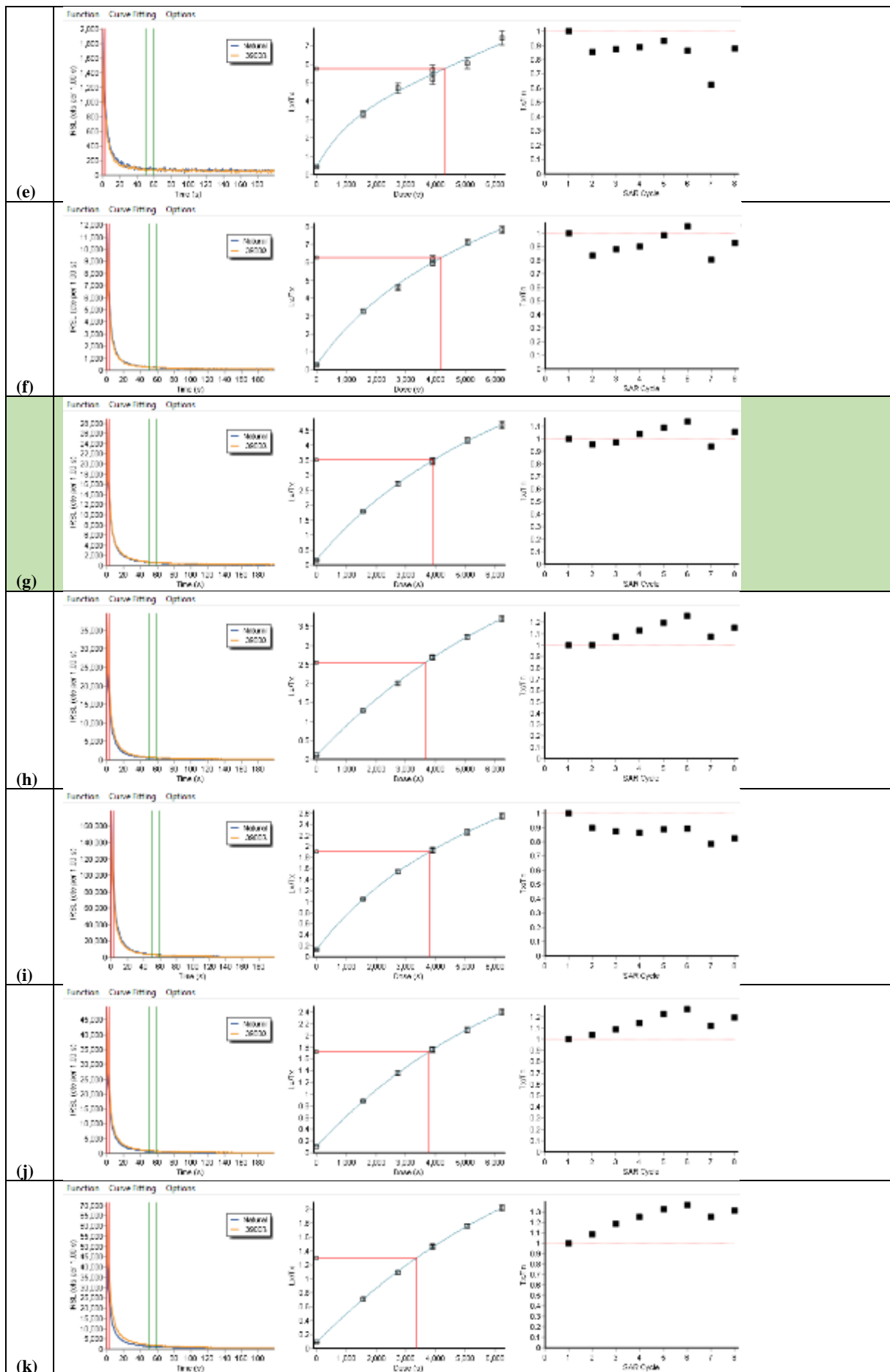
Normalisation dose test

A test to determine a suitable normalisation dose (also “test dose”) for the SAR D_e measurements (Colarossi et al. 2018) was performed on 15 supertiny aliquots of sample HDS-1776, with varying normalisation doses (NRM) set at 20 s, 39 s, 98 s, 195 s, 293 s, 390 s, 780 s, 1170 s, 1560 s, 1800 s, 2340 s, 2730 s, 3120 s, 3510 s and 3900 s Δ -irradiation time (one aliquot each), corresponding to 0.5 %, 1 %, 2.5 %, 5 %, 7.5 %, 10 %, 20 %, 30 %, 40 %, 50 %, 60 %, 70 %, 80 %, 90 % and 100 % of the expected dose (administered laboratory dose of 3900 s, corresponding to ca 314 Gy at the time of measurement). Prior to administering the laboratory dose (LAB), the aliquots were bleached for 3 h under a solar simulator (Sol 2, Dr. Hönle), while covering the aliquot holder with a UVILEX glass filter to better align the light spectrum with that of the natural sun light, and placing the aliquot holder on a water cooled copper plate (ca 22 °C). Prior to measurement the aliquots were stored for at least 24 h in the dark to allow for any electron excitation to decay. This procedure (bleaching and storage) was applied in the here described manner to all aliquots that were bleached and dosed for OSL dating pretests in the present study, including those on polymineral and quartz fine grains (cf. respective supplements).

While dose response curves for the lowest applied normalisation doses are quite strongly curved, they stretch with increasing normalisation doses (Fig. S5.95). Aliquots measured *with normalisation doses* <20 % of the expected dose mostly overestimate the expected value, and show comparably large errors, while those measured with a *normalisation dose* >20 % mostly *underestimate the given dose* (Fig. S5.96).

Neither the model of the dose response curve fitting (single exponential; exponential plus linear), nor the length of the D_e integral have an influence on the results (Table S5.28). Only one aliquot (second aliquot, measurement position 3, NRM 1 % of LAB) which showed below average luminescence counts, *could not be analysed* for the *earliest* D_e integral (0–1 s) (Table S5.28). As a result a *normalisation dose* of 20 % (ca 62.8 Gy) of the expected dose (Fig. S5.95g) appears appropriate for the here *applied SAR protocol* (cf. Fig. S5.92). For further tests the exponential plus linear fit was used together with the D_e integral 0–4 s and an integral 51–60 s for late light subtraction.





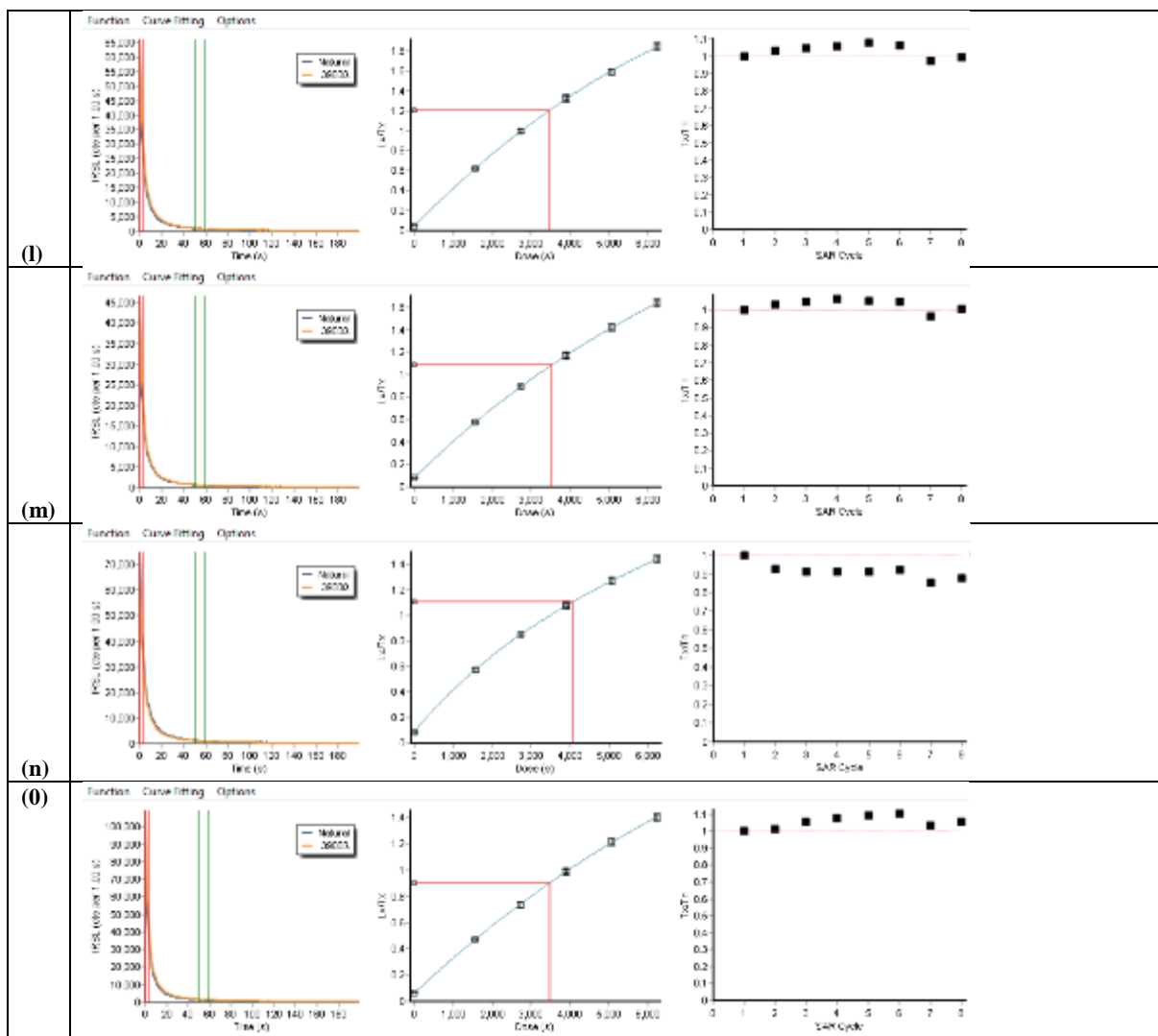


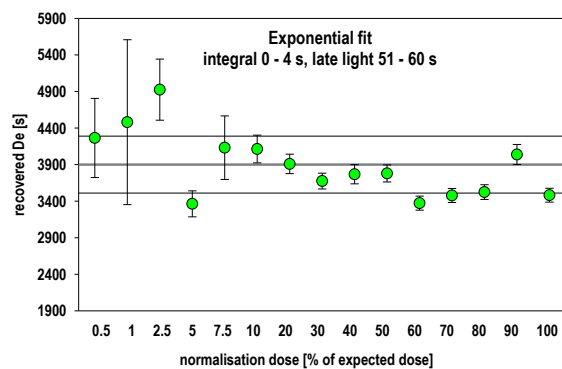
Figure S5.95: Normalisation dose test on bleached aliquots of sample HDS-1776 with a laboratory dose of 3900 s (ca. 314 Gy). Single exponential fit for dose response modelling. Late light subtraction 51–60 s; D_e integral 0–4 s. A normalisation dose of 20 % (780 s) of the laboratory dose (3900 s) appears most appropriate (g, highlighted in green). Most results for normalisation doses below 20 % dose overestimate the expected value, while most results above 20 % underestimate it.

Table S5.28: Results of the normalisation dose test for different D_e integrals. (a) Single exponential fit. (b) Exponential plus linear fit. A normalisation dose of 20 % (780 s) of the laboratory dose (3900 s) appears most appropriate.

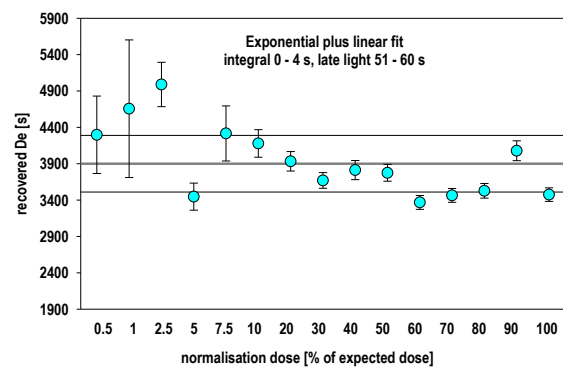
aliquot position	normalisation dose		single exponential						
	[% of expected dose] [s]		late light 51 - 60 s						
			I 1 - 1 s	I 1 - 4 s		I 1 - 10 s			
			D_e [s]	D_e [s]	D_e [s]	D_e [s]	D_e [s]		
1	1	0.5	20	4552.69	699.98	4264.29	540.90	4244.01	526.59
2	3	1.0	39	n.a.		4480.05	1127.75	5360.43	no error
3	5	2.5	98	5302.15	570.95	4925.08	418.10	4978.54	418.71
4	7	5.0	195	3236.62	196.28	3363.22	178.13	3365.74	177.51
5	9	7.5	293	4132.75	613.03	4131.52	434.41	4236.60	508.80
6	11	10.0	390	4247.37	244.99	4113.25	189.26	4051.86	178.04
7	13	20.0	780	3955.19	148.89	3909.27	132.79	3923.29	131.75
8	15	30.0	1170	3647.43	114.83	3674.82	108.22	3652.83	107.22
9	17	40.0	1560	3728.15	129.11	3767.91	130.58	3775.07	132.00
10	19	46.2	1800	3763.56	120.21	3779.29	116.10	3748.00	114.37
11	21	60.0	2340	3397.89	98.57	3372.88	96.16	3362.15	95.87
12	23	70.0	2730	3469.13	97.63	3477.65	96.34	3442.27	96.19
13	25	80.0	3120	3518.98	102.53	3524.28	100.66	3507.59	101.03
14	27	90.0	3510	4056.56	137.47	4038.26	136.71	4030.54	139.59
15	29	100.0	3900	3468.01	94.91	3481.79	94.02	3485.27	94.74

aliquot position	normalisation dose		exponential plus linear							
	[% of expected dose] [s]		late light 51 - 60 s							
			l 1 - 1 s	l 1 - 4 s		l 1 - 10 s				
			De [s]	De [s]	De [s]	De [s]	De [s]	De [s]	De [s]	De [s]
1	1	0.5	20	4596.03	653.76	4297.77	532.26	4283.19	517.61	
2	3	1.0	39	n.a.		4656.58	945.91	5356.48	1463.09	
3	5	2.5	98	5253.50	326.54	4989.70	304.59	5029.61	303.32	
4	7	5.0	195	3341.49	210.07	3447.28	186.13	3434.94	185.30	
5	9	7.5	293	4298.44	581.15	4316.07	378.52	4421.72	433.73	
6	11	10.0	390	4312.28	243.60	4179.39	189.69	4093.35	178.88	
7	13	20.0	780	3987.66	149.38	3933.23	133.40	3949.38	132.34	
8	15	30.0	1170	3658.36	115.41	3669.88	107.87	3646.26	106.71	
9	17	40.0	1560	3775.29	130.05	3812.63	131.60	3819.49	133.01	
10	19	46.2	1800	3763.30	120.20	3774.91	115.87	3747.46	114.34	
11	21	60.0	2340	3387.68	97.26	3367.96	95.61	3355.01	95.03	
12	23	70.0	2730	3457.73	96.47	3464.17	95.16	3429.89	95.12	
13	25	80.0	3120	3510.58	101.39	3527.43	100.90	3510.72	101.26	
14	27	90.0	3510	4093.43	137.77	4077.94	136.55	4084.28	138.76	
15	29	100.0	3900	3460.87	94.11	3475.07	93.32	3479.18	94.22	

(b)



(a)



(b)

Figure S5.96: Normalisation dose test on bleached aliquots of sample HDS-1776 with a laboratory dose of 3900 s (ca 314 Gy). A normalisation dose of 20 % (780 s) of the laboratory dose (3900 s) appears most appropriate.

Dose recovery test

The suggested normalisation dose (20 % of LAB) was investigated in a further test on 8 artificially bleached and dosed aliquots. The dose recovery test supports the results of the normalisation dose test, giving a central dose of 3939.6 ± 78.6 s, with an overdispersion (OD) of 4.3 % for the exponential plus linear fit. All recovered D_{es} meet the expected dose within an error range of 10 % (Fig. S5.97).

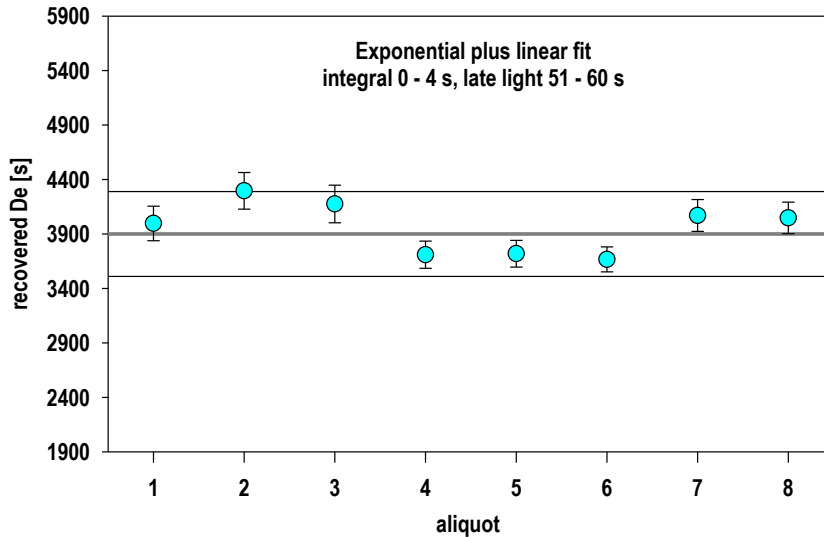


Figure S5.97: Dose recovery test on bleached aliquots of sample HDS-1776 with a laboratory dose of 3900 s (ca 314 Gy) and a normalisation dose of 780 s (ca 62.7 Gy; 20 % of the laboratory dose).

PIR₆₀IR₂₂₅ SAR protocol

Based on the pretests presented above the SAR protocol for D_e determination on supertiny aliquots (100 grains) of potassium coarse grains (125–212 μm) from the 6 block samples was adapted as outlined in Fig. S5.98. The SAR measurements were processed after flooding the measurement chamber of the luminescence reader for 4 min with liquid nitrogen without applying the run-one-at-a-time mode. 24 aliquots were measured of each sample, placed on every second turntable position to avoid cross talk (Kreutzer et al. 2013).

As for the lowermost sample (HDS-1799), the D_e of some aliquots was near/beyond the largest regeneration dose point (REG) (6240 s resp. 501.50 Gy), for these aliquots two more recycling dose points were added at the upper end of the dose response curve (7410 s resp. 595.5 Gy; 8580 s resp. 689.6 Gy), starting the continuation measurement with the repetition of the 3900 s and the 6240 s dose point to test the recycling ratio again and finishing it with the zero dose point and the 3900 s dose point to test the recuperation and the recycling ratio.

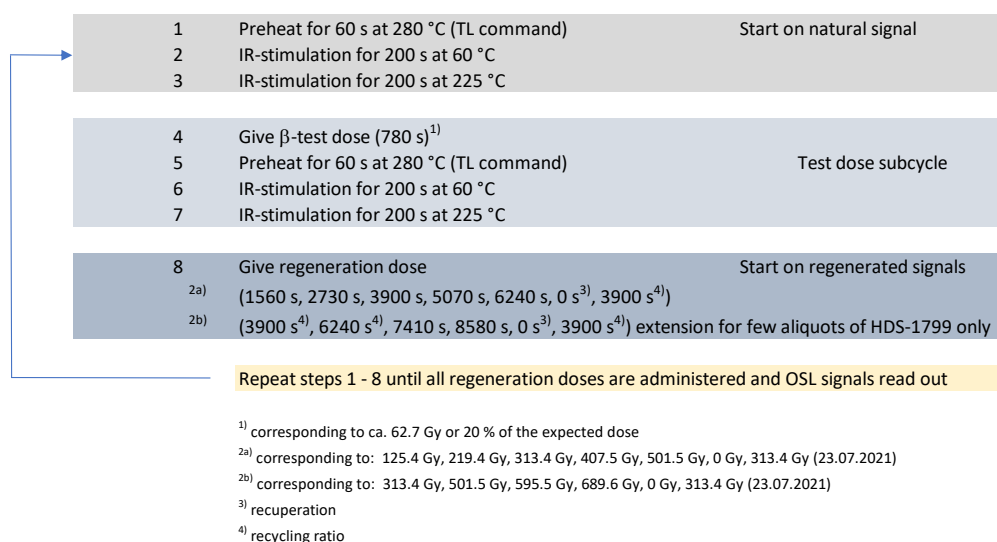


Figure S5.98: Schematic representation of the $pIR_{60}IR_{225}$ SAR protocol applied to potassium coarse grains (125–212 μm) of the 6 block samples HDS-1776 to HDS-1778 and HDS-1799 to HDS-1801. For the uppermost sample HDS-1778 also aliquots with recuperation values >10 % were accepted.

D_e determination

The D_e determination occurred with the software Analyst (version 4.31.09; Duller, 2015) applying the parameters of data analysis as depicted in Fig. S5.99.

Assuming similarly large absolute recuperation, samples/aliquots with a comparatively smaller D_e possess a comparatively larger relative recuperation, as the zero dose signal is compared to the natural signal. This explains why several aliquots of the uppermost sample HDS-1778 exhibit recuperation values >10 % (see Fig. S5.102). As these aliquots did not show any conspicuous characteristics, but only comparatively low D_e values with associated comparatively large recuperation values, we did not eliminate these aliquots from the data set.

Software:	Luminescence Analyst, version 4.31.9 (Duller 2015)
Curve fitting:	Exponential plus linear
Integral [channel]:	1 - 4 (0 - 4 s)
Background [channel]:	51 - 60 (51 - 60 s)
Use recycled points for fitting:	Yes
Measurement error [%]:	1.5
Incorporate error on curve fitting:	Yes
Use errors when applying criteria:	Yes
Recycling ratio limit [%]:	10
Maximum test dose error [%]:	10
Maximum recuperation [% of N]:	10
Tn signal > 3 sigma above background:	Yes

Figure S5.99: Parameters of the D_e determination. For the uppermost sample HDS-1778 also aliquots with recuperation values >10 % were accepted (cf. Fig. S5.101 of this supplement).

The analysis of the counts of the first data channel resp. first second of the shine down curve of sample HDS-1776 shows that the signal of the subsequently read out IR_{225} signal is on average ca 2–3 times stronger than the previously read out IR_{60} signal. This is in contrast to

the polymineral fine grains, extracted and analysed from the same OSL block samples (cf. supplement sect. 5.4.1).

Table S5.29: Comparison of the signal strength of the IR_{60} and IR_{225} signals. The comparison is based on the mean counts of the initial signal (0–1 s) of all normalisation doses (set number 9 (IR_{60}) and 10 (IR_{225}); 8 records each) of the 24 measured aliquots.

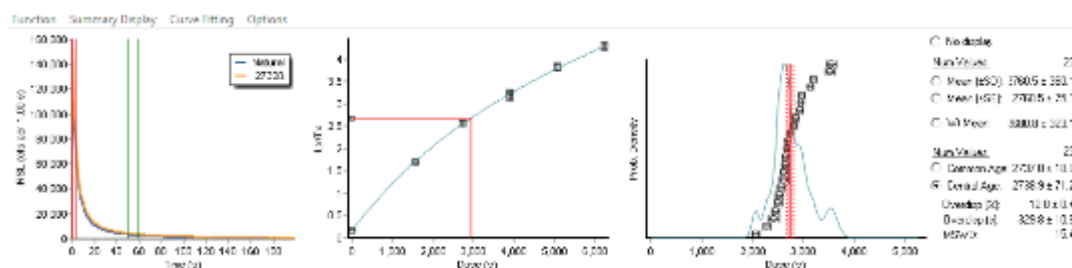
Position	NRM - IR_{60}			NRM - IR_{225}			NRM - IR_{225} / NRM - IR_{60}
	Mean [cts]	SD [cts]	SD [%]	Mean [cts]	SD [cts]	SD [%]	
1	25933.8	3463.8	13.4	66566.5	8725.7	13.1	2.6
3	1952.9	123.0	6.3	4213.4	536.7	12.7	2.2
5	5974.0	420.6	7.0	16040.4	1631.4	10.2	2.7
7	11281.1	1297.8	11.5	24534.4	3926.3	16.0	2.2
9	2630.0	61.2	2.3	7002.3	576.5	8.2	2.7
11	19605.0	2333.6	11.9	36133.0	5743.5	15.9	1.8
13	1306.1	76.5	5.9	3811.4	361.0	9.5	2.9
15	2152.4	128.5	6.0	8139.4	801.3	9.8	3.8
17	4463.0	449.8	10.1	15941.0	2377.2	14.9	3.6
19	11685.9	1686.2	14.4	27919.6	5274.3	18.9	2.4
21	26702.8	2535.9	9.5	44038.6	3829.1	8.7	1.6
23	23059.3	1999.8	8.7	24876.0	3979.3	16.0	1.1
25	5290.4	487.8	9.2	15973.9	1494.7	9.4	3.0
27	19298.8	3813.6	19.8	41612.1	10177.4	24.5	2.2
29	20910.3	1580.3	7.6	64418.9	4637.6	7.2	3.1
31	10883.4	1108.8	10.2	44802.0	6681.4	14.9	4.1
33	44634.5	3630.5	8.1	86530.0	10708.9	12.4	1.9
35	18118.6	1844.6	10.2	41047.0	5231.2	12.7	2.3
37	5607.3	945.3	16.9	11970.3	2781.8	23.2	2.1
39	28841.5	3383.3	11.7	51855.1	10507.4	20.3	1.8
41	1591.8	147.6	9.3	4078.4	688.8	16.9	2.6
43	4504.3	587.9	13.1	8228.1	1677.1	20.4	1.8
45	2566.5	153.2	6.0	15036.0	1556.7	10.4	5.9
47	7798.5	846.1	10.9	25086.8	3663.2	14.6	3.2

MEAN:	2.6
MIN:	1.1
MAX:	5.9

SAR measurements

Results of the D_e measurements are compiled in Fig. S5.100 to Fig. S5.105. Comparison of the very early D_e integral 0–1 s vs. the integral 0–4 s shows no systematic differences for the two intervals. For the uppermost sample HDS-1778 also the recuperation values are given, which for this sample may be above 10 %.

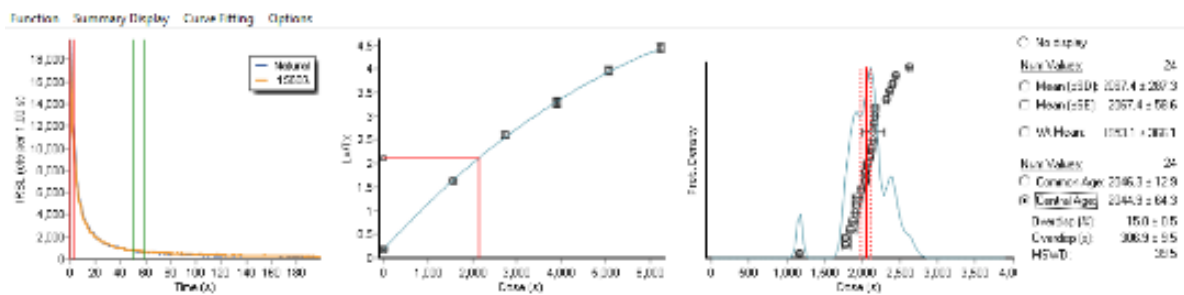
HDS-1776



turntable position [#]	aliquot [#]	determined dose [s irradiation time]		determined dose [s irradiation time]		Diff long vs. short De interval [s irradiation time] [0 - 4 s] - [0 - 1 s]
		[0 - 1 s]	[0 - 4 s]	[0 - 1 s]	[0 - 4 s]	
1	1	2951.53	96.78	2945.67	95.18	-5.86
3	2	2702.90	118.91	2662.48	96.40	-40.42
5	3	2626.76	87.63	2646.23	83.01	19.47
7	4	2487.33	84.63	2461.29	78.25	-26.04
9	5	2639.41	103.44	2630.97	91.86	-8.44
11	6	2627.29	78.73	2631.26	78.40	3.97
13	7	3402.51	147.31	3535.99	126.85	133.48
15	8	2278.23	79.37	2281.39	71.79	3.16
17	9	2725.76	87.73	2834.26	84.40	108.50
19	10	2600.89	75.60	2673.12	75.85	72.23
21	11	2344.51	110.50	2409.90	116.23	65.39
23	12	2707.56	87.42	2744.31	83.76	36.75
25	13	2509.07	76.71	2558.31	75.33	49.24
27	14	2986.67	84.29	2954.98	80.61	-31.69
29	15	2805.22	91.81	2852.35	92.90	47.13
31	16	n.a.		n.a.		
33	17	2696.17	77.56	2697.15	76.96	0.98
35	18	3155.04	100.51	3144.17	99.98	-10.87
37	19	3227.81	115.12	3197.45	102.99	-30.36
39	20	3011.29	85.41	2981.53	84.64	-29.76
41	21	2008.77	80.95	2057.09	68.46	48.32
43	22	2509.08	88.51	2520.23	75.74	11.15
45	23	3532.65	133.90	3547.10	126.94	14.45
47	24	2527.97	74.58	2523.19	72.26	-4.78
central dose:		2720.50	71.20	2738.90	71.20	

Figure S5.100: D_e determination on sample HDS-1776. Example of shine down curve and dose response curve (exponential plus linear fit), and weighted histogram of all analysable aliquots ($N = 23$).

HDS-1777

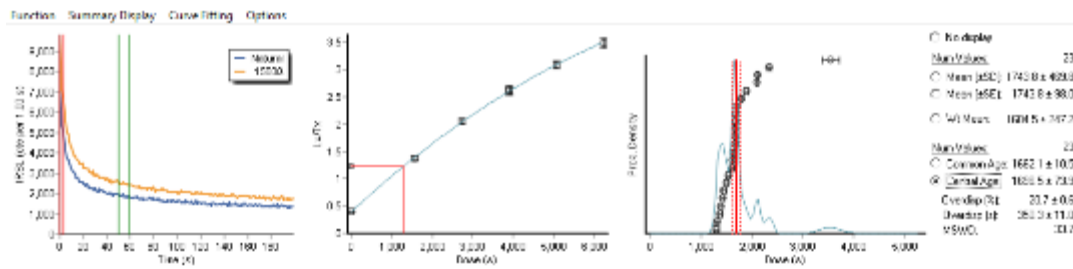


turntable position [#]	aliquot [#]	determined dose [s irradiation time]		determined dose [s irradiation time]		Diff long vs. short De interval [s irradiation time] [0 - 4 s] - [0 - 1 s]
		[0 - 1 s]	[0 - 1 s]	[0 - 4 s]	[0 - 4 s]	
1	1	2212.18	72.14	2139.75	63.26	-72.43
3	2	2342.01	68.31	2331.34	65.41	-10.67
5	3	2128.16	61.98	2177.93	58.84	49.77
7	4	1767.78	85.94	1853.24	67.70	85.46
9	5	1790.37	53.36	1783.68	50.92	-6.69
11	6	2588.31	94.11	2623.26	80.10	34.95
13	7	1891.19	62.70	1884.74	54.47	-6.45
15	8	2042.29	80.64	2062.89	67.77	20.60
17	9	1960.15	66.15	1911.46	53.37	-48.69
19	10	2322.94	82.28	2409.60	73.54	86.66
21	11	2095.96	58.28	2155.88	58.74	59.92
23	12	2015.64	71.17	2052.88	67.49	37.24
25	13	1769.73	58.14	1792.98	54.08	23.25
27	14	2143.48	76.24	2180.13	68.70	36.65
29	15	1165.10	40.94	1166.68	34.79	1.58
31	16	2071.85	63.29	2105.29	62.07	33.44
33	17	1866.37	59.35	1926.13	56.64	59.76
35	18	2017.80	62.86	2044.96	58.28	27.16
37	19	n.a.		2150.22	184.57	
39	20	2067.67	65.11	2115.12	64.90	47.45
41	21	2042.96	190.74	1937.36	94.50	-105.60
43	22	2372.43	78.60	2449.24	75.12	76.81
45	23	2387.40	76.92	2373.03	68.60	-14.37
47	24	1987.72	61.79	1988.85	59.57	1.13

central dose: 2024.30 65.00 2044.90 64.30

Figure S5.101: D_e determination on sample HDS-1777. Example of shine down curve and dose response curve (exponential plus linear fit), and weighted histogram of all analysable aliquots ($N = 23$).

HDS-1778

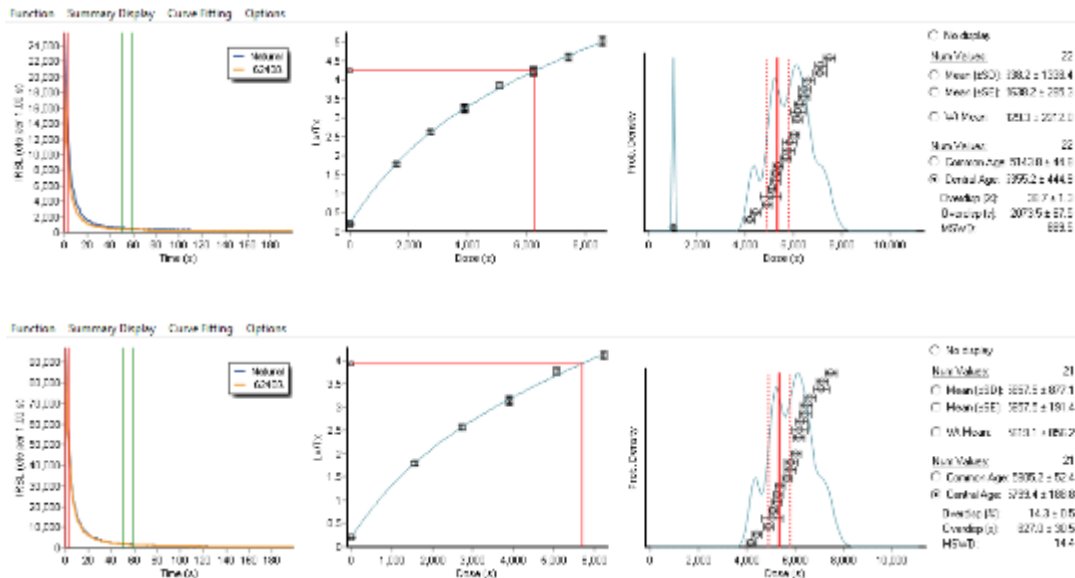


turntable position [#]	aliquot [#]	determined dose [s irradiation time]		determined dose [s irradiation time]		Diff long vs. short De interval [0 - 4 s] - [0 - 1 s]	recuperation [% signal of N]		recuperation [% signal of N]		
		[0 - 1 s]	[0 - 1 s]	[0 - 4 s]	[0 - 4 s]		[0 - 1 s]	[0 - 1 s]	[0 - 4 s]	[0 - 4 s]	
1	1	1366.46	68.45	1296.55	54.71		-69.91	27.92	1.46	32.03	1.30
3	2	2149.02	80.12	2113.00	65.71		-36.02	8.80	0.46	8.69	0.35
5	3	1653.14	49.42	1667.30	47.51		14.16	12.04	0.44	11.79	0.38
7	4	1367.17	43.13	1375.47	39.51		8.30	12.69	0.45	12.61	0.41
9	5	1682.96	50.44	1673.86	47.80		-9.10	9.53	0.35	9.63	0.31
11	6	± no signal		± no signal							
13	7	1464.10	63.23	1538.43	52.40		74.33	10.58	0.57	10.15	0.41
15	8	2439.56	88.05	2338.56	70.48		-101.00	8.60	0.40	9.19	0.33
17	9	1296.49	41.98	1322.63	39.19		26.14	11.16	0.45	10.85	0.37
19	10	3734.02	307.33	3542.20	199.24		-191.82	5.22	0.71	6.42	0.53
21	11	1681.31	49.90	1693.93	47.82		12.62	11.16	0.37	11.08	0.35
23	12	1329.60	47.85	1389.36	45.92		59.76	10.71	0.53	10.30	0.40
25	13	1593.73	46.16	1618.98	44.59		25.25	10.67	0.36	10.50	0.33
27	14	1699.78	58.88	1715.94	55.19		16.16	12.69	0.52	12.62	0.44
29	15	1954.33	83.27	1899.68	65.90		-54.65	9.87	0.58	9.39	0.41
31	16	2068.96	63.02	2093.60	61.85		24.64	8.86	0.30	8.58	0.27
33	17	1645.23	52.06	1640.69	47.02		-4.54	11.04	0.44	11.04	0.38
35	18	1648.84	50.79	1666.89	48.15		18.05	10.91	0.42	10.52	0.35
37	19	1672.71	51.75	1695.28	48.51		22.57	9.93	0.36	9.91	0.32
39	20	1787.08	54.08	1810.59	52.60		23.51	11.00	0.36	11.21	0.35
41	21	1598.36	45.92	1619.44	45.01		21.08	8.78	0.29	8.56	0.27
43	22	1428.80	39.31	1433.41	38.45		4.61	10.90	0.36	10.79	0.34
45	23	1458.16	41.65	1506.37	42.35		48.21	13.07	0.43	13.06	0.41
47	24	1462.62	48.03	1454.46	41.91		-8.16	11.61	0.49	11.43	0.41

central dose: 1704.80 78.90 1716.90 75.20

Figure S5.102: D_e determination on sample HDS-1778. Example of shine down curve and dose response curve (exponential plus linear fit), and weighted histogram of all analysable aliquots ($N = 23$).

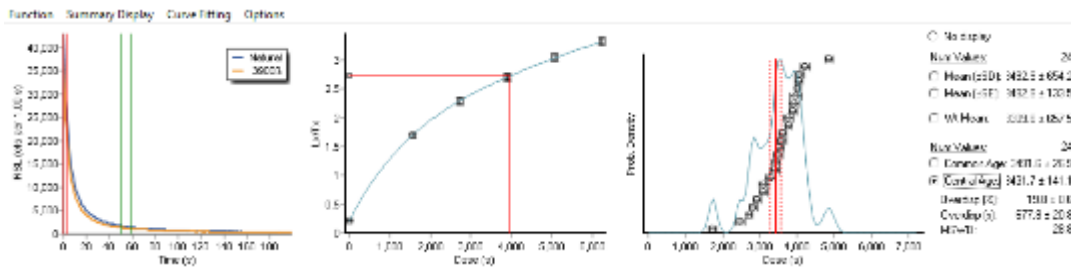
HDS-1799



turntable position [#]	aliquot [#]	determined dose [s irradiation time]		determined dose [s irradiation time]		Diff long vs. short De interval [s irradiation time] [0 - 4 s] - [0 - 1 s]
		[0 - 1 s]	[0 - 1 s]	[0 - 4 s]	[0 - 4 s]	
1	1	5633.82	224.57	5701.99	220.81	68.17
3	2					
5	3	6165.17	292.93	6268.38	270.16	103.21
7	4	5258.52	232.57	5383.84	221.21	125.32
9	5	4957.40	193.27	5092.62	176.20	135.22
11	6	4555.94	218.32	4905.23	183.42	349.29
13	7	6732.82	404.82	7108.30	330.66	375.48
15	8	5633.98	296.34	5850.92	276.97	216.94
17	9	6435.99	259.77	6623.27	266.33	187.28
19	10	6460.18	269.38	6488.72	263.25	28.54
21	11	5028.20	199.89	5291.50	200.79	263.30
23	12	5948.78	271.54	6095.03		146.25
25	13	7234.39	290.32	7133.57	279.53	-100.82
27	14	6153.27	259.09	6459.34	258.61	306.07
29	15	4293.66	249.19	4212.91	195.22	-80.75
31	16	5033.45	225.20	5251.29	205.16	217.84
33	17	4971.01	596.62	5079.13	419.52	108.12
35	18	5632.52	217.64	5826.09	237.49	193.57
37	19	7385.55	343.65	7487.23	311.13	101.68
39	20	967.45	41.99	1031.84	33.94	64.39
41	21	4439.07	267.43	4431.83	188.55	-7.24
43	22	6086.88	239.62	6171.11	229.78	84.23
45	23	5889.52	385.21	6200.70	333.50	311.18
47	24	6029.54	229.50	6039.63	220.38	10.09
central dose:		5246.70	426.30	5355.20	444.90	
no outlier:		5684.50	176.30	5799.40	188.80	

Figure S5.103: D_e determination on sample HDS-1799. Example of shine down curve and dose response curve (exponential plus linear fit), and weighted histogram of all analysable aliquots ($N = 22$, including outlier at lower end; $N = 21$, excluding outlier).

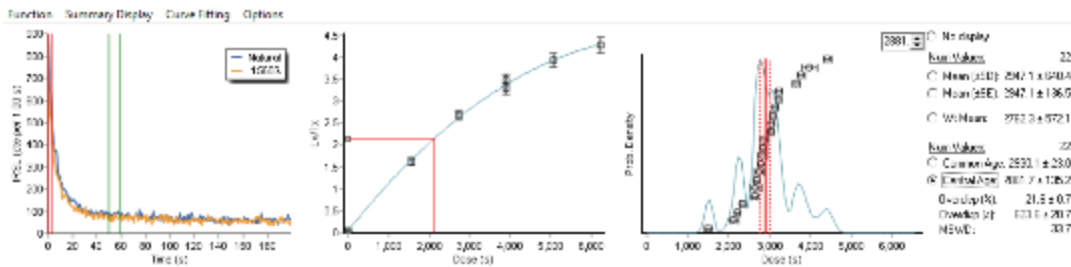
HDS-1800



turntable position [#]	aliquot [#]	determined dose [s irradiation time]		determined dose [s irradiation time]		Diff long vs. short De interval [s irradiation time] [0 - 4 s] - [0 - 1 s]
		[0 - 1 s]	[0 - 1 s]	[0 - 4 s]	[0 - 4 s]	
1	1	3936.19	203.65	3960.73	197.31	24.54
3	2	3866.35	165.36	3891.87	155.41	25.52
5	3	3367.19	133.56	3482.94	132.30	115.75
7	4	3538.10	123.94	3593.08	127.65	54.98
9	5	1593.58	145.64	1738.51	113.00	144.93
11	6	3660.80	159.53	3618.97	149.61	-41.83
13	7	2355.50	139.35	2480.86	120.24	125.36
15	8	3983.21	169.80	4081.95	174.64	98.74
17	9	2872.59	134.34	3108.91	128.17	236.32
19	10	2935.79	104.79	2917.38	96.80	-18.41
21	11	3310.05	124.33	3448.84	122.78	138.79
23	12	3973.95	148.52	4037.54	151.39	63.59
25	13	2756.09	94.12	2731.87	85.25	-24.22
27	14	3056.19	113.35	3107.16	111.40	50.97
29	15	3218.21	126.16	3282.57	126.36	64.36
31	16	3487.97	128.79	3541.25	125.64	53.28
33	17	2785.54	101.97	2836.67	97.01	51.13
35	18	4173.69	174.19	4218.41	167.60	44.72
37	19	3897.38	124.58	4033.68	125.80	136.30
39	20	4848.55	156.10	4853.63	156.77	5.08
41	21	3362.35	133.01	3410.98	133.47	48.63
43	22	3716.81	133.50	3764.53	123.12	47.72
45	23	3769.94	171.34	3765.92	159.77	-4.02
47	24	3870.74	167.88	3921.44	157.53	50.70
central dose:		3372.00	143.00	3431.70	141.10	

Figure S5.104: D_e determination on sample HDS-1800. Example of shine down curve and dose response curve (exponential plus linear fit), and weighted histogram of all analysable aliquots ($N = 24$).

HDS-1801



turntable position [#]	aliquot [#]	determined dose [s irradiation time] [0 - 1 s]		determined dose [s irradiation time] [0 - 4 s]		Diff long vs. short De interval [s irradiation time] [0 - 4 s] - [0 - 1 s]
1	1	2960.88	96.09	3053.04	98.39	92.16
3	2	2653.68	94.52	2679.06	85.44	25.38
5	3	2704.47	131.24	2744.22	113.91	39.75
7	4	3775.62	292.94	3975.57	237.01	199.95
9	5	3132.24	115.03	3226.42	112.55	94.18
11	6	3183.13	115.55	3149.82	103.71	-33.31
13	7	2518.55	215.15	2658.76	142.67	140.21
15	8	recup. > 10 %		recup. > 10 %		
17	9	2855.81	106.37	3036.13	107.78	180.32
19	10	2767.17	107.44	2855.72	107.71	88.55
21	11	1389.51	129.11	1510.40	92.61	120.89
23	12	2804.99	99.92	2806.95	94.96	1.96
25	13	2336.72	73.82	2330.56	65.86	-6.16
27	14	2556.11	137.54	2819.70	125.53	263.59
29	15	3639.81	129.45	3644.97	129.05	5.16
31	16	2795.30	120.12	2866.58	98.63	71.28
33	17	3110.77	142.86	3247.61	121.34	136.84
35	18	3024.33	106.57	3070.58	101.89	46.25
37	19	4530.16	169.49	4410.97	146.57	-119.19
39	20	3691.45	136.47	3771.09	137.19	79.64
41	21	2587.17	104.42	2642.29	92.87	55.12
43	22	n.a.		n.a.		
45	23	2083.42	199.62	2122.92	125.76	39.50
47	24	2218.57	98.80	2213.74	72.78	-4.83
central dose:		2820.00	134.50	2881.70	135.20	

Figure S5.105: D_e determination on sample HDS-1801. Example of shine down curve and dose response curve (exponential plus linear fit), and weighted histogram of all analysable aliquots ($N = 22$).

Investigating the suitability of T_x/T_n sensitivity curves as a proxy of varying material source

Pfaffner et al. (2024) used the IRSL/pIR-BLSL signal ratio (signal detection in the UV around 340 nm) of the minimally prepared Baix samples as a proxy of material source. Here we tested whether also the course of the luminescence signals during a complete SAR measurement (here 8 cycles) associated with the normalisation dose (also test dose; T_n = test dose signal following the readout of the natural dose or the laboratory dose in a dose recovery test, respectively, here SAR cycle 1); T_x = test dose signal induced by the regeneration doses (REG) during a SAR measurement, here SAR cycles 2–8). The normalised signals (T_x/T_n) are illustrated in Fig. S5.106a–f (D_e determination on natural samples) and Fig. S5.105g (dose recovery on artificially bleached and dosed sample HDS-1776). All measurements were carried out applying a 3.900 s dose response curve (313.4 Gy) and NRM 20 % (62.7 Gy). However, while the T_x/T_n values of the natural samples lie for the lowermost sample HDS-1779 mainly below 1 they are for the upper samples HDS-1776 to HDS-1778 mainly above 1, with those of HDS-1800 and HDS-1801 trending around the balance line. Thus, from bottom to top of the Baix stratigraphy, the T_x/T_n curves appear to rise from below 1 to above 1 while simultaneously expanding from a narrow range around 1 (ca 0.6–1.17) for HDS-1799 to a wider range (ca 0.8–2.1, with extreme values up to 2.4–2.5) for the upper three samples HDS-1776 to HDS-1778.

As compared to the natural sample HDS-1776, the dose recovery test (DRT) on 8 aliquots of HDS-1776 (Fig. S5.106g) shows a comparable narrow scatter in the range 0.8–1.4. This compares to sample HDS-1800 (ca 0.7–1.4), which yielded a central dose of 3431.70 ± 141.10 s, which is close to LAB 3900 s as administered in the DRT. It is possible that the expansion of the T_x/T_n curves is dependent on the dose (natural palaeodose or laboratory dose) a sample had received prior to the $pIR_{60}IR_{225}$ SAR measurement. If this is the case, larger primary doses would lead to T_x/T_n curves more narrowly stretched around 1, while smaller primary doses would cause a wider expansion of the T_x/T_n values, especially above the balance line.

Similarly, the size of the normalisation dose modulates the course of the T_x/T_n curves (Fig. S5.95a–o; right graph in each case). While smaller NRMs lead to a zigzag appearance larger NRMs provide T_x/T_n courses stretched narrowly around 1. As the T_x/T_n values, or de facto the ratio of the signal strength of a regeneration dose (REG) signal (L_x) compared to T_x , are used to correct (normalise) the regeneration dose points of a SAR dose response curve, the more sensitive (zigzagged) courses of T_x/T_n lead to a stronger curved SAR curve, while the less sensitive (zigzagged) courses of T_x/T_n lead to a more stretched SAR curve (cf. the trend from Fig. S5.95a–o).

The sensitivity curves show that the course of the T_x/T_n values are also dependent on the size of the associated REG, increasing for the curves trending above 1 with larger REGs (e.g. run 2 with the smallest REG to run 6 with the largest REG) and decreasing with a smaller REG (cf. zero dose of run 7). Around the T_x/T_n value around the zero dose point this positive trend with higher REGs and negative trend with smaller REGs is also observed for T_x/T_n curves trending below the balance line. Therefore, the trend of the T_x/T_n curves seems to be dependent, among others, on the degree of refilling of the OSL traps after the previous SAR readouts and/or the electron redistribution by IRSL readout of the respective amount of refilled electrons due to artificial dosing (REG). If the latter case applies the ionized electrons associated with NRM (which is the same for each SAR cycle) may possibly not be able to occupy the OSL traps which they would search if they had not already been occupied by electrons associated with the REG dosing or its OSL readout, thus increasing T_x/T_n .

Concluding: The different behaviour of the T_x/T_n curves of the lower samples (stretched curves, narrow data scatter around 1) which possess a dominant component of reworked Eem Bt as compared to the T_x/T_n curves of the upper samples (larger expansion of the data values and curves, especially above the balance line, and increasing expansion in the upward direction) which possess a strong (and in the upward direction increasing) component of Last Glacial loess input might at first sight suggest a correlation of T_x/T_n behaviour and material source. However, including the results of the DRT and NRM test as well as the response of individual T_x/T_n values to previous regeneration doses (REGs) and considering the decreasing size of

the natural palaeodoses with decreasing depth below ground level, the amount of electrons in the OSL traps might dominantly modulate the course of the T_x/T_n curves rather than differing source materials. This finding would conform to the observations of Chen et al. (2013), who observed differences in the trends of T_x/T_n curves between artificially well bleached and dosed samples as compared to artificially poorly bleached and dosed samples. The issue needs further investigation in future studies.

Investigating the suitability of T_x/T_n sensitivity curves as a proxy of poor bleaching

As Chen et al. (2013) observed different behaviour of T_x/T_n sensitivity curves for artificially well and poorly bleached and subsequently dosed samples, here we investigate whether such phenome can be observed for the Baix OSL block samples and therefore whether the trend of the T_x/T_n curves may serve as a proxy to indicate poor bleaching of the mineral grains. If one assumes the aliquots producing a larger D_e to having been poorly bleached prior to deposition and those producing the smaller D_{es} having been well bleached, then one could expect a correlation such that smaller T_x/T_n values (and negative trends) would be typical of aliquots with well bleached grains while aliquots dominated by poorly bleached grains would deliver larger T_x/T_n values (and positive trends) (cf. Chen et al. 2013). In Fig. S5.107 we plotted the D_e values of each aliquot gained by the SAR measurements (cf. also Fig. S5.100 –S5.105) against an aliquots mean T_x/T_n value to illustrate a possible correlation between the two parameters. Next to the measurements of the natural samples (Fig. S5.107a–f) we also show the results of the dose recovery test (DRT) on 8 aliquots of sample HDS-1776 (Fig. S5.107g), which had received a laboratory dose (LAB) of 3900 s (ca 320 Gy), whereas the natural sample delivered a ca 30 % smaller central dose of 2738.90 ± 71.20 s (ca 218.6 Gy). As a result no convincing correlation is observed between T_x/T_n and D_e . Of the natural samples, only HDS-1778 shows one large outlier D_e with an unusually small T_x/T_n value (cf. also Fig. S5.106a, T_x/T_n curve (triangles with yellow filling) below the balance line), while the narrow scatter of the mean T_x/T_n values of the DRT on sample HDS-1776 may also suggest a tendency of slightly smaller T_x/T_n values for larger D_{es} (less well bleached aliquots under the solar simulator?) and slightly larger T_x/T_n values for smaller D_{es} (likely better bleached aliquots?). Although it cannot be excluded that different aliquots were bleached to a slightly different degree under the solar simulator, the experimental setup of the bleaching procedure does not make that scenario very likely. Anyway, no distinctly differing T_x/T_n values and T_x/T_n curve trends as observed by Chen et al. (2013) were observed for the Baix samples. Presently we therefore conclude that T_x/T_n cannot be used as a proxy of poor bleaching of a sample at the LPS Baix. The issue needs further investigation.

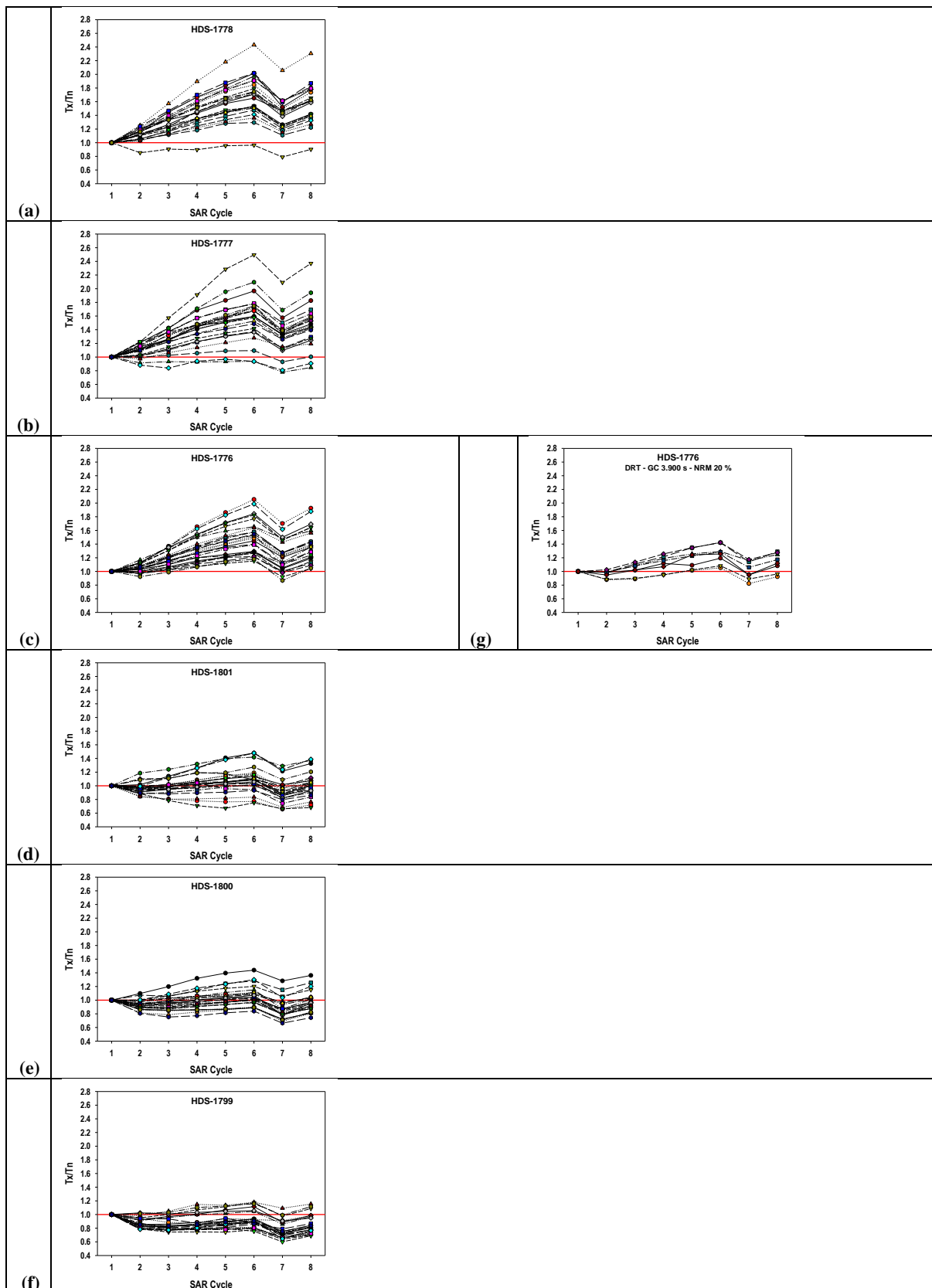


Figure S5.106: T_x/T_n sensitivity curves over the 8 measured SAR cycles for the six block samples HDS-1799 to HDS-1801 and HDS-1776 to HDS-1778 in stratigraphical order. (a–f) D_e determination on 24 natural samples; (g) dose recovery on 8 artificially bleached and dosed aliquots (LAB 3900 s; ca 313.4 Gy); (c) 23 analysable of 24 measured aliquots providing a central dose of 2738.9 ± 71.2 s (cf. Fig. S5.99). All samples were measured with a 3.900 s (ca 313.4 Gy) SAR dose response curve with NRM 20 % (780 s; ca 62.7 Gy).

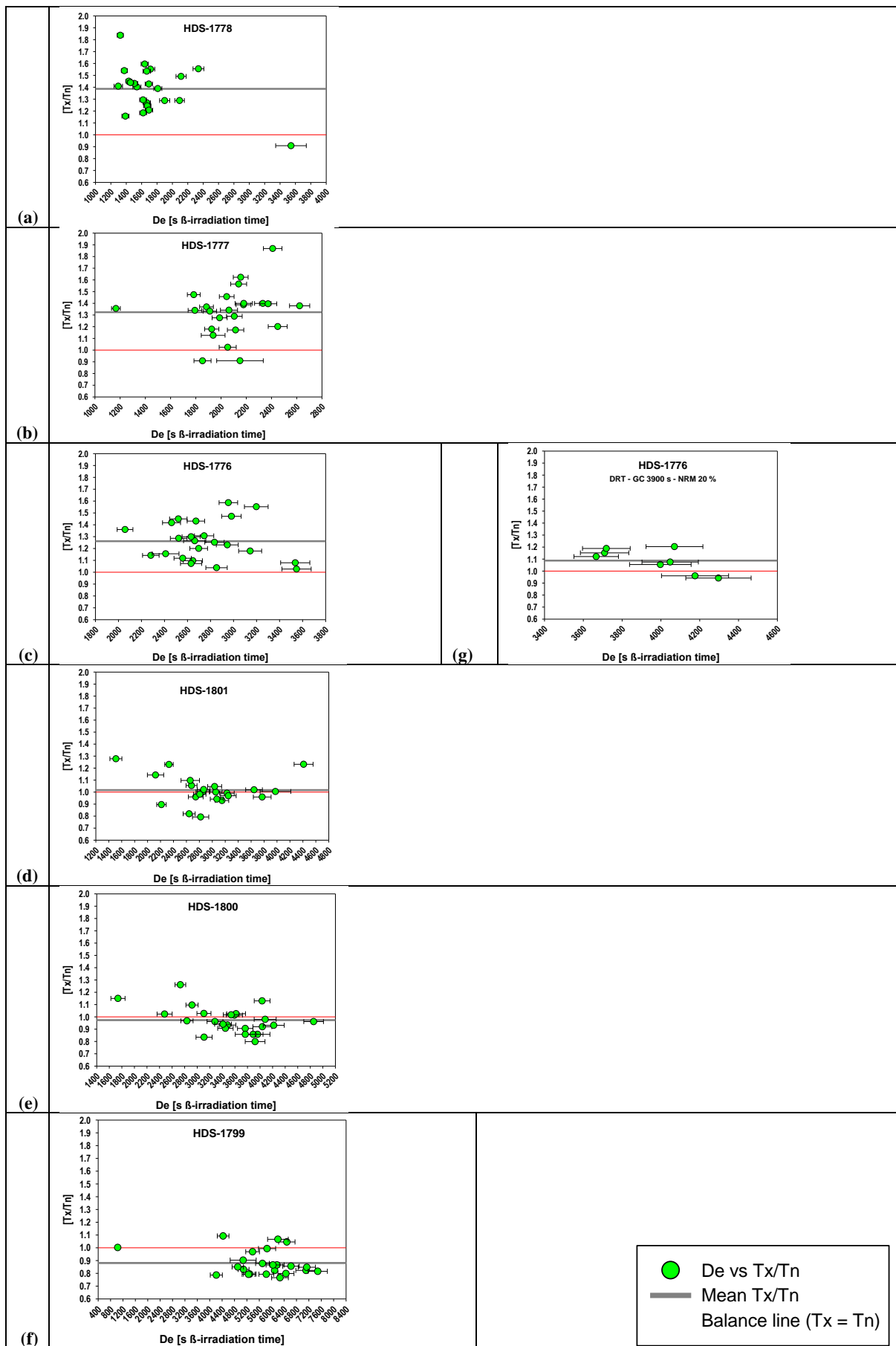


Figure S5.107: Mean T_x/T_n values per aliquot (y-axis) versus D_e value (x-axis) for the six block samples HDS-1799 to HDS-1801 and HDS-1776 to HDS-1778 in stratigraphical order. (a–f) D_e determination on

24 natural samples; (g) dose recovery on 8 artificially bleached and dosed aliquots (LAB 3900 s; ca 313.4 Gy); (c) 23 analysable of 24 measured aliquots providing a central dose of 2738.9 ± 71.2 s (cf. Fig. S5.99). All samples were measured with a 3.900 s (ca 313.4 Gy) SAR dose response curve with NRM 20 % (780 s; ca 62.7 Gy).

S5.4.3 Report quartz fine grains – pir-BLSL SAR

Instrumentation

Blue light stimulated luminescence (BLSL) single aliquot regeneration (SAR) (Murray and Wintle, 2001) measurements of quartz fine grains (4–11 μm) were carried out on a luminescence reader model Risø DA20 (serial no. 245; Kadereit and Kreutzer, 2013), equipped as depicted in Fig. S5.108.

Luminescence reader: Risø model TL/OSL DA20 (No. 245)			
turntable: 48 measurement positions			
use every 2 nd position (or wider spacing) to avoid IR cross talk (ignore)			
IR stimulation: bleaching of IR signal from feldspar			
IR-LEDs; 3 clusters; 7 LEDs each; 870 Δ 40 nm			
measurements with 90 % diode-power, after 10 s warmup			
Blue light stimulation: detection of BLSL ₁₂₅ signal assumed to originate (mostly) from quartz			
blue light emitting diodes; four clusters; 7 LEDs each; 470 Δ 30 nm			
measurements with 90 % diode-power, after 10 s warmup			
Detection: bialkali PMT EMI 9235QB15			
Detection filter: U340 (Schott; 3 x 2.5 mm thick)			
Detected emission: ultra-violet, around 340 nm			
β -dose rate:	0.08497 ± 0.00297	Gy/s	28. June 2021 (start this study)
	5.10 ± 0.18	Gy/min	
	0.08309 ± 0.00291	Gy/s	02. June 2022 (end this study)
	5.0 ± 0.2	Gy/min	
Nitrogen use: ca. 3 minutes at start of measurement			

Figure S5.108: Equipment of the luminescence reader model Risø TL/OSL DA20 used for BLSL SAR measurements of the quartz fine grains (4–11 μm).

Tests on possible contamination with feldspar

A possible feldspar contamination of the fine grain separates was investigated by applying a not yet optimized BLSL SAR protocol to aliquots with the natural luminescence signal. While the regeneration dose points (REG) for constructing the dose response curve were as in Pfaffner et al. (2024) and as in the pIR₆₀IR₂₂₅ protocol for feldspar coarse grains (cf. supplementary, sect. 5.4.2), preheat 1 was 260 °C and preheat 2 was 160 °C, both for 10 s. Blue light stimulated luminescence (BLSL) was performed for 40 s at 125 °C. The normalisation dose (NRM; also “test dose”) was set at 293 s (ca 24.9 Gy), corresponding to ca 7.5 % of the expected dose of 3900 s (ca 331.4 Gy). Feldspar contamination was investigated with a repeatedly measured dose point of which the BLSL readout occurred after IR-bleaching (OSL IR depletion ratio; Duller, 2003).

A first test was performed on polymineral fine grains (no etching with hydrofluoric acid (H₂SiF₆)); a second test was performed on material etched for 3 d with H₂SiF₆. Further tests

and D_e measurements were performed on material etched for 5 d with H_2SiF_6 . The tests on contamination with feldspar show that the unetched polymineral fine grains possess a significant amount of feldspar, whereas the fine grains do not possess any significant amount of feldspar after 3 d of etching (OSL IR depletion ratio <10 %) (Fig. S5.109).

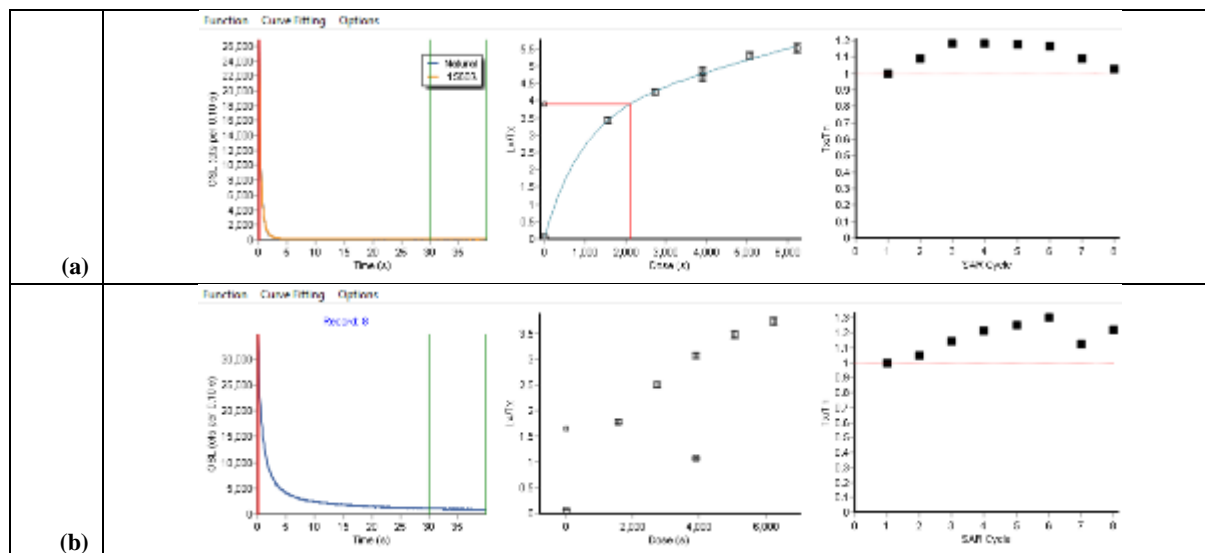


Figure S5.109: Typical examples of shine down curve, dose response curve (with an exponential plus linear fit in (b)) and sensitivity. Whereas unetched samples show OSL IR depletion ratios of 0.24–0.35 for the signal of the first two data channels; 0–0.2 s (a), they are always >0.9 after 3 d of etching with H_2SiF_6 (b).

Test on the palaeodose range

The preliminary SAR protocol applied for the test of feldspar contamination was also used for a test on the range of the equivalent doses (D_{es}) to be expected from the natural samples. For this test the lower three samples HDS-1799, HDS-1800 and HDS-1801 were measured (2 aliquots each). The D_e range was for the oldest sample (HDS-1799) ca 4900–7500 s (ca 411–629 Gy) and for the two younger samples ca 2400–2600 s (ca 201–218 Gy).

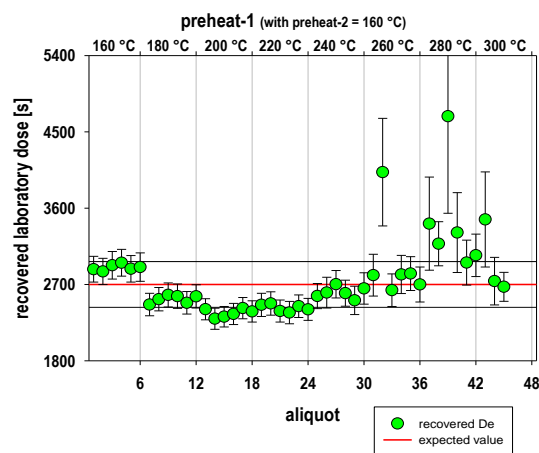
Combined preheat and dose recovery tests

A first set of combined preheat and dose recovery tests was performed on sample HDS-1776. The aliquots were bleached under a solar simulator (type Dr. Hönle, SOL 2; 3 h; samples covered with UVILEX glass filter; sample holders placed on water-cooled copper plate at ca 22 °C) before they received a laboratory dose of 2700 s (ca 226 Gy). The regeneration dose points were placed at 40 %, 70 %, 100 %, 130 %, 160 %, 0 %, 40 % and 100 % of the expected dose, corresponding to 1080 s (90.3 Gy), 1890 s (158.1 Gy), 2700 s (225.8 Gy), 3510 s (293.6 Gy), 4320 s (361.3 Gy), 0 s (0 Gy; to test for recuperation), 1080 s (90.3 Gy; to test the recycling ratio of a repeatedly measured dose point) and 2700 s (225.8 Gy; to test the OSL IR depletion ratio (feldspar contamination) of a dose point which prior to BLSL readout had been read out with IR-stimulation) (cf. also Fig. S5.109). The normalisation dose was set at 10 % of the expected dose (270 s; 22.6 Gy). Preheat 1 was increased from 160 °C to 300 °C (TL for 10 s)

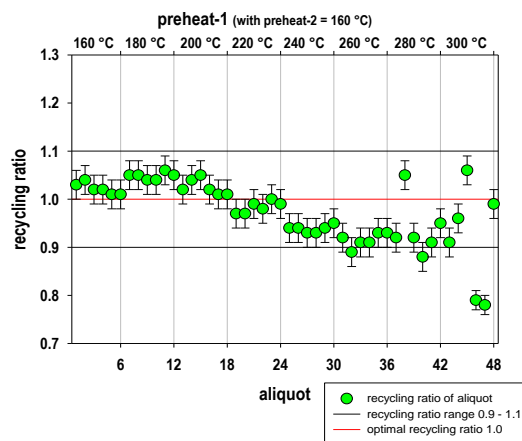
in steps of $\Delta 20\text{ }^\circ\text{C}$ (8 groups; 6 aliquots each), while preheat 2 was kept at $160\text{ }^\circ\text{C}$ (TL for 10 s) in a first test, and equal preheat 1 in a second test. In a third test preheat 2 was $\Delta 40\text{ }^\circ\text{C}$ lower than preheat 1. In all tests recycling ratios were around 1 and recuperation $<1\%$ of the recovered dose. The interval 30.1–40 s (channel 301–400) was used for background subtraction and the early integrals 0–0.1 s (channel 1–1) and 0–0.4 s (channel 1–4) were used for D_e determination.

Feldspar contamination was no issue as tested by the OSL IR depletion ratio, allowing depletion ratios of 0.9–1.0. With very few exceptions in the aliquot groups with the hottest preheat, in all tests recycling ratios were >0.9 and <1.1 and recuperation was $<1\%$. Recycling ratios are best (around 1) for lower preheat temperatures. No significant differences in D_e values were observed between the two different D_e intervals (Table S5.30). The expected D_e was met by most aliquots within a range of $\pm 10\%$, with the exception of the aliquot groups measured with the two hottest preheat temperatures (preheat 1 $\geq 280\text{ }^\circ\text{C}$; omitted in the $\Delta 40\text{ }^\circ\text{C}$ test (see Fig. S5.112)). The expected D_e was recovered best by a preheat combination $180\text{ }^\circ\text{C}/180\text{ }^\circ\text{C}$, with a central dose of the respective aliquot group of $2698.70 \pm 58.30\text{ s}$ (Fig. S5.111; Table S5.30).

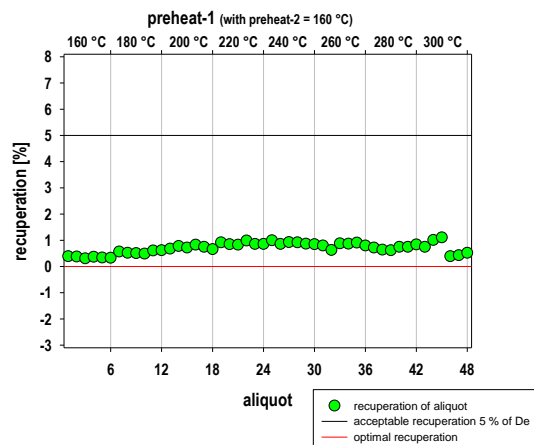
Combined preheat and dose recovery test with preheat 2 equal $160\text{ }^\circ\text{C}$



(a)



(b)



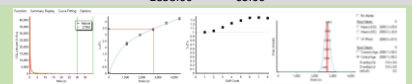
(c)

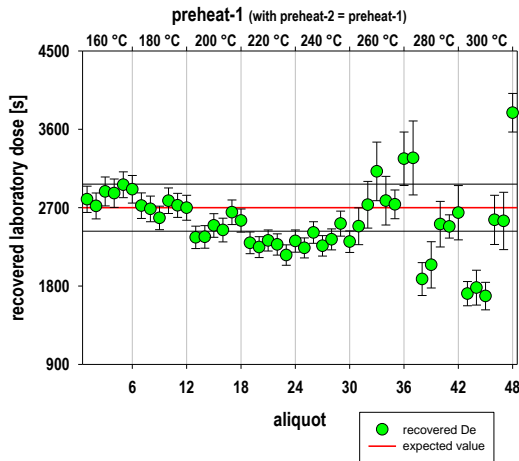
Figure S5.110: Combined preheat and dose recovery test: Laboratory dose 2700 s (225.8 Gy), normalisation dose 270 s (22.6 Gy). Six aliquots per group. Preheat 1 increasing from 160 °C to 300 °C, in steps of 20 °C. Preheat 2 always at 160 °C. BLSL readout at 125 °C for 40 s in 400 data channels (0.1 s per data channel). Dose response curve modelled with exponential plus linear fit. Results for D_e interval 0–0.4 s, with late light interval 30.1–40 s. (a) Recovered D_e values, (b) recycling ratios, (c) recuperation.

Combined preheat and dose recovery test with preheat 2 equal preheat 1

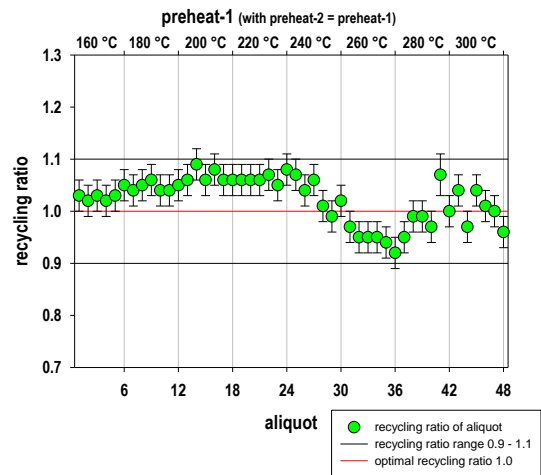
Table S5.30: Combined preheat and dose recovery test: Laboratory dose 2700 s (225.8 Gy), normalisation dose 270 s (22.6 Gy). Six aliquots per group. Preheat 1 and preheat 2 increasing from 160 °C to 300 °C, in steps of 20 °C. BLSL readout at 125 °C for 40 s in 400 data channels (0.1 s per data channel). Dose response curve modelled with exponential plus linear fit. Results for D_e interval 0–0.4 s, with late light interval 30.1–40 s. (a) Recovered D_e values, (b) recycling ratios, (c) recuperation. The expected dose was recovered best by a preheat combination 180 °C/180 °C (central dose of aliquot group 2698.70 ± 58.30 s). Data analysis with software Luminescence Analyst (version 4.31.9; Duller 2015).

Aliquot	recovered dose		recovered dose		recovered dose		recovered dose		recovered dose		recovered dose		recovered dose	
	0 - 0.1 s, LL 30.1 - 40 s	151.83	0 - 0.2 s, LL 30.1 - 40 s	151.83	0 - 0.4 s, LL 30.1 - 40 s	150.60	0 - 0.6 s, LL 30.1 - 40 s	150.60	0 - 0.1 s, LL 30.1 - 40 s	65.50	0 - 0.2 s, LL 30.1 - 40 s	63.60	0 - 0.4 s, LL 30.1 - 40 s	63.60
1	2846.37	151.83			2796.04	150.60								
2	2804.58	162.69			2719.81	149.21								
3	2865.95	176.15			2886.41	166.39								
4	2885.84	165.59			2866.16	163.31								
5	3029.68	148.10			2963.18	148.46								
6	2787.99	162.03			2911.26	158.87			2878.40	65.50		2858.60	63.60	
7	2650.56	148.01			2722.96	146.83								
8	2689.28	150.30			2685.88	147.59								
9	2694.69	137.49			2582.07	135.16								
10	2815.65	162.26			2779.76	146.93								
11	2924.19	139.07			2726.18	137.92								
12	2703.62	145.59			2699.00	143.43			2752.10	59.90		2698.70	58.30	
13	2443.75	139.15			2359.09	128.58								
14	2388.23	132.71			2364.49	129.57								
15	2420.47	135.70			2495.72	135.68								
16	2422.27	132.53			2443.04	136.10								
17	2599.11	140.11			2647.35	141.45								
18	2481.88	143.77			2551.41	133.17			2459.50	56.00		2477.40	54.70	
19	2346.59	124.51			2295.77	124.59								
20	2300.97	120.86			2246.47	119.84								
21	2408.04	124.12			2322.95	120.88								
22	2264.68	121.58			2277.44	121.70								
23	2156.20	119.52			2155.80	117.55								
24	2341.65	130.68			2316.52	127.79			2304.30	50.40		2269.10	49.80	
25	2172.72	106.63			2237.79	114.97								
26	2451.80	133.59			2414.73	124.08								
27	2273.98	116.95			2261.82	117.56								
28	2387.17	122.90			2336.01	120.60								
29	2518.64	147.62			2516.97	143.73								
30	2303.78	125.31			2309.43	123.17			2337.60	50.60		2339.50	50.30	
31	2563.15	211.04			2486.28	211.33								
32	2651.09	239.01			2733.59	268.07								
33	3188.87	339.18			3116.62	336.27								
34	2962.27	303.54			2780.03	279.60								
35	2585.63	156.33			2737.95	165.18								
36	3275.19	266.85			3261.66	306.96			2819.20	119.00		2802.10	98.20	
37	3270.92	413.81			3271.00	424.74								
38	2018.40	217.57			1879.78	189.13								
39	2163.25	294.89			2043.31	265.49								
40	2595.81	277.24			2510.73	261.66								
41	2440.83	142.30			2484.02	133.65								
42	2756.86	313.62			2642.06	311.88			2493.60	134.50		2420.10	159.20	
43	1765.89	154.06			1712.50	139.15								
44	1846.89	207.21			1781.90	200.11								
45	1765.72	194.16			1684.47	157.86								
46	2656.28	303.39			2559.75	282.53								
47	2574.98	337.63			2547.48	329.11								
48	3992.46	257.60			3789.88	221.54			2334.70	294.00		2249.80	280.50	

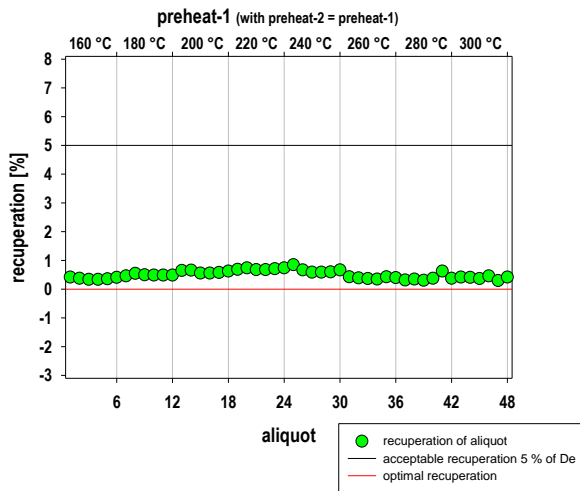




(a)



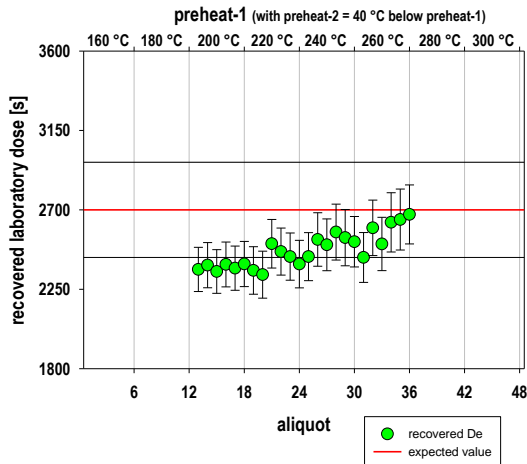
(b)



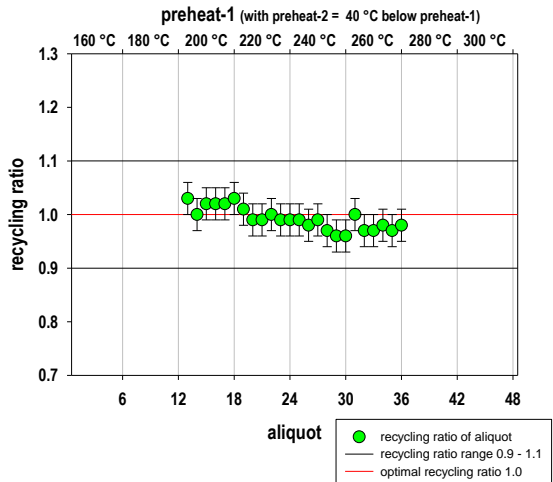
(c)

Figure S5.111: Combined preheat and dose recovery test: Laboratory dose 2700 s (225.8 Gy), normalisation dose 270 s (22.6 Gy). Six aliquots per group. Preheat 1 and preheat 2 increasing from 160 °C to 300 °C, in steps of 20 °C. BLSL readout at 125 °C for 40 s in 400 data channels (0.1 s per data channel). Dose response curve modelled with exponential plus linear fit. Results for De interval 0–0.4 s, with late light interval 30.1–40 s. (a) Recovered De values, (b) recycling ratios, (c) recuperation. The expected dose was recovered best by a preheat combination 180 °C/180 °C (central dose of aliquot group 2698.70 ± 58.30 s).

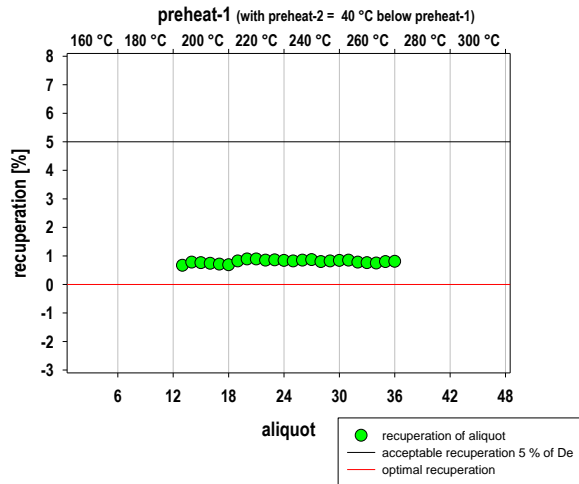
Combined preheat and dose recovery test with preheat 2 Δ 40 °C below preheat 1



(a)



(b)

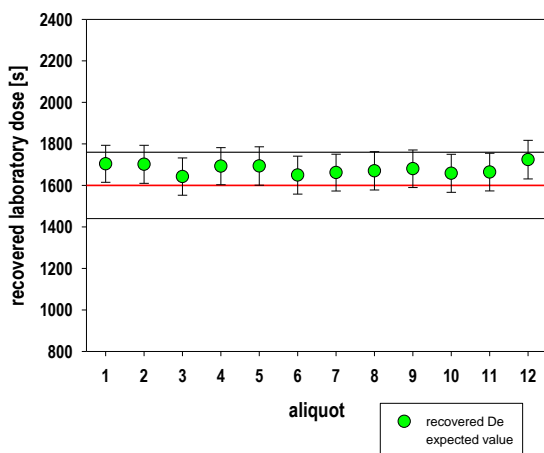


(c)

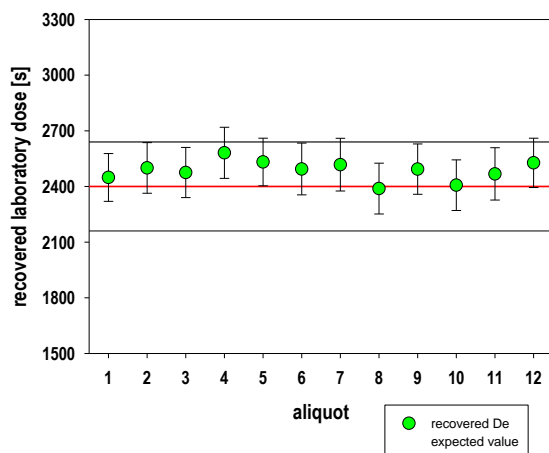
Figure S5.112: Combined preheat and dose recovery test: Laboratory dose 2700 s (225.8 Gy), normalisation dose 270 s (22.6 Gy). Six aliquots per group. Preheat 1 increasing from 200 °C to 260 °C, in steps of 20 °C. Preheat 2 Δ 40 °C lower than preheat 1. BLSL readout at 125 °C for 40 s in 400 data channels (0.1 s per data channel). Dose response curve modelled with exponential plus linear fit. Results for D_e interval 0–0.4 s, with late light interval 30.1–40 s. (a) Recovered D_e values, (b) recycling ratios, (c) recuperation.

Dose recovery tests with administered doses of 1600 s and 2400 s

Using the same SAR protocol as for the combined preheat and dose recovery tests and the best performing preheat combination of 180 °C/180 °C, bleached aliquots of sample HDS-1776 with laboratory doses (LAB) of 1600 s (133.8 Gy) and 2400 s (200.7 Gy) were subjected to dose recovery tests (12 aliquots each). For D_e determination the integral 0–0.4 s (channel 1–4) was used, for late light subtraction the integral 30.1–40 s (channel 301–400). The central doses of 1678.8 ± 26.3 s and 2487.80 ± 39.20 s met the expected doses reasonably well. All aliquots met the expected value within a range of ± 10 % and most aliquots met the expected value within the error range of the D_e value (Fig.S5.113).



(a)



(b)

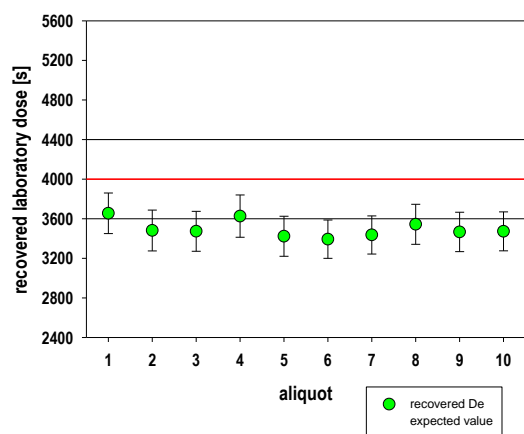
Figure S5.113: Dose recovery tests on sample HDS-1776: Laboratory doses (a) 1600 s (133.8 Gy) and (b) 2400 s (200.7 Gy). Normalisation dose 270 s (22.6 Gy). 12 aliquots per test. Preheat 1 and preheat 2 equal 180 °C. BLSL readout at 125 °C for 40 s in 400 data channels (0.1 s per data channel). Dose response curve modelled with exponential plus linear fit. Results for D_e interval 0–0.4 s, with late light interval 30.1–40 s.

Dose recovery tests with extended dose response curve and laboratory doses of 4000 s and 5000 s

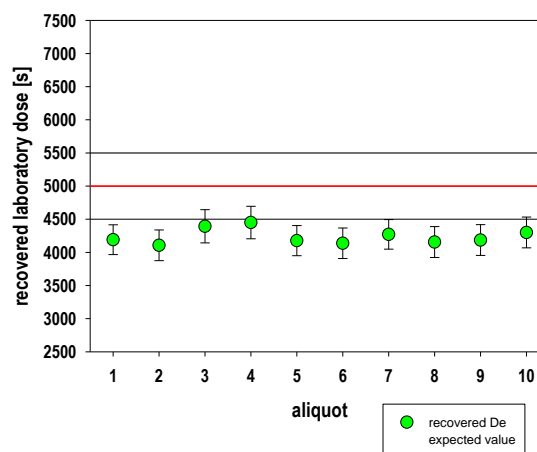
As for the lowermost samples HDS-1799 and HDS-1800 D_{es} of various aliquots were above the highest regeneration dose point (see Fig. S5.121, Fig. S5.122), the dose response curve was extended for the SAR D_e determination of these two samples. Subsequent to the measurement as described above, further regeneration dose points were added at 2700 s (225.8 Gy; repetition of another recycling dose point), 5130 s (429.1 Gy), 5940 s (496.8 Gy), 0 s (0 Gy) and 2700 s (225.8 Gy) (see Fig. S5.116). Therefore two further dose recovery tests were carried out on bleached and dosed aliquots of sample HDS-1776 with 4000 s (334.6 Gy) and 5000 s (418.2 Gy). 10 aliquots were measured for LAB 4000 s and 12 aliquots for LAB 5000. In addition, another 10 aliquots were measured for LAB 4000 with a hotbleach (40 s BLSL at 280 °C) at the end of each SAR subcycle.

As a result the dose recovery tests without hotbleach underestimate the expected doses with an increasing trend towards larger D_{es} , i.e. 12.6 % for 4000 s (central dose 3496.30 ± 63.70 s) and 15.8 % for 5000 s (4208.20 ± 66.80 s) (Fig. S5.114a, Fig. S5.114b). As the two lowermost samples HDS-1799 and HDS-1800 gave central doses of 4956.5 ± 88.4 Gy and 4130.3 ± 45.8 Gy (D_e integral 0–4 s; see Fig. S5.121, Fig. S5.122), it is possible that the palaeodose of the second lowest sample was underestimated by ca 16 % and that of the lowermost sample by >16 %, if the trend of increasing underestimation increases with increasing D_e .

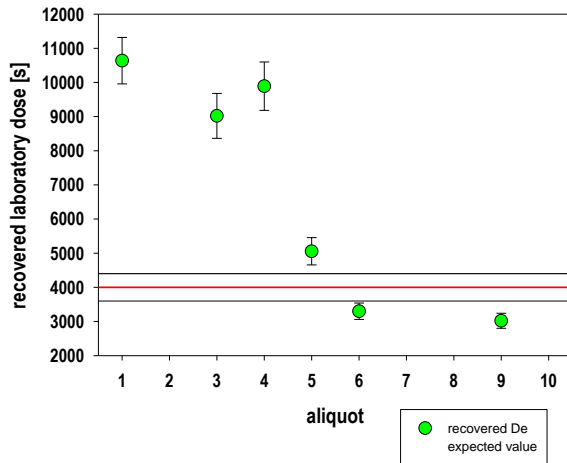
Including a hotbleach reduces the recuperation to (almost) zero, but significantly worsens the measurement results (Fig. S5.115c). Only 6 of 10 measured aliquots are analysable, which show a wide scatter of recovered D_{es} between ca 3021 s and 10638 s, the latter value way beyond the largest regeneration dose point (REG). Two aliquots give indefinitely large D_{es} , i.e. above an unusually strongly curved and early saturating dose response curve. Therefore, a hotbleach does not help to avoid slight D_e underestimation of larger D_{es} .



(a)



(b)



(c)

Figure S5.114: Dose recovery tests on sample HDS-1776: Laboratory doses (a) 4000 s (334.6 Gy) and (b) 5000 s (418.2 Gy). (c) Like (a), but including a hotbleach of 40 s BLSL at 280 °C at the end of each SAR subcycle. Normalisation dose 270 s (22.6 Gy). Extended dose response curve. 12 aliquots per test. Preheat 1 and preheat 1 equal 180 °C. BLSL readout at 125 °C for 40 s in 400 data channels (0.1 s per data channel). Dose response curve modelled with exponential plus linear fit. Results for D_e interval 0–0.4 s, with late light interval 30.1–40 s.

Normalisation dose test

Finally, another dose recovery test with a laboratory dose of 2700 s (225.8 Gy) and a preheat combination of 180 °C/180 °C was performed using the not extended dose response curve. In this test the size of the normalisation dose was varied from 7.5 % (203 s; 17.0 Gy) to 10 % (270 s; 22.6 Gy), 20 % (540 s; 45.2 Gy) and 30 % (810 s; 67.7 Gy) of the expected dose. All D_{es} were recovered within an error range of 10 % of LAB (Fig. S5.115). Nevertheless, the recovered central doses show a slight trend towards lower D_{es} with increasing NRM giving 2720.70 ± 62.80 s and 2732.10 ± 62.00 s for the aliquot groups which had received 7.5 % and 10 % of LAB, respectively, and 2687.60 ± 58.50 s for NRM 20 % of LAB and 2641.20 ± 57.20 s for NRM 30 % of LAB. Anyway, modulating the normalisation dose would not help to improve the results of the underestimated recovered large D_{es} (4000 s, 5000 s).

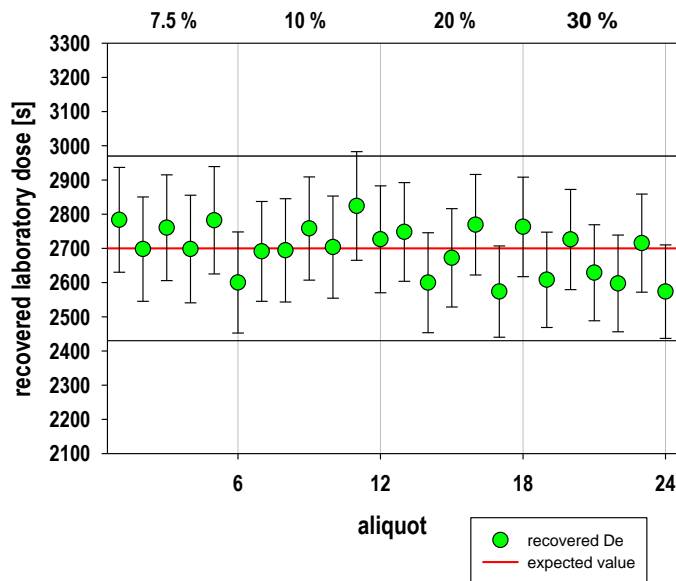


Figure S5.115: Dose recovery tests on sample HDS-1776 with a laboratory dose of 2700 s (225.8 Gy), a preheat combination of 180 °C/180 °C and normalisation doses of 7.5 % (203 s; 17.0 Gy; aliquot 1–6), 10 % (270 s; 22.6 Gy; aliquot 7–12), 20 % (540 s; 45.2 Gy; aliquot 13–18) and 30 % (810 s; 67.7 Gy; aliquot 19–24) of the expected dose. BLSL readout at 125 °C for 40 s in 400 data channels (0.1 s per data channel). Dose response curve modelled with exponential plus linear fit. Results for D_e interval 0–0.4 s, with late light interval 30.1–40 s.

SAR protocol

Based on the sequence of pretests (D_e range, preheat temperature, normalisation dose) the BLSL SAR protocol for quartz fine grains (4–11 μm) was adapted as illustrated in Fig. S5.116.

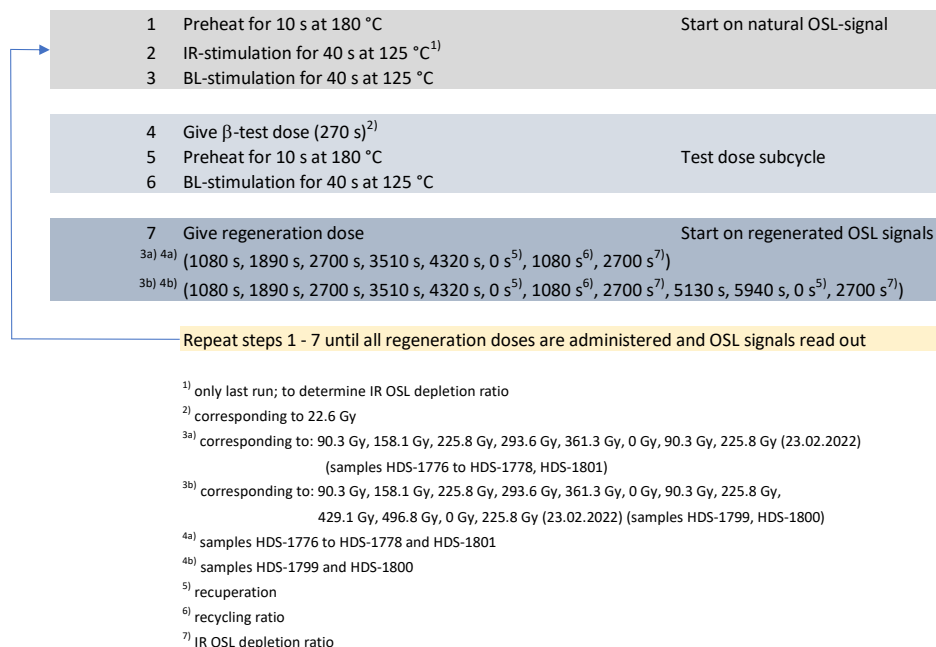


Figure S5.116: Schematic representation of the BLSL₁₂₅ SAR protocol adapted to quartz fine grain separates (4–11 μm) of the LPS Baix.

D_e determination

The D_e determination occurred with the software Analyst (version 4.31.09; Duller, 2015) applying the parameters of data analysis as depicted in Fig. S5.117.

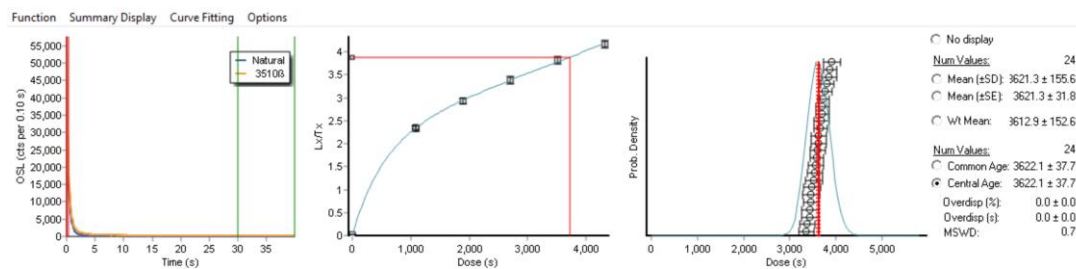
Software:	Luminescence Analyst, version 4.31.9 (Duller 2015)
Curve fitting:	Exponential plus linear fit
Integral [channel]:	1 - 4 (0 - 0.4 s)
Background [channel]:	301 - 400 (30.1 - 40 s)
Use recycled points for fitting:	Yes
Measurement error [%]	1.5
Incorporate error on curve fitting:	Yes
Use errors when applying criteria:	Yes
Recycling ratio limit [%]:	10
Maximum test dose error [%]:	10
Maximum recuperation [% of N]:	5
Tn signal > 3 sigma above background:	Yes
Maximum IR OSL depletion ratio [%]:	10

Figure S5.117: Parameters of the D_e determination.

SAR measurements

Results of the D_e determination for samples HDS-1776 to HDS-1779 and HDS-1799 to HDS-1801 are given in Fig. S5.118 to Fig. S5.123. 24 aliquots were measured per sample. D_e determination occurred for the D_e integral 0–0.1 s and 0–0.4 s, respectively, to investigate if the samples show insufficient bleaching, but no systematic differences were observed. While 23 aliquots of sample HDS-1777 and 22 aliquots of sample HDS-1799 were analysable, all aliquots of the other samples were analysable. IRSL signals as emitted by feldspar are no issue (only 2 aliquots, one of sample HDS-1777 and one of sample HDS-1779, did not pass the OSL IR depletion test). It is interesting to note that OSL IR depletion ratio may also help eliminate aliquots with a comparably strong mica (muscovite) luminescence signal (Antohti-Trandafir et al. 2018), an issue relevant for samples rich in non-eliminable mica (see below, SEM-EDX measurements).

HDS-1776

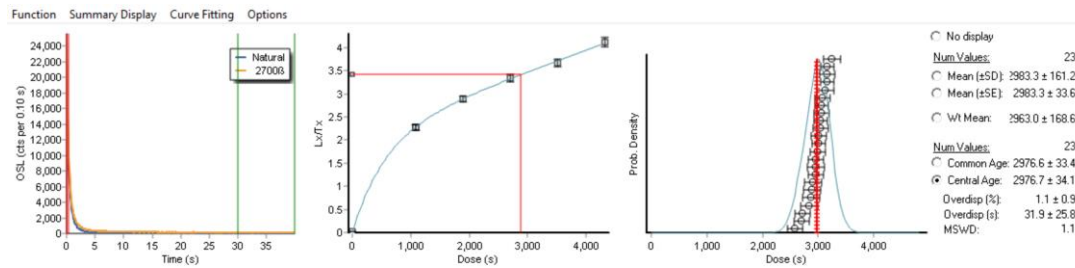


turntable position [#]	aliquot [#]	determined dose [s irradiation time]		determined dose [s irradiation time]		Diff long vs. short De interval [s irradiation time]	
		[0 - 0.1 s]	[0 - 0.1 s]	[0 - 0.4 s]	[0 - 0.4 s]	[0 - 0.4 s] - [0 - 0.1 s]	[0 - 0.4 s] - [0 - 0.1 s]
	1	3615.03	192.29	3716.65	176.79		101.62
	2	3614.51	191.59	3590.48	183.23		-24.03
	3	3796.90	211.58	3868.42	191.75		71.52
	4	3868.22	205.48	3822.60	191.11		-45.62
	5	3860.47	239.52	3909.41	219.31		48.94
	6	3539.42	198.03	3633.44	188.99		94.02
	7	3818.35	187.18	3765.23	189.66		-53.12
	8	3661.78	200.58	3680.56	192.64		18.78
	9	3649.30	192.82	3708.96	180.20		59.66
	10	3700.02	171.21	3734.71	166.75		34.69
	11	3612.68	201.60	3615.23	188.49		2.55
	12	3691.75	204.48	3669.61	173.22		-22.14
	13	3824.30	194.18	3850.46	199.46		26.16
	14	3437.90	189.76	3470.79	181.83		32.89
	15	3388.82	175.29	3552.42	182.61		163.60
	16	3507.90	190.94	3562.44	181.42		54.54
	17	3388.95	185.97	3521.36	183.92		132.41
	18	3730.03	200.44	3632.53	187.96		-97.50
	19	3444.39	169.60	3466.34	168.13		21.95
	20	3316.19	182.76	3447.05	180.72		130.86
	21	3423.50	223.68	3485.61	199.25		62.11
	22	3616.70	201.81	3452.66	186.23		-164.04
	23	3393.81	182.82	3390.35	175.49		-3.46
	24	3308.28	205.00	3362.90	173.26		54.62

central dose: 3594.20 39.70 3622.10 37.70

Figure S5.118: D_e determination on sample HDS-1776. Example of shine down curve, dose response curve with an exponential plus linear fit and weighted histogram of all analysable aliquots ($N = 24$ for D_e interval 0–0.4 s). No systematic difference for D_{eS} determined for the two different D_e intervals 0–0.1 s and 0–0.4 s, respectively.

HDS-1777

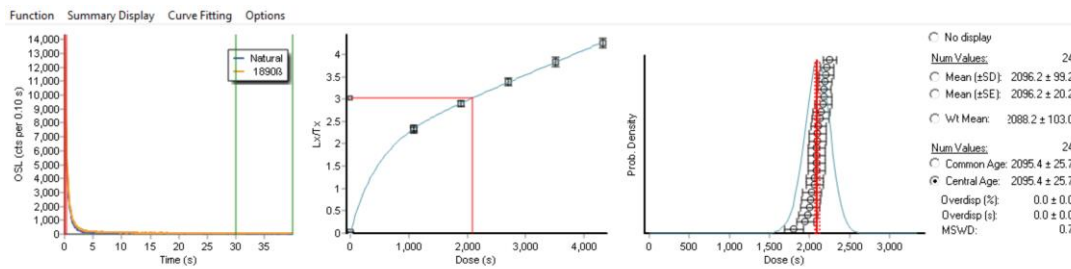


turntable position [#]	aliquot [#]	determined dose [s irradiation time] [0 - 0.1 s]		determined dose [s irradiation time] [0 - 0.4 s]		Diff long vs. short De interval [s irradiation time] [0 - 0.4 s] - [0 - 0.1 s]
1	1	2879.85	164.25	2875.82	159.30	-4.03
2	2	3048.99	161.23	2955.62	145.71	-93.37
3	3	3093.86	179.47	3168.38	169.61	74.52
4	4	3186.00	191.45	3133.90	183.30	-52.10
5	5	2910.06	180.91	3018.03	167.43	107.97
6	6	2786.21	164.87	2590.12	134.67	-196.09
7	7	2879.20	177.83	2956.21	163.07	77.01
8	8	3113.32	172.72	3170.86	157.13	57.54
9	9	2994.86	190.02	2904.67	166.12	-90.19
10	10	3044.64	170.27	3000.51	157.11	-44.13
11	11	2851.30	162.78	3049.52	155.88	198.22
12	12	3130.60	215.09	3242.60	199.76	112.00
13	13	3023.54	196.99	2896.73	164.91	-126.81
14	14	2948.42	164.34	3017.78	155.13	69.36
15	15	3213.17	170.30	3160.45	162.57	-52.72
16	16	3014.83	164.46	3065.37	157.53	50.54
17	17	2836.47	168.06	2842.95	156.51	6.48
18	18	3128.30	165.72	3081.58	169.27	-46.72
19	19	2908.58	181.74	3059.35	172.08	150.77
20	20			n.a.	n.a.	
21	21	3158.00	168.80	3040.52	172.19	-117.48
22	22	2818.12	157.94	2698.89	145.08	-119.23
23	23	2992.62	170.60	2959.24	157.29	-33.38
24	24	2871.96	154.61	2726.98	141.23	-144.98
central dose:		2993.40	36.00	2976.70	34.10	

IRSL 0-4 s

Figure S5.119: D_e determination on sample HDS-1777. Example of shine down curve, dose response curve with an exponential plus linear fit and weighted histogram of all analysable aliquots ($N = 23$ for D_e interval 0–0.4 s). No systematic difference for D_{es} determined for the two different D_e intervals 0–0.1 s and 0–0.4 s, respectively.

HDS-1778

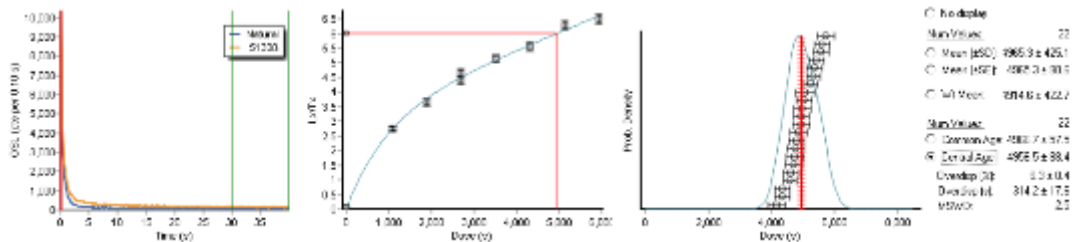


turntable position [#]	aliquot [#]	determined dose [s irradiation time]		determined dose [s irradiation time]		Diff long vs. short D_e interval [s irradiation time] [0 - 0.4 s] - [0 - 0.1 s]
		[0 - 0.1 s]	[0 - 0.1 s]	[0 - 0.4 s]	[0 - 0.4 s]	
	1	2019.50	132.86	2085.60	122.19	66.10
	2	2231.57	154.29	2064.63	124.43	-166.94
	3	2287.66	164.27	2178.92	136.40	-108.74
	4	2181.98	147.78	2219.94	132.57	37.96
	5	2075.24	139.37	2069.14	121.15	-6.10
	6	2193.66	146.45	1989.28	125.30	-204.38
	7	2100.83	136.51	2198.72	129.26	97.89
	8	1976.11	149.40	2016.52	128.04	40.41
	9	1982.62	146.92	2106.05	126.40	123.43
	10	2169.99	154.09	2208.68	135.00	38.69
	11	2176.75	136.49	2103.38	125.03	-73.37
	12	1838.49	130.48	1806.84	113.28	-31.65
	13	2021.90	134.29	2006.22	118.35	-15.68
	14	1930.56	133.24	2110.68	126.54	180.12
	15	2044.24	140.50	2094.17	127.35	49.93
	16	1955.54	142.88	2140.81	131.99	185.27
	17	2124.05	142.87	2182.47	129.35	58.42
	18	2030.73	134.59	2033.75	122.38	3.02
	19	1868.34	124.69	1943.57	112.84	75.23
	20	2024.43	133.84	2092.87	125.04	68.44
	21	2105.98	136.09	2167.57	130.24	61.59
	22	2114.80	144.72	2151.86	132.94	37.06
	23	2148.92	139.87	2086.19	124.59	-62.73
	24	2276.09	144.14	2251.33	128.49	-24.76

central dose: 2078.60 28.80 2095.40 25.70

Figure S5.120: D_e determination on sample HDS-1778. Example of shine down curve, dose response curve with an exponential plus linear fit and weighted histogram of all analysable aliquots ($N = 24$ for D_e interval 0–0.4 s). No systematic difference for D_{es} determined for the two different D_e intervals 0–0.1 s and 0–0.4 s, respectively.

HDS-1779

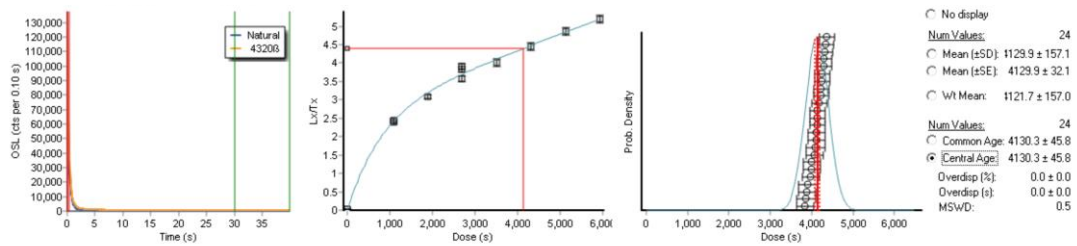


turntable position [#]	aliquot [#]	determined dose [s irradiation time] [0 - 0.1 s]		determined dose [s irradiation time] [0 - 0.4 s]		Diff long vs. short De interval [s irradiation time] [0 - 0.4 s] - [0 - 0.1 s]
1	1	5194.83	369.96	4946.84	277.24	-247.99
2	2	5937.04	406.23	5718.64	310.01	-218.40
3	3	4778.75	358.95	4852.58	274.37	73.83
4	4	4679.28	350.45	4797.61	250.39	118.33
5	5	3609.41	245.50	n.a.	n.a.	
6	6	4793.88	354.18	5423.79	295.44	629.91
7	7	5244.07	380.90	5046.08	262.48	-197.99
8	8	n.a.	n.a.	4163.90	257.84	
9	9	4508.19	292.41	4713.94	271.65	205.75
10	10	4781.87	338.09	4947.00	262.95	165.13
11	11	n.a.	n.a.	4734.36	280.06	
12	12	4502.34	335.60	4340.64	246.44	-161.70
13	13	n.a.	n.a.	4362.46	228.50	
14	14	4634.57	355.08	4628.17	243.15	-6.40
15	15	4684.02	401.73	4760.16	275.27	76.14
16	16	4662.18	274.38	4598.06	227.85	-64.12
17	17	5473.43	340.04	n.a.	n.a.	
18	18	5964.15	484.60	5367.97	284.95	-596.18
19	19	5678.82	334.95	5597.03	290.18	-81.79
20	20	5089.16	339.47	5261.13	269.54	171.97
21	21	5030.60	334.70	5566.26	291.82	535.66
22	22	4795.37	348.84	4990.87	284.24	195.50
23	23	5357.58	346.71	5345.23	262.28	-12.35
24	24	5387.19	452.96	5074.63	306.11	-312.56
central dose:		4961.90	120.60	4956.50	88.40	

IRSL	
Floating point problem	
RecRat	

Figure S5.121: D_e determination on sample HDS-1799. Example of shine down curve, dose response curve with an exponential plus linear fit and weighted histogram of all analysable aliquots ($N = 22$ for D_e interval 0–0.4 s). No systematic difference for D_e s determined for the two different D_e intervals 0–0.1 s and 0–0.4 s, respectively. Please note that dose recovery tests suggest that doses ≥ 5000 s (ca 418 Gy) may underestimate the true value by $\geq 16\%$.

HDS-1800

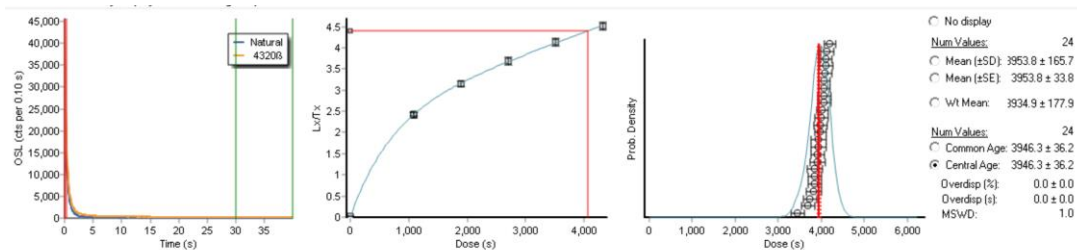


turntable position [#]	aliquot [#]	determined dose [s irradiation time] [0 - 0.1 s]		determined dose [s irradiation time] [0 - 0.4 s]		Diff long vs. short De interval [s irradiation time] [0 - 0.4 s] - [0 - 0.1 s]
	1	4206.64	215.79	4143.76	218.97	-62.88
	2	4062.86	224.63	3908.06	221.50	-154.80
	3	4332.60	235.92	4345.01	236.25	12.41
	4	3986.52	210.76	3979.48	214.46	-7.04
	5	3887.98	232.53	3872.80	232.55	-15.18
	6	4289.28	233.04	4264.50	230.92	-24.78
	7	4392.61	246.90	4320.36	236.56	-72.25
	8	4031.48	222.49	4138.01	222.66	106.53
	9	3926.39	218.99	3840.49	211.61	-85.90
	10	4003.65	232.68	4103.96	228.33	100.31
	11	4205.09	223.57	4233.46	225.78	28.37
	12	4238.19	231.80	4294.13	234.91	55.94
	13	4142.11	219.93	4126.13	220.82	-15.98
	14	3966.92	220.11	4063.48	223.08	96.56
	15	3968.06	221.37	3999.16	219.91	31.10
	16	4167.06	237.60	4144.21	229.63	-22.85
	17	4314.82	232.54	4362.90	237.14	48.08
	18	4260.31	235.84	4235.72	230.17	-24.59
	19	4061.07	220.87	4002.61	213.93	-58.46
	20	4194.84	226.48	4111.56	216.92	-83.28
	21	4262.86	234.22	4294.33	232.23	31.47
	22	4128.39	210.76	4253.96	220.03	125.57
	23	4165.53	222.85	4188.21	224.84	22.68
	24	3868.47	206.15	3890.60	207.90	22.13

central dose:	4127.50	46.00	4130.30	45.80
---------------	---------	-------	---------	-------

Figure S5.122: D_e determination on sample HDS-1800. Example of shine down curve, dose response curve with an exponential plus linear fit and weighted histogram of all analysable aliquots ($N = 24$ for D_e interval 0–0.4 s). No systematic difference for D_{es} determined for the two different D_e intervals 0–0.1 s and 0–0.4 s, respectively. Please note that dose recovery tests suggest that D_{es} of ca. 4000 s (ca 335 Gy) may underestimate the true value by ca 13–16 %.

HDS-1801



turntable position [#]	aliquot [#]	determined dose [s irradiation time]		determined dose [s irradiation time]		Diff long vs. short D_e interval [s irradiation time] [0 - 0.4 s] - [0 - 0.1 s]
		[0 - 0.1 s]	[0 - 0.1 s]	[0 - 0.4 s]	[0 - 0.4 s]	
1	1	3909.01	190.39	4058.22	195.72	149.21
2	2	4191.74	206.30	3992.15	187.18	-199.59
3	3	3894.55	193.09	3933.26	182.47	38.71
4	4	3471.75	164.14	3453.30	148.71	-18.45
5	5	4100.64	204.19	4138.31	197.32	37.67
6	6	3990.51	190.63	4060.79	186.07	70.28
7	7	4086.86	209.72	4083.00	188.76	-3.86
8	8	4253.68	213.78	4122.70	183.15	-130.98
9	9	3855.82	175.99	3922.01	170.60	66.19
10	10	4366.32	210.51	4192.91	186.61	-173.41
11	11	4271.69	202.39	4064.39	174.81	-207.30
12	12	4191.69	188.00	4063.14	179.05	-128.55
13	13	3909.04	222.94	3930.54	187.51	21.50
14	14	3789.15	180.12	3990.46	178.55	201.31
15	15	3962.38	167.35	3988.20	165.47	25.82
16	16	4137.28	204.04	4117.04	193.52	-20.24
17	17	3875.72	183.15	3854.13	168.09	-21.59
18	18	3994.01	177.71	4028.78	173.07	34.77
19	19	3576.16	172.71	3833.64	180.07	257.48
20	20	3828.31	184.30	3919.06	180.41	90.75
21	21	3691.92	175.07	3746.25	161.31	54.33
22	22	3715.82	179.91	3685.41	161.84	-30.41
23	23	3990.07	198.45	3858.43	178.80	-131.64
24	24	3881.58	166.01	3855.27	168.69	-26.31
central dose:		3947.90	44.30	3946.30	36.20	

Figure S5.123: D_e determination on sample HDS-1801. Example of shine down curve, dose response curve with an exponential plus linear fit and weighted histogram of all analysable aliquots ($N = 24$ for D_e interval 0–0.4 s). No systematic difference for D_{es} determined for the two different D_e intervals 0–0.1 s and 0–0.4 s, respectively.

Additional tests on the quartz fine grains

As the apparent age overestimations of the BLSL SAR dating on the quartz fine grains of the six Baix OSL-samples was surprising we performed additional tests on the quartz extracts to investigate whether any unwanted luminescence signals may have intervened with the BLSL quartz signal used for dating. Therefore we investigated whether: unwanted fluorides had formed during the sample preparation; feldspar was not efficiently eliminated; and/or whether there is any indication of a latent unbleached “geologic” luminescence component present in the quartz fine grain fraction that was not reset during the last sediment reworking but may have been (partially) read out by the here applied BLSL SAR procedure. Such a palaeodose in saturation of a mineral grain could possibly arise from quartz grains from the in situ Cretaceous bedrock if the mineral grains had been incorporated into hillwash processes but were not (significantly) bleached during the sediment reworking.

SEM-EDX measurements

Both, polymineral and quartz fine grains of the six Baix OSL-samples were subjected to scanning electron microscope (SEM) and energy dispersive X-ray (EDX) analyses at the Department of Geosciences of the University of Heidelberg (team Prof. Dr. Lucie Tajcmanova, Dr. Sebastian Cionoiu). The measurements were performed on powder samples coated with carbon on a JEOL FEG-SEM JSM-IT800. The EDS-detector used is an Oxford Instruments

Ultim Max 100 mm². SEM and EDX measurements and data analyses were kindly performed by Dr. Alexander Varychev and Dr. Hans-Peter Meyer. Of each OSL sample one polymineral and one quartz fine grain aliquot were investigated. For each aliquot 15 (HDS-1776, quartz fine grains) to 32 element analyses (HDS-1800, polymineral fine grains) were performed at spots each representing a well delimitable mineral grain on the scanning electron micrographs. The analyses showed (Fig. S5.124) that fluorides that might have formed and not been efficiently eliminated during the sample preparation and therefore might have emitted an unwanted luminescence signal during the SAR BLSL dating measurements was no issue. Fluor was detected only once, in a polymineral fine grain extract (HDS-1801), where it accounted for 1.3 wt % of all detected elements in the investigated mineral grain, likely a hornblende. Feldspar that was present in the polymineral fine grains (both potassium and sodium feldspars; potassium feldspar with 12.6 – 14.8 wt % K) was also no issue for the quartz fine grains. However, next to accessory minerals rich in Ti (mostly identified as rutile or titaniferous magnetite), Fe- (titaniferous magnetite; hornblende; iron oxides, in connection with nodular shapes likely products of the in situ soil forming processes under hydromorphic conditions) and Mg (mostly in hornblende) the polymineral fine grains contained plenty of micas, which were present also after etching in fluorosilicic acid in the quartz separates. Unlike other minerals which were in the expected grain size range (4–11 µm) the micas often exceeded the presumed upper grain size limit. This observation is not surprising, as the foliated crystal structure of the micas makes them settle during the gravitational grain-size separation in water much more slowly than a more roundish mineral grain of equal mass density. Summarising, the SEM and EDX analyses do not reveal any shortcomings of the sample preparation which could possibly explain the age overestimation of the quartz fine grains.

Polymineral fine grains SEM micrograph	EDX element analysis	Quartz fine grains SEM micrograph	EDX element analysis
(a)	(g)	(m)	(s)
(b)	(h)	(n)	(t)
(c)	(i)	(o)	(u)
(d)	(j)	(p)	(v)
(e)	(k)	(q)	(w)
(f)	(l)	(r)	(x)

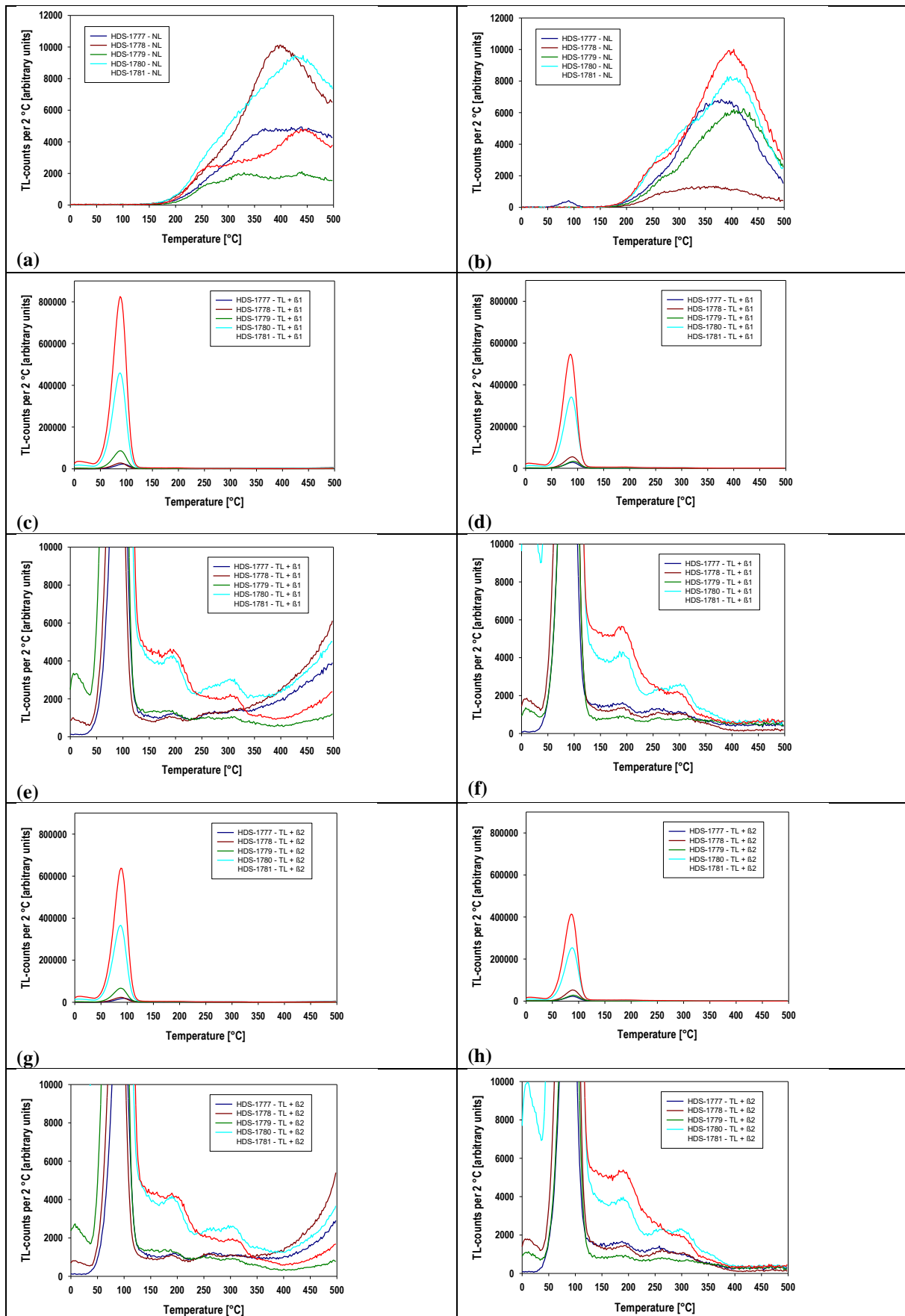
Figure S5.124: Exemplary results of the scanning electron microscope (SEM) analyses (a–f, m–r) and the energy dispersive X-ray (EDX) analyses (g–l, s–x) of the polymineral fine grains (left two columns) and the quartz fine grains (right two columns).

TL up to 500 °C

It is not possible to extract mica-free quartz extracts from mica-containing sediments with standard laboratory procedures (Antohti-Trandafir et al. 2018), at best they can be reduced,

e.g., by soaking and rinsing mica-contaminated quartz separates with certain detergents (Kortekaas and Murray, 2005). Antoni-Trandafir et al. (2018) observed in the mica (muscovite) samples investigated by them a broad TL-peak around 200 °C (ramp 5 °C; UV detection filter U-340, Hoya). Therefore, we measured TL up to 500 °C (ramp 2 °C) of five of the Baix samples with prepared aliquots at hand (one aliquot each) using the SAR BLSL detection filter utilized for the dating of the quartz fine grains (U-340, Hoya, 3 x 2.5 mm) to investigate if the TL curves could give any indication of a luminescence signal contribution in the UV detection band. We measured both a sample's natural signal and subsequently, from the same aliquot, twice (repetitive) a regenerated signal after applying a laboratory dose of the size of the expected dose (cf. Fig. S5.112; dose recovery test with 2700 s irradiation time; ca 225.8 Gy; ca half of the size of the laboratory dose applied by Antohi-Trandafir et al. (2018)). Two measurements were performed, one without (Fig. S5.125; for better comparison with Antohi-Trandafir et al. (2018)) and one with background subtraction (Fig. S5.126; to eliminate any potential influence on the shape of the TL curve by black-body radiation), using for the latter the automated subtraction routine of the Risø TL/OSL sequence editor, v. 4.36. As we used a smaller ramp than Antoni-Trandafir et al. (2018) a luminescence signal from micas that could possibly interfere with the signal from quartz during the BLSL SAR dating measurements should be indicated by a broad peak somewhat below 200 °C. The results of our TL-measurements, not for the natural but only for the regenerated signal, show a peak around ca. 190 °C, which could possibly conform to the TL peak as identified by Antohi-Trandafir et al. (2018) for micas. However, Antohi-Trandafir et al. (2018) also showed that – if muscovite exhibited above negligible IRSL and/or BLSL response (after all, three out of five of their samples did not) – the OSL IR depletion ratio test with a threshold value <0.9 as also applied in the present study reliably rejects mica-contaminated aliquots not suitable for D_e determination. Anyway, unwanted OSL IR depletion ratios were not a major issue and relevant only for single aliquots of samples HDS-1777 and HDS-1779 (cf. Figs. S5.119 and S5.121). The TL-curves show another peak at ca. 300 – 310 °C – likely the 325 °C quartz peak at a higher temperature ramp – which is regarded as the OSL sensitive quartz peak as sampled for BLSL SAR measurements like in the present study. In addition to that the natural TL curve of three samples (HDS-1779 to HDS-1801; Fig. S5.125b) possess a high temperature peak around ca 400 °C ca 4–5 times the size of the regenerated 325 °C peak. Schmidt and Woda (2018) observed a peak around ca. 420 °C in the blue detection window when measuring TL of a quartzitic sandstone sample (BT1629) from Venezuela with a “geologic” dose (Precambrian age; ca 1.5 Ga). Like in the Baix samples the high temperature peak was present only in the natural and not in the regenerated TL curves. It is possible, that in the Baix samples the tail of a blue TL peak was observed in the UV detection window. Anyway, the observation of a high temperature TL peak in the natural samples may support the assumption that not properly

bleached material with a “geological dose has been incorporated into the Baix loess deposits, likely during slope wash processes.



(i)	(j)
-----	-----

Figure S5.125: Samples HDS-1777 to HDS-1781, one aliquot each. TL-curves up to 500 °C, heating rate 2 °C/s. Left column (a, c, e, g, i) without background subtraction. Right column (b, d, f, h, j) without background subtraction. (a, b) Natural luminescence. (c, d) post-TL beta-dose signal. (e, f) Like (c, d), enlarged viewing. (g, h) Like (c, d) but measured after (c, d) (repeated measurement). (i, j) Like (g, h), enlarged viewing. Beta irradiation 2700 s (ca 225.8 Gy). (b) The natural signal of the first aliquot measured with background subtraction shows a slight 110 °C peak (here ca 85 °C) due to cross talk next to a position with 2700 s beta irradiation. (a, b) The aliquots with the natural signal do not exhibit a TL peak around 200 °C. (c, d) (g, h) In the presence of the 110 °C peak all other peaks are markedly subdued. (e, f) (i, j) The enlarged viewings of the artificially irradiated aliquots show a narrow peak around ca 190 °C which could possibly conform to the typical broad mica peak as identified by Antohi-Trandafir et al. (2018). Please note that different aliquots were measured without (a, c, e, g, i) and with (b, d, f, h, j) background subtraction, as the measurements on each aliquot started with the TL readout of the natural signal, followed by two regenerated signals (2700 s, 225.8 Gy).

Linearly modulated (LM) OSL measurements

In a further test, one aliquot of each of the samples HDS-1777 to HDS-1781 was measured in the linearly modulated (LM) OSL mode (Singarayer and Bailey, 2003) to investigate whether the samples are possibly dominated by a hard to bleach medium and/or slow component, which could possibly explain age overestimation of the quartz fine grains. We measured both, the natural signal and a regenerated signal of the size of the expected palaeodose (2700 s beta irradiation, ca 225.8 Gy). LM BLSL readout in the UV detection window (Hoya, U340, 3 x 2.5 mm) was performed for 4000 s (4000 data channels, 1 s per data channel) at 125 °C, like for the dating measurements after a preheat of 10 s at 180 °C and with a LED power of 90 %, estimated to result in 80 mW/cm² at the sample position. In addition, the aliquots' IR OSL depletion ratio was determined by repeatedly measuring the BLSL signal at 125 °C for 40 s and comparing the signals without previous IR bleach with the signal with IR bleach (40 s at 125 °C) prior to BLSL readout. As a result, the values were all within the acceptable range 0.9–1 (minimum 0.94 ± 0.03: HDS-1779; maximum 0.98 ± 0.03: HDS-1777). The natural and regenerated LM-OSL curves conform well with each other (Fig. S5.126). Following Bulur (1996), a nonlinear least squares fit for the LM-OSL curves was performed with the function „fit_LMCurve()“ (Kreutzer et al. 2022) of the R Luminescence package, version 0.9.18 (Kreutzer et al. 2022). The LM-OSL curves were best modelled with four components (Fig. S5.126a) or five components (Fig.S5.127b). While for sample HDS-1779, dominated by a slow component, no fit could be applied, the LM-curves of the other samples each possess a first component with cross sections in the range ca 10⁻¹⁷ cm², which may be regarded as a fast component. Thus, the analyses of the LM-OSL curves do not give an indication that the quartz fine-grain separates from the Baix samples may exhibit hard to bleach slower components which could possibly explain the age overestimation by the SAR BLSL dating.

--	--

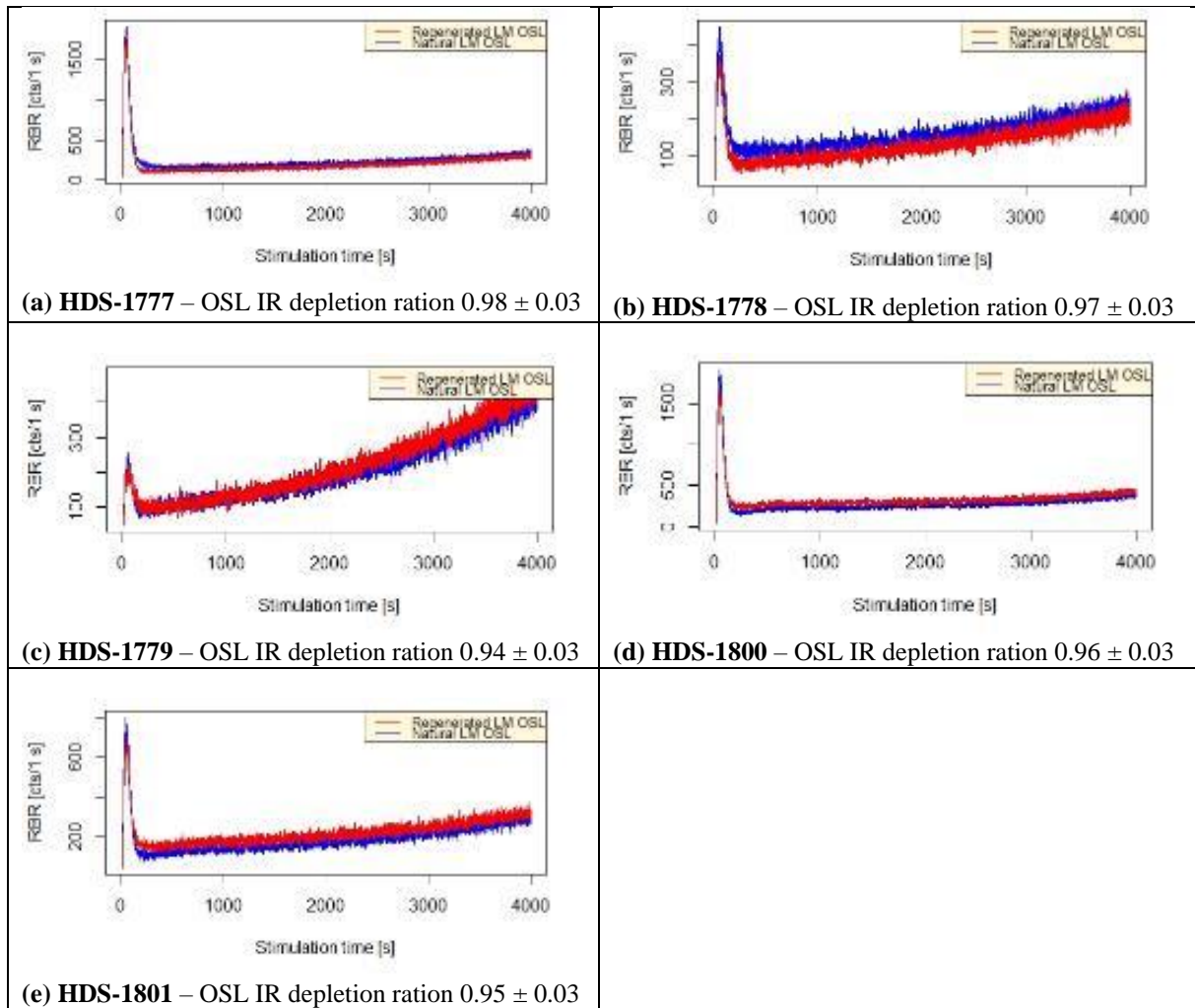


Figure S5.126: LM OSL measurements of the samples HDS-1777 to HDS-1801 (one aliquot each), natural and regenerated signals.

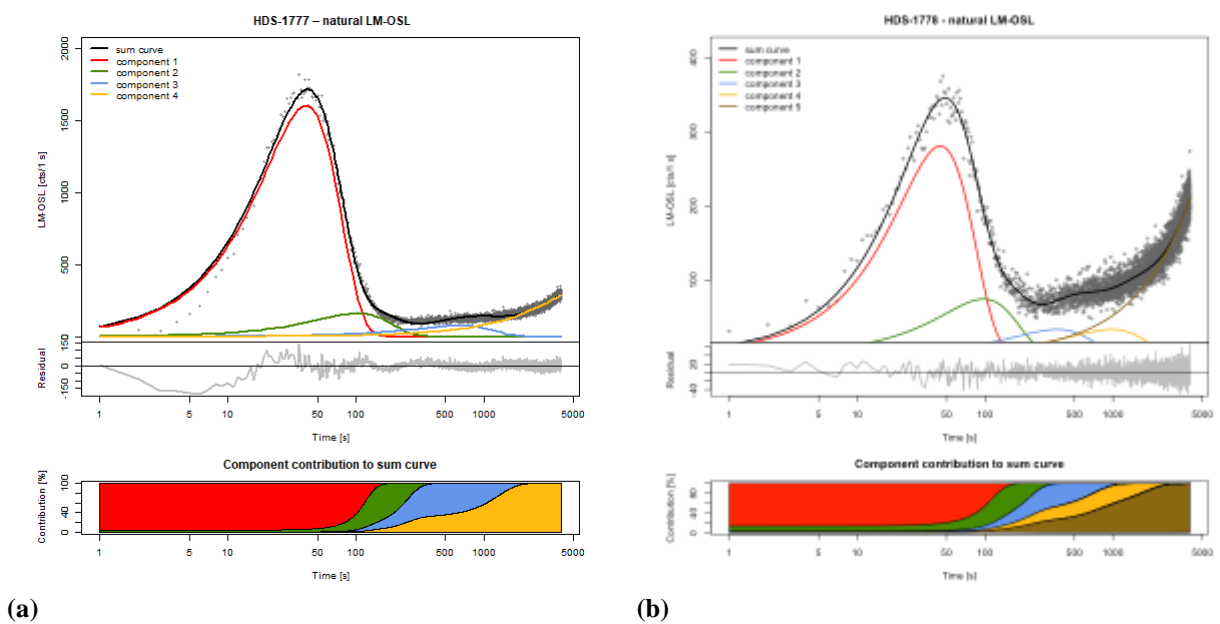
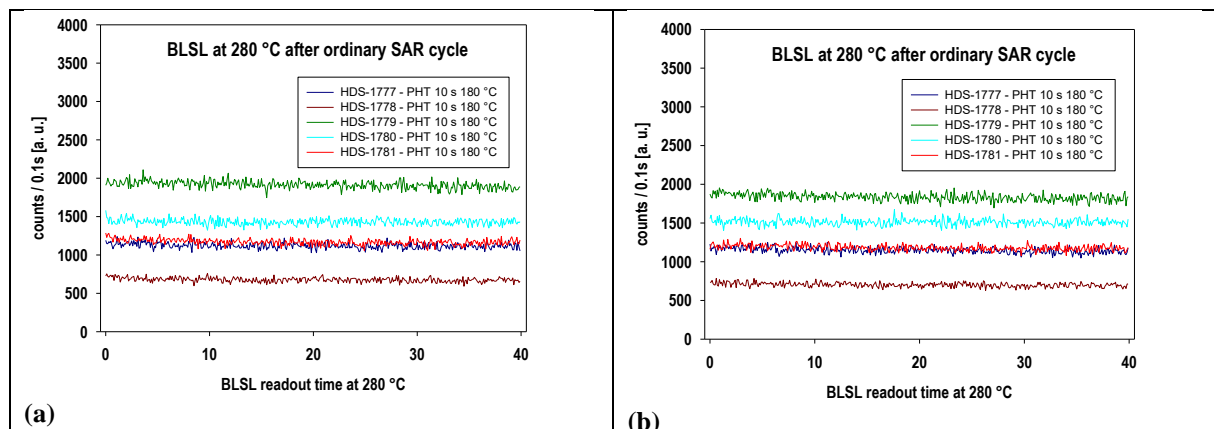


Figure S5.127: Four-component analyses of the natural LM-OSL curve of sample (a) HDS-1777 with a dominant fast component and (b) HDS-1778, the modelled photoionization cross section of the first component does not qualify as a fast component.

High background signal of hotbleach (BLSL at 280 °C)

A dose recovery test which included a hotbleach at the end of each SAR cycle of 40 s BLSL at 280 °C (cf. Fig. S5.114c) showed an unusually high background luminescence of several 10^2 to few 10^3 counts per 0.1 s readout time. Therefore, we investigated whether this was the result of the comparably low preheat temperature of 180 °C. For this test we used the five aliquots previously utilized for the LM test (HDS-1777 to HDS-1801, one aliquot each). The aliquots were subjected to SAR cycles for which they received always the same laboratory dose of 2700 s (225.8 Gy), and each SAR cycle was finalised with a respective hotbleach. For the test sequence the preheat temperature was increased from 160 °C to 280 °C in steps of Δ 20 °C. The preheat duration was always 10 s. The results, presented in Fig. S5.128, show that the preheat temperature has only a marginal influence on the size of the background signal. An initial BLSL curve is not present in any of the hotbleach measurements following the usual SAR BLSL readout at 125 °C. We also tested whether the background signals of hotbleaches without previous BLSL readouts at 125 °C change with varying preheat temperatures (duration always 10 s), but found hardly any effect either (Fig. S5.129). Only the initial BLSL signal of the shine down decreases with increasing preheat temperature. Finally we extended the preheat duration to 240 s, testing only preheat temperatures of 160 °C and 280 °C (Fig. S5.129). While the hotbleach measurement following a 160 °C preheat shows a BLSL shine down curve with a reduced initial signal, the hotbleach following a 280 °C preheat revealed only a background signal. Again, the pretreatment did not have any marked effect on the size of the background signal. Summarising, the unusually large level of the hotbleach background signal is not a result of the samples pretreatment, but rather an intrinsic feature of the Baix samples. Whether the presence of mica in the quartz separates is the reason for the unusually large level is beyond the scope of the present study, as it is not possible to extract pure mica from the fine grains.



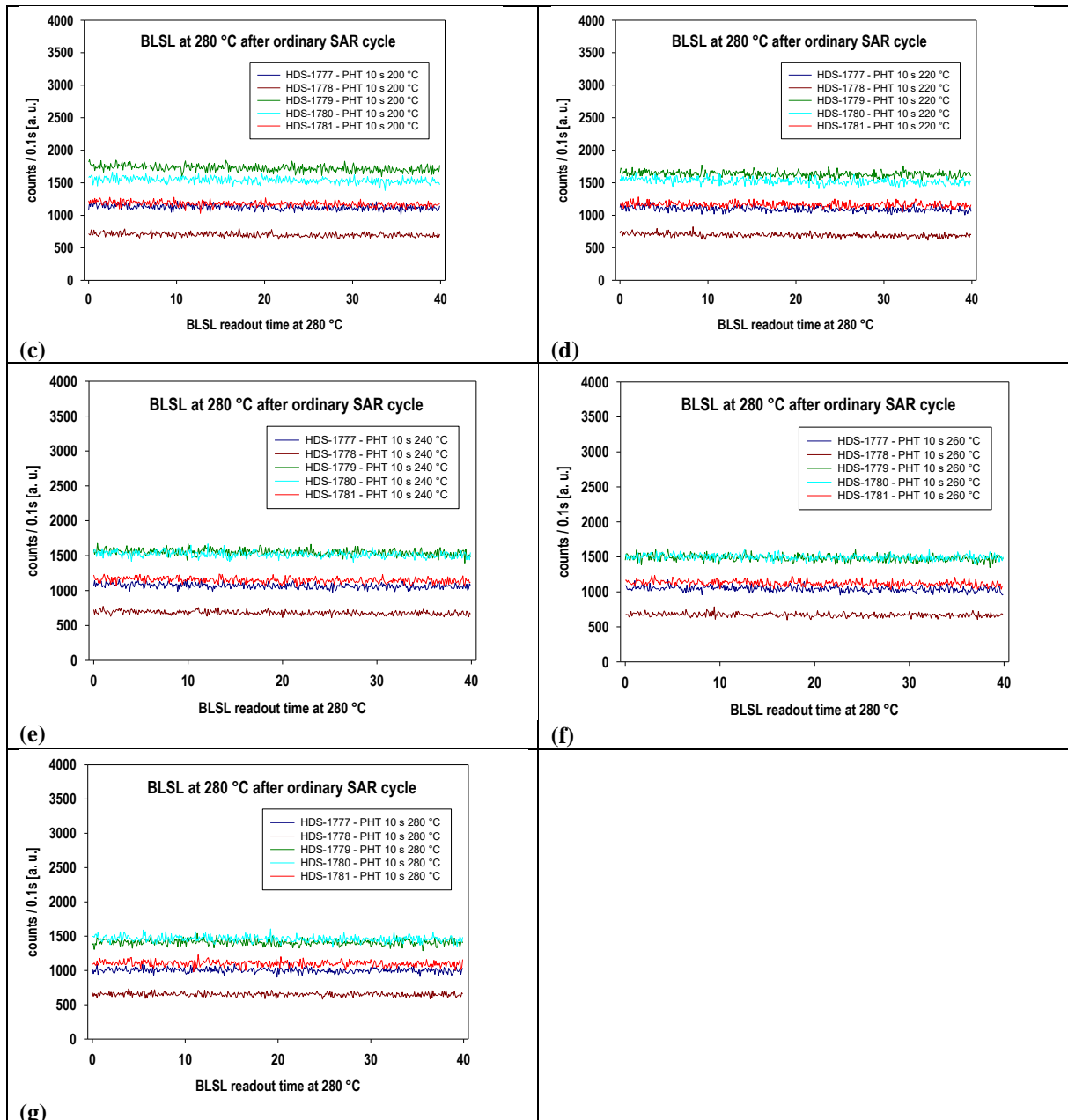
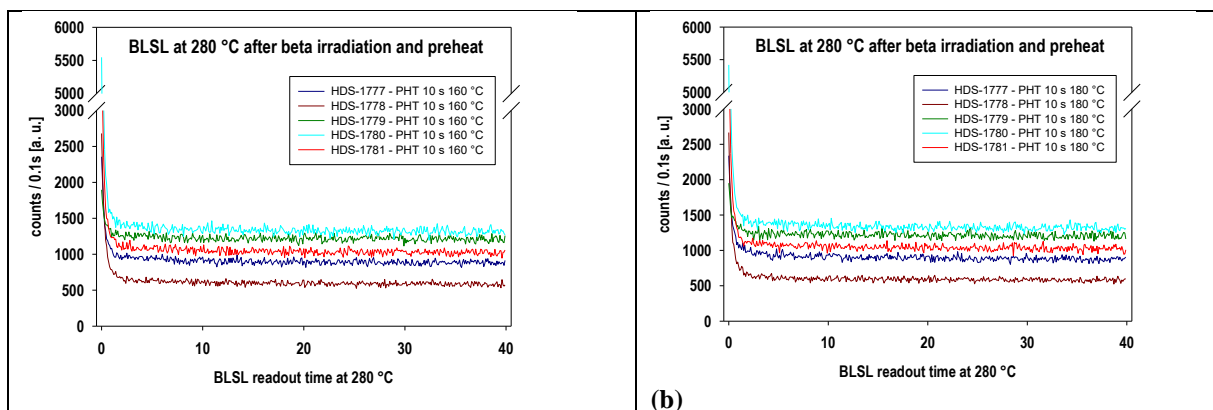


Figure S5.128: Samples HDS-1777 to HDS-1781, one aliquot each. Hotbleach measurements (40 s BLSL at 280 °C) following an ordinary SAR regeneration cycle: irradiation 2700 s (225.8 Gy); preheat (here increased from 160 °C to 280 °C, by $\Delta 20$ °C); 40 s BLSL at 125 °C; normalisation dose (270 s, 22.6 Gy); 40 s BLSL at 125 °C. The duration of the preheat is always 10 s. Hardly any effect of the preheat temperature on the size of the hotbleach background signal. Used aliquots previously utilized for the LM test (Fig. S5.126).



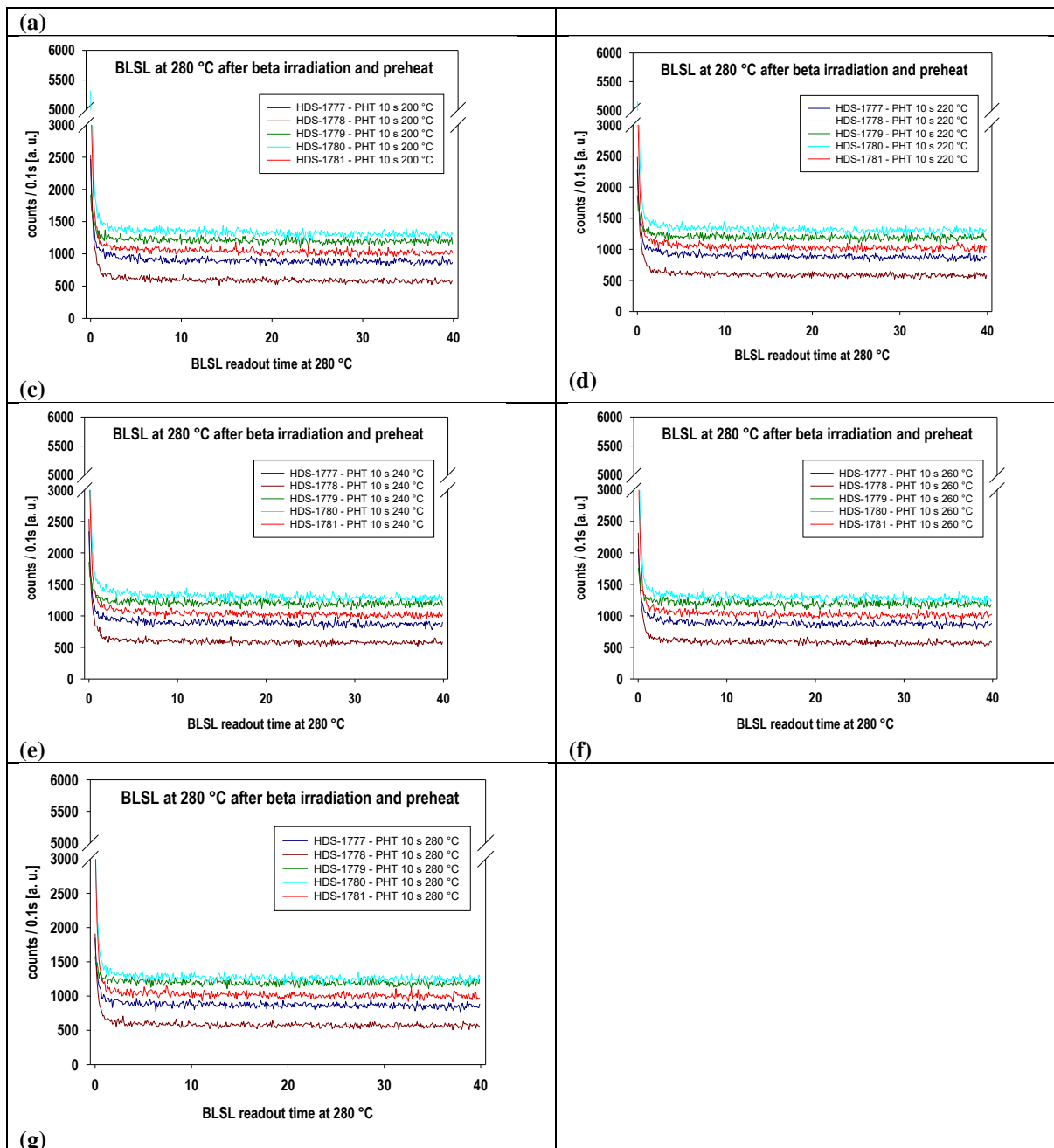


Figure S5.129: Samples HDS-1777 to HDS-1781, one aliquot each. Hotbleach measurements (40 s BLSL at 280 °C) following sample irradiation (2700 s, 225.8 Gy) and preheat (here increased from 160 °C to 280 °C, by $\Delta 20$ °C). The duration of the preheat is always 10 s. Hardly any effect of the preheat temperature on the size of the hotbleach background signal. Used aliquots previously utilized for the LM test (Fig. S5.126) and the previous hotbleach test (Fig. S5.128).

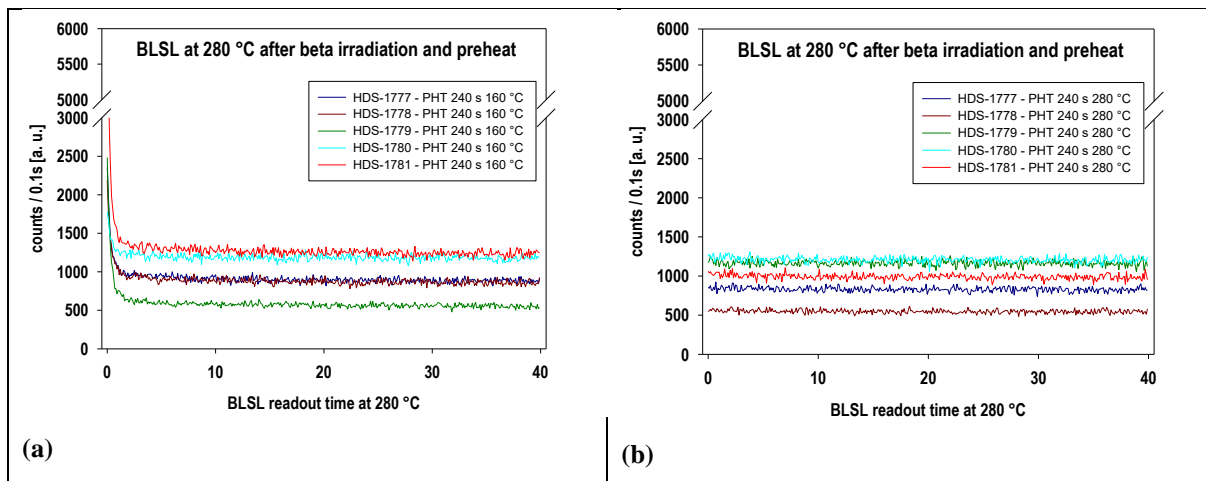


Figure S5.130: Samples HDS-1777 to HDS-1781, one aliquot each. Hotbleach measurements (40 s BLSL at 280 °C) following sample irradiation (2700 s, 225.8 Gy) and preheat, (a) 160 °C and (b) 280 °C. The duration of the preheat is always 240 s. Hardly any effect of the preheat temperature on the size of the hotbleach background signal. Used aliquots previously utilized for the LM test (Fig. S5.126) and the previous hotbleach tests (Fig. S5.128, S5.129).

S5.5 Discussion

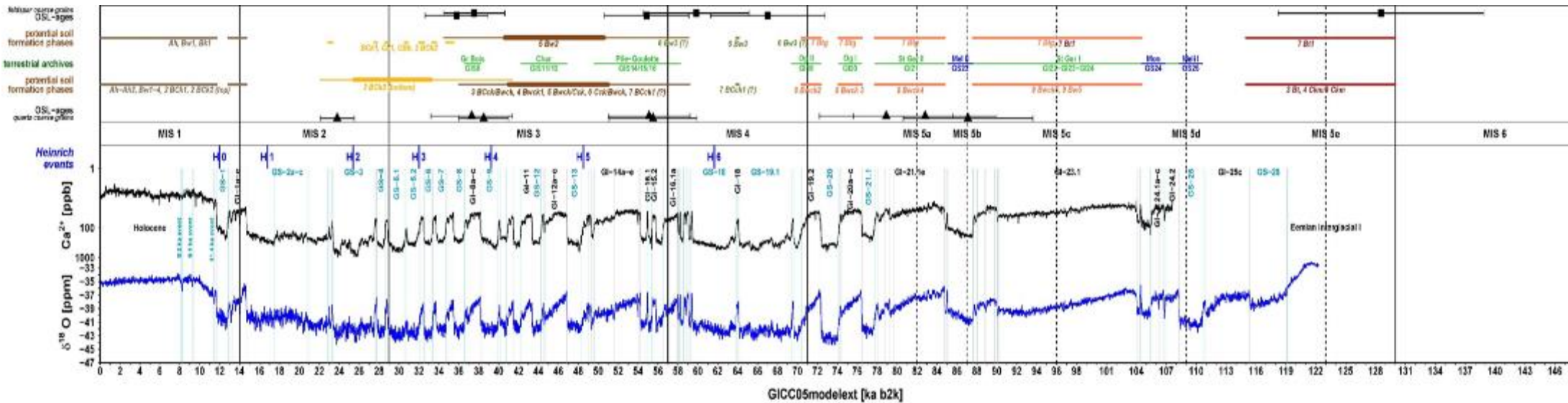


Figure S5.131: Timeline of Loess-palaeosol sequences (LPS) Baix and Collias. Feldspar coarse grain ages (black squares with error margins) and potential soil formation phases at the LPS Baix (top) reflected against: Quartz coarse grain ages (black triangles with error margins) and potential soil formation phases at the LPS Collias (Bosq et al. 2020b), terrestrial interstadials at La Grande Pile (Helmens, 2013; Wohlfahrt, 2013), marine isotope stages (MIS) (Lisiecki and Raymo 2005), Heinrich events (Allard et al. 2021) and the Greenland-ice-core based INTIMATE event stratigraphy (Rasmussen et al. 2014) with Greenland interstadials (GI) and Greenland stadials (GS).

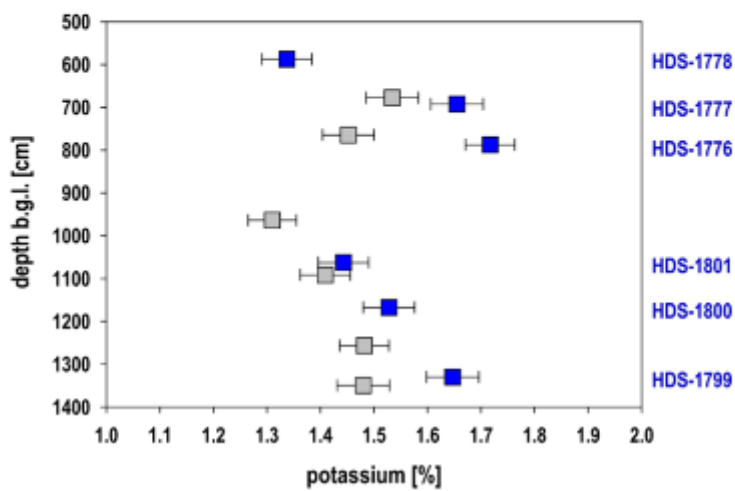
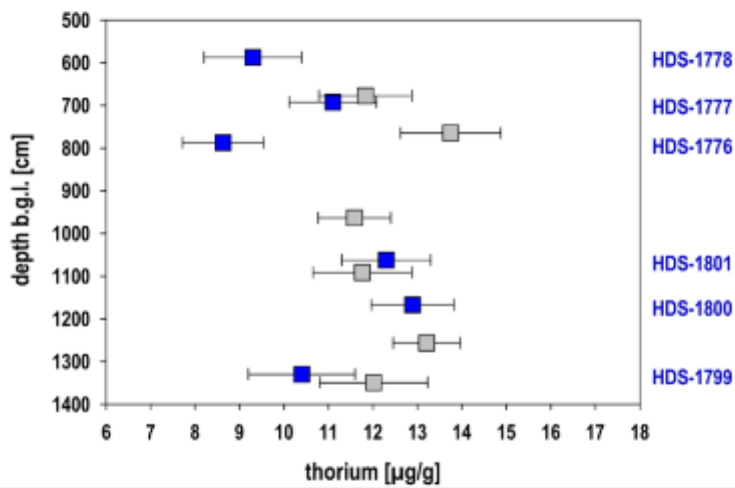
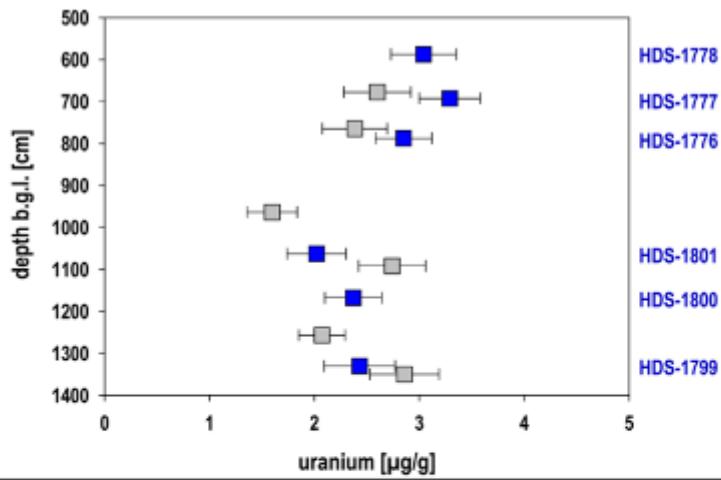


Figure S5.132: Uranium, thorium and potassium contents as determined with the μ Dose system. Results for block samples in blue and with laboratory numbers, for box samples in grey.

Chapter 6: General discussion

6.1 Research objectives and hypotheses

The stated objectives of the thesis were to I) identify possible stratigraphic marker horizons/complexes in the LPS along the Rhône Rift Valley and to II) establish a reliable chronostratigraphy of the Baix and Collias LPSs. In consideration of these objectives our findings from the studies allowed to test the stated hypotheses as followed:

- i) The Mediterranean zone extended further north during the Last Interglacial (Eemian, marine isotope stages (MIS) 5e).

Our findings exposed a less intense rubefied Luvisol at Baix LPS (sect. 5.5.1) compared to the intense rubefied Luvisol from Collias LPS (sect. 3.3.1). Thus, the characteristics of the Eemian Luvisol of LPS Baix rather coincide with soil characteristics described from central Europe LPS.

Generally, the intensity of the rubefication process depends on the moisture regime, temperature, as well as the parent material and its permeability (Boero and Schwertmann, 1987; Federoff and Courty, 2013). Thus, two possible scenarios may explain the slight rubefication of the Eemian soil of Baix LPS. Firstly, the climate conditions were the same as in central Europe during the Eemian and stated hypotheses can't be confirmed. Secondly, the "formation conditions" for the rubefication process at Baix LPS were different compare to Collias LPS. In fact, the underlying molasse sediments of the early Miocene at LPS Collias (sect. 3.4.1) are assumed to be more permeable as the limestones and marls of the Lower Cretaceous at Baix LPS (sect. 4.3.1), thus favouring rubefication at Collias compare to Baix. Furthermore, the Eemian soil at Baix was clearly truncated and possibly more intense rubefied material was eroded as it is also stated for the Collias-Wood LPS (sect. 3.3.1). Also, the geomorphological position of the Baix LPS at the slope foot may favoured moisture availability and necessary dry periods for the rubefication process could not take place. Additionally, pollen stratigraphies (Beaulieu and Reille, 1984a) and more recent studies on insect remains (Gandouin et al. 2007) of Les Échets indicated a thermal optimum during the Eemian within the northern Rhône Rift Valley. Defleur and Desclaux (2019) concluded from findings from the archaeological cave site of Baume Moula-Guercy, right next to the Baix LPS, that hot and dry Eemian Mediterranean climate must have extended much further north than present. Thus, we still assume a northwards expansion of the Mediterranean conditions over the recent climatic boarder in the Rhône Rift Valley.

Unfortunately, so far, no other in situ Interglacial soil within LPS in this climatic transition zone was described and can't be used for comparison. Thus, based solely on the Eemian soil-sediment characteristics of Baix LPS, we can't confirm with certainty and had to falsify this

stated hypothesis. So far, we have to assume, that similar climate conditions all over central Europe during the Eemian reaching towards to the recent climatic period (Figs: 6.133, 6.134).

- ii) During the Middle Pleniglacial (MIS 3) more pronounced temperate conditions (i.e. higher precipitation) prevailed in the Rhône Rift Valley compared to central Europe.

At Baix and LPS Collias LPSs, a prominent MIS 3 Cambisol-complex spanning from GI 15.1 or GI 14 to GI 9 with a striking carbonate nodule horizon was observed, respectively (sect. 3.3.3, 4.4.2, 5.4.1). This complex or at least the striking nodule horizon was also observed in several other LPS along the Rhône Rift Valley during field investigations. Thus, this horizon serves an ideal stratigraphic marker horizon for the Rhône Rift Valley and for correlations with central Europe LPS (objectives I and II). The presence of the prominent nodules suggest one leaching phase of high intensity or several leaching phases of low intensity for the early/middle MIS 3. As large nodules are missing or have not been described for MIS 3 soils in central European LPS, we attributed this feature to more humid conditions in the Rhône Rift Valley. Hence, the hypothesis could be confirmed.

- iii) During the Upper Pleniglacial (MIS 2) the transition zone was marked by less pronounced cold and arid conditions compared to central Europe.

Frost-thaw related features were described for LPS of the northern Rhône as well as for central European LPS (sect. 3.4.5, 5.5.2). None of these features could be detected neither at Baix LPS, nor at Collias LPS. Instead, we observed various intensively weathered yellow-brown to brown loess horizons (sect. 3.3.5, 5.5.2) (Fig. 6.133). We attributed it to less dry and cold climate conditions during loess accumulation phases at the LPS, and thus affirming the hypothesis.

6.2 Synthesis

Two main LPSs, Baix and Collias, were investigated with multiple state-of-the-art-methods (from macro to micro scale) in order to establish reliable chronostratigraphies, respectively (sect. 1.3). The LPSs displayed various loess and loess-like sediment depositions, interlaced by weakly to strongly developed palaeosols (-remains), according to the chronological development. The following comparison of the pedo- and loess units of both LPSs allowed to discuss where possible climatic boundaries were located regionally in Rhône Rift Valley and how these boundaries may fluctuated along the N-S European transect.

Both LPSs cover the Last Interglacial and Glacial period (MIS 5 to MIS 1) and can be structured in up to 4 pedo-sedimentary units (Last Interglacial soil-complex, lower interstadial soil, upper interstadial soil-complex and Holocene soil) and two loess units (Fig. 6.133).

The Last Interglacial soil-complex comprises soil formations of the Last Interglacial (MIS 5e) and Early Glacial (MIS 5c, 5a) and their loess- (soil) sediment deposits (MIS 5d, 5b).

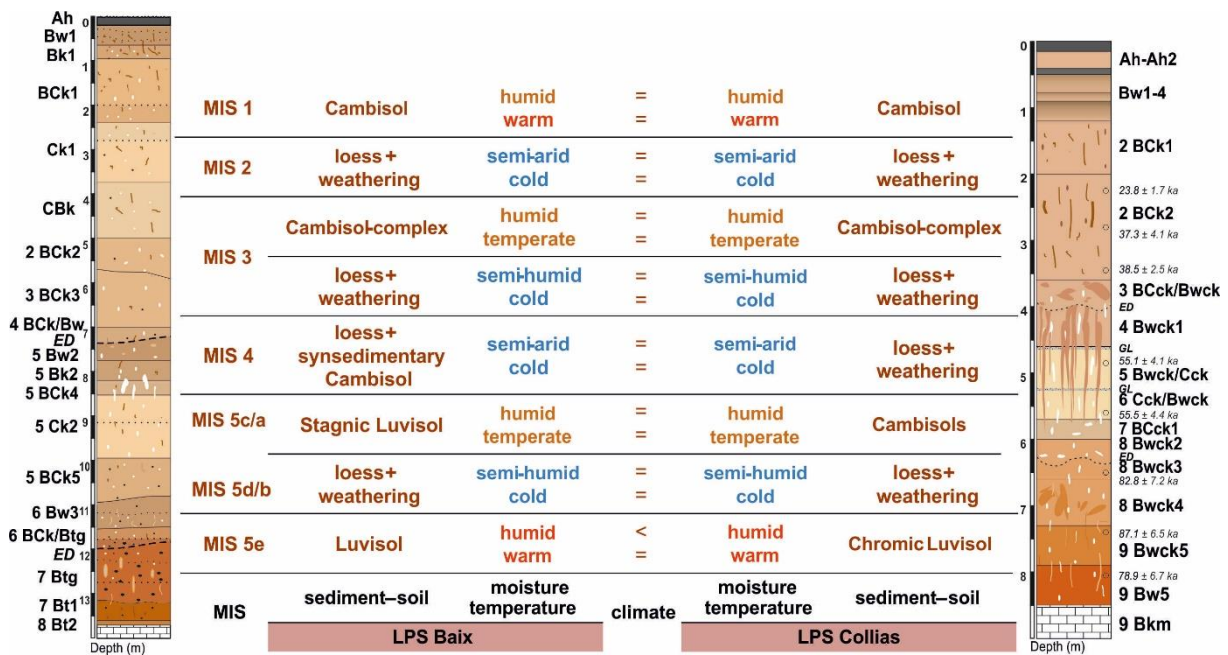


Figure 6.133: Chronostratigraphies of Baix and Collias loess-palaeosol sections with soil types and sediment units and derived palaeoenvironments for the Last Interglacial-Glacial cycle. The terms arid and humid describe the soil moisture regime and to picture tendencies within the dryness, the terms semi-humid and semi-arid is used, blue colour: cold, brown colour: temperate, red colour = warm.

At Collias LPS, the Eemian soil is represented by a Chromic Luvisol soil sediment, which is underlain by a 50 cm thick petrocalcic layer, assumed to be formed within this period. Hence, we interpreted the Eemian climate at Collias LPS as Mediterranean conditions with warm, arid summers and mild, humid winters. In contrast, at Baix LPS, the Eemian soil sediment is part of a polygenetic Stagnic Luvisol-complex, represented by a slightly rubefied Bt horizon (Fig. 6.133). The Luvisol formation of the Baix LPS suggest similar climate conditions, although with at least temporarily different moisture regime that, allowed a slight rubefication process. So far, we have to conclude, that the region at Baix might still represented the climatic transition zone during the Eemian, whereas Mediterranean fauna and flora co-existed. Thus, the climatic boundary did not seem to have been shifted northwards during the Eemian as we initially hypothesised (sect. 6.1), but further investigations will be needed.

To evaluate possible Eemian climate settings, we further compared this soil formation with the recent soil formation processes. Even though the Eemian is supposed to have lasted longer (approx. 17.000–18.000 years) and being warmer than the ongoing Holocene (sect. 1.1), it may help to assess recent and potential future climate conditions. The intensity of rubefication illuviation-processes in the Holocene loess soils of the Mediterranean region ranges from Calcisols (NE Spain) to Cambisols (SE Spain, SE France, NW Croatia) and (chromic) Luvisols (N Italy, NW Croatia) (sect. 3.4.6). Within the Collias and Baix LPSs, the recent soils were

classified as a Cambisol, respectively. In contrast to Baix LPS (sect. 4.3.1), the colluvial Bw horizons of Collias LPS showed a brown-orange colour matrix (sect. 3.3.5), indicating the presence of goethite, which is an indication for moist conditions. With reference to soil erosion and corresponding colluvial processes, which destroyed/eroded possible clay accumulation horizons of the current in situ soil development, the climate conditions are generally favourable for a Luvisol development. However, the exceeding ETp over MAP in the Mediterranean region as well as in the transition area (Fig. 1.1), does not support clay-illuviation processes. Therefore, a future development into a Luvisol with the present prevailing conditions seems unlikely for the region.

Thus, we conclude that for the Eemian period, the soils throughout the entire European climate transect were marked by more warm and humid conditions than the recent climate. The intensity of rubefication seemed to increase southwards within the transect (Fig. 6.134). Although an assumed northern expansion of Mediterranean conditions during the Eemian solely based on the soil characteristics of Baix could not be conclusively verified, other archives still do support a northwards expansion

The Early Glacial (mid and late MIS 5) at Baix LPS is marked by a slow climate deterioration with temperate, humid phases during interstadials and cold, semi-humid conditions during stadials introducing a polygenetic Stagnic Luvisol (sect. 4.4.2, 5.5.1). Similar conditions were reconstructed for the Collias LPS, reflected by several Bw horizons (sect. 3.3.3). We attributed the varying magnitudes of erosions and weathering of the horizons to the different positions within their respective slope positions. Thus, compared to central European LPS, where increasing continentality is represented by humus-enriched horizons, we interpret a slower climatic deteriorating in the Rhône Rift Valley with temperate moist phases during interstadials (soil formation) and semi-humid conditions during stadials (surface run off-processes and loess accumulation) (Fig. 6.133, 6.134).

Thus, we conclude, that in contrast to central Europe, the interstadials of the MIS 5 in the Rhône Rift Valley stayed more humid at both climatic zones (Mediterranean and climatic transitions zones). Most probably, this effect was also favoured by their valley positions.

Lower interstadial soil and loess deposits of the Lower Pleniglacial (MIS 4)

Both LPS begin with a major erosional discordance, which we interpreted as the transition from MIS 5 to MIS 4. The MIS 4 loess deposits of both LPSs show generally higher accumulations rates, reworking, the least weathering and no features related to permafrost (sections 3.3.2, 5.4.2). The silty and sandy loamy MIS 4 deposits display a polymodal grain-size distribution and they are interlaced by fine gravel bands (sect. 2.3.4, 3.3.2). Their olive-coloured sandy

deposits suggest either increased wind intensities or a more proximal source (local reworked glauconitic sandstone) of sediment supply (sect. 3.3.1, 3.3.2). In contrast, the silty and sandy loess deposits of the Baix LPS showed a unimodal grain-size distribution, which also suggest less proximal sources (sect. 5.5.1). Furthermore, a brown MIS 4/MIS 3 Bw horizon was observed in Baix LPS, in contrast to Collias LPS. We assume, that after relocation of the interglacial soil and loess sediment-mixture, the (re-)formation of the 6 Bw3 horizon began in the climatically mild excursions of GI 18, or more likely GI 17.2–GI 16.1 a (or GI 15.1) and continued as syn-sedimentary process within a younger phases (sect. 4.4.2, 5.5.2). Although the LPSs display different grain-size distributions, we defined the derived climate conditions for both LPS in the Rhône Rift Valley as generally cold and drier, allowing deposition, reworking, weathering of loess and loess-like sediments (Fig. 6.133). In central Europe LPS, MIS 4 to MIS 4/MIS 3 loess deposits as well as palaeosol relicts of the Cambisol or Regosol-Cambisol types have been evidenced.

We conclude, that during MIS 4 along the entire European transect, including the Rhône Rift Valley, generally cold and arid conditions prevalent. However, as there were no permafrost features detected in the Baix and Collias LPS, less severe conditions compare to central Europe can be interpreted.

Upper interstadial palaeosol-complex of the Middle Pleniglacial (MIS 3).

At both LPSs, we observed the same truncated Cambisol-complex with prominent in situ carbonate nodules, which formation began in GI 15.1 or more likely in GI 14 until perhaps GI 9. At Collias LPS, the Cambisol-complex is underlain by a large vertical former biopores system, suggesting intense rooting during MIS 3 interstadials, whereas the biopore system of the Cambisol-complex at Baix LPS is less pronounced (sect. 3.4.3, 3.3.6, 4.3.1). The derived climate conditions with the Rhône Rift Valley are interpreted as (i) semi-humid conditions allowing moderate accumulation of loess and pre-weathering in the form of carbonate leaching during stadial phases, and (ii) brunification during temperate and humid interstadial phases with efficient carbonate leaching (sect. 3.5.3, 5.5.2). Comparably intense developed brown truncated soil horizons (Cambisol) are found in most of the European LPSs, although without the description of the prominent carbonate nodules. Both, Baix and Collias LPS, don't display significant soil formation above the MIS 3 Bw palaeosol-complex, only loess horizons of different weathering intensities. They seem to be influenced by more constant climate conditions, in contrast to other European loess landscapes after ca 40 ka (Heinrich 4 event; GS 9), showing e.g. the formation of the Lohne soil complex.

We conclude, that during MIS 3 the climate in the Rhône Rift Valley was generally marked by decreasing loess input and the formation of brown soils, followed by an

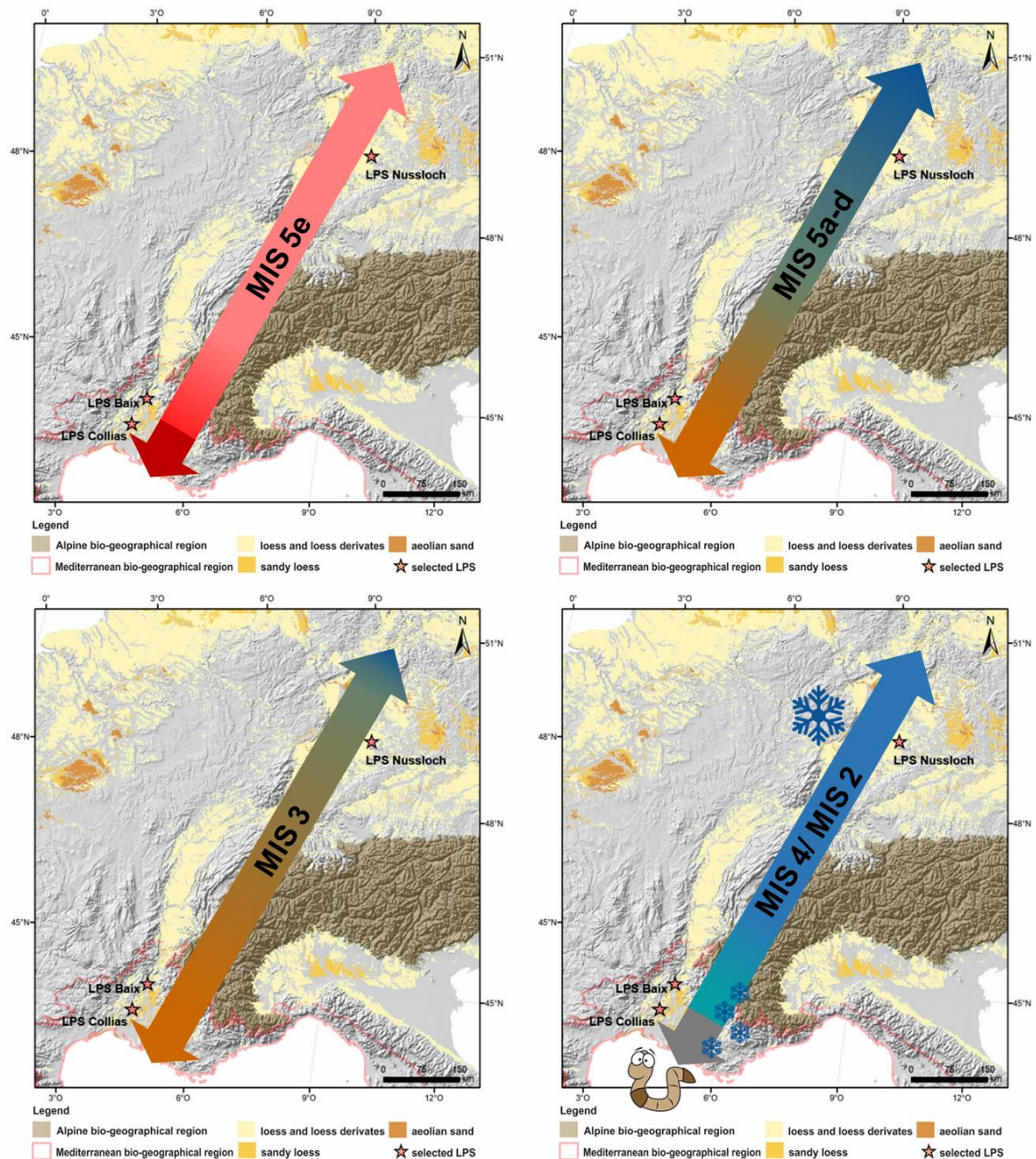


Figure 6.134: Derived climate conditions from Baix and Collias loess-palaeosol sections (LPS) and known western European LPSs (e.g. Nussloch) for the Last Interglacial and Glacial period (MIS 5 to MIS 2) and possible climatic boundaries along the N-S European transect, blue colour: cold, brown colour: temperate, red colour = warm, earthworm symbolises intense bioturbation (data: Bertran et al. 2021, Lehmkuhl et al. 2021).

increase of loess depositions and leaching processes. As the observed prominent carbonate nodules are missing or have not been described for MIS 3 soils in central European LPS, we attributed this feature to a more intense humidity during the early and mid MIS 3, in contrast to central Europe

Loess deposits of the Upper Pleniglacial (MIS 2).

Aeolian input of mainly silt and/or sand sized grains becomes dominant from ca 36 ka onwards for the Baix and Collias LPSs. Both LPSs don't show in these loess horizons (weak) soil formation, e.g. tundra gley soils, or redoximorphic features related to freeze-thaw dynamics, like European LPS (Figs. 5.74, 6.133). Instead, they are strongly bioturbated and marked by slope-wash processes (sect. 2.3.1, 3.3.4, 5.5.1). Hence, we defined for the transition MIS 3/MIS 2 and the ongoing MIS 2, including the Last Glacial Maximum, cold and mainly dry conditions, which are required for loess accumulation (Fig. 6.133). Furthermore, we assumed with respect to seasonality, shifting moisture conditions that allows pre-weathering by carbonate leaching and run-off processes as well as redeposited pre-weathered material at the foot slopes.

We concluded, that the LPS of the Rhône Rift Valley correlates in terms of recorded acceleration of loess input rates with central European LPS. However, the various intensively weathered loess horizons of the Baix and Collias LPS, suggest less severe conditions, which also explains together with the lacking permafrost why this LPS are so intensively bioturbated in contrast to central European LPS (Fig. 6.134).

6.3 Final conclusions and outlook

Firstly, we conclude that within the Rhône Rift Valley during the Eemian period, a northwards expansion of Mediterranean conditions above the recent climatic transitions zone could not be certainly verified solely based on the determined soil characteristics of the Baix LPS (strongly rubefied Luvisol). However, other archives do support a northern expansion of Mediterranean conditions and we can conclude that the climate conditions in the central and southern Rhône Rift Valley seemed to be significantly more humid than today. The comparison of the last Interglacial and the recent soil formation to determine similarities and differences of the climate conditions is challenging due to various factors (e.g. different insolation, geomorphological position, anthropogenic use). However, it seems unlikely that under present conditions in the NW Mediterranean region the Cambisol will develop into a Luvisol. Although the Eemian is described to have lasted somewhat longer than the ongoing Holocene, it is rather likely, that assumed future increase of precipitation intensity and increased frequency and length of dry periods effects the soil moisture regime and increases the risk of soil erosion.

Nevertheless, regarding our inconclusive results, statements how (far) the recent Mediterranean boundary in the mid-Rhône Rift Valley may will expand northwards in the future, as projected from climate models, have to be carefully made.

In contrast, throughout the whole Last Glacial period, the Collias and Baix LPSs showed similar characteristics, whereas their position within the valley and at the slopes most likely favoured moisture availability and potentially higher temperatures. Thus, on a regional scale I can

conclude that Baix LPS and Collias LPS formed in the same weak periglacial environment, whereas moisture availability favoured chemical weathering and syn-sedimentary processes during stable phases, and higher erosion and slope-wash processes during unstable phases.

Secondly, we assessed that the general characteristic of the LPSs of the Rhône Rift Valley coincide with central and western European LPS. Striking pedo-stratigraphic marker horizons (e.g. MIS 5e–Luvisol, MIS 3–Cambisol) clearly showed commonalities. However, marker horizons of the Rhône Rift Valley are exclusively reflected as polygenetic soil complexes that integrate possible equivalent palaeosol formations (e.g. MIS 5 soils, MIS 3 Cambisols) known from central European LPS.

Finally, we can summarise that the determined syn-sedimentary, intensively reworked and bioturbated character of the Rhône Rift Valley loess deposits as well as their partly polygenetic soils and soil-complexes reflect a gradient of decreasing magnitude of Late Pleistocene climate changes from central Europe to southern Europe.

Outlook

In this thesis, we have demonstrated that loess-palaeosol sections (LPS) of the Rhône Rift Valley with respect to their disturbances, are suitable archives to reconstruct palaeoenvironments. However, as our results concerning the expansions boundaries of Mediterranean conditions in terms of intensity of rubefication are inconclusive, other suitable archives need to be investigated to conclusively verify our derived climate conditions for this area. Furthermore, more inter-latitudinal reconstructions from north to south from numerical dated LPS are needed to support or deny palaeoenvironmental conditions and their distributions. Especially, LPS expanding north of Lyon (Dombes plateau, Saône valley) will be highly interesting to investigate with state-of-the-art-methods as the LPSs are according to Bourdier (1958) covers the whole last Interglacial-Glacial cycle, too. The Collias LPS serves also as an ideal tie-point to be connected with higher located LPSs within the eastern valley of the Durance River (Mirabeau, Saint-Paul, Aubagne and Cuges (Bourdier 1958; Alimen 1965; Bonifay 1965)). So far, the chronostratigraphies of these LPSs are only supported by numerical ages of ¹⁴C dated mollusc shells. Furthermore, some of the underlying sediments were correlated to the Middle and Upper Pleniglacial (Bonifay, 1965), but without any numerical confirmation.

References

- Aitken, M.J., 1998. An introduction to optical dating: the dating of Quaternary sediments by the use of photon-stimulated luminescence, Oxford University Press, Oxford, UK, 280 pp. ISBN 0198540922.
- Alessandri, A., Felice, M. de, Zeng, N., Mariotti, A., Pan, Y., Cherchi, A., Lee, J.-Y., Wang, B., Ha, K.-J., Ruti, P., Artale, V., 2014. Robust assessment of the expansion and retreat of Mediterranean climate in the 21st century. *Sci. Rep.* 4, (7211). <https://doi.org/10.1038/srep07211>.
- Alimen, H., 1965. Pétrographie des limons de Provence. *B. Assoc. Fr. Étud. Quat. (Quaternaire)* 2, 35–65. <https://doi.org/10.3406/quate.1965.979>.
- Allard, J., Hughes, P.D., Woodward; J. C., 2021. Heinrich Stadial aridity forced Mediterranean-wide glacier retreat in the last cold stage. *Nat. Geosci.*, 14 (4). <https://doi.org/10.1038/s41561-021-00703-6>.
- Allen, J.R.M., Brandt, U., Brauer, A., Hubberten, H.-W., Huntley, B., Keller, J., Kraml, M., Mackensen, A., Mingram, J., Negendank, J.F.W., Nowaczyk, N.R., Oberhänsli, H., Watts, W.A., Wulf, S., Zolitschka, B., 1999. Rapid environmental changes in southern Europe during the last glacial period. *Nature* 400, 740–743. <https://doi.org/10.1038/23432>.
- Amante, C., Eakins, B.W., 2009. ETOPO1 Global Relief Model Converted to PanMap Layer Format. NOAA-National Geophysical Data Center. <https://doi.org/10.1594/PANGAEA.769615>.
- Andrieux, E., Bertran, P., Saito, K., 2016. Spatial analysis of the French Pleistocene permafrost by a GIS database. *Permafrost Periglac.* 27 (1), 17–30. <https://doi.org/10.1002/ppp.1856>.
- Antohi-Trandafir, O., Timar-Gabor, A., Vulpoi, A., Bălc, R., Longmann, J., Veres, D., Simon, S., 2018. Luminescence properties of natural muscovite relevant to optical dating of contaminated quartz samples. *Radiat. Meas.* 109, 1–7. <https://doi.org/10.1016/j.radmeas.2017.12.004>.
- Antoine, P., Rousseau, D., Lautridou J.-P., Hatté, C., 1999. Last Interglacial-Glacial climatic cycle in loess-palaeosol successions of north-western France. *Boreas* 28, 551–563. <https://doi.org/10.1111/j.1502-3885.1999.tb00241.x>.
- Antoine, P., Rousseau, D., Zöller, L., Lang, A., Munaut, A.-V., Hatté, C., Fontugne, M., 2001. High-resolution record of the Last Interglacial–glacial cycle in the Nussloch loess–palaeosol sequences, Upper Rhine Area, Germany. *Quatern. Int.* 76-77, 211–229. [https://doi.org/10.1016/S1040-6182\(00\)00104-X](https://doi.org/10.1016/S1040-6182(00)00104-X).
- Antoine, P., Bahain, J.J., Debenham, N., Frechen, M., Gauthier, A., Hatté, C., Limondin-Lozouet, N., Locht, J. L., Raymond, P., Rousseau, D.D., 2003. Nouvelles données sur le Pléistocène du nord du Bassin parisien: les séquences loessiques de Villiers-Adam (Val d'Oise, France). *Quaternaire* 14 (4), 219–235. <https://dx.doi.org/10.3406/quate.2003.1744>.
- Antoine, P., Rousseau, D.D., Moine, O., Kunesch, S., Hatté, C., Lang, A., Tissoux, H., Zöller, L., 2009a. Rapid and cyclic aeolian deposition during the Last Glacial in European loess: a high-resolution record

from Nussloch, Germany. *Quaternary Sci. Rev.* 28, 2955–2973. <https://doi.org/10.1016/j.quascirev.2009.08.001>.

Antoine, P., Rousseau, D.D., Fuchs, M., Hatté, C., Gauthier, C., Marković, S.B., Jovanović, M., Gaudenyi, T., Moine, O., Rossignol, J., 2009b. High-resolution record of the last climatic cycle in the southern Carpathian Basin (Surduk, Vojvodina, Serbia). *Quatern. Int.* 198, 19–36. <https://doi.org/10.1016/j.quaint.2008.12.008>.

Antoine, P., Coutard, S., Guerin, G., Deschodt, L., Goval, E., Loch, J.-L., Paris, C., 2016. Upper Pleistocene loess-palaeosol records from northern France in the European context: environmental background and dating of the Middle Palaeolithic. *Quatern. Int.* 411, 4–24. <https://doi.org/10.1016/j.quaint.2015.11.036>.

Antoine, P., Coutard, S., Bahain, J.-J., Loch, J.-L., Hérison, D., Goval, E., 2021. The last 750 ka in loess–palaeosol sequences from northern France: environmental background and dating of the western European Palaeolithic. *J. Quaternary Sci.* 36 (8), 1293–1310. <https://doi.org/10.1002/jqs.3281>.

Armitage, S.J., Bailey, R.M., 2005. The measured dependence of laboratory beta dose rates on sample grain size. *Radiat. Meas.* 39, 123–127. <https://doi.org/10.1016/j.radmeas.2004.06.008>.

Arnal, H., 1971. Phénomènes périglaciaires dans la basse vallée du Rhône. Formations quaternaires du rebord sud et alluvions du fond de l'étang de Pujaut. *B. Assoc. Fr. Étud. Quat. (Quaternaire)* 8, 145–149. <https://doi.org/10.3406/quate.1971.1177>.

Arnal, H., 1974. Les multiples terrasses rhodaniennes de la partie nord de la Costière nîmoise; leurs prolongements vers Montpellier et leurs sols. *B. Soc. Étud. Sci. Nat. Nîmes* 54, 35–50.

Arnaud-Fassetta, G., 2003. River channel changes in the Rhone Delta (France) since the end of the little Ice Age: geomorphological adjustment to hydroclimatic. *Catena* 51, 141–172. [https://doi.org/10.1016/S0341-8162\(02\)00093-0](https://doi.org/10.1016/S0341-8162(02)00093-0).

Arnaud-Fassetta, G., Provansal, M., 2014. The lower Valley and the Delta of the Rhône River: Water Landscapes of Nature and History. In: Landscapes and Landforms of France. Fort, M., André, M.-F. (eds). Springer Netherlands: Dordrecht, s.l.; 207–218. ISBN 978-94-007-7021-8.

Auclair, M., Lamothe, M., Huot, S., 2003. Measurement of anomalous fading for feldspar IRSL using SAR. *Radiat. Meas.*, 37, 487–492. [https://doi.org/10.1016/S1350-4487\(03\)00018-0](https://doi.org/10.1016/S1350-4487(03)00018-0).

Bagnold, R.A., Barndorff-Nielsen, O., 1980. The pattern of natural size distributions. *Sedimentology* 27, 199–207. <https://doi.org/10.1111/j.1365-3091.1980.tb01170.x>.

Bambier, A., Bornand, M., Chenevoy, M., Combier, J., Debromez, J.-F., Mandier, P., Monjuvent, G., 1979. Notice Explicative de la Feuille Tournon à 1/50 000. Bureau de recherches géologiques et minières (BRGM).

- Banerjee, D., Murray, A., Bøtter-Jensen, L., Lang, A., 2001. Equivalent dose estimation using a single aliquot of polymineral fine grains. *Radiat. Meas.* 33, 73–94. [https://doi.org/10.1016/S1350-4487\(00\)00101-3](https://doi.org/10.1016/S1350-4487(00)00101-3).
- Banks, W.E., Bertran, P., Ducasse, S., Klaric, L., Lanos, P., Renard, C., Mesa, M., 2019. An application of hierarchical Bayesian modelling to better constrain the chronologies of Upper Palaeolithic archaeological cultures in France between ca 32,000-21,000 calibrated years before present. *Quaternary Sci. Rev.* 220, 188–214. <https://doi.org/10.1016/j.quascirev.2019.07.025>.
- Barta, G., 2011a. The structure and origin of loess dolls - a case study from the loess-paleosoil sequence of Süttö, Hungary, J. Environ. Geography, 1–10. <https://doi.org/10.14232/jengeo-2011-43789>.
- Barta, G., 2011b. Secondary carbonates in loess-paleosoil sequences: a general review. *Open Geosci.* 3, 203. <https://doi.org/10.2478/s13533-011-0013-7>.
- Barta, G., 2016. Analysis of secondary carbonates from the young loess-paleosol sequences of the Carpathian Basin - especially regarding their paleoenvironmental role. PhD thesis. Eötvös Loránd University, Faculty of Science. https://edit.elte.hu/xmlui/bitstream/handle/10831/33462/PhD_dissertation_Barta_Gabriella_2016.pdf.
- Bašić, F., 2013. The Soils of Croatia. World Soil Book Series Publisher: Springer Dordrecht Heidelberg New York London. Eds. Prof. Hartemink, A., ISBN: 978-94-007-5815.
- Bateman, M.D., Stein, S., Ashurst, R.A., Selby, K., 2015. Instant luminescence chronologies? High resolution luminescence profiles using a portable luminescence reader. *Quat. Geochronol.*, 30, 141–146. <https://doi.org/10.1016/j.quageo.2014.12.007>.
- Bazile, F., 2007. Le Gravettien de la France méditerranéenne. *PALEO. Revue d'archéologie préhistorique* 19, 89–103. <https://doi.org/10.4000/paleo.534>.
- Beaudouin, C., Suc, J.-P., Acherki, N., Courtois, L., Rabineau, M., Aloisi, J.-C., Sierro, F.J., Oberlin, C., 2005. Palynology of the northwestern Mediterranean shelf (Gulf of Lions): First vegetational record for the last climatic cycle. *Mar. Petrol. Geol.*, 22, 845–863. <https://doi.org/10.1016/j.marpetgeo.2005.03.005>.
- Beaudouin, C., Jouet, G., Suc, J.-P., Berné, S., Escarguel, G., 2007. Vegetation dynamics in southern France during the last 30 ky BP in the light of marine palynology. *Quaternary Sci. Rev.* 26, 1037–1054. <https://doi.org/10.1016/j.quascirev.2006.12.009>.
- Beaulieu, J.-L. d., Reille, M., 1984a. A long Upper Pleistocene pollen record from Les Échets, near Lyon, France. *Boreas* 111–132. <http://dx.doi.org/10.1111/j.1502-3885.1984.tb00066.x>.
- Beaulieu, J.-L. de, Reille, M., 1984b. The Pollen Sequence of Les Échets (France): A New Element for the Chronology of the Upper Pleistocene. *Geogr. Phys. Quatern.* 38 (1), 3–9. <https://doi.org/10.7202/032531ar>.

- Beaulieu, J.-L. de, Reille, M., 1989. The transition from temperate phases to stadials in the long upper Pleistocene sequence from Les Echets (France). *Palaeogeogr., Palaeoecol.* 72, 147–159. [https://doi.org/10.1016/0031-3501\(89\)90139-9](https://doi.org/10.1016/0031-3501(89)90139-9).
- Beaulieu, J.-L., Reille, M., 1992. The last cycle at La Grande Oile (Vosges, France). *Quaternary Sci. Rev.*, 11, 431–438. [https://doi.org/10.1016/0277-3791\(92\)90025-4](https://doi.org/10.1016/0277-3791(92)90025-4).
- Beaulieu, J.-L. de, Miras, Y., Andrieu-Ponel, V., Guiter, F., 2005. Vegetation dynamics in north-western Mediterranean regions: Instability of the Mediterranean bioclimate. *Plant Biosystems – Int. J. Plant Biol.* 139, 114–126. <https://doi.org/10.1080/11263500500197858>.
- Becze-Deák, J., Langohr, R., Verrecchia, E. P., 1997: Small scale secondary CaCO₃ accumulations in selected sections of the European loess belt. Morphological forms and potential for paleoenvironmental reconstruction. *Geoderma* 76, 221–252. [https://doi.org/10.1016/S0016-7061\(96\)00106-1](https://doi.org/10.1016/S0016-7061(96)00106-1).
- Bell, W.T., 1979. Attenuation Factors for the Absorbed Radiation Dose in Quartz Inclusion for Thermoluminescence Dating. *Ancient TL* 8, 2–13. http://ancienttl.org/ATL_L3-3.pdf (accessed: 14 December 2023).
- Benoit, E., 1858. Esquisse de la Carte géologique et agronomique de la Bresse et de la Dombes. *Bull. Soc. Géol. France* 2 (15), 315-344.
- Berger-Levrault, F., 1968. Notice Explicative de la Feuille Uzès à 1:50.000 - XXIX-41, Service de la Carte Géologique de la France - Paris, Nancy.
- Bertran, P., Sitzia L., Banks, W.E., Bateman, M.D., Demars P.-Y., Hernandez, M., Lenoir, M., Mercier, N., Prodeo, F., 2013. The Landes de Gascogne (Southwest France): periglacial desert and cultural frontier during the Palaeolithic. *J. Archaeol. Sci.* 40 (5), 2274–2285. https://www.academia.edu/2650842/The_Landes_de_Gascogne_southwest_France_periglacial_desert_and_cultural_frontier_during_the_Palaeolithic (accessed: 20 May 2020).
- Bertran, P., Andrieux, E., Antoine, P., Deschodt, L., Gardère, P., Hernandez, M., Legentil, C., Lenoble, A., Liard, M., Mercier, N., Moine, O., Sitzia, L., van Vliet-Lanoë, B., 2014. Distribution and chronology of Pleistocene permafrost features in France: Database and first results. *Boreas* 43, 699–711. <https://doi.org/10.1111/bor.12025>.
- Bertran, P., Liard, M., Sitzia, L., Tissoux, H., 2016. A map of Pleistocene aeolian deposits in Western Europe, with special emphasis on France. *J. Quaternary Sci.* 31. e2909 <https://doi.org/10.1002/jqs.2909>.
- Bertran, P., Bosq, M., Borderie, Q., Coussot, C., Coutard, S., Deschodt, L., Franc, O., Gardère, P., Liard, M., Wuscher, P., 2021. Revised map of European aeolian deposits derived from soil texture data. *Quaternary Sci. Rev.* 266, 107085. <https://doi.org/10.1016/j.quascirev.2021.107085>.
- Beuselinck, L., Govers, G., Poesen, J., Degraer, G., Froyen, L., 1998. Grain-size analysis by laser diffractometry: comparison with the sieve-pipette method. *Catena* 32 (3-4), 193–208. [https://doi.org/10.1016/S0341-8162\(98\)00051-4](https://doi.org/10.1016/S0341-8162(98)00051-4).

- Bibus, E., Semmel, A., 1977. Stratigraphische Leithorizonte im Würmlöß des Mittelrhein-Gebietes. *Geol. Jb. Hessen* (105), 141–147.
- Bibus, E., Frechen, M., Kösel, M., Rähle, W., 2007. Das jungpleistozäne Lößprofil von Nußloch (SW-Wand) im Aufschluss der Heidelberger Zement AG. *E&G Quaternary Sci. J.* 56 (4): 227–255.
- Blume, H.P., Brummer, G.W., Horn, R., Kandeler, E., Kögel-Knabner, I., Kretzschmar, R., Stahr, K., Wilke, B.M., 2010. *Lehrbuch der Bodenkunde (Scheffer/Schachtschabel)*. volume 16.
- Blume, H.P., Stahr, K., Leinweber, P., 2011. *Bodenkundliches Praktikum: Eine Einführung in pedologisches Arbeiten für Ökologen, insbesondere Land- und Forstwirte, und für Geowissenschaftler*. Spektrum Akademischer Verlag, Heidelberg, 255 pp. ISBN 9783827415530.
- Boero, V., Schwertmann, U., 1987. Occurrence and transformations of iron and manganese in a colluvial terra rossa toposequence of northern Italy. *Catena* 6 (14), 519–531. [https://doi.org/10.1016/0341-8162\(87\)90003-8](https://doi.org/10.1016/0341-8162(87)90003-8).
- Boero, V., Schwertmann, U., 1989. Iron oxide mineralogy of terra rossa and its genetic implications. *Geoderma* 44, 319–327. [https://doi.org/10.1016/0016-7061\(89\)90039-6](https://doi.org/10.1016/0016-7061(89)90039-6).
- Bognar, A., Schweitzer, F., Ször, G., 2003. Susak. Environmental reconstruction of a loess island in the Adriatic. *Elmélet, módster, gyakorlat* 60. http://real-eod.mtak.hu/3678/1/MTA_ElmeletModszerGyakorlat_60_000823211.pdf.
- Boixadera, J., Poch, R.M., Lowick, S.E., Balasch, J.C., 2015. Loess and soils in the eastern Ebro basin. *Quatern. Int.* 376, 114–133. <https://doi.org/10.1016/j.quaint.2014.07.046>.
- Bokhorst, M.P., Beets, C.J., Marković, S.B., Gerasimenko, N.P., Matviishina, Z.N., Frechen, M., 2009. Pedo-chemical climate proxies in Late Pleistocene Serbian-Ukrainian loess sequences. *Quatern. Int.* 198, 113–123. <https://doi.org/10.1016/j.quaint.2008.09.003>.
- Bonifay, E., 1952. Les limons loessiques de la région de Marseille (Bouches-du-Rhône). *Bull. Soc. Géolog. France* 6 (7-9), 461–466. <http://dx.doi.org/10.2113/gssgfbull.S6-II.7-9.461>.
- Bonifay, E., 1962. *Les Terrains quaternaires dans le Sud-Est de la France*. Bordeaux, Institut de Préhistoire, 194 p. (Publications de l'Institut de préhistoire de l'Université de Bordeaux ; 2).
- Bonifay, E., 1965. Stratigraphie des loess anciens et récents dans le Sud-Est de la France. *B. Assoc. Fr. Étud. Quat. (Quaternaire)* 2, 21–34. <https://doi.org/10.3406/quate.1965.978>.
- Bonnet, A., Bornand, M., 1970. Pédologie et Quaternaire dans la vallée du Rhône. *B. Assoc. Fr. Étud. Quat. (Quaternaire)* 7 (2), 105–116. <https://doi.org/10.3406/quate.1970.1152>.
- Boretto, G., Zanchetta, G., Ciulli, L., Bini, M., Fallick, A. E., Lezzerini, M., Colonese, A.C., Zembo, I., Trombino, L., Regattieri, E., Sarti, G., 2017. The loess deposits of Buca Dei Corvi section (Central Italy): Revisited. *Catena* 151, 225–237. <https://doi.org/10.1016/j.catena.2017.01.001>.

- Bornand, M., 1978. Altération des matériaux fluvio-glaciaires, genèse et évolution des sols sur terrasses quaternaires dans la moyenne vallée du Rhône. Géomorphologie. Université Montpellier II - Sciences et Techniques du Languedoc. Français. <https://hal.archives-ouvertes.fr/tel-02859745/>.
- Bosq, M., Bertran, P., Degeai, J.-P., Kreutzer, S., Queffelec, A., Moine, O., Morin, E., 2018. Last Glacial aeolian landforms and deposits in the Rhône Valley (SE France): spatial distribution and grain-size characterization. *Geomorphology* 318, 250–269. <https://doi.org/10.1016/j.geomorph.2018.06.010>.
- Bosq, M., Bertran, P., Degeai, J.-P., Queffelec, A., Moine, O., 2020a. Geochemical signature of sources, recycling and weathering in the Last Glacial loess from the Rhône Valley (southeast France) and comparison with other European regions. *Aeolian Res.* 42, 100561. <https://doi.org/10.1016/j.aeolia.2019.100561>.
- Bosq, M., Kreutzer, S., Bertran, P., Degeai, J.-P., Dugas, P., Kadereit, A., Lanos, P., Moine, O., Pfaffner, N., Queffelec, A., Sauer, D., 2020b. Chronostratigraphy of two Late Pleistocene loess-palaeosol sequences in the Rhône Valley (southeast France). *Quaternary Sci. Rev.* 245, 106473. <https://doi.org/10.1016/j.quascirev.2020.106473>.
- Bouchez, J., Gaillardet, J., Lupker, M., Louvat, P., France-Lanord, C., Maurice, L., Armijos, E., Moquet, J.-S., 2012. Floodplains of large rivers: weathering reactors or simple silos? *Chem. Geol.* 332e333, 166–184. <https://doi.org/10.1016/j.chemgeo.2012.09.032>.
- Bourdier, F., 1985. Le Bassin du Rhône au Quaternaire, géologie et préhistoire. PhD thesis, Faculté des Sciences de l'Université de Paris, 337 pp. <https://theses.hal.science/tel-00682737> (accessed: 17 December 2023).
- Boyer, J., Duvail, C., Le Strat, P., Gensous, B., Tesson, M., 2005. High resolution stratigraphy and evolution of the Rhône delta plain during Postglacial time, from subsurface drilling data bank. *Mar. Geol.* 222–223, 267–298. <https://doi.org/10.1016/j.margeo.2005.06.017>.
- Brennan, R., Quade, J., 1997. Reliable late-Pleistocene stratigraphic ages and shorter groundwater travel times from 14 C in fossil snails from the southern Great Basin. *Quaternary Res.* 47, 329–336. <https://doi.org/10.1006/qres.1997.1895>.
- Brewer, S., Guiot, J., Sánchez-Goñi, M.F., Klotz, S., 2008. The climate in Europe during the Eemian: A multi-method approach using pollen data. *Quaternary Sci. Rev.* 27, 2303–2315. <https://doi.org/10.1016/j.quascirev.2008.08.029>.
- BRGM, 2021. Bureau de Recherches Géologiques et Minières, Cartes géologiques France 1/1 000 000 access through <http://infoterre.brgm.fr/viewerlite/MainTileForward.do> (accessed: 14 May 2021).
- Bronger, A., 1966. Löss, ihre Verbraunungszonen und fossilen Böden. Ein Beitrag zur Stratigraphie des oberen Pleistozäns in Südbaden. In: *Schriften des Geographischen Institutes der Universität Kiel*, Schmieder, O., Schlenger, H., Wilhelm, F., (eds). *Schr. Geogr. Inst. Univ. Kiel* 2, 98 pp.
- Bronger, A., 1976. Zur quartären Klima- und Landschaftsentwicklung des Karpatenbeckens auf (paläo) pedologischer und bodengeographischer Grundlage. *Kieler Geogr. Schriften*, XIV, 268 pp.

- Bronger, A., Heinkele, T., 1990. Mineralogical and clay mineralogical aspects of loess research. *Quatern. Int.* 7 (8), 37–51. [https://doi.org/10.1016/1040-6182\(90\)90037-5](https://doi.org/10.1016/1040-6182(90)90037-5).
- Brosche, K.-U., Walther, M., 1977. Geomorphologische und bodengeographische Analyse Holozäner, Jung- und Mittelpleistozäner Sedimente und Böden in Spanien und Südfrankreich. *Catena* 3, 311–342. [https://doi.org/10.1016/0341-8162\(77\)90036-4](https://doi.org/10.1016/0341-8162(77)90036-4).
- Brunnacker, K., 1974. Löss und Paläoböden der letzten Kaltzeit im mediterranen Raum, *E&G Quaternary Sci. J.* 25, 62–95. <https://doi.org/10.3285/eg.25.1.07>.
- Buggle, B., Glaser, B., Hambach, U., Gerasimenko, N., Marković, S., 2011. An evaluation of geochemical weathering indices in loess-paleosol studies. *Quatern. Int.* 240, 12–21. <https://doi.org/10.1016/j.quaint.2010.07.019>.
- Buggle, B., Hambach, U., Müller, K., Zöller, L., Marković, S.B., Glaser, B., 2014. Iron mineralogical proxies and Quaternary climate change in SE-European loess-paleosol sequences. *Catena* 117, 4–22. <https://doi.org/10.1016/j.catena.2013.06.012>.
- Bulur, E., 1996. An alternative technique for optically stimulated luminescence (OSL) experiment. *Radiat. Meas.* 26 (5), 701–709. [https://doi.org/10.1016/S1350-4487\(97\)82884-3](https://doi.org/10.1016/S1350-4487(97)82884-3).
- Buoncrisiani, J.-F., Campy, M., 2004. Expansion and retreat of the Jura Ice sheet (France) during the last glacial maximum. *Sediment. Geol.* 165 (3), 253–264. <http://dx.doi.org/10.1016/j.sedgeo.2003.11.007>.
- Buoncrisiani, J.-F., Campy M., 2011. Quaternary glaciations in the French Alps and Jura. In: Elhers, J., Gibbard, P.L., Hughes, P.D., (eds.) *Quaternary Glaciations – Extent and Chronology: A Closer Look, Developments in Quaternary Science*. Elsevier, Amsterdam, 117–126. <http://dx.doi.org/10.1016/B978-0-444-53447-7.00010-6>.
- Burbidge, C. I., Sanderson, D. C. W., Housley, R. A., Allsworth Jones, P., 2007. Survey of Palaeolithic sites by luminescence profiling, a case study from Eastern Europe. *Quat. Geochronol.*, 2, 296–302. <https://doi.org/10.1016/j.quageo.2006.05.024>.
- Calvo, F.R., Sanchez, J., Acosta, A., Wolf, D., Faust, D., 2016. Granulometrical, mineralogical and geochemical characterization of loess deposits in the Tajo Basin. *Quatern. Int.* 407, 14–28. <https://doi.org/10.1016/j.quaint.2015.11.122>.
- Candy, I., Black, S., 2009. The timing of Quaternary calcrete development in semi-arid southeast Spain: Investigating the role of climate on calcrete genesis. *Sediment. Geol.* 218, 6–15. <https://doi.org/10.1016/j.sedgeo.2009.03.005>.
- Canti, M.G., Pearce, T.G., 2003. Morphology and dynamics of calcium carbonate granules produced by different earthworm species. *Pedobiologia* 47, 511–521. <https://doi.org/10.1078/0031-4056-00221>.
- Canti, M.G., 2007. Deposition and taphonomy of earthworm granules in relation to their interpretative potential in Quaternary stratigraphy. *J. Quaternary Sci.* 22, 111–118. <https://doi.org/10.1002/jqs.1017>.

- Carignan, J., Hild, P., Mevelle, G., Morel, J., & Yeghicheyan, D., 2001. Routine Analyses of Trace Elements in Geological Samples using Flow Injection and Low Pressure On-Line Liquid Chromatography Coupled to ICP-MS: A Study of Geochemical Reference Materials BR, DR-N, UB-N, AN-G and GH. *Geostandards Newsletter* 25(2–3), 187–198. <https://doi.org/10.1111/j.1751-908X.2001.tb00595.x>
- Catt, J. A., 1991. Soils as indicators of Quaternary climatic change in mid-latitude regions. *Geoderma* 51 (1-4), 167–187. [https://doi.org/10.1016/0016-7061\(91\)90070-A](https://doi.org/10.1016/0016-7061(91)90070-A).
- Chapotat, G., 1935. La vallée du Rhône de Vienne à Tain, notes de morphologie. *Étud. Rhodaniennes* 4, 397–432. <https://doi.org/10.3406/geoca1935.7112>.
- Chen, J.H., Curran, H.A., White, B., Wasserburg, G. J., 1991. Precise chronology of the Last Interglacial period: ²³⁴U-²³⁰Th data from fossil coral reefs in the Bahamas. *Geol. Soc. Am. Bull.* 103, 82–97. [https://doi.org/10.1130/0016-7606\(1991\)103%3C0082:PCOTLI%3E2.3.CO;2](https://doi.org/10.1130/0016-7606(1991)103%3C0082:PCOTLI%3E2.3.CO;2).
- Chen, J., Ji, J., Balsam, W., Chen, Y., Liu, L., An, Z., 2002. Characterization of the Chinese loess–paleosol stratigraphy by whiteness measurement. *Palaeogeogr., Palaeoecol.* 183 (3-4), 287–297. [https://doi.org/10.1016/S0031-0182\(02\)00246-8](https://doi.org/10.1016/S0031-0182(02)00246-8).
- Chen, Y., Li, S.-H., Li, B., 2013. Residual doses and sensitivity change of post IR IRSL signals from potassium feldspar under different bleaching conditions. *Geochronometria* 40 (4): 229–238. <https://doi.org/10.2478/s13386-013-0128-3>.
- Chenevoy, M., Elmi, S., Lorenchet de Montjamont, M., Combier, J., Michel, R., 1977. Notice Explicative de la Feuille Crest à 1/50 000. Bureau de recherches géologiques et minières (BRGM) <http://ficheinfoterre.brgm.fr/Notices/0842N.pdf> (accessed: 17 December 2023).
- CIE, 1976. Colorimetry: Official Recommendations of the International Commission on Illumination. Bureau central de la CIE, Paris.
- Clark, P.U., Dyke, A.S., Shakun, J.D., Carlson, A.E., Clark, J., Wohlfarth, B., Mitrovica, J.X., Hostetler, S.W., McCabe, A.M., 2009. The last glacial maximum. *Science* 325, 710–714. <https://doi.org/10.1126/science.1172873>.
- Colarossi, D., Duller, G., Roberts, H.M., 2018. Exploring the behaviour of luminescence signals from feldspars: Implications for the single aliquot regenerative dose protocol. *Radiat. Meas.* 109, 35–44. <https://doi.org/10.1016/j.radmeas.2017.07.005>.
- Combès, B., Philippe, A., Lanos, P., Mercier, N., Tribolo, C., Guerin, G., Guibert, P. Lahaye, C., 2015. A Bayesian central equivalent dose model for optically stimulated luminescence dating. *Quat. Geochronol.* 28, 62–70. <https://doi.org/10.1016/j.quageo.2015.04.001>.
- Costantini, E.A.C., Carnicelli, S., Sauer, D., Priori, S., Andreetta, A., Kadereit, A., Lorenzetta, R., 2018. Loess in Italy: genesis, characteristics and occurrence. *Catena* 168, 14–33. <https://doi.org/10.1016/j.catena.2018.02.002>.

- Coudé-Gaussen, G., 1990. The loess and loess-like deposits along the sides of the western Mediterranean Sea: Genetic and palaeoclimatic significance. *Quatern. Int.* 5, 1–8. [https://doi.org/10.1016/1040-6182\(90\)90020-5](https://doi.org/10.1016/1040-6182(90)90020-5).
- Coutterand, S., Schoeneich, P., Gérard N., 2009. Le lobe glaciaire lyonnais au maximum würmien glacier du Rhône ou/et glaciers savoyard? Neige et glace de montagne Reconstitution, dynamique, pratiques. Collection EDYTEM, 11–22. https://www.persee.fr/doc/edyte_1762-4304_2009_num_8_1_1069.
- Coutterand, S. 2010. Étude géomorphologique des flux glaciaires dans les Alpes nord-occidentales au Pléistocène récent. Du maximum de la dernière glaciation aux premières étapes de la déglaciation. Thèse Université Savoie Mont Blanc. HAL-ID: tel-00517790. <https://hal.univ-smb.fr/tel-00517790v2> (accessed: 15 May 2021).
- Cremschi, M., 1990a. The Loess in Northern and Central Italy: a Loess Basin between the Alps and the Mediterranean Region. CNR Centro di Studio per la Stratigrafia e la Petrografia delle Alpi Centrali, Milano. ISBN 88-85329-00-4.
- Cremschi, M., 1990b. Stratigraphy and palaeoenvironmental significance of the loess deposits on Susak Island (Dalmatian archipelago). *Quatern. Int.* 5, 97–106. [https://doi.org/10.1016/1040-6182\(90\)90029-4](https://doi.org/10.1016/1040-6182(90)90029-4).
- Cremschi, M., van Vliet-Lanoë, B., 1990. Traces of frost activity and ice segregation in Pleistocene loess deposits and till of northern Italy: Deep seasonal freezing or permafrost? *Quatern. Int.* 5, 39–48. [https://doi.org/10.1016/1040-6182\(90\)90023-W](https://doi.org/10.1016/1040-6182(90)90023-W).
- Cremschi, M., Fedoroff, N., Guerreschi, A., Huxtable, J., Colombi, N., Castelletti, L., Maspero, A., 1990. Sedimentary and pedological processes in the Upper Pleistocene loess of northern Italy. The Bagaggera sequence. *Quatern. Int.* 5, 23–38. [https://doi.org/10.1016/1040-6182\(90\)90022-V](https://doi.org/10.1016/1040-6182(90)90022-V).
- Cremschi, M., Zerboni, A., Nicosia, C., Negrino, F., Rodnight, H., Spötl, C., 2015. Age, soil-forming processes, and archaeology of the loess deposits at the Apennine margin of the Po plain (northern Italy): new insights from the Ghiardo area. *Quatern. Int.* 376, 173–188. <https://doi.org/10.1016/j.quaint.2014.07.044>.
- Cullers, R.L., 2000. The geochemistry of shales, siltstones and sandstones of Pennsylvanian-Permian age, Colorado, USA: implications for provenance and metamorphic studies. *Lithos* 51, 181–203. [https://doi.org/10.1016/S0024-4937\(99\)00063-8](https://doi.org/10.1016/S0024-4937(99)00063-8).
- Dansgaard, W., Johnsen, S.J., Clausen, H.B., Dahl-Jensen, D., Gundestrup, N.S., Hammer, C.U., Hvidberg, C.S., Steffensen, J.P., Sveinbjörnsdóttir, A.E., Jouzel, J., Bond, G., 1993. Evidence for general instability of past climate from a 250-kyr ice-core record. *Nature* 364, 218–220. <https://doi.org/10.1038/364218a0>.
- Datar, 2022. Les territoires français face au changement climatique. https://cartotheque.anct.gouv.fr/media/record/eyJpIjoizGVmYXVsdCIsIm0iOm51bGwslmQiOjEsInliOjQ1Mn0= (accessed: 5 January 2022).

- Daujeard, C., Fernandes, P., Guadelli, J.-L., Moncel, M.-H., Santagata, C., Raynal, J.-P., 2012. Neanderthal subsistence strategies in Southeastern France between the plains of the Rhone Valley and the mid-mountains of the Massif Central (MIS 7 to MIS 3). *Quatern. Int.* 252, 32–47. <https://doi.org/10.1016/j.quaint.2011.01.047>.
- Dearing, J., Livingstone, I., Zhou, L.-P., 1996. A late Quaternary magnetic record of Tunisian loess and its climatic significance. *Geophys. Res. Lett.* 23, 189–192. <https://doi.org/10.1029/95GL03132>.
- Debelmas J., 1974. *Géologie de la France. Les Chaines plissées du cycle Alpin et leur avant-pays.*: Volume 2. DOIN: Paris.
- Debelmas, J., Balleisio, R., Brochier J.-L., Fourneaux, L., Moûtier, L., Triat J.-M., 2004. Notice Explicative de la Feuille Valréas à 1/50 000, 2 édition. Bureau de recherches géologiques et minières (BRGM).
- Dee, M.W., Palstra, S.W.L., Aerts-Bijma, A.T., Bleeker, M.O., de Bruijn, S., Ghebru, F., Jansen, H.G., Kuitens, M., Paul, D., Richie, R.R., 2020. Radiocarbon dating at Groningen: new and updated chemical pretreatment procedures. *Radiocarbon* 62, 63–74. <https://doi.org/10.1017/RDC.2019.101>.
- Defleur, A., Desclaux, E. 2019. Impact of the Last Interglacial climate change on ecosystems and Neanderthals behavior at Baume Moula-Guercy, Ardèche, France. *J. Archaeol. Sci.* 104, 114–124. <https://doi.org/10.1016/j.jas.2019.01.002>.
- Delhon, C., Thiébault, S., Berger, J.-F., 2009. Environment and landscape management during the Middle Neolithic in Southern France: Evidence for agro-sylvo-pastoral systems in the Middle Rhone Valley. *Quatern. Int.* 200 (1–2), 50–65. <https://doi.org/10.1016/j.quaint.2008.05.008>.
- Dèzes, P., Schimid S.M., Ziegler, P.A., 2004. Evolution of the European Cenozoic rift system: interaction of the Alpine and Pyrenean orogens with their foreland lithosphere. *Tectonophysics* 389 (1–2), 1–33. <https://doi.org/10.1016/j.tecto.2004.06.011>.
- Dietze, E., Hartmann, K., Diekmann, B., IJmker, J., Lehmkuhl, F., Opitz, S., Stauch, G., Wünnemann, B., Borchers, A., 2012. An end-member algorithm for deciphering modern detrital processes from lake sediments of Lake Donggi Cona, NE Tibetan Plateau, China. *Sediment. Geol.* 243, 169–180. <https://doi.org/10.1016/j.sedgeo.2011.09.014>.
- Dietze, M., Kreutzer, S., Burow, C., Fuchs, M.C., Fischer, M., Schmidt, C., 2016. The abanico plot: visualising chronometric data with individual standard errors. *Quat. Geochronol.* 31, 12–18. [doi:10.1016/j.quageo.2015.09.003](https://doi.org/10.1016/j.quageo.2015.09.003).
- Dietze, E., Dietze, M., 2019. Grain-size distribution unmixing using the R package EMMAgeo. *E&G Quaternary Sci. J.* 68, 29–46. <https://doi.org/10.5194/egqsj-68-29-2019>.
- Diodato, N., Bellocchi, G., Romano, N., Guadagno, F.M., 2016. Modelling the Rainfall Erosivity of the Rhone Region (Southeastern France). Associated with Climate Variability and Storminess. *Adv. Meteorol.* 2016, 1–9. <https://doi.org/10.1155/2016/7626505>.

- Dixit, Y., Toucanne, S., Fontanier, C., Pasquier, V., Lora, J.M., Jouet, G., Tripathi, A., 2020. Enhanced western mediterranean rainfall during past interglacials driven by North Atlantic pressure changes. *Quatern. Int.* 553, 1–13. <https://doi.org/10.1016/j.quaint.2020.08.017>.
- Doyen, É., Vanni re, B., Rius, D., B geot, C., Millet, L., 2015. Climate and Biomass Control on Fire Activity during the Late-Glacial/Early-Holocene Transition in Temperate Ecosystems of the Upper Rhone Valley (France). *Quaternary Res.* 83 (1), 94–104. <https://doi.org/10.1016/j.yqres.2014.08.004>.
- Drake, L., 2018. CloudCal v3.0. GitHub. <https://github.com/leedrake5/CloudCal>. doi:10.5281/zenodo.2596154.
- Dubar, M., 1979. I.-Les caract res s dimentologiques des terrasses fluviales et leur couverture limoneuse en Moyenne Durance. *B. Assoc. Fr.  tud. Quat. (Quaternaire)* 16 (3), 109–120. https://www.persee.fr/doc/quate_0004-5500_1979_num_16_3_1354 (accessed 04: February 2022).
- Duller, G.A.T., 2007. Assessing the error on equivalent dose estimates derived from single aliquot regenerative dose measurements. *Ancient TL*, 25 (1), 15–24. http://ancienttl.org/ATL_25-1_2007/ATL_25-1_Duller_p15-24.pdf (accessed: 14 August 2021).
- Duller, G.A.T., 2013. Distinguishing quartz and feldspar in single grain luminescence measurements. *Radiat. Meas.* 37 (2), 161–165. [https://doi.org/10.1016/S1350-4487\(02\)00170-1](https://doi.org/10.1016/S1350-4487(02)00170-1).
- Duller, G.A.T., 2015. The Analyst software package for luminescence data: overview and recent improvements. *Ancient TL*, 33, 35–42. http://ancienttl.org/ATL_33-1_2015/ATL_33-1_Duller_p35-42.pdf (accessed: 15 August 2021).
- Duprat-Oualid, F., Rius, D., B geot, C., Magny, M., Millet, L., Wulf, S., Appelt, O., 2017. Vegetation response to abrupt climate changes in Western Europe from 45 to 14.7 k cal a BP: the Bergsee lacustrine record (Black Forest, Germany). *J. Quaternary Sci.* 32, 1008–1021. <https://doi.org/10.1002/jqs.2972>.
- Durcan, J.A., King, G.E., Duller, G.A., 2015. DRAC: dose rate and age calculator for trapped charge dating. *Quat. Geochronol.* 28, 54–61. <https://doi.org/10.1016/j.quageo.2015.03.012>.
- Durn, G., 2003. Terra Rossa in the Mediterranean Region: Parent Materials, Composition and Origin, *Geol. Croat.* 56, 83–100. <http://dx.doi.org/10.4154/GC.2003.06>.
- Durn, G., Rubini c, V., Wacha, L., Patekar, M., Frechen, M., Tsukamoto, S., Tadej, N., Husnjak, S., 2018a. Polygenetic soil formation on Late Glacial Loess on the Susak Island reflects paleo-environmental changes in the Northern Adriatic area. *Quatern. Int.* 494, 236–247. <https://doi.org/10.1016/j.quaint.2017.06.072>.
- Durn, G., Wacha, L., Bartolin, M., Rolf, C., Frechen, M., Tsukamoto, S., Tadej, N., Husnjak, S., Li, Y., Rubini c, V., 2018b. Provenance and formation of the red palaeosol and lithified terra rossa-like infillings on the Island of Susak: a highresolution and chronological approach. *Quatern. Int.* 494, 105–129. <https://doi.org/10.1016/j.quaint.2017.11.040>.

- dwd, deutscher Wetterdienst, 2021a. Heidelberg, Station 2080, Temperatur: vieljährige Mittelwerte 1981-2010. https://www.dwd.de/DE/leistungen/klimadatendeutschland/mittelwerte/temp_8110_fest_html.html%3Fview%3DnasPublication (accessed: 04 March 2023).
- dwd, deutscher Wetterdienst, 2021b. Heidelberg, Station 2080, Niederschlag: vieljährige Mittelwerte 1981-2010. https://www.dwd.de/DE/leistungen/klimadatendeutschland/mittelwerte/nieder_8110_fest_html.html?view=nasPublication&nn=16102 (accessed: 04 March 2023).
- Eckmeier, E., Gerlach, R., Gehrt, E., Schmidt, M.W., 2007. Pedogenesis of chernozems in central Europe—a review. *Geoderma* 139, 288–299. <https://doi.org/10.1016/j.geoderma.2007.01.009>.
- Ehlers, J., Gibbard, P.L., 2004. Quaternary Glaciations-Extent and Chronology: Part I: Europe. Elsevier, Amsterdam. ISBN 0 444 51462 7.
- European Environment Agency (EEA), 2021. Elevation map of Europe. Hillshade 1 km x 1km. <https://www.eea.europa.eu/data-and-maps/data/digital-elevation-model-of-europe>. Shapefiles of biogeographical regions: <https://www.eea.europa.eu/data-and-maps/data/biogeographical-regions-europe-3> (accessed: 25 August 2020).
- Evin, J., Marechal, J., Pachiardi, C., Puissegur, J., 1980. Conditions involved in dating terrestrial shells. *Radiocarbon* 22, 545–555. <https://doi.org/10.1017/S0033822200009875>.
- FAO, 2006. Guidelines for soil description. Food and Agriculture Organization of the United Nations, Rome, Italy, ISBN 92-5-105521-1.
- Falsan, A., Chantre, E., 1879. Monographie géologique des anciens glaciers et du terrain erraique de la partie moyenne du bassin du Rhône T 1 (Éd.1879-1880). *Ann. Soc. Agric. Lyon*, 205–474.
- Fedoroff, N., Courty, M.-A., 2013. Revisiting the genesis of red Mediterranean soils. *Turk. J. Earth Sci.* 22, 359–375. <https://doi.org/10.3906/yer-1205-10>.
- Ferraro, F., Terhorst, B., Ottner, F. Cremaschi, M. 2004. Val Sorda: An upper Pleistocene loess-paleosol sequence in northeastern Italy. *Rev. Mex. Cienc. Geol.* 21 (1), 30–47. <https://www.redalyc.org/pdf/572/57221105.pdf> (accessed: 05 April 2020).
- Ferraro, F., 2009. Age, sedimentation, and soil formation in the Val Sorda loess sequence, Northern Italy. *Quatern. Int.* 204, 54–64. <https://doi.org/10.1016/j.quaint.2008.12.002>.
- Field, J.P., Breshears, D.D., Whicker, J.J., Zou, C.B., 2012. Sediment capture by vegetation patches: Implications for desertification and increased resource redistribution. *J. Geophys. Res.* 117 (G1), 273. <https://doi.org/10.1029/2011JG001663>.
- Fischer, P., Hambach, U., Klasen, N., Schulte, P., Zeeden, C., Steininger, F., Lehmkuhl, F., Gerlach, R., Radtke, U., 2019. Landscape instability at the end of MIS 3 in western Central Europe: evidence from a multi proxy study on a Loess-Palaeosol-Sequence from the eastern Lower Rhine Embayment, Germany. *Quatern. Int.* 502, 119–136. <https://doi.org/10.1016/j.quaint.2017.09.008>.

- Fischer, P., Jöris, O., Fitzsimmons, K.E., Vinnepond, M., Prud'homme, C., Schulte, P., Hatté, C., Hambach, U., Lindauer, S., Zeeden, C., Peric, Z., Lehmkuhl, F., Wunderlich, T., Wilken, D., Schirmer, W., Vött, A., 2021. Millennial-scale terrestrial ecosystem responses to Upper Pleistocene climatic changes: 4D-reconstruction of the Schwalbenberg Loess-Palaeosol-Sequence (Middle Rhine Valley, Germany). *Catena* 196, 104913. <https://doi.org/10.1016/j.catena.2020.104913>.
- Fitzsimmons, K.E., Perić, Z., Nowatzki, M., Lindauer, S., Vinnepond, M., Prud'homme, C., Dave, A.K., Vött, A., Fischer, P., 2022. Luminescence Sensitivity of Rhine Valley Loess: Indicators of Source Variability? *Quaternary* 5, 1. <https://doi.org/10.3390/quat5010001>.
- Fletcher, W. J., Sánchez-Goñi, M.F., 2008. Orbital- and sub-orbital-scale climate impacts on vegetation of the western Mediterranean Basin over the last 48,000 yr. *Quaternary Res.* 70, 451–464. doi:10.1016/j.yqres.2008.07.002.
- Fletcher, W.J., Goni, M. F.S., Allen, J.R., Cheddadi, R., Combourieu-Nebout, N., Huntley, B., Lawson, I., Londeix, L., Magri, D., Margari, V., 2010. Millennial-scale variability during the last glacial in vegetation records from Europe. *Quaternary Sci. Rev.* 29, 2839–2864. <https://doi.org/10.1016/j.quascirev.2009.11.015>.
- Franc, O., Moine, O., Fülling, A., Auguste, P., Pasty, J.-F., Gadiolet, P., Gaertner, V., Robert, V., 2017. Les séquences alluvio-lössiques du Würm moyen/supérieur de Quincieux et de Lyon (Rhône-Alpes, France) premières interprétations paléoenvironnementales et corrélations. *Quaternaire* 423–453. <https://doi.org/10.4000/quaternaire.8453>.
- Frechen, M., van Vliet-Lanoë, B., van den Haute, P., 2001. The Upper Pleistocene loess record at Harmignies/Belgium – high resolution terrestrial archive of climate forcing. *Palaeogeogr., Palaeoecol.* 173 (3-4), 175–195. <https://doi.org/10.3285/eg.60.1.05>.
- Frechen, M., Terhorst, B., Rähle, W., 2007. The Upper Pleistocene loess/palaeosol sequence from Schatthausen in North Baden-Württemberg. *E&G Quaternary Sci. J.* 212–227. <https://doi.org/10.3285/eg.56.3.05>.
- Frechen, M., Schirmer, W., 2011. Luminescence chronology of the Schwalbenberg II loess in the Middle rhine valley. *E&G Quaternary Sci. J.* 60, 78–89. <https://doi.org/10.3285/eg.60.1.05>.
- Frouin, M., Huot, S., Kreutzer, S., Lahaye, C., Lamothe, M., Philippe, A., Mercier, N., 2017. An improved radiofluorescence single-aliquot regenerative dose protocol for K-feldspars. *Quat. Geochronol.* 38, 13–24. <https://doi.org/10.1016/j.quageo.2016.11.004>.
- Fuchs, M., Kreutzer, S., Rousseau, D.D., Antoine, P., Hatté, C., Lagroix, F., Moine, O., Gauthier, C., Svoboda, J., Lisa, L., 2013. The loess sequence of dolní vestonice, Czech Republic: a new OSL-based chronology of the last climatic cycle. *Boreas* 42, 664–677. <https://doi.org/10.1111/j.1502-3885.2012.00299.x>.

- Galbraith, R.F., Roberts, R.G., Laslett, G.M., Yoshida, H., Olley, J. M., 1999. Optical dating of single grains of quartz from Jinmium rock shelter, northern Australia. Part I: experimental design and statistical models. *Archaeometry*, 339–364. <https://doi.org/10.1111/j.1475-4754.1999.tb00987.x>.
- Gandouin, W., Ponel, P., Andrieu-Ponel, V., Franquet, É., de Beaulieu, J.-L., Reile, M., Guiter, F., Brulhet, J., Lallier-Vergès, É., Keravis, D., von Grafenstet, U., Veres, D., 2007. Past environment and climate changes at the Last Interglacial/Glacial transition (Les Échets, France) inferred from subfossil chironomids (Insecta). *C.R. Geosci.* 339, 337–346. <https://doi.org/10.1016/j.crte.2007.03.002>.
- Gao, X., Giorgi, F., 2008. Increased aridity in the Mediterranean region under greenhouse gas forcing estimated from high resolution simulations with a regional climate model. *Global Planet. Change* 62 (3), 195–209. <http://dx.doi.org/10.1016/j.gloplacha.2008.02.002>.
- García-Ruiz, J. M., Nadal-Romero, E., Lana-Renault, N., Beguería, S., 2013. Erosion in Mediterranean landscapes: Changes and future challenges. *Geomorphology* 198, 20–36. <https://doi.org/10.1016/j.geomorph.2013.05.023>.
- Gilbert, E.R., de Camargo, M.G., Sandrini-Neto, L., 2014. rysgran: Grain size analysis, textural classifications and distribution of unconsolidated sediments. CRAN version 2.1.0. <https://CRAN.R-project.org/package=rysgran>.
- Giorgi F., 2006. Climate change hot-spots. *Geophys. Res. Lett.* 33 (8): L08707. <https://doi.org/10.1029/2006GL025734>.
- Giorgi, F., Lionello, P., 2008. Climate change projections for the Mediterranean region. *Global Planet. Change* 63, 90–104. <https://doi.org/10.1016/j.gloplacha.2007.09.005>.
- GisSol, 1999. Description de l'Unité Cartographique de Sol (UCS) numéro 30102. Référentiel Régional Pédologique du Languedoc-Rousillon. Groupement d'intérêt scientifique Sol.
- Gocke, M., Gulyás, S., Hambach, U., Jovanović, M., Kovács, G., Marković, S.B., Wiesenberg, G.L., 2014. Biopores and root features as new tools for improving paleoecological understanding of terrestrial sediment-paleosol sequences. *Palaeogeogr., Palaeoecol.* 394, 42–58. <https://doi.org/10.1016/j.palaeo.2013.11.010>.
- Godfrey-Smith, D. I., Huntley, D. J., Chen, W.-H., 1988. Optical dating studies of quartz and feldspar sediment extracts. *Quaternary Sci. Rev.* 373–380. [https://doi.org/10.1016/0277-3791\(88\)90032-7](https://doi.org/10.1016/0277-3791(88)90032-7).
- Goldstein, S.L., Hemming, S.R., 2014. Long-lived Isotopic Tracers in Oceanography, Paleoceanography, and Ice-sheet Dynamics. *Treatise on Geochemistry Elsevier* 453–483. <https://doi.org/10.1016/B978-0-08-095975-7.00617-3>.
- González-Sampériz, P., Valero-Garcés, B.L., Carrión, J.S., Peña-Monné, J.L., García-Ruiz, J.M., Martí-Bono, C., 2005. Glacial and Lateglacial vegetation in northeastern Spain: New data and a review. *Quatern. Int.* 140-141, 4–20. <https://doi.org/10.1016/j.quaint.2005.05.006>.

- Goodfriend, G.A., Stipp, J.J., 1983. Limestone and the problem of radiocarbon dating of land-snail shell carbonate. *Geology* 11, 575–577. [https://doi.org/10.1130/0091-7613\(1983\)11<575:LATPOR>2.0.CO;2](https://doi.org/10.1130/0091-7613(1983)11<575:LATPOR>2.0.CO;2).
- Goubanva, K., Li, J., 2007. Extremes in temperature and precipitation around the Mediterranean basin in an ensemble of future climate scenario simulations. *Global Planet. Change* 57, 27–42. <https://doi.org/10.1016/j.gloplacha.2006.11.012>.
- Guenard, V., Drobinski, P., Caccia, J.-L., Campistron, B., Benech, B., 2005. An observational study of the mesoscale Mistral dynamics. *Bound-Lay. Meteorol.* 115, 263–288. <https://doi.org/10.1007/s10546-004-3406-z>.
- Guenther, E.W., 1961. Sedimentpetrographische Untersuchungen von Lössen. Zur Gliederung des Eiszeitalters und zur Einordnung paläolithischer Kulturen. In: *Fundamenta zur Urgeschichte, Schwabedissen H* (ed). Böhlau Verlag, Köln. <https://doi.org/10.7485/qu.1963.14.82750>.
- Guenther E.W., 1987. Zur Gliederung der Lössen des südlichen Oberrheintals. *E&G Quaternary Sci. J.* 37 (1), 67–78. <https://doi.org/10.3285/eg.37.1.07>.
- Guérin, G., Mercier, N., 2011a. Determining gamma dose rates by field gamma spectroscopy in sedimentary media: Results of Monte Carlo simulations. *Radiat. Meas.* 46 (2), 190–195. doi:10.1016/j.radmeas.2010.10.003.
- Guérin, G., Mercier, N., Adamiec, G., 2011. Dose-rate conversion factors: update. *Ancient TL* 5–8. <https://www.aber.ac.uk/en/media/departamental/dges/ancienttl/pdf/vol29no1/atl-issue29-1.pdf#page=9> (accessed: 15 November 2022).
- Guérin, G., Mercier, N., Nathan, R., Adamiec, G., Lefrais, Y., 2012. On the use of the infinite matrix assumption and associated concepts: A critical review. *Radiat. Meas.* 47 (9), 778–785. <https://doi.org/10.1016/j.radmeas.2012.04.004>.
- Guérin, G., Antoine, P., Schmidt, E., Goval, E., Hérison, D., Jamet, G., Reyss, J.-L., Shao, Q., Philippe, A., Vibet, M.-A., 2017a. Chronology of the Upper Pleistocene loess sequence of Havrincourt (France) and associated Palaeolithic occupations: a Bayesian approach from pedostratigraphy, OSL, radiocarbon, TL and ESR/Useries data. *Quat. Geochronol.* 42, 15–30. <https://doi.org/10.1016/j.quageo.2017.07.001>.
- Guérin, G., Christophe, C., Philippe, A., Murray, A.S., Thomsen, K.J., Tribolo, C., Urbanova, P., Jain, M., Guibert, P., Mercier, N., Kreutzer, S., Lahaye, C., 2017b. Absorbed dose, equivalent dose, measured dose rates, and implications for OSL age estimates: introducing the Average Dose Model. *Quat. Geochronol.* 41, 163–173. <https://doi.org/10.1016/j.quageo.2017.04.002>.
- Guibert, P., Schvoerer, M., 1991. TL dating: low background gamma spectrometry as a tool for the determination of the annual dose. *Int. J. Radiat. Appl. Instrum. Nucl. Tracks. Radiat. Meas.* 18, 231–238. [https://doi.org/10.1016/1359-0189\(91\) 90117-Z](https://doi.org/10.1016/1359-0189(91) 90117-Z).

- Guibert, P., Lahaye, C., Bechtel, F., 2009. The importance of U-series disequilibrium of sediments in luminescence dating: A case study at the Roc de Marsal Cave (Dordogne, France). *Radiat. Meas.* 44 (3), 223–231. <https://doi.org/10.1016/j.radmeas.2009.03.024>.
- Guido, M. A., Molinari, C., Moneta, V., Branch, N., Black, S., Simmonds, M., Stastney, P., Montanari, C., 2020. Climate and vegetation dynamics of the Northern Apennines (Italy) during the Late Pleistocene and Holocene. *Quaternary Sci. Rev.* 231, 106206. <https://doi.org/10.1016/j.quascirev.2020.106206>.
- Guilloré, P., 1980. *Méthode de fabrication mécanique et en série des lames minces*. Institut National Agronomique, Paris-Grignon.
- Guillevic, M., Bazin, L., Landais, A., Stowasser, C., Masson-Delmotte, V., Blunier, T., Eynaud, F., Falourd, S., Michel, E., Minster, B., Popp, T., Prié, F., Vinther, B. M., 2014. Multi-proxy fingerprint of Heinrich event 4 in Greenland ice core records. *Clim. Past. Discuss.* 10, 1179–1222. <https://doi.org/10.1016/j.gca2018.02.015>.
- Guiot, J., Beaulieu, J. L. de, Cheddadi, R., David, F., Ponel, P., Reille, M., 1993. The climate in Western Europe during the last Glacial/Interglacial cycle derived from pollen and insect remains, *Palaeogeogr., Palaeoecol.* 103, 73–93. [https://doi.org/10.1016/0031-0182\(93\)90053-L](https://doi.org/10.1016/0031-0182(93)90053-L).
- Güiter, F., Andrieu-Ponel, V., Beaulieu, J.-L. de, Cheddadi, R., Calvez, M., Ponel, P., Reille, M., Keller, T., Goeury, C., 2003. The last climatic cycles in Western Europe: a comparison between long continuous lacustrine sequences from France and other terrestrial records. *Quatern. Int.* 111, 59–74. [https://doi.org/10.1016/S1040-6182\(03\)00015-6](https://doi.org/10.1016/S1040-6182(03)00015-6).
- Günster, N., 1999. *Paläopedologische Untersuchungen an pliozänen und pleistozänen Sedimenten im Becken von Granada/Südspanien*. Rheinische Friedrich-Wilhelm-Universität. Bonner bodenkundliche Abhandlungen, 26.
- Günster, N., Eck, P., Skowronek, A., Zöller, L., 2001. Late Pleistocene loess and their paleosols in the Granada Basin, Southern Spain. *Quatern. Int.* 76-77, 241–245. [https://doi.org/10.1016/S1040-6182\(00\)00106-3](https://doi.org/10.1016/S1040-6182(00)00106-3).
- Guo, Y., Yang, S., Su, N., Li, C., Yin, P., Wang, Z., 2018. Revisiting the effects of hydrodynamic sorting and sedimentary recycling on chemical weathering indices. *Geochem. Cosmochim. Acta* 227, 48–63.
- Haase, D., Fink, J., Haase, G., Ruske, R., Pécsi, M., Richter, H., Altermann, M., Jäger, K.-D., 2007. Loess in Europe—its spatial distribution based on a European Loess Map, scale 1:2,500,000. *Quaternary Sci. Rev.* 26 (9-10), 1301–1312. <https://doi.org/10.1016/j.quascirev.2007.02.003>.
- Hädrich, F., 1985. Löß und Paläoböden im südlichen Oberrheingebiet. In *Exkursionsführer der 22. wiss. Tagung der Deutschen Quartärvereinigung*, Schreiner, A., Metz, B. (eds): Freiburg i. Br; 71–88.
- Hädrich, F., Stahr, K., 1992. Die Böden in der Umgebung von Freiburg i.Br. In *Freiburger Geographische Hefte*, Mäckel, R., Metz, B. (eds). Selbstverlag des Institutes für Physische Geographie der Albert-Ludwig-Universität Freiburg i.Br.

- Haesaerts, P., Damblon, F., Gerasimenko, N., Spagna, P., Pirson, S., 2016. The Late Pleistocene loess-palaeosol sequence of Middle Belgium. *Quatern. Int.* 411, 25–43. <https://doi.org/10.1016/j.quaint.2016.02.012>
- Hansen, V., Murray, A., Buylaert, J.P., Yeo, E.Y., Thomsen, K., 2015. A new irradiated quartz for beta source calibration. *Radiat. Meas.* 81, 123–127. <https://doi.org/10.1016/j.radmeas.2015.02.017>.
- Heier, K. S., Billings, G.K., 1970. Rubidium. In: Wedepohl, K.H. (Ed.), *Handbook of Geochemistry*. Springer, Berlin, pp. 37B1–37N1.
- Helmens, K. F., 2014. The Last Interglacial–Glacial cycle (MIS 5–2) re-examined based on long proxy records from central and northern Europe. *Quaternary Sci. Rev.* 86, 115–143. <https://doi.org/10.1016/j.quascirev.2013.12.012>.
- Heydari, M., Guérin, G., 2018. OSL signal saturation and dose rate variability: Investigating the behaviour of different statistical models. *Radiat. Meas.* 120, 96–103. <https://doi.org/10.1016/j.radmeas.2018.05.005>.
- Hopcroft, P.O., Valdes, P.J., Woodward, S., Joshi, M.M., 2015. Last glacial maximum radiative forcing from mineral dust aerosols in an Earth system model: LGM dust in an earth system model. *J. Geophys. Res. Atmosphere* 120, 8186–8205. <https://doi.org/10.1002/2015JD023742>.
- Hughes, A.L., Gyllencreutz, R., Lohne, Ø.S., Mangerud, J., Svendsen, J.I., 2016. The last Eurasian ice sheets—a chronological database and time-slice reconstruction, DATED-1. *Boreas* 45, 1–45. <http://dx.doi.org/10.1111/bor.12142>.
- Huntley, D.J., Godfrey-Smith, D.I., Thewalt, M.L., 1985. Optical dating of sediments. *Nature* 313, 105–107. <https://doi.org/10.1038/313105a0>.
- Huntley, D.J., Baril, M.R., 1997. The K content of the K-feldspars being measured in optical dating or in the thermoluminescence dating. *Ancient TL* 15 (1), 11–13. http://ancienttl.org/ATL_15-1_1997/ATL_15-1_Huntley_p11-13.pdf (accessed: 04 January 2024).
- Hütt, G., Jaek, I., Tchonka, J., 1988. Optical dating: K-feldspar optical response stimulation spectra. *Quaternary Sci. Rev.* 7 (3-4), 381-385. [https://doi.org/10.1016/0277-3791\(88\)90033-9](https://doi.org/10.1016/0277-3791(88)90033-9).
- IGN-FRa: l'Institut national de l'information géographique et forestière. <https://geoservices.ign.fr> (accessed : 24 May 2020).
- IGN-FRb: l'Institut national de l'information géographique et forestière. <https://geoservices.ign.fr/documentation/diffusion/telechargement-donnees-libres.html#rge-alti-1-m> (accessed: 18 March 2021).
- ISO 11277, 2020. Soil quality: Determination of particle size distribution in mineral soil material.
- ISO 13320, 2009. Particle Size Analysis - Laser Diffraction Methods.
- ISO 13320, 2020. Particle size analysis - Laser diffraction methods.

- IUSS Working Group WRB, 2015. World Reference Base for Soil Resources 2014, Update 2015: International Soil Classification System for Naming Soils and Creating Legends for Soil Maps. FAO, Rome.
- IUSS Working Group WRB, 2022. World Reference Base for Soil Resources, International soil classification system for naming soils and creating legends for soil maps, 4th edn., International Union of Soil Sciences (IUSS), Vienna, Austria, ISBN: 979-8-9862451-1-9.
- Ivy-Ochs, S., Kerschner, H., Kubik, P. W., Schlüchter, C., 2006. Glacier response in the European alps to Heinrich event 1 cooling: the Gschnitz stadial. *J. Quaternary. Sci.* 21, 115–130. <https://doi.org/10.1002/jqs.955>.
- Ivy-Ochs, S., Kerschner, H., Reuther, A., Preusser, F., Heine, K., Maisch, M., Kubik, P.W., Schlüchter, C., 2008. Chronology of the last glacial cycle in the European Alps. *J. Quaternary Sci.* 23, 559–573. <https://doi.org/10.1002/jqs.1202>.
- Ivy-Ochs, S., 2015. Glacier variations in the European Alps at the end of the last glaciation. *Cuadernos de investigación geográfica* 41, 295–315. <https://doi.org/10.18172/cig.2750>.
- Ivy-Ochs, S., Lucchesi, S., Baggio, P., Fioraso, G., Gianotti, F., Monegato, G., Graf, A.A., Akçar, N., Christl, M., Carraro, F., 2018. New geomorphological and chronological constraints for glacial deposits in the Rivoli-Avigliana end-moraine system and the lower Susa Valley (Western Alps, NW Italy). *J. Quaternary Sci.* 33, 550–562. <https://doi.org/10.1002/jqs.3034>.
- Ivy-Ochs, S., Monegato, G., Reitner, J.M., 2022. The Alps: glacial landforms from the Last Glacial Maximum. Chapter 85. In: Palacios, D., García-Ruis, J., Hughes, P. D., Andrés, N. *European Glacial Landscapes. Maximum Extent of Glaciations.* <https://doi.org/10.1016/B978-0-12-823498-3.00030-3>.
- Jacq, V., Philippe Albert, P. Delorme, R., 2005. Le mistral - Quelques aspects des connaissances actuelles. *Météorologie* 50, 30–38. https://lameteorologie.fr/issues/2005/50/meteo_2005_50_30.
- Jamagne, M., Eimberck, M., Desbourdes, S., 2011. Grands paysages pédologiques de France, Collection Synthèses, Éditions Quæ, Versailles, 535 pp. ISBN: 9782759210367.
- Ji, J., Balsam, W., Chen, J., 2001. Mineralogic and climatic interpretations of the Luochuan loess section (China) based on diffuse reflectance spectrophotometry. *Quaternary Res.* 56, 23–30. <https://doi.org/10.1006/qres.2001.2238>.
- Johnsen, S.J., Clausen, H.B., Dansgaard, W., Fuhrer, K., Gundestrup, N., Hammer, C.U., Iversen, P., Jouzel, J., Stauffer, B., Steffensen, J.P., 1992. Irregular glacial interstadials recorded in a new Greenland ice core. *Nature* 359, 311–313. <https://doi.org/10.1038/359311a0>.
- Joly, D., Brossard, T., Cardot, H., Cavailhes, J., Hilal, M., Wavresky, P., 2010. Ley types de climats en France, une construction spatiale. *Cybergeo, Eur. J. Geogr., Cartographie, Imagerie, SIG*, document 501. <https://doi.org/10.4000/cybergeo.23155>.

- Jones, R.M., 2003. Particle size analysis by laser diffraction: ISO 13320, standard operating procedures, and Mie theory. *Am. Lab. (Shelton)* 35, 44–47.
- Kadereit, A., Kreutzer, S., 2013. Ris0 calibration quartz - A challenge for β -source calibration. An applied study with relevance for luminescence dating. *Measurement* 2238–2250. <https://doi.org/10.1016/j.measurement.2013.03.005>.
- Kadereit, A., Kind, C.-J., Wagner, G.A., 2013. The chronological position of the Lohne Soil in the Nussloch loess section – re-evaluation for a European loess-marker horizon. *Quaternary Sci. Rev.* 59: 67–86. <https://doi.org/10.1016/j.quascirev.2012.10.026>.
- Kadereit, A., Kreutzer, S., Schmidt, C., DeWitt, R., 2020. Author Comment 1, AC1: 'A closer look at IRSL SAR fading data and their implication for luminescence dating. <https://doi.org/10.5194/gchron-2020-3-AC1>.
- Kautz, T., 2015. Research on subsoil biopores and their functions in organically managed soils: A review. *Renew. Agric. Food Syst.* 30, 318–327. <https://doi.org/10.1017/S1742170513000549>.
- Kehl, M., 2010. Quaternary loesses, loess-like sediments, soils and climate change in Iran. Gebr. Borntraeger Science Publishers, Stuttgart, .210 pp. ISBN 978-3-443-09024-1.
- Kehl, M., Seeger, K., Pötter, S., Schulte, P., Klasen, N., Zickel, M., Pastoors, A., Claßen, E., 2024. Loess formation and chronology at the Palaeolithic key site Rheindahlen, Lower Rhine Embayment, Germany. *E&G Quaternary Sci. J.*, 73, 41–67. <https://doi.org/10.5194/egqsj-73-41-2024>.
- Kemp, R. A., 2001. Pedogenic modification of loess: significance for palaeoclimatic reconstructions. *Earth-Sci. Rev.* 54, 145–156. [https://doi.org/10.1016/S0012-8252\(01\)00045-9](https://doi.org/10.1016/S0012-8252(01)00045-9).
- Kinnaird, T.C., Sanderson, D.C.W., Woodward, N.L., 2012. Applying luminescence methods to geoarchaeology: a case study from Stronsay, Orkney. *Earth Env. Sci. T. R. So.*, 102, 191–199. <https://doi.org/10.1017/S1755691012011115>.
- Kjellström, E., Brandefelt, J., Nälsund, J.-O., Smith, B., Strandberg, G., Voelker, A.H.L., Wohlfarth, B., 2010. Simulated climate conditions in Europe during the Marine Isotope Stage 3 stadial. *Boreas* 39, 436–456. <https://doi.org/10.1111/j.1502-3885.2010.00143.x>.
- Kolb, T., Tudyka, K., Kadereit, A., Lomax, J., Poręba, G., Zander, A., Zipf, L., Fuchs, M., 2022. The μ Dose-system: determination of environmental dose rates by combined alpha and beta counting – performance tests and practical experiences. *Geochronology* 4, 1–31. <https://doi.org/10.5194/gchron-4-1-2022>.
- Konert, M., Vandenberghe, J., 1997. Comparison of laser grain size analysis with pipette and sieve analysis: a solution for the underestimation of the clay fraction. *Sedimentology* 44 (3), 523–535. <https://doi.org/10.1046/j.1365-3091.1997.d01-38.x>.
- Kortekass, M, Murray, A.S., 2005. Method for the removal of mica from quartz separates. *Ancient TL* 23 (2).[https://www.aber.ac.uk/en/media/departmental/dges/ancienttl/pdf/vol23no2/kortekaas_atl_23\(2\)_43-46.pdf](https://www.aber.ac.uk/en/media/departmental/dges/ancienttl/pdf/vol23no2/kortekaas_atl_23(2)_43-46.pdf) (accessed: 16 February 2024).

- Kovda, I., Sycheva, S., Lebedeva, M., Inozemtzev, S., 2009. Variability of carbonate pedofeatures in a loess-paleosol sequence and their use for paleoreconstructions. *J. Mt. Sci.* 6, 155–161. <https://doi.org/10.1007/s11629-009-1032-4>.
- Krauss, L., Klasen, N., Schulte, P., Lehmkuhl, F., 2021. New results concerning the pedo- and chronostratigraphy of the loess–palaeosol sequence Attenfeld (Bavaria, Germany) derived from a multi-methodological approach. *J. Quaternary Sci.* 1–15. <https://doi.org/10.1002/jqs.3298>.
- Kreutzer, S., Fuchs, M., Meszner, S., Faust, D., 2012a. OSL chronostratigraphy of a loess-palaeosol sequence in Saxony/Germany using quartz of different grain sizes. *Quat. Geochronol.* 10, 102–109. <https://doi.org/10.1016/j.quageo.2012.01.004>.
- Kreutzer, S., Schmidt, C., Fuchs, M.C., Dietze, M., Fischer, M., Fuchs, M., 2012b. Introducing an R package for luminescence dating analysis. *Ancient TL* 30, 1–8. <https://hal.science/hal-01846159>.
- Kreutzer, S., Hülle, D., Jørkov Thomsen, K., Hilgers, A., Kadereit, A., Fuchs, M., 2013. Quantification of cross-bleaching during infrared (IR) light stimulation. *Ancient TL*, 31 (1), 1–10. http://www.ancienttl.org/ATL_31-1_2013/ATL_31-1_Kreutzer_p1-10.pdf.
- Kreutzer, S., Schmidt, C., DeWitt, R., Fuchs, M., 2014. The a-value of polymineral fine grain samples measured with the post-IR IRSL protocol. *Radiat. Meas.*, 69, 18–29. <https://doi.org/10.1016/j.radmeas.2014.04.027>.
- Kreutzer, S., Duval, M., Bartz, M., Bertran, P., Bosq, M., Eynaud, F., Verdin, F., Mercier, N., 2018a. Deciphering long-term coastal dynamics using IR-RF and ESR dating: A case study from Médoc, south-West France. *Quaternary Geochronology* 48, 108–120. <https://doi.org/10.1016/j.quageo.2018.09.005>.
- Kreutzer, S., Martin, L., Dubernet, S., Mercier, N., 2018b. The IR-RF alpha-Efficiency of K-feldspar. *Radiat. Meas.* 120, 148–156. <https://doi.org/10.1016/j.radmeas.2018.04.019>.
- Kreutzer, S. and Burow, C., 2020. Analyse_FadingMeasurement: Analyse fading measurements and returns the fading rate per decade (g-value). Function version 0.1.14. In: Kreutzer, S., Burow, C., Dietze, M., Fuchs, M.C., Schmidt, C., Fischer, M., Friedrich, J., 2020. Luminescence: Comprehensive Luminescence Dating Data Analysis. R package version 0.9.8.9000-17, <https://CRAN.R-project.org/package=Luminescence>.
- Kreutzer, S., Burow, C., Dietze, M., Fuchs, M.C., Schmidt, C., Fischer, M., Friedrich, J., Mercier, N., Smedley, R.K., Christophe, C., Zink, A., Durcan, J., King, G.E., Philippe, A., Guerin, G., Riedesel, S., Autzen, M., Guibert, P., Fuchs, M., 2020. Luminescence: Comprehensive Luminescence Dating Data Analysis. CRAN version 0.9.5. <https://CRAN.R-project.org/package=Luminescence>.
- Kreutzer, S., Valladas, H., Texier, P.-J., Moineau, V., Mologni, C., Mercier, N., 2021. The Mousterian loess sequence La Combette (France) and its chronological framework: A re-investigation. *Comptes Rendus Palevol.*, 20 (14), 225–255. <https://doi.org/10.5852/cr-palevol2021v20a14>.

- Kreutzer, S., Mercier, M., Lamothe, M., 2022. Infrared-radiofluorescence: Dose saturation and long-term signal stability of a K-feldspar sample. *Radiat. Meas.* 156, 106818. <https://doi.org/10.1016/j.radmeas.2022.106818>.
- Kukla, G.J., Bender, M.L., Beaulieu, J.-L. d., Bond, G., Broecker, W.S., Cleveringa, P., Gavin, J.E., Herbert, T.D., Imbrie, J., Jouzel, J., Keigwin, L.D., Knudsen, K.-L., McManus, J.F., Merkt, J., Muhs, D. R., Müller, H., Poore, R.Z., Porter, S.C., Seret, G., Shackleton, N.J., Turner, C., Tzedakis, P.C., Winograd, I.J., 2002. Last Interglacial Climates. *Quaternary Res.* 58, 2–13. <https://doi.org/10.1006/qres.2001.2316>, 2002.
- Kühn, P., Terhorst, B., Ottner, F., 2006. Micromorphology of middle Pleistocene palaeosols in northern Italy. *Quatern. Int.* 156–157. <https://doi.org/10.1016/j.quaint.2006.05.026>.
- Laag, C., Lagroix, F., Kreutzer, S., Chapkanski, S., Zeeden, C., Guyodo, Y., 2023. Measuring and evaluating colorimetric properties of samples from loess-paleosol sequences. *MethodsX* 10, 102159. <https://doi.org/10.1016/j.mex.2023.102159>.
- Lai, Z., Zöller, L., Fuchs, M., Brückner, H., 2008. Alpha efficiency determination for OSL of quartz extracted from Chinese loess. *Radiat. Meas.*, 43, 767–770. <https://doi.org/10.1016/j.radmeas.2008.01.022>.
- Lambeck, K., Rouby, H., Purcell, A., Sun, Y., Sambridge, M., 2014. Sea level and global ice volumes from the last glacial maximum to the Holocene. *Proc. Natl. Acad. Sci. Unit. States Am.* 111, 15296–15303. <https://doi.org/10.1073/pnas.1411762111>.
- Lanos, P., Philippe, A., 2015. Hierarchical Bayesian modeling for combining dates in archaeological context. *Journal de la Société Française de Statistique, Société Française de Statistique et Société Mathématique de France* 158, 72–88. <https://hal.science/hal-01162404v3>.
- Lanos, P., Philippe, A., 2017. Event date model: a robust Bayesian tool for chronology building. *Communications for Statistical Applications and Methods* 25, 131–157. <https://doi.org/10.29220/CSAM.2018.25.2.131>.
- Lanos, P., Dufresne, P., 2019. ChronoModel Version 2.0: Software for Chronological Modelling of Archaeological Data Using Bayesian Statistics. Centre National de la Recherche Scientifique.
- Lapp, T., Jain, M., Thomsen, K.J., Murray, A.S., Buylaert, J.-P., 2012. New luminescence measurement facilities in retrospective dosimetry. *Radiat. Meas.*, 47, 803–808. <https://doi.org/10.1016/j.radmeas.2012.02.006>.
- Lapp, T., Kook, M., Murray, A.S., Thomsen, K.J., Buylaert, J.-P., Jain, M., 2015. A new luminescence detection and stimulation head for the Risø TL/OSL reader. *Radiat. Meas.* 81, 178–184. <https://doi.org/10.1016/j.radmeas.2015.02.001>.
- Laroche, M., Parisot, N., Recq, C., Orgeval, M., Remicourt, M., Renaud, A., Grange, G., Charbouillot, S., Battentier, J., Marquebielle, B., Rué, M., Lafont, V., Chateauneuf, F., Curé, A.-M., Magnin, F., 2020. L'occupation fonbuxienne de Mitra 5 à Garons (Gard) (archaeological survey report). *Paléotime*, Villard-de-Lans.

- Lee, J.-Y., Marotzke, J., Bala, G., Cao, L., Corti, S., Dunne, J.P., Engelbrecht, F., Fischer, E., Fyfe, J.C., Jones, C., Maycock, A., Mutemi, J., Ndiaye, O., Panickal, S., Zhou, T., 2021. Future Global Climate: Scenario-Based Projections and Near-Term Information. In *Climate Change 2021: The Physical Science Basis. Contribution of Working Group I to the Sixth Assessment Report of the Intergovernmental Panel on Climate Change*. Masson-Delmotte, V., P. Zhai, A., Pirani, S.L., Connors, C. Péan, S., Berger, N., Caud, Y., Chen, L. Goldfarb, M. I., Gomis, M., Huang, K., Leitzell, E., Lonnoy, J. B. R., Matthews, T. K., Maycock, T., Waterfield, O., Yelekçi, R., Yu, Zhou, B. (eds.). Cambridge University Press, Cambridge, United Kingdom and New York, NY, USA, pp. 553–672, doi:10.1017/9781009157896.006.
- Legros, J.-P., 2006. Classification Systems: French, in: *Encyclopedia of soil science*, 2nd ed., edited by: Lal, R., Taylor & Francis, New York, Abingdon, Oxon. ISBN 0-8493-5053-0.
- Lehmkuhl, F., Zens, J., Krauß, L., Schulte, P., Kels, H., 2016. Loess-paleosol sequences at the northern European loess belt in Germany: distribution, geomorphology and stratigraphy. *Quaternary Sci. Rev.* 153, 11–30. <https://doi.org/10.1016/j.quascirev.2016.10.008>.
- Lehmkuhl, F., Nett, J.J., Pötter, S., Schulte, P., Sprafke, T., Jary, Z., Antoine, P., Wacha, L., Wolf, D., Zerboni, A., Hošek, J., Marković, S.B., Obreht, I., Sümegi, P., Veres, D., Zeeden, C., Boemke, B., Schaubert, V., Viehweger, J., Hambach, U., 2021. Loess landscapes of Europe – Mapping, geomorphology, and zonal differentiation. *Earth-Sci. Rev.* 215, 103496. <https://doi.org/10.1016/j.earscirev.2020.103496>.
- Lelièvre, F., Sala, S., Volaire, F., 2010. Climate change at the temperate-Mediterranean interface in Southern France and impacts on grasslands production. In: Porqueddu, C., Ríos, S. (ed). *The contributions of grasslands to the conservation of Mediterranean biodiversity. Options Méditerranéennes, Série A. Séminaires Méditerranéens* 92: 187–192.
- Lewis, C.J., McDonald, E.V., Sancho, C., Peña, J.L., Rhodes, E.J., 2009. Climatic implications of correlated Upper Pleistocene glacial and fluvial deposits on the Cinca and Gállego Rivers (NE Spain) based on OSL dating and soil stratigraphy. *Global Planet. Change* 67 (3-4), 141–152. <https://doi.org/10.1016/j.gloplacha.2009.01.001>.
- Li, Y., Song, Y., Fitzsimmons, K.E., Chang, H., Orozbaev, R., Li, X., 2018a. Eolian dust dispersal patterns since the last glacial period in eastern Central Asia: insights from a loess-paleosol sequence in the Ili Basin. *Clim. Past* 14, 271. <https://doi.org/10.5194/cp-14-271-2018>.
- Li, Y., Zhang, W., Aydin, A., Deng, X., 2018b. Formation of calcareous nodules in loess-paleosol sequences: Reviews of existing models with a proposed new “per evapotranspiration model”. *J. Asian Earth Sci.* 154, 8–16. <https://doi.org/10.1016/j.jseaes.2017.12.002>.
- Liang, L., Sun, Y., Beets, C.J., Prins, M. A., Wu, F., Vandenberghe, J., 2013. Impacts of grain size sorting and chemical weathering on the geochemistry of Jingyuan loess in the northwestern Chinese Loess Plateau. *J. Asian Earth Sci.* 69, 177–184. <https://doi.org/10.1016/j.jseaes.2012.12.015>.
- Lin, Y., Mu, G., Xu, L., Zhao, X., 2016. The origin of bimodal grain-size distribution for aeolian deposits. *Aeolian Res.* 20, 80–88. <https://doi.org/10.1016/j.aeolia.2015.12.001>.

- Lindner, H., Lehmkuhl, F., Zeeden, C., 2017. Spatial loess distribution in the eastern Carpathian Basin: a novel approach based on geoscientific maps and data. *J. Maps* 13, 173–181. <https://doi.org/10.1080/17445647.2017.1279083>.
- Lindvall, A., Stjern, R., Alexanderson, H., 2017. Bleaching of quartz OSL signals under natural and laboratory light conditions. *Ancient TL* 35 (2), 12–20. http://www.ancienttl.org/ATL_35-2_2017/ATL_35-2_Lindvall_p12-20.pdf (accessed: 25 September 2022).
- Lionello, P., Malanotte-Rizzoli, P., Boscolo, R., Alpert, P., Artale, V., Li, L., Luterbacher, J., May, W., Trigo, R., Tsimplis, M., Ulbrich, U., Xoplaki, E., 2007. The Mediterranean climate: An overview of the main characteristics and issues, in: *Global warming and global cooling: Evolution of climate on earth*, edited by: Sorochtin, O.G., Chilingar, G.V., and Chiljuk, L.F., Elsevier, Amsterdam, 1–26. [https://doi.org/10.1016/S1571-9197\(06\)80003-0](https://doi.org/10.1016/S1571-9197(06)80003-0).
- Lionello, P., Scarascia, L., 2018. The relation between climate change in the Mediterranean region and global warming. *Reg. Environ. Change* 18, 1481–1493. <https://doi.org/10.1007/s10113-018-1290-1>.
- Lisiecki, L.E., Raymo, M.E., 2005. A Pliocene-Pleistocene stack of 57 globally distributed benthic $\delta^{18}\text{O}$ records. *Paleoceanography*, 20 (1), PA1003. <https://doi.org/10.1029/2004PA001071>.
- Lomax, J., Fuchs, M., Preusser, F., Fiebig, M., 2014. Luminescence based loess chronostratigraphy of the Upper Palaeolithic site Krems-Wachtberg, Austria. *Quatern. Int.* 351, 88–97. <https://doi.org/10.1016/j.quaint.2012.10.037>.
- Løvborg, L., Kirkegaard, P., 1974. Response of 3" x 3"Nal (TI) detectors to terrestrial gamma radiation. *Nucl. Instrum. Methods* 121, 239–251. [https://doi.org/10.1016/0029-554X\(74\)90072-X](https://doi.org/10.1016/0029-554X(74)90072-X).
- Lucas-Tooth, H. J., Price, B. J., 1961. A mathematical method for investigation of interelement effects in X-ray fluorescence analysis. *Metallurgia* 64, 149–152.
- Luetscher, M., Boch, R., Sodemann, H., Spötl, C., Cheng, H., Edwards, R.L., Frisia, S., Hof, F., Müller, W., 2015. North atlantic storm track changes during the last glacial maximum recorded by alpine speleothems. *Nat. Commun.* 6, 1–6. <https://doi.org/10.1038/ncomms7344>.
- Lukić, T., Basarin, B., Bugge, B., Marković, S.B., Tomovic, V.M., Raljić, J.P., Hrnjak, I., Timar-Gabor, A., Hambach, U., Gavrilov, M.B., 2014. A joined rock magnetic and colorimetric perspective on the Late Pleistoceneclimate of Orlovat loess site (Northern Serbia). *Quatern. Int.* 334, 179–188. <https://doi.org/10.1016/j.quaint.2014.03.042>.
- Lunt, D. J., Valdes, P. J., 2002. Dust deposition and provenance at the Last Glacial Maximum and present day. *Geophys. Res. Lett.* 29 <https://doi.org/10.1029/2002GL015656>, 42-51-42–4.
- Lüthgens, C., Böse, M., 2011. Chronology of Weichselian main ice marginal positions in north-eastern Germany. *E&G Quaternary Sci. J.*, 60, 17. <https://doi.org/10.3285/eg.60.2-3.02>.
- Macdonald, P., Du, J., 2015. Package 'mixdist': Finite Mixture Distribution Models. CRAN version 0.9.5. <https://CRAN.R-project.org/package=Luminescence>.

- Magnin, F., 1993. Quaternary non-marine Mollusca and palaeoclimates in Mediterranean France. *Scripta Geol. Spec. Issue 2*: 275–289. <https://repository.naturalis.nl/pub/317352/SG1993S002013.pdf>.
- Magnin, F., 2014. Middle pleniglacial to Holocene molluscan assemblages in the marseille-aubagne basin (provence, France). *Quaternaire* 25, 113–125. <https://doi.org/10.4000/quaternaire.7006>.
- Magnin, F., Bonnet, S., 2014. Une succession malacologique du pléniglaciaire moyen et du postglaciaire à Aix-en-Provence (France) éléments de datation, taphonomie des assemblages et paléoenvironnements. *Quaternaire* 163–185. <https://doi.org/10.4000/quaternaire.7040>.
- Maher, B.A., Taylor, R.M., 1988. Formation of ultrafine-grained magnetite in soils. *Nature* 336, 368–370. <https://doi.org/10.1038/336368a0>.
- Mahowald, N.M., Muhs, D. R., Levis, S., Rasch, P.J., Yoshioka, M., Zender, C. S., Luo, C., 2006. Change in atmospheric mineral aerosols in response to climate: last glacial period, preindustrial, modern, and doubled carbon dioxide climates. *J. Geophys. Res.: Atmosphere* 111, D10202. <https://doi.org/10.1029/2005JD006653>.
- Mandier, P., 1969. La vallée épigénique du Rhône d'Andance à Tournon, et le contact du socle avec l'avant-pays mollassique. Essai de mise au point morphologique. *Rev. Géogr. Lyon* 44 (2), 117–168. <https://doi.org/10.3406/geoca1969.2641>.
- Mandier, P., 1974. Les passages du Rhône dans la dépression de Saint-Péray. *Géocarrefour* 49 (2), 139–154. <https://doi.org/10.3406/geoca1974.1644>.
- Mandier, P., 1984. Le relief de la moyenne vallée du Rhône au Tertiaire et au Quaternaire. *Bull. Lab. Rhod. Géomorphol.* 15-16, 27–36. https://www.persee.fr/doc/rga_0035-1121_1987_num_75_1_2669_t1_0087_0000_1.
- Mandier, P., 1988. Les problèmes chronologiques posés par les phases de la récession würmienne dans la moyenne vallée du Rhône. *B. Assoc. Fr. Étud. Quat. (Quaternaire)* 25, 123–128. <https://doi.org/10.3406/quate.1988.1873>.
- Mandier, P., Evin, J., Argant, J., Petiot, R., 2003. Chronostratigraphie des accumulations würmiennes dans la moyenne vallée du Rhône. L'apport des dates radiocarbone. *Quaternaire* 14 (2), 113–127. <https://doi.org/10.3406/quate.2003.1735>.
- Marcelin, P., 1926. Contribution à l'étude géographique de la garrigue nîmoise. *Géocarrefour* 2, 35–180. <https://doi.org/10.3406/geoca1926.3816>.
- Marcelin, P., 1950. Phénomène du vent et du froid au Quaternaire Supérieur dans la région Nimoise. *Bull. Soc. Languedocienne Géogr.* 21, 85–122.
- Marković, S.B., Hambach, U., Catto, N., Jovanović, M., Buggle, B., Machalett, B., Zöller, L., Glaser, B., Frechen, M., 2009. Middle and Late Pleistocene loess sequences at batajnica, vojvodina, Serbia. *Quatern. Int.* 198, 255–266. <https://doi.org/10.1016/j.quaint.2008.12.004>.

- Mathieu, J., Davies, T.J., 2014. Glaciation as an historical filter of below-ground biodiversity. *J. Biogeogr.* 41, 1204–1214. <https://doi.org/10.1111/jbi.12284>.
- Mauz, B., Martin, L., Discher, M., Tribolo, C., Kreutzer, S., Bahl, C., Lang, A., Mercier, N., 2021. Technical note: On the reliability of laboratory beta-source calibration for luminescence dating. *Geochronology* 3, 371–381. <https://doi.org/10.5194/gchron-3-371-2021>.
- May, J.-H., Marx, S.K., Reynolds, W., Clark-Balzana, L., Jacobsen, G.E., Preusser, F., 2018. Establishing a chronological framework for a late Quaternary seasonal swamp in the Australian 'Top End'. *Quat. Geochronol.*, 47, 81–92. <https://doi.org/10.1016/j.quageo.2018.05.010>.
- Mazenot, G., 1956. Recherches sur les faunes malacologiques du loess récent würmien et de divers limons terrestres holocènes dans le sud-est de la France (pp. 1–16). *Pub. Soc. Lin. Lyon*, 25, 9–24. <https://doi.org/10.3406/linly.1956.7784>.
- Mazenot, G., 1957. Nouvelles recherches pétrographiques et malacologiques sur le loess et limons de Basse-Provence. *Bull. Mens. Soc. Linn. Lyon* 26, 271–281.
- Mazenot, G., 1959. Présence du loess fossilifère würmien en amont des moraines internes, dans les collines du Bas-Dauphiné à l'est de Lyon. In: *Bull. Soc. Lyon*, 28 n (10), 309–311. https://www.persee.fr/doc/linly_0366-1326_1959_num_28_10_8104 (accessed: 29 May 2020).
- Mazenot, G., 1965. Existe-t-il à tout prix, en France, une faune de loess ? *Bull. Assoc. Fr. Étud. Quat. (Quaternaire)* 2, 78–84. https://www.persee.fr/doc/quate_0004-5500_1965_num_2_1_982 (accessed: 20 July 2020).
- McManus, J. F., Bond, G.C., Broecker, W.S., Johnsen, S., Labeyrie, L., Higgins, S., 1994. High-resolution climate records from the North-Atlantic during the last interglacial. *Nature* 371, 326–329. <https://doi.org/10.1038/371326a0>.
- Mejdahl, V., 1987. Internal radioactivity in quartz and feldspar grains. *Ancient TL* 5 (2), 10–17.
- Meschede, M., Warr, L.N., 2019. *The Geology of Germany. A Process-Oriented Approach*. Springer Spektrum: Berlin. <http://dx.doi.org/10.1007/978-3-319-76102-2>.
- Mercier, N., Falguères, C., 2007. Field gamma dose-rate measurement with a NaI (TI) detector: re-evaluation of the “threshold” technique. *Ancient TL* 25, 1–4. [https://www.aber.ac.uk/en/media/departamental/dges/ancienttl/pdf/vol25no1/mercier_atl25\(1\)_1-4.pdf](https://www.aber.ac.uk/en/media/departamental/dges/ancienttl/pdf/vol25no1/mercier_atl25(1)_1-4.pdf) (accessed: 17 September 2022).
- Mercier, N., Kreutzer, S., Christophe, C., Guérin, G., Guibert, P., Lahaye, C., Lanos, P., Philippe, A., Tribolo, C., 2016. Bayesian statistics in luminescence dating: the 'baSAR'-model and its implementation in the R package 'Luminescence'. *Ancient TL* 34, 14–21. http://ancienttl.org/ATL_34-2_2016/ATL_34-2_Mercier_p14-21.pdf.
- Meteo-France, 2020. *Le climat en France métropolitaine*. <https://meteofrance.com/comprendre-climat/france/le-climat-en-france-metropolitaine> (accessed: 06 July 2022).

- Meteo-France, 2022a. Fiche Climatologique. Statistiques 1991-2020 et records Lyon-Bron. https://donneespubliques.meteofrance.fr/?fond=produit&id_produit=117&id_rubrique=39 (accessed: 06 July 2022).
- Meteo-France, 2021b. Fiche Climatologique. Statistiques 1991-2020 et records Valence-Chabeui. https://donneespubliques.meteofrance.fr/?fond=produit&id_produit=117&id_rubrique=39 (accessed: 17 December 2023).
- Meteo-France, 2022c. Fiche Climatologique. Statistiques 1991-2020 et records Arles. https://donneespubliques.meteofrance.fr/?fond=produit&id_produit=117&id_rubrique=39 (accessed: 06 July 2022).
- Meteo-France, 2022d. Fiche Climatologique. Statistiques 1991-2020 et records Nîmes. https://donneespubliques.meteofrance.fr/?fond=produit&id_produit=117&id_rubrique=39 (accessed: 06 July 2022).
- Meteo-France, 2022e. Fiche Climatologique. Statistiques 1991-2020 et records Uzès. https://donneespubliques.meteofrance.fr/?fond=produit&id_produit=117&id_rubrique=39 (accessed: 06 July 2022).
- Miall, A., 1996. *The Geology of Fluvial Deposits, Sedimentary Facies, Basin Analysis and Petroleum Geology*. Springer, Berlin. ISBN 978-3-540-59186-3.
- Mikulčić-Pavlaković, S., Crnjaković, M., Tibljaš, D., Šoufek, M., Wacha, L., Frechen, M., Lacković, D., 2011. Mineralogical and geochemical characteristics of Quaternary sediments from the Island of Susak (Northern Adriatic, Croatia). *Quatern. Int.* 234, 32–49. <https://doi.org/10.1016/j.quaint.2010.02.005>.
- Moine, O., Rousseau, D.D., Antoine, P., 2005. Terrestrial molluscan records of Weichselian Lower to Middle Pleniglacial climatic changes from the Nussloch loess series (Rhine Valley, Germany): the impact of local factors. *Boreas* 34, 363–380. <https://doi.org/10.1080/03009480510013060>.
- Moine, O., Antoine, P., Hatté, C., Landais, A., Mathieu, J., Prud'homme, C., Rousseau, D.D., 2017. The impact of Last Glacial climate variability in west-European loess revealed by radiocarbon dating of fossil earthworm granules. *Proc. Natl. Acad. Sci. Unit. States Am.* 114, 6209–6214. <https://doi.org/10.1073/pnas.1614751114>.
- Molnár, M., Rinyu, L., Veres, M., Seiler, M., Wacker, L., Synal, H.-A., 2013. Environ-MICADAS: a mini 14 C AMS with enhanced gas ion source interface in the Hertelendi Laboratory of Environmental Studies (HEKAL), Hungary. *Radiocarbon* 55, 338–344. <https://doi.org/10.1017/S0033822200057453>.
- Molliex, S., Siame, L.L., Bourlès, D.L., Bellier, O., Braucher, R., Clauzon, G., 2013. Quaternary evolution of a large alluvial fan in a periglacial setting (Crau Plain, SE France) constrained by terrestrial cosmogenic nuclide (^{10}Be). *Geomorphology*, 195, 45–52. <https://doi.org/10.1016/j.epsl.2016.03.043>.
- Mologni, C., Purdue, L., Audiard, B., Dubar, M., Kreutzer, S., Texier, P.-J., 2021. Sedimentary processes and palaeoenvironments from La Combette sequence (southeastern France): climatic insights on the

- Last Interglacial/Glacial transition. *Palaeogeogr., Palaeoecol.* 576, 110503. <https://doi.org/10.1016/j.palaeo.2021.110503>.
- Moncel, M.-H., Allué, E., Bailon, S., Barshay-Szmidt, C., Béarez, P., Crégut, É., Daujeard, C., Desclaux, E., Debard, É., Lartigot-Campin, A.-S., Puaud, S., Roger, T., 2015. Evaluating the integrity of palaeoenvironmental and archaeological records in MIS 5 to 3 karst sequences from southeastern France. *Quatern. Int.* 378, 22–39. <https://doi.org/10.1016/j.quaint.2013.12.009>.
- Monegato, G., Ravazzi, C., Donegana, M., Pini, R., Calderoni, G., Wick, L., 2007. Evidence of a two-fold glacial advance during the last glacial maximum in the Tagliamento end moraine system (eastern Alps). *Quaternary Res.* 68, 284–302. <https://doi.org/10.1016/j.yqres.2007.07.002>.
- Monegato, G., Scardia, G., Hajdas, I., Rizzini, F., Piccin, A., 2017. The Alpine LGM in the boreal ice-sheets game. *Sci. Rep.* 7, 1–8. <https://doi.org/10.1038/s41598-017-02148-7>.
- Monjuvent, G., Masse, J.-P., Ballesio, R., Alabouvette, B., Blavoux, B., Dupias, G., Granier, J., Philip, J., 1991. La carte géologique à 1/50 000. Nîmes est recouverte par les coupures suivantes de la carte géologique de la France à 1 / 80 000.
- Moska, P., Jary, Z., Adamiec, G., Bluszcz, A., 2015. OSL chronostratigraphy of a loesspalaeosol sequence in Złota using quartz and polymineral fine grains. *Radiat. Meas.* 81, 23–31. <https://doi.org/10.1016/j.radmeas.2015.04.012>.
- Moska, P., Jary, Z., Adamiec, G., Bluszcz, A., 2019. Chronostratigraphy of a loesspalaeosol sequence in Biały Kościół, Poland using OSL and radiocarbon dating. *Quatern. Int.* 502, 4–17. <https://doi.org/10.1016/j.quaint.2018.05.024>.
- Muhs, D.R., Bettis III, E.A., 2003. Quaternary loess-paleosol sequences as examples of climate-driven sedimentary extremes. *Spec. Pap. Geol. Soc. Am.* 370, 53–74. <http://dx.doi.org/10.1130/0-8137-2370-1.53>.
- Muñoz-Salinas, E., Bishop, P., Sanderson, D.C.W., Zamorano, J.-J., 2011. Interpreting luminescence data from a portable OSL reader: three case studies in fluvial settings. *Earth Surf. Proc. Land.*, 36, 651–660. <https://doi.org/10.1002/esp.2084>.
- Muñoz-Salinas, E., Bishop, P., Sanderson, D., Kinnaird, T., 2014. Using OSL to assess hypotheses related to the impacts of land use change with the early nineteenth century arrival of Europeans in south-eastern Australia: an exploratory case study from Grabben Gullen Creek, New South Wales. *Earth Surf. Proc. Land.*, 39, 1576–1586. <https://doi.org/10.1002/esp.3542>.
- Munsell, A.H., 2000. Munsell Soil Color Charts. GretagMacbeth, Shanghai.
- Murray, A.S., Wintle, A.G., 2000. Luminescence dating of quartz using an improved single-aliquot regenerative-dose protocol. *Radiat. Meas.* 32, 57–73. [https://doi.org/10.1016/S1350-4487\(99\)00253-X](https://doi.org/10.1016/S1350-4487(99)00253-X).
- NEEM community members, 2013. Eemian interglacial reconstructed from a Greenland folded ice core. *Nature* 493, 489–494. <https://doi.org/10.1038/nature11789>.

- Nesbitt, H. W., Markovics, G., Price, R.C., 1980. Chemical processes affecting alkalis and alkaline earths during continental weathering. *Geochem. Cosmochim. Acta* 44, 1659–1666. [https://doi.org/10.1016/0016-7037\(80\)90218-5](https://doi.org/10.1016/0016-7037(80)90218-5).
- Nesbitt, H. W., Young, G.M., 1982. Early Proterozoic climates and plate motions inferred from major element chemistry of lutites. *Nature* 299, 715. <https://doi.org/10.1038/299715a0>.
- Nesbitt, H. W., Young, G.M., 1989. Formation and diagenesis of weathering profiles. *J. Geol.* 97, 129–147. <https://doi.org/10.1086/629290>.
- North-GRIP Members, 2004. High-resolution record of Northern Hemisphere climate extending into the Last Interglacial period. *Nature* 431, 147. <https://doi.org/10.1038/nature02805>.
- Nottebaum, V., Stauch, G., Hartmann, K., Zhang, J., Lehmkuhl, F., 2015. Unmixed loess grain size populations along the northern Qilian Shan (China): relationships between geomorphologic, sedimentologic and climatic controls. *Quatern. Int.* 372, 151–166. [https://doi.org/10.1016/S1350-4487\(99\)00253-X](https://doi.org/10.1016/S1350-4487(99)00253-X).
- Novothy, Á., Frechen, M., Horváth, E., Wacha, L., Rolf, C., 2011. Investigating the penultimate and last glacial cycles of the Süttő loess section (Hungary) using luminescence dating, high-resolution grain size, and magnetic susceptibility data. *Quatern. Int.* 234, 75–85. <https://doi.org/10.1016/j.quaint.2010.08.002>.
- Obrecht, I., Zeeden, C., Hambach, U., Veres, D., Marković, S.B., Lehmkuhl, F., 2019. A critical reevaluation of palaeoclimate proxy records from loess in the Carpathian Basin. *Earth-Sci. Rev.* 190, 498–520. <https://doi.org/10.1016/j.earscirev.2019.01.020>.
- Obermann, A., Bastin, S., Belamari, S., Conte, D., Gaertner, M.A., Li, L., Ahrens, B., 2018. Mistral and Tramontane wind speed and wind direction patterns in regional climate simulations. *Clim. Dyn.* 3 (51), 1059–1076. <https://doi.org/10.1007/s00382-016-3053-3>.
- Olivier, J.-M., Amoros, C., Carrel, G., Malard, F., Lamouroux, N., Bravard, J.-P., 2009. Chapter 7 – The Rhône River Basin. In: Rivers of Europe. Tockner, K., Uehlinger, U., Robinson, C.T.(eds). Academic Press: London; 247–295. <http://dx.doi.org/10.1016/B978-0-12-369449-2.00007-2>.
- Ollivier, V., 2006. Continuités, instabilités et ruptures morphogéniques en Provence depuis la dernière glaciation. Unpublished Ph.D. dissertation. In: Travertinisation, détritisme et incisions sur le piémont sud du Grand Luberon (Vaucluse, France). Relations avec les changements climatiques et l’anthropisation. University of Provence, Aix-Marseille I. https://theses.hal.science/tel-00358962v1/file/These_Vincent_Ollivier_2006_Continuites_instabilites_et_ruptures_morphogeniques_en_Provence_depuis_la_derniere_glaciation.pdf.
- Ollivier, V., Magnin, F., Guendon, J. L., Miramont, C., 2014. Regards sur les dynamiques paysagères du Pléistocène Supérieur du Luberon et de Basse Provence (SIM 3 et SIM 2, France). *Quaternaire* 91–111. <https://doi.org/10.4000/quaternaire.7002>.
- Ottlé, C., Etchevers, P., Golaz, C., Habets, F., Noilhan, J., Martin, E., Ledoux, E., Leblois, E., Sauquet, E., Amraoui, N., Artinian, E., Champeaux, J.L., Guérin, P., Lacarrère, P., Le Molgne, P., Saulnier, G.M.,

- Thiéry, D., Vidal-Madjar, D., Voirin, S., 2001. Hydro-Meteorological Modelling of the Rhône Basin: General Presentation and Objectives. *Phy. Chem. Earth* 26 (5–6), 443–453. [https://doi.org/10.1016/S1464-1909\(01\)00033-8](https://doi.org/10.1016/S1464-1909(01)00033-8).
- Party, J.-P., 2001. Cartographie des sols de l'Ardeche: Description de l'Unité Cartographique de Sol (UCS) numéro 22, Référentiel Régional Pédologique de l'Ardèche. Chambre Régionale d'Agriculture Auvergne-Rhône-Alpes - AGRAPOLE.
- Pasquetti, F., Zanchetta, G., Bini, M., Paffi, J., Coltorti, M., Lezzerini, M., Arienzo, I., Cremaschi, M., 2023. Potential dust sources for loess deposits in Central Italy: A geochemical case study from the Loess-Paleosol-Sequence of Ponte Crispiero (Marche). *Catena* 226 (1), 107064. <https://doi.org/10.1016/j.catena.2023.107064>.
- Pasquier, V., Toucanne, S., Sansjofre, P., Dixit, Y., Revillon, S., Mokeddem, Z., Rabineau, M., 2019. Organic matter isotopes reveal enhanced rainfall activity in Northwestern Mediterranean borderland during warm substages of the last 200 kyr. *Quaternary Sci. Rev.* 205, 182–192. <https://doi.org/10.1016/j.quascirev.2018.12.007>.
- Pastre, J.-F., Singer, B.S., Guillou, H., Pupin, J.-P., Riou, B., 2004. Chronostratigraphy of the key Upper Miocene (Lower Turolian) sequence of la Montagne d'Andance (Ardèche, France). Implications of new $^{40}\text{Ar}/^{39}\text{Ar}$ laser fusion and unspiked K-Ar dating of trachytic tephra and basalts. *Quaternaire* 175 (1), 3–10. <https://dx.doi.org/10.2113/175.1.3>.
- Paterson, G.A., Heslop, D., 2015. New methods for unmixing sediment grain size data. *G-cubed* 16, 4494–4506. <https://doi.org/10.1002/2015GC006070>.
- Pécsi, M., Richter, G., 1996. Löss: Herkunft - Gliederung - Landschaften; gewidmet dem 14. INQUA-Kongress in Berlin. *Zeitschrift für Geomorphologie Supplementband 98*. Borntraeger, Berlin, 391 pp. ISBN 9783443210984.
- Pedersen, R.A., Langen, P.L., Vinther, B.M., 2017. The Last Interglacial climate: comparing direct and indirect impacts of insolation changes. *Clim. Dynam.* 48, 3391–3407. <https://doi.org/10.1007/s00382-016-3274-5>.
- Penck, A., Brückner, E., 1909. Die Alpen im Eiszeitalter. Dritter Band. Die Eiszeiten in den Südalpen und im Bereich der Ostabdachung der Alpen. *Chr. Herm. Tauchnitz, Leipzig*. https://opac.geologie.ac.at/ais312/dokumente/Penck_1909_Eiszeitalter_Bd_1.pdf.
- Perrin, A., 1948. A propos du loess récent du Mont d'Or lyonnais. *Étud. Rhodaniennes* 23 (3), 176–182. <https://doi.org/10.3406/geoca1948.5293>.
- Pigati, J.S., Rech, J.A., Nekola, J.C., 2010. Radiocarbon dating of small terrestrial gastropod shells in North America *Quat. Geochronol.* 5, 519–532. <https://doi.org/10.1016/j.quageo.2010.01.001>.
- Pfaffner, N., Kadereit, A., Karius, V., Kolb, T., Kreutzer, S., Sauer, D., 2024. Reconstructing the Eemian to Middle Pleniglacial pedosedimentary evolution of the Baix loess–palaeosol sequence (Rhône Rift

- Valley, southern France) – basic chronostratigraphic framework and palaeosol characterisation, *E&G Quaternary Sci. J.*, 73, 1–22. <https://doi.org/10.5194/egqsj-73-1-2024>.
- Plata, J., Rodríguez, R., Preusser, F., Boixadera, J., Balasch, J.C., Antúnez, M., Poch, R.M., 2021. Red soils in loess deposits of the Eastern Ebro Valley. *Catena* 204 (1–2), 105430. <https://doi.org/10.1016/j.catena.2021.105430>.
- Pletsch, A., Uterwedde, H., 2003. Frankreich: Geographie, Geschichte, Wirtschaft, Politik. Wiss. Buchges: Darmstadt. ISBN 9783534160426.
- Portenga, E.W., Bishop, P., 2016. Confirming geo-morphological interpretations based on portable OSL reader data. *Earth Surf. Proc. Land.*, 41, 427–432. <https://doi.org/10.1002/esp.3834>.
- Potts, P., 1987. *A Handbook of Silicate Rock Analysis - Classical and rapid methods of analysis*, Blackie Academics & Professional. ISBN 978-0216932098.
- Prescott, J.R., Hutton, J.T., 1994. Cosmic ray contributions to dose rates for luminescence and ESR dating: Large depths and long-term time variations. *Radiat. Meas.* 23 (2-3), 497–500. [https://doi.org/10.1016/1350-4487\(94\)90086-8](https://doi.org/10.1016/1350-4487(94)90086-8).
- Preusser, F., Degering, D., Fuchs, M., Hilgers, A., Kadereit, A., Klasen, N., Krbetschek, M., Richter, D., Spencer, J.Q., 2008. Luminescence dating: basics, methods and applications. *E&G Quaternary Sci. J.* 57, 95–149. <https://doi.org/10.3285/eg.57.1-2.5>.
- Preusser, F., Graf, H. R., Keller, O., Krayss, E., Schlüchter, C., 2011. Quaternary glaciation history of northern Switzerland. *E&G Quaternary Sci. J.* 60, 282–305. <https://doi.org/10.3285/eg.60.2-3.06>.
- Profe, J., Zolitschka, B., Schirmer, W., Frechen, M., Ohlendorf, C., 2016. Geochemistry unravels MIS 3/2 paleoenvironmental dynamics at the loessepaleosol sequence Schwalbenberg II, Germany. *Palaeogeogr., Palaeoecol.* 459, 537–551. <https://doi.org/10.1016/j.palaeo.2016.07.022>.
- Profe, J., Wacha, L., Frechen, M., Ohlendorf, C., Zolitschka, B., 2018. XRF scanning of discrete samples – A chemostratigraphic approach exemplified for loess-paleosol sequences from the Island of Susak, Croatia. *Quatern. Int.* 494, 34–51. <https://doi.org/10.1016/j.palaeo.2016.07.022>.
- Puaud, S., Nowak, M., Pont, S., Moncel, M.-H., 2015. Minéraux volcaniques et alpins à l’abri du Maras (Ardèche, France). *Comp. Rend. Palevol.* 4 (14), 331–341. <https://doi.org/10.1016/j.crpv.2015.02.007>.
- Pye, K., 1995. The nature, origin and accumulation of loess. *Quaternary Sci. Rev.* 14, 653–667. [https://doi.org/10.1016/0277-3791\(95\)00047-X](https://doi.org/10.1016/0277-3791(95)00047-X).
- Qiang, M., Lang, L., Wang, Z., 2010. Do fine-grained components of loess indicate westerlies: insights from observations of dust storm deposits at Lenghu (Qaidam Basin, China). *J. Arid Environ.* 74, 1232–1239. <https://doi.org/10.1016/j.jaridenv.2010.06.002>.
- Qin, X., Cai, B., Liu, T., 2005. Loess record of the aerodynamic environment in the east Asia monsoon area since 60,000 years before present. *J. Geophys. Res.: Solid Earth* 110, B01204. <https://doi.org/10.1029/2004JB003131>.

- Quénard, L., Samouëlian, A., Laroche, B., Cornu, S., 2011. Lessivage as a major process of soil formation: A revisit of existing data. *Geoderma* 167–168, 135–147. <https://doi.org/10.1016/j.geoderma.2011.07.031>.
- R Core Team, 2019. R: a Language and Environment for Statistical Computing. version 3.0. 2. R Foundation for Statistical Computing, Vienna, Austria, 2013.
- Railsback, B., Gibbard, P.L., Head, M.J., Voarintsoa, N.R.G., Toucanne, S., 2015. An optimized scheme of lettered marine isotope substages for the last 1.0 million years, and the climatostratigraphic nature of isotope stages and substages. *Quaternary Sci. Rev.* 111, 94–106. <https://doi.org/10.1016/j.quascirev.2015.01.012>.
- Railsback, B., 2021. Ages of boundaries between marine isotope stages. Railsbeck's fundamentals of Quaternary Science. <http://railsback.org/FQS/FQSSubstages02-Update1.jpg> (accessed: 05 August 2021).
- Rasmussen, S.O., Bigler, M., Blockley, S.P., Blunier, T., Buchardt, S.L., Clausen, H.B., Cvijanovic, I., Dahl-Jensen, D., Johnsen, S.J., Fischer, H., 2014. A stratigraphic framework for abrupt climatic changes during the Last Glacial period based on three synchronized Greenland ice-core records: refining and extending the INTIMATE event stratigraphy. *Quaternary Sci. Rev.* 106, 14–28. <https://doi.org/10.1016/j.quascirev.2014.09.007>.
- Reille, M., Beaulieu, J.-L. de, 1990. Pollen analysis of a long upper Pleistocene continental sequence in a Velay maar (Massif Central, France). *Palaeogeogr., Palaeoecol.* 80, 35–48. [https://doi.org/10.1016/0031-0182\(90\)90032-3](https://doi.org/10.1016/0031-0182(90)90032-3).
- Reille, M., Beaulieu, J.-L. de, Svobodova, H., Andrieu-Ponel, V., Goeury, C., 2000. Pollen analytical biostratigraphy of the last five climatic cycles from a long continental sequence from the Velay region (Massif Central, France). *J. Quaternary Sci.* 15, 665–685. [https://doi.org/10.1002/1099-1417\(200010\)15:7<665:AID-JQS560>3.0.CO;2-G](https://doi.org/10.1002/1099-1417(200010)15:7<665:AID-JQS560>3.0.CO;2-G).
- Reimann, C., Birke, M., Demetriades, A., Filzmoser, P., O'Connor, P., 2014. Part A: Chemistry of Europe's Agricultural Soils: Methodology and Interpretation of the GEMAS Data Set. *Geologisches Jahrbuch, Hannover*. ISBN 978-3-510-96846-6.
- Reimer, P.J., Bard, E., Bayliss, A., Beck, J.W., Blackwell, P.G., Ramsey, C.B., Buck, C.E., Cheng, H., Edwards, R.L., Friedrich, M., 2013. IntCal13 and Marine13 radiocarbon age calibration curves 0–50,000 years cal BP. *Radiocarbon* 55, 1869–1887. https://doi.org/10.2458/azu_js_rc.55.16947.
- Reimer, P.J., Austin, W.E.N., Bard, E., Bayliss, A., Blackwell, P.G., Bronk Ramsey, C., Butzin, M., Cheng, H., Edwards, R.L., Friedrich, M., Grootes, P.M., Guilderson, T.P., Hajdas, I., Heaton, T.J., Hogg, A.G., Hughen, K.A., Kromer, B., Manning, S.W., Muscheler, R., Palmer, J.G., Pearson, C., van der Plicht, J., Reimer, R.W., Richards, D.A., Scott, E.M., Southon, J.R., Turney, C.S.M., Wacker, L., Adolphi, F., Büntgen, U., Capano, M., Fahrni, S.M., Fogtmann-Schulz, A., Friedrich, R., Köhler, P., Kudsk, S., Miyake, F., Olsen, J., Reinig, F., Sakamoto, M., Sookdeo, A., Talamo, S., 2020. The IntCal20 Northern

- Hemisphere Radiocarbon Age Calibration Curve (0–55 cal kBP). *Radiocarbon* 62 (4), 725–757. <https://doi.org/10.1017/RDC.2020.41>.
- Reynaud, J.-Y., Dalrymple, R.W., Vennin, E., Parize, O., Besson, D., Rubino, J.-L., 2006. Topographic Controls on Production and Deposition of Tidal Cool-Water Carbonates, Uzès Basin, SE France. *J. Sediment. Res.* 76, 117–130. <https://doi.org/10.2110/jsr.2006.07>.
- Reynaud, J.-Y., Vennin, E., Parize, O., Rubino, J.-L., Bourdillon, C., 2012. Incised valleys and tidal seaways: the example of the Miocene Uzès-Castillon basin, SE France. *Bull. Soc. Géol. France* 183, 471–486. <https://doi.org/10.2113/gssgfbull.183.5.471>.
- Richard, M., Falguères, C., Pons-Branchu, E., Bahain, J.-J., Voinchet, P., Lebon, M., Valladas, H., 2015. Contribution of ESR/U-series dating to the chronology of late Middle Palaeolithic sites in the middle Rhône valley, southeastern France. *Quat. Geochronol.* 30, 529–534. <https://doi.org/10.1016/j.quageo.2015.06.002>.
- Richter, D., Richter, A., Dornich, K., 2013. Lexsygda new system for luminescence research. *Geochronometria* 40, 220–228. <https://doi.org/10.2478/s13386-013-0110-0>.
- Richter, D., Woda, C., Dornich, K., 2020. A new quartz for γ -transfer calibration of radiation sources. *Geochronometria* 47, 23–34. <https://doi.org/10.2478/geochr-2020-0020>.
- Rivals, F., Moncel, M.-H., Patou-Mathis, M., 2009. Seasonality and intra-site variation of Neanderthal occupations in the Middle Palaeolithic locality of Payre (Ardèche, France) using dental wear analyses. *J. Archaeol. Sci.* 36, 1070–1078. <https://doi.org/10.1016/j.jas.2008.12.009>.
- Roberts, H.M., 2008. The development and application of luminescence dating to loess deposits: a perspective on the past, present and future. *Boreas* 37 (4), 483–507. <https://doi.org/10.1111/j.1502-3885.2008.00057.x>.
- Rose, J., Meng, X., Watson, C., 1999. Palaeoclimate and palaeoenvironmental responses in the western Mediterranean over the last 140 ka: evidence from Mallorca, Spain. *J. Geol. Soc. London* 156, 435–448. <https://doi.org/10.1144/gsjgs.156.2.0435>.
- Rousseau, D., Antoine, P., Hatté, C., Lang, A., Zöller, L., Fontugne, M., Othman, D., Luck, J., Moine, O., Labonne, M., Bentaleb, I., Jolly, D., 2002. Abrupt millennial climatic changes from Nussloch (Germany) Upper Weichselian eolian records during the Last Glaciation. *Quaternary Sci. Rev.* 21 (14-15), 1577–1582. [http://dx.doi.org/10.1016/S0277-3791\(02\)00034-3](http://dx.doi.org/10.1016/S0277-3791(02)00034-3).
- Rousseau, D., Derbyshire, E., Antoine, P., Hatté, C., 2018. European Loess Records, in: Reference Module in Earth Systems and Environmental Sciences. Elsevier. <https://doi.org/10.1016/B978-0-12-409548-9.11136-4>.
- Ruth, U., Wagenbach, D., Steffensen, J.P., Bigler, M., 2003. Continuous record of microparticle concentration and size distribution in the central Greenland NGRIP ice core during the last glacial period. *J. Geophys. Res.: Atmosphere* 108. <https://doi.org/10.1029/2002JD002376>.

- Saint Martin, M., 2009. Carte géologique harmonisée du département de l'Ardèche notice technique: BRGM, BRGM/RP-57097-FR, 423 pp., <http://infoterre.brgm.fr/rapports/RP-57097-FR.pdf> (accessed: 11 February 2022).
- Sánchez-Goñi, M.F., Eynaud, F., Turon, J.L., Shackleton, N.J., 1999. High resolution palynological record off the Iberian margin: direct land-sea correlation for the Last Interglacial complex. *Earth Planet. Sc. Lett.* 177 (1), 123-137. [https://doi.org/10.1016/S0012-821X\(99\)00141-7](https://doi.org/10.1016/S0012-821X(99)00141-7).
- Sánchez-Goñi, M.F., Loutre, M.F., Crucifix, M. Peyron, O., Santos, L., Duprat, J., Malaizé, B., Turon, J.-L., Peyrouquet, J.-P., 2005. Increasing vegetation and climate gradient in Western Europe over the Last Glacial Inception (122-110 ka): data-model comparison. *Earth Planet Sc. Lett.* 231, 111–130. <https://doi:10.1016/j.epsl.2004.12.010>.
- Sánchez-Goñi, M. F., Harrison, S. P., 2010. Millennial-scale climate variability and vegetation changes during the Last Glacial: concepts and terminology. *Quaternary Sci. Rev.* 29, 2823–2827. <https://doi.org/10.1016/j.quascirev.2009.11.014>.
- Sanderson, D.C.W., Bishop, P., Stark, M.T., Spencer, J.Q., 2003. Luminescence dating of anthropogenically reset canal sediments from Angkor Borei, Mekong Delta, Cambodia. *Quaternary Sci. Rev.*, 22, 1111–1121. [https://doi.org/10.1016/S0277-3791\(03\)00055-6](https://doi.org/10.1016/S0277-3791(03)00055-6).
- Satterfield, D., Rollinson, H., Suthren, R., 2019. The eastern French Pyrenees: from mountain belt to foreland basin. *Geology Today* 35, 228–240. <https://doi.org/10.1111/gto.12291>.
- Sauer, D., Stein, C., Glatzel, S., Kühn, J., Zarei, M., Stahr, K., 2015. Duricrusts in soils of the Alentejo (southern Portugal)—types, distribution, genesis and time of their formation. *J. Soils Sediments* 15, 1437–1453. <https://doi.org/10.1007/s11368-015-1066-x>.
- Sauer, D., 2016. Soil Development: Numerical Indices. In: *International Encyclopedia of Geography: People, the Earth, Environment and Technology*, edited by: Richardson, D., Castree, N., Goodchild, M. F., Kobayashi, A., Liu, W., and Marston, R. A., John Wiley & Sons, Ltd, Oxford, UK, 1–8. <https://doi.org/10.1002/9781118786352.wbieg0909>.
- Sauer, D., Kadereit, A., Kühn, P., Kösel, M., Miller, C. E., Shinonaga, T., Kreutzer, S., Herrmann, L., Fleck, W., Starkovich, B.M., Stahr, K., 2016. The loess-palaeosol sequence of Datthausen, SW Germany: characteristics, chronology, and implications for the use of the Lohne Soil as a marker soil. *Catena* 146, 10–29. <https://doi.org/10.1016/j.catena.2016.06.024>.
- Schaffernicht, E.J., Ludwig, P., Shao, Y., 2020. Linkage between dust cycle and loess of the last glacial maximum in Europe. *Atmos. Chem. Phys.* 20, 4969–4986. <https://doi.org/10.5194/acp-20-4969-2020>.
- Schirmer W., 2000. Eine Klimakurve des Oberpleistozäns aus dem rheinischen Löss. *E&G Quaternary Sci. J.* 50: 25–49. <https://doi.org/10.3285/eg.50.1.02>.
- Schirmer, W., 2002. Compendium of the Rhein loess sequence, At: Ikinge, A. and Schirmer, W. (Eds.): *Loess units and solcomplexes in the Niederrhein and Maas area. Terra Nostra*, 1, 102–104.

- Schirmer W., 2012. Rhine loess at Schwalbenberg II - MIS 4 and 3. *E&G Quaternary Sci. J.* 61: 32–47. <https://doi.org/10.3285/eg.61.1.03>.
- Schirmer, W., 2016. Late Pleistocene loess of the lower rhine. *Quatern. Int.* 411, 44–61. <https://doi.org/10.1016/j.quaint.2016.01.034>.
- Schmidt, M.W., Noack, A.G., 2000. Black carbon in soils and sediments: analysis, distribution, implications, and current challenges. *Global Biogeochem. Cycles* 14, 777–793. <https://doi.org/10.1029/1999GB001208>.
- Schmidt, C., Woda, C., 2019. Quartz thermoluminescence spectra in the high-dose range. *Phys. Chem. Miner.* 46, 861–875. <https://doi.org/10.1007/s00269-019-01046-w>.
- Schoeneich, P. 1998. Corrélation du dernier maximum glaciaire et de la déglaciation alpine avec l'enregistrement isotopique du Groenland [Correlation of the alpine LGM and déglaciation with the Greenland isotopic record]. *Quaternaire* 9 (3), 203–215. <https://doi.org/10.3406/quate.1998.1603>.
- Schulte, P., Lehmkuhl, F., Steininger, F., Loibl, D., Lockot, G., Protze, J., Fischer, P., Stauch, G., 2016. Influence of HCl pretreatment and organo-mineral complexes on laser diffraction measurement of loess-paleosol sequences. *Catena* 137, 392–405. <https://doi.org/10.1016/j.catena.2015.10.015>.
- Schulte, P., Lehmkuhl, F., 2018. The difference of two laser diffraction patterns as an indicator for post-depositional grain size reduction in loess-paleosol sequences. *Palaeogeogr., Palaeoecol.* 509, 126–136. <https://doi.org/10.1016/j.palaeo.2017.02.022>.
- Schulte, P., Sprafke, T., Rodrigues, L., Fitzsimmons, K.E., 2018. Are fixed grain size ratios useful proxies for loess sedimentation dynamics? Experiences from Remizovka, Kazakhstan. *Aeolian Res.* 31, 131–140. <https://doi.org/10.1016/j.aeolia.2017.09.002>.
- Schulze, T., Schwahn, L., Fülling, A., Zeeden, C., Preusser, F., Sprafke, T., 2022. Investigating the loess-palaeosol sequence of Bahling-Schönberg (Kaiserstuhl), southwestern Germany, using a multi-methodological approach. *E&G Quaternary Sci. J.* 71, 45–162. <https://doi.org/10.5194/egqsj-71-145-2022>.
- Schwertmann, U., 1993. Relations between Iron Oxides, Soil Color, and Soil Formation. In: *Soil color: Proceedings of a symposium sponsored by Divisions S-5 and S-9 of the Soil Science Society of America in San Antonio, Texas, 21-26 Oct. 1990*, edited by: Bigham, J.M., Ciolkosz, E.J., and Luxmoore, R.J., Soils Science Society of America, Madison, Wis, USA, 51–69. <https://doi.org/10.2136/sssaspecpub31.c4>.
- Seelos, K., Sirocko, F., Dietrich, S., 2009. A continuous high-resolution dust record for the reconstruction of wind systems in central Europe (Eifel, Western Germany) over the past 133 ka. *Geophys. Res. Lett.* 36, L20712. <https://doi.org/10.1029/2009GL039716>.
- Seguinot, J., Ivy-Ochs, S., Juvet, G., Huss, M., Funk, M., Preusser, F., 2018. Modelling last glacial cycle ice dynamics in the Alps. *Cryosphere* 12, 3265–3285. <https://doi.org/10.3929/ethz-b-000297918>.

- Semmel, A., 1968. Studien über den Verlauf jungpleistozäner Formung in Hessen. Frankfurter Geogr. Hefte (45).
- Semmel, A., 1998. Lokalisationen von Stratotypen jungpleistozäner äolischer und solifluidaler Sedimente im Rhein-Main-Gebiet. *Geo. Archaeo. Rhein* (2), 35–45.
- Shackleton, N.J., Sánchez-Goñi, M.F., Pailler, D., Lancelot, Y., 2003. Marine Isotope Substage 5e and the Eemian Interglacial. *Global Planet. Change* 36, 151–155. [https://doi.org/10.1016/S0921-8181\(02\)00181-9](https://doi.org/10.1016/S0921-8181(02)00181-9).
- Sheffer, N.A., Rico, M., Enzel, Y., Benito, G., Grodek, T., 2008. The Palaeoflood record of the Gardon River, France: A comparison with the extreme 2002 flood event. *Geomorphology* 98, 71–83. <https://doi.org/10.1016/j.geomorph.2007.02.034>.
- Sheldon, N.D., Tabor, N.J., 2009. Quantitative paleoenvironmental and paleoclimatic reconstruction using paleosols. *Earth-Sci. Rev.* 95, 1–52. <https://doi.org/10.1016/j.earscirev.2009.03.004>.
- Shepard, F.P., 1954. Nomenclature Based on Sand-silt-clay Ratios. *J. Sedimentary Petrology* 24 (3), 151–158.
- Sierro, F.J., Andersen, N., Bassetti, M.A., Berné, S., Canals, M., Curtis, J.H., Dennielou, B., Flores, J.A., Frigola, J., Gonzalez-Mora, B., Grimalt, J.O., Hodell, D.A., Jouet, G., Pérez-Folgado, M., Schneider, R., 2009. Phase relationship between sea level and abrupt climate change. *Quaternary Sci. Rev.* 28, 2867–2881. <https://doi.org/10.1016/j.quascirev.2009.07.019>.
- Singarayer, J.S., Bailey, R.M., 2003. Further investigations of the quartz optically stimulated luminescence components using linear modulation. *Radiat. Meas.* 37 (4), 451-458. [https://doi.org/10.1016/S1350-4487\(03\)00062-3](https://doi.org/10.1016/S1350-4487(03)00062-3).
- Sirocko, F., Knapp, H., Dreher, F., Förster, M.W., Albert, J., Brunck, H., Veres, D., Dietrich, S., Zech, M., Hambach, U., Röhner, M., Rudert, S., Schwibus, K., Adams, C., Sigl, P., 2016. The ELSA-vegetation-stack: reconstruction of landscape evolution zones (LEZ) from laminated Eifel maar sediments of the last 60,000 years. *Global Planet. Change* 142, 108–135. <https://doi.org/10.1016/j.gloplacha.2016.03.005>.
- Sitzia, L., Bertran, P., Sima, A., Chery, P., Queffelec, A., Rousseau, D.D., 2017. Dynamics and sources of last glacial aeolian deposition in southwest France derived from dune patterns, grain-size gradients and geochemistry, and reconstruction of efficient wind directions. *Quaternary Sci. Rev.* 170, 250–268. <https://doi.org/10.1016/j.quascirev.2017.06.029>.
- Sgubin, G., Swingedouw, D., Dayon, G., de Cortázar-Atauri, I.G., Ollat, N., Pagé, C., van Leeuwen, C., 2018. The risk of tardive frost damage in French vineyards in a changing climate. *Agr. Forest Meteorol.* 250–251, 226–242. <http://doi.org/10.1016/j.agrformet.2017.12.253>.
- Sparks, D.L., Bartels, J.M., 1996. *Methods of soil analysis, Part 3: Chemical Methods*. Soil Science Society of America, Inc. American Society of Agronomy, Inc., Madison, Wisconsin, USA. ISBN: 978-0891188254.

- Sprafke, T., 2015. Löss in Niederösterreich: Archiv quartärer Klima- und Landschaftsveränderungen. Dissertation. https://opus.bibliothek.uni-wuerzburg.de/files/12778/978-3-95826-039-9_Sprafke_Tobias_OPUS_12778.pdf (accessed: 10 November 2022).
- Sprafke, T., Schulte, P., Meyer-Heintze, S., Händel, M., Einwögerer, T., Simon, U., Peticzka, R., Schäfer, C., Lehmkuhl, F., Terhorst, B., 2020. Paleoenvironments from robust loess stratigraphy using high-resolution color and grain-size data of the last glacial Krems-Wachtberg record (NE Austria). *Quaternary Sci. Rev.* 248, 106602. <https://doi.org/10.1016/j.quascirev.2020.106602>.
- Stoops, G., 2003. *Guidelines for Analysis and Description of Soil and Regolith Thin Sections*. Soil Science Society of America, Madison. ISBN: 978-0891188421.
- Stoops, G., 2021. *Guidelines for Analysis and Description of Soil and Regolith Thin Sections*. 2nd edn., ASA, CSSA, and SSSA Bks, American Society of Agronomy, Newark, 259 pp., ISBN: 978-0891189756.
- Stuiver, M., Reimer, P.J., 1993. Extended 14 C data base and revised CALIB 3.0 14 C age calibration program. *Radiocarbon* 35, 215–230. <https://doi.org/10.1017/S0033822200013904>.
- Stuiver, M., Reimer, P.J., Reimer, R.W., 2021. CALIB 8.2 [WWW Program] at <https://calib.org>.
- Suen, T.-Y., 1934. *Le Loess de la Vallée du Rhône*, Lyon : Bosc frères, M. et L. Riou, PhD Thèse, Université de Lyon-Faculté des Lettres, 163 pp.
- Sun, Y., Lu, H., An, Z., 2000. Grain size distribution of quartz isolated from Chinese loess/paleosol. *Chin. Sci. Bull.* 45, 2296–2298. <https://doi.org/10.1007/BF02886372>.
- Sun, D., Bloemendal, J., Rea, D.K., Vandenberghe, J., Jiang, F., An, Z., Su, R., 2002. Grain-size distribution function of polymodal sediments in hydraulic and aeolian environments, and numerical partitioning of the sedimentary components. *Sediment. Geol.* 152, 263–277. [http://dx.doi.org/10.1016/S0037-0738\(02\)00082-9](http://dx.doi.org/10.1016/S0037-0738(02)00082-9).
- Sun, D., Chen, F., Bloemendal, J., Su, R., 2003. Seasonal variability of modern dust over the Loess Plateau of China. *J. Geophys. Res.: Atmosphere* 108. <https://doi.org/10.1029/2003JD003382>.
- Surić, M., Juračić, M., 2010. Late Pleistocene– Holocene environmental changes – records from submerged speleothems along the Eastern Adriatic coast (Croatia). *Geol. Cro.* 63. <https://doi.org/10.4154/gc.2010.13>.
- Terhorst, B., Sedov, S., Sprafke, T., Peticzka, R., Meyer-Heintze, S., Kühn, P., Solleiro Rebolledo, E., 2015. Austrian MIS 3/2 loess–palaeosol records—Key sites along a west–east transect. *Palaeogeogr., Palaeoecol.* 418: 43–56. <https://doi.org/10.1016/j.palaeo.2014.10.020>.
- Thiel, C., Buylaert, J.-P., Murray, A.S., Terhorst, B., Tsukamoto, S., Frechen, M., Sprafke, T., 2011a. Investigating the chronostratigraphy of prominent palaeosols in Lower Austria using post-IR IRSL dating. *E&G Quaternary Sci. J.* 60, 137–152. <https://doi.org/10.3285/eg.60.1.10>.
- Thiel, C., Buylaert, J.-P., Murray, A.S., Terhorst, B., Hofer, I., Tsukamoto, S., Frechen, M., 2011b. Luminescence dating of the Stratzing loess profile (Austria) – Testing the potential of an elevated

temperature post-IR IRSL protocol. *Quatern. Int.* 234, 23–31.
<https://doi.org/10.1016/j.quaint.2010.05.018>.

Thirault, E., Ancel, M.J., Ayasse, A., Baradat, A., Deparnay, X., Moreau, C., Rue, M., 2020. Favary, Rousset (Bouches-Du-Rhône) Archaeological Survey Report. Paléotime, Villard-de-Lans.

Thompson, R., Oldfield, F., 1986. *Environmental Magnetism*. Allen and Unwin, London.
<https://doi.org/10.1007/978-94-011-8036-8>.

Thomsen, K.J., Murray, A.S., Jain, M., Bøtter-Jensen, L., 2008. Laboratory fading rates of various luminescence signals from feldspar-rich sediment extracts. *Radiat. Meas.* 43 (9-10), 1474–1486.
<https://doi.org/10.1016/j.radmeas.2008.06.002>.

Trautmann, T., Krbetschek, M.R., Dietrich, A., Stolz, W., 1998. Investigations of feldspar radioluminescence: potential for a new dating technique. *Radiat. Meas.* 29 (3-4), 421–425.
[https://doi.org/10.1016/S1350-4487\(98\)00012-2](https://doi.org/10.1016/S1350-4487(98)00012-2).

Trautmann, T., Krbetschek, M.R., Dietrich, A., Stolz, W., 1999. Feldspar radioluminescence: a new dating method and its physical background. *J. Luminescence* 85 (1-3), 45–58. [https://doi.org/10.1016/S0022-2313\(99\)00152-0](https://doi.org/10.1016/S0022-2313(99)00152-0).

Tribolo, C., Kreutzer, S., Mercier, N., 2019. How reliable are our beta-source calibrations? *Luminescence Dosimetry Laboratory. Ancient TL* 1–10. <https://hal.archives-ouvertes.fr/hal-02165583/document>.

Tricart, J., 1952. Paléoclimats quaternaires et morphologie climatique dans le Midi méditerranéen. *E&G Quaternary Sci. J.* 2, 172–188. <https://doi.org/10.3285/eg.02.1.20>.

Tsoar, H., Pye, K., 1987. Dust transport and the question of desert loess formation. *Sedimentology* 34, 139–153. <https://doi.org/10.1111/j.1365-3091.1987.tb00566.x>.

Tudyka, K., Miłosz, S., Adamiec, G., Bluszcz, A., Poręba, G., Paszkowski, Ł., Kolarczyk, A., 2018. μ Dose: A compact system for environmental radioactivity and dose rate measurement. *Radiat. Meas.* 118, 8–13. <https://doi.org/10.48550/arXiv.1804.09714>.

Tudyka, K., Bluszcz, A., Poręba, G., Miłosz, S., Adamiec, G., Kolarczyk, A., Kolb, T., Lomax, J., Fuchs, M., 2020. Increased dose rate precision in combined α and β counting in the μ Dose system - a probabilistic approach to data analysis. *Radiat. Meas.* 134, 106310.
<https://doi.org/10.1016/j.radmeas.2020.106310>.

Tzedakis, P.C., 2007. Seven ambiguities in the Mediterranean palaeoenvironmental narrative. *Quaternary Sci. Rev.* 26, 2042–2066. <https://doi.org/10.1016/j.quascirev.2007.03.014>.

Tzedakis, P.C., Emerson, B.C., Hewitt, G.M., 2013. Cryptic or mystic? Glacial tree refugia in northern Europe. *Trends Ecol. Evol.* 28 (12), 696–704. <https://doi.org/10.1016/j.tree.2013.09.001>.

Újvári, G., Kok, J.F., Varga, G., Kovács, J., 2016a. The physics of wind-blown loess: implications for grain size proxy interpretations in Quaternary paleoclimate studies. *Earth-Sci. Rev.* 154, 247–278.
<https://doi.org/10.1016/j.earscirev.2016.01.006>.

- Újvári, G., Molnár, M., Páll-Gergely, B., 2016b. Charcoal and mollusc shell 14C-dating of the Dunaszekcső loess record, Hungary. *Quat. Geochronol.* 35, 43–53. <https://doi.org/10.1016/j.quageo.2016.05.005>.
- Valladas, G., 1978. A gamma ray irradiator. *PACT 3 - Revue du Réseau Européen de Sciences et Techniques appliquées au Patrimoine Culturel*, 439–442.
- Valladas, H., Mercier, N., Ayliffe, L.K., Falguères, C., Bahain, J.-J., Dolo, J.-M., Froget, L., Joron, J.-L., Masaoudi, H., Reyss, J.-L., Moncel, M.-H., 2008. Radiometric dates for the Middle Palaeolithic sequence of Payre (Ardèche, France). *Quat. Geochronol.* 3, 377–389. <https://doi.org/10.1016/j.quageo.2008.01.001>.
- van Vliet-Lanoë, B., 1985. Frost effects in soils. In: Boardman, J. (Ed.), *Soils and Quaternary Landscape Evolution*. John Wiley & Sons, New York, pp. 115-156. ISBN -10. 9780471905288.
- Vandenberghe, J., Múcher, H. J., Roebroeks, W., Gemke, D., 1985. Lithostratigraphy and palaeoenvironment of the Pleistocene deposits at Maastricht-Belvédère, southern Limburg, The Netherlands. *Analecta* 18, 12. <https://scholarlypublications.universiteitleiden.nl/access/item%3A2721128/view> (accessed: 12 November 2022).
- Vandenberghe, D., De Corte, F., Buylaert, J.P., Kucera, J., Van den haute, P., 2008. On the internal radioactivity in quartz. *Radiat. Meas.* 43 (2-6), 771–775. <https://doi:10.1016/j.radmeas.2008.01.016>.
- Vandenberghe, J., 2013. Grain size of fine-grained windblown sediment: a powerful proxy for process identification. *Earth-Sci. Rev.* 121, 18–30. <https://doi.org/10.1016/j.earscirev.2013.03.001>.
- Vandenberghe, J., Sun, Y., Wang, X., Abels, H.A., Liu, X., 2018. Grain-size characterization of reworked fine-grained aeolian deposits. *Earth-Sci. Rev.* 177, 43–52. <https://doi.org/10.1016/j.earscirev.2017.11.005>.
- Varennes, G., Ajas, A., Brochier, J. L., Delhon, C., Durand, F., Nicolle, B., Parisot, N., Picavet, R., Roux, L., Vital, J., 2015. *Les Croisières, Guilhaud-Granges, Ardèche (Archaeological Survey Report)*. Paléotime, Villard-de-Lans.
- Varga, G., Újvári, G., Kovács, J., 2019. Interpretation of sedimentary (sub)populations extracted from grain size distributions of Central European loess-paleosol series. *Quatern. Int.* 502, 60–70. <https://doi.org/10.1016/j.quaint.2017.09.021>.
- Vella, C., Provansal, M., 2000. Relative sea-level rise and neotectonic events during the last 6500 yr on the southern eastern Rhône delta. France. *Mar. Geol.* 170 (1-2), 27–39. [https://doi.org/10.1016/S0025-3227\(00\)00063-3](https://doi.org/10.1016/S0025-3227(00)00063-3).
- Veres, D., Tecsá, V., Gerasimenko, N., Zeeden, C., Hambach, U., Timar-Gabor, A., 2018. Short-term soil formation events in last glacial east European loess, evidence from multi-method luminescence dating. *Quaternary Sci. Rev.* 200, 34–51. <https://doi.org/10.1016/j.quascirev.2018.09.037>.

- Vermeesch, P., 2012. On the visualisation of detrital age distributions. *Chem. Geol.* 312, 190–194. <https://doi.org/10.1016/j.chemgeo.2012.04.021>.
- Viret, J., 1948. Une contribution à l'histoire des glaciations alpines : la faune du loess durci de Saint-Vallier (Drôme). *Étud. rhodaniennes* 23 (4), 227–232. <https://doi.org/10.3406/geoca1948.5298>.
- Viscarra Rossel, R.A., Minasny, B., Roudier, P., McBratney, A.B., 2006. Colour space models for soil science. *Geoderma* 133, 320–337. <https://doi.org/10.1016/j.geoderma.2005.07.017>.
- Voelker, A. H., 2002. Global distribution of centennial-scale records for Marine Isotope Stage (MIS) 3: a database. *Quaternary Sci. Rev.* 21, 1185–1212. [https://doi.org/10.1016/S0277-3791\(01\)00139-1](https://doi.org/10.1016/S0277-3791(01)00139-1).
- Vriend, M., Prins, M.A., 2005. Calibration of modelled mixing patterns in loess grain-size distributions: an example from the north-eastern margin of the Tibetan Plateau, China. *Sedimentology* 52, 1361–1374. <https://doi.org/10.1111/j.1365-3091.2005.00743.x>.
- Wacha, L., Mikulčić Pavlaković, S., Frechen, M., Crnjaković, M., 2011a. The Loess Chronology of the Island of Susak, Croatia. *E&G Quaternary Sci. J.* 60, 153–169 <https://doi.org/10.3285/eg.60.1.11>.
- Wacha, L., Mikulčić Pavlaković, S., Novothny, Á., Crnjaković, M., Frechen, M., 2011b. Luminescence dating of Upper Pleistocene loess from the Island of Susak in Croatia. *Quatern Int.* 234, 50–61. <https://doi.org/10.1016/j.quaint.2009.12.017>.
- Wacha, L., Rolf, C., Hambach, U., Frechen, M., Galović, L., Duchoslav, M., 2018. The Last Glacial aeolian record of the Island of Susak (Croatia) as seen from a highresolution grain–size and rock magnetic analysis. *Quatern. Int.* 494, 211–224. <https://doi.org/10.1016/j.quaint.2017.08.016>.
- Wagner, S., Eckmeier, E., Skowronek, A., Günster, N., 2014. Quaternary paleosol and sediments on the Balearic Islands as indicator of climate changes. *Catena* 112, 112–124. <http://dx.doi.org/10.1016/j.catena.2013.06.022>.
- Wang, Q., Song, Y., Zhao, Z., Li, J., 2016. Color characteristics of Chinese loess and its paleoclimatic significance during the last glacial–interglacial cycle. *J. Asian Earth Sci.* 116, 132–138. <https://doi.org/10.1016/j.jseaes.2015.11.013>.
- Weltje, G.J., 1997. End-member modeling of compositional data: numerical-statistical algorithms for solving the explicit mixing problem. *Math. Geol.* 29, 503–549. <https://doi.org/10.1007/BF02775085>.
- Weltje, G.J., Prins, M.A., 2007. Genetically meaningful decomposition of grain-size distributions. *Sediment. Geol.* 202, 409–424. <https://doi.org/10.1016/j.sedgeo.2007.03.007>.
- Wilcox, P.S., Honiat, C., Trüssel, M., Edwards, R.L., Spötl, C., 2020. Exceptional warmth and climate instability occurred in the European Alps during the Last Interglacial period. *Commun. Earth Environ.* 1. <https://doi.org/10.1038/s43247-020-00063-w>.
- Wintle, A.G., 1973. Anomalous fading of thermo-luminescence in mineral samples. *Nature* 245, 143–144. <https://www.nature.com/articles/245143a0>.

- Wohlfarth, B., 2013. A review of Early Weichselian climate (MIS 5d-a) in Europe. Technical report / Svensk kärnbränslehantering AB, 70p. <https://archimer.ifremer.fr/doc/00499/61046/>.
- Woillard, G., 1987. Grand Pile peat bog: a continuous pollen record for the last 140,000 years. *Quaternary Res.*, 9, 1–21. [https://doi.org/10.1016/0033-5894\(78\)90079-0](https://doi.org/10.1016/0033-5894(78)90079-0).
- Wolf, D., Kolb, T., Alcaraz-Castaño, M., Heinrich, S., Baumgart, P., Calvo, R., Sanchez, J., Ryborz, K., Schäfer, I., Bliedtner, M., 2018. Climate deteriorations and Neanderthal demise in interior Iberia. *Sci. Rep.* 8, 1–10. <https://doi.org/10.1038/s41598-018-25343-6>.
- Wolf, D., Ryborz, K., Kolb, T., Zapata, R.C., Vizcaino, J.S., Zöller, L., Faust, D., 2019. Origins and genesis of loess deposits in central Spain, as indicated by heavy mineral compositions and grain-size variability. *Sedimentology* 66, 1139–1161. <https://doi.org/10.1111/sed.12539>.
- Woodward, J.C., Hamlin, R.H.B., Macklin, M.G., Hughes, P.D., Lewin, J., 2008. Glacial activity and catchment dynamics in northwest Greece: Long-term river behaviour and the slackwater sediment record for the last glacial to interglacial transition. *Geomorphology* 101, 44–67. doi:10.1016/j.geomorph.2008.05.018
- Wronkiewicz, D.J., Condie, K.C., 1990. Geochemistry and mineralogy of sediments from the ventersdorp and transvaal supergroups, South Africa: cratonic evolution during the early proterozoic. *Geochem. Cosmochim. Acta* 54, 343–354. [https://doi.org/10.1016/0016-7037\(90\)90323-D](https://doi.org/10.1016/0016-7037(90)90323-D).
- Yaalon, D.H., 1997. Soils in the Mediterranean region: what makes them different? *Catena* 28, 157–169. [https://doi.org/10.1016/S0341-8162\(96\)00035-5](https://doi.org/10.1016/S0341-8162(96)00035-5).
- Young, G.M., Nesbitt, H.W., 1998. Processes controlling the distribution of Ti and Al in weathering profiles, siliciclastic sediments and sedimentary rocks. *J. Sediment. Res.* 68, 448–455. <https://doi.org/10.2110/jsr.68.448>.
- Zamanian, K., Pustovoytov, K., Kuzyakov, Y., 2016. Pedogenic carbonates: Forms and formation processes. *Earth-Sci. Rev.* 157, 1–17. <https://doi.org/10.1016/j.earscirev.2016.03.003>.
- Zech, M., Rass, S., Buggle, B., Löscher, M., Zöllner, L., 2012. Reconstruction of the late Quaternary paleoenvironments of the Nussloch loess paleosol sequence, Germany, using n-alkane biomarkers. *Quaternary Res.* 78 (02): 226–235. <https://doi.org/10.1016/j.yqres.2012.05.006>.
- Zeeden, C., Krauß, L., Kels, H., Lehmkuhl, F., 2017. Digital image analysis of outcropping sediments: Comparison to photospectrometric data from Quaternary loess deposits at Şanoviţa (Romania) and Achenheim (France). *Quatern. Int.* 429, 100–107. <http://dx.doi.org/10.1016%2Fj.quaint.2016.02.047>.
- Zens, J., Schulte, P., Klasen, N., Krauß, L., Pirson, S., Burow, C., Brill, D., Eckmeier, E., Kels, H., Zeeden, C., Spagna, P., Lehmkuhl, F., 2018. OSL chronologies of paleoenvironmental dynamics recorded by loess-paleosol sequences from Europe: case studies from the Rhine-Meuse area and the Neckar Basin. *Palaeogeogr., Palaeoecol.* 509, 105–125. <https://doi.org/10.1016/j.palaeo.2017.07.019>.

- Zerboni, A., Trombino, L., Frigerio, C., Livio, F., Berlusconi, A., Michetti, A.M., Rodnigh, H., Spötl, C., 2015. The loess-paleosol sequence at Monte Netto: a record of climate change in the Upper Pleistocene of the central Po Plain, northern Italy. *J. Soils Sediments* 15, 1329–1350. <https://doi.org/10.1007/s11368-014-0932-2>.
- Zhang, Y., Zhang, M., Niu, J., Zheng, H., 2016. The preferential flow of soil: A widespread phenomenon in pedological perspectives. *Eurasian Soil Sci.* 49, 661–672. <https://doi.org/10.1134/S1064229316060120>.
- Zhang, J., Rolf, C., Wacha, L., Tsukamoto, S., Durn, G., Frechen, M., 2018. Luminescence dating and palaeomagnetic age constraint of a last glacial loess-palaeosol sequence from Istria, Croatia. *Quatern. Int.* 494, 19–33. <https://doi.org/10.1016/j.quaint.2018.05.045>.
- Zickel, M., Becker, D., Verheul, J., Yener, Y., Willmes, C., 2016. Paleocoastlines GIS Dataset. CRC806-Database. <https://doi.org/10.5880/SFB806.20>.
- Ziegler, P.A., Dèzes P., 2007. Cenozoic Uplift of Variscan Massifs in the Alpine Foreland: Timing and Controlling Mechanisms. *Glob. Planet. Change* 58, 237–269. <https://doi.org/10.1016/j.gloplacha.2006.12.004>.
- Zöller, L., Stremme, H., Wagner, G.A., 1988. Thermolumineszenzdatierung an Lösspaläobodensequenzen von nieder-, mittel- und Oberrhein Bundesrepublik Deutschland. *Chem. Geol. Isotope Geoscience section* 73 (1): 39–62. [https://doi.org/10.1016/0168-9622\(88\)90020-6](https://doi.org/10.1016/0168-9622(88)90020-6).
- Zöller, L., 2010. New approaches to European loess: a stratigraphic and methodical review of the past decade. *Cent. Eur. J. Geosci.* 2 (1): 19-31. <https://doi.org/10.2478/v10085-009-0047-y>.
- Zöller, L., Richter, D., Masuth, S., Wunner, L., Fischer, M., Antl-Weiser, W., 2013. Luminescence chronology of the Grub-Kranawetberg site, Austria. *E&G Quaternary Sci. J.* 62, 127–135. <https://doi.org/10.3285/eg.62.2.04>.